Structural and Functional Characterisation of the A6 – A11 Dicarba Insulin Analogues

BY

ONG SHEE CHEE

A thesis submitted to

FLINDERS UNIVERSITY OF SOUTH AUSTRALIA

for the degree of

Doctor of Philosophy

COLLEGE OF MEDICINE & PUBLIC HEALTH

- 5th Nov 2018 -

SUPERVISOR

PROFESSOR BRIONY E. FORBES

TABLE OF CONTENTS

THESIS SUMMARY

Insulin is an indispensable treatment for type 1 and late stage type 2 diabetes. While current insulin and insulin analogue treatments are effective for many patients, further improvements could provide better blood glucose control and minimise long term diabetic complications. New insulin analogue design aims to improve the pharmacokinetic and pharmacodynamic profiles and stability. In addition, concerns raised recently over some insulin analogues that have greater mitogenic potential than native insulin also calls for the design of insulin analogues that are metabolically-biased with low risk of promoting cancer growth.

Defining the physiologically relevant, active conformation of insulin is essential for the development of improved insulin mimetics. This project explored the possibility to improve insulin analogues through unconventional manipulation of the intra-chain A6–A11 disulfide bond. In collaboration with the Robinson laboratory (Prof. A. Robinson, Monash), the A6–A11 disulfide of native insulin, rapid-acting insulin lispro and long-acting insulin glargine were substituted with a rigid, non-reducible C=C (dicarba) linkage *via* chemical synthesis. During the synthesis, two non-interconvertible dicarba stereoisomers were generated with either a *cis* or *trans* configuration of the dicarba bond. It was discovered that the dicarba isomers exhibit completely different biological properties; *cis* isomer being active and *trans* isomer being inactive.

This study also discovered that while the *cis* dicarba insulins are not more stable than insulin, they are more rapid-acting, effectively lower blood glucose levels in mice and also exhibit significantly lower mitogenic potential. Importantly, through the biophysical analyses of these dicarba insulin analogues, this thesis describes the roles of A6–A11 bond that are critical for the regulation of insulin action, stability and signalling outcomes that have never been described before. These new insights into the insulin structure and function should hopefully provide a meaningful basis to the future design of improved insulin analogues.

STATEMENT OF ORIGINALITY

I certify that this thesis does not incorporate without acknowledgement any material previously submitted for a degree or diploma in any university; and that to the best of my knowledge and belief it does not contain any material previously published or written by another person except where due reference is made in the text.

I give consent to this copy of my thesis when deposited in Flinders University, being made available for loan and photocopying, subject to provisions of the Copyright Act 1968. The author acknowledges that copyright of published works contained within this thesis resides with the copyright holder(s) of those works.

I also give permission for the digital version of my thesis to be made available on web, via the Flinders University's digital research repository, the Library catalogue, and also through web search engines, unless permission has been granted by the University to restrict access for a period of time.

Ong Shee Chee

ACKNOLEDGEMENTS

I would like to express my deepest appreciation to Prof. Briony Forbes for the guidance and support as my supervisor and mentor. I am very grateful for all the great advice and opportunities that you have given me throughout the years.

I would also like to thank everyone that has been part of this project and for the assistance provided particularly Prof. Andrea Robinson, Prof. Michael Lawrence, Prof. Ray Norton, Prof. Sofianos Andrikopoulos, Dr Alessia Belgi, Dr Bianca van Lierop, Dr Naomi Haworth, Dr Christopher MacRaild, Dr Tim Chataway, Dr Alex Colella, Dr Daniel Jardine, John Menting, Carlie Delaine, Kerrie McNeil and Jason Young.

I also acknowledge that this project and the conference attendances during the candidature were supported by the fundings listed in the following as well as the funding bodies acknowledged in the published papers.

I thank all the beautiful souls in my life that have been supporting and encouraging me. I am forever grateful for having you all in my life and I cherish every moment we spend together. Particularly, thanks to my dearest Dr Sally Sun, Dr Olivia He, Dr Cher-Lynn Soh and my colleagues in Flinders University, Jastrow Canlas, Alyce Martin, Emily Sun and Lauren Jones.

Special thanks to my family and Kurt Siu for always being there for me and believing in me. Thanks to Gatsby and Fluffy for their unconditional love.

"Life is a series of thousands of miracles.

I am blessed to share the miracles with you all."

PUBLICATIONS

PUBLICATIONS:

I. **Ong, S. C.**, Belgi, A., Van Lierop, B., Delaine, C., Andrikopoulos, S., Macraild, C. A., Norton, R. S., Haworth, N. L., Robinson, A. J. & Forbes, B. E. 2018. Probing the correlation between insulin activity and structural stability through introduction of the rigid A6–A11 bond. *J. Biol. Chem.*, doi:10.1074/jbc.RA118.002486.
Accepted June 13 2018

II. Van Lierop, B.*, **Ong, S. C.***, Belgi, A., Delaine, C., Andrikopoulos, S., Haworth, N. L., Menting, J. G., Lawrence, M. C., Robinson, A. J. & Forbes, B. E. 2017. Insulin in motion: The A6–A11 disulfide bond allosterically modulates structural transitions required for insulin activity. *Sci. Rep.,* 7, 17239.
* Co-first author
Published Dec 8 2017

CONFERENCES, COMPETITION & WORKSHOPS

ORAL PRESENTATIONS:

2017

I. **Ong, S.C.,** van Lierop, B., Belgi, A., Delaine, C., Menting, J.G., Lawrence, M.C., Andrikopoulos, S., Robinson, A. J. & Forbes, B.E. *"A mechanistic insight into insulin A6–A11 disulfide bond in regulating hormone activity and structural stability."* COMBIO 2017 (ADELAIDE, SA, AUSTRALIA 2017)

2016

II. **Ong, S.C.,** Belgi, A., van Lierop, B., McNeil, K.A., Delaine, C., Menting, J.G., Lawrence, M.C., Andrikopoulos, S., Robinson, A. J. & Forbes, B.E. *"Novel observations of the critical role of insulin A6–A11 disulfide bond: Dicarba insulin analogues."* IGF-OZ 2016 (PARKVILLE, VIC, AUSTRALIA 2016)

III. **Ong, S.C.,** Belgi, A., van Lierop, B., Delaine, C., Andrikopoulos, S., Robinson, A.J. & Forbes, B.E.*"Novel insulin analogues with improved therapeutic benefits: Dicarba insulin exhibit reduced mitogenic potential."* Adelaide Protein Group (APG) Awards Event (ADELAIDE, SA, AUSTRALIA 2016)

2014

IV. **Ong, S.C.,** Belgi, A., van Lierop, B., Delaine, C., Andrikopoulos, S., Robinson, A. J. & Forbes, B.E. "Dicarba insulin peptides results in lower mitogenic activity signalled via IGF-1R and IR than insulin." 7th International Congress of the GRS & IGF Society (SINGAPORE 2014)

POSTER PRESENTATIONS:

2016

I. **Ong, S.C.,** Belgi, A., van Lierop, B., McNeil, K.A., Delaine, C., Menting, J.G., Lawrence, M.C., Andrikopoulos, S., Robinson, A. J. & Forbes, B.E. *"Novel insulin analogues with improved therapeutic benefits: Dicarba insulin exhibit reduced mitogenic potential."* 52nd European Association for the Study of Diabetes (EASD) Annual Meeting (MUNICH, GERMANY 2016)

II. **Ong, S.C.,** Belgi, A., van Lierop, B., McNeil, K.A., Delaine, C., Menting, J.G., Lawrence, M.C., Andrikopoulos, S., Robinson, A. J. & Forbes, B.E. *"Fundamental mechanism of insulin receptor binding revealed by structural and functional studies of novel dicarba insulin analogues ([A6^{C}-A11^{C}]-Insulin)"* Adelaide Protein Group (APG) Awards Event (ADELAIDE, SA, AUSTRALIA 2016)

2015

III. **Ong, S.C.,** Belgi, A., van Lierop, B., McNeil, K.A., Delaine, C., Andrikopoulos, S., Robinson, A. J. & Forbes, B.E. *"Novel insulin analogues with improved therapeutic benefits: Dicarba insulin exhibit reduced mitogenic potential."* Gordon Research Conference: IGF & Insulin System in Physiology & Disease (CALIFORNIA, LA, USA 2015)

IV. **Ong, S.C.,** Belgi, A., van Lierop, B., McNeil, K.A., Delaine, C., Andrikopoulos, S., Robinson, A. J. & Forbes, B.E. *"Novel insulin analogues with improved therapeutic benefits: Dicarba insulin exhibit reduced mitogenic potential."* 5TH Adelaide Cell & Developmental Biology Meeting (ADELAIDE, SA, AUSTRALIA 2015)

V. **Ong, S.C.,** Belgi, A., van Lierop, B., McNeil, K.A., Delaine, C., Andrikopoulos, S., Robinson, A. J. & Forbes, B.E. *"Novel insulin analogues with improved therapeutic benefits: Dicarba insulin exhibit reduced mitogenic potential."* Flinders University School of Medicine PhD Student Day (ADELAIDE, SA, AUSTRALIA 2015)

VI. **Ong, S.C.,** Belgi, A., van Lierop, B., McNeil, K.A., Delaine, C., Andrikopoulos, S., Robinson, A. J. & Forbes, B.E. *"Novel insulin analogues with improved therapeutic benefits: Dicarba insulin exhibit reduced mitogenic potential."* CNS Collaborator Day: Women in Science (BEDFORD PARK, SA, AUSTRALIA 2015)

VII. **Ong, S.C.,** Belgi, A., van Lierop, B., McNeil, K.A., Delaine, C., Andrikopoulos, S., Robinson, A. J. & Forbes, B.E. *"Design of novel insulin mimetics for diabetes treatments."* Australian Diabetes Society and The Australian Educators Association (ADS-ADEA) Annual Scientific Meeting (ADELAIDE, SA, AUSTRALIA 2015)

2014

VIII. **Ong, S.C.,** Belgi, A., van Lierop, B., McNeil, K.A., Delaine, C., Andrikopoulos, S., Robinson, A. J. & Forbes, B.E. *"Design of novel insulin mimetics for diabetes treatments."* Adelaide Protein Group (APG) Awards Event (ADELAIDE, SA, AUSTRALIA 2014)

COMPETITION:

I. *"IS OUR HERO CAUSING DAMAGE?"* 3-MINUTE THESIS (BEDFORD PARK, SA, AUSTRALIA 2016)

PROFESSIONAL DEVELOPMENT:

I. THE INTERNATIONAL SUMMER SCHOOL OF TECHNOLOGY TRANSFER IN LIFE SCIENCES (DRESDEN UNIVERSITY OF TECHNOLOGY, GERMANY 2016)
II. STEM WOMEN BRANCHING OUT LEADER LAB MENTORING PROGRAM (FLINDERS UNIVERSITY, AUSTRALIA 2016)
III. ACADEMIC INTERNSHIP PROGRAM FOR DOCTORAL STUDENTS (FLINDERS UNIVERSITY, AUSTRALIA 2016)

AWARDS & FUNDINGS

2014 – 2017

I. Australian Postgraduate Award (APA) Scholarship

2016

II. Faculty Of Medicine Student Conference Travel
III. International Network On Diabetes & Depression (IN2D) Travel Grant
IV. Academic Internship Program For Doctoral Student Special Support Grant
V. Runner-Up Prize For 3-Minute Thesis (3MT) School Heat
VI. Runner-Up Prize For 3-Minute Thesis (3MT) Faculty Heat
VII. Best Poster Award For Adelaide Protein Group (APG) Student Awards Event 2016

2015

VIII. Gordon Research Conference (GRC) Travel Grant
IX. Centre Of Neurosciences (CNS) Scientific-Exchange Travel Grant
X. Academic Internship Program For Doctoral Student Support Grant
XI. Faculty Of Medicine Student Conference Travel Grant
XII. Best Poster Award For 5TH Adelaide Cell And Developmental Biology Meeting
XIII. Runner-Up Of Best Poster For Flinders University School Of Medicine PhD Student Day

2014

XIV. GRS & IGF Society Travel Grant
XV. Best Poster Award For Adelaide Protein Group (APG) Student Awards Event 2014

ABBREVIATIONS

ACN	*Acetonitrile*
AFM	*Atomic force microscopy*
BSA	*Bovine serum albumin*
CD	*Circular Dichroism*
Dicarba	*Unsaturated carbon-carbon bond (C=C)*
DMEM	*Dulbecco's modified Eagle's medium*
DTT	*dithiothreitol*
EDTA	*Ethylene diamine tetra-acetate*
ERK1/2	*Extracellular-related kinases 1/2*
Eu	*Europium*
FCS	*Foetal calf serum*
GdnHCl	*Guanidine hydrochloride*
GSK-3β	*Glycogen synthase kinase-3β*
HEPES	*N-2-Hydroxyethylpiperazine-N-2-ethanesulphonic acid*
EC_{50}	*Concentration of inhibitor which reduces binding by 50%*
HCCA	*α-cyano-4-hydroxycinnamic acid*
IAA	*Iodoacetic acid*
IAM	*Iodoacetamide*
IGFBP	*Insulin-like growth factor binding protein*
IGF-I	*Insulin-like growth factor I*
IGF-1II	*Insulin-like growth factor II*
IR	*Insulin receptor*
IR-A	*Insulin receptor isoform A*
IR-B	*Insulin receptor isoform B*
IRS-1	*Insulin receptor substrate 1*
IRS-2	*Insulin receptor substrate 2*
IU	*International units*
KP insulin	*$Lys^{B28}Pro^{B29}$ insulin*
L	*Litre*
MAPK	*Mitogen activated protein kinase*
MALDI	*Matrix-assisted laser desorption/ionisation*
MD	*Molecular Dynamics*

MS	*Mass spectrometry*
PD	*Pharmacodynamics*
PDB	*Protein Data Bank*
PDK-1	*3-phosphoinositide-dependent protein kinase 1*
PH	*Pleckstrin homology*
PI3K	*Phophatidyl-inositol 3' phosphate kinase*
PK	*Pharmacokinetics*
PKB/Akt	*Protein kinase B*
pY20	*Phosphotyrosine antibody*
rpHPLC	*Reverse- phase high-performance liquid chromatography*
SA	*Sinapinic acid*
SDS	*Sodium dodecyl sulphate*
S.E.M	*Standard error of mean*
S–S	*Disulfide bond*
T1D	*Type 1 Diabetes*
T2D	*Type 2 Diabetes*
TEMED	*N,N.N,N'N'-tetrametylethylene-diamine*
TFA	*Trifluoroacetic acid*
ThT	*Thioflavin T*
TOF	*Time-of-flight*

LIST OF TABLES

LIST OF FIGURES

LIST OF APPENDICES

CHAPTER 1

Introduction

CHAPTER 1 INTRODUCTION

1.1 OVERVIEW

Insulin is a small peptide hormone produce in pancreatic β-cells for the regulation of blood glucose homeostasis. Progressive resistance to the effect of insulin hormone (insulin resistance) and/or the inability to produce sufficient insulin leads to the onset of diabetes. Treatment of type 1 diabetes (T1D) and late stage type 2 diabetes (T2D) depends on the use of insulin compounds that effectively lower blood glucose levels through activation of insulin receptor signalling.

Human insulin is a two-chain polypeptide comprised of a 21-residue A-chain and a 30-residue B-chain. Critical to its stability, insulin is stored in β-cells as Zn^{2+}-hexamer form and the insulin monomer is stabilised by three disulfide bonds – one intra-chain Cys^{A6}-Cys^{A11} linkage and two inter-chain Cys^{A7}-Cys^{B7} and Cys^{A20}-Cys^{B19} linkages. Insulin can also form dimers and higher order oligomers (insulin fibrils and aggregates). Importantly, only the monomeric form has the ability to engage the two receptor isoforms of insulin receptor that arise due to alternative splicing – IR-A and IR-B. Activation of IR-B predominantly regulates PI3K-dependent metabolic responses such as glucose uptake *via* GLUT4 transporters in insulin responsive tissues; whereas activation of IR-A preferentially regulates mitogenic responses *via* MAPK signalling pathway. Native insulin binds poorly to the growth promoting insulin-like growth factor receptor 1 (IGF-1R).

The physiological insulin secretion profile consists of a steady release of basal insulin throughout the day with several bursts of biphasic insulin secretion (bolus) upon food intake. Current insulin analogues aim to emulate this endogenous insulin secretion profile – rapid-acting insulins mimicking bolus insulin and long-acting insulin mimicking basal insulin. However, current insulin analogues are still suboptimal. Several limitations that require immediate attention include: (1) the suboptimal pharmacokinetics/pharmacodynamics properties of insulin analogues that do not perfectly mimic endogenous insulin action, (2) poor stability of insulin analogues; particularly for monomeric insulin analogues that have higher propensity to fibrillate at elevated temperatures, and (3) undesirable side effects for example weight gain and the debatable carcinogenic risk in some analogues.

Defining the physiologically relevant insulin active conformation and understanding the molecular mechanism(s) that regulates insulin action and stability is essential for the

development of improved insulin mimetics. Previous investigations of insulin structure and function focus on mapping the functional surface of insulin. Lacking is a detailed understanding of the insulin disulfide bonds and their role in insulin action and conformational dynamics. Fortunately, the continuing innovation in chemical synthesis methodologies now allows modern design of peptide analogues with unconventional disulfide isosteres that can shed new light on our understanding of insulin's structure-function relationship.

This chapter provides an overview of diabetes, current understanding of insulin and insulin analogues, as well as the recent trend of exploring the functional roles of insulin disulfide bonds. Relevant to the overarching aims of this thesis, the discussion focuses on three major aspects: insulin action, insulin structure and stability, and insulin metabolic-mitogenic signalling.

1.2 DIABETES MELLITUS

Diabetes mellitus is a life-long chronic disease in which patients suffered from uncontrolled and elevated blood glucose levels due to the progressive resistance to the effect of insulin hormone and/or the inability to produce sufficient insulin. It is a serious and complex condition that could affects the entire body over time. Diabetes is associated with increased risk of vascular and neuronal related diseases such as heart attack, stroke, kidney failure, blindness, diabetic ulcers and mental health disorders. If untreated, diabetes is fatal. An overview of diabetes mellitus and its associated complications were recently reviewed in (Ahmad, 2013).

Diabetes is Australia's and the world's fastest growing chronic disease. In 2013, there were 382 million diabetics and 5.1 million diabetes related deaths globally (Diabetes Austalia). With the rapidly increasing prevalence of the disease at a rate of 25 % every decade, diabetes has been declared as a global epidemic (International Diabetes Federation). Currently in Australia, 4 % (1.1 million people) of the population has diabetes with 100, 000 new cases diagnosed each year (AIHW). Diabetes is also ranked in the top 10 leading causes of death in the country (AIHW, Baker IDI Heart & Diabetes Institute, 2012).

There are 3 major classifications of diabetes mellitus, Type 1 diabetes (T1D), Type 2 diabetes (T2D) and gestational diabetes (Maraschin Jde et al., 2010). T1D is characterised by the complete loss of insulin production due to autoimmune destruction of β-cells in the pancreatic islets of Langerhans (Atkinson et al., 2014). Approximately 5 – 10 % of diabetics are diagnosed with T1D, mostly arising in children or young adults (< 35 years old) (Ahmad, 2013). On the other hand, T2D is characterised by a combination of insulin resistance and the progressive β-

cell dysfunction (Mayfield and White, 2004). It is the most common type of diabetes and contributes to 85 – 90 % of diabetic cases (AIHW). Although T2D is most prevalence in the older age group, increasing number of younger adults are also diagnosed with T2D in recent years (Reinehr, 2013). A major contributing factor to the early development of T2D is the progressive insulin resistance associated to obesity (Wali et al., 2014). Gestational diabetes is defined as diabetes that developed at the time of pregnancy (Subiabre et al., 2018).

The initial treatment of T2D aims to restore blood glucose homeostasis by improving the functionality of β-cells in the pancreas. Patients are usually encouraged to acquire a healthy lifestyle through exercise, weight control and healthy diet. Lifestyle treatments are also often augmented with anti-diabetic medications to improve insulin sensitivity and stimulate insulin secretion. In Australia, there are seven classes of available medications for T2D; all in tablet form, except for incretin mimetics that are administered *via* subcutaneous injection (see Table 1.1).

Table 1.1 Anti-diabetic non-insulin medications.

For more details on anti-diabetic medication, see recent reviews in (Rhee et al., 2017, Otto-Buczkowska and Jainta, 2018). This list provides examples of drugs but is not exhaustive.

Medication	Drug Names	Action
Biguanides	Metformin	Insulin sensitizer which reduces gluconeogenesis in liver
Thialzolidinediones	Rosiglitazone, Pioglitazone	Insulin sensitizer which improves insulin sensitivity of peripheral tissues, especially muscle and adipose.
Sulfonylureas	Gliclazide, Glibenclamide, Glipizide, Glimepiride	Insulin secretagogues which stimulate insulin secretion from pancreas
α-glycosidase inhibitors	Acarbose	Reduce rate of digestion and absorption of carbohydrates
Dipeptidyl peptidase 4 (DPP4) inhibitors	Alogliptin, Linagliptin, Saxagliptin, Sitagliptin, Vildagliptin	Inhibit cleavage of two incretin hormones; glucagon-like peptide-1 (GLP-1) and glucose-dependent insulinotropic peptide (GIP).
Glucagon-like peptide 1 (GLP-1) receptor agonists (incretin mimetics)	Exenatide, Exenatide, Liraglutide	Injected subcutaneously. Stimulate insulin secretion and block glucagon production.
Sodium-glucose transporter (SGLT2) inhibitors	Canagliflozin, Dapagliflozin	Inhibit glucose reabsorption in kidney

Medications listed in *Table 1.1* are only effective when insulin can still be endogenously secreted to levels sufficient for normal glycemic control. Thus, these medications are not effective treatments of T1D. Patients with T1D rely on daily insulin injections. While early stage T2D can be managed effectively with oral medications, the progressive loss of β-cells in the later stage of T2D demand combination treatment with insulin (Freeman, 2009, Mayfield and White, 2004).

1.3 INSULIN THERAPY

The introduction of insulin therapy aims to restore glucose homeostasis in diabetes patients by reintroducing insulin or insulin mimetics that emulate the physiological insulin action. In a healthy pancreas, insulin is produced in the β-cells and stored as Zn^{2+}-coordinated hexamers; consisting of three insulin dimers. Physiologically, insulin is most stable in its hexameric form. Upon release into the blood circulation, insulin hexamers dissociate into its active monomeric form, which allows receptor engagement and activation to promote glucose uptake into myocytes or adipocytes. As illustrated in *Figure 1.1*, the physiological insulin secretion involves a steady release of basal insulin throughout the day in response to hepatic glucose production and biphasic prandial (bolus) insulin secretion in response to elevated blood glucose level after food intake (see. Fig. 1.1) (Thompson et al., 2006). Immediately after food ingestion, phase 1 insulin secretion peaks within 2 minutes and lasts for 10 minutes, suppressing hepatic glucose production and initiating phase 2 insulin secretion, which lasts for 2 hours until normoglycemia is restored (Campbell and White, 2002).

In the 1920s, Banting and Best were the first to introduce treatment for diabetes using insulins extracted from animals (Bliss, 1982). Since then, coupled with our better understanding of insulin structure and function, major advancements have been made in the production of insulin, design of new insulin analogues, methods of insulin administration and reduction of risks associated with insulin therapy. Current insulin treatments for diabetes include the use of recombinant human insulin and a range of rapid- and long-acting insulin analogues; described in the following sections (Freeman, 2009).

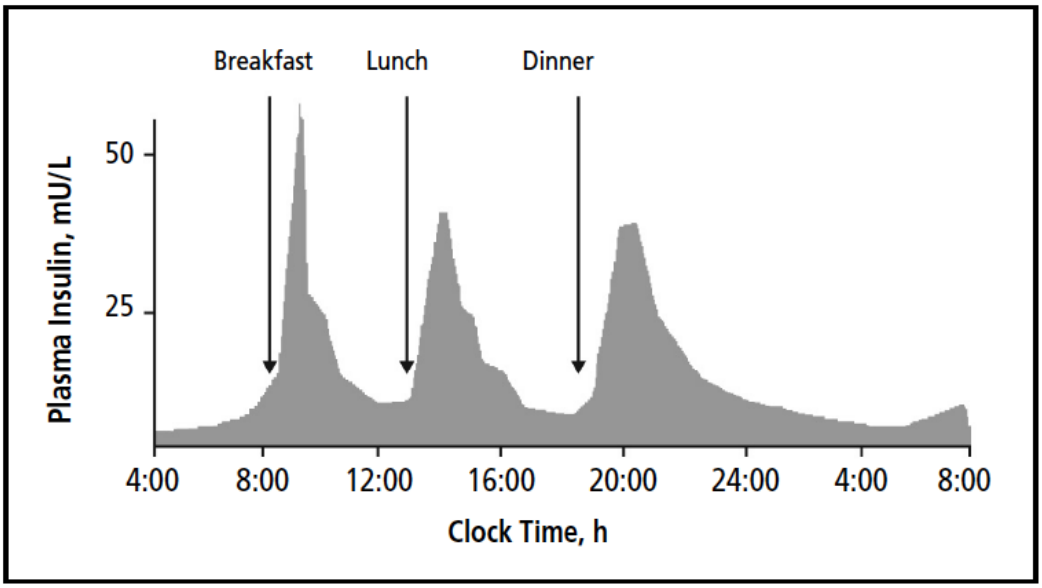

Figure 1.1 Physiological insulin secretion in healthy individuals. The physiological insulin secretion profile consists of a steady release of basal insulin throughout the day with several bursts of biphasic insulin secretion (bolus) upon food intake. From (Thompson et al., 2006).

1.3.1 Recombinant Human Insulin

Eli Lilly & Co. developed the first generation of recombinant human insulins, including the short-acting regular insulin (Humalin® R) and the intermediate-acting neutral protamine Hagedorn (NPH) insulin (Humulin® N) (Eli Lilly & Co.). However, the use of regular human insulin has many limitations. Regular human insulin has a slow onset of action at 30–60 minutes after injection and long duration of action (6–8 hours) resulting in increased risk of hypoglycaemia in between meals and post-prandial hyperglycemia (see. Figs. 1.3*A* & 1.4) (Vajo et al., 2001). The NPH insulin is essentially formulated regular human insulin that co-crystallises with protamine allowing slower absorption and action; designed to emulate basal insulin. However, the major drawback of the NPH insulin is its high variability in absorption rate and its considerably short duration of action (10–16 hours) that leads to an increased risk of nocturnal hypoglycaemia (Heinemann et al., 2000) (see. Fig. 1.3*B* & 1.4).

To overcome the shortcomings of the recombinant human insulins, insulin analogues were engineered with amino acid modifications that allow better mimicking of the basal or bolus insulin action (see Fig. 1.2). Rapid-acting insulin analogues (see *section 1.3.2*) were designed to mimic bolus insulin action; injected before each meal. While long-acting insulin analogues (see *section 1.3.3*) are intended for one injection per day to provide continuous basal insulin. Pharmacokinetics (PK) and pharmacodynamics (PD) properties of rapid- and long-acting insulin analogues were recently reviewed in (Sciacca et al., 2018, Mathieu et al., 2017, Home, 2012) and described briefly in the following sections.

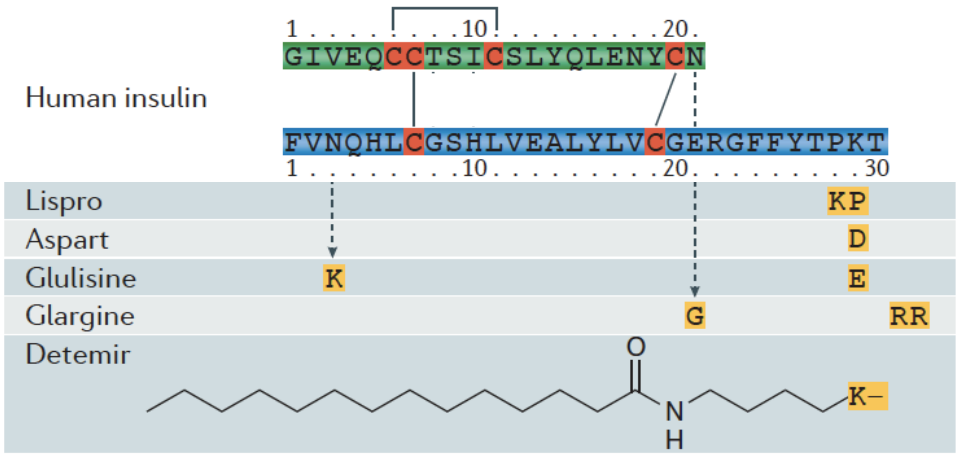

Figure 1.2 Structure of human insulin and its analogues. Human insulin is comprised of a 21-residue A-chain (highlighted in *green*) and 30-residue B-chain (highlighted in *blue*). The hormone is stabilized by two A7—B7 and A20 – B19 inter-chain disulfide bonds and one A6–A11 intra-chain disulfide bond. Cysteine residues for disulfide pairings are highlighted in *red*. Sequence modifications of insulin analogues are highlighted in *yellow* in the bottom panel. Rapid-acting insulin analogues: insulin lispro, aspart and glulisine; long-acting insulin analogues: glargine and determir, From (Zaykov et al., 2016), reproduced with modification.

1.3.2 Rapid-acting Insulin Analogues

Classic rapid-acting insulin analogues currently in clinical use are insulin lispro (Humalog®; Eli Lilly) (Howey et al., 1994), insulin aspart (NovoLog®; Novo Nordisk) and insulin glulisine (Apidra®; Sanolfi-Aventis) (see Figs. 1.2 – 1.4). As insulin is only active in its monomeric form, these analogues were designed to increase the propensity to self-dissociate into monomers upon administration; thus, allowing rapid absorption immediately after injection and shorter duration of insulin action compared to regular human insulin and NPH insulin (Figs. 1.3*A* and 1.4). (Yamada, 2009, Kapustin, 2012)

The design of rapid-acting insulins was made possible due to our improved understanding of insulin self-assembly behaviour and the delineation of insulin dimer- and hexamer-forming surfaces. Insulin lispro (or KP insulin) was designed with an inversion of amino acids from $Pro^{B28}Lys^{B29}$ to $Lys^{B28}Pro^{B29}$ that allows insulin to adopt an IGF-I-like motif with impaired self-dimerization (Figs. 1.2 and 1.4). Similarly, insulin aspart also has a modification at position B28, substituting proline with a highly negatively charged aspartate residue (Figs. 1.2 and 1.4). The increased charge repulsion prevents dimer/hexamer formation. Finally, insulin glulisine was designed with the asparagine residue at position B3 replaced by lysine and the lysine at position B29 replaced by glutamic acid (Figs. 1.2 and 1.4). Clinical studies confirmed that the pharmacokinetic and pharmacodynamic performance of all three rapid-acting insulin analogues is similar (Fig. 1.3) (Dreyer et al., 2005, Becker et al., 2005).

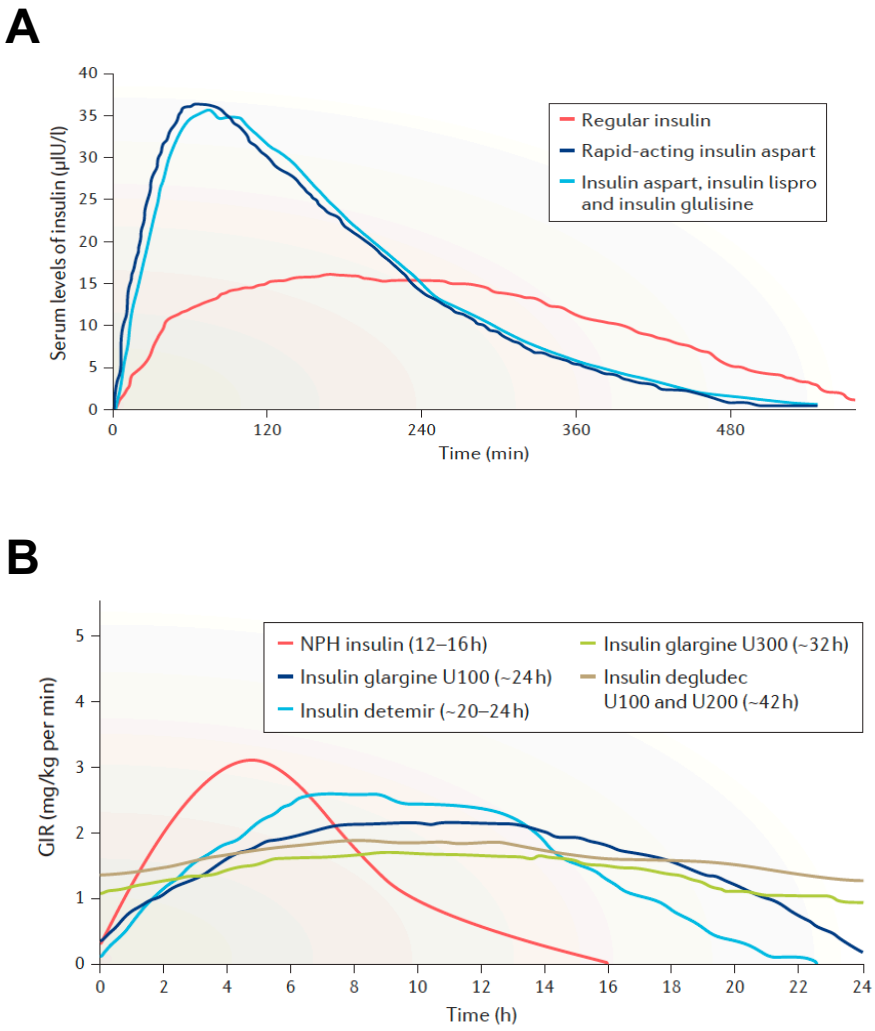

Figure 1.3 Pharmacokinetic action profiles of rapid-acting and long-acting insulins. (A) The rapid-acting insulins (insulin aspart, insulin lispro and insulin glulisine) have faster onset of action and shorter duration of action compared to the short-acting human regular insulin. The pharmacokinetics of the three rapid-acting insulins are very similar to each other. (B) In steady state, the long-acting insulins (insulin glargine, insulin detemir and insulin degludec) have flatter and longer duration of action compared to the neutral protamine Hagedorn (NPH) insulin. Concentrated formulation of insulin glargine U300 extends the duration of action to > 32 hours in treating patients with T1D. IU, international units. From (Mathieu et al., 2017).

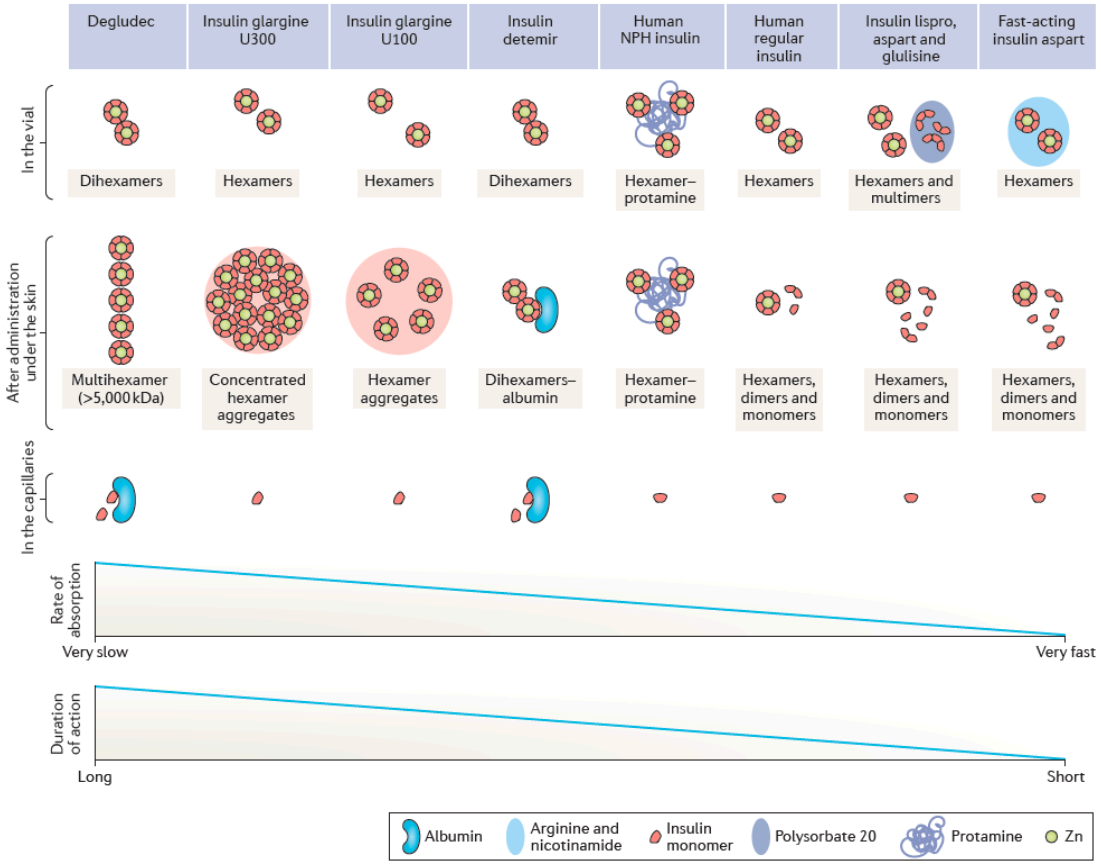

Figure 1.4 Different determinants of the rate of absorption and duration of action of recombinant human insulin and insulin analogues. Insulin degludec forms multihexamers upon subcutaneous injection and reversibly bind to plasma albumin in circulation, thereby slowing its absorption and provide the longest duration of action among all insulins. Neutralization of insulin glargine upon injection leads to precipitation that allows slow absorption of the long-acting analogue. The insulin glargine U300 is a more concentrated formulation of insulin glargine U100. Insulin determir is stabilized as dihexamers. Binding to plasma albumin further stabilizes insulin detemir that delays its absorption and prolongs the duration of action. Human Neutral protamine Hagedorn (NPH) insulin is essentially regular human insulin that co-crystalizes with protamine to allow slower rate of absorption and action. The rapid-acting insulin analogues (insulin lispro, insulin aspart and insulin glulisine) have increased propensity to rapidly dissociate into the active monomeric form that allows rapid absorption and shorter duration of action than regular human insulin injected subcutaneously. Polysorbate 20 in the formulation for insulin glulisine prevents Zn-dependent hexamer formation. Formulation improvement for insulin aspart by addition of arginine and nicotinamide further accelerates the dissociation rate of insulin aspart to monomers, thereby increasing the rate of absorption. From (Mathieu et al., 2017).

1.3.3 Long-acting Insulin Analogues

Contrary to the rapid-acting insulin analogues, the long-acting insulin analogues aim to provide stable, smooth and continuous insulin levels, mimicking endogenous basal insulin. Currently available for clinical use are insulin glargine (Lantus®; Sanolfi-Aventis), insulin determir (Levemir®) and the recently approved insulin degludec (Tresiba®) (Novo Nordisk) (see Figs. 1.2 – 1.4). Insulin glargine is the most widely used long-acting insulin analogue in the current market due to its high demand for treatment of T2D (Aggarwal, 2014).

Long-acting insulin analogues are commonly modified at the *C*-terminus of B chain to improve insulin stability in its hexameric form. Glargine has an extended B chain with addition of two arginine residues at the *C*-terminal end that increases the hormone's isoelectric point, and substitution of asparagine in position A21 to glycine that enhances its stability in the acidic formulation. Upon injection, neutralisation of glargine leads to isoelectric precipitation, thereby allowing the slow release of insulin glargine into the circulation (Figs. 1.2 and 1.4). Compared to NPH insulin, insulin glargine provides a longer and flatter insulin action (Fig. 1.3*B*). Nevertheless, duration of insulin glargine action is variable in each individual, ranging from 22–26 hours. Some patients may require more than one injection per day. A new generation of insulin glargine was released more recently by concentrating the formulation of insulin glargine from U100 to U300 (U= international units). The duration of action was extended from ~24 hours (U100) to > 32 hours in treating patients with T1D with the new insulin glargine U300 formulation (Fig. 1.3*B*) (Becker, 2015). The evolution, development and the clinical implication of insulin glargine was discussed in detail in (Hilgenfeld et al., 2014).

Alternatively, another approach to reduce the absorption rate and extend insulin half-life in blood circulation has been to add a long fatty acid chain to the *C*-terminal end of insulin B chain that has high affinity for serum albumin. For example, insulin detemir was constructed by deletion of Thr^{B30} residue and addition of a 14-carbon myristoyl fatty acid at Lys^{B29} (Fig. 1.2). Stabilisation of insulin detemir in its hexamer form and the binding to albumin delays its absorption and increases its duration of action (Fig. 1.4) (Sørensen et al., 2010).

Similar to insulin determir, insulin degludec also has Thr^{B30} removed and a 16-carbon fatty acid is attached to the Lys^{B29} residue through a glutamic acid spacer. The modification allows insulin degludec to form unique multihexamer chains following subcutaneous injection. In circulation, insulin degludec monomers also bind to albumin (Fig. 1.4). Clinically, among the available long-acting insulin analogues, degludec provides the most effective and even glucose-lowering effects

for the longest duration (~ 42 hours) (Fig. 1.3). The improved stability also reduces risk of nocturnal hypoglycaemia and allows increased flexibility in the timing of administration (Jonassen et al., 2012).

1.3.4 Limitations of Current Insulin Analogues

Despite significant innovation in insulin design and the resultant improved biological performance, there remain significant shortfalls in insulin therapies. Clinically, a common problem with T2D treatment is often caused by the delay in introduction of insulin therapy despite inadequate glycemic control with anti-diabetic oral medications. The delay in the initiation of insulin therapy leads to glycemic burden that causes early onset of diabetes-associated complications. Reluctance to initiate insulin treatment (including the use of insulin analogues) is often due to psychological resistance arising from fear and concerns over the invasive administration method through subcutaneous injection, cost of treatment, convenience and effectiveness of treatment and potential risks of post-prandial hyperglycemia and nocturnal hypoglycaemia. Further side effects include, allergic reaction, weight gain and the debatable carcinogenic risk of some analogues. Nonetheless, recent clinical evidence suggests that early initiation of insulin therapy in T2D may in fact provide long term clinical benefits by preventing complications due to prolonged glycaemic burden and also may also delay disease progression (Retnakaran and Zinman, 2012, Owens, 2013). Thus, in addition to the increasing prevalence of diabetes, the anticipated increasing demand for insulin therapy introduced at earlier stages of T2D further urge the need to develop better insulin treatments.

Insulin analogues currently used clinically are suboptimal. First and foremost, they do not fully mimic the endogenous insulin profile, which imposes risks of postprandial hypo- and hyperglycaemia in many patients. The increasing global prevalence of diabetes mellitus especially in the third world countries of warmer climate also urgently demands analogues with improved stability. More recently, controversy over the potential increased risk of cancer promoted by some analogues and the use of highly potent insulin analogues has highlighted the need for analogues to be designed to avoid such properties. This has driven the need for a greater understanding of the structure and function of insulin and the underlying mechanisms of insulin signalling regulation.

1.3.4.1 Suboptimal Pharmacokinetic/Pharmacodynamics (PK/PD)

While rapid-acting insulin analogues may have improved rates of absorption and onset of action, the PK/PD profiles do not accurately mimic the biphasic bolus insulin secretion stimulated in

response to elevated blood glucose levels. The glucose lowering action of these analogues is relatively slow and lacks precision compared endogenous insulin. Clearance of rapid-acting insulin analogues is also substantially slower, with duration of action ranging from 6–8 hours as opposed to endogenous insulin that is essentially undetected from circulation within 2 hours after the first peak of insulin. On the other hand, long-acting insulin analogues have relatively short duration of action compared to endogenous basal insulin. Another downside of these analogues is the dose-to-dose and patient-to-patient variabilities in the onset and duration of action; which may increase risk of nocturnal hyperglycemia in some patients (Freeman, 2009).

1.3.4.2 ***Poor Insulin Stability***

Besides safety assurance and therapeutic efficiency of insulin analogues, another major issue of insulin therapy is insulin instability, a major bottleneck of insulin development that greatly affects the cost and availability for the treatment itself. Diabetes mellitus is a global pandemic and it is a costly burden especially for the developing countries. Current insulin formulations required transportation and storage of insulin vials at 4–8 °C with a short shelf life of 2 years. Once vials are opened, they must be kept below 30°C and discarded within 2–4 weeks. This is because the existing insulin and insulin analogues are highly susceptible to chemical and physical degradation especially at elevated temperatures. The rapid chemical denaturation in vials causes wastage or glycemic excursions when inconsistent dosage of active insulin is injected each time. Likewise, physical degradation in the form of fibrillation also poses significant issue in the production and storage of insulin analogues in warmer climates (Groenning et al., 2009, Nielsen et al., 2001b). On rare occasions, injecting aggregated insulin may lead to detrimental problems such as lipoatrophy resulting from an inflammatory response towards insulin crystals (Cabrera-Freitag et al., 2011, Holstein et al., 2010). Of more severe consequences, insulin aggregates may lead to obstruction of insulin pumps that leads to rapid onset of ketoacidosis in T1D patients (Lindenbaum et al., 1993, Pryce, 2009).

In addition to the clinical impacts, insulin instability has also cause a tremendous economic burden globally as majority of insulin wastage was due to the short expiration of insulin (Smallwood et al., 2017, Rosenbloom et al., 1994). The need for improving insulin stability was further emphasized in a model study conducted by Novo Nordisk® that clearly demonstrated a substantial savings to both the healthcare system and patients in a scenario of extending the regimen of using fast-acting insulin aspart [rDNA origin] (Novolog) in pumps from 2 to 6 days (Weiss et al., 2011).

1.3.4.3 Potential Mitogenic Risk

The continuing debate on the potential cancer risk associated with the use of insulin analogues reinforces the need to perform further investigation on ways to reduce mitogenic potency of existing and emerging insulin analogues. As evident in several examples, including the well-known super mitogenic insulin X10 ($His^{B10} \rightarrow Asp^{B10}$), even minimal modification of human insulin can significantly alter its receptor binding potency and its associated biological outcomes. Insulin X10 was a promising rapid-acting insulin, however, clinical trial for the analogue was suspended shortly after it was shown to stimulate mammary gland proliferation and promote breast cancer in Sprague-Dawley rats. It was later revealed that improving insulin potency in insulin X10 by modification of the B10 residue also increased its binding affinity for the type 1 IGF receptor (IGF-1R) that most likely contributed to its increased mitogenic activity *in vivo* (Stammberger et al., 2006, Hansen et al., 2011). Disappointingly, even after 30 years since it was first developed, the underlying mechanisms of how some insulin analogues promote differential signalling and functional selectivity are still not fully understood.

The long-acting insulin glargine is another example of insulin analogue that is continuously debated for its possible mitogenic risk (see review (Rendell et al., 2013, Sciacca et al., 2018)). Although the mitogenic potential of glargine in *in vivo* studies remains debatable, its significantly increased binding affinity for the IGF-1R (6–8-fold) and its increase mitogenic activity in *in vitro* studies are undeniably alarming ((Varewijck et al., 2010, Kurtzhals et al., 2000, Rendell et al., 2013). It has also been found that glargine increases serum IGF-I in diabetic patients which may indirectly lead to enhanced mitogenic signalling of IGF-I *via* IGF-1R (Slawik et al., 2006). However, glargine is rapidly metabolised once in the circulation to metabolites with equal activity to native insulin and therefore poses relatively low risk.

1.3.5 Insulin Analogues in Development

In line with the renewed interest in insulin development, the primary objectives for designing new insulin analogues focuses on refining the PK/PD profile of rapid- and long-acting insulins, improving thermodynamic stability of insulin analogues and identifying possible ways to enhanced receptor selectivity for metabolic outcome. Recently reviewed by Zaykov, A. N., Mayer, J. P. and Mirachi, R.D. are some of the most promising insulin analogues that were recently approved for clinical use or are in development (Zaykov et al., 2016). Some examples are discussed in the following:

1.3.5.1 *New Insulins with Improved PK/PD Profile*

To better emulate the biphasic bolus and basal of endogenous insulin profile, several strategies were explored to develop new ultra-rapid and ultra-long acting insulin analogues. New bolus insulin mimetics were developed with the aim to improve precision of action, *i.e.* even faster onset of action and shorter duration of action. Preclinical studies of [B22Ala] insulin and [B26Ala] insulin showed two-fold increase in blood glucose lowering effects in pigs (Zhang et al., 2003). Concurrently, recent efforts were also made to improve formulations for existing rapid-acting insulin analogues; the BIOD-123 (Krasner et al., 2014) and the BioChaperone lispro (Andersen et al., 2015) are two relatively successful examples.

On the other hand, new basal insulin mimetics have been designed with aim to increase duration of action and reduce glycaemic variability. Several advances were made that successfully delay the rate of absorption from the subcutaneous injection site through polymeric encapsulation (*e.g.* AB101 (Roberts et al., 2016)), biosynthesis fusion of insulin (*e.g.* ^{LAPS}Insulin115 (Hwang et al., 2014, Huh et al., 2015) and Insumera (Arnold et al., 2015, Marquez et al., 2015)) or prolonged precipitation at the site of injection (*e.g.* lapidated insulin NN1436 and NN1438 (Global Clinical Registry and Novo Nordisk A/S, 2016)).

Aside from the independent progress in the development of bolus and basal insulin mimetics, emerging evidence also supports the possibility of implementing insulin-incretin co-therapy for T2D treatment. Treatment with IDegLira, that combines long-acting insulin degludec and the GLP-1 analogue liraglutide, showed promising therapeutic outcomes with reduced hypoglycaemic episode and reduced weight gains in treated patients (Rodbard et al., 2016, Gough et al., 2016, Billings et al., 2018).

1.3.5.2 *New Insulins with Improved Stability*

In an endeavour to develop the ideal ultra-rapid insulin analogue, there is also a pressing need to improve its stability. Current rapid-acting insulin analogues were engineered to allow increased availability of active insulin monomers upon injection. However, a major drawback of maintaining insulin in its monomeric form is its concomitant increased propensity to fibrillation, particularly when stored in elevated temperatures (Brange et al., 1997a, Groenning et al., 2009, Nielsen et al., 2001a, Yang et al., 2010a). Therefore, the design of a highly potent but thermodynamically stable insulin has also proven to be a challenging task with only very few successes. Inspired by the stabilising attributes of disulfide bonds, variants of insulin analogues with an additional disulfide bond (4SS-insulins) were developed. Astoundingly, one of the

variants, A10C-B4C insulin, showed an improved glucose lowering effect and improved stability with its melting point increased by ~35 °C compared to native insulin (Vinther et al., 2013, Vinther et al., 2015b).

Another appealing breakthrough in insulin design is the ability to achieve insulin stability through the development of several forms of single chain insulins (SCIs), with the A and B chains connected through a 6-residue C-domain. The SCI-57 (also known as SCI-c) and its improved variants; SCI-a and SCI-b, demonstrated particularly promising results possessing improved potency and superior thermodynamic stability (Hua et al., 2008, Glidden et al., 2018b, Glidden et al., 2018a). Furthermore, the ability to produce functional single chain insulin also opens up new avenue to simplify recombinant insulin production.

Lastly, other examples of recently emerging insulin analogues are those that are chlorinated or halogenated on the aromatic ring of phenylalanine at position B24. The Phe^{B24} residue is thought to sit at the hydrophobic edge of the high affinity receptor binding pocket (described below in Section 1.7.1) surrounded by an asymmetric electrostatic environment. A chlorine or halogen group introduces a near-symmetric effect that enhances the general hydrophobicity of the molecule that attributes to its enhanced protein stability and activity (Weiss, 2014, Weiss, 2015).

1.3.5.3 New Insulins with Improved Metabolic: Mitogenic Profile

Correlation of insulin use and cancer progression is still under investigation. Nevertheless, any possibility of imposing life-threating risk to the treatment of diabetes should warrant an immediate attention. The classical example of 'highly mitogenic' insulin analogue, such as insulin X10, suggests that increased mitogenic potential is most likely associated with increased residence time on the growth-promoting IGF-1R and/or the IR-A. Insulin metabolic action is preferentially activated through the IR-B isoform. Correspondingly, an insulin analogue with increased binding preference for IR-B compared to IR-A and/or IGF-IR would result in a metabolically-biased IR agonist. There has been, however, very little success in this regard. Novo Nordisk has recently presented a receptor-selective insulin analogue (INS-B) that has 2–4-fold greater binding preference for IR-B compared to IR-A *in vitro*. The analogue also exhibits a tissue-selective biological response (Glendorf et al., 2011, Vienberg et al., 2011). Although promising, the investigation of INS-B analogue is still under early experimental stages.

Despite the many challenges and limitations, insulin therapy is inevitable for many diabetes patients. Thus, it remains an unwavering priority to develop better insulin analogues with improved therapeutic index and safety assurance. The rapid advances in insulin development

have so far relied on the constant improved understanding of insulin's structure and function. In the next sections I will describe the prevailing knowledge of insulin and its mechanisms of action and stabilization that have led to the development of current insulin analogues. The revolutionary advances in chemical synthesis of insulin with disulfide isosteric linkages is also discussed in the later sections of this chapter to aid the understanding of the principles for the strategic design of the dicarba insulin analogues used in my investigation for this thesis.

1.4 OVERVIEW OF INSULIN & IGF SYSTEM

The insulin and insulin-like growth factor (IGF) signalling system is complex and key to the regulation of diverse biological responses including metabolism, cellular growth, proliferation, differentiation, survival and apoptosis (see Fig 1.5). Initiation of these responses is stimulated by insulin, IGF-I and IGF-II ligands that bind and activate receptor tyrosine kinases (RTK) – the insulin receptor (IR) and insulin-like growth factor-I receptor (IGF-1R). Six IGF binding proteins (IGFBPs) and the IGF-2R regulate IGF levels in circulation and within tissues (reviewed in (Denley et al., 2005)). In the circulation, IGFs are usually bound to the IGFBPs that prevent their interaction with the receptors (Forbes et al., 2012). The IGF-2R, also known as cation-independent mannose-6-phosphate, is a large single chain transmembrane protein with 15 extracellular contiguous repeats. High affinity binding of IGF-II to IGF-2R regulates the bioavailability of IGF-II by targeting the hormone to degradation *via* endocytosis and lysosomal enzyme degradation (Brown et al., 2009).

The IR and IGF-1R share high structural similarity, with each receptor dimer comprised of two extracellular α-subunits and two transmembrane β-subunits covalently linked by three disulfide bonds in a β-α-α-β coordination. The two isoforms of insulin receptor, IR-A and IR-B, are encoded by 22 exons and 21 introns and are translated as a single chain pre-proreceptor (Ullrich et al., 1985). Alternative splicing of exon 11 that encodes a 12-amino acid (717-729) segment at the carboxyl-terminus of α-subunits, results in the formation of the exon 11- isoform (IR-A) (Seino and Bell, 1989). High structural homology of the receptors also allows the formation of hybrid receptors (IR-A/IGF-1R or IR-B/IGF-1R) in certain tissues (Federici et al., 1998).

Similarly, insulin also shares high sequence and structural homology to the IGFs (see Fig. 1.6, *A* and *B*). However, as part of the key regulatory function of the hormones, the ligands bind to each receptor with different affinities (see Table 1.2) that leads to the activation of distinct biological outcomes. Generally, insulin binds to both IR isoforms with high affinity and predominantly regulates metabolic responses *via* the IR-B. On the other hand, IGFs binds to the IGF-1R with

high affinities and promote mitogenic signalling responses. The IR-A binds both insulin and IGF-II (3 to 10-fold lower than insulin) with high affinities (Frasca et al., 1999, Rajapaksha, 2013). Although the IR-A is capable of promoting metabolic signalling when stimulated by insulin, there is increasing evidence demonstrating the importance of the IR-A in promoting prenatal growth as well as cancer development when activated by IGF-II (Malaguarnera et al., 2012, Giani et al., 2002, Manousos et al., 1999, Sacco et al., 2009). Other possible contributing factors to the differential roles of the two IR isoforms are the different tissue distribution, ligand association/dissociation rates, receptor internalisation rates and phosphorylation patterns of the receptor intercellular domains. These are recently discussed in several reviews (Belfiore et al., 2009, Belfiore et al., 2017, Haeusler et al., 2018).

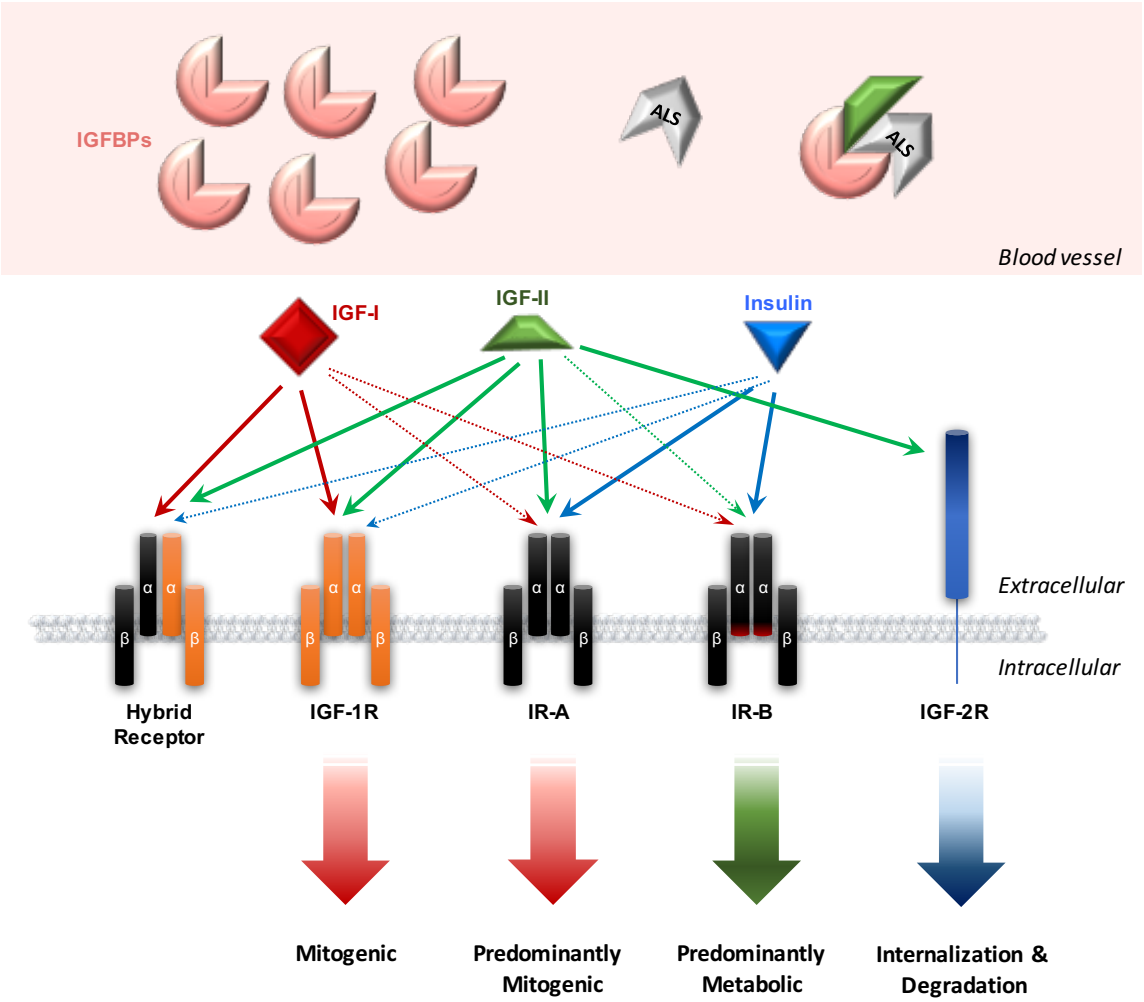

Figure 1.5 A schematic representation of the insulin/IGF system. The insulin/insulin-like growth factor (IGF) system system is comprised of three peptide hormones: insulin, IGF-I and IGF-II. Each ligand binds the different receptor tyrosine kinase (IR, IGF-1R and hybrid receptors) with different affinities (high affinity represented by *solid line arrows*; low affinity represented by *dotted line arrow,* refer *Table 1.2* for binding affinities) and differentially activates a diverse biological outcomes. Alternative splicing of exon 11 gives rise to the two IR isoform; exon 11-lacking IR-A and exon 11-containing IR-B (exon 11 encoded segment highlighted in red). Insulin activation of IR-B predominantly stimulates metabolic responses, while activation of IGF-1R by IGF ligands promotes mitogenic responses. IGF-II also has high affinity for the IR-A and predominantly activates mitogenic signalling through IR-A. IGFs binding to IR: IGF-1R hybrid receptors activate IGF-1R-like signalling. IGF-2R regulates the bioavailability of IGF-II *via* receptor internalisation and lysosomal enzyme degradation. Within blood circulation, the IGFs are bound to the six high affinity IGF binding proteins (IGF-BPs). Binding of acid labile subunit (ALS) and IGFBP to the IGFs prolongs the half-life of IGFs. The release of IGFs from IGF-BPs occurs *via* IGF-BPs proteolysis or extracellular matrix binding.

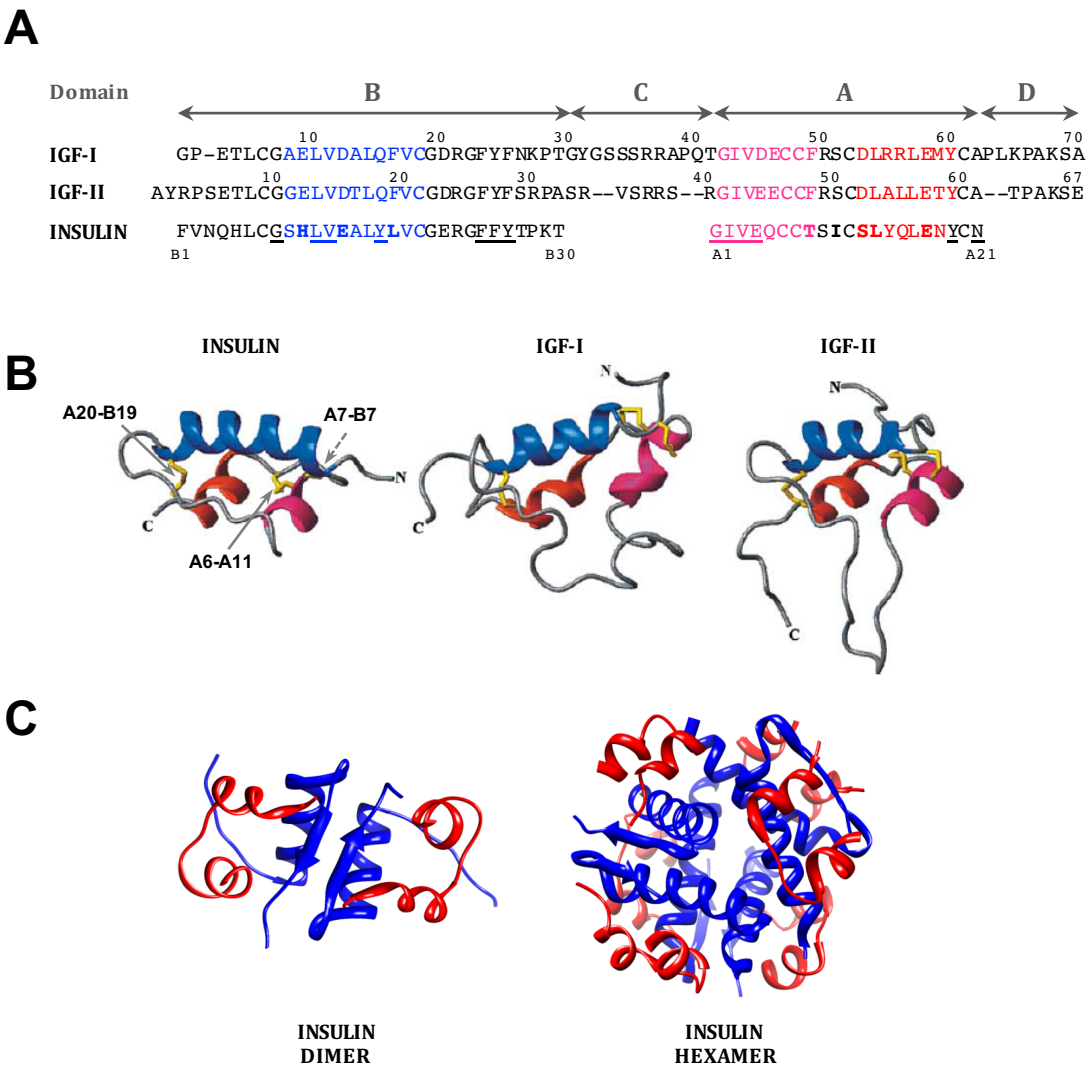

Figure 1.6 Sequence alignment and ribbon structures of insulin, IGF-I and IGF-II. (A) Sequence alignment of IGF-I, IGF-II and insulin. IGFs are single chain peptides comprised of B, C, A and D domains; whereas insulin in a 2-chain polypeptide comprised of a 21-residue A-chain and 30-residue B-chain. Insulin sequence highlighting site 1-binding residues (*underlined*) and site 2-binding residues (*bold*). (B) Insulin and IGFs share high structural homology; each contains two α-helices on A-chain (highlighted in *red* and *pink*) and a central helix on B-chain (highlighted in *blue*) and three disulfide bonds (highlighted in *yellow*). *Figure B* from (Denley et al., 2005). (C) Ribbon structure of an insulin dimer and hexamer.

Table 1.2 EC_{50} values (nM) of insulin, IGF-I and IGF-II for binding of IR-A, IR-B and IGF-1R.

	IR-A	IR-B	IGF-1R	References
Insulin	0.91 ± 0.3	1.0 ± 0.4	N. A.	(Frasca et al., 1999)
	0.40 ± 0.10	0.49 ± 0.05	> 1000	(Sciacca et al., 2010)
	1.57 ± 0.33	N. A.	N. A.	(Rajapaksha and Forbes, 2015)
	2.7 ± 0.6	2.6 ± 0.7	N.A.	(Pierre-Eugene et al., 2012)
IGF-I	> 30	> 30	0.2 ± 0.3	(Pandini et al., 2002)
	N. A.	N. A.	1.49 ± 0.14	(Versteyhe et al., 2013)
	34 ± 13	50 ± 13	N. A.	(Pierre-Eugene et al., 2012)
IGF-II	3.3 ± 0.4	36 ± 3.8	N. A.	(Frasca et al., 1999)
	15.2 ± 0.2	N. A.	N. A.	(Rajapaksha and Forbes, 2015)
	4 ± 0.4	N. A.	3.4 ± 0.2	(Ziegler et al., 2014)
	N. A.	N. A.	0.6	(Pandini et al., 2002)

N.A.: not analysed.

1.5 INSULIN

1.5.1 Insulin Biosynthesis

Insulin is a small globular peptide hormone produced exclusively in the β-cells of pancreatic islets. In humans, insulin is encoded within a single *INS* gene on chromosome 11. Transcription of *INS* is promoted in response to glucose and regulated *via* autocrine insulin signalling (Andrali et al., 2008). Insulin is initially translated in the form of a single chain pre-proinsulin. Within the rough endoplasmic reticulum, the precursor hormone is further processed *via* post-translational modification; removing the *N*-terminal signal sequence followed by the formation of three disulfide bonds, correct folding and cleavage of the connecting C peptide to yield a mature insulin (Steiner, 1988).

The mature human insulin comprises a 21-residue A chain that includes two α helices (residues A1 to A8 and A12 to A18, respectively), and a 30-residue B chain that includes a single α helix (residues B9 to B19) (Adams et al., 1969a). Integral to insulin's structure are its three disulfide bonds — one intra-chain (Cys^{A6}-Cys^{A11}) and two inter-chain (Cys^{A7}-Cys^{B7} and Cys^{A20}-Cys^{B19}) (Fig. 1.6*B*). Formation of these disulfide linkages ensures both the correct folding of the insulin precursor polypeptide and the structural stability of the mature hormone (Weiss, 2009b, Chang et al., 2003). Finally, the insulin monomer is further stabilised by dimer formation and as it is packaged and stored as 2Zn hexamers within insulin granules (Fig. 1.6*C*) (Steiner, 1988). Although insulin is most stable in its hexameric form it is the zinc-free monomeric form that engages the insulin receptor (Lawrence and Ward, 2015b).

1.5.2 Insulin Function

The primary role of insulin is the regulation of blood glucose homeostasis. High blood glucose signals the release of insulin into the circulation to promote glucose uptake in muscle and adipose tissue (see Fig. 1.7). Upon insulin binding to its receptors on myoblasts or adipocytes, the receptor undergoes conformational change and induces autophosphorylation of a series of tyrosine residues that serve as docking sites for the recruitment and activation of insulin receptor substrate (IRS) proteins (Taniguchi et al., 2006). Activated IRS proteins recruit PI3K to the plasma membrane which rapidly converts phosphatidylinositol (3,4)-bis-phosphate ($P1P_2$) to phosphatidylinositol (3,4,5)-tris-phosphate ($P1P_3$) (Katso et al., 2001). Membrane enriched with $P1P_3$ attracts Akt/PKB (protein kinase B), allowing its phosphorylation by PDK1 at Thr 308 and by mTORC2 at Ser 473; effectively initiating the activation of the PI3K-Akt signalling cascade for the regulation of glucose metabolism (Alessi et al., 1997). The fully activated Akt phosphorylates Akt substrate of 160 kDa (AS160) and subsequently promotes glucose transporter type 4 (GLUT4) translocation to the plasma membrane for glucose uptake (Kramer et al., 2006). Akt activation also promotes glycolysis *via* phosphorylation of 6-phosphofructo-2-kinase/fructose-2,6-biphosphatase 2 (PFKFB2) (Deprez et al., 1997) and induces glycogen synthesis *via* inhibition of glycogen synthase kinase 3β (GSK-3β) (Frame and Cohen, 2001).

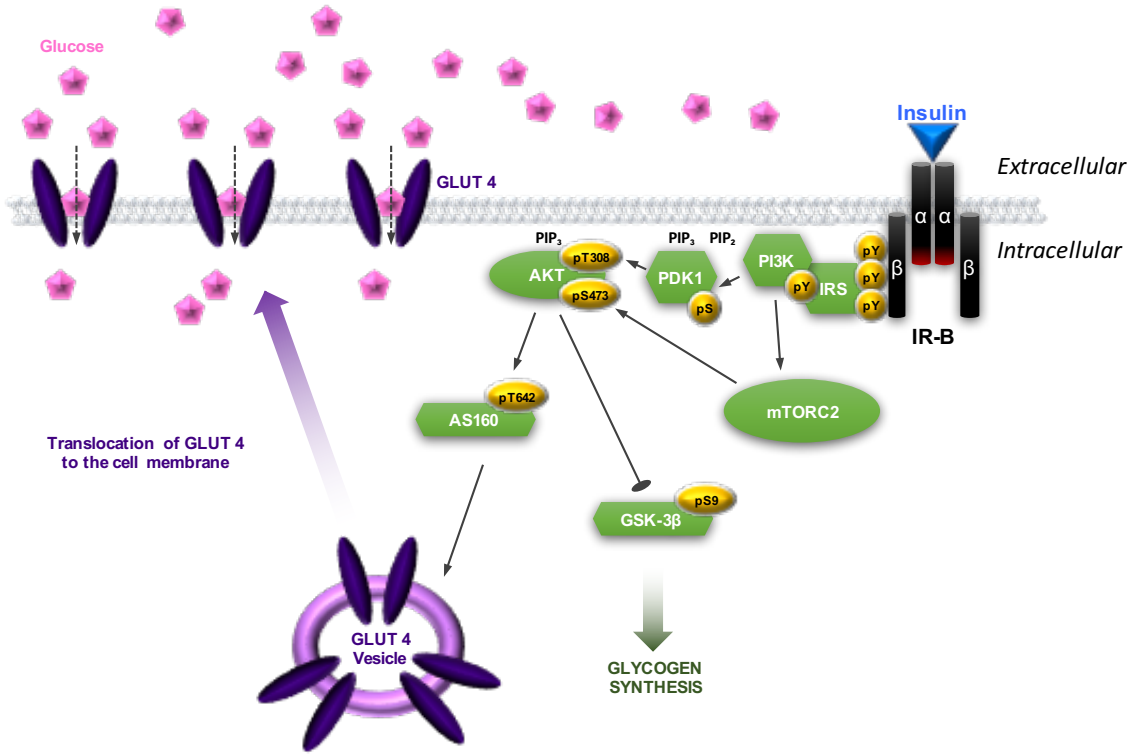

Figure 1.7 Insulin metabolic action *via* insulin receptor. At high blood glucose conditions, insulin binding to the insulin receptor stimulates PI3K signalling to promote glucose uptake and glycogen synthesis in muscles and adipose tissues. Upon receptor binding, conformational change of insulin receptor allows autophosphorylation of the receptor intracellular domains that act as docking sites for the recruitment and activation of *insulin receptor substrate* (IRS) proteins. Subsequent recruitment and activation of *phosphoinositide 3-kinase* (PI3K) and *phosphoinositide-dependent kinase 1* (PDK1) allows phosphorylation of Akt (also known as protein kinase B) at T308 and S473 residues. Fully activated Akt acts a master kinase protein that phosphorylates *Akt substrate of* 160 kDa (AS160) that regulates *glucose transporter type* 4 (GLUT 4) translocation to plasma membrane for glucose uptake. Akt also phosphorylates *glycogen synthetase kinase-3β* (GSK-3β); whereby its inhibition allows promotion of glycogen synthesis.

1.6 INSULIN RECEPTOR

The IR is a dimeric receptor tyrosine kinase where each monomer consists of an α-subunit and a transmembrane β-subunit (see Fig. 1.8) (De Meyts and Whittaker, 2002). The α-subunit comprises leucine-rich repeats (L1 and L2 domains) that are separated by a Cys-rich (CR) region. These are followed by the fibronectin type III domains (FnIII-1, FnIII-2, FnIII-3), which are separated by an insert (ID) domain that is also being split to form the *N*-terminus of β-subunit. The β-subunit constitutes most of the intracellular domains, in which the tyrosine-kinase domain (TK) is located between a juxtamembrane (JM) domain and a carboxyl-terminal tail (CT) (Marino-Buslje et al., 1999). The crystal structure of the ectodomain dimer of the IR-A (*apo* receptor) revealed a folded over conformation with each α-β monomer of the receptor dimer forming an 'inverted-V' layout relative to the surface of the cell membrane. The L1-CR-L2 domains from one monomer combine with the FnIII domains of the other monomer to form one leg of the inverted 'V' (see Fig. 1.8*B*). The anti-parallel symmetry arrangement of IR brings together the binding surfaces of alternative receptor monomers in close proximity thus defining the two ligand binding pockets: *site 1*/*site 2'* and *site 1'*/*site 2* (McKern et al., 2006).

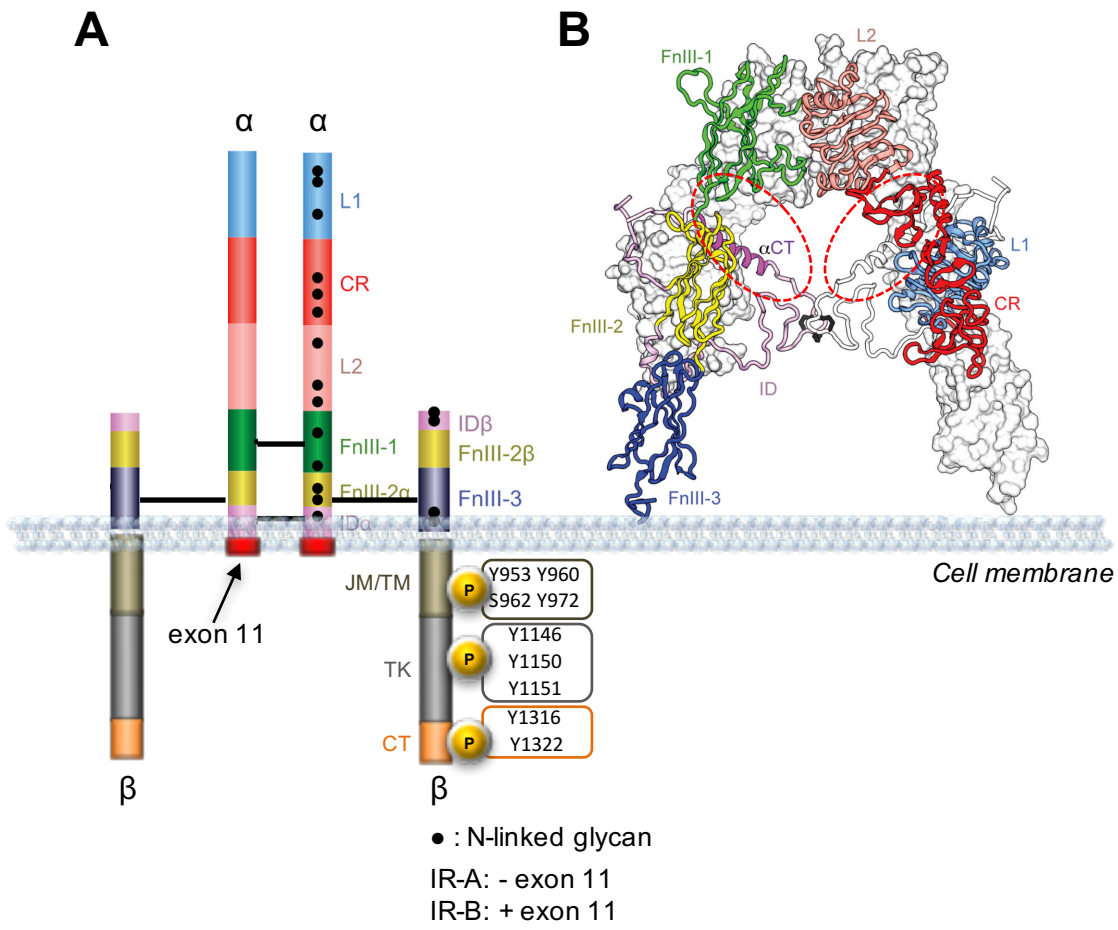

Figure 1.8 Structure of Insulin Receptor. (A) Schematic representation of IR in β-α-α-β chain coordination. Insulin receptor domains: L1, large domain 1 rich in leucine; CR, domain rich in cysteine; L2, large domain 2; Fn, fibronectin III type domain; TM, transmembrane domain; JM, juxtamembrane domain; TK, tyrosine kinase domain; CT, C-terminal domain. In the JM, TM, TK, and CT domains, several key phosphorylation residues are indicated. (B) X-ray crystallographic structure of insulin receptor ectodomain in 'inverted-V' layout. One α-β monomer in ribbon structure (domains colour corresponds to the schematic representation in (A). The other α-β monomer in white sphere structure. Insulin binding pockets highlighted in *red ovals*. From (Croll et al., 2016b); reproduced with modification.

1.7 INSULIN BINDING & RECEPTOR ACTIVATION

1.7.1 Insulin Binding Surfaces

The mechanism and kinetics of insulin binding to its receptor are not fully understood and require further investigation. This is also one of the major emphases of this project discussed in *Chapter 3*. Insulin achieves high affinity binding to its receptor when two binding sites of an insulin monomer crosslinks with two binding surfaces formed by anti-parallel α-subunits of the receptor dimer (De Meyts, 1994). Each binding pocket comprises receptor domains from the two receptor halves (*ie. site 1/site 2'* and *site 1'/site2*). At physiological insulin concentrations, insulin binds to IR in *site 1/site 2'* at stoichiometry of 1: 1 ratio (Fig. 1.9) (Kiselyov et al., 2009). Numerous studies also have proposed that a second insulin molecule binds to the other binding pocket (*site 1'/site2*), thereby accelerating the dissociation of the pre-bound insulin molecule on the receptor, suggesting insulin: IR engagement involves negative cooperativity (Christoffersen et al., 1994, De Meyts et al., 1978, Surinya et al., 2008, de Meyts et al., 1973, Whittaker et al., 2008).

Extensive alanine scanning studies from various groups have successfully mapped the two binding surfaces on insulin classified as site 1 (also known as "classical" binding surface) and site 2 (see Figs. 1.6*A* and 1.10; reviewed in (De Meyts, 2015)). The site 1 binding residues include Gly^{A1}, Ile^{A2}, Val^{A3}, Glu^{A4}, Tyr^{A19} and Asp^{A21} on the A chain as well as Gly^{B8}, Ser^{B9}, Leu^{B11}, Val^{B12}, Tyr^{B16}, Phe^{B24}, Phe^{B25} and Tyr^{B26} on the B chain (Inouye et al., 1981, Nakagawa and Tager, 1992, Jensen, 2000a, Nakagawa et al., 2000, Kristensen et al., 1997). Many of the site 1 residues also overlap with the insulin dimerization surfaces (Zoete et al., 2005). Despite their importance in receptor binding, some of these site 1 binding residues are buried suggesting insulin conformational change is required to allow receptor engagement. Particularly, several studies confirm the importance of the B23 –26 segment in receptor binding (Mirmira et al., 1991, Mirmira and Tager, 1989, Zakova et al., 2004, Zakova et al., 2013). Furthermore, natural mutations of several of these residues were also discovered in insulin from type 1 diabetic patients suffering from the lack of active insulin, further highlighting the vital role of these surfaces. For example, Insulin Chicago has Phe → Leu mutation at B25, Insulin Los Angeles has Phe → Ser mutation at B24 and Insulin Wakayama has Val → Leu mutation at A3 (Shoelson et al., 1983, Xu et al., 2004).

Site 2 binding residues identified by alanine scanning mutagenesis include Thr^{A8}, Ile^{A10}, Ser^{A12}, Leu^{A13}, Glu^{A17}, His^{B10}, Glu^{B13} and Leu^{B17} (Jensen, 2000a, Kristensen et al., 1997, Gauguin et al.,

2008b). Some of these residues (Leu^{A13}, Glu^{A17}, Glu^{B13} and $LeuB^{17}$) lie within the insulin hexamer-forming surface (reviewed in (De Meyts et al., 2004, Jensen and De Meyts, 2009)).

1.7.2 Insulin Receptor Binding Surfaces

Studies for the identification of residues involved in site 1 and site 2 binding surfaces on the insulin receptor are far more complicated and incomplete due to the complexity involved in the production of the large whole IR (~460 kDa; α-subunit 135 kDa and β-subunit 95 kDa), as well as the technical limitations of structural studies. The primary sequence of the IR was reported in 1980s (Seino et al., 1989). However, structural determination of both unliganded (*apo*) and liganded (*holo*) receptor has been a challenge. Thus, initial identification of site 1 and site 2 binding surfaces on IR relied upon biochemical approaches using site-directed alanine mutants, chimeric receptors and photoaffinity crosslinking (reviewed in (De Meyts and Whittaker, 2002, De Meyts, 2004). From these studies, it was proposed that IR site 1 binding surfaces are located within the L1 domain (amino acids 1-137) in the *N*-terminus of α-subunit and in the αCT domain located at the *C*- terminus of the insert domain (amino acid 704-715) (see Fig. 1.8) (Williams et al., 1995, Mynarcik et al., 1996, Mynarcik et al., 1997). Critically, it was later confirmed in photo-crosslinking study that the insulin site 1 Val^{A3} residue interacts with αCT domain upon receptor engagement (Huang et al., 2007). Several key site 1 contact sites were reported including His 710. Asn 711, Phe 714, Val 715, Pro 718 in the αCT domain and Asp 12, Arg 14, Asn 15, Leu 37, Phe 39, Phe 64 and Arg 65 in the L1 domain (De Meyts, 2015). Through mutagenesis the IR site 2 was located in the loop between the FnIII-1 and FnIII-2 domains (Whittaker et al., 2008).

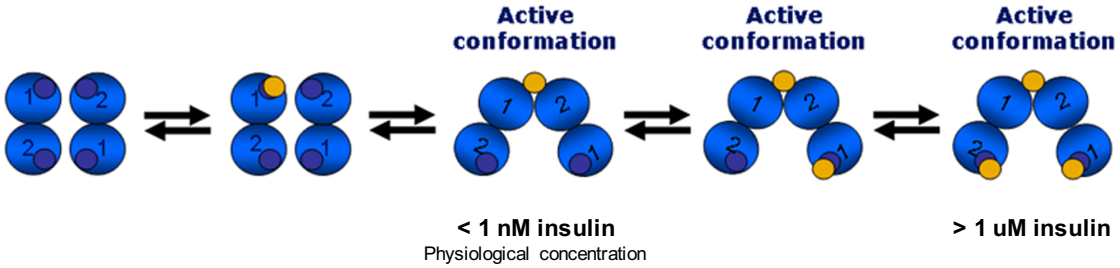

Figure 1.9 Current model of insulin receptor binding mechanism. In this model, the IR dimer has two identical binding pockets crosslinking partial sites (site 1 and site 2) from each receptor monomer arranged in an anti-parallel way. At physiological insulin concentrations, insulin binds to IR in *site 1/site 2'* at stoichiometry of 1: 1 ratio. The crosslinked state of the receptor corresponds to the activated state of the receptor (De Meyts 1994; Schaffer 1994). At higher insulin concentration, it was proposed that insulin binding also exhibit a phenomenon of negative cooperativity; whereby a second insulin molecule binds to the other available binding pocket (*site 1'/site2*); accelerating the dissociation of the pre-bound insulin molecule on the receptor. From (Kiselyov et al., 2009).

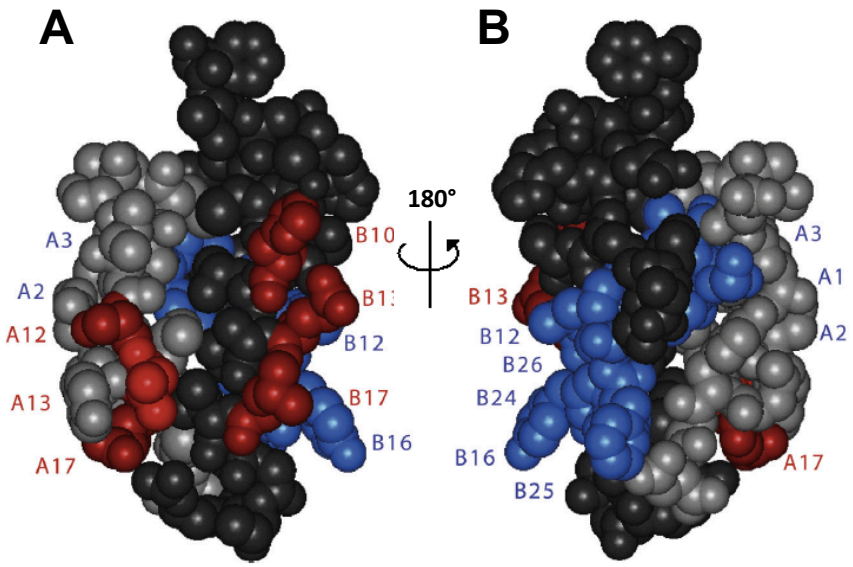

Figure 1.10 Insulin binding surfaces. (A) Front view and (B) back view of insulin molecule based on an R crystallographic protomer. Site-1 binding residues for insulin receptor engagement are highlighted in blue; while site-2 binding residues are highlighed in red. Many of the site 1 residues also overlap with the insulin dimerization surfaces. Several site-2 binding residues (Leu^{A13}, Glu^{A17}, Glu^{B13} and $LeuB^{17}$) also lie within the insulin hexamer-forming surface. Insulin A- and B-chains that are not involved in binding are shown in light grey and dark grey, respectively. From (Weiss, 2013b)

1.7.3 Insulin Receptor Activation

Upon insulin binding, the IR undergoes conformational change that induce receptor activation and/or receptor internalisation. The mechanisms of the structural transitions of the IR upon insulin binding are not well understood. Conformational change within the extracellular α-subunits is transmitted through the TM domains to the intracellular TK domains on the β-subunits, leading to further conformational change and activation of the kinase. There are 59 potential phosphorylation sites on the β-subunit of IR: 13 tyrosines (Tyr, Y), 30 serines (Ser, S) and 16 threonines (Thr, T). However, only 24 phosphorylation sites (9 tyrosines, 12 serines and 3 threonines) on JM, TK (including activation loop) and CT domains were reported upon stimulation in different cell lines (Hornbeck et al., 2012). Specific phosphorylated residues act as docking sites for a number of intracellular adaptor proteins. Subsequent phosphorylation events of the recruited signalling molecules allow initiation of insulin-dependent signalling cascades.

The first events after the TK domain activation and ATP binding are autophosphorylation of three tyrosine residues (Y1146, Y1150 and Y1151) located in the activation loop of TK domain (Fig. 1.8*A*) (Shoelson et al., 1991, Ward and Lawrence, 2009, Hubbard and Miller, 2007). Phosphorylation of these three tyrosines is known as a critical step for IR activation and is required for a sustained IR signalling. Site-directed mutagenesis of any of the three tyrosine residues to a phenylalanine (Phe, P) drastically impairs IR activation by 45 – 60%, and substitution of all three tyrosines to phenyalanines almost completely abolishes the IR activity (Wilden et al., 1992).

Furthermore, several residues on the JM (Y953, Y960, S962 and Y972) (Murakami and Rosen, 1991) and CT domains (Y1316, Y1322, S1275, S1293, S1294, S1309, S1315, T1323, T1336) (Fig. 1.8*A*) (Hornbeck et al., 2012) are also phosphorylated upon insulin stimulation. Although it has been shown that truncated IR with deletion of either JM (Sattar et al., 2007) or CT domain (Myers et al., 1991) can activate normal receptor activation and the stimulation of downstream signalling, there are also studies that suggest these domains may play important roles in regulating differential signalling of IR; as described below.

Phosphorylated Y960 is an important docking site for a number of signalling molecules, including the IRS family that is involved in PI3K signalling to promote metabolic and mitogenic responses (Xu et al., 1999, Sesti, 2000, Wu et al., 2008, Sawka-Verhelle et al., 1996, Inoue et al., 1998, Hribal et al., 2000, Abe et al., 1998) and the Shc protein involved in activation of mitogenic MAPK signalling (Farooq et al., 1999). Deletion of a 12-amino acid segment on the

JM domain including the Y960 residue leads to reduced glycogen and DNA synthesis (Backer et al., 1991).

More recently, the Y960 residue was also found preferentially phosphorylated when IR-A is stimulated by the highly mitogenic X10 insulin analog (Hansen et al., 2011). In contrast, stimulation with a "less mitogenic" insulin agonist peptide (S597) induced a delayed phosphorylation of Y960 residue (Rajapaksha and Forbes, 2015). The S597 peptide also promoted lower activation of IRS-1 (Jensen et al., 2007); suggesting its activation may be dependent on Y960 phosphorylation. Furthermore, independent of Y960 phosphorylation, the JM domain was also found to be important for regulating IR internalisation (Backer et al., 1992); a mechanism that is still poorly understood but is increasingly associated with IR mitogenic signalling. These evidence suggest that preferential phosphorylation of the IR Y960 within the conserved NPEY motif in JM domain may be associated with increased mitogenic signalling.

Compared to the JM domain, the role of CT region is less well understood. Several older reports demonstrated a deletion or mutation on the two key phosphorylation sites on CT domains (Y1316 and Y1322) (see Fig. 1.8*A*) can lead to either reduce mitogenicity (Takata et al., 1991), reduce metabolic signalling (Maegawa et al., 1988) or have no effect on both signalling pathways (Myers et al., 1991, Murakami and Rosen, 1991). More recently, Rajapaksha & Forbes demonstrated that increased phosphorylation of Y1316 and Y1322 is associated with stimulation with a "less metabolic" qIGF-I peptide but phosphorylation of these sites does not appear to be selectively reduced when stimulated by a "less mitogenic" S597 peptide (Rajapaksha and Forbes, 2015). Whether phosphorylation of these residues on CT domain has any significant role in IR differential signalling remains controversial.

In summary, the significance of each phosphorylation site on the JM, TK and CT domains remains unclear. Many research groups, including our group, propose that the fate of activating differential signalling outcomes is encoded within the different phosphorylation events and kinetics of phosphorylation within these domains. Phosphorylation of some of these specific residues are essential docking sites for a number of signalling proteins that drives the activation of specific signalling cascades and may also dictate the initiation of receptor internalisation.

1.8 INSULIN STRUCTURE & STABILITY

In the 1950s, insulin was the first peptide to be amino acid sequenced (Ryle and Sanger, 1955), and its Zn^{2+} hexameric form also was the first hormone to have its tertiary structure characterised by x-ray crystallography (Blundell et al., 1971a, Blundell et al., 1971b). Since then, the structure of insulin has been studied quite extensively in a variety of monomeric, dimeric and hexameric crystals (Bentley et al., 1976, Baker et al., 1988b, Derewenda et al., 1989, Smith and Ciszak, 1994, Ciszak and Smith, 1994, Ciszak et al., 1995, Smith et al., 2000, Menting et al., 2013). Solution structures of insulin have also been determined using nuclear magnetic resonance (NMR) spectroscopy (Roy et al., 1990, Hua and Weiss, 1991, Kaarsholm and Ludvigsen, 1995, Olsen et al., 1996). More recently, the structural dynamics and the structural properties of insulin have also been investigated using computational approaches such as molecular dynamics (MD) simulations (Zoete et al., 2004, Zakova et al., 2013, Zakova et al., 2014, Papaioannou et al., 2015, Papaioannou et al., 2017). Highlighted in these structural studies and numerous other reports are the importance of maintaining a fine balance between competing requirements for stability and conformational plasticity needed for optimal insulin activity. Structural flexibility of the insulin molecule is important for its correct folding, dimerization, hexamer assembly, receptor binding and activating potency, while structural stability of insulin is important for its bioavailability, function, storage and also to prevent complications associated with misfolding and fibrillation.

Key to the structural flexibility and stability of insulin are the three evolutionarily conserved disulfide linkages that hold the insulin molecule together — one intra-chain (Cys^{A6}-Cys^{A11}) and two inter-chain (Cys^{A7}-Cys^{B7} and Cys^{A20}-Cys^{B19}) disulfides. Insulin stability is also associated with its self-association/dissociation ability and the tendency to fibrillate. Depending on the different solution conditions, insulin maintains self-association equilibria between its monomeric, dimeric and hexameric forms. Partially unfolded insulin can also form insulin fibrils or higher-order insulin aggregates in extreme conditions, such as low pH, increased temperature and agitation. Thus, further to our understanding of insulin: receptor binding sites, it is also increasingly evident that understanding the structural dynamics of insulin both in physiological conditions and in external storages (in the vial and in the reservoir of a pump) is required for the design of new insulin analogues.

1.8.1 Insulin Conformations: T- & R-state

Extensive mutagenesis and structural studies of the molecule revealed that insulin adopts multiple conformations most commonly categorized into the "classical" T-state and R-state (or R^f-state) (see Fig. 1.11). The T-state conformation includes the *N*-terminal A chain α-helix spanning residues A1 to A8, the second α-helix spanning residues A12 to A18 and the single B chain α-helix from residues B9 to B19 (Adams et al., 1969a). The transition from the T- to R-state is characterised by the extension of the *N*-terminus of the B chain α-helix to include residues B1 – B19 α-helix (Derewenda et al., 1989). Under different crystallisation conditions the B1 –B3 segment unravels into a non-helical extension resulting in a frayed R^f-state (Ciszak and Smith, 1994). The long extension in the R-state creates a significant structural change moving away from the insulin core by nearly 30Å (Kaarsholm and Ludvigsen, 1995).

Under different X-ray crystallography conditions, 3 families of insulin hexamers are observed T_6, T_3R_3 (or T_3R^f) and R_6 (reviewed in (Weiss, 2009b)) (see Fig. 1.12). The T_6 hexamer is stabilized by two zinc ions. At high chloride concentration a 4Zn-T_3R_3 (or 4Zn-$T_3R^f_3$) can be observed. Finally, the transition to R_6 hexamer requires binding of 6 phenols. The $T_6 \leftrightarrow T_3R_3/T_3R^f_3 \leftrightarrow R_6$ transition of insulin hexamers was first observed in crystals (Bentley et al., 1978). The transition was also later observed in solution and it was also suggested that the 3 forms of hexamers can coexist in solution in a dynamic equilibrium and can be regulated *via* the change of ionic strength; with the T_6 state being the dominant form (Roy et al., 1989, Thomas and Wollmer, 1989, Jacoby et al., 1993, Shneine et al., 2000). Crystal (Bi Ru et al., 1984, Whittingham et al., 2006) and in-solution (Olsen et al., 1996, Hua and Weiss, 1990, Hua and Weiss, 1991) structures of insulin monomers and dimers resemble T-state conformations. Interestingly, R-state has never been observed in the monomeric or dimeric form, while the R_6 hexamer was only observed in the presence of cyclic alcohols such as of phenol or m-cresol that are routinely used in formulation as anti-bacterial agents (Ciszak and Smith, 1994, Smith et al., 2000).

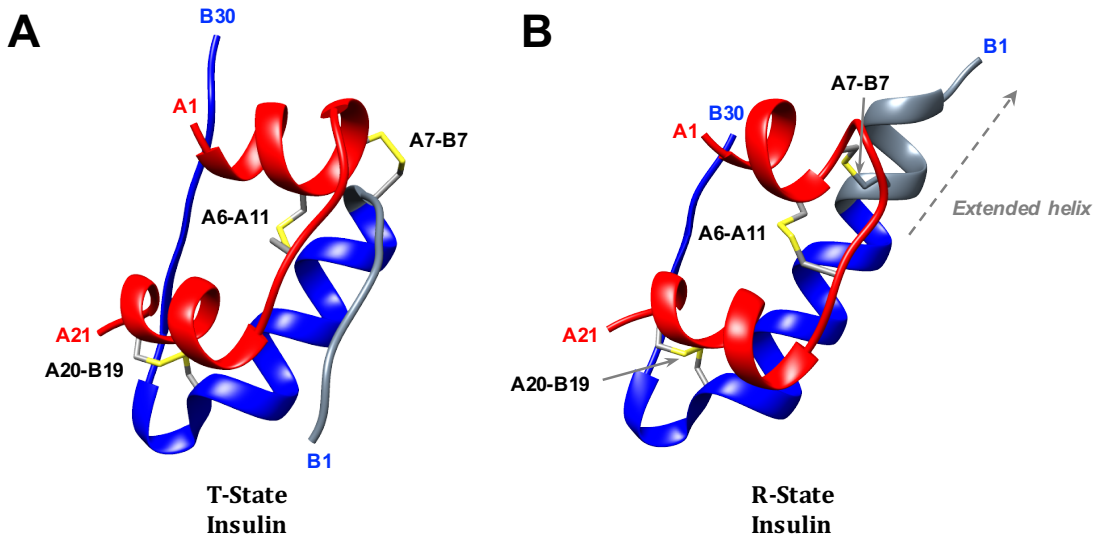

Figure 1.11 Ribbon structures of insulin in (A) T-state and (B) R-state. Both T- and R-state insulin structures are comprised of two A-chain α-helices (highlighted in *red* and *pink*), a B-chain central helix (highlighted in *blue*) and three disulfide bonds (highlighted in *yellow*). T-state insulin from T_6 insulin hexamer (PDB: 1MSO (Smith et al., 2003)) includes an *N*-terminal A-chain α-helix spanning residues A1 to A8, the second α-helix spanning residues A12 to A18 and the single B chain α-helix from residues B9 to B19. R-state from a R_6 insulin hexamer (PDB: 4E7V (Frankaer et al., 2012)) is characterized by the extended B-chain helix that includes B1-B8 segment (highlighted in *grey).*

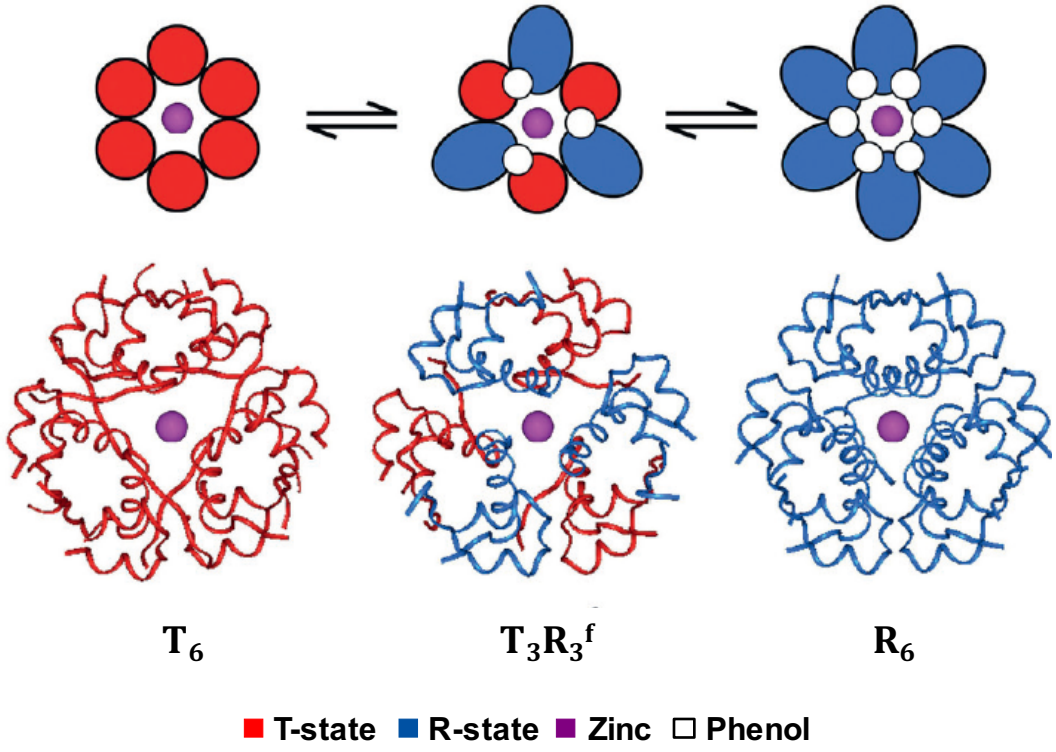

Figure 1.12 Insulin hexamers in T_6, $T_3R_3^f$ and R_6 coordinations. Schematic representation (*top*) and crystal structures (*bottom*) depicting transition of T_6, ⇌ $T_3R_3^f$ ⇌ R_6 states of insulin hexamers**.** The T-state protomers are shown in red and R-state protomers in blue. Zinc ions are shown in purple and phenol in white. Protein Data Bank accession numbers: 4INS (T_6; (Baker et al., 1988b)) , 1TRZ ($T_3R_3^f$; (Ciszak and Smith, 1994)) and 1ZNJ (R_6). From (Weiss, 2013a).

1.8.2 Defining the Active Insulin Conformation

Currently, there are over 300 reported structures of insulin from different organisms, insulin mutants and in various states (monomer, dimer, hexamer and receptor-bound) in the PDB database. Nevertheless, the ultimate receptor-ready active conformation of an insulin molecule has not been fully defined. It has long been suggested that the transition between T- and R states could play a crucial role in the transformation between active and inactive conformation of insulin. However, the physiological implication of the two states is not clear. Whether T- or R-state could represent the insulin active conformation has been a subject of robust debate. Particularly, the discussions have been concentrated on the flexibility of B chain *N*- and *C*-terminal segments during receptor engagement.

In several publications, Weiss and colleagues suggested that the stable T-state insulin represents an inactive conformation while the more flexible R-state has a closer resemblance to the receptor-bound or active conformation of the hormone (Weiss, 2009b). By comparing the structural and functional properties of insulin mutants with isomeric amino acid substitutions of the Gly^{B8} residue ($_{D}$- or $_{L}$-Ala^{B8} and $_{D}$- or $_{L}$-Ser^{B8}), the importance of insulin Gly^{B8} residue in the transition of "stable but inactive" T-like state ($_{D}$-analogues) to the "flexible but active" R-like state ($_{L}$-analogues) was described. Weiss *et al.* conclude that the stability of T-like state is key for disulfide pairing and correct folding of insulin monomer, while the flexibility of R-like state is essential for insulin's activity (Nakagawa et al., 2005, Hua et al., 2006, Hua et al., 2011, Weiss, 2009b).

However, there are also several reports suggesting the R-state is not required for receptor binding and thus is unlikely to represent the ultimate active conformation. For instance, Vinther *et al.* has demonstrated that an insulin analogue which is constrained by an additional disulfide linkage (A10C-B4C) is unable to adopt the R-state conformation (characterised by the B-chain *N*-terminal helical extenstion) but still binds the IR with high affinity (Vinther et al., 2013). Furthermore, the R-state is only detected in structures crystallised under non-physiological conditions in the presence of cyclic alcohols such as of phenol or m-cresol and was never observed in the monomeric form. Using a similar approach described by Prof. Weiss, Kosinová *et al.* also attempted to design two analogues that represent a 'locked T-state' ([*N*MeAlaB8]-insulin) and a 'locked R-state' ([AibB8]-insulin) through modification of the Gly^{B8} residue (Kosinova et al., 2014). Interestingly, however, they reported that introduction of an unusual chiral amino group is not necessarily sufficient to constraint the R-state. Instead, both analogues adopted T-like conformations (classified as I-states; intermediate states between T- and R-state).

Although both analogues are inactive, the study emphasized the complexity in inducing a full T $\rightarrow$ R transition and highlights the importance of Gly^{B8} flexibility in receptor binding. Hence, they suggest both R-state and the "classical" T-state are unlikely to represent the active conformation and neither represent the flexible conformation of B1-B8 segment required for receptor binding (Kosinova et al., 2014).

Contrary to the ambiguity surrounding the *N*-terminus of insulin B chain, several reports provide convincing evidence that conformational changes in *C*-terminal end of B chain are required for receptor engagement. Hua *et al.* proposed that the movement of the *C*-terminal segment (B24-B30) of the B chain from the hormone core is required for engagement with the IR αCT and L1 domains (Hua et al., 1991). Crystallographic studies of an IR fragment comprised of the ectodomain and the αCT segment in complex with insulin through site 1 residues confirmed a structural change of insulin at the *C*-terminal end of B chain to enable receptor engagement (see Fig. 1.13) (Menting et al., 2013, Menting et al., 2014b). Both groups suggest that the movement of *C*-terminal B chain away from the hydrophobic core of insulin is required to allow accessibility to insulin site 1-binding residues (Ile^{A2}, Val^{A3}, Val^{B12}, Phe^{B24} and Phe^{B25}) that otherwise remain buried (Menting et al., 2014b, Hua et al., 1991). Menting *et al.* also suggest that such movement is driven by a 60° rotation at Phe^{B24} residue which then promotes the movement of the *C*-terminal end of B chain away from the core. More recently, molecular dynamic simulations of insulin suggests that the end of the B chain opens in a zipper-like fashion (Fig. 1.14) (Papaioannou et al., 2015).

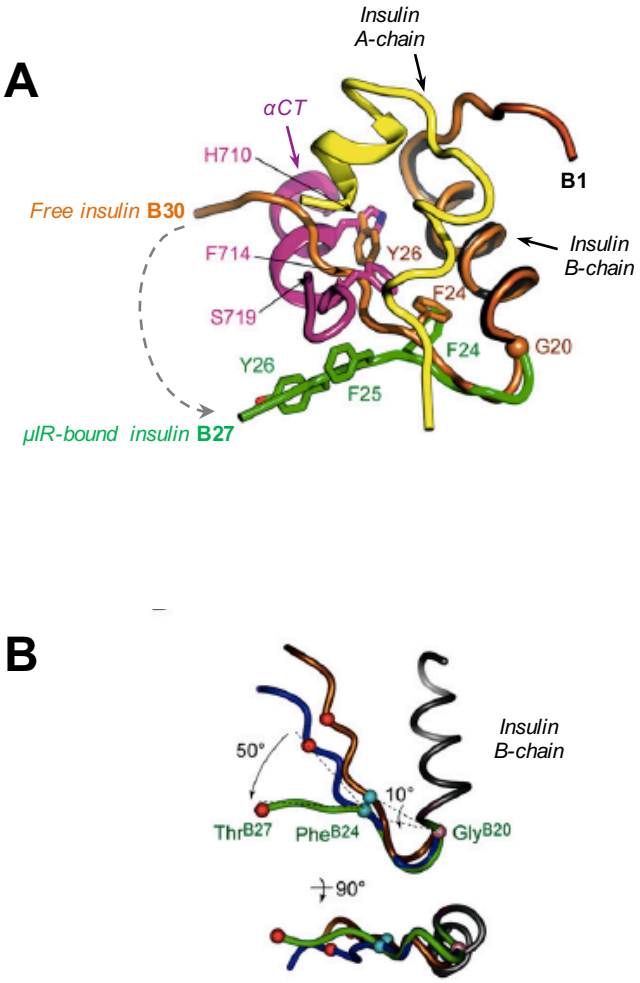

Figure 1.13 Structural movement of B-chain *C*-terminal segment upon μIR engagement. (A) Overlay of the B-chain of free insulin (B1–B30: *orange*) and μIR-bound insulin (B7–B19: black; B20–B27: *green*) ribbon structures. In the μIR: insulin complex, insulin A-chain is depicted in *yellow* and the αCT segment of μIR is in *magenta*. To prevent steric clash between the insulin B-chain *C*-terminal segment and the αCT segment (as depicted in free insulin), structural movement of insulin B-chain *C*-terminal segment away from the hydrophobic core is required. This would allow the sidechain of His710 and Phe714 residues on the IR αCT segment to fill in the volume that would otherwise occupied by the TyrB26 residue in free insulin. (B) Overlay of insulin B-chain (*black*) highlighting the hinge-like movement of B20–B30 conformation transitioning from the free insulin conformation (*orange*) to the intermediate conformation that involves a ~10° rotation of B20–B23 β-turn (*blue*) and eventually a ~50° rotation of B24–B30 hinged around Phe^{B24} residue to achieve the μIR-bound conformation (*green*). From (Menting et al., 2014b); reproduced with slight modification.

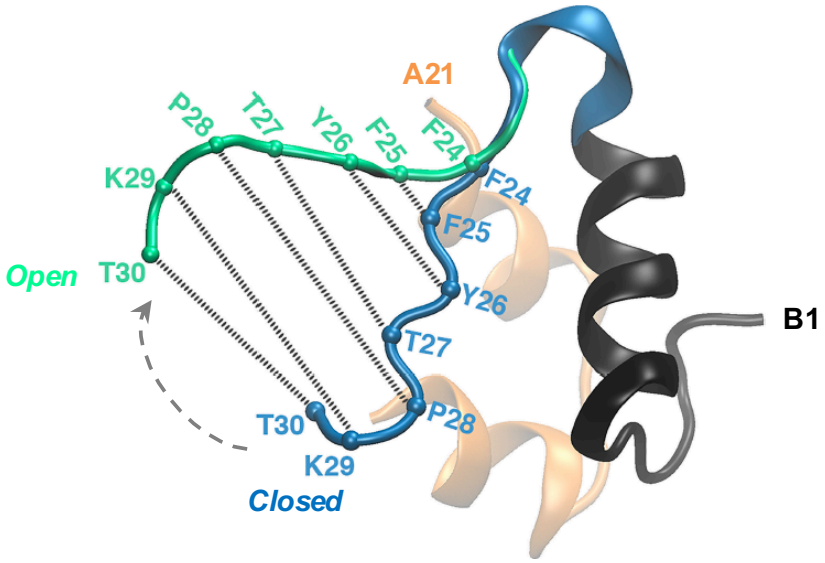

Figure 1.14 Molecular dynamics simulations of insulin highlighting the zipper-like opening of B-chain *C*-terminus. Molecular dynamics simulations demonstrating a zipper-like opening of the B-chain *C*-terminus hinged at $PheB^{24}$ residue upon receptor binding. Insulin B-chain *C*-terminus in its closed (*blue*) and open (*green*) conformations depict the movement of B-chain *C*-terminus away from the insulin hydrophobic core to allow receptor binding. The Cα atoms of residues in B24–B30 segment are represented in spheres. Insulin A-chain is in *orange* and the remaining B-chain in *black*. From (Papaioannou et al., 2015); reproduced with slight modification.

Although the 'opening' of *C*-terminal end of B chain seems to be required for receptor engagement, insulin analogues adopting a permanently 'open' B chain *C*-terminus are not necessarily potent. For instance, an insulin analogue with a truncated *C*-terminal segment of B-chain, such as in the desheptapeptide [B26-30]-insulin, only retains 25.7% of receptor binding potency and further truncation of Phe^{B24} residue results in complete inactivity of the molecule (Bao et al., 1997).

Nevertheless, Jiracek and colleagues demonstrate that the truncation of insulin's B26-B30 segment is not the leading contributor to the loss of receptor binding potency. By introducing a new β-turn structure through N-methylated L-amino acids at the B25-B26 peptide bond (eg. [*N*MeAla^{B26}]-DTI-NH_2) or by the insertion of D-amino acids at B26 ([D-Pro^{B26}]-DTI-NH_2), the insulin analogues with a truncated B26-B30 segment regained receptor binding potency (300 – 500%), suggesting the β-turn at the B24-B26 segment is a key element for optimal receptor binding. Interestingly, these analogues exhibit poor downstream metabolic potency in *in vitro* lipogenesis assays and *in vivo* blood glucose lowering tests. It is possible that these analogues engage with receptor differently to the native insulin; possibly due to the unique conformation at the B chain *N*-terminus that is neither T-like nor R-like (Zakova et al., 2008, Jiracek et al., 2010).

Critically, Jiracek *et al.* also noted an influence of B chain *C*-terminal truncation on conformation of the *N*-terminal end of the A chain (Jiracek et al., 2010). Weiss *et al.* also reported that the removal of A6–A11 linkage severely perturbed insulin activity as a result of the disordered *N*-terminal A-chain, suggesting the flexibility and movement of the A chain may play a role in receptor binding; and the helical conformation of the A1-A8 region might be an important receptor recognition element (Weiss et al., 2000). The structural dynamics of insulin in this region and the key mechanisms that regulate such movements are still poorly characterised. Nonetheless, both of these observations are highly relevant to my investigation and will be discussed in detail in *Chapter 3*.

1.8.3 Mechanism of Insulin Degradation

Although the active conformation of insulin has not been fully defined, it is clear that such conformation reveals hydrophobic surfaces that are key to receptor binding (De Meyts, 2015) but at the same time may also prime the molecule to instability (Brange and Langkjoer, 1993, Hua and Weiss, 2004, Yang et al., 2010a, Nielsen et al., 2001a). Insulin instability increases its vulnerability to chemical denaturation and/or physical denaturation.

Chemical denaturation is a process that involves a change in the covalent structure of a protein when subjected to denaturing agents such as elevated temperature, extremes pH, high concentration of organic solvents, guanidine hydrochloride, urea etc. The susceptibility of a protein to chemical denaturation is defined by its thermodynamic properties and its tendency to unfold from its tertiary structure upon perturbation. Chemical denaturation can occur *via* several mechanisms, including: pH-dependent deamidation of asparagine residue, formation of dimers and oligomers through transpeptidation between amine groups, and formation of covalent polymers *via* disulfide exchange (Brange and Langkjaer, 1992, Brange et al., 1992b, Brange et al., 1992a, Brange, 1992, Brange et al., 1992d, Brange et al., 1992c).

On the other hand, physical denaturation can involve an irreversible physical change of the protein without a change in its covalent structure – also known as protein fibrillation; characterized by the cross-β assembly of linear polymers (Dobson and Karplus, 1999). The mechanism of insulin fibrillation is still poorly understood. Nevertheless, it has been suggested that the initiation of insulin fibrillation involves nucleation of insulin monomers in conditions of elevated temperatures and physical agitation. Subsequent growth into fibrils involves conformational transition of α→β of insulin monomers, elongation and stacking of anti-parallel β-sheets (Bouchard et al., 2000, Yu et al., 1974).

Fink and coworkers also proposed that in the absence of receptor, the increased flexibility of insulin monomer primes the transition towards a partially-folded intermediate that can either further unfold completely or form nucleus that rapidly initiates the process of insulin fibrillation (Nielsen et al., 2001a) (see Fig. 1.15). Importantly, the increased abundance of insulin in the monomeric form has also been suggested to correlate to increase propensity of insulin fibrillation (Brange et al., 1997a, Brange et al., 1997b). Nevertheless, the fibrillation behaviour of the monomeric rapid-acting insulin analogues evidently displays different behaviours depending on the experimental conditions used to measure fibrillation. For example, monomeric insulin lispro (KP) that was predicted to readily fibrillate has also been reported to be relatively

slow in forming fibrils under conditions of low pH at room temperatures. Interestingly, in conditions where the insulin molecules are pre-nucleated, insulin lispro fibrillated faster than native insulin (Woods et al., 2012, Ludwig et al., 2011); suggesting an ambiguity in the understanding of insulin fibrillation mechanism.

Within the insulin monomer, the structural flexibility of the molecule also contributes to its tendency to unfold during the fibrillation process. As seen in the monomeric KP insulin, the movement of the *C*-terminal end of B-chain away from the hydrophobic core is known to promote insulin fibrillation (Brange et al., 1997a, Hua and Weiss, 2004, Phillips et al., 2012, Hua et al., 2011). Furthermore, it has also been proposed that the transition of $\alpha \rightarrow \beta$ occurs at the *N*-terminal helix of the A-chain; a process that also requires A-chain *N*-terminal helix to move away from the hormone core (Hua et al., 2011, Yang et al., 2010a).

Generally, increased flexibility of insulin molecule tends to increased its susceptibility to degradation. However, conformational flexibility and movement are also important elements to receptor engagement. Lacking is the understanding of the underlying mechanism that regulates the "tolerable" conformation flexibility that allows gain of optimal insulin activity without potentiating insulin fibrillation. Unravelling such insight would open up a limitless possibility in refining insulin therapy and its production process.

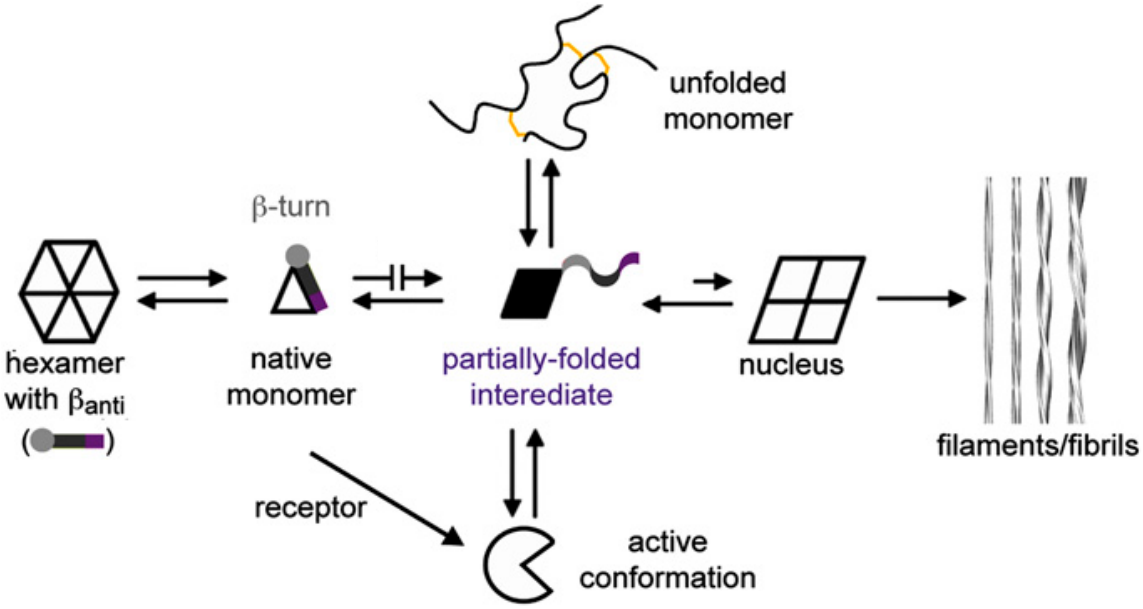

Figure 1.15 Mechanism of insulin fibrillation. Under physiological conditions native insulin monomers (*triangles*) are stabilized in a Zn^{2+}-coordinated hexamer form (*far left*) comprised of 3 sets of insulin dimers coordinated *via* the anti-parallel β -sheet (β -anti). Within the native monomer, the B-chain *C*-terminus is highlighted in segments: B20–B23 β -turn (*light grey circle*), B24–B28 β-stand (*dark grey bar*) and the less ordered B29 and B30 residues (*purple bar*). For receptor engagement, the insulin hexamer needs to dissociate to a monomer and undergo a structural change to adopt the active conformation (*open circle*). During this process, native monomer may also enter a partially-folded intermediate state (*black trapezoid*) leading to the formation of an amylogenic nucleus that initiates the process of insulin fibrillation. Alternatively, in extreme conditions, such as elevated temperature, insulin could also unfold completely into an unordered state (*top*); constrained by the 3 disulfide bonds (*yellow*). From (Menting et al., 2014b).

1.9 INSULIN SIGNALLING

Conventionally, insulin is known as a metabolic hormone that regulates glucose and lipid metabolism. The hormone also promotes mitogenic responses such as gene expression, protein synthesis, cell proliferation, differentiation, growth, apoptosis and survival. Regulation of such diverse biological outcomes involves a complex insulin signalling network commonly promoted by activation of two major pathways – the phosphatidylinositol 3-kinase (PI3K) pathway and mitogen-activated protein kinase (MAPK) pathway (see Fig. 1.16). Generally, the PI3K pathway is known as the regulator for both metabolic and mitogenic responses while the activation of MAPK pathway predominantly leads to mitogenic outcomes (Katso et al., 2001, Gehart et al., 2010, Avruch, 1998, Taniguchi et al., 2006).

1.9.1 PI3K-Akt and MAPK-Erk signalling pathways

As described earlier, upon insulin stimulation, autophosphorylation of the IR at the intracellular domain recruits insulin receptor substrate (IRS) proteins to the plasma membrane that allows initiation of PI3K signalling *via* the key protein kinase Akt (also known as protein kinase B or PKB). Phosphorylation of Akt at Thr308 and Ser473 indicates the activation of PI3K signalling. Fully activated Akt activates and inhibits a wide range of downstream proteins that regulate metabolic processes (Taniguchi et al., 2006). For instance, phosphorylation of AS160 promotes glucose uptake *via* GLUT4 (Kramer et al., 2006), phosphorylation of PFKFB2 promotes glycolysis (Deprez et al., 1997) and phosphorylation of GSK-3β induces glycogen synthesis (Frame and Cohen, 2001).

On the other hand, autophosphorylation of the activated IR also creates a docking site for growth factor receptor-bound protein-2 (Grb2) that subsequently attracts the guanine nucleotide-exchange factor son of sevenless (SOS) to the receptor (Pronk et al., 1993, Li et al., 1993, Chardin et al., 1993). As the name suggests, the SOS protein catalyses the conversion of GDP to GTP resulting in the activation of the Ras protein that is required for subsequent activation of the cascade of Raf protein kinase, Erk kinases (MEK) 1/2 and extracellular signal-regulated kinases (Erk) 1/2. In the cytosol, activated Erk1/2 phosphorylates and activates the 90 kDa ribosomal S6 kinase ($p90^{RSK}$) family; an important group of proteins involve in the regulation of translation during cell growth, proliferation and survival (Anjum and Blenis, 2008). Activated Erk1/2 can also translocate into the nucleus where it regulates gene expression *via* activation of mitogen- and stress-activated kinases (MSK) and a variety of transcription factors such as Elk-1, FoxO3, c-Myc, c-Fos etc (Mendoza et al., 2011, Chen et al., 1992).

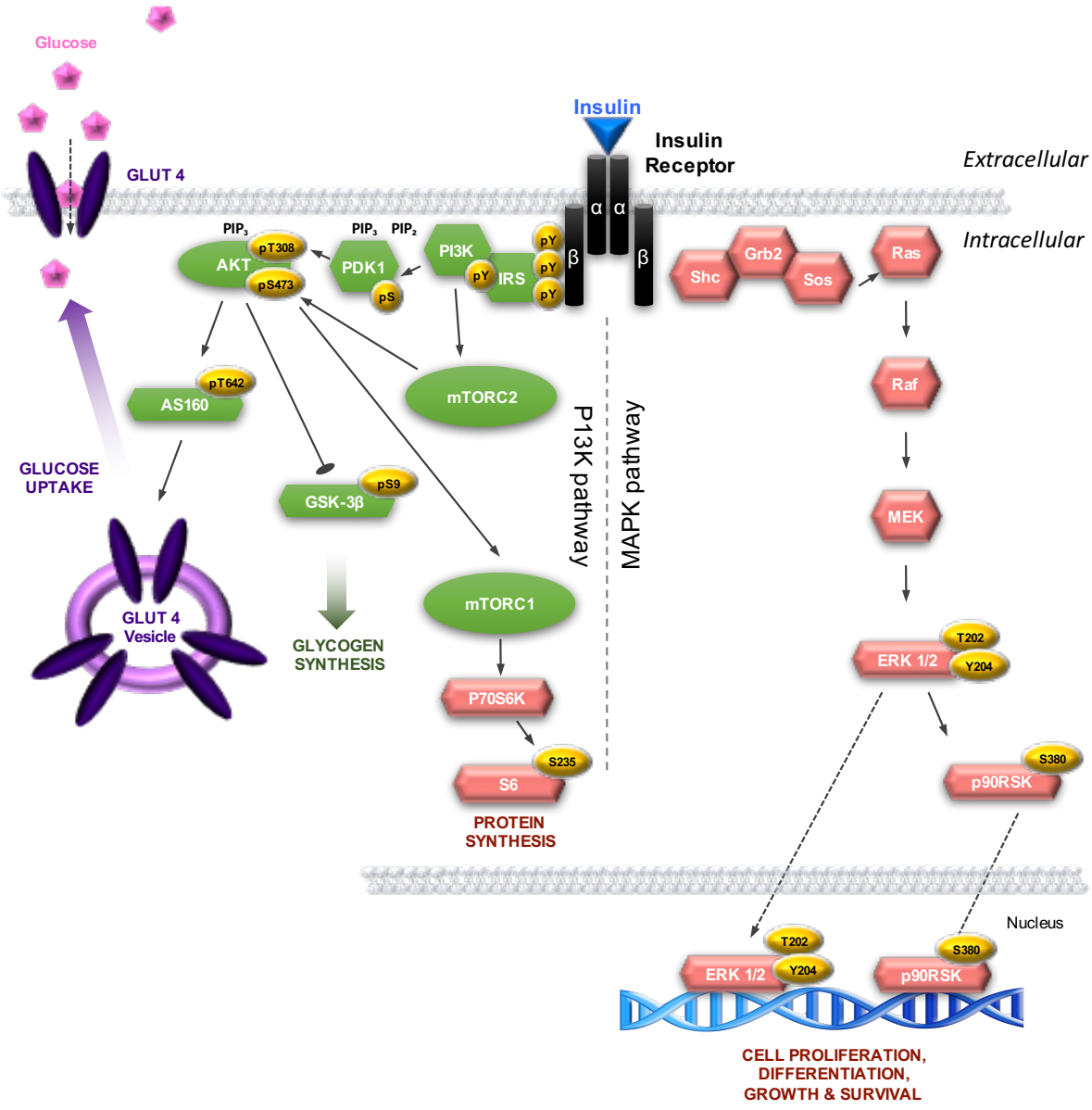
Glucose
GLUT 4
Insulin
Insulin Receptor
Extracellular
Intracellular
α
α
β
β
PIP3
PIP3
PIP2
AKT
pT308
pS473
PDK1
pS
PI3K
IRS
pY
pY
pY
pY
Shc
Grb2
Sos
Ras
Raf
MEK
ERK 1/2
T202
Y204
p90RSK
S380
AS160
pT642
mTORC2
GSK-3β
pS9
GLUCOSE UPTAKE
GLUT 4 Vesicle
GLYCOGEN SYNTHESIS
mTORC1
P70S6K
S6
S235
PROTEIN SYNTHESIS
P13K pathway
MAPK pathway
Nucleus
CELL PROLIFERATION, DIFFERENTIATION, GROWTH & SURVIVAL

Figure 1.16 Insulin signalling *via* Akt/PI3K and Erk/MAPK pathways. Insulin (*blue; triangle*) actions *via* insulin receptor (IR; *black complex*) by modulating a cascade of intracellular mediators through a series of phosphorylation/dephosphorylation events. Insulin stimulation results in two major signalling pathways: *phosphatidylinositol 3-kinase* (PI3K) pathway and *mitogen-activated protein kinase* (MAPK) pathway for regulations of a diverse cellular functions generally categorized to metabolic (adaptor proteins in *green*) or mitogenic (adaptor proteins in *pink*) responses. Activated IR undergoes conformational change and autophosphorylations that allow recruitment and activation of *insulin receptor substrate* (IRS) proteins for the subsequent activation of PI3K regulatory subunit and *phosphoinositide-dependent kinase 1* (PDK1). In the proximity of cell membrane, Akt (also known as *protein kinase B*; PKB) is partially activated when phosphorylated at Thr308 by the PDK. Full activation of Akt requires phosphorylation of Ser473 by the *mammalian target of rapamycin complex 2* (mTORC2). Akt plays an important role in PI3K pathway as a key kinase modulator for a diverse range of downstream effector proteins. In muscle and fat cells, the activated Akt regulates metabolism through activation of *Akt substrate of 160 kDa* (AS160; originally known as TBC1D4) *via* phosphorylation at multiple sites including Thr642. Activated AS160 promotes translocation of *glucose transporter type 4* (GLUT4) to the plasma membrane for glucose uptake. Akt also induces glycogen synthesis *via* inhibition of *glycogen synthase kinase-3β* (GSK-3β) *via* phosphorylation of Ser9. Through activation of mTORC1 complex, Akt also regulates mitogenic responses such as upregulation of protein synthesis *via* activations of *70 kDa ribosomal s6 kinase* (p70-S6K) and S6 ribosomal protein. The mitogenic Erk/MAPK pathway is activated by insulin following the formation of Shc/Grb2/SOS complex. Shc: *src homology 2 domain containing*; Grb 2: *growth factor receptor-bound protein 2*; SOS: *Son of Sevenless*. The complex recruits and activates the small GTPase Ras that initiates a phosphorylation cascade of activating *rapidly accelerated fibrosarcoma* (Raf), *mitogen-activated protein kinase* (MEK1/2) and *extracellular-signal-regulated kinase 1/2* (ERK1/2). Activated ERKs promote several mitogenic responses including cell growth, survival and cellular differentiation. For instance, activated ERKs can act as a transcription factor and also as a kinase that phosphorylates and activates *p90 ribosomal protein s6 kinase* (p90 RSK) for increasing gene expression critical for cell growth.

However, it is important to not overly simplify the insulin signalling network as signal integration and crosstalk can exist at multiple levels between PI3K and MAPK signalling pathways (Carel et al., 1996, Katso et al., 2001, Dann et al., 2007, Shaul and Seger, 2007, Franke, 2008, Gehart et al., 2010, Mendoza et al., 2011, De Luca et al., 2012, Vadlakonda et al., 2013). For instance, Akt and Erk share an overlapping role in the regulation of protein synthesis (mitogenic response). In an mTORC-dependent pathway, both Akt and Erk can phosphorylate and inhibit tuberous sclerosis complex-1/2 (TSC1/2) that subsequently leads to the downstream activation of mammalian target of rapamycin complex 1 (mTORC1) and 70 kDa ribosomal S6 kinase-1/2 (p70-S6K) for the upregulation of protein translation (reviewed in (Mendoza et al., 2011)). Furthermore, negative feedback also exists between the two pathways; where Akt negatively regulates Raf and Erks negatively regulate IRS for PI3K docking (recently summarised in (Arkun, 2016)).

1.9.2 Signalling Bias *via* Insulin Receptor

The complexity of IR signalling suggests possibilities to design insulin analogues that could promote desirable biased-signalling. In the case of insulin analogues for diabetes treatment, efforts have been made to design new analogues that selectively activate PI3K signalling for metabolic responses (glucose uptake) but do not promote mitogenic MAPK signalling *via* the IR (Glendorf et al., 2011, Vienberg et al., 2011, Jiracek and Zakova, 2017). The design of metabolically-biased insulin analogues allows a refined efficacy of glucose lowering action and would remove any safety concerns of insulin-related cancer risk. Nonetheless, the journey to such accomplishment has been challenging as we have yet been able to define the key determinants of IR signalling selectivity.

Only limited examples of signalling-biased insulin analogues or mimetics are available for the investigation. These include the mitogenically-biased insulin X10 (Hansen et al., 2011) and the metabolically-biased S597 peptide (Jensen et al., 2007, Rajapaksha and Forbes, 2015) and IR-A48 aptamer (Yunn et al., 2015). Two major mechanisms that have been proposed to promote signalling bias are the rate of receptor internalisation and the preferential phosphorylation pattern/kinetics of receptor β-subunits.

1.9.3 Insulin Receptor Internalisation & Signalling Selectivity

Insulin receptor internalisation and its association to differential signalling is a relatively new concept in the understanding of IR signalling bias. In recent years, several groups propose that ligand-dependent IR internalisation and sorting can directly modulate the duration and intensity

of receptor signalling. Particularly, emerging evidence supports that IR-A internalisation is a required mechanism to promote optimal and sustainable IR-A-dependent mitogenic signalling (Rajapaksha and Forbes, 2015, Giudice et al., 2013, Giudice et al., 2011, Jensen et al., 2007, Foti et al., 2004, Leof, 2000).

The mechanism of ligand-mediated endocytosis of IR and its role in receptor signalling is not fully understood (see review (Morcavallo et al., 2014)). Briefly, based on the current understanding, IR internalisation involves two steps: first, upon ligand binding, IR autophosphorylation promotes receptor redistribution from the microvilli to the nonvillous domain of the cell. Second, the translocated IR is either anchored within clathrin-coated pits to allow internalisation into an endosome (Carpentier et al., 1993) or internalised through a clathrin-independent pathway (Smith et al., 1991, Smith and Jarett, 1990, McClain and Olefsky, 1988, Fagerholm et al., 2009). The low pH environment within the endosome leads to rapid release of ligand from the IR, which is then targeted to lysosomal degradation, effectively downregulating receptor signalling. The receptor can also be recycled back to cell surface ready for another ligand binding (Morcavallo et al., 2014).

Receptor sorting and trafficking directly modulates the availability of cell surface receptors for ligand binding and initial receptor activation, thereby effectively regulating IR signalling. Based on this model, Marcavollo *et al.* suggests that ligands with lower binding affinity for the IR-A, (such as IGF-II compared to insulin) are significantly less effective in promoting IR-A internalisation for degradation. Thus, IGF-II is able to promote sustainable mitogenic signalling *via* cell surface IR-A (Morcavallo et al., 2012). Interestingly, they also reported that, upon prolonged stimulation by insulin, IR-A internalisation *via* clathrin-dependent pathway was found preferentially to activate Akt, whereas IR-A internalised *via* an clathrin-independent pathway preferentially activates Erk (Morcavallo et al., 2012). This suggests that in addition to the potency of promoting IR internalisation, the process of endocytosis is also an important "check-point" for the regulation of differential signalling within the cell.

In contrast, other groups including our laboratory, proposed that IR internalisation is an important mechanism that ensures sustainable mitogenic signalling *via* intracellular interaction and activation of Shc and SOS (see Fig. 1.17). Prior to receptor degradation or recycling, ligand that is able to promote receptor internalisation continues to activate MAPK signalling within the early endosome. Contrary to Morcavollo *et al.*'s study, Giudice *et al.* demonstrated that IGF-II promotes faster IR-B internalisation compared to insulin and this correlates with its mitogenic responses stimulated through the internalised endosome. On the other hand, insulin seems to

promote metabolic responses mainly *via* cell surface IR-B (Giudice et al., 2013, Giudice et al., 2011). Also, using a metabolically-biased insulin mimetic (S597), two separate groups demonstrated that perturbed IR-A internalisation correlates strongly with reduced mitogenic potentials *via* Shc and Erk activation; while retaining full metabolic action *via* Akt activated at the cell surface (Jensen et al., 2007, Rajapaksha and Forbes, 2015).

Although the mechanisms that regulate the fate of the IR are still poorly understood, the process clearly plays a critical role in fine-tuning the signalling intensity and outcome of the activated receptor. A major limitation in the previously described studies is the possible signalling bias that exists between peptides have different binding affinities for the receptor and are also structurally different from each other. What is required is a study of signalling-biased insulin analogues that have equipotent IR binding affinities to native insulin, for their resultant mitogenic and metabolic responses.

In addition to measuring the rate of receptor internalisation, studies of signalling molecule cellular localisation also provide further evidence to support the correlation between receptor internalisation and mitogenic signalling. Endosomally located IR-A is also found to co-localise with signalling proteins such as Grb2, Shc and Erk 1/2 that are associated with mitogenic MAPK signalling (Pol et al., 1998, Di Guglielmo et al., 1994). Disruption of IR internalisation significantly reduces insulin-induced phosphorylation and activation of Shc and Erk; but does not affect phosphorylation of IRS-1 and Akt (Jensen et al., 2007, Ceresa et al., 1998, Hamer et al., 2002, Biener et al., 1996). Additionally, *ex vivo* subcellular fractionation of rat skeletal muscles also leads to an increased membrane localisation of Akt2 and AS160 upon insulin stimulation (Zheng and Cartee, 2016).

The different mechanisms of promoting Akt/PI3K and Erk/MAPK signalling is also reflected in the different activation kinetics of the two pathways, recently reviewed in (Haeusler et al., 2018). Phosphorylation of Akt2 occurs rapidly and peaks within 2 minutes after insulin stimulation, while phosphorylation of Erk peaks between 2 – 5 minutes (Humphrey et al., 2015). Essentially, the temporal activation and subcellular distribution profiles of the key adaptor proteins of PI3K and MAPK signalling pathways suggest that Akt/PI3K activation required for a metabolic response is most likely promoted *via* activation of cell surface IR, while a sustainable mitogenic Erk/MAPK signalling can only be achieved when coupled with activation through endosomal IR-A.

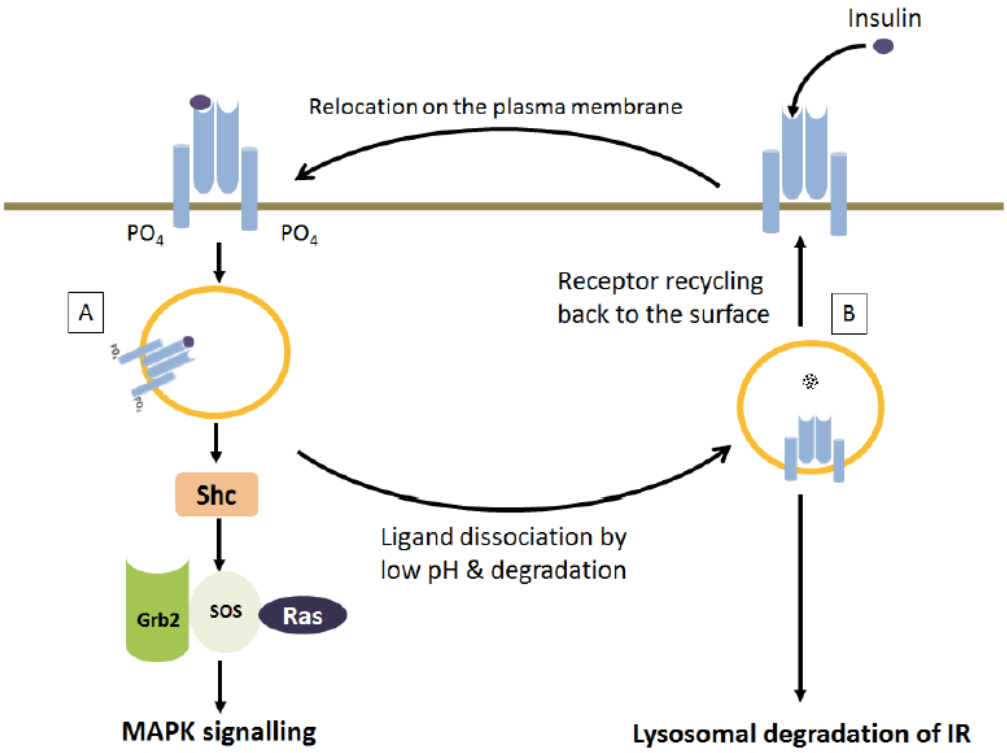

Figure 1.17 Insulin-mediated internalisation and trafficking of insulin receptor. Insulin binding promotes insulin receptor (IR) activation, relocation and internalisation into an endosome. (A) Within the endosome, the insulin-bound IR activates MAPK signalling pathway *via* a sequential phosphorylations of SHC, Grb2, SOS and Ras. Low pH within the endosome leads to the dissociation of insulin from the IR. (B) The free IR can either be targeted to lysosomal degradation or recycled back to the cell surface for binding of a new insulin molecule. From (Rajapaksha, 2013).

1.9.4 IR Phosphorylation Pattern & Signalling Selectivity

Understanding of the receptor internalisation and its role in influencing signalling bias can be gained by deciphering the signals that initiate or prevent IR internalisation. Several studies suggest that the process is dependent on the phosphorylation pattern, potency or kinetics at different intracellular domains of the β-subunits. Carpentier *et al.* reported that phosphorylation of Y1146, Y1150 and Y1151 sites located within the activation loop, but not Y1316 and Y1322 (on CT region) is required for the process (Carpentier et al., 1993). Braiman *et al.* reported that protein kinase C δ (PKCδ) plays an important role by phosphorylating the T1336 residue located at the CT region and is required for insulin-stimulated IR internalisation (Braiman et al., 2001). Furthermore, Y960 on the JM domain is associated with IR mitogenic signalling and may also play a role in the regulation of receptor internalisation (Backer et al., 1991, Backer et al., 1992). Interestingly, it appears that rather than the phosphorylation of Y960 site, the structural integrity around this residue is more important for promoting receptor internalisation. Mutation of the Y960 residue to an alanine significantly disrupts receptor internalisation, whereas Y960 mutation to a phenylalanine, that also has an aromatic side chain, has no effect on IR endocytosis (Carpentier et al., 1993).

Furthermore, recent investigation of the IR phosphorylation pattern in response to insulin mimetics reveals several important but contradictory insights. Based on a dose-response study using the "highly mitogenic" insulin analogue X10, Hansen *et al*. suggested that the preferential phosphorylation of the Y972 and Y1158 promotes mitogenic responses, whereas preferential phosphorylation of the *C*-terminal end of IR (Y1334) leads to metabolic signalling (Hansen et al., 2011). Using a "highly metabolic" agonistic aptamer (IR-A48) that binds to the IR Yunn *et al.* revealed metabolic-biased signalling is associated with preferential phosphorylation of the Y1150 residue (Yunn et al., 2015). In the same year, Rajapaksha *et al.* from our laboratory also suggested that depending on the type of stimulating ligand, IR-A internalisation and its associated mitogenic potential can be independently regulated by modulating either the phosphorylation potency or kinetics of several receptor tyrosine residues (Y960, Y1146, Y1150, Y1151, Y1316 and Y1322). Compared to insulin, reduced mitogenic potential of IGF-II ligand is associated with its reduced potency for stimulating IR-A tyrosine phosphorylation and receptor internalisation. In contrast, the reduced IR-A internalisation rate promoted by the poorly mitogenic S597 insulin mimetic is associated with slower IR-A tyrosine phosphorylation kinetics.

In summary, current evidence that describe insulin signalling bias is lacking and highly controversial. One major limitation in these studies are bias arising from the use of insulin mimetics with different structural properties or different receptor binding potency. Ultimately, a better understanding of insulin signalling regulation will open a new avenue for designing insulin analogues with selective therapeutic traits that is ideally metabolically effective and mitogenically safe.

1.10 INSULIN DISULFIDE BONDS

1.10.1 Evolution, Properties and Formation of Disulfide Bonds

Disulfide bonds are covalent linkages formed between the thiol groups (–SH) of two cysteine (Cys) residues under oxidative conditions. The cysteine residue is the only residue that allows disulfide pairing. It is also the second most evolutionarily conserved amino acid, surpassed by tryptophan (Gonnet et al., 1992). The number, position and the characteristic of protein disulfide bonds are also highly conserved among all insulin-like proteins in vertebrates (Steiner, 1988), including the closely related members of the insulin superfamily; insulin, IGF-I, IGF-II (Humbel, 1990), relaxin (Schwabe and McDonald, 1977) and bombyxin (Nagata et al., 1995).

The formation of disulfide bonds involves reduction of oxygen, presence of oxidized glutathione (GSSG), flavin cofactor and other disulfide bonds. Under *in vitro* oxidative conditions protein disulfide pairing can occur spontaneously, where oxygen acts as the electron acceptor. In eukaryotes, disulfide bond formation occurs mainly within the endoplasmic reticulum (ER) and the process is often catalysed by oxidoreductases such as thioredoxin (Trx) (Mahmood et al., 2013) and the members of protein disulfide isomerase (PDI) family (Hatahet and Ruddock, 2009, Feige and Hendershot, 2011, Sevier and Kaiser, 2002).

The formation and stability of a disulfide linkage is defined by its redox potential, *ie.* the tendency to be reduced in a redox environment (Jensen et al., 2009). Redox potential is measured relative to glutathione and can range from –95 to –470 mV. The more negative the redox potential, the more stable the disulfide bond (Wouters et al., 2010). Several factors that may affect the redox potential and the rate of disulfide bond formation include (1) the redox environment, whereby oxidizing conditions favour disulfide formation; (2) thiol pKa of both nucleophilic-cysteine and the leaving thiol group, whereby decreased pKa increases rate of thiol-disulfide exchange; (3) entropy barriers influenced by the physical proximity of two cysteine groups, whereby closer cysteine proximity reduces the entropic cost and thus allows a faster rate

of disulfide formation; and finally (4) protein structural strain exerted by the disulfide bond also affects disulfide stability, whereby disulfide bond distorted from the ideal torsional angle of ± 90° may significantly reduce disulfide stability (Sato and Inaba, 2012, Bechtel and Weerapana, 2017).

1.10.2 Classification of Disulfide Bonds

The classification of disulfide bonds is based on their two major functional roles: structural disulfides and redox disulfides; the latter is also subcategorised into small molecule disulfides, catalytic disulfides and allosteric disulfides (see review (Bechtel and Weerapana, 2017)). Each disulfide bond constitutes of 6 atoms: C_α– C_β – S_γ – S_γ' – C_β' – C_α'. The rotation of each bond linking between two atoms defines the torsional angle of the disulfide bond. In 2006, Prof. Hogg P. J. and colleagues analysed the geometry and torsional strain of 6874 disulfide bonds in 2776 protein X-ray crystal structures and identified a total of 20 disulfide bond configurations based on 5 torsional angles (χ_1, χ_2, χ_3, χ_2'and χ_1') that define the cysteine residues (see Fig. 1.18*A*) (Schmidt et al., 2006). Later, they also confirmed the same disulfide configurations can exist in NMR structures (Schmidt and Hogg, 2007). More recently, Haworth *et al.* further refined the disulfide classification through computational studies correlating disulfide torsional energies to the disulfide redox potentials in proteins (Haworth et al., 2010).

Generally, the torsional angles of the χ_2, χ_3 and χ_2'defines the three types of disulfide bonds; which include the low energy spiral ($\chi_2 \sim 60°$, $\chi'_2 \sim 60°$ and $\chi_3 < 80°$), hooks ($\chi_2 \sim 60°$, $\chi'_2 \sim 300°$ and $\chi_3 = 80°$ or 90°) and the high energy staple ($\chi_2 \sim 280°$, $\chi'_2 \sim 280°$ and $\chi_3 = 120°$). A positive or negative χ_3 torsional angle is further characterised as having a right- or left-handed configuration, respectively. The torsional angles of χ_1 and χ_1' can also be treated symmetrically (– or +) or asymmetrically (–/+ or +/–) (Schmidt et al., 2006, Schmidt and Hogg, 2007). The categorisation of disulfides based on their configurations and torsional energies has vastly enhanced our understanding and prediction for the different functions of disulfide bond further described below.

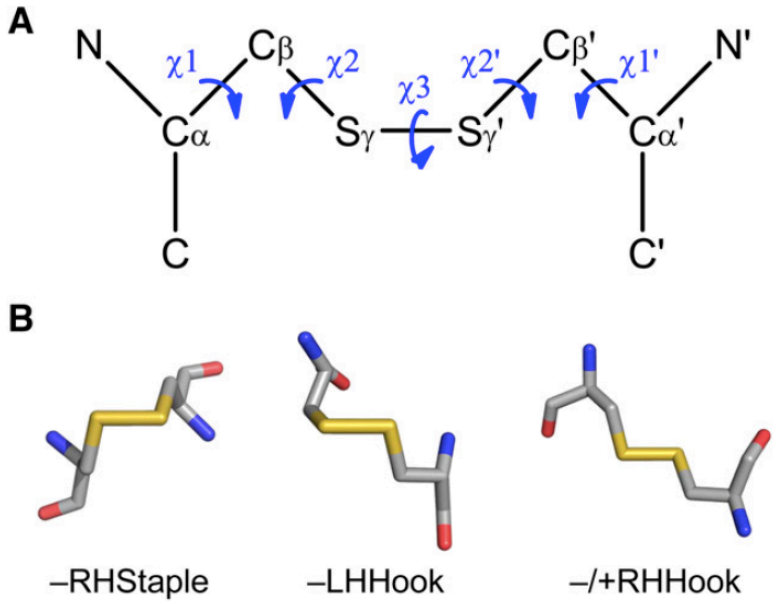

Figure 1.18 Classification of disulfide bonds and configurations of allosteric disulfide bonds. (A) The disulfide bond can adopt up to 20 known configurations. Each disulfide bond is comprised of 6 atoms: C_α– C_β – S_γ – S_γ' – C_β' – C_α'. The classification of disulfide bond is based on their geometry defined by the 5 torsional angles (χ_1, χ_2, χ_3, χ_2'and χ_1') linking the 2 Cα of the cystine residue. The C_α is the main chain carbon atom while the C_β is the side chain carbon atom of each cysteine residue. The χ angles can either be positive or negative. The 3 basic types of bond configurations are spirals, hooks, and staples defined based on the signs of the central 3 angles. The bond is denoted as being either right-handed (RH) or left-handed (LH) on the basis whether the χ_3 angle is positive or negative, respectively. (B) Examples allosteric disulfide bond configurations: –RH Staple, –LH Hook, and -/+RH Hook. From (Butera et al., 2014).

1.10.2.1 *Structural Disulfides*

Traditionally, a structural disulfide bond is understood to act as a motif important for maintaining protein structure and stability. Unsurprisingly, the structural disulfides are predominantly found in the low energy –LHspiral and +RHspiral configurations (Schmidt et al., 2006) and can have redox potentials as low as –470mV (Gilbert, 1990). The correct pairing of structural disulfides is particularly important for proteins destined as plasma proteins or secreted proteins. Exposure to the highly oxidizing extracellular environment can induce spontaneous disulfide pairing that may disrupt the protein structure Thus to prevent protein instability, formation of structural disulfides usually occurs within the oxidizing environment of the ER or other cellular compartments in a controlled manner catalysed by oxidoreductases. Once established, the structural disulfides remain static and usually do not undergo breakage and reformation (Depuydt et al., 2011).

1.10.2.2 *Redox Disulfides*

More recently, the functional role of disulfide bond in the regulation of protein activity and localization through redox reactions has been recognised. Redox disulfides generally have greater redox potentials (more positive) than structural disulfides and can adopt different configurations upon breakage and reformation of these bonds. The formation of redox disulfides can be achieved *via* thiol-disulfide exchange between a protein cysteine thiol and a small molecule thiol or within intramolecular thiol groups such as in the catalytic and allosteric disulfides.

1.10.2.2.1 *Small Molecule Disulfides*

The formation of small molecule disulfides can be achieved *via* glutathionylation or cysteinylation pathways. Glutathionylation involves thiol-disulfide exchange between a thiol group on a protein and thiol group of an oxidised glutathione (GSSG) forming a mixed disulfide linkage (Pastore and Piemonte, 2012). Cysteinylation refers to the formation of mixed disulfide bonds involving linkage between a thiol group on the protein cysteine and a thiol group from a free cysteine residue (Couvertier et al., 2014). Examples of small molecule disulfides include the glutathionylation of nuclear factor kappa light chain enhancer of activated B cells (NF-κβ) that modulates transcriptional activity (Pineda-Molina et al., 2001, Siebenlist et al., 1994) and cysteinylation of superoxide dismutase 1 (SOD1) that is protective against oxidative damage (Auclair et al., 2013).

1.10.2.2.2 Catalytic Disulfides

Catalytic disulfides are found in oxidoreductases such as, protein disulfide isomerases (PDI), thioredoxin (Trx) and glutaredoxin (Grx). Most oxidoreductases catalyse the formation of disulfides, reduction and isomerisation *via* redox reaction between the catalytic disulfide on their active motif and the thiol group on the target proteins. Critical to their function, the catalytic disulfides have redox potentials ranging from –95 to –330 mV (Wunderlich and Glockshuber, 1993, Huber-Wunderlich and Glockshuber, 1998, Lin and Kim, 1989, Aslund et al., 1997). The catalytic disulfides are predominantly in the +/–RHhook configuration (Schmidt et al., 2006). Dysregulated formation of catalytic disulfides can be detrimental and has been associated with several diseases, such as Parkinson's disease, HIV-1 viral infection, thrombosis, cancer and aging ((Mahmood et al., 2013, Lillig and Holmgren, 2007, Auwerx et al., 2009), reviewed in (Bechtel and Weerapana, 2017)).

1.10.2.2.3 Allosteric Disulfides

The allosteric disulfide is a relatively new disulfide class characterised by its ability to modulate the function of its residing protein. As its name would suggest, the bond is able to regulate the conformational change of a distantly located region of the protein upon breakage and reformation of the linkage through redox reaction.

Among the 20 different disulfide bond configurations, the allosteric disulfides were found predominantly in three configurations (–RHstaple, –LHhook and –/+RHhook bonds; see Fig. 1.18*B*) that constitute to ~20 % of the total disulfide bonds analysed in X-ray crystals (Schmidt et al., 2006). It was also found that the prevalence of the allosteric –RHstaple bond is higher than the catalytic +/ -RHHook bond suggesting an allosteric disulfide bond may have significant biological roles. Currently, just over 30 examples of redox sensitive allosteric disulfides have been described; some are involved in regulating protein function for normal biological processes such as thrombosis and haemostasis (Butera et al., 2014); others are involved in pathological processes such as cancer (Hogg, 2013) and viral infections (Wouters et al., 2004).

Owning to its short history, the mechanism of allosteric disulfide action has not been fully elucidated. Interestingly, two out of the 3 configurations (–RHstaple and –/+RHhook bonds) were shown to be under more topology stress compared to the other 18 disulfide configurations. Hence, it was hypothesized that the "pre-stressed" condition may be an important feature of an allosteric disulfide and the stress primes these bonds for an accelerated reduction/cleavage required for protein function. The –LHhook, however, is not under more stress compared to the

other disulfide configurations and its underlying mechanism associated with its allosteric function is still unclear (Zhou et al., 2014, Schmidt et al., 2006).

In summary, it is now evident that disulfide bonds play important roles in protein function beyond their roles in maintaining protein stability. The ability to better define the different classes of disulfide bonds has improved our understanding of protein structure and function.

1.10.3 Insulin Disulfide Bonds

Human insulin consists of three disulfide bonds — one intra-chain (Cys^{A6}-Cys^{A11}) and two inter-chain (Cys^{A7}-Cys^{B7} and Cys^{A20}-Cys^{B19}) (Fig. 1.6*B*). Formation of these disulfide linkages ensures both the correct folding of the insulin precursor polypeptide and the structural stability of the mature hormone (Weiss, 2009b, Chang et al., 2003). In the endoplasmic reticulum, the disulfide pairings play an important role in directing the correct folding of the single chain proinsulin before it is being processed into a mature two-chained insulin molecule. The formation of the two inter-chain disulfide bonds is necessary for holding the two polypeptide chains in place and formation of the insulin core, while the Cys^{A6}–Cys^{A11} further stabilises the hormone. (Miller et al., 1993). In its correctly-folded conformation, most non-polar hydrophobic residues are clustered within the core. The inter-chain Cys^{A20}–Cys^{B19} bond is buried deepest within the core with minimal accessibility and is most likely a structural disulfide. The other inter-chain disulfide bond, Cys^{A7}–Cys^{B7}, is relatively flexible and is partly surface exposed. The intra-chain Cys^{A6}–Cys^{A11} bond is also buried within the hydrophobic core sandwiched between the two chains (Weiss et al., 2000). The functional roles of Cys^{A7}–Cys^{B7} and Cys^{A6}–Cys^{A11} are not well understood.

Insulin is a relatively small and compact molecule. To ensure correct folding of such a small hormone, correct pairing of disulfides in the correct order is essential. The oxidative folding and the order of successive disulfide pairings of insulin were probed *via* kinetic trapping of insulin folding-intermediates. This approach also integrates the knowledge of classical disulfide pairing and biophysical paradigms of protein folding. The current proposed mechanism of insulin disulfide pairing has been reviewed in (Weiss, 2009a). Based on the equilibrium models, the proposed pathways of insulin disulfide pairings begin with the formation of Cys^{A20}–Cys^{B19} which brings together the conserved aliphatic and aromatic side chains within the hydrophobic core. Subsequently, insulin folding can proceed *via* alternative pathways to form either the inter-chain Cys^{A7}–Cys^{B7} first or the intra-A-chain Cys^{A6}–Cys^{A11} linkage first, and then eventually forming the native insulin conformation.

Regardless of the order of insulin formation, it is undeniable that all three disulfide bonds are required for the optimal function and stability of insulin. Insulin analogues with deletion of any of the 3 disulfide linkages (Dai and Tang, 1996, Hua et al., 1996, Chang et al., 2003), elongated linkages ([$Hcy^{7,20}$-A] insulin; homocysteine inter-chain disulfide linkages of sheep insulin) (Cosmatos and Katsoyannis, 1975), rearranged linkages ([A7–A11, A6–B7-cystine]- and [A6–A7, A11–B7-cystine]-insulin) (Sieber et al., 1978) or with disulfide bond with altered configurations ($_{D\text{-form}}$ cysteine isomers) (Marki et al., 1979) all result in poor activity of insulin and, in some cases, loss of structural integrity.

Intriguingly, introducing an additional disulfide bond to insulin provided a surprising insight into the structural dynamics of insulin. In an attempt to improve protein stability through incorporating an additional disulfide bond to the native insulin, six analogues were designed containing additional linkages from A10 residue to the first 6 residues on the *C*-terminal end of B-chain (B1-B6). However, only two analogues (A10C–B3C and A10C–B4C) gained stability and only the A10C-B4C analogue showed improved activity. The other analogues showed reduced activity and stability to various extents, suggesting that, although disulfide bonds are known to provide structural stability to insulin, an additional linkage does not necessarily provide an added benefit. Subtle changes in the location of the residing disulfide bond can result in drastically different effects on the activity and stability of insulin (Vinther et al., 2015a, Vinther et al., 2013, Vinther et al., 2015b).

Collectively, these studies suggest that the modification of evolutionarily conserved insulin disulfide linkages are generally not well tolerated and can severely affect insulin function and structural integrity. Importantly, it also appears that the location, length, configuration and correct pairing of each insulin disulfide bond can critically affect the functionality of the linkages.

1.10.3.1 ***Understanding the Cys^{A6}–Cys^{A11} Insulin Disulfide Bond***

Deletion of the two structural disulfides Cys^{A20}–Cys^{B19} and Cys^{A7}–Cys^{B7} has severe consequences, resulting in inactive analogues with significantly disrupted secondary structures. Deletion of the intra-chain Cys^{A6}–Cys^{A11} linkage has the least impact on the overall structure of insulin with most of its helical contents retained. However, the analogue binds poorly to the IR, with a relative binding affinity of less than 0.02% of native insulin (Dai and Tang, 1996, Hua et al., 1996, Chang et al., 2003, Li et al., 2012). Coincident with reduced structural intergrity, all analogues with a deleted disulfide linkage(s) are also more susceptible to enzymatic proteolysis and amyloidogenicity (Chang et al., 2003, Li et al., 2012).

Loss of the Cys^{A6}–Cys^{A11} disulfide linkage within the monomeric insulin analogue [Asp^{B10}, Lys^{B28}, Pro^{B29}]-human insulin (DKP-insulin) also has similar effects; retaining overall structure of an insulin molecule but having very poor receptor binding and metabolic signalling potency (Weiss et al., 2000, Hua et al., 1996). While most of the three-dimensional structure is maintained, the short A1–A8 segment that usually forms the first helix A chain is unfolded due to the loss of Cys^{A6}–Cys^{A11} bond. The structure and functional analysis of this analogue provides several insights to the understanding of function of the insulin Cys^{A6}–Cys^{A11} disulfide bond: (1) The folding of insulin native structure is independent on the A1–A8 region and Cys^{A6}–Cys^{A11} disulfide bond. (2) The native A1–A8 α-helix is also not required to nucleate the hydrophobic core or to specify the orientation between chains for the other two inter-chain disulfide to pairing. (3) The helical conformation of stabilisation of the A1–A8 segment by Cys^{A6}–Cys^{A11} disulfide bond is essential for optimal insulin activity (Hua et al., 1996, Weiss et al., 2000).

In summary, although not directly involved in ligand: receptor interaction, all 3 disulfide bonds play important roles in maintaining and regulating the biologically active conformation of insulin. Although it is not surprising that the loss of either inter-chain disulfide bonds significantly affects insulin's functionality due to the loss of structural integrity, it was not apparent how Cys^{A6}–Cys^{A11} bond plays a role in insulin function. Critically, surrounding the Cys^{A6}–Cys^{A11} bond are several receptor binding hotspots; including the Gly^{A1}, Ile^{A2}, Val^{A3} and Gln^{A5} residues (De Meyts et al., 2004, Huang et al., 2004). While the loss of Cys^{A6}–Cys^{A11} apparently causes the least perturbation of insulin's structure, the configuration and flexibility of Cys^{A6}–Cys^{A11} linkage may be an important regulatory mechanism that influences the flexibility of A1–A8 segment that forms the receptor recognition α-helix. Similar flexibility in the region of Cys^{A6}–Cys^{A11} disulfide bond is also found in IGF-I (Guo et al., 2002) and relaxin (Tang et al., 2003).

1.11 CHEMICAL SYNTHESIS & DISULFIDE ISOSTERES

1.11.1 Chemical Synthesis of Insulin and Insulin-related Peptides

Chemical synthesis of peptides within the insulin superfamily serves as a new strategy to produce insulin-related peptides. Although yield from chemical synthesis method does not permit scale up to large-scale manufacture, this method provides the abillity to synthesise unique and unconventional insulin-related peptides. The continuing innovation in chemical synthesis methodologies allows modern design of peptide analogues that can aid our understanding of

insulin's structure-function relationship and that correspondingly inspire fundamental structural refinements for drug discovery.

The two most challenging obstacles of insulin chemical synthesis are (1) the correct pairing and formation of disulfide bonds and (2) the assembly of the A-chain and B-chain. The history and methods of insulin chemical synthesis have been extensively reviewed previously ((Belgi et al., 2011, Liu et al., 2016, Hossain and Wade, 2017)) and are discussed briefly here.

The first series of successful total chemical synthesis of insulins was achieved *via* solution phase synthesis by three independent groups (Katsoyannis et al., 1966, Kung et al., 1965, Meienhofer et al., 1963). Although the overall yield was poor (< 1%), the success signifies one of the most significant scientific achievements in protein chemistry. In 1963, Merrifield introduced a solid-phase peptide synthesis (SPPS) approach that significantly improved yields to 20 – 40% (Marglin and Merrifield, 1966, Merrifield, 1963), which became the basis of today's chemical synthesis approach. The ongoing refinement of the SPPS method has led to a substantial improvement in the synthesis of individual A- and B-chain of insulin peptide. However, successful combination of the two individual chains to yield the final product requires correct pairing of disulfide bonds.

The disulfide pairing of the chemically synthesized peptides can be achieved *via* two general approaches. The first approach involves spontaneous disulfide formation either through random chain combination or *via* assisted-folding through synthesis of a single chain biomimetic. The random chain combination method relies on the instinctive protein folding of the peptide under oxidative condition in the presence of reducing agent. Although this method has been later optimised by Du *et al.* from 5% to 70 % yield, the method is laborious and inefficient (Du et al., 1961, Du et al., 1965). The highly efficient folding of the single chain proinsulin inspired an alternate single chain insulin (SCI) method. The SCI precursor demonstrated improved folding efficacy (> 70% yield) that is subjected to a second step of selective proteolysis for the harvest of the final two-chain active insulin analogues (Zaykov et al., 2014, Qiao et al., 2001, Chang et al., 1998, Markussen et al., 1985).

Application of the two strategies described above to the production of insulin analogues with varied stabilities has not been particularly successful. A low yield of insulin analogues with reduced thermodynamic stability synthesized is seen with this method (Mayer et al., 2007). To overcome this, an alternative method was developed; utilizing orthogonally protected cysteines that enable directed and sequential regioselective disulfide pairings (Akaji et al., 1993, Burnley

et al., 2015, Hossain and Wade, 2017, Karas et al., 2014, Robinson et al., 2009, Shabanpoor et al., 2013). Several orthogonal cysteine protective groups used include acetamidomethyl (Acm), trityl (Trt) and *tert*-butyl (*t*Bu) which can be deprotected with iodine, acidic and silyl chloride-sulfoxide treatment, respectively (Akaji et al., 1993). A major advantage of this method is its improved disulfide pairing accuracy and the ability to monitor and purify each synthesis step through liquid chromatography.

1.11.2 Disulfide Isostreic Replacement within the Insulin Superfamily

As evident in the previously described studies, manipulation of insulin disulfide bonds is not well tolerated, whether it is the removal (Dai and Tang, 1996, Chang et al., 2003, Hua et al., 1996), elongation (Cosmatos and Katsoyannis, 1975), rearrangement (Sieber et al., 1978) or even addition (Vinther et al., 2013) of the linkage. Such limitations partially account for the delayed understanding of the functional role of insulin's disulfide bonds.

The successful introduction of an isosteric bond that closely resembles the native disulfide bond would provide new possibilities to further elucidate the characteristic of the disulfide bonds and their role in the regulation of insulin structure and function. Although disulfide bonds are traditionally known as the foundation to protein stability, reduction of disulfides is also the leading cause of protein degradation. Thus, replacement of a redox sensitive disulfide bond with a non-reducible linkage can prevent disulfide reduction, disulfide rearragement and disulfide isomerisation that could also potentially enhance protein stability *in vivo*.

Prior to this investigation, several attempts were made to synthesize insulin-related peptides incorporating different classes of disulfide isosteres, including diselenium (Armishaw et al., 2006), lactam (Karas et al., 2013) and dicarba (Noda et al., 1987, Stymiest et al., 2003, Hossain et al., 2009, Zhang et al., 2010, van Lierop et al., 2013, Chhabra et al., 2014); each has its own advantages and limitations when being used as a disulfide alternative. There are several factors to take into consideration when designing peptide with disulfide isosteres, including assessment of the effect of the bond length and configuration on the tertiary structure of synthesized peptide, scalability of the peptide synthesis and biological toxicity of the end product.

As a reference, the distance of a cysteine bond (Sγ–Sγ') measured between the two sulphur groups is 2.03Å. In comparison, the diselenium bond is 2.33 Å, lactam amide bond is approximately 1.47 Å, and dicarba bond lengths are 1.54 Å for saturated dicarba (C–C) and 1.34 Å for unsaturated dicarba (C=C) (disulfide bond *versus* dicarba bond; see Fig. 1.19). Amongst the three disulfide isosteres, diselenium linkage is most similar in length to the cysteine linkage.

However, selenocysteine has been associated with the potential risk of toxicity, suggesting it may be inappropriate to incorporate in the design of analogue for clinical use (Plateau et al., 2017).

Insulin-like peptide 3 (INSL3) disulfide bond(s) replaced with a single (mono-lactam A24-B22) or double (bis-lactam A11-B10, A24, B22) inter-molecular lactam linkage(s) have been shown to retain receptor binding affinity for RXFP2 receptor, suggesting these linkages are well tolerated as disulfide substitutions in INSL3 (Karas et al., 2013). Unfortunately, the yield of both analogues were fairly poor, thus structural analyses of these analogues were not feasible.

On the other hand, several examples of dicarba replacement in insulin-related peptides demonstrated improvements in peptide stability and activity; described in the followings. The current method of chemical synthesis for dicarba-containing insulin-related peptides involves a microwave-accelerated solid phase peptide synthesis (SPPS) approached coupled with hydrocarbon crosslink *via* ring-closing olefin metathesis (RCM) of the incorporated allyglycine residues (Gleeson et al., 2017, van Lierop et al., 2011a, van Lierop et al., 2010, Hossain and Wade, 2017, Liu et al., 2016). Unique to the unsaturated dicarba bond, the linkage can exist in *cis* and *trans* configurations. Thus, synthesis of dicarba analogues typically results in two distinct isomers separable through chromatographic purifications.

Dicarba substitution of A-chain intra-molecular disulfide bond in INSL3 (Zhang et al., 2010) and INSL7 (also known as human relaxin-3) (Hossain et al., 2009) yields analogues that exhibit similar biological potentials compared to their respective native form. In both examples, both dicarba isomers showed equal binding affinities to their cognate receptors (both G-coupled protein receptors) and exhibit similar secondary structures to their respective native forms. Importantly, the majority of the synthesized INSL7 is in the *cis* form, a configuration that more closely resembles the native disulfide bond in that position. Using a similar approach, Hossain *et al.* also synthesized the intra-chain dicarba analogue of human relaxin 2, yielding two isomers that both bind the RXFP1 receptor with high affinity. Surprisingly, both relaxin 2 dicarba isomers show less *in vitro* serum stability even though the secondary structure is only subtly different from their native form (Hossain et al., 2015). Dicarba bonds introduced into other small polypeptides such as α-conotoxin (van Lierop et al., 2013, Chhabra et al., 2014), oxytocin (Stymiest et al., 2003) and calcitonin (Noda et al., 1987) also improves their stability, and in some cases, their activity.

In summary, the substitution of disulfide bonds in peptides can have several benefits: (1) ability to probe the function of specific disulfide bond within the peptide; whether it is a structural disulfide or redox disulfide that is involves in the regulation of peptide function, (2) elucidate the role of disulfide bond in the structure-function relationship of peptide (3) increase biological activity through improved peptide stability.

1.12 PROJECT OVERVIEW

1.12.1 Project Inspiration & Goal

Insulin is an indispensable and effective treatment for diabetes. Nevertheless, current insulin treatments could be improved to provide better blood glucose control and to minimise long-term diabetic complications. Designing new ultra-rapid insulin analogues that are also more stable and have low risk of promoting cancer growth is a global ambition.

To this end, an improved understanding of insulin's structure-function relationship is necessary. The role of individual residues in the mature insulin molecule have been extensively characterised to probe their role in insulin structure and function. However, an indepth understanding of the physio-chemical nature, stereochemistry and structural contribution of insulin disulfide bonds to function is still lacking. Hence, the overarching goal of this project is to improve understanding of the insulin disulfide bonds, with the long-term aim to develop insulin analogues with enhanced activity, stability and metabolic signalling outcomes.

This project aimed to characterise the structure, biophysical properties and function of insulin analogues in which the A6–A11 disulfide bond was substituted with a rigid, non-reducible C=C linkage (dicarba insulins) *via* chemical synthesis (see Fig. 1.19).

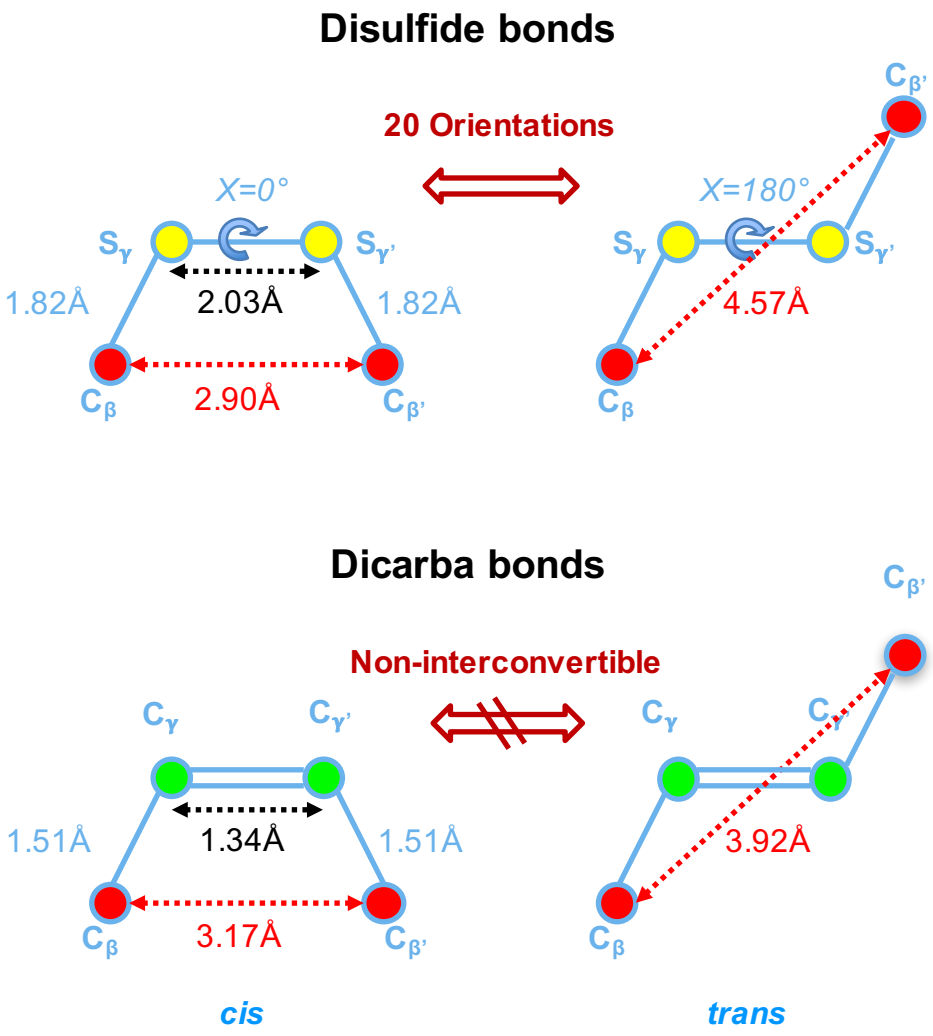

Figure 1.19 Disulfide bond *versus* unsaturated dicarba (C=C) bonds in *cis* and *trans* configurations. The disulfide bond (*top*) can adopt up to 20 different configurations and can undergo redox reaction. The dicarba bond is an ideal disulfide isosteres that can adopt is non-reducible and non-interconvertible *cis* or *trans* configuration. The distance between C_β–C_β' (*red arrows*), S_γ– S_γ' and C_γ=C_γ' (*black arrows*) are also indicated.

Specifically, the project focuses on investigating the role of the insulin intra-chain A6–A11 disulfide bond for a number of reasons.

1. Amongst the three insulin disulfide bonds, the A6–A11 is considered the least important linkage in the process of protein folding and maintaining structural stability. Introduction of a rigid bond in that position is least likely to change the overall conformation of the molecule.
2. Technically, it is also most feasible to establish an A6–A11 dicarba linkage compared to the two inter-chain linkages. It is the last disulfide linkage made during chemical synthesis and during chain combination.
3. The A6–A11 bond resides in a receptor binding 'hotspot', neighbouring several classical site 1 binding residues. Also, conformational dynamics is a key element to insulin high affinity binding. Thus, it is not unreasonable to speculate that the flexibility and configuration of A6–A11 bond may have a regulatory influence to insulin activity.
4. Introduction of a dicarba linkage into the equivalent intra-chain position in other insulin-related peptides has been shown to improve peptide stability and also improve potency in several cases (Hossain et al., 2009, Noda et al., 1987, Stymiest et al., 2003, van Lierop et al., 2013).

1.12.2 Aims & Experimental Strategies

The establishment of this project arose from a collaboration between Professor Briony Forbes (my primary supervisor) and Professor Andrea Robinson from Monash University. The Robinson Laboratory specializes in chemical biology and organic synthesis and synthesized all dicarba insulin analogues used for this project, while our laboratory specializes in investigation of protein structure and function relationship through biochemical and biophysical studies and *in vitro* cell biology systems.

The initial inspiration of designing intra-A-chain dicarba insulin analogues aspired to improve insulin stability and activity as had been seen in the several successes demonstrated in the dicarba analogues of insulin-related peptides. While dicarba bonds had been previously introduced into insulin-like peptides INSL3 and INSL7, Professor Robinson's group had to develop the strategy to generate A6–A11 intra-chain dicarba analogues of human insulin. The development and further refinement of the solid phase peptide synthesis (SPPS)-catalysis and ring closing metathesis approach necessary for the chemical synthesis of the dicarba insulin analogues is described in *Chapter 2*. As expected from the chemical synthesis of other insulin-

related dicarba analogues, synthesis of A6–A11 dicarba insulin also resulted in two stereoisomers (*cis*- and *trans* isomers).

Preliminary data of the insulin dicarba analogues demonstrated several surprising outcomes that subsequently defined the course of this PhD project.

Preliminary data suggested that:

1. Only the *cis* isomer of dicarba insulin is equipotent to insulin in IR binding and activation; the *trans* isomer is inactive (see Fig. 2.2, *A* and *B*).
2. *Cis* dicarba insulin showed significantly reduced mitogenic potency evident in the *in vitro* DNA synthesis assay while retaining its metabolic potency in glucose uptake assay (see Fig. 2.2, *C* and *D*).

Based on these observations it was hypothesised that the A6–A11 disulfide bond acts as a "toggle" between the active and inactive conformations. The dicarba insulins could therefore allow us to define the active insulin conformation. It was also proposed that *cis* dicarba must engage with the receptor in a subtly different way to insulin to promote signalling biased towards metabolic signalling. Therefore, *cis* dicarba insulin would be a good tool for investigating insulin signalling bias.

My aims for this project were to comprehensively characterize the biochemical, biophysical and biological nature of the dicarba insulin analogues in order to understand why *cis* and *trans* dicarba insulin have these unique attributes.

It was speculated that the introduction of dicarba bond into rapid-acting lispro insulin and long-acting glargine insulin would introduce stability and possibly different biological activities (including lower mitogenic potential). Therefore, to broaden the scope of this investigation, A6–A11 dicarba analogues of the rapid-acting lispro and the long-acting glargine insulin were also included in this study.

The specific aims to prove the hypotheses stated above were to:

Aim 1: Define the role of the Cys^{A6}–Cys^{A11} linkage in the regulation of insulin activity.

1. Investigate the biological potency of insulin dicarba analogues through a series of *in vitro* activity testings (receptor binding and activation, glucose uptake assay, DNA synthesis assay) and *in vivo* insulin tolerance tests in mice.

2. Perform biophysical studies to predict secondary structure of dicarba insulin analogues. X-ray crystallographic studies of dicarba insulin were performed in collaboration with Professor Mike Weiss from WEHI, Victoria, Australia.
3. Predict the "active" conformation of insulin through structural comparison of the active *cis* dicarba insulin with the existing x-ray crytal structures in the PDB database.
4. Identify the key mechanism(s) by which the insulin A6–A11 bond regulates insulin activity by comparing *cis* and *trans* dicarba configurations to the native A6–A11 disulfide bond configurations.

Aim 2: Define the role of the Cys^{A6}–Cys^{A11} linkage in the regulation of insulin stability.

1. Investigate thermal and chemical (guanidine hydrochloride) stability of dicarba insulin analogues monitored through circular dicroism.
2. Investigate enzymatic stability of dicarba insulin analogues.
3. Investigate the role of A6–A11 linkage in regulating insulin conformational dynamics and stability by comparing the species of proteolytic peptides generated from native insulin and dicarba insulin analogues using mass spectrometry. The investigation was also assisted by molecular dynamic performed by Dr Naomi Haworth.

Aim 3: Define the role of the Cys^{A6}–Cys^{A11} linkage in the regulation of signalling bias.

1. Investigate the downstream metabolic and mitogenic signalling bias through dose-dependent stimulation of dicarba insulin analogues.
2. Investigate the kinetics of stimulated metabolic and mitogenic signalling in response to dicarba insulin analogues.
3. Investigate the association between signalling bias and receptor internalisation.
4. Investigate the association between insulin receptor phosphorylation kinetics and signalling bias.

Collectively, through the detailed study of dicarba insulins this project aimed to provide understanding of the role of the A6–A11 bond in insulin's action, stability and IR signalling bias. Ultimately this research seeks to inform the future design of novel insulins with the highly desirable properties of reduced mitogenicity, rapid action and enhanced stability.

CHAPTER 2

"Insulin in Motion:

The A6 – A11 disulfide bond allosterically modulates structural transitions required for insulin activity."

The following chapter was co-first authored with Dr Bianca van Lierop and has been published in Nature Scientific Report Vol 7; Article No.: 17239 on the 8th Dec 2017.

CHAPTER 2 INSULIN IN MOTION: THE A6–A11 DISULFIDE BOND ALLOSTERICALLY MODULATES STRUCTURAL TRANSITIONS REQUIRED FOR INSULIN ACTIVITY

2.1 INTRODUCTION

Insulin is fundamental to the physiological regulation of blood glucose concentration (Saltiel and Kahn, 2001). A deficiency in insulin results in diabetes, a major economic and primary health care burden across both developed and developing countries. Insulin therapy is essential in both type 1 diabetes and late-stage type 2 diabetes, with current therapeutic insulins being designed to restore the normal biphasic insulin response to food intake (Pandyarajan and Weiss, 2012, Hirsch, 2005). While such therapeutic analogues are largely successful in controlling blood glucose levels, their means of administration and their pharmacokinetic and pharmacodynamic profiles are far from ideal, putting patients at risk of both hyper- and hypoglycemia. Notably, none of the currently available therapeutic insulin analogues have employed in their design an atomic-level understanding of how insulin engages its receptor, as such detail has only recently begun to emerge (Menting et al., 2013, Menting et al., 2014a). A thorough understanding of the conformational changes involved in insulin / insulin receptor interaction therefore has the potential to lead to a new generation of insulin analogues with improved pharmacological properties.

Insulin is a two-chain polypeptide, comprising an A chain of 21 residues that includes two α helices (residues A1 to A8 and A12 to A18, respectively), and a B chain of 30 residues that includes a single α helix (residues B9 to B19) (Fig. 2.1*A*) (Adams et al., 1969b). Integral to insulin's structure are its three disulfide bonds — one intra-chain (Cys^{A6}-Cys^{A11}) and two inter-chain (Cys^{A7}-Cys^{B7} and Cys^{A20}-Cys^{B19}) (Fig. 2.1*A*). Formation of these disulfide linkages ensures both the correct folding of the insulin precursor polypeptide and the structural stability of the mature hormone (Weiss, 2009b, Chang et al., 2003). Both the A6–A11 and the A20–B19 cystines are buried within the core of the hormone, whereas the A7–B7 cystine is partly surface exposed. Insulin is stored as a 2Zn hexamer in pancreatic β-cells, but it is the monomeric form that engages the insulin receptor (IR, a receptor tyrosine kinase) (Lawrence and Ward, 2015a).

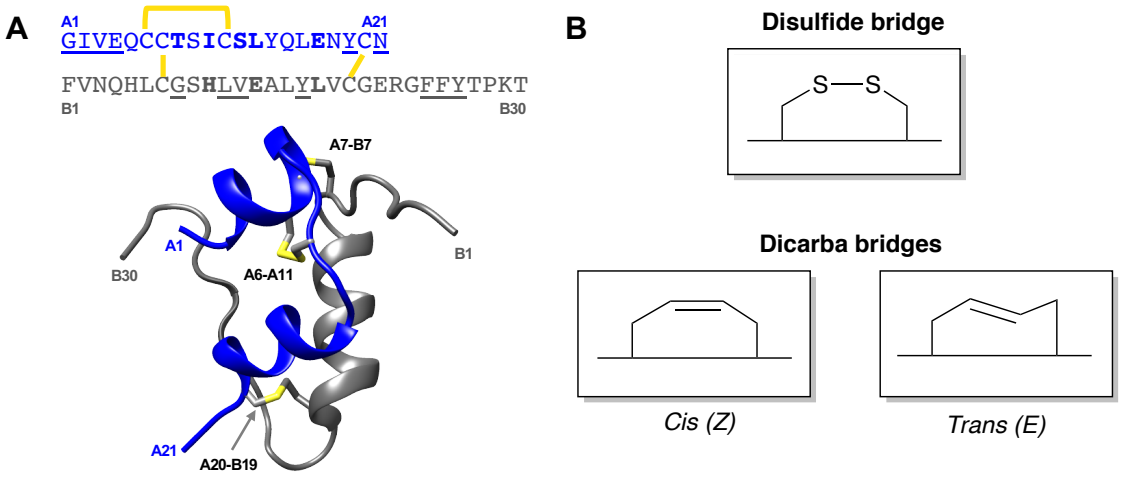

Figure 2.1 Insulin sequence and structure. (A) Primary sequence (*top*) of the A (*blue*) and B (*grey)* chains of human insulin, highlighting disulfide bonds (*yellow*), site 1-binding residues (*underlined*) and site 2-binding residues (*bold*) (De Meyts, 2015). Ribbon diagram of insulin (2-Zn-coordinated T6 conformation (Baker et al., 1988b) PDB entry 1MSO) showing the location of the three α-helices and the three disulfide bonds. (B) Schematic diagram of native cystine and isomeric *cis*- and *trans*-dicarba bridges.

The insulin receptor is a disulfide-linked $(\alpha\beta)_2$ homodimer, the ectodomain of which in its *apo* form adopts a folded-over Λ-shaped conformation (McKern et al., 2006, Croll et al., 2016a). Insulin binding to the insulin receptor is currently understood to involve the hormone forming a high-affinity cross-link between two distinct sites (1 and 2) on the receptor surface (Menting et al., 2013, Jensen, 2000b). A number of the insulin residues involved in site 1 binding are also involved in forming the insulin dimer within the classical 2Zn insulin hexamer (Fig. 2.1*A*) (Menting et al., 2013, Menting et al., 2014a, Whittaker et al., 2008, De Meyts, 2015). The location of IR site 2 is not well defined (Menting et al., 2013, McKern et al., 2006) but evidence exists that it is engaged by insulin residues involved in the hexamer-forming surface of the hormone (Jensen, 2000b, De Meyts, 2015) (Fig. 2.1*A*).

Recent crystallographic studies of insulin in complex with domain-minimized insulin receptor constructs comprising site 1 alone revealed two key insights into the mechanism of interaction: (i) both the insulin B chain and the αCT segment of the receptor undergo conformational change upon their mutual engagement (Menting et al., 2013, Menting et al., 2014a); in the case of insulin, such change involves the long-predicted folding out of the B-chain *C*-terminal segment (residues B24-B30) away from the hormone core (Hua et al., 1991) and (ii) within the complex, the B-chain *N*-terminal segment does not form the *N*-terminal α-helical extension to the B8-B20 helix that is characteristic of the so-called R- or R^f states of the hormone that occur in crystals grown in the presence of phenolic derivatives (Weiss, 2009b) but rather it adopts a conformation similar to that in the classical T-state structures of insulins (Baker et al., 1988a), wherein the B-chain *N*-terminal segment is folded back against the hormone.(Weiss, 2009b)

Lacking from our current understanding is the role of disulfide bond flexibility in insulin's engagement with the IR. Here, we specifically seek to explore the influence of the A6–A11 disulfide bond on insulin structure and function through strategic use of olefin metathesis to replace the A6–A11 disulfide bond of insulin with a C=C double bond (Fig. 2.1*B*) (Robinson and van Lierop, 2011). An unsaturated C=C dicarba bond is considerably more rigid than a disulfide bond and adopts either a *cis* or *trans* configuration, with an insurmountable barrier to exchange under physiological conditions. Introduction of a dicarba bond into a number of small polypeptides (Gleeson et al., 2017) including oxytocin (Stymiest et al., 2003), calcitonin (Noda et al., 1987) and H3-relaxin (Hossain et al., 2009) has been shown to improve their stability and, in some cases, their activity. Our synthetic techniques permit generation of both the *cis* and *trans* configuration of the A6–A11 dicarba bond within insulin (Fig. 2.1*B*). Taken together with a re-analysis of extant T-state insulin crystal structures, our structural, molecular dynamics and

biological characterization of these dicarba insulin isomers leads to a new understanding of the critical interplay between A-chain conformational flexibility and restraint that is allosterically regulated by the A6–A11 disulfide bond. Such structural transitions are required for insulin / insulin receptor engagement.

2.2 MATERIALS & METHODS

2.2.1 Materials

Actrapid® insulin was purchased from Lyppard Australia Pty Ltd. Hybridoma cells expressing antibodies specific for the IR α subunit (83-7) and the IGF-1R α subunit (24-31) were a gift from Prof. K Siddle (Soos and Siddle, 1989, Soos et al., 1989, Ganderton et al., 1992). [^{3}H]-Thymidine was purchased from Perkin Elmer Life Sciences. hIR-A and hIR-B over-expressing R$^-$fibroblast cells (derived from IGF-1R knockout mouse embryonic fibroblasts, a gift from Prof. R. Baserga (Philadelphia, USA) (Sell et al., 1994) were produced according to Denley *et al.*(Denley et al., 2004). hIR-A over expressing L6 myoblasts were provided by Dr B.F. Hansen (Novo Nordisk A/S, Denmark). P6 cells (BALB/c3T3 cells overexpressing the human IGF-1R) were from Prof. R. Baserga (Pietrzkowski et al., 1992).

2.2.2 Cell Lines and Cultures Conditions

hIR-A and hIR-B overexpressing cells (R$^-$IR-A and R$^-$IR-B, respectively) were constructed as described in (Denley et al., 2004) using R$^-$fibroblasts (derived from IGF-1R knockout mouse embryonic fibroblasts) - a kind gift from Professor R. Baserga (Philadelphia, PA)(Sell et al., 1994). L6 rat skeletal myoblasts overexpressing human IR-A (hIR-A L6) were kindly provided by Dr B.F. Hansen (Novo Nordisk A/S, Denmark) (Bonnesen et al., 2010). P6 cells (BALB/c3T3 cells overexpressing the human IGF-1R) were from Professor R. Baserga (Pietrzkowski et al., 1992). All cells were maintained at 37 °C; 5% CO_2. R$^-$IR-A, R$^-$IR-B, hIR-A L6 and P6 cells were maintained in Dulbecco's minimal essential medium (DMEM) High Glucose (4.5 g/mL) supplemented with 10% FCS, 2 mM L-glutamine, 100 U/l penicillin and 100 µg/L streptomycin. All cell culture media and supplements were purchased from Thermo Fisher Scientific Australia.

2.2.3 Synthesis of Dicarba Insulins

Chemical synthesis of all dicarba insulin analogues in this thesis were generated by our collaborator Dr Bianca van Lierop, Dr Alessia Belgi and Prof. Andrea J. Robinson in the School

of Chemistry, Monash University. Clayton, Victoria, Australia. Methodology is briefly described here; details are provided in the *Chapter 2 Appendices 2A – E*.

An interrupted solid-phase peptide synthesis (SPPS)-catalysis approach(Van Lierop et al., 2011b) was developed to overcome deleterious aggregation and achieve quantitative ring-closing metathesis of the dicarba insulin A chain. Construction of the complementary insulin B chain was achieved through microwave-accelerated SPPS. The monocyclic A-B conjugates were prepared by combination of the dicarba insulin A chains with the insulin B chain under basic conditions resulting in spontaneous oxidation of the liberated free thiol groups to give the two target isomeric *trans* and *cis* dicarba peptides.

2.2.4 Receptor Competition Binding Assays

IR-A, IR-B and IGF-1R binding was measured essentially as described by Denley *et al.* ((Denley et al., 2004). Human IR isoform A (IR-A), isoform B (IR-B) and IGF-1R were solubilized from R$^-$IR-A, R$^-$IR-B and P6 cells, respectively. Briefly, cells were serum-starved for 4 h before lysis in lysis buffer (20 mM HEPES, 150 mM NaCl, 1.5 mM $MgCl_2$, 10% (v/v) glycerol, 1% (v/v) Triton X-100, 1 mM EGTA, and 1 mM phenylmethylsulfonyl fluoride, pH 7.5) for 1 h at 4 °C. Lysates were centrifuged for 10 min at 2,200 × *g*, then 100 µL lysate was added per well to a white Greiner Lumitrac 600 96-well plate previously coated with anti-IR antibody 83-7 or anti-IGF-1R antibody 24-31 (250 ng/well in bicarbonate buffer pH 9.2). Approximately 500,000 fluorescent counts of europium-labelled insulin (Eu-insulin, prepared in-house) was added to each well along with increasing concentrations of unlabelled competitor in a final volume of 100 µl and incubated for 16 h at 4 °C. Wells were washed four times with 1 x TBST (20 mM Tris pH 7.4, 150 mM NaCl, and 0.1% (v / v) Tween 20). Then 100 µL per well DELFIA enhancement solution (PerkinElmer Life Sciences) was added. After 10 min time-resolved fluorescence was measured using 340 nm excitation and 612 nm emission filters with a BMG Lab Technologies Polarstar fluorometer (Mornington, Australia). Assays were performed in triplicate in at least three independent experiments.

2.2.5 Kinase Receptor Activation Assays (KIRA)

IR-A, IR-B and IGF-1R phosphorylation was detected essentially as described by Denley *et al.* (Denley et al., 2004). Briefly, R$^-$IR-A, R$^-$IR-B or P6 cells (5×10^4 cells/well) were plated in a 96-well flat bottom plate and grown overnight at 37°C, 5% CO_2. Cells were starved in serum-free medium for 4 h before treatment with insulin or dicarba insulins in 100 µl of Dulbecco's minimal essential medium with 1% bovine serum albumin for 10 min or in a time course (0, 2, 5,

8, 12, 20, 30 min) at 37°C, 5% CO_2. Cells were lysed with ice-cold lysis buffer containing 2 mM Na_3VO_4 and 100 mM NaF, and receptors were captured onto white Greiner Lumitrac 600 96-well plates pre-coated with anti-IR antibody 83-7 (Soos et al., 1986) or anti-IGF-IR antibody 24-31 (250 ng / well) (Soos et al., 1992) and blocked with 20 mM Tris-HCl pH7.4, 150 mM NaCl, and 0.1% (v/v) Tween 20 (TBST) / 0.5% bovine serum albumin. Following overnight incubation at 4°C, the plates were washed three times with TBST. Phosphorylated receptor was detected by incubation with Eu-pY20 (76 ng / well) at room temperature for 2 h. Wells were washed four times with TBST, and time-resolved fluorescence was detected as described above. Assays were performed in triplicate in at least three independent experiments.

2.2.6 DNA synthesis Assay

DNA synthesis was carried out as described in Gaugin *et al.*(Gauguin et al., 2008a). Briefly, L6 rat skeletal myoblasts overexpressing human IR-A, were plated in a 96 well flat bottom plate (1.5×10^4 cells / well) and grown overnight at 37°C, 5% CO_2. Cells were starved in serum-free medium for 4 h before treatment with with increasing ligand concentrations for 18 h in Dulbecco's minimal essential medium with 1% bovine serum albumin. The cells were incubated with 0.13 µCi / well [^{3}H]-thymidine for 4 h, shaken for 2h with 50µL disrupting buffer (40mM Tris pH 7.5 / 10mM EDTA/150mM NaCl) and then harvested onto glass fibre filters (Millipore®) using a MICRO 96™ Skatron harvester (Molecular Devices). The filters were counted in a Wallac MicroBeta counter (PerkinElmer Life Sciences). Assays were performed in triplicate in at least three independent experiments.

2.2.7 Glucose Uptake Assay

Briefly, NIH3T3-L1 myoblasts (up to passage 20) grown in DMEM supplemented with 10% newborn calf serum, 2mM L-glutamine, 100U/l penicillin, 100µg/L streptomycin at 37°C were seeded into 24-well plates at $5x10^3$ cells/well and grown for 8 days to confluence and were then differentiated into adipocytes as described in (Govers et al., 2004). Glucose uptake in response to insulin and the *cis* isomer was measured essentially as described in (van Dam et al., 2005). Briefly, 3T3-L1 adipocytes were serum starved in serum free DMEM/1%BSA for 4 h, washed twice with Krebs-Ringer phosphate buffer (KRP, 12.5mM HEPES, 120mM NaCl, 6mM KCl, 1.2mM $MgSO_4$, 1mM CaCl2, 0.4mM Na_2HPO_4, 0.6mM Na_2HPO_4 (pH7.4)) containing 1%BSA and incubated for 15min at 37°C. Insulin or the *cis* isomer was added at decreasing concentrations (100 – 0.3nM) for 30min at 37°C. For the final 10 min 2-deoxyglucose (DOG) uptake was initiated by the addition of 50µM cold deoxyglucose and 1µCi ^{3}H –deoxyglucose per

well. The assay was terminated by rapidly washing the cells three times with ice-cold KRP buffer. Cells were solubilized in 0.5M NaOH/0.1% SDS and ^{3}H content was determined by scintillation counting. Nonspecific 2-DOG uptake was determined in the presence of 50μM cytochalasin B.

2.2.8 Insulin Tolerance Test

Insulin tolerance tests were performed by our collaborator Assoc. Prof. Sofianos Andrikopoulos in the University of Melbourne, Department of Medicine, Parkville, Victoria, Australia.

Eight-week-old C57BL6 male mice were fed either a standard rodent chow diet containing (wt / wt) 77% carbohydrate, 20% protein, and 3% fat from Ridley AgriProducts (Pakenham, Victoria, Australia) or a high fat diet (HFD) containing (wt / wt) 57% carbohydrate, 19% protein and 15% fat from Specialty Feeds (SF08-044, Glen Forrest, Western Australia, Australia) for 12 weeks. Mice (5 or 6 mice per group) were injected ip with 0.75I U/kg insulin or *cis* isomer under non-fasting conditions and tail vein blood glucose was measured *via* glucometer at indicated times.(Wong et al., 2011) Experimental procedures were carried out in accordance to the protocols approved by the Austin Health Animal Ethics Committee (AEC 2011/04396). Native insulin (Actrapid) were administered as formulated peptide diluted to the correct dose in phosphate-buffered saline pH 7.4 (semi-formulated). *Cis* dicarba insulin was dissolved in 10mM HCl and diluted to the correct dose in phosphate-buffered saline pH 7.4 (non-formulated).

2.2.9 Circular Dichroism

Circular dichroism (CD) was carried out as previously described (Weiss et al., 2000, Alvino et al., 2009). CD spectra were recorded on a Jasco J-815 CD spectrometer (Biophysical Characterisation Facility, South Australia).

2.2.9.1 Spectra

CD spectra were measured from 260 to 190 nm with a 1.0 nm step size using a 1.0 s response time and 1.0 nm bandwidth in a quartz cuvette with a 0.1 cm path length. Insulin and dicarba insulin analogues were diluted in 10 mM phosphate buffer (pH 7.4) to a concentration of 0.22 mg/mL (38 μM). Spectra were background-corrected by subtraction of the spectrum of buffer alone.

2.2.9.2 *Thermal denaturation*

Temperature denaturation of insulin and dicarba insulin analogues was achieved by automated thermal control increasing by 2°/min at 1° intervals monitored at far-UV wavelength at 222 nm.

2.2.9.3 *Chemical denaturation*

Insulin or dicarba insulin analogues were diluted to final concentration of 10 μM for equilibrium denaturation studies in guanidine hydrochloride (0 - 8.0 M). Each sample was incubated at room temperature for 30 minutes prior to CD spectrum measurement from 230 – 210 nm. Function of Gu.HCl denaturation was plotted as ellipticity value at 222 nm *vs* concentration of Gu.HCl.

2.2.9.4 *Analyses*

The machine unit collected, θ in millidegrees, is converted to mean residue ellipicity (MRE), [θ] in degrees.cm^{2}dmol^{-1}residue^{-1}, as follows:

Equation 2.1:

$$[\theta] = \theta \times \frac{(0.1 \times MRW)}{(P \times Conc.)}$$

where *MRW* is the protein mean weight ((atomic mass units/daltons) / number of residues)), *P* is pathlength (cm) and *Conc.* is protein concentration in mg/mL. $[\theta]_{222}$ is the molar ellipicity per residue at wavelength 222 nm.

2.2.10 Bioinformatics

A dataset of insulin structures was constructed from all medium- and high-resolution X-ray crystal structures (better than 2.8 Å) in PDB Archive Version 4.0 (Jul 2011). 275 unique insulin structures were found in 105 PDB files; these included human, bovine and porcine insulins and synthetic mutants. 152 structures were found to exhibit the R (or R_f) state (data not shown) and 123 the T state. (Note: structures with A6–A11 Sγ-Sγ bond lengths outside the range of 1.95 to 2.05 Å (indicative of poor modelling of the disulfide), as well as structures involving insulin in complex with the insulin degrading enzyme, were not included in the dataset.) Analyses were performed only on T-state insulins (*i.e.*, T-state insulins from monomeric, T_2, T_6, T_3R_3 or $T_3R^f_3$ structures). Of the T-state structures, 30 exhibited a Class 1 conformation and 93 a Class 2 conformation. Custom programs were used to extract the $C\alpha^{A6}$-to-$C\alpha^{A11}$ and $C\alpha^{A7}$-to-$C\alpha^{B7}$ distances and A6–A11 disulfide conformations, as well as the hydrogen bonding pairs, from each structure (see *Chapter 2 Appendices, 2F and 2G*). The approach used to determine the

relative azimuthal positioning of residues within the segment A1–A10 of each insulin is also described in the *Appendix 2G*.

2.2.11 Molecular Dynamics

Molecular dynamics analyses were conducted by our collaborator, Dr Naomi L. Haworth in the School of Chemistry, Monash University, Clayton, Victoria, Australia.

Molecular dynamics simulations were performed using the AMBER14 program package.(D.A. Case et al., 2014) Amber ff14SB force field parameters (Maier et al., 2015) were used for all standard amino acid residues. RESP charges (Bayly et al., 1993) and force-field parameters for the dicarba linkages were determined using the PyRED program (Dupradeau et al., 2010, F. Wang, 2013) (see *Chapter 2 Appendices, 2F and 2G*). Initial atomic coordinates were taken from three high-resolution T-state insulin PDB entries: 1G7B E, F; 1MSO A,B; and 3I3Z A,B. Each of these structures has a different conformation for the A6–A11 disulfide bond. *Cis* and *trans* isomers were created from each entry, giving a total of nine different starting structures. After minimization and equilibration (see *Chapter 2 Appendices, 2F and 2G*), the system was heated to 400K and the dynamics simulated for 10 ns. Each high-temperature simulation was analysed to identify distinct conformations of the insulin analogue. Four structures (or 8 in the case of the *cis* isomer) were chosen from each run to use as starting geometries for subsequent 200 ns room-temperature MD simulations. Full details of simulation protocols are provided in *Chapter 2 Appendices, 2F and 2G*. Processing of simulations and cluster analysis was performed using CPPTRAJ.(Roe and Cheatham, 2013) The same custom programs as described above under *Bioinformatics* were used to assess the backbone hydrogen-bonding patterns, interatomic distances and A6–A11 disulfide conformations in each MD simulation frame. DSSP (Kabsch and Sander, 1983) was also used to identify residue backbone conformations.

2.2.12 Crystallization

Crystallography experiments were performed by our collaborator, John G. Menting and Prof. Mike C. Lawrence in The Walter and Eliza Hall Institute of Medical Research, Parkville, Victoria, Australia.

trans isomer: An initial sparse-matrix sitting-drop vapor-diffusion crystallization screen was conducted at the CSIRO Collaborative Crystallisation Centre (CSIRO C3; Parkville, Australia). Based on hit conditions determined, a *ca* 50 μm crystal was then grown at 20 °C in a 24-well Linbro plate by vapor diffusion from a hanging drop of 1 μL of 1 mg/ml protein dissolved in 10

mM HCl mixed with 2 μL crystallant solution (0.9 M potassium sodium tartrate, 0.1 M Tris HCl (pH 8.5), 0.5% PEG 5000 MME) on a siliconized coverslip (Hampton Research) placed over 0.4 mL crystallant. The crystal was placed in a second hanging drop vapor diffusion condition, a 2 μL drop of 1.0 M potassium sodium tartrate, 0.1 M Tris HCl pH 8.5 and equilibrated against 0.4 mL of 1.5 M potassium sodium tartrate overnight at 20°C, after which the well solution was exchanged for saturated potassium sodium tartrate and incubated for 24 h. The crystal was cryo-cooled by direct plunging into liquid nitrogen (without addition of a cryo-stabilizing solution). *cis* isomer: Following an initial sparse-matrix screen identical to that described above for the *trans* isomer, a *ca* 25 μm crystal was subsequently grown at CSIRO C3 in a 96-well additive screen using a SWISSCI plate in vapor diffusion format at 20 °C using a sitting drop of 150 nL of 1 mg/ml protein dissolved in 10 mM HCl mixed with 150 nL 0.8 M potassium sodium tartrate, 0.1 M Tris-HCl pH 8.5, 0.5 % PEG 5000 MME, 4% acetonitrile. This crystal was briefly dipped in paraffin oil (Hampton Research) and cryo-cooled by direct plunging into liquid nitrogen.

2.2.13 Diffraction Data Collection and Processing

Diffraction data for both crystals were collected at the MX2 beamline at Australian Synchrotron (McPhillips et al., 2002) at ~100 K and at λ= 0.9537 Å. Diffraction data were processed and merged using XDS;(Kabsch, 2010) statistics are presented in *Table 2.1*.

2.2.14 Crystallographic Structure Solution and Refinement

Molecular replacement solutions for both isomers were obtained using PHASER,(McCoy et al., 2007) with the starting model in both cases being a porcine insulin monomer obtained from PDB entry 1B2A.(Diao, 2003) Structure refinement was performed with PHENIX(McCoy et al., 2007) iterated with manual model building within COOT.(Emsley and Cowtan, 2004) In the case of the *cis* isomer, the density remained exceptionally poor for the A chain *N*-terminal helix and for residues in vicinity of the dicarba bond. Attempts were made to refine the structure as an ensemble,(Burnley et al., 2012) but without success. Final refinement statistics are presented in *Table 2.1*.

2.2.15 Statistical Analyses

Statistical analysis of receptor binding, receptor activation and DNA synthesis assays were performed using a 2-way ANOVA with a Dunnett's multiple comparison. Data for glucose uptake assay and significance of the overall change of blood glucose levels in insulin tolerance

test were analysed with paired *t*-test. Significance of the change of blood glucose levels at each time-point was also determined by 2-way ANOVA followed by Holm Sidak's multiple comparison test. Significance was accepted at $P < 0.05$.

2.3 RESULTS

2.3.1 Chemical Synthesis of *cis*- and *trans* dicarba insulins

Outline: Chemical synthesis of A6–A11 dicarba insulin generates two isomeric cis- and trans dicarba insulin peptides.

While dicarba bonds have been previously introduced into the analogous bond of insulin-like peptides INSL3 and INSL7 (Hossain et al., 2009, Zhang et al., 2010, Hossain et al., 2015) no strategy exists in the literature to generate A6–A11 intra-chain dicarba analogues of human insulin. Here, the highly hydrophobic *N*-terminus of the insulin A-chain necessitated the development of an interrupted solid phase peptide synthesis (SPPS)-catalysis approach (Van Lierop et al., 2011b) to overcome deleterious aggregation and achieve quantitative ring closing metathesis (see *Chapter 2 Appendices, 2C and 2D*). Additionally, to ensure exclusive generation of the required *C*-terminal asparagine residue on resin cleavage, Fmoc-L-Asp-O^{t}Bu was loaded onto Rink amide resin *via* its side chain. Microwave-accelerated SPPS in combination with HATU–DIPEA activation and Fmoc-protected amino acids were used to generate the truncated peptide sequence **1** (Schematic 2.1), carrying through each intermediate without purification and characterization. Two strategically placed L-allylglycine residues were incorporated into the primary sequence to facilitate formation of the intra-chain dicarba bridge, and cysteine residues were orthogonally protected to later aid regioselective disulfide oxidation and tethering of the B chain (Schematic 2.1). It was critically important to perform the catalysis without the five *N*-terminal residues; performing the ring closure on the full A-chain sequence (21 mer), unlike other insulin-super family molecules, gave only poor conversion. Hence, ring-closing metathesis (RCM) of the fully protected, truncated resin-tethered peptide **1** (16 mer) was performed in the presence of 20 mol% second-generation Grubb's catalyst in DCM with 0.4 M w/v LiCl in DMF.

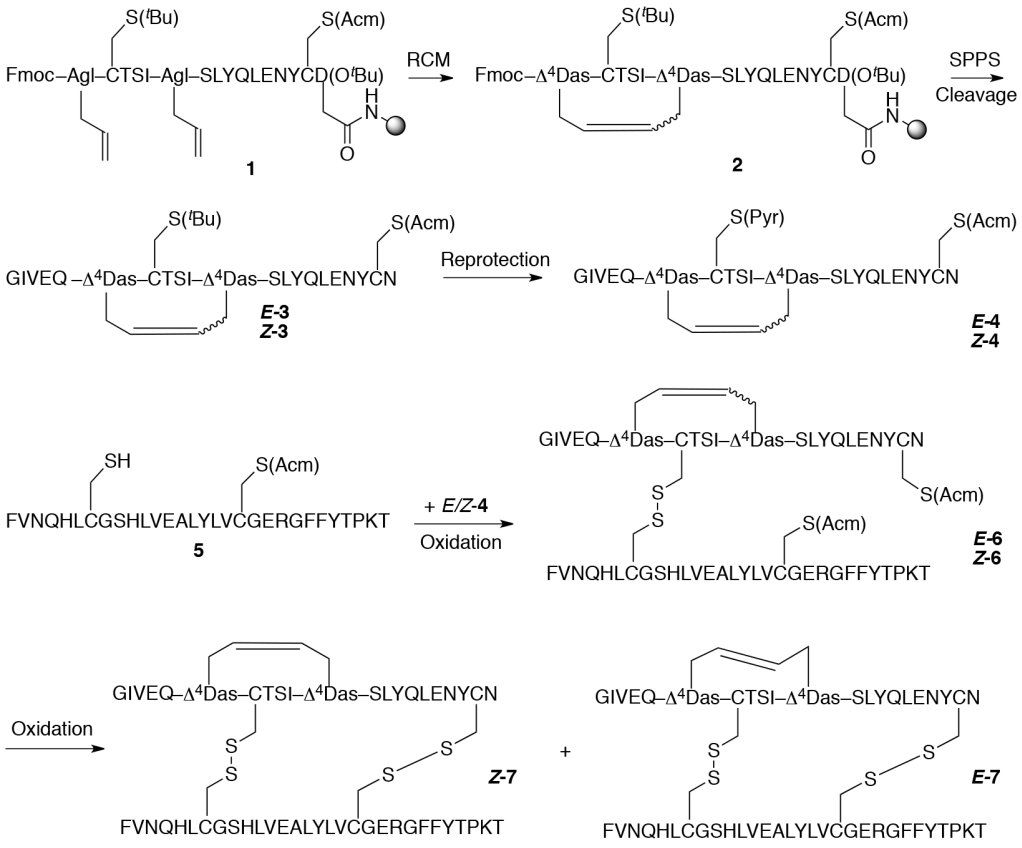

Schematic 2.1 Synthesis of dicarba insulins was performed *via* ring-closing metathesis (RCM) and an interrupted solid phase peptide synthesis (SPPS)-catalysis approach. L-Allylglycine (Agl), tert-butyl (^{t}Bu), acetamidomethyl (Acm), pyridinyl (Pyr), cis isomer (Z), trans isomer (E).

Under these conditions, microwave irradiation of the peptidyl-resin at 100 °C for 2 h resulted in near quantitative conversion to the desired carbocycle **2**. Continued microwave-accelerated SPPS was then performed and the remaining five residues (GIVEQ) were appended to the *N*-terminus to deliver the complete dicarba insulin A chain. Mass spectral analysis of the 21-mer gave the required molecular ions for carbocycle **3** and the RP-HPLC trace showed the formation of two geometric isomers (***E*-3** and ***Z*-3**) in a 3:1 ratio (see Appx. Fig. 2.1*C*). Following resin cleavage, crude peptide **3** was exposed to an acidic cleavage mixture containing 2,2'-dipyridyl disulfide to facilitate concerted *tert*-butyl-deprotection and pyridinyl-reprotection of residue CysA7. Each of the resultant isomeric dicarba insulin peptides **4** were then purified before being subjected to regioselective chain coupling. Construction of the complementary insulin B chain **5** was achieved through microwave-accelerated SPPS, in combination with HBTU/HOBt–DIPEA activation and Fmoc-protected amino acids, on preloaded Fmoc-Thr(^{t}Bu)-PEG-PS resin. During chain elongation, orthogonally protected Cys(Trt) and Cys(Acm) residues were strategically incorporated into the primary sequence in positions B7 and B19 respectively. Preparative RP-HPLC gave the required insulin B chain **5** in 30% yield and 90% purity. The monocyclic A-B conjugates were prepared by combination of the dicarba insulin A chains (***E*-4**, ***Z*-4**) with the insulin B chain **5** under basic conditions. In all cases, oxidation was complete within minutes giving the required 51 amino acid peptides (Schematic 2.1, ***E*-6** and ***Z*-6**). Mass spectral analysis of the isolated solids supported formation of the covalent A-B dimers. The final disulfide bridge in the c[Δ^4A6,11]-dicarba human insulins (Schematic 2.1, ***E*-7** and ***Z*-7**) was formed on exposure of each of the monocyclic A-B conjugates (***E*-6**, ***Z*-6**) to iodine under acidic conditions. Removal of the acetamidomethyl (Acm) protecting groups at positions A20 and B19 resulted in spontaneous oxidation of the liberated free thiol groups to give the two target isomeric *trans*- and *cis*-dicarba insulin peptides (Schematic 2.1, peptides ***E*-7** and ***Z*-7**, respectively) (Robinson and van Lierop, 2011), which were then purified by RP-HPLC and independently subjected to biological testing and structural analysis.

2.3.2 Stereochemical Assignment of the Dicarba Bridge

The C^{β} chemical shifts of peptides comprising Δ^4-diaminosuberic acid (Δ^4Sub) residues show appreciable differences between the *cis-(Z)* and *trans-(E)* configurations (Gleeson et al., 2016). These features were used to identify the stereochemistry of the insulin A-chain A6–A11 dicarba bridge without the need for structural calculations. Hence, TOCSY and ^{13}C-HSQC spectra were acquired on each of the dicarba insulin A-chain peptides (***E*-4** and ***Z*-4**). Δ^4Sub H^{γ} resonances for each *E*- and *Z*-dicarba isomer were readily identifiable at ~5.6 ppm, which facilitated the

assignment of associated Δ^4Sub H^{β} resonances as well as Δ^4Sub C^{β} resonances in the ^{13}C HSQC. As with other dicarba peptide sequences, only minor differences in carbon chemical shifts were observed between the two isomers, with the major difference occurring at the C^{β} atoms of the dicarba bridge (Appx. Fig. 2.2).(Gleeson et al., 2016) Consistent with the previously reported model for stereochemical assignment, the upfield C^{β} shifts for the *cis* isomer presented at δ30.9 and δ32.8 and those for the *trans* isomer appeared at δ36.4 and δ36.9. The stereochemistry of the *trans* isomer ***E*-7** was also confirmed by X-ray crystallography. Additionally, an independent, stereoselective synthesis of *cis*-[A6-11]-dicarba insulin A chain (***Z*-3**) (Appx. Fig. 2.1*L*) was achieved using a preformed, orthogonally protected *Z*-configured diaminosuberic acid residue (*cis*-**S1**) (Gleeson et al., 2016) and SPPS (Appx. Fig 2.3) and found to be identical to material obtained *via* RCM (Appx. Fig. 2.1*C*).

2.3.3 Receptor Binding & Activation

Outline: Cis dicarba insulin is equipotent to native insulin in receptor binding and activation; whereas trans dicarba insulin is inactive.

The affinities of the two dicarba insulin isomers for the human insulin receptor isoforms IR-A and IR-B and the human type 1 insulin-like growth factor receptor (IGF-1R) were determined using ligand competition binding assays.(Denley et al., 2004) The *cis* isomer ***Z*-7** was found to bind IR-B and IR-A with similar affinity to native insulin, whereas the *trans* isomer ***E*-7** had a ~50-fold lower affinity for IR-B and IR-A than native insulin (Fig. 2.2*A*, Appx. Table 2.1 and Appx. Fig. 2.4*A*). The *cis* isomer ***Z*-7** bound IGF-1R with similar affinity to insulin (Appx. Table 2.1 and Appx. Fig 2.4*C*), whereas *trans* isomer ***E*-7** exhibited negligible affinity to IGF-1R.

In receptor phosphorylation assays, the *cis* isomer was equipotent to insulin in activation of IR-B (Fig. 2.2*B*) and IR-A (Appx. Fig 2.4*B*), but slightly poorer than insulin in activation of IGF-1R (Appx. Fig 2.4*D*), whereas the *trans* isomer was ~1000 fold less potent than insulin in activating IR-B (Fig. 2.2*B*). The *trans* isomer had very low binding affinity for the IR-A and IGF-1R and its activity at these receptors was left undetermined.

In summary, these data indicate that (i) only one of the two stereochemical isomers of A6–A11 dicarba insulin (*viz.*, the *cis* isomer) is a potent analogue, and (ii) the equipotency of the *cis* analogue to native insulin is maintained despite the increase in rigidity across the A6–A11 connection afforded by the unsaturated dicarba bond.

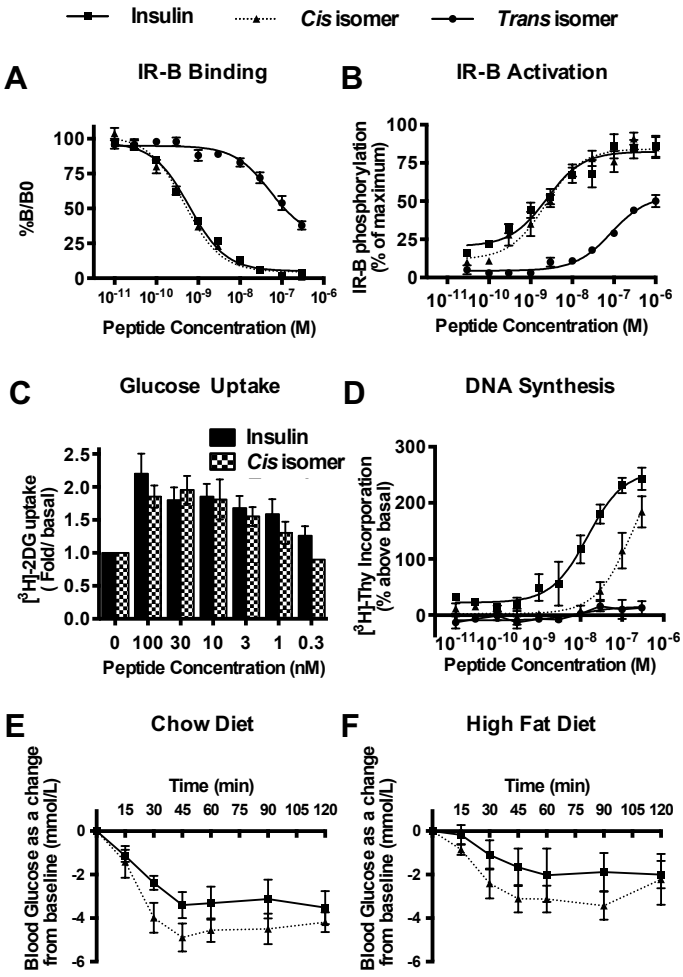

Figure 2.2 Insulin receptor binding, activation and biological activities of *cis*- and *trans* isomers.(A) Competition binding of insulin (*squares*), *cis*- (triangles) and *trans*- (*circles*) isomers with europium-labelled insulin. Results are expressed as a percentage of binding in the absence of competing ligand (%B/B0). (B) Activation of IR-B by increasing concentrations of dicarba insulins (10 min stimulation) is expressed as receptor phosphorylation as a percentage of the maximal phosphorylation induced by insulin. Insulin *vs cis* isomer (non significant); insulin *vs trans* isomer **** ($P \leq 0.0001$) (2-way ANOVA; Dunnett's multiple comparison) (C) Glucose uptake stimulated by increasing concentrations of insulin or *cis* isomer is expressed as fold glucose uptake (pmol/min/mg) above basal. Insulin *vs cis* isomer (ns) (paired *T-test*). (D) DNA synthesis in response to increasing concentrations of dicarba insulins is shown as percentage incorporation of ^{3}H-thymidine (^{3}H-Thy) above basal. All data in (A–D) are the mean ± S.E.M. n = at least 3 independent experiments. (E) Insulin tolerance test in mice fed on a normal diet (chow), or (F) on a high fat diet were administered through intraperitoneal injection (ip) with 0.75 IU/kg insulin (squares; solid lines) or *cis* isomer (triangles; dotted lines) under non-fasting conditions and tail vein blood glucose was measured *via* glucose meter at indicated times (Wong et al., 2011). n = 5–6 per group. Blood glucose levels are expressed as change over basal levels (mmol / L). Chow diet, insulin *vs cis* isomer ** ($P \leq 0.01$); high fat diet, insulin *vs cis* isomer ** ($P \leq 0.01$) (paired *T-test*).

2.3.4 *In vitro* Metabolic and Mitogenic Activity

Outline: Cis dicarba insulin is significantly less potent than native insulin in promoting DNA synthesis while effectively promoting glucose uptake in vitro.

The *cis* isomer was equipotent to native insulin in promoting glucose uptake by NIH3T3-L1 adipocytes (Fig. 2.2*C*), aligning with its equipotency in the above receptor binding and receptor activation assays. However, the *cis* isomer was 5-10 fold less potent than native insulin in promoting DNA synthesis (Fig. 2.2*D*), despite its equal affinity for IR and IGF-1R. The *trans* isomer was unable to stimulate DNA synthesis significantly above basal levels, correlating with its poor receptor binding ability.

2.3.5 Insulin Tolerance Test

Outline: Cis dicarba insulin effectively lowers blood glucose levels in mice.

The *cis* isomer lowered blood glucose more effectively than native insulin in an insulin tolerance test in mice (Fig. 2.3*E*) measured as described (Wong et al., 2011). This was also evident in insulin-resistant mice fed on a high-fat diet (Fig. 2.2*F*).

2.3.6 Biophysical Characterisation

Outline: Cis dicarba insulin is themordynamically less stable than native insulin.

The effect of introduction of a dicarba bond at A6–A11 on protein secondary structure and stability was monitored by circular dichroism (CD; Fig. 2.3). Far UV spectra indicate (Appx. Table 2.2) that both the *cis*- and *trans* isomers have significantly lower helical content (37% and 23%, respectively) than native insulin (48% in my assay, similar to that reported by others(Hua and Weiss, 2004)). In my experiments, native insulin exhibits a sigmoidal thermal denaturation curve (as monitored by ellipticity at 222 nm) with apparent midpoint T_m = ~60 °C (Fig. 2.3*A* and Appx. Fig 2.5*B*), similar to the previously-reported value.(Weiss et al., 2000) In contrast, both dicarba isomers exhibit only a small decrease in ellipticity with increasing temperature (Fig. 2.3*B* and Appx. Fig 2.5*C*). The slope of the *trans* isomer denaturation curve appears slightly lower than that of the *cis* isomer, most likely because the *trans* isomer has a much lower initial helical content. Insulin exhibits a two-state transition upon chemical denaturation (ΔG = 4.74 kcal.mol-^{1}; Fig. 2.3*C*). The dicarba insulin analogues are considerably less stable, with inferred ΔG = 1.98 kcal mol^{-1} for the *cis* isomer and ΔG = 1.6 kcal mol^{-1} for the *trans* isomer (Fig. 2.3*C*).

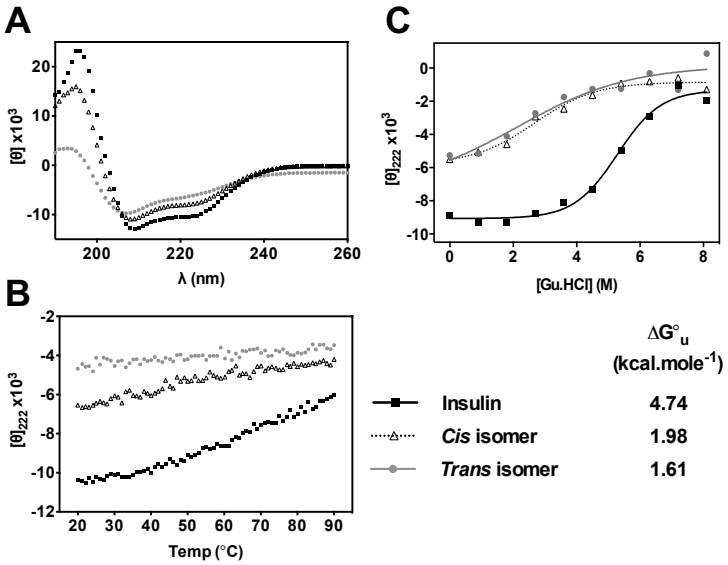

Figure 2.3 Thermal and chemical stability of *cis*- and *trans* isomers.(A) Circular dichroism far-UV spectra reveal lower helical propensities in both the *cis*- and *trans* isomers. θ = ellipticity. (B) Differences in thermal unfolding are monitored by ellipticity at 222 nm and show both the *cis*- and *trans* isomers are considerably less stable than insulin. (C) Unfolding in the presence of guanidine demonstrates that both isomers are considerably destabilized compared to insulin. ΔG values derived from guanidine denaturation studies are listed.

2.3.7 Crystal Structure Determination

Outline: Cis- and trans dicarba insulins crystal structures exhibit a T-state-like conformation.

The X-ray crystal structures of the *cis*- and *trans* isomers were determined using diffraction data to 2.70 Å and 1.55 Å resolution, respectively, with the crystals being grown under similar conditions (see *Methods*). Data processing and refinement statistics are presented in *Table 2.1*. Both crystal structures exhibit a T-state-like conformation in that the B chain *N*-terminal segment adopted an extended conformation folded back against the interface between the B chain helix and the polypeptide linker between the two A chain helices (Figs. 2.4, *A* and *B*). Both crystal structures also contain dimers formed in a fashion closely similar to that of the classical insulin T-state dimer. In the crystal structure of the *cis* isomer, residues A1 to A10 appear largely disordered, with the A chain *N*-terminal helix being represented by no more than a relatively featureless "blob" of difference electron density (Fig. 2.4*D*). The dimensions of this blob loosely approximate that of the polypeptide core of the 8-mer α-helix of the native hormone and likely reflect a crystallographic superposition of the helix in a variety of azimuthal and axial orientations. Various unsuccessful attempts were made to obtain alternative crystals of the *cis* isomer with higher structural definition of the A-chain *N*-terminal helix. Nevertheless, we were able to build a tentative model of the *cis* isomer into the available electron density and to refine this model crystallographically to acceptable R_{work} / R_{free} statistics, though with poor overall stereochemistry (as evidenced by the root-mean-square deviations (RMSDs) of the bond angle and bond lengths from ideality; Table 2.1). The Ramachandran plot statistics for the two structures are: *trans* isomer: 99% in the favoured region, none in the disallowed region; *cis* isomer: 72% in the favoured region, 11% in the disallowed region (the latter values aligning with the poor stereochemical nature of the model). We note that, in the *trans* isomer structure, the A1–A10 segment is involved in crystal contacts whereas in the *cis* isomer structure the A1–A10 segment is not involved in crystal contacts (or at least not in the putative conformation in which it has been modelled).

Table 2.1 X-ray diffraction data processing and refinement statistics

	***cis* isomer**	***trans* isomer**
Data collection[1]		
Space group	$I2_13$	$P2_13$
Cell dimensions *a*, *b*, *c* (Å)	79.78, 79.78, 79.78	77.28, 77.28, 77.28
Resolution (Å)	28.20 - 2.70 (2.80 - 2.70)[2]	30 - 1.55 (1.60 - 1.55)[2]
R_{merge}	0.066 (1.653)	0.144 (5.03)
$I / \sigma (I)$	16.19 (1.13)	11.72 (0.38)
$CC_{1/2}$	0.999 (0.280)	0.999 (0.107)
Completeness (%)	98.8 (98.9)	0.999 (1.00)
Redundancy	6.0 (6.2)	10.8 (10.4)
Molecules / asymmetric unit	1	2
Refinement		
Resolution (Å)	28.20 - 2.70	30.0 - 1.55
No. reflections	2403	22449
R_{work} / R_{free}	0.223 / 0.282[3]	0.195 / 0.215[3]
No. atoms		
Protein	404	827
Ligand/ion	0	0
Water	0	97
***B*-factors**		
Protein (Å^2)	120.	33.4
Water	n.a.	46.7
R.m.s. deviations		
Bond lengths (Å)	0.011	0.006
Bond angles (°)	1.5	0.8

[1] Diffraction data are from a single crystal in both instances.
[2] Resolution limits were set based on the $CC_{1/2}$ correlation statistic being assessed significant at the P=0.001 level of probability.
[3] Free set comprised 5% of the reflections.

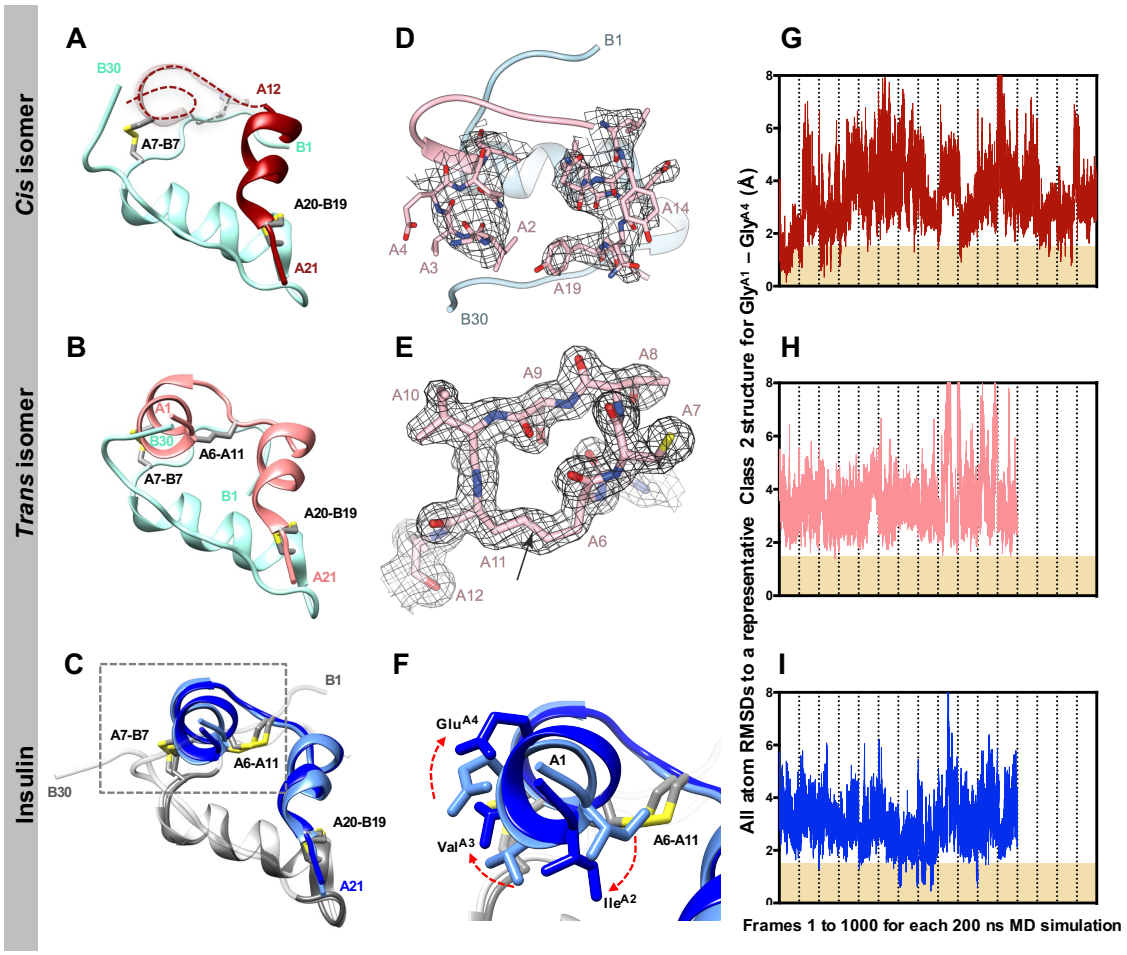

Figure 2.4 Structural comparison of *cis*- and *trans* isomers with T-state insulin structures.(A) The *cis*- and (B) *trans* isomers represent T-state insulins with conserved B-chain structures (*green*). The *cis* isomer has a poorly defined A1–A8 helix (*dotted line*), whereas the two *trans* isomers in the crystallographic asymmetric unit both display a Class 1 A1–A8 helix. (C) Alignment of the two insulin structures within the asymmetric unit of PDB entry 1MSO are aligned across their B chain helices, showing both a Class 1 (*light blue*) and Class 2 (*dark blue*) A1–A8 helix. (D) ($2mF_{obs}$ - DF_{calc}) difference electron density associated with the residues within the *N*- and *C*-terminal helices of the A chain of the *cis* isomer; contour level: 1 σ. (E) ($2mF_{obs}$ - DF_{calc}) difference electron density in the vicinity of the A6–A11 dicarba bond (*arrowed*) within the *trans* isomer, contour level = 1.3 σ. (F) A zoom-in view of the boxed selection in panel (C) highlighting the differences in the A2, A3 and A4 side-chain positions of the two different classes. (G–I) Analysis of molecular dynamics data, showing RMSDs of all atoms of residues Gly^{A1} to Glu^{A4} for each simulation frame with respect to a representative Class 2 conformation structure. Regions corresponding to the Class 2 conformation are shaded *yellow*. Average RMSDs over all simulation frames for insulin, *cis* isomer and *trans* isomer are 3.0 ± 0.9 Å, 3.4 ± 1.3 Å and 3.5 ± 1.0 Å, respectively. Note that each bin between pairs of tick marks on the horizontal axis represents a separate 200 ns simulation.

2.3.8 Structural Comparison

Outline: The T-state insulin can be partitioned into two classes on the basis of the conformation of A-chain N-terminal helix; in which the Class 2 adopts a wider helix than the Class 1.

In order to compare the three-dimensional structure of the *trans* isomer determined here with those of native insulin, we began by analysing the conformations of residues A1–A11 in extant insulin crystal structures in the Protein Data Bank (PDB; see Appx. Table 2.3). Inspection of T-state structures of (receptor-free) insulin monomers, including monomers from T_2, T_6, T_3R_3 and $T_3R^f_3$ assemblies by alignment of the respective B-chain helices (residues B8–B20) revealed that they could be partitioned into two classes on the basis of the conformation of the A-chain *N*-terminal helix: Class 1 (30 structures), in which residues A1 to A9 exhibit the classical (*i*, *i*+4) α-helical hydrogen-bonding pattern; and Class 2 (93 structures), wherein residues A1 to A5 form a single α-helical turn and residues A3 to A9 adopt a wider helix conformation, approximating an (*i*, *i*+5) π-helix (Fig. 2.4, *C* and *F*). The distinction between these two classes is most apparent in the hydrogen bonding exhibited by the backbone amide of Thr^{A8}: in Class 1 structures the amide forms a canonical α-helical (*i*, *i*+4) hydrogen bond with the backbone carbonyl oxygen of Glu^{A4}; however, in the Class 2 structures, the amide hydrogen bonds to the backbone carbonyl of Val^{A3}. In many cases, these two classes occur within the same crystallographic asymmetric unit structure, with 27 out of 30 Class 1 structures being from crystals that also contain within their asymmetric unit an insulin of Class 2 conformation.

Concomitant with these differences in helical conformation are differences in the relative azimuthal positioning of residues A1–A5 about the helix axis (Fig. 2.4*F* and Appx. Table 2.4). In addition, the corresponding mean $C\alpha^{A6}$-to-$C\alpha^{A11}$ distance of the Class 1 insulins (4.78 ± 0.13 Å) is slightly longer than the mean $C\alpha^{A6}$-to-$C\alpha^{A11}$ distance of the Class 2 insulins (4.55 ± 0.37 Å). Concomitantly, the mean $C\alpha^{A7}$-to-$C\alpha^{B7}$ distance of the Class 1 insulins (4.62 ± 0.12 Å) is slightly shorter than the mean $C\alpha^{A7}$-to-$C\alpha^{B7}$ distance of the Class 2 insulins (4.76 ± 0.11 Å) (Appx. Table 2.5).

The crystal structure of the *trans* isomer corresponds to a Class 1 insulin conformation. Residues A1–A9 exhibit a classical α-helical geometry, with the azimuthal positioning of residues A1–A5 being closely similar to that of native insulins within Class 1 (Fig. 2.5*A*). In addition, the $C\alpha^{A6}$-to-$C\alpha^{A11}$ distance (5.17 Å) in the *trans* isomer is more similar to the corresponding average

$C\alpha^{A6}$-to-$C\alpha^{A11}$ distance of the Class 1 insulins than the average $C\alpha^{A6}$-to-$C\alpha^{A11}$ distance of the Class 2 and IR-bound native insulin (PDB entries 4OGA, 3W12, 3W13) (Appx. Table 2.5).

These analyses are consistent with the report of Kaarlsholm *et al*.(Kaarsholm et al., 1993) of two forms of insulin that differ at residues A1–A5 through a rotation of 32° about the Cys^{A6} Cα-NH bond in the crystal structure of 2Zn porcine insulin.(Baker et al., 1988a) The Class 2 conformation of the A chain *N*-terminal helix is also observed in insulin analogues synthetically engineered to reposition the B chain *C*-terminal segment away from the hormone core, *e.g.* des[23-30]-insulin (PDB 1DEI) (Bao et al., 1997) and NMeAla-B26-DTI insulin analogue (PDB 2WRX).(Jiracek et al., 2010) This study is, however, the first to recognize the allosteric role played by the A6–A11 disulfide bond in this conformational switch without movement of the B chain *C*-terminal segment.

As far as we can ascertain from the structures of the insulin / IR Site 1-complexes (PDB entries 4OGA, 3W12 and 3W13, at resolution (3.5 - 3.9 Å)), the A-chain *N*-terminal helix of insulin (and insulin analogues) exhibits a Class 2-like structure when bound to IR (see Fig. 2.5). This is apparent in the larger-diameter A-chain *N*-terminal helix and shorter $C\alpha^{A6}$-to-$C\alpha^{A11}$ distance than those observed for Class 1 insulins, and in a similar azimuthal positioning of the constituent Cα atoms to those within Class 2 structures. The ability of the insulin A-chain *N*-terminal helix to adopt these two classes of structure indicates both (i) a degree of conformational flexibility in the three covalent bonds that connect that helix to the remainder of the hormone (*viz*., the A6–A11 and A7–B7 disulfide bonds and the downstream peptide bond), and (ii) rotameric plasticity of the side chains of the residues that form the interface between that helix and the remainder of the hormone (Fig. 2.4, *C* and *F*).

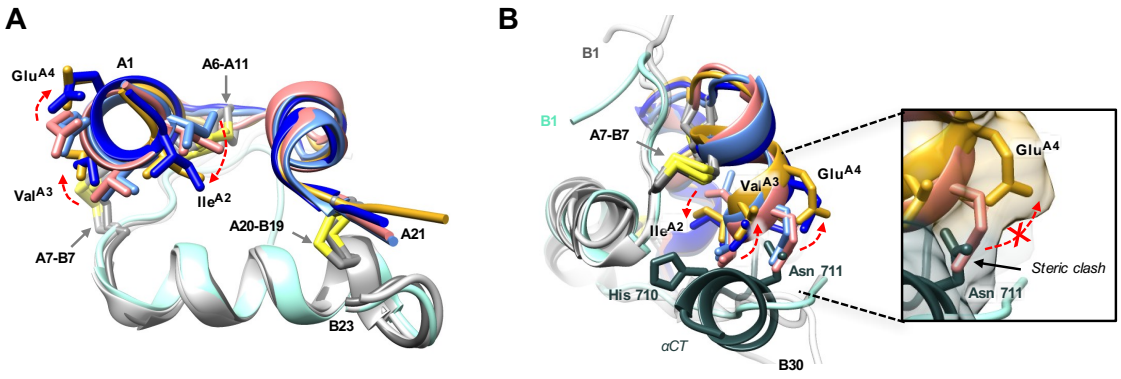

Figure 2.5 Structural comparison of the *trans* isomer with native insulin in its IR site-1 bound and receptor-free forms. (A) Overlay of *trans* isomer (*pink*) with T6 insulin (PDB entry 1MSO, Class 1 (*light blue*), Class 2 (*dark blue*)) and with IR site-1 bound insulin (PDB entry 4OGA, *gold*). Differences in the A2, A3 and A4 side-chain positions arise through rotation of the A1–A8 helix. In the complex, this allows accommodation of the IR αCT (not shown). (B) In the IR site-1 bound conformation, insulin's A1–A8 helix adopts a Class 2 conformation and the A2-A4 residues rotate to enable engagement with IR αCT (*dark green*), with insulin A3 and A4 residues flanking Asn711 of IR αCT. Colours are otherwise as in (A).

2.3.9 Molecular Dynamics

Outline: Insulin A-chain N-terminal helix is highly mobile, and native insulin and cis dicarba insulin can interchange between classes; whereas trans dicarba insulin never adopt Class 2.

Molecular dynamics simulations were conducted to explore the significance of conformational flexibility in the A6–A11 linkage and the A1–A9 helix — in particular, the distinction between the Class 1 and Class 2 conformations. Three high-resolution X-ray crystal structures were selected, each having a different conformation of the A6–A11 disulfide linkage (PDB entry 1G7B chains E and F, Class 2; PDB entry 1MSO chains A and B, Class 1; and PDB entry 3I3Z chains A and B, Class 2). Each structure was also modified to contain *cis* and *trans* isomers, resulting in nine starting structures. Multiple 200 ns MD simulations were then conducted based on each starting structure. In all simulations, it was evident that the A-chain *N*-terminal helix was highly mobile and, in many cases, interchange between classes was also observed. Indeed, although each starting structure belonged initially to a particular Class, that distinction appeared not to survive the pre-optimization phase, and hence did not bias the simulations.

Root mean square deviations (RMSDs) with respect to a representative Class 2 structure were calculated for all atoms of residues A1 to A4 for each frame of each MD simulation. From the RMSD plots (Figs. 2.4, *G* – *I*), it is seen that both insulin and the *cis* isomer can approach the Class 2 conformation (RMSD < ~1.5 Å), albeit rarely (Figs. 2.4, *G* and *I*). In contrast, the *trans* isomer almost never adopted a Class 2 conformation, with RMSD values being generally >2 Å and very rarely <1.5 Å (two disparate frames out of 12,000 had an RMSD <1.5 Å) (Fig. 2.4*H*). Interestingly, three different hydrogen-bonding partners for the backbone amide of Thr^{A8} were observed in the structures generated in the MD simulations: Val^{A3} (*i*, *i*+5; π-helix), Glu^{A4} (*i*, *i*+4; α-helix) and Gln^{A5} (*i*, *i*+3; 3_{10}-helix) (Appx. Table 2.6). For both insulin and the two dicarba isomers, Glu^{A4} and Gln^{A5} were the dominant hydrogen bonding partners. A backbone hydrogen bond between Thr^{A8} and Val^{A3} was seen only in ~4% of simulation frames for insulin and the *cis* isomer and never in any of the *trans* isomer MD runs. Cluster analysis suggests that structures with Thr^{A8}-Glu^{A4} and Thr^{A8}-Gln^{A5} backbone hydrogen bonds are not distinct conformations and transitions between them are part of a natural "breathing" mode of the helix, possibly explaining why Thr^{A8}-Gln^{A5} backbone hydrogen bonds have not been found in extant crystal structures. The average $C\alpha^{A6}$-to-$C\alpha^{A11}$ distance for Class 1 insulin and for *cis* isomer structures were effectively the same within the MD trajectories and the X-ray structures (Appx. Table 2.5). Curiously, the average $C\alpha^{A6}$-to-$C\alpha^{A11}$ distances for Class 2 structures in the MD simulations (4.05 Å and 3.97 Å for the *cis* isomer and insulin, respectively) were found to be shorter than seen in the crystal

structures (4.50 Å and 4.55 Å for the *cis* isomer and insulin, respectively), suggesting that the distance is possibly distorted from its optimal value in the crystalline phase, or that there are differences in the respective stereochemical libraries that underpin MD and crystallographic refinement methodologies.

It is important to note that the variations in the RMSDs through the time course of the simulations (Figs. 2.4, *G* – *I*) are larger for the *cis* isomer (σ = 1.3 Å) than for either the *trans* isomer (σ = 1.0 Å) or insulin itself (σ = 0.9 Å). This indicates that the *N*-terminus of the *cis* isomer is more conformationally flexible than that of the other analogues, suggesting an explanation for the disorder of this helix in the X-ray crystallographic maps. Although the *cis* isomer is seen to access the Class 2 conformation in MD simulations and the *trans* isomer is not, their average RMSDs from the Class 2 conformation across all simulation frames are similar (3.4 and 3.5 Å, respectively) and are higher than for insulin (3.0 Å). These increased RMSDs for the dicarba insulin analogues correlate with statistically significant decreases in the helicity of the *N*-terminal A chain residues (as measured by the backbone conformations of the relevant resides) in comparison with that of insulin (see Appx. Table 2.7).

2.4 DISCUSSION

Whereas the role of individual insulin surface residues in receptor binding has been intensively investigated, there has been less examination of the physico-chemical nature of the disulfide bonds, their stereochemistry, and their structural contribution to insulin / IR engagement and resultant biological activities. Here, we have synthesized the two stereoisomers of an A6–A11 dicarba insulin, determined their crystal structures and characterized their biochemical and biophysical nature. Ruthenium-alkylidene catalyzed ring-closing metathesis of insulin A-chain sequences bearing a pair of allylglycine residues provided an expedient route to intra-chain dicarba insulin analogues with different stereochemical configurations.

The dicarba stereoisomers exhibit two intriguing biological characteristics. First, the *cis* isomer is active and the *trans* inactive, as evidenced in *in vitro* assays (receptor binding, receptor activation and glucose uptake by adipocytes). The *cis* isomer also demonstrates promising therapeutic potential, evident from its ability to lower blood glucose more rapidly than native insulin in both normal and insulin-resistant mice. Second, the *cis* isomer is significantly less potent than native insulin in stimulating DNA synthesis, indicating its reduced ability to promote cell growth/replication. The unique biological characteristics of the dicarba stereo-isomers reflect the structural outcomes of the respective rigid configurations of the dicarba linkages.

These findings thus presented us with an opportunity to utilize the stereoisomers as tools to scrutinize further the mechanistic role of A6–A11 bond and its influence in mediating the structural transitions of insulin to its active conformation.

To this end I sought to identify structural features that might account for the differences in biological activities of the *cis* and *trans* isomers. Intriguingly, both isomers exhibit reduced helical content as assessed by CD and by MD. In the case of the *cis* isomer, such reduced helical content in solution is consistent with the disorder of the A-chain *N*-terminal helix observed in its crystal structure. In the case of the *trans* isomer, CD measurement indicates a lower helical content than the *cis* isomer. However, both molecules within the crystallographic asymmetric unit of the *trans* isomer show an ordered A chain *N*-terminal helix. Unlike in the structure of the *cis* isomer, the respective A-chain *N*-terminal helices of the two *trans* isomers are involved in crystal contacts, suggesting their crystallographic order may be brought about by these contacts: in solution, the *trans* isomer A chain is likely disordered. In support, preliminary atomic force microscopy analysis (see *Chapter 3*) shows an increased rate of fibrillation of both dicarba isomers compared to that of insulin. A key feature of fibril formation is proposed to be loss of helical structure as the A-chain *N*-terminal helix transitions to a β sheet (Brange et al., 1997a). Consistent with the CD and MD data, earlier studies show that the A-chain *N*-terminal helix is susceptible to perturbation through removal of the A6–A11 disulfide bond (Weiss et al., 2000, Hua et al., 1996, Liu et al., 2004) or residue substitution elsewhere within the helix (Yang et al., 2010b, Huang et al., 2007, Hua et al., 2002a, Chen and Feng, 1998) and that it can undergo conformational fluctuation (Yang et al., 2010b, Olsen et al., 1998).

An explanation for the *cis* isomer being active and the *trans* isomer being inactive arises from the analysis of extant T-state insulin structures. The existence of the two Classes (1 and 2) of T-state insulin structures suggests that the hormone is capable of transition between the two forms. As far as can be ascertained at the resolution of the IR-site-1-complexed structures of insulin, the IR-bound conformation of the hormone corresponds to Class 2. The crystal structure of the *trans* isomer indicates that it has a Class 1 conformation, and its inactivity suggests that it is incapable of transitioning to a Class 2 structure. This hypothesis is supported by the MD simulations, which show that, although the *trans* isomer is capable of transiently adopting a range of structures, the Class 2 conformation appears to be precluded. An overlay of *trans* isomer and Class 1 insulin X-ray structures onto those of Class 2 and receptor-bound (PDB entry 4OGA) insulins shows a distinction between the two sets of structures (Fig. 2.5*A*), with the *N*-terminal end of the helix axis adopting different rotational configurations with respect to the hormone

core (highlighted in Movie (https://static-content.springer.com/esm/art%3A10.1038%2Fs41598-017-16876-3/MediaObjects/41598_2017_16876_MOESM2_ESM.mov; see also Appx. Fig 2.8 for a snap shots of the movie). The overlay also indicates that there would be a significant steric clash between side chain of Glu^{A4} of the Class 1 / *trans* isomer structures and the side chains of Asn^{711} within the receptor αCT helix (Fig. 2.5*B*).

Hence, introduction of the *cis* and *trans* dicarba linkages is seen to affect the structural dynamics of the A chain *N*-terminal helix in three ways: (i) increased short-range motion: both *cis* and *trans* linkages disrupt the residue backbone conformations (*i.e.*, helicity), as evidenced in both the CD spectroscopy and the MD simulations—this possibly due to the increased rigidity of the dicarba linkages transmitting more vibrational energy from the rest of the molecule into the helix in comparison with the less rigid disulfide bond of insulin; (ii) increased long-range motion in the *cis* isomer, evidenced by the increased range of RMSDs (Fig. 2.4*G*) and the corresponding increased standard deviation seen in the MD simulations, as well as in the disorder apparent in the *cis* isomer X-ray structure; and (iii) decreased conformational flexibility in the *trans* isomer: the longer *trans*-dicarba bond (Appx. Table 2.5) changes the conformation of the A6–A11 loop, preventing the formation of a Thr^{A8}-Val^{A3} hydrogen bond and hence the adoption of a Class 2 conformation. The inability of the *trans* isomer to adopt a Class 2 conformation (as seen within the MD simulations) then precludes its engagement with IR site 1 and results in its observed biological inactivity.

The activity of the *cis* isomer demonstrates that reduction-oxidation of the native A6–A11 disulfide bond (if it occurs) does not play an obligatory role in IR binding and activation. Rather, we suggest that the A6–A11 disulfide bond is able to modulate the insulin conformation through allostery, key elements of which are revealed by this study. The ability of the A6–A11 cystine bridge to adopt a range of disulfide conformations (Appx. Table 2.3) allows switching of the *N*-terminal region of the insulin A chain between active (Class 2) and inactive (Class 1) conformations. The active conformation requires a short A6–A11 Cα-Cα distance and a concomitant lengthening of the distance between the Cα atoms of A7 and B7 (Appx. Table 2.5). The short A6–A11 Cα-Cα distance of the Class 2 structures appears to result in a "pulling" of the *N*-terminal end of A1–A8 helix away from the volume that would be occupied by IR αCT in a putative receptor complex (a conformation also adopted by mutation of B26 to NMeAla or NMeTyr (Jiracek et al., 2010)). In contrast, the longer A6–A11 linkage seen in Class 1 structures results in the base of the A chain *N*-terminal helix being closer to the B chain as a direct consequence of the A7–B7 disulfide bond length (Appx. Table 2.5). Critically, the short A6–

A11 Cα-Cα distance seen in the active Class 2 conformations appears to be necessary to allow a precise rotation of the A-chain *N*-terminal helix, which in turn positions the side chains of residues A2 to A4 in an orientation compatible with receptor binding. In insulin, it is the adoption of a particular A6–A11 disulfide conformation that gives the required Cα-Cα distance and hence access to the active conformation. While both *cis* and *trans* A6–A11 dicarba bonds promote flexibility in the A1–A8 helix, it is only the *cis* dicarba linkage that can allow the A6 and A11 Cα atoms to come into the close proximity required to adopt a Class 2 structure. The increased interchain length resulting from the presence of a *trans* carbon-carbon double bond means that the active conformation is not accessible to the *trans* isomer.

2.5 CONCLUSION

Through detailed analysis of the structure and function of the two dicarba insulin isomers generated through novel chemistry, this investigation provides the first description of the key role that the evolutionarily-conserved A6–A11 cystine bridge plays as an allosteric switch of insulin activity. This study reveals that both the configuration and flexibility of the A6–A11 disulfide linkage are essential elements in insulin's adoption of an active conformation. Additionally, it was concluded that the A6–A11 dicarba linkage of the *cis* isomer can also adopt a configuration that enables insulin receptor binding. This leads to effective lowering of blood glucose levels in mice and a significantly reduced ability to promote mitogenic signaling, a highly desirable biological property. Thus, the *cis* isomer represents an analogue with promising clinical potential. In conclusion, this investigation revealed a novel mechanism underlying insulin receptor engagement that dictates downstream biological outcomes. Using these findings as a basis we can now design improved insulin analogues for the treatment of diabetes.

CHAPTER 2

APPENDICES

CHAPTER 2 APPENDICES

APPENDIX 2A Peptide materials and reagents

4-Amino-2-pentenoic acid (allylglycine, Agl) was used as supplied by Peptech. Trifluoroacetic acid (TFA) and *N*,*N*-dimethylformamide (DMF) were supplied by Auspep and the latter was stored over 4 Å molecular sieves. Dichloromethane (DCM) and piperidine were supplied by Merck and stored over 4 Å molecular sieves. *N*,*N'*-Diisopropylcarbodiimide (DIC), diisopropylethylamine (DIPEA), 2,2'-dipyridyl disulfide (2,2'-DPDS), *N*-methylmorpholine (NMM), trifluoromethanesulfonic acid (TfOH) and triisopropylsilane (TIPS) were used as supplied by Aldrich. *O*-(7-Azabenzotriazol-1-yl)-*N*,*N*,*N'*,*N*'-tetramethyluronium hexafluorophosphate (HATU), *O*-(benzotriazol-1-yl)-*N*,*N*,*N'*,*N*'-tetramethyluronium hexafluorophosphate (HBTU), *O*-(benzotriazol-1-yl)-tripyrrolidinophosphonium hexafluorophosphate (PyBOP) and *N*-hydroxybenzotriazol (HOBt) were used as supplied by GL Biochem. Fmoc-amino acids were also used as supplied by GL Biochem and reactive sidechains were protected with the Acm, Boc, Pbf, ^{t}Bu, and Trt protection groups. Fmoc-Asp-O^{t}Bu loaded Rink-amide resin was used as supplied by Applied Biosystems.

APPENDIX 2B Catalysts and materials

Tricyclohexylphosphine[1,3-bis(2,4,6-trimethylphenyl)-4,5-dihydro-imidazol-2-ylidene] (benzylidene) ruthenium (II) dichloride (2nd generation Grubbs' catalyst) was used as supplied by Aldrich. The solvents used in all metal-catalysed metathesis reactions (DCM and a 0.4 M solution of LiCl in DMF) were degassed prior to use with high purity argon and subjected to a general freeze-pump-thaw procedure. CEM Benchmate™ microwave reactor vessels, equipped with stirrer beads, were employed for ring closing metathesis reactions.

APPENDIX 2C Synthesis of dicarba insulins.

c[Δ^4A6,11]-Dicarba human insulin transformations

*1. des_{A1-5}-[A6,11]-Agl-[A7]-Cys(^{t}Bu)-[A20]-Cys(Acm) human insulin A chain **1**.*

An automated, microwave-accelerated procedure (outlined below and in Robinson et al.(Robinson and van Lierop, 2011)) was used for the synthesis of peptide **1** (Schematic 2.1) on Fmoc-Asp-O^{t}Bu loaded Rink-amide resin (164 mg, 100 μmol). Quantities of HATU, DIPEA, piperidine and each Fmoc-amino acid were used as described by the automated protocols of the instrument. After sequence completion, the resin-bound peptide was transferred into a fritted syringe and treated with an acetic anhydride solution (7 mL; DMF : acetic anhydride : NMM; 94 : 5 : 1) for 2 h. The resin was washed with DMF (7 mL; 3 × 1 min), DCM (7 mL; 3 × 1 min) and MeOH (7 mL; 3 × 1 min), then left to dry in vacuo for 1 h. Prior to treatment with MeOH, a small aliquot of the resin-bound peptide was removed and subjected to Fmoc-deprotection and to TFA-mediated cleavage (outlined below) for RP-HPLC and mass spectral analysis (Appx. Fig 2.1*A*). This supported formation of the desired peptide **1** in 90% purity. Mass spectrum (ESI^+, MeCN : H_2O : TFA): m/z 658.3 $[M + 3H]^{3+}$, ⅓($C_{87}H_{137}N_{20}O_{28}S_2$) requires 658.0; 986.6 $[M + 2H]^{2+}$, ½($C_{87}H_{136}N_{20}O_{28}S_2$) requires 986.5; 1315.7 $[2M + 3H]^{3+}$, ⅓($C_{174}H_{271}N_{40}O_{56}S_4$) requires 1314.9. RP-HPLC (Agilent: Vydac C18 analytical column, 15 → 50% buffer B over 35 min): t_R = 18.4 min. Buffer A: 0.1% Aqueous TFA; Buffer B: 0.1% TFA in MeCN.

*2. des_{A1-5}-c[Δ^4A6,11]-Dicarba-[A7]-Cys(^{t}Bu)-[A20]-Cys(Acm) human insulin A chain **2**.*

Resin-bound peptide **1** was subjected to the general microwave-accelerated RCM procedure(Van Lierop et al., 2011b, van Lierop et al., 2013) under the following conditions: Resin-bound **1** (420 mg, 100 μmol), DCM (4 mL), 0.4 M LiCl in DMF (0.2 mL), 2nd generation Grubbs' catalyst (17 mg, 20 μmol), 100 W μwave, 100 ºC, 2 h, >95% conversion into **2** (Schematic 2.1). Post metathesis, a small aliquot of resin-bound peptide was subjected to Fmoc-deprotection and to TFA-mediated cleavage for RP-HPLC and mass spectral analysis (Appx. Fig 2.1*B*). RP-HPLC (Agilent: Vydac C18 analytical column, 15 → 50% buffer B over 35 min): t_R = 17.3 min. ESI^+, (MeCN : H_2O : TFA): m/z 649.0 $[M + 3H]^{3+}$, ⅓($C_{85}H_{133}N_{20}O_{28}S_2$) requires 648.6; 972.5 $[M + 2H]^{2+}$, ½($C_{85}H_{132}N_{20}O_{28}S_2$) requires 972.4; 1296.6 $[2M + 3H]^{3+}$, ⅓($C_{170}H_{263}N_{40}O_{56}S_4$) requires 1296.3.

*3. c[Δ^4A6,11]-Dicarba-[A7]-Cys(^{t}Bu)-[A20]-Cys(Acm) human insulin A-chain **3**.*

Method A: The automated, microwave-accelerated procedure described above was used to attach the remaining five residues on resin-bound peptide **2** (1.46 g, 200 μmol). Quantities of HATU, DIPEA, piperidine and each Fmoc-amino acid were used as described by the automated protocols of the instrument. After sequence completion, the resin-bound peptide was transferred into a fritted syringe and subjected to Fmoc-deprotection in the presence of 20% v/v piperidine in DMF (7 mL; 1 × 1 min, 2 × 10 min). The resin was washed with DMF (7 mL; 5 × 1 min), DCM (7 mL; 3 × 1 min) and MeOH (7 mL; 3 × 1 min), then left to dry in vacuo for 1 h. The resin-bound peptide was subjected to TFA-mediated cleavage. RP-HPLC and mass spectral analysis of the resultant off-white solid supported formation of the desired peptide **3** as cis- and trans isomers in a 3 : 1 ratio (Appx. Fig 2.1, *C* and *D*). Cis isomer 3: Mass spectrum (ESI^+, MeCN : H_2O : TFA): m/z 824.5 $[M + 3H]^{3+}$, ⅓($C_{108}H_{171}N_{26}O_{36}S_2$) requires 824.1; 1235.8 $[M + 2H]^{2+}$, ½($C_{108}H_{170}N_{26}O_{36}S_2$) requires 1235.6. RP-HPLC (Agilent: Vydac C18 analytical column, 15 → 50% buffer B over 35 min): t_R = 17.9 min. Trans-**3**: Mass spectrum (ESI^+, MeCN : H_2O : TFA): m/z 824.2 $[M + 3H]^{3+}$, ⅓($C_{108}H_{171}N_{26}O_{36}S_2$) requires 824.1; 1235.5 $[M + 2H]^{2+}$, ½($C_{108}H_{170}N_{26}O_{36}S_2$) requires 1235.6. RP-HPLC (Agilent: Vydac C18 analytical column, 15 → 50% buffer B over 35 min): t_R = 18.9 min.

Method B: Peptide **3** was synthesised with the automated, microwave-accelerated procedure outlined above using Fmoc-Asp-O^{t}Bu loaded Rink-amide resin (164 mg Rink-amide resin, 100 μmol). Quantities of HATU, DIPEA, piperidine and each Fmoc-amino acid were used as described by the automated protocols of the instrument. After construction of the 10-mer (*i.e.* SLYQLENYCN), the pre-fabricated residue (2S,7S)-2-((((9H-Fluoren-9-yl)methoxy)carbonyl)amino)-8-((4-nitrobenzyl)oxy)-7-((((4-nitrobenzyl)oxy)carbonyl)amino)-8-oxooct-4-enoic acid(Gleeson et al., 2016) (cis-**S1**, 2 eq, E/Z ratio = 1:25) was manually coupled into the sequence. Analysis of the filtrate following coupling showed unreacted acid cis-**S1** in unchanged isomeric ratio. After mass spectral analysis of an aliquot of resin-cleaved peptide supported incorporation of the bridging unit, three additional residues were incorporated (*i.e.*, TSI) before the pNb and pNz protecting groups were removed *via* treatment with $SnCl_2$ (6 M) and HCl/DMF (5 mM) in DMF (3 x 2 mL) for 0.5 h. The resin-tethered peptide (12.5 μmol) was then subjected to cyclisation using a solution of PyBOP (65 mg, 125 μmol), HOBt (16.9 mg, 125 μmol) and NMM (27.5 μL, 250 μmol) in DMF (3 mL) and shaken for 6 h at RT. The automated, microwave-accelerated procedure described above was then used to attach the remaining five residues (*i.e.* GIVEQ) to afford resin-bound peptide **3**. After sequence completion, the peptide

was transferred into a fritted syringe and subjected to Fmoc-deprotection in the presence of 20% v/v piperidine in DMF (7 mL; 1 × 1 min, 2 × 10 min). The resin was washed with DMF (7 mL; 5 × 1 min), DCM (7 mL; 3 × 1 min) and MeOH (7 mL; 3 × 1 min), then left to dry in vacuo for 1 h. The resin-bound peptide was subjected to TFA-mediated cleavage and RP-HPLC and mass spectral analysis (Appx. Fig 2.1*L*). The E/Z ratio of the two insulin A-chain isomers, *cis*-**3** and trans-**3**, was found to be ~ 1:25 which is consistent with the original isomeric ratio of the incorporated bridging unit *cis*-**S1**. Additionally, the retention times of the two peaks were consistent with previously prepared dicarba insulin A chains prepared *via* Method A described above.

*4. c[Δ^{4}A6,11]-Dicarba-[A7]-Cys(Pyr)-[A20]-Cys(Acm) human insulin A chain **4**.*

The concerted tert-butyl-deprotection and pyridinyl-reprotection of Cys_7 was carried out according to a procedure described by Bullesbach et al.(Bullesbach and Schwabe, 2001) A solution of ice-cold TFA : TfOH (13.4 mL; 4 : 1) was added to a stirred solution of the cyclic peptide **3** (516.1 mg, 0.2 mmol) and 2,2'-DPDS (227.1 mg, 1.0 mmol) in TFA : anisol (13.4 mL; 9 : 1) at 0 °C. After 1.5 h, the reaction mixture was reduced under a constant stream of air and ice-cold Et_2O (70 mL) was added to induce peptide precipitation. The resultant solid was then collected by centrifugation (3 × 6 min) and analysed by RP-HPLC and mass spectrometry (Appx. Fig 2.1, *E* and *F*). This supported formation of the S-activated peptide **4** as two isomers, *cis*-**4** and trans-**4**, in a 3 : 1 ratio. The solid was lyophilised and purified by RP-HPLC (Agilent: Vydac C18 preparative column, 15 → 45% buffer B over 40 min, t_R = 22.8 and 24.4 min). Selected fractions were combined and lyophilised to give two isomers, *cis*-**4** and trans-**4**, of the desired peptide as colourless solids (*cis*-**4**: 43.6 mg, 11.3% and trans-**4**: 14.7 mg, 11.6%) in >95% purity. *Cis*-**4**: Mass spectrum (ESI^+, MeCN : H_2O : TFA): m/z 842.1 $[M+3H]^{3+}$, ⅓($C_{109}H_{166}N_{27}O_{36}S_3$) requires 841.7; 1262.7 $[M + 2H]^{2+}$, ½($C_{109}H_{165}N_{27}O_{36}S_3$) requires 1262.1. RP-HPLC (Agilent: Vydac C18 analytical column, 15 → 50% buffer B over 35 min): t_R = 16.7 min. Trans-**4**: Mass spectrum (ESI^+, MeCN : H_2O : TFA): m/z 842.1 $[M+3H]^{3+}$, ⅓($C_{109}H_{166}N_{27}O_{36}S_3$) requires 841.7; 1262.7 $[M + 2H]^{2+}$, ½($C_{109}H_{165}N_{27}O_{36}S_3$) requires 1262.1. RP-HPLC (Agilent: Vydac C18 analytical column, 15 → 50% buffer B over 35 min): t_R = 18.2 min.

*5. [B19]-Cys(Acm) human insulin B chain **5**.*

The synthesis of the peptide was performed according to the automated, microwave-accelerated SPPS procedure described above on Fmoc-Thr(^{t}Bu)-PEG-PS resin (667 mg, 100 μmol).

Quantities of DIPEA (N,N-Diisopropylethylamine), HBTU (2-(1H-benzotriazol-1-yl)-1,1,3,3-tetramethyluronium hexafluorophosphate), HOBt (1-hydroxy-benzotriazole), piperidine and each Fmoc-amino acid were used as described by the automated protocols of the instrument. A small aliquot of resin-bound peptide was subjected to the cleavage procedure outlined above (Fmoc-deprotection followed by TFA-mediated cleavage) for RP-HPLC and mass spectral analysis (Appx. Fig 2.1*G*). This supported formation of the desired peptide **5**. Following global Fmoc-deprotection and TFA-mediated cleavage of the remaining peptide **5** from the resin (1.11 g), the resultant pale yellow solid was purified by RP-HPLC (Agilent: Vydac C18 preparative column, 25 → 45% buffer B over 30 min, t_R = 16.0 min). Selected fractions were combined and lyophilised to give the desired peptide **5** as a colourless solid (106 mg, 30%) in 90% purity. Mass spectrum (ESI^+, MeCN : H_2O): m/z 876.0 $[M + 4H]^{4+}$, ¼($C_{161}H_{243}N_{41}O_{43}S_2$) requires 875.7; 1167.6 $[M + 3H]^{3+}$, ⅓($C_{161}H_{242}N_{41}O_{43}S_2$) requires 1167.2. RP-HPLC (Agilent: Vydac C18 analytical column, 25 → 45% buffer B over 30 min): t_R = 15.0 min.

6. Monocyclic A-B heterodimer of c[Δ⁴A6,11]-dicarba human insulin ***6****.*

<u>*Cis* isomer:</u> The modified insulin B chain **5** (14.6 mg, 4.17 μmol) in H_2O (12 mL) was added dropwise to a stirred solution of the insulin A chain *cis*-**4** (13.2 mg, 5.23 μmol) in 50 mM NH_4HCO_3 solution (8 mL). Reaction progress was monitored by RP-HPLC and mass spectrometry and after 45 min (Appx. Fig 2.1, *H* and *I*) the oxidation was terminated by addition of AcOH and lyophilised to give a crude pale yellow solid (51.2 mg) which was used without purification in the next step. *Cis*-**6**: Mass spectrum (ESI^+, MeCN : H_2O : TFA): m/z 1183.4 $[M + 5H]^{5+}$, ⅕($C_{265}H_{402}N_{67}O_{79}S_4$) requires 1183.0; 1479.0 $[M + 4H]^{4+}$, ¼($C_{265}H_{401}N_{67}O_{79}S_4$) requires 1478.5. RP-HPLC (Vydac C18 analytical column, 0 → 25% buffer B over 5 min then 25 → 50% buffer B over 30 min): t_R = 18.9 min.

<u>*Trans* isomer:</u> The modified insulin B chain **5** (3.53 mg, 1.00 μmol) in H_2O (6 mL) was added dropwise to a stirred solution of the modified insulin A chain trans-**4** (4.94 mg, 1.96 μmol) in 50 mM NH_4HCO_3 (4 mL). Reaction progress was monitored by RP-HPLC and mass spectrometry and after 45 min (Appx. Fig 2.1), the oxidation was terminated by addition of AcOH and lyophilised to give a crude pale yellow solid (8.3 mg) which was used without purification in the next step. Trans-**6**: Mass spectrum (ESI^+, MeCN : H_2O : TFA): m/z 1183.8 $[M + 5H]^{5+}$, ⅕($C_{265}H_{402}N_{67}O_{79}S_4$) requires 1183.0; 1478.7 $[M + 4H]^{4+}$, ¼($C_{265}H_{401}N_{67}O_{79}S_4$) requires 1478.5. RP-HPLC (Vydac C18 analytical column, 0 → 25% buffer B over 5 min then 25 → 50% buffer B over 30 min): t_R = 18.5 min.

*7. c[Δ^4A6,11]-Dicarba human insulin **7**.*

<u>*Cis* isomer:</u> A 10 mM solution of iodine in glacial acetic acid (22.5 mL) was added to a stirred solution of the crude reaction mixture above (51.2 mg) containing the monocyclic peptide *cis*-**6** (4.17 μmol (max.)) in glacial acetic acid (22.5 mL) and 60 mM HCl (1.5 mL). Reaction progress was monitored by RP-HPLC and after 2.75 h, ice-cold Et_2O (245 mL) was added to induce peptide precipitation. The resultant yellow solid was collected by centrifugation (1 × 10 min) and 20 mM ascorbic acid (2 mL) was then added to quench any excess iodine before analysis *via* RP-HPLC and mass spectrometry (Appx. Fig 2.1, *J* and *K*). The resultant solid was then purified by RP-HPLC (Agilent: Vydac C18 preparative column, 0 → 30% buffer B over 5 min then 30 → 40% buffer B over 60 min: t_R = 16.4 min). Selected fractions were combined and lyophilised to give *cis*-**7** of the desired c[Δ^4A6,11]-dicarba human insulin analogue as a colourless solid (6.1 mg, 26%) in >99% purity. *Cis*-**7**: Mass spectrum (ESI$^+$, MeCN : H_2O : TFA): m/z 1154.6 $[M + 5H]^{5+}$, $^1/_5(C_{259}H_{390}N_{65}O_{77}S_4)$ requires 1154.1; 1443.1 $[M + 4H]^{4+}$, $¼(C_{259}H_{389}N_{65}O_{77}S_4)$ requires 1442.4. RP-HPLC (Agilent: Vydac C18 analytical column, 0 → 30% buffer B over 5 min then 30 → 40% buffer B over 30 min): t_R = 18.7 min.

<u>*Trans* isomer:</u> A 10 mM solution of iodine in glacial acetic acid (7.5 mL) was added to a stirred solution of the crude reaction mixture above (8.3 mg) containing the monocyclic peptide *trans*-**6** (1.00 μmol (max.)) in glacial acetic acid (7.5 mL) and 60 mM HCl (0.5 mL). Reaction progress was monitored by RP-HPLC and after 2.75 h, ice-cold Et_2O (70 mL) was added to induce peptide precipitation. The resultant solid was collected by centrifugation (1 × 10 min) and 20 mM ascorbic acid (1 mL) was then added to quench any excess iodine before purification by RP-HPLC (Agilent: Vydac C18 preparative column, 0 → 30% buffer B over 5 min then 30 → 40% buffer B over 60 min: t_R = 17.3 min). Selected fractions were combined and lyophilised to give *trans*-**7** of the desired c[Δ^4A6,11]-dicarba human insulin analogue as a colourless solid (0.52 mg, 9%) in >99% purity (Appx. Fig 2.1). *Trans*-**7**: Mass spectrum (ESI$^+$, MeCN : H_2O : TFA): m/z 1154.8 $[M + 5H]^{5+}$, $^1/_5(C_{259}H_{390}N_{65}O_{77}S_4)$ requires 1154.1; 1443.3 $[M + 4H]^{4+}$, $¼(C_{259}H_{389}N_{65}O_{77}S_4)$ requires 1442.4. RP-HPLC (Agilent: Vydac C18 analytical column, 0 → 30% buffer B over 5 min then 30 → 40% buffer B over 30 min): t_R = 14.6 min.

APPENDIX 2D Automated microwave-accelerated peptide synthesis.

Automated microwave-accelerated SPPS was carried out using a CEM Liberty-Discover™ synthesiser. This involved the flow of dissolved reagents from external nitrogen pressurised bottles to a resin-containing microwave reactor vessel fitted with a porous filter. Coupling and deprotection reactions were carried out within this vessel and were aided by microwave energy. Each reagent delivery, wash and evacuation step was carried out according to automated protocols of the instrument controlled by PepDriver software. In a 50 mL centrifuge tube, the resin was swollen with DMF : DCM (10 mL; 1 : 1; 1 × 60 min) and connected to the Liberty™ resin manifold. The Fmoc-amino acids (0.2 M in DMF), activators (0.5 M HBTU/HOBt or HATU in DMF), activator base (2 M DIPEA in NMP) and deprotection agent (20% v/v piperidine in DMF) were measured out and solubilised in an appropriate volume of specified solvent as calculated by the PepDriver software program. The default microwave conditions used in the synthesis of each linear peptide included: Initial deprotection (40 W, 75 ºC, 0.5 min), deprotection (40 W, 75 ºC, 3 min) and coupling (20 W, 75 ºC, 5 min). Cysteine and histidine residues were subjected to modified and lower temperature microwave conditions including: Initial deprotection (40 W, 75 ºC, 0.5 min), deprotection (40 W, 75 ºC, 3 min), pre-activation (0 W, 50 ºC, 2 min) and coupling (25 W, 50 ºC, 4 min). On synthesis completion, the resin-bound peptides were automatically returned to the Liberty™ resin manifold as a suspension in DMF : DCM (1 : 1) and filtered through fritted plastic syringes (5 or 10 mL) prior to acid-mediated cleavage described below. Prior to catalysis, the resin-bound peptides were optionally capped with an acetic anhydride solution (4 mL; 94 : 5 : 1; DMF : acetic anhydride : NMM) for 2 hr, filtered through fritted plastic syringes (5 or 10 mL), washed with DMF (3 x 1 min), DCM (3 x 1 min) then MeOH (3 x 1 min), and dried *in vacuo* for 30 min.

APPENDIX 2E TFA cleavage procedures.

A small aliquot of resin-bound peptide (approx. 5 mg) was suspended in cleavage solution (1 mL; TFA : TIPS : water : thioanisol; 95 : 2 : 2 : 1) and shaken gently for 2 h. The mixture was filtered through a fritted syringe and the beads rinsed with TFA (1 × 0.2 mL). The filtrate was concentrated under a constant stream of air and the resultant oil was induced to precipitate in ice-cold Et_2O (1 mL). Cleaved peptides were collected by centrifugation (3 × 5 min) and dried for analysis by analytical RP-HPLC and mass spectrometry. For full scale resin cleavages, 20 mL of cleavage solution was used and after 4 h, the resin was rinsed with TFA (3 × 2 mL). The filtrate was concentrated under a constant stream of air and the resultant oil was induced to precipitate in ice-cold Et_2O (35 mL). Collection by centrifugation was carried out over 5 × 6 min spin times.

APPENDIX 2F Molecular Dynamics

Molecular dynamics simulations were performed using the AMBER14 software package.(D.A. Case et al., 2014) Amber ff14SB force field parameters(Maier et al., 2015) were used for all standard amino-acid residues. RESP charges(Bayly et al., 1993) and force-field parameters for the dicarba linkages were determined using the PyRED program(Dupradeau et al., 2010, F. Wang, 2013) from R.E.D. Server Development,(Vanquelef et al., 2011) available at http://q4md-forcefieldtools.org/REDServer-Development/, in conjunction with Gaussian 09.(Frisch, Gaussian, Inc., Wallingford CT, 2009) In all simulations, the Particle-Mesh Ewald (PME) technique (non-bonded cutoff 9.0 Å) was used to calculate long-range electrostatic interactions. Temperature was maintained with a Langevin thermostat, and bonds involving hydrogen atoms were constrained using the SHAKE algorithm. Initial atomic coordinates were taken from three high-resolution T-state insulin PDB entries: entry 1G7B chains E and F, entry 1MSO chains A and B and entry 3I3Z chains A and B. Each of these structures has a different conformation for the A6–A11 disulfide bond. *Cis* and *trans* isomers were created from each entry, giving a total of nine different starting structures. Charges were balanced by the addition of Na^+ ions and the structures solvated with a truncated octahedral box of TIP3P water molecules with a buffer of 9.0 Å surrounding the solute.

The following simulation protocol was used for all starting structures: (i) Atomic coordinates of the two residues of each dicarba linkage were minimised for 500 cycles using the steepest decent algorithm followed by 500 cycles with the conjugate gradient algorithm. All other atomic coordinates were held fixed with a force constant of 500 kcal mol^{-1} $Å^2$ (dicarba insulin simulations only). (ii) Solvent coordinates were minimised (500 cycles steepest descent, 500 cycles conjugate gradient). All other atomic coordinates were held fixed with a force constant of 500 kcal mol^{-1} $Å^2$. (iii) Coordinates of all atoms were minimised (2000 cycles steepest descent, 3000 cycles conjugate gradient). (iv) The system was then heated to 400 K over 20 ps with constant volume periodic boundary conditions. In this phase the solute coordinates restrained with a force constant of 10 kcal mol^{-1} $Å^2$ and the solvent left unrestrained. (v) The entire system was then allowed to equilibrate at 400 K for a further 100 ps with constant pressure periodic boundary conditions. Isotropic position scaling with a relaxation time of 2 ps was used to maintain the pressure at 1 atm. (vi) Finally, the simulation was allowed to run for a further 10 ns at 400 K, again with constant pressure dynamics, with snapshots being recorded every 2 ps.

Each of the high-temperature simulations was analysed to identify distinct conformations of the insulin analogue. Four structures were chosen from each run to use as starting geometries for room-temperature simulations. Note: eight structures were chosen from the *cis* isomer simulation based on PDB entry 1MSO as these had a different orientation of the dicarba bond to those based on PDB entries 1G7B and 3I3Z, giving a total of eight simulations with the *cis* dicarba bond in each orientation.

For each of the resulting 40 structures, the following protocol was used for the production MD runs: (i) The solvent was cooled to 300 K over 10 ps with constant volume periodic boundary conditions and the solute coordinates restrained with a force constant of 10 kcal mol^{-1} $Å^2$. (ii) The entire system was equilibrated at 300 K for a further 100 ps with constant pressure periodic boundary conditions. Isotropic position scaling with a relaxation time of 2 ps was used to maintain the pressure at 1 atm. (iii) MD runs of 200 ns were carried out with constant pressure dynamics at 300 K. Snapshots were saved every 2 ps.

Processing of simulations and cluster analysis was performed using CPPTRAJ.(Roe and Cheatham, 2013) The same custom programs as described above under *Bioinformatics* were used to assess the backbone hydrogen bonding patterns, interatomic distances and A6–A11 disulfide conformations in each MD simulation frame. DSSP(Kabsch and Sander, 1983) was also used to identify residue backbone conformations.

APPENDIX 2G Bioinformatics and Molecular Dynamics Structure Analysis

A custom program was also used to assess the backbone hydrogen-bonding pattern within each insulin structure, the program being based on the energy of NH-CO interaction as calculated from the electrostatic function within the DSSP algorithm.(Kabsch and Sander, 1983)

Appendix Equation 2A

$$E = q_1 q_2 \left[\frac{1}{r_{ON}} + \frac{1}{r_{CH}} - \frac{1}{r_{OH}} - \frac{1}{r_{CN}}\right] \times 1390 \text{ kJ mol}^{-1}$$

Interactions with E < -2.1 kJ mol^{-1}, r(H…O) ≤ 2.45 Å, a(N-H…O) ≥ 125º and a(H…O-C) ≥ 90º were identified as hydrogen bonds.

The relative azimuthal positioning of residues within the segment A1–A10 of each insulin was computed as follows. First, the direction vectors $\vec{a}$ and $\vec{b}$ of the helices defined by residues A1–A8 and B9-B19 respectively were computed using the program HELIXANG within the CCP4 suite,(Winn et al., 2011) as well as the vector $\vec{d}$ defining the line of closest approach between the two helical axes $\vec{a}$ and $\vec{b}$. The azimuthal angle ϕ_n of the *n*'th residue within the segment A1–A10 was then defined as the angle between the vector $\vec{d}$ and the vector $\vec{n}$, where $\vec{n}$ is defined as the vector defining the line and direction of closest approach of the Cα atom of residue *n* and the helical axis $\vec{a}$ (see Appx. Fig 2.7).

APPENDIX TABLES 2

APPENDIX TABLE 2.1

Inhibition of europium-labeled insulin and IGF-I for binding to the IR-B and IGF-1R, respectively, by insulin, dicarba insulin isomers and IGF-I.

	IR-B		**IGF-1R**	
	IC_{50} (nM)	Affinity (% Insulin ± SEM)	IC_{50} (nM)	Affinity (% Insulin ± SEM)
Insulin	1.07 ± 0.09	100	> 300	100
cis isomer	1.07 ± 0.30	100 ± 26[ns]	> 300	~100
trans isomer	40.4 ± 7.2[a]	1.8 ± 0.3****	-	-
IGF-I	-	-	0.60 ± 0.07	4704 ±468 ****

n = 3 or more, [a]n=2, - not performed, n.a. not analysed, [ns]non-statistically significant, [ψ]derived from Kurtzhals *et al.*, $P > 0.05$, ** $P \leq 0.01$, *** $P \leq 0.001$, **** $P \leq 0.0001$. Errors shown are S.E.M

APPENDIX TABLE 2.2

Secondary structure content of insulin and dicarba insulin isomers from CD analysis.

	Helix (%)	Sheet (%)	Turn (%)	Unordered (%)
Insulin	48	12	14	26
***cis* isomer**	37	16	20	27
***trans* isomer**	23	24	22	31

Secondary structure content was calculated using the CONTINLL algorithm for deconvolution against the protein database reference set SP43. The program is available on the DICROWEB website (http://dichroweb.cryst.bbk.ac.uk/html/home.shtml).

APPENDIX TABLE 2.3

Bioinformatics study of T state structures within medium- to high-resolution X-ray crystal structures of insulins (<2.8 Å, including T_2 (TT) or T_6 (TT), T_3R_3 (TR), $T_3R^f_3$ (TR) and T monomers (T_M)) grouped into two classes based on the conformation of the A chain *N*-terminal helix. Chain identifiers are used to distinguish between different insulin molecules within the same crystallographic asymmetric unit. Structures used as starting points for the MD simulations are highlighted in bold. Amino acid sequences are given for each polypeptide chain of each structure; hyphens are used to represent amino acids that are missing or not resolved in the X-ray crystallographic maps as well as non-standard residues. For the critical A6–A11 disulfide bond, both the conformation and the distance between the cysteine Cα atoms ($r(C_\alpha\text{-}C_\alpha)$ /Å) are reported; mean Cα-Cα distances for each structural class are in *Appendix Table 2.5*. The hydrogen-bonding pattern in the *N*-terminal region of the A chain is reported in terms of the hydrogen-bonding partners of the carbonyl oxygens of residues Gly^{A1} to Gln^{A5}. The relative backbone azimuthal angle ϕ of each residue in the A chain *N*-terminal helix is also given; the method of calculation of ϕ is as described in the *Methods* section of *Chapter 2* and illustrated in *Appendix Figure 2.7*. The mean ϕ values for each class are in *Appendix Table 2.4*. Diagrams of the disulfide bond conformations are provided in *Appendix Figure 2.6*.

PDB Code	Chain IDs in PDB		Context	A Chain Sequence	B Chain Sequence	A6–A11		H bond partner of CO					Azimuthal angles Φ/°										Class
						$r(C_\alpha\text{-}C_\alpha)$ /Å	Conformation	A1	A2	A3	A4	A5	A1	A2	A3	A4	A5	A6	A7	A8	A9	A10	
1IZB	A	B	TR	GIVEQCCTSICSLYQLENYCN	FVNQHLCGSHLVQALYLVCGERGFFYTPKT	4.6	right-handed G'GT	5	6		8	9	17.4	262.7	170.1	95.4	340.4	250.2	170.5	50.2	333.2	287.7	1
1M5A	A	B	TT	GIVEQCCTSICSLYQLENYCN	FVNQHLCGSHLVEALYLVCGERGFFYTPKA	4.6	right-handed G'GT	5	6		8	9	25.6	265.1	169.0	91.6	338.6	250.6	169.4	49.9	329.7	286.2	1
1MSO	A	B	TT	GIVEQCCTSICSLYQLENYCN	FVNQHLCGSHLVEALYLVCGERGFFYTPKT	4.9	right-handed G'GT	5	6		7,8	9	24.8	266.8	169.3	91.8	337.8	247.1	167.9	47.9	328.7	284.2	1
1OS3	A	B	TT	GIVEQCCTSICSLYQLENYCN	FVNQHLCGSHLVEALYLVCGERGFFYTPK-	4.8	right-handed G'GT	5	6		7,8	9	43.0	289.3	188.8	107.4	347.2	250.9	174.5	55.3	339.9	296.0	1
1OS4	A	B	TT	GIVEQCCTSICSLYQLENYCN	FVNQHLCGSHLVEALYLVCGERGFFYTPK-	4.6	right-handed G'GT	5	6	7	8	9	58.1	288.3	193.1	109.3	348.1	254.2	178.8	58.2	342.8	296.4	1
1OS4	E	F	TT	GIVEQCCTSICSLYQLENYCN	FVNQHLCGSHLVEALYLVCGERGFFYTP--	4.6	right-handed G'GT	5	6		8	9	46.4	286.0	186.8	101.2	345.0	251.2	172.5	53.4	336.0	291.6	1
1OS4	I	J	TT	GIVEQCCTSICSLYQLENYCN	FVNQHLCGSHLVEALYLVCGERGFFYTP--	4.7	right-handed G'GT	5	6		8	9	45.9	292.7	189.4	101.8	344.8	249.9	174.1	56.7	336.5	291.7	1
2A3G	A	B	TT	GIVEQCCASVCSLYQLENYCN	FVNQHLCGSHLVEALYLVCGERGFFYTPKA	4.7	right-handed G'GT	5	6		7,8	9	28.1	265.5	168.1	89.2	339.7	249.4	172.5	51.5	333.6	287.9	1
2R35	C	D	TR	GIVEQCCTSICSLYQLENYCN	FVNQHLCGSHLVEALYLVCGERGFFYTPKT	4.4	right-handed hook			7			18.4	203.1	140.4	50.6	316.6	246.4	165.1	49.7	324.7	283.8	1

2VK0	C	D	TT	GIVEQCCTSICSLYQLENYCN	--NQHLCGSHLVEALYLVCGERGFFYTPK-	4.7	left-handed GGT	5	6	8	9	29.2	266.0	173.1	97.0	338.9	247.7	169.7	44.7	330.1	294.5	1
2ZP6	A	B	TT	GIVEQCCASVCSLYQLENYCN	FVNQHLCGSHLVEALYLVCGERGFFYTPKA	4.8	right-handed G'GT		6	8	9	19.8	259.3	163.6	78.1	338.1	244.8	170.8	48.2	333.2	286.3	1
3BRR	A	B	TT	GIVEQCCTSICSLYQLENYCN	FVNQHLCGSHLVEALYLVCGERGFFYTPKA	4.8	right-handed G'GT	5	6	8	9	23.7	263.8	169.6	92.7	338.3	249.2	171.6	53.1	334.3	289.8	1
3BXQ	A	B	TT	GIVEQCCTSICSLYQLENYCN	FVNQRLCGSHLVEALYLVCGERGFFYTPKT	4.9	right-handed G'GT	5	6	7,8	9	27.5	267.8	170.7	92.3	339.3	249.1	172.5	51.8	331.4	286.2	1
3E7Y	C	D	TT	GIVEQCCTSICSLYQLENYCN	FVNQHLCGSHLVEALYLVCGERGFFYTPK-	4.8	right-handed G'GT	4,5	6	7,8	9	31.8	279.5	173.8	95.3	340.0	249.8	170.1	50.7	333.1	288.6	1
3E7Z	C	D	TT	GIVEQCCTSICSLYQLENYCN	FVNQHLCGSHLVEALYLVCGERGFFYTPK-	4.8	right-handed G'GT	5	6	8	9	28.5	259.3	169.6	89.5	335.7	249.6	171.0	50.6	332.8	287.8	1
3EXX	A	B	TT	GIVEQCCTSICSLYQLENYCN	FVNQHLCGSHLVEALYLVCGERGFFYTPKT	4.9	right-handed G'GT	5	6	8	9	23.9	266.6	265.3	169.9	92.8	337.4	248.4	169.1	48.8	329.9	1
3FHP	A	B	TT	GIVEQCCTSICSLYQLENYCN	FVNQHLCGSHLVEALYLVCGERGFFYTPKA	4.8	right-handed G'GT	5	6	8	9	31.9	269.1	171.4	92.5	338.5	248.0	169.8	49.0	328.8	284.6	1
3FQ9	A	B	TT	-IVEQCC-SICSLYQLENYCN	FVNQHLCGSHLVEALYLVCGERGFFYTPKT	4.8	right-handed G'GT		6			28.4	268.6	172.3	94.0	339.3	249.8	173.8	53.9	334.8	290.3	1
3ILG	A	B	TT	GIVEQCCTSICSLYQLENYCN	FVNQHLCGSHLVEALYLVCGERGFFYTPKT	4.8	right-handed G'GT	5	6	8	9	23.7	264.4	169.4	91.2	338.8	248.9	168.7	49.7	334.6	287.7	1
3INC	A	B	TT	GIVEQCCTSICSLYQLENYCN	FVNQHLCGSHLVEALYLVCGERGFFYTPKT	4.8	right-handed G'GT	5	6	8	9	26.7	264.8	170.7	93.1	336.7	248.7	168.5	49.9	333.3	288.2	1
3INS	A	B	TT	GIVEQCCTSICSLYQLENYCN	FVNQHLCGSHLVEALYLVCGERGFFYTPKA	4.8	right-handed G'GT	5	6	8	9	23.1	266.4	171.0	93.8	340.6	249.6	171.5	50.3	332.3	288.1	1
3IR0	A	B	TT	GIVEQCCTSICSLYQLENYCN	FVNQHLCGSHLVEALYLVCGERGFFYTPKT	5.0	right-handed G'GT	5	6	7,8	9	14.9	260.1	168.2	88.1	346.9	252.0	171.7	45.7	326.8	284.5	1
3IR0	E	F	TT	-IVEQCCTSICSLYQLENYCN	FVNQHLCGSHLVEALYLVCGERGFFYTPKT	4.8	right-handed G'GT		6	8												1
3IR0	I	J	TT	GIVEQCCTSICSLYQLENYCN	FVNQHLCGSHLVEALYLVCGERGFFYTPKT	4.9	right-handed G'GT	5	6	7,8	9	12.0	256.2	160.6	82.7	336.0	240.5	164.6	40.4	320.3	275.8	1
3IR0	M	N	TT	GIVEQCCTSICSLYQLENYCN	FVNQHLCGSHLVEALYLVCGERGFFYTPKT	5.0	right-handed G'GT	5	6	7,8	9	20.0	264.9	169.2	91.0	344.8	248.5	172.1	47.4	325.8	282.2	1
3IR0	R	S	TT	GIVEQCCTSICSLYQLENYCN	FVNQHLCGSHLVEALYLVCGERGFFYTPKT	4.7	right-handed G'GT	5	6	8	9	31.9	246.0	160.8	79.7	338.5	252.6	179.4	53.0	331.5	291.3	1

3IR0	V	W	TT	GIVEQCCTSICSLYQLENYCN	-VNQHLCGSHLVEALYLVCGERGFFYTPKT	4.9	right-handed G'GT	5	6		7,8	9	18.3	260.2	167.1	88.4	344.1	250.6	177.4	51.7	332.1	286.3	1
3Q6E	A	B	TT	GIVEQCCTSICSLYQLENYCN	FVNQHLCGSHLVEALYLVCGERGFFYTPK-	4.9	left-handed GGT	5	6		7,8	9	17.1	262.0	169.8	91.9	345.8	257.3	172.0	52.8	331.6	288.8	1
3RTO	A	B	TT	GIVEQCCTSICSLYQLENYCN	FVNQHLCGSHLVEALYLVCGERGFFYTPKA	4.8	right-handed G'GT	5	6		8	9	22.2	259.7	257.9	169.3	88.2	338.4	248.5	171.8	53.2	333.5	1
4INS	A	B	TT	GIVEQCCTSICSLYQLENYCN	FVNQHLCGSHLVEALYLVCGERGFFYTPKA	4.8	right-handed G'GT	5	6		8	9	22.4	264.2	170.2	93.8	341.6	249.4	171.9	48.7	332.0	287.5	1
1B17	A	B	T_M	GIVEQCCTSICSLYQLENYCN	FVNQHLCGSHLVEALYLVCGERGFFYTPKA	3.8	right-handed hook	5	6	7,8			52.4	213.6	139.7	44.1	314.1	247.3	169.2	65.9	340.3	289.7	2
1B18	A	B	T_M	GIVEQCCTSICSLYQLENYCN	FVNQHLCGSHLVEALYLVCGERGFFYTPKA	3.9	right-handed hook	5	6	7,8			54.0	212.7	140.7	44.0	313.9	247.5	169.7	66.4	340.4	289.8	2
1B19	A	B	T_M	GIVEQCCTSICSLYQLENYCN	FVNQHLCGSHLVEALYLVCGERGFFYTPKA	3.9	right-handed hook	5	6	7,8			53.1	213.2	141.5	45.2	313.9	248.2	169.9	66.1	341.1	290.7	2
1B2A	A	B	T_M	GIVEQCCTSICSLYQLENYCN	FVNQHLCGSHLVEALYLVCGERGFFYTPKA	3.8	right-handed hook	5	6	7,8			52.3	212.6	141.0	44.9	314.3	248.0	170.2	66.5	341.0	290.5	2
1B2B	A	B	T_M	GIVEQCCTSICSLYQLENYCN	FVNQHLCGSHLVEALYLVCGERGFFYTPKA	3.9	right-handed hook	5	6	7,8			52.9	213.1	141.8	45.5	313.9	248.1	170.2	66.3	341.0	290.5	2
1B2C	A	B	T_M	GIVEQCCTSICSLYQLENYCN	FVNQHLCGSHLVEALYLVCGERGFFYTPKA	3.9	right-handed hook	5	6	7,8			55.0	213.1	141.5	45.3	314.1	248.5	170.0	66.6	341.8	291.1	2
1B2D	A	B	T_M	GIVEQCCTSICSLYQLENYCN	FVNQHLCGSHLVEALYLVCGERGFFYTPKA	3.9	right-handed hook	5	6	7,8			52.6	213.0	141.8	45.3	314.6	248.1	169.7	65.8	340.9	290.2	2
1B2E	A	B	T_M	GIVEQCCTSICSLYQLENYCN	FVNQHLCGSHLVEALYLVCGERGFFYTPKA	3.9	right-handed hook	5	6	7,8			54.0	212.6	141.6	46.4	315.2	248.9	171.4	67.5	341.7	291.3	2
1B2F	A	B	T_M	GIVEQCCTSICSLYQLENYCN	FVNQHLCGSHLVEALYLVCGERGFFYTPKA	3.9	right-handed hook	5	6	7,8			53.8	212.0	141.7	46.1	315.3	249.1	170.7	67.3	339.9	290.0	2
1B2G	A	B	T_M	GIVEQCCTSICSLYQLENYCN	FVNQHLCGSHLVEALYLVCGERGFFYTPKA	3.9	right-handed hook	5	6	7,8			57.3	214.6	141.6	47.4	316.3	248.6	172.2	67.8	340.6	290.7	2
1B9E	A	B	TT	GIVEQCCTSICSLYQLENYCN	FVNQHLCGEHLVEALYLVCGERGFFYTPKT	4.8	right-handed G'GT	5	6	7,8	9		38.6	213.5	139.3	47.3	316.7	246.4	168.8	61.3	337.5	288.0	2
1B9E	C	D	TT	GIVEQCCTSICSLYQLENYCN	FVNQHLCGEHLVEALYLVCGERGFFYTPKT	4.8	right-handed G'GT	5	6	7,8			36.7	212.3	139.7	49.1	315.1	246.3	168.8	60.6	337.2	287.4	2
1BEN	A	B	TR	GIVEQCCTSICSLYQLENYCN	FVNQHLCGSHLVEALYLVCGERGFFYTPKT	4.7	left-handed GGT	5	6	7,8	9		39.9	210.1	137.7	45.4	316.5	248.5	171.4	63.9	337.8	286.0	2

1BPH	A	B	T_M	GIVEQCCASVCSLYQLENYCN	FVNQHLCGSHLVEALYLVCGERGFFYTPKA	3.9	right-handed hook	5	6	7,8		68.0	236.1	156.7	64.9	334.6	265.8	189.3	83.0	355.0	305.0	2
1DEI	A	B	TT	GIVEQCCTSICSLYQLENYCN	FVNQHLCGSHLVEALYLVCGERG-------	4.7	right-handed G'GT	5	6	7,8	9	36.7	217.7	139.5	43.5	315.0	248.5	168.9	65.6	340.7	287.2	2
1DEI	C	D	TT	GIVEQCCTSICSLYQLENYCN	FVNQHLCGSHLVEALYLVCGERG-------	4.7	right-handed G'GT	5	6	7,8	9	26.8	215.8	142.1	48.1	313.7	246.5	167.6	60.7	339.2	289.6	2
1DPH	A	B	T_M	GIVEQCCASVCSLYQLENYCN	FVNQHLCGSHLVEALYLVCGERGFFYTPKA	4.0	right-handed hook	5	6	7,8		65.1	242.5	171.4	78.7	346.2	277.8	201.1	92.3	6.7	317.9	2
1G7A	A	B	TR	GIVEQCCTSICSLYQLENYCN	FVNQHLCGSHLVEALYLVCGERGFFYTPKT	4.6	left-handed GGT	5	6	7,8		52.3	205.0	133.0	41.7	313.3	246.9	170.7	64.0	334.2	283.6	2
1G7A	E	F	TR	GIVEQCCTSICSLYQLENYCN	FVNQHLCGSHLVEALYLVCGERGFFYTPKT	4.6	left-handed GGT	5	6	7,8	9	45.3	210.7	137.6	45.9	317.4	316.2	248.9	171.1	64.1	338.5	2
1G7B	A	B	TR	GIVEQCCTSICSLYQLENYCN	FVNQHLCGSHLVEALYLVCGERGFFYTPKT	4.5	left-handed GGT	5	6	7,8		53.1	205.9	133.7	42.5	313.6	247.8	170.9	65.1	334.3	284.6	2
1G7B	E	F	TR	GIVEQCCTSICSLYQLENYCN	FVNQHLCGSHLVEALYLVCGERGFFYTPKT	4.6	left-handed GGT	5	6	7,8		44.1	211.8	137.7	45.5	316.4	248.6	171.0	63.9	338.4	338.3	2
1GUJ	A	B	TT	GIVEQCCTSICSLYQLENYCN	FVNQHLCGSHLVEALYLVCGERGFFYTPKT	4.6	right-handed G'GT	5	6	7,8	9	29.0	212.5	138.5	48.0	316.4	247.5	170.1	62.7	339.3	288.6	2
1GUJ	C	D	TT	GIVEQCCTSICSLYQLENYCN	FVNQHLCGSHLVEALYLVCGERGFFYTPKT	4.7	right-handed G'GT	5	6	7,8	9	27.6	210.3	135.9	42.2	311.5	244.9	165.2	60.2	336.9	285.0	2
1IZA	C	D	TR	GIVEQCCTSICSLYQLENYCN	FVNQHLCGSHLVQALYLVCGERGFFYTPKT	5.0	right-handed G'GT	5	6	8		29.5	204.7	133.6	42.4	313.9	252.4	170.7	66.9	340.2	287.0	2
1IZB	C	D	TR	GIVEQCCTSICSLYQLENYCN	FVNQHLCGSHLVQALYLVCGERGFFYTPKT	4.9	right-handed G'GT	5	6	7,8	9	56.4	214.2	142.6	44.8	314.2	246.4	168.7	61.9	341.0	289.2	2
1J73	A	B	TR	GIVEQCCTSICSLYQLENYCN	FVNQHLCGSHLVEALYLVCGERGFFYTPKT	4.8	left-handed GGT	5	6	7		24.5	213.2	138.0	49.9	316.7	246.5	170.3	58.1	330.9	279.9	2
1JCA	A	B	TR	GIVEQCCKSICSLYQLENYCN	FVNQHLCGSHLVEALYLVCGERGFFYTPKT	4.7	left-handed GGT	4	6	8		39.0	215.6	133.3	39.4	310.6	242.4	167.0	58.2	329.1	276.9	2
1LPH	A	B	TR	GIVEQCCTSICSLYQLENYCN	FVNQHLCGSHLVEALYLVCGERGFFYTKPT	4.7	left-handed GGT		6	7,8		45.2	213.6	137.9	43.6	314.6	246.7	166.8	65.2	337.4	279.6	2
1M5A	C	D	TT	GIVEQCCTSICSLYQLENYCN	FVNQHLCGSHLVEALYLVCGERGFFYTPKA	4.6	right-handed G'GT	5	6	7,8	9	39.0	217.2	141.3	47.0	315.0	249.5	172.8	65.6	345.7	288.8	2
1MPJ	C	D	TR	GIVEQCCTSICSLYQLENYCN	FVNQHLCGSHLVEALYLVCGERGFFYTPKA	4.7	right-handed G'GT	5	6	7,8		45.1	204.0	137.7	45.7	315.6	249.6	170.2	61.4	335.3	284.2	2

1MSO	C	D	TT	GIVEQCCTSICSLYQLENYCN	FVNQHLCGSHLVEALYLVCGERGFFYTPKT	4.8	right-handed G'GT	5	6	7,8	9	51.9	214.5	140.7	47.3	316.0	314.9	249.5	171.4	65.8	344.8	2
1OS3	C	D	TT	GIVEQCCTSICSLYQLENYCN	FVNQHLCGSHLVEALYLVCGERGFFYTP--	4.7	right-handed G'GT	5	6	7,8	9	56.5	213.7	142.5	48.1	315.4	248.4	169.5	63.2	342.1	287.0	2
1OS4	C	D	TT	GIVEQCCTSICSLYQLENYCN	FVNQHLCGSHLVEALYLVCGERGFFYTP--	4.8	right-handed G'GT		6	7,8		70.5	210.8	146.0	50.2	317.2	251.0	170.5	66.4	346.5	292.0	2
1OS4	G	H	TT	-IVEQCCTSICSLYQLENYCN	FVNQHLCGSHLVEALYLVCGERGFFYTP--	4.6	right-handed G'GT		6	8												2
1OS4	K	L	TT	GIVEQCCTSICSLYQLENYCN	FVNQHLCGSHLVEALYLVCGERGFFYTP--	4.8	right-handed G'GT		6	7,8		48.0	215.9	146.6	44.3	307.3	247.0	164.6	62.8	341.5	285.6	2
1PID	A	B	TT	GIVEQCCASVCSLYQLENYCN	FVNQHLCGSHLVEALYLVCGERGFF-----	4.7	right-handed G'GT	5	6	7,8	9	23.1	218.6	146.0	52.8	318.6	248.3	171.8	63.9	342.5	292.0	2
1PID	C	D	TT	GIVEQCCASVCSLYQLENYCN	FVNQHLCGSHLVEALYLVCGERGFF-----	4.7	right-handed G'GT	5	6	7,8		48.4	214.6	139.6	47.0	315.7	248.1	170.9	64.9	339.0	290.5	2
1Q4V	A	B	TR	GIVEQCCTSICSLYQLENYCN	FVNQHLCGSHLVEALYLVCGERGFFYTPKT	4.7	left-handed GGT	5		7,8		8.2	200.9	134.5	41.8	311.0	243.3	169.5	57.3	333.0	286.3	2
1QJ0	C	D	TR	GIVEQCCTSICSLYQLENYCN	FVNQYLCGSHLVEALYLVCGERGFFYTPKT	5.0	right-handed G'GT	5	6	7,8		45.6	199.7	138.9	47.6	312.2	248.8	168.5	60.2	334.4	287.0	2
1RWE	A	B	TR	GIVEQCCHSICSLYQLENYCN	FVNQHLCGSHLVEALYLVCGERGFFYTPKT	4.7	left-handed GGT	5	6	7,8		49.2	215.6	138.1	46.4	317.4	247.4	170.6	63.3	332.3	280.9	2
1SDB	A	B	T_M	GIVEQCCTSICSLYQLENYCN	--NQHLCGSHLVEALYLVCGERGFF-----	4.9	right-handed G'GT	5	6	7,8	9	29.2	210.6	137.9	45.5	316.2	246.8	168.4	61.1	336.4	285.0	2
1TRZ	A	B	TR	GIVEQCCTSICSLYQLENYCN	FVNQHLCGSHLVEALYLVCGERGFFYTPKT	4.8	left-handed GGT	5	6	7,8	9	63.6	226.1	149.5	57.3	327.8	259.4	180.7	72.6	347.7	297.4	2
1TYL	A	B	TR	GIVEQCCTSICSLYQLENYCN	FVNQHLCGSHLVEALYLVCGERGFFYTPKT	4.8	left-handed GGT		6	7,8		31.3	214.7	139.0	47.4	317.7	248.1	171.4	64.2	336.6	285.6	2
1TYM	A	B	TR	GIVEQCCTSICSLYQLENYCN	FVNQHLCGSHLVEALYLVCGERGFFYTPK-	4.6	left-handed GGT	5	6	7,8	9	24.0	212.3	138.4	46.5	315.8	249.3	171.8	63.7	340.0	287.5	2
1ZNI	C	D	TR	GIVEQCCTSICSLYQLENYCN	FVNQHLCGSHLVEALYLVCGERGFFYTPKA	4.5	left-handed GGT	5	6	7,8		34.6	208.7	136.6	45.2	314.6	248.9	170.3	63.6	336.9	284.4	2
2A3G	C	D	TT	GIVEQCCASVCSLYQLENYCN	FVNQHLCGSHLVEALYLVCGERGFFYTPKA	4.8	right-handed G'GT	5	6	7,8	9	51.8	218.2	146.8	53.8	318.3	246.8	170.4	61.4	340.2	287.9	2
2BN3	A	B	T_M	GIVEQCCTSVCSLYQLENYCN	FVNQHLCGSHLVEALYLVCGERGFFYTPKA	3.9	right-handed hook	5	6	7,8		38.8	215.1	140.3	45.5	315.7	248.6	171.4	66.5	338.5	338.2	2

2C8Q	A	B	T_M	GIVEQCCTSICSLYQLENYCN	FVNQHLCGSHLVEALYLVCGERGFFYTPK-	3.9	right-handed hook	5	6	7,8		38.5	215.6	141.0	47.2	316.3	248.1	171.8	66.2	337.3	288.8	2
2CEU	A	B	TT	GIVEQCCTSICSLYQLENYCN	-VNQHLCGSHLVEALYLVCGERGFF-----	4.6	right-handed G'GT	5	6	7,8	9	39.3	217.9	145.2	50.0	315.0	247.1	168.0	60.3	339.0	288.8	2
2CEU	C	D	TT	GIVEQCCTSICSLYQLENYCN	-VNQHLCGSHLVEALYLVCGERGFF-----	4.6	right-handed G'GT	5	6	7,8	9	38.1	217.3	145.2	50.0	314.6	247.1	167.9	60.4	339.0	288.8	2
2EFA	A	B	T_M	GIVEQCCTSICSLYQLENYCN	FVNQHLCGSHLVEALYLVCGERGFFYTPKA	3.8	right-handed hook	5	6	7,8		44.0	215.7	140.4	46.8	316.6	250.2	173.7	69.6	340.8	287.5	2
2G4M	A	B	T_M	GIVEQCCTSICSLYQLENYCN	FVNQHLCGSHLVEALYLVCGERGFFYTPKA	3.9	right-handed hook	5	6	7,8		37.1	215.1	140.6	46.9	317.6	248.0	171.7	65.9	337.5	288.6	2
2QIU	C	D	TR	GIVEQCCTSICSLYQLENYCN	FVNQHLCGSHLVEALYLVCGERGFFYTPKT	5.0	right-handed G'GT	5	6	7,8		47.2	198.0	141.8	48.5	314.9	249.2	172.5	61.7	330.9	287.7	2
2R34	C	D	TR	GIVEQCCTSICSLYQLENYCN	FVNQHLCGSHLVEALYLVCGERGFFYTPK-	4.5	left-handed GGT	5	6	7,8	9	50.0	206.2	139.7	51.3	316.4	251.2	175.5	59.5	338.2	290.4	2
2R36	A	B	TT	GIVEQCCTSICSLYQLENYCN	FVNQHLCGSHLVEALYLVCGERGFFYTPKT	5.1	right-handed G'GT		6	7,8		33.9	206.4	139.8	50.2	318.3	246.8	168.6	59.2	332.8	285.4	2
2R36	C	D	TT	GIVEQCCTSICSLYQLENYCN	FVNQHLCGSHLVEALYLVCGERGFFYTPKT	4.9	right-handed G'GT		6	7,8		44.7	210.1	140.2	51.2	318.7	248.3	171.5	60.9	338.7	291.3	2
2TCI	C	D	TR	GIVEQCCTSICSLYQLENYCN	FVNQHLCGSHLVEALYLVCGERGFFYTPKA	4.7	right-handed G'GT	5	6	7,8		59.3	210.0	137.6	46.6	317.3	250.2	172.8	65.7	338.2	287.7	2
2VJZ	A	B	TR	GIVEQCCTSICSLYQLENYCN	FVNQHLCGSHLVEALYLVCGERGFFYTPK-	4.5	left-handed GGT	5	6	7,8	9	38.4	207.5	136.0	44.0	314.6	314.2	248.5	170.7	63.4	337.6	2
2VK0	A	B	TT	GIVEQCCTSICSLYQLENYCN	--NQHLCGSHLVEALYLVCGERGFFYTPKT	4.7	left-handed hook	5	6	7,8		65.8	206.2	136.8	42.4	311.3	248.2	169.2	64.9	337.9	289.0	2
2WRU	A	B	T_M	GIVEQCCTSICSLYQLENYCN	-VNQHLCGSHLVEALYLVCGERGFF-----	4.6	right-handed G'GT	5	6	7,8	9	35.8	212.8	137.0	45.2	313.6	247.1	168.6	62.3	339.4	288.3	2
2WRV	A	B	T_M	GIVEQCCTSICSLYQLENYCN	-VNQHLCGSHLVEALYLVCGERGFF-----	4.7	right-handed G'GT	5	6	7,8	9	40.1	210.7	137.1	45.6	314.4	247.6	169.9	62.1	337.8	290.2	2
2WRW	A	B	T_M	GIVEQCCTSICSLYQLENYCN	-VNQHLCGSHLVEALYLVCGERGFF-----	4.6	right-handed G'GT	5	6	7,8	9	48.2	212.2	137.9	45.5	315.9	247.8	170.1	64.5	338.6	288.6	2
2WRX	A	B	TT	GIVEQCCTSICSLYQLENYCN	-VNQHLCGSHLVEALYLVCGERGFF-TP--	4.7	right-handed G'GT	5	6	7,8	9	33.3	214.3	137.0	44.9	313.8	246.1	168.5	62.1	338.5	288.5	2
2WRX	C	D	TT	GIVEQCCTSICSLYQLENYCN	-VNQHLCGSHLVEALYLVCGERGFF-TP--	4.6	right-handed G'GT	5	6	7,8	9	33.9	215.0	137.6	46.1	315.0	247.8	168.7	62.9	339.6	288.9	2

2WS0	A	B	T_M	GIVEQCCTSICSLYQLENYCN	FVNQHLCGSHLVEALYLVCGERGFF-T---	4.7	right-handed G'GT	5	6	7,8	9	46.2	210.8	136.9	45.7	315.5	247.3	171.8	63.5	337.8	289.1	2
2WS1	A	B	T_M	GIVEQCCTSICSLYQLENYCN	-VNQHLCGSHLVEALYLVCGERGFF-TP--	4.6	right-handed G'GT	5	6	7,8	9	33.8	212.0	136.5	43.6	312.8	245.7	167.2	60.9	337.6	286.8	2
2WS4	A	B	T_M	GIVEQCCTSICSLYQLENYCN	-VNQHLCGSHLVEALYLVCGERGFFP----	4.6	right-handed G'GT	5	6	7,8	9	42.5	215.5	141.3	47.2	316.4	248.6	170.6	63.3	339.5	285.8	2
2ZP6	C	D	TT	GIVEQCCASVCSLYQLENYCN	FVNQHLCGSHLVEALYLVCGERGFFYTPKA	4.9	right-handed G'GT	4,5	6	7,8	9	4.8	215.4	141.1	41.1	312.2	241.2	164.9	60.7	335.8	284.2	2
2ZPP	A	B	TT	GIVEQCCTSICSLYQLENYCN	FVNQHLCGSHLVEALYLVCGERGFFYTPKA	3.9	right-handed hook	4,5	6	7,8		61.8	216.5	143.3	47.8	314.3	249.0	171.4	67.7	342.8	291.0	2
3BXQ	C	D	TT	GIVEQCCTSICSLYQLENYCN	FVNQRLCGSHLVEALYLVCGERGFFYTPKT	4.8	right-handed G'GT			6,7		56.8	217.9	148.8	50.1	318.6	243.5	168.2	62.2	337.3	288.4	2
3E7Y	A	B	TT	GIVEQCCTSICSLYQLENYCN	FVNQHLCGSHLVEALYLVCGERGFFYTPK-	4.6	right-handed G'GT	5	6	7,8		45.4	218.5	142.9	47.1	313.1	248.3	171.1	64.8	342.2	288.5	2
3E7Z	A	B	TT	GIVEQCCTSICSLYQLENYCN	FVNQHLCGSHLVEALYLVCGERGFFYTPK-	4.6	right-handed G'GT	5	6	7,8		45.3	219.3	143.3	47.0	311.1	248.8	170.6	63.7	342.2	288.7	2
3FHP	C	D	TT	GIVEQCCTSICSLYQLENYCN	FVNQHLCGSHLVEALYLVCGERGFFYTPKA	4.8	right-handed G'GT	5	6	7,8	9	57.0	215.4	144.6	49.6	317.3	247.2	169.2	64.2	342.2	289.5	2
3FQ9	C	D	TT	-IVEQCC-SICSLYQLENYCN	FVNQHLCGSHLVEALYLVCGERGFFYTPKT	4.6	right-handed G'GT		6	7		41.0	203.2	130.5	36.6	304.4	234.3	157.7	51.1	330.4	277.5	2
3GKY	A	B	TR	GIVEQCCHSICSLYQVENYCN	FVNQHLCGSHLVEALYLVCGERGFFYTPKA	4.8	right-handed G'GT	5	6	7,8		28.9	191.8	115.4	24.9	293.5	221.5	145.7	36.2	305.2	256.7	2
3I3Z	A	B	T_M	GIVEQCCTSICSLYQLENYCN	FVNQHLCGSHLVEALYLVCGERGFFYTPKA	3.9	right-handed hook	5	6	7,8		50.4	213.7	140.5	46.7	315.8	250.1	171.9	67.1	338.2	288.6	2
3I40	A	B	T_M	GIVEQCCTSICSLYQLENYCN	FVNQHLCGSHLVEALYLVCGERGFFYTPKA	3.9	right-handed hook	5	6	7,8		47.1	216.0	140.9	44.9	314.1	248.3	169.4	65.5	338.5	288.5	2
3ILG	C	D	TT	GIVEQCCTSICSLYQLENYCN	FVNQHLCGSHLVEALYLVCGERGFFYTPKT	4.7	right-handed G'GT	5	6	7,8	9	44.2	214.7	139.7	45.4	312.5	248.1	170.9	65.6	344.3	287.9	2
3INC	C	D	TT	GIVEQCCTSICSLYQLENYCN	FVNQHLCGSHLVEALYLVCGERGFFYTPKT	4.7	right-handed G'GT	5	6	7,8	9	50.6	212.8	140.4	46.9	313.4	248.2	171.0	64.4	341.7	287.8	2
3INS	C	D	TT	GIVEQCCTSICSLYQLENYCN	FVNQHLCGSHLVEALYLVCGERGFFYTPKA	4.7	right-handed G'GT	5	6	7,8	9	64.1	229.7	156.2	60.5	328.5	262.4	185.0	79.4		303.9	2
3IR0	C	D	TT	GIVEQCCTSICSLYQLENYCN	FVNQHLCGSHLVEALYLVCGERGFFYTPKT	4.9	right-handed G'GT	4,5	6	8		76.9	204.8	142.1	38.2	310.4	254.1	175.6	66.1	348.4	294.9	2

3IR0	G	H	TT	GIVEQCCTSICSLYQLENYCN	FVNQHLCGSHLVEALYLVCGERGFFYTPKT	4.9	right-handed G'GT	5	6	8	9	56.5	205.1	140.0	44.5	312.7	247.2	173.5	63.9	340.9	287.7	2
3IR0	K	L	TT	GIVEQCCTSICSLYQLENYCN	FVNQHLCGSHLVEALYLVCGERGFFYTPKT	4.9	right-handed G'GT	5	6	7,8		52.6	194.1	128.0	36.5	307.2	245.4	164.4	56.8	335.4	288.1	2
3IR0	O	P	TT	GIVEQCCTSICSLYQLENYCN	FVNQHLCGSHLVEALYLVCGERGFFYTPKT	4.9	right-handed G'GT	5	6	7,8		45.8	195.1	130.1	37.7	308.6	245.8	165.5	56.8	335.9	288.5	2
3IR0	T	U	TT	GIVEQCCTSICSLYQLENYCN	FVNQHLCGSHLVEALYLVCGERGFFYTPKT	4.9	right-handed G'GT	4,5	6	8		54.3	214.6	147.0	52.2	317.9	252.4	182.5	70.1	346.2	293.3	2
3IR0	X	Y	TT	GIVEQCCTSICSLYQLENYCN	FVNQHLCGSHLVEALYLVCGERGFFYTPKT	5.0	right-handed G'GT	4	5,6			31.3	228.2	145.5	55.2	317.2	252.0	172.0	61.9	347.6	296.2	2
3JSD	A	B	TR	GIVEQCCTSICSLYQLENYCN	FVNQHLC-SHLVEALYLVCGERGFFYTPKT	4.9	left-handed GGT	5	6	7,8		45.7	218.0	140.7	50.9	314.8	245.7	170.9	55.6	329.4	286.1	2
3KQ6	A	B	TR	GIVHQCCHSICSLYQLENYCN	FVNQHLCGSHLVEALYLVCGERGFFYTPKT	4.8	left-handed GGT	5	6	7,8	9	54.9	221.0	144.0	53.0	318.9	250.7	170.3	62.2	336.8	287.0	2
3MTH	C	D	TR	GIVEQCCTSICSLYQLENYCN	FVNQHLCGSHLVEALYLVCGERGFFYTPKA	4.4	left-handed GGT	5	6	7,8		49.8	206.7	135.9	45.2	315.7	249.4	170.8	63.8	337.3	287.0	2
3Q6E	C	D	TT	GIVEQCCTSICSLYQLENYCN	FVNQHLCGSHLVEALYLVCGERGFFYTPKT	4.7	right-handed G'GT	5	6	7,8	9	39.2	212.3	138.1	43.9	312.6	247.1	167.4	63.0	338.9	288.7	2
3RTO	C	D	TT	GIVEQCCTSICSLYQLENYCN	FVNQHLCGSHLVEALYLVCGERGFFYTPKA	4.7	right-handed G'GT	5	6	7,8	9	36.6	213.7	141.9	49.0	315.4	246.1	170.0	60.5	341.2	289.6	2
4INS	C	D	TT	GIVEQCCTSICSLYQLENYCN	FVNQHLCGSHLVEALYLVCGERGFFYTPKA	4.7	right-handed G'GT	5	6	7,8	9	40.6	214.2	141.1	46.4	313.2	247.6	170.9	63.7	341.4	288.0	2
9INS	A	B	T_M	GIVEQCCTSICSLYQLENYCN	FVNQHLCGSHLVEALYLVCGERGFFYTPKA	3.9	right-handed hook	5	6	7,8		44.1	213.3	140.8	46.6	317.1	248.3	171.4	65.7	340.3	290.3	2

APPENDIX TABLE 2.4

Average azimuthal angles ϕ (in degrees) for each conformation class. Values are mean over all unique X-ray crystal structures used in the bioinformatics study (Appx. Table 2.3) for each of the ten residues of the A-chain *N*-terminal helix.

	Residue									
	A1	**A2**	**A3**	**A4**	**A5**	**A6**	**A7**	**A8**	**A9**	**A10**
Class 1	27±10	265±16	177±25	97±23	323±65	256±23	177±20	59±31	313±73	291±12
Class 2	45±12	213±7	140±6	47±6	315±6	250±13	173±15	67±20	326±60	291±13

APPENDIX TABLE 2.5

Mean distances (Å) between the Cα atoms of the A6–A11 linkage from X-ray crystal structures and MD simulations.

A6–A11	**Class 1**	**Class 2**
X-ray – insulin	4.78 ± 0.13	4.55 ± 0.37
X-ray – insulin bound to μIR	-	4.50 ± 0.15
X-ray – *trans* isomer	5.17 ± 0.13	-
MD – insulin	4.86 ± 0.46	3.97 ± 0.18
MD – *cis* isomer	4.42 ± 0.31	4.05 ± 0.27
MD – *trans* isomer	5.18 ± 0.22	-

A7—B7		
X-ray – insulin	4.62 ± 0.13	4.76 ± 0.11
X-ray – insulin bound to μIR	-	5.53
X-ray – *trans* isomer	4.36	-
MD – insulin	4.36±0.28	4.76±0.20
MD – *cis* isomer	4.47±0.30	4.81±0.21
MD – *trans* isomer	4.42±0.27	-

APPENDIX TABLE 2.6

The percentage of frames in the molecular dynamics simulations where the NH of residue Thr^{A8} forms hydrogen bonds with the carbonyl group of residues Val^{A3}, Glu^{A4} and Gln^{A5}. Detail of the hydrogen bond formation criterion is provided in *Methods* (q.v.).

Thr^{A8} hydrogen bonding partner (C=O)	Insulin	*cis* isomer	*trans* isomer
Val^{A3}	4 ± 8	4 ± 8	0
Glu^{A4}	55 ± 9	48 ± 20	52 ± 20
Gln^{A5}	32 ± 10	29 ± 15	32 ± 16

APPENDIX TABLE 2.7

The conformation of various regions of structure, based on MD simulations. Secondary structure types were assigned to each residue in all simulation frames using DSSP (Kabsch and Sander, 1983). The percentage of frames in which each residue adopted each structure type was determined across all simulations, then the values averaged over all residues in the relevant region to obtain the final results. Where the deviations of the values for the dicarba insulin isomers from those of insulin are statistically significant at the 95% confidence limit (Student's t-test), these numbers are highlighted in bold. HB=hydrogen bonded.

		Insulin	*cis* isomer	*trans* isomer
A3-A8	αhelix	50	**39**	**32**
	3_{10} helix	3	7	5
	π helix	0	0	0
	HB turn	38	39	**45**
	nHB turn	7	9	**11**
	other	1	5	7
A13-A19	α helix	38	**31**	36
	3_{10} helix	16	19	17
	π helix	0	0	0
	HB turn	34	**39**	38
	nHB turn	11	11	10
	other	0	0	0
B29-B40	α helix	72	**64**	**69**
	3_{10} helix	3	5	4
	π helix	0	0	0
	HB turn	16	**22**	18
	nHB turn	9	10	10
	other	0	0	0

APPENDIX FIGURES 2

APPENDIX FIGURE 2.1

Synthesis of *cis*- and *trans* dicarba insulins monitored *via* RP-HPLC and ESI mass spectrometry.

APPENDIX FIGURE 2.1A

des$_{A1\text{-}5}$-[A6,11]-Agl-[A7]-Cys(^{t}Bu)-[A20]-Cys(Acm) human insulin A-chain 1

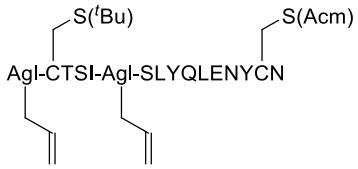

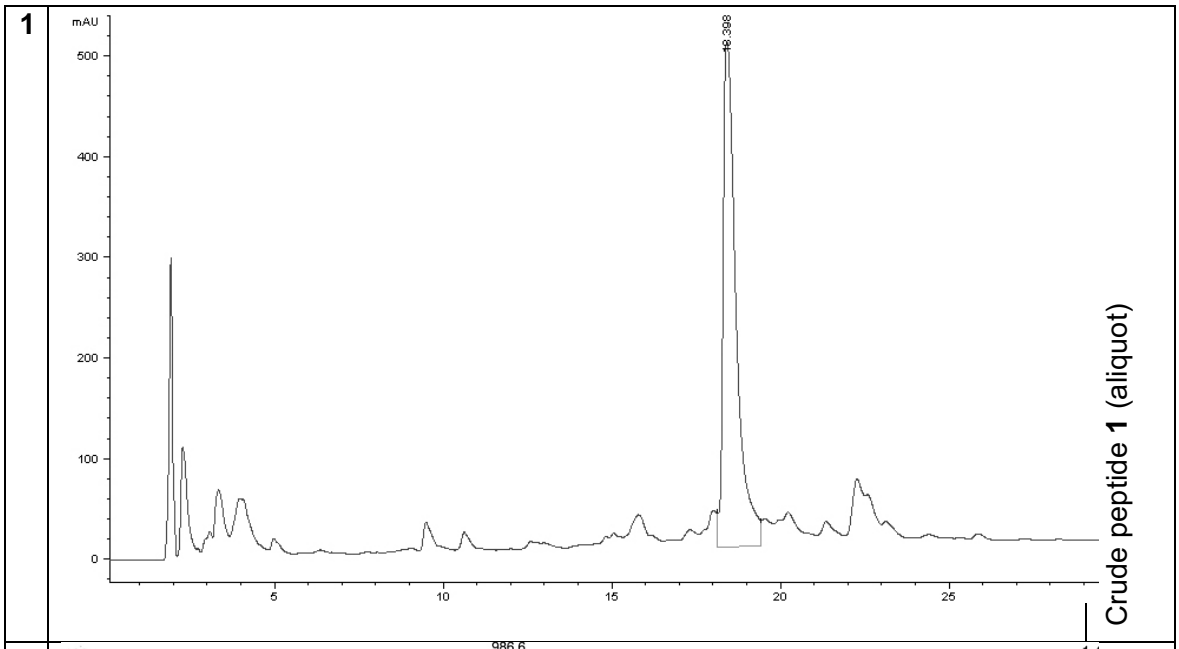

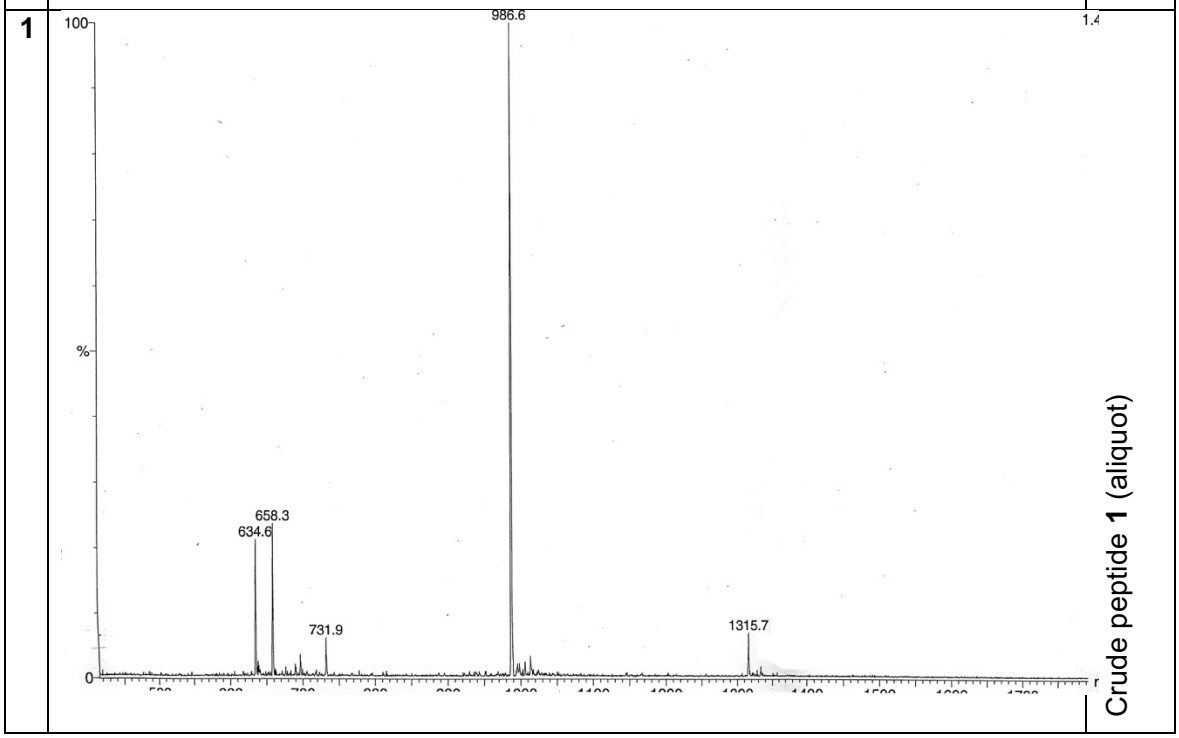

APPENDIX FIGURE 2.1B

$des_{A1\text{-}5}$-c[Δ^4A6,11]-Dicarba-[A7]-Cys(^{t}Bu)-[A20]-Cys(Acm) human insulin A chain 2

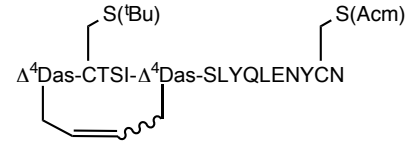

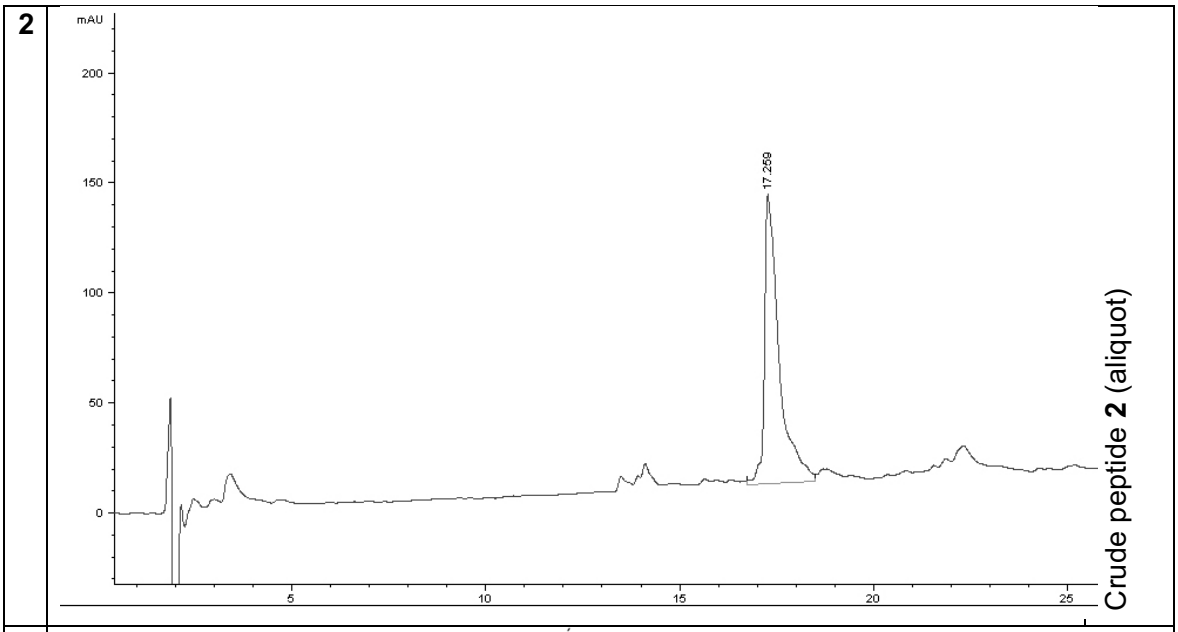

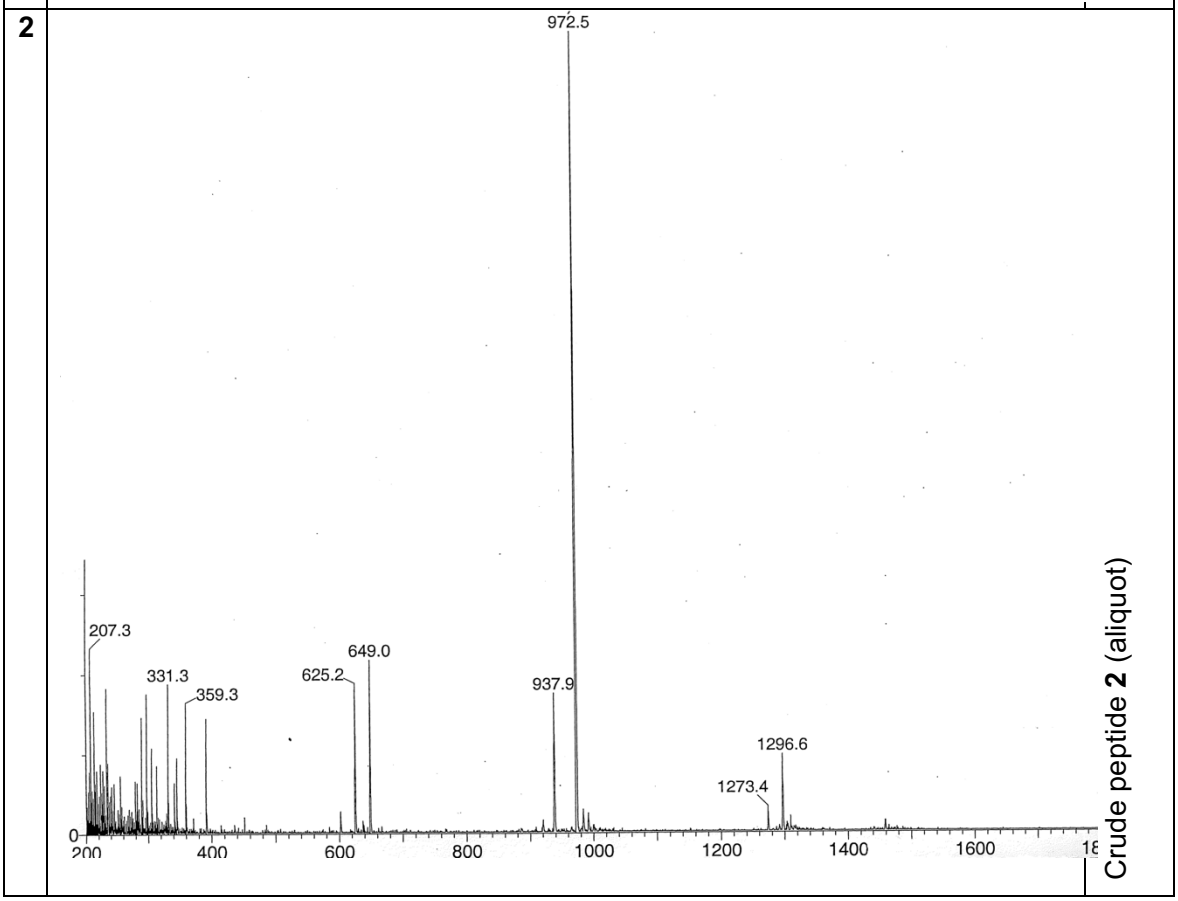

APPENDIX FIGURE 2.1C

c[Δ^4A6,11]-Dicarba-[A7]-Cys(^{t}Bu)-[A20]-Cys(Acm) human insulin A-chain *Z*-3

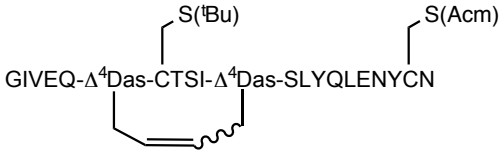

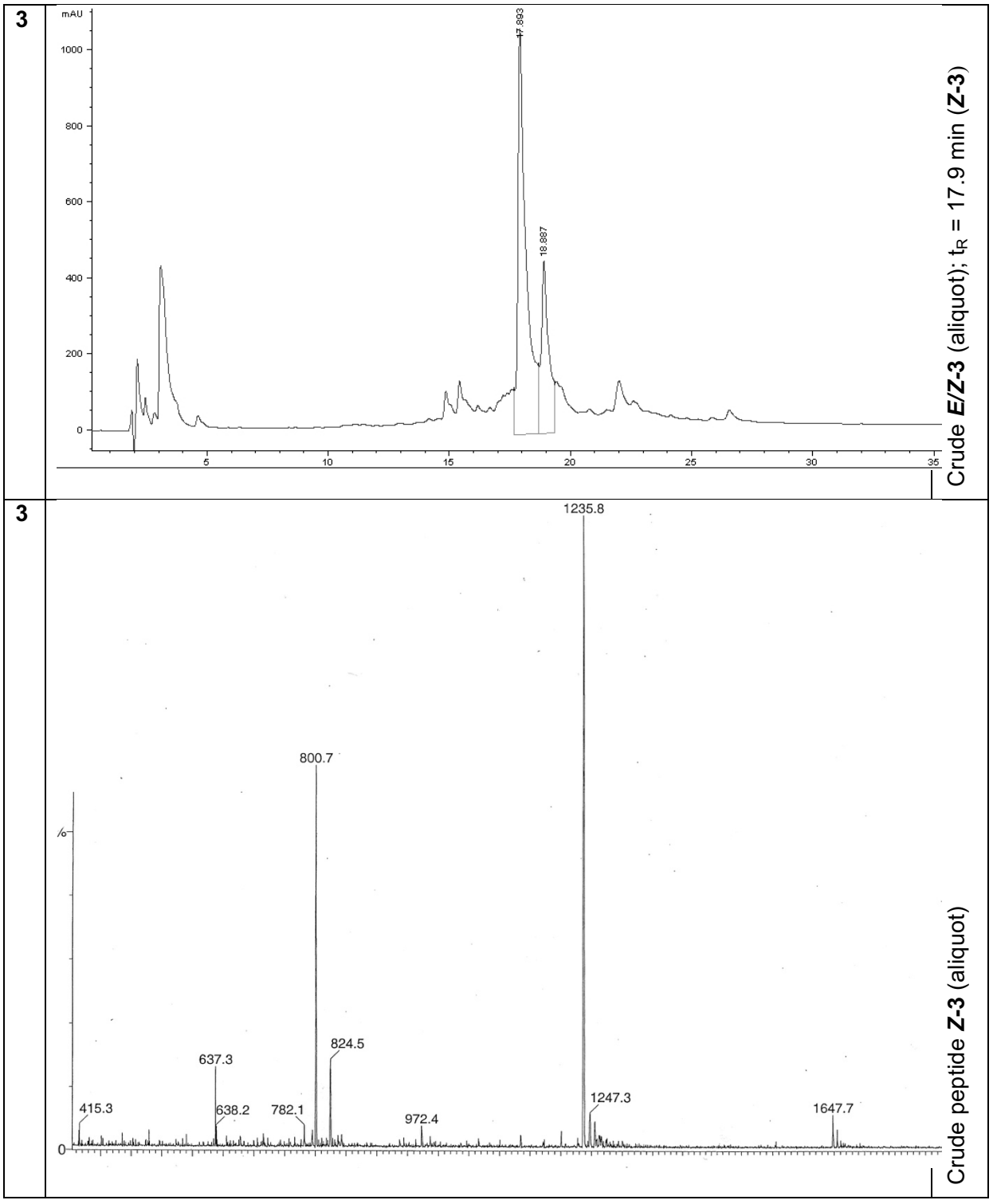

APPENDIX FIGURE 2.1D

c[Δ^4A6,11]-Dicarba-[A7]-Cys(tBu)-[A20]-Cys(Acm) human insulin A-chain E-3

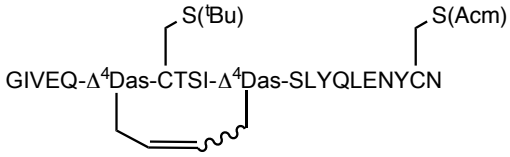

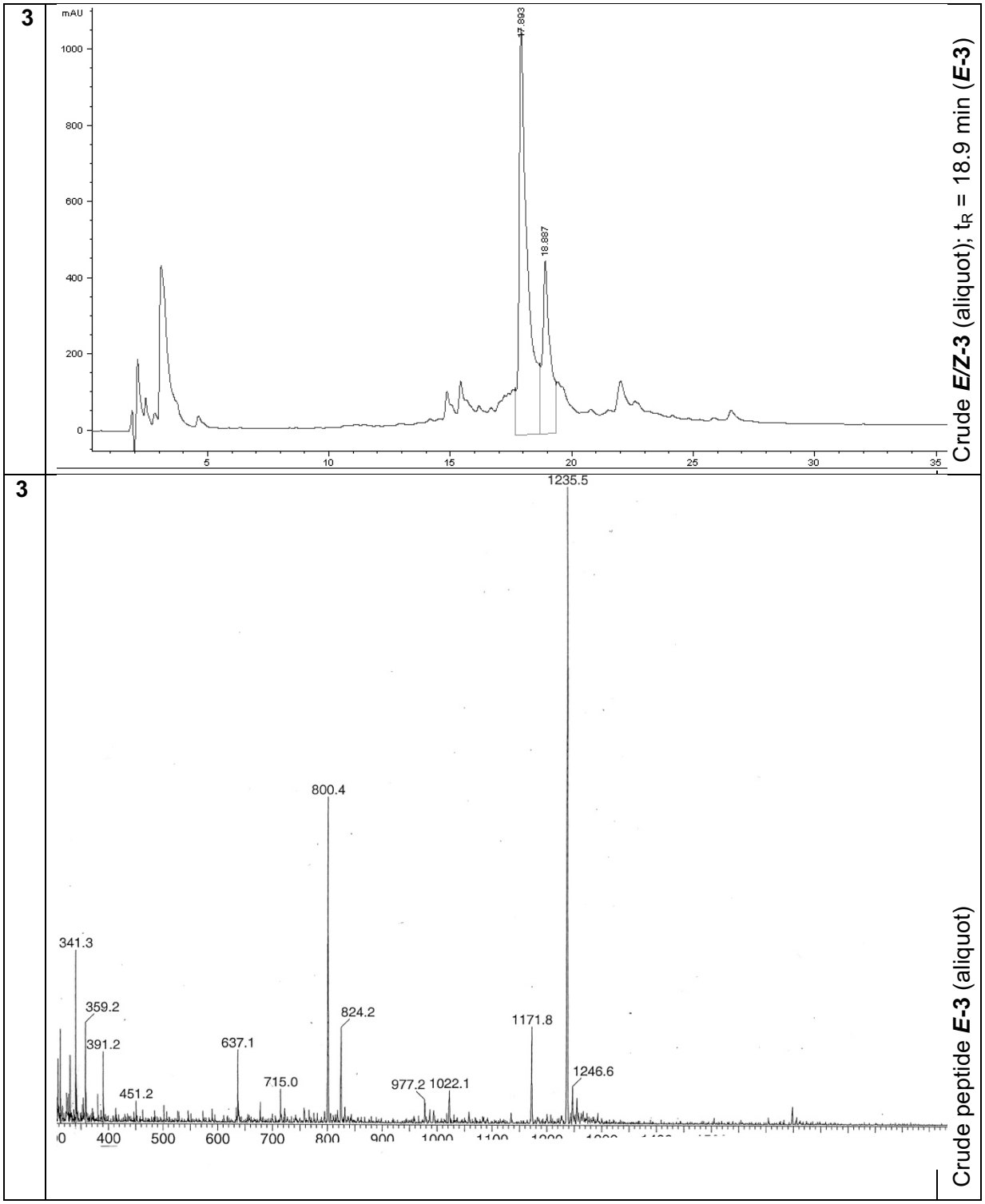

APPENDIX FIGURE 2.1E

c[Δ^4A6,11]-Dicarba-[A7]-Cys(Pyr)-[A20]-Cys(Acm) human insulin A-chain *Z*-4

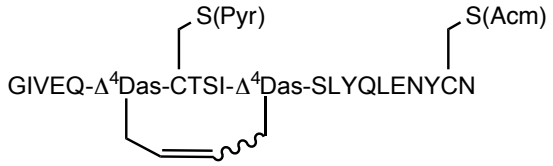

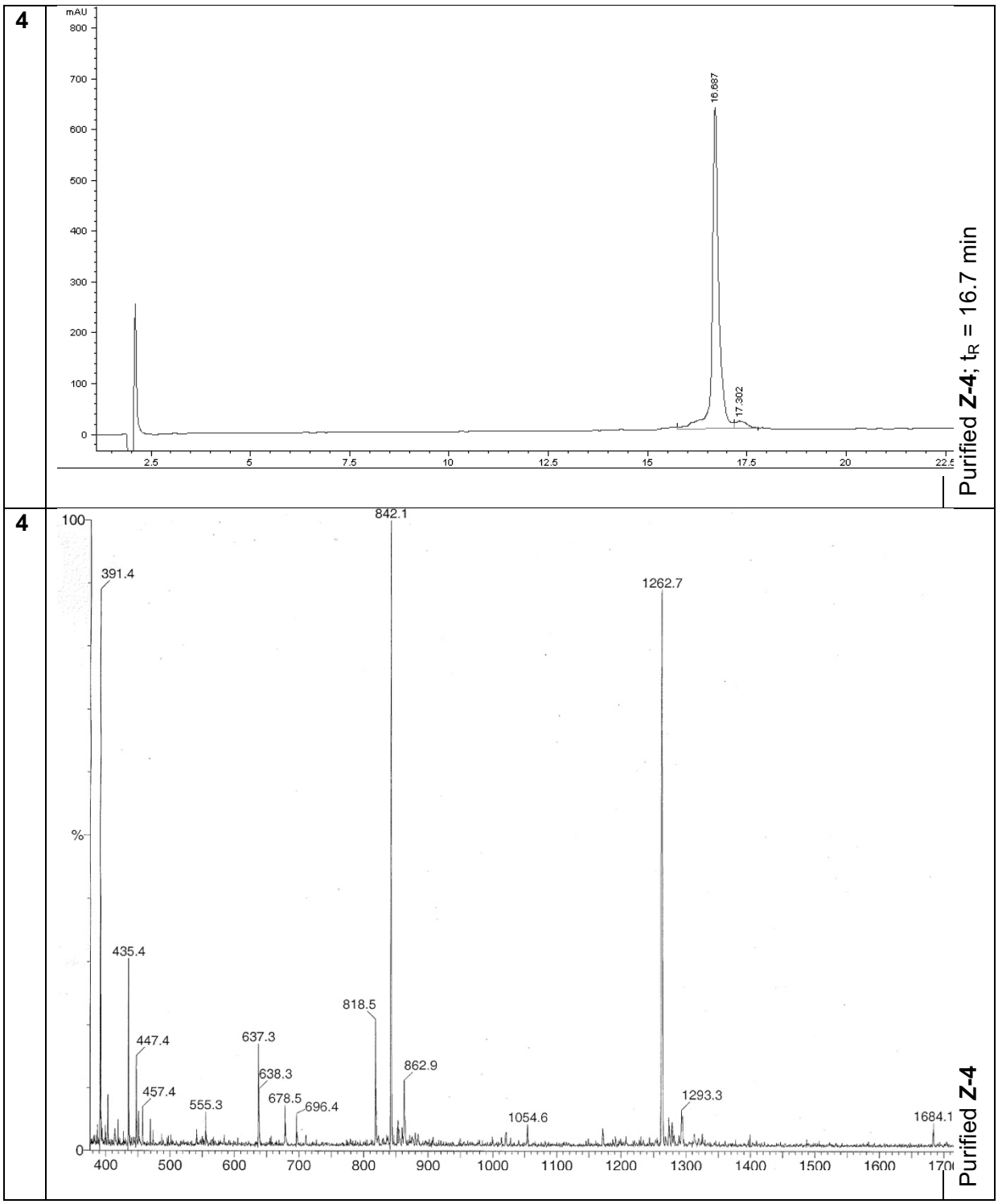

APPENDIX FIGURE 2.1F

c[Δ^4A6,11]-Dicarba-[A7]-Cys(Pyr)-[A20]-Cys(Acm) human insulin A-chain *E*-4

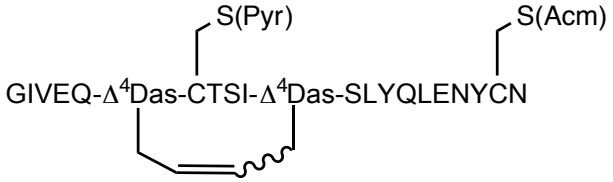

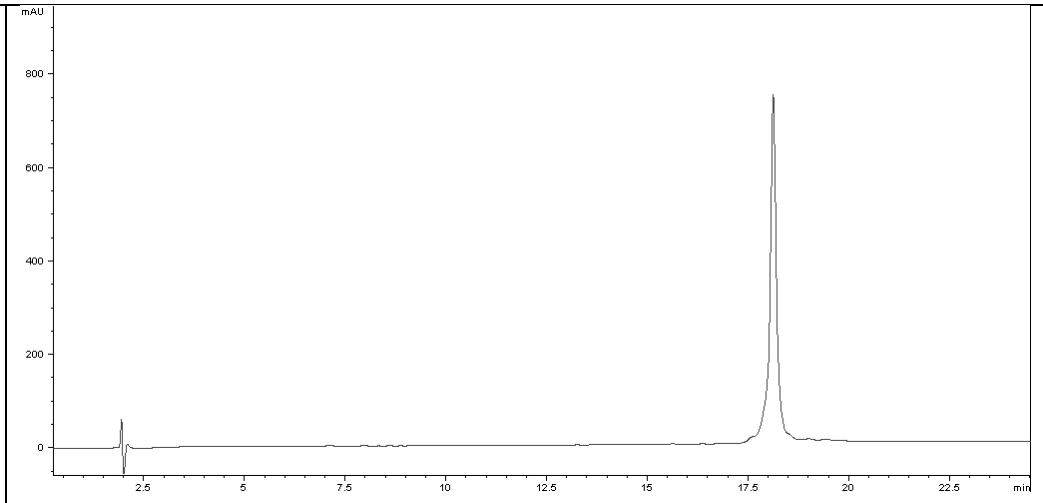

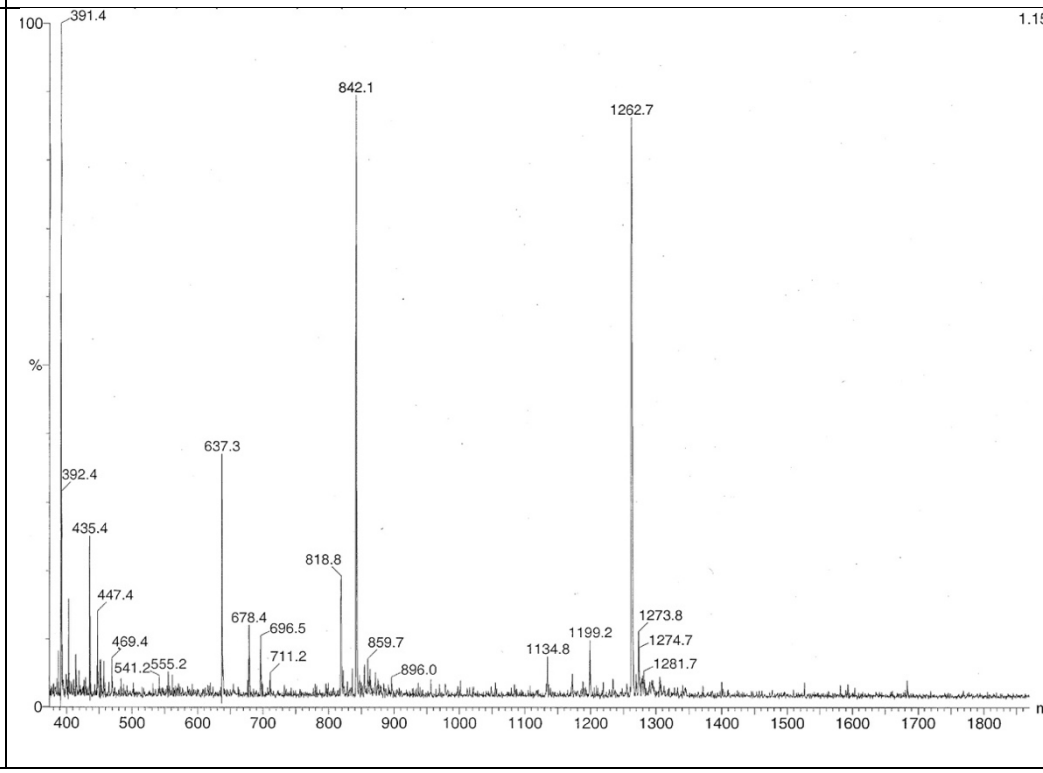

APPENDIX FIGURE 2.1G

[B19]-Cys(Acm) human insulin B-chain 5

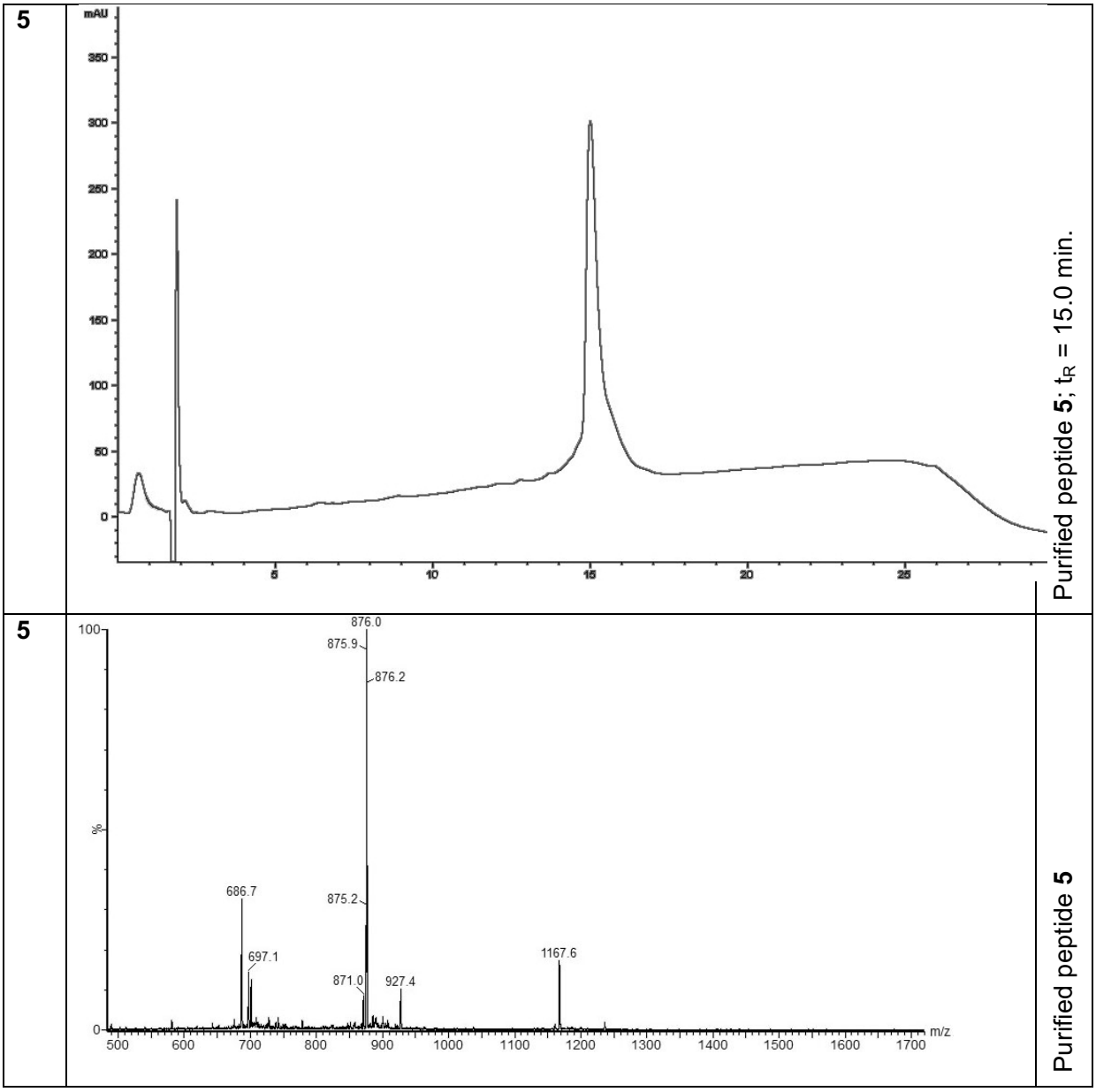

APPENDIX FIGURE 2.1H

Monocyclic A-B heterodimer of *c*[Δ^4A6,11]-dicarba human insulin *Z*-6

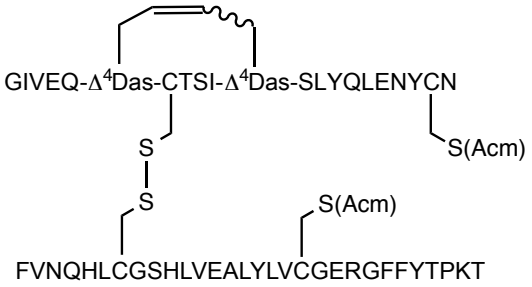

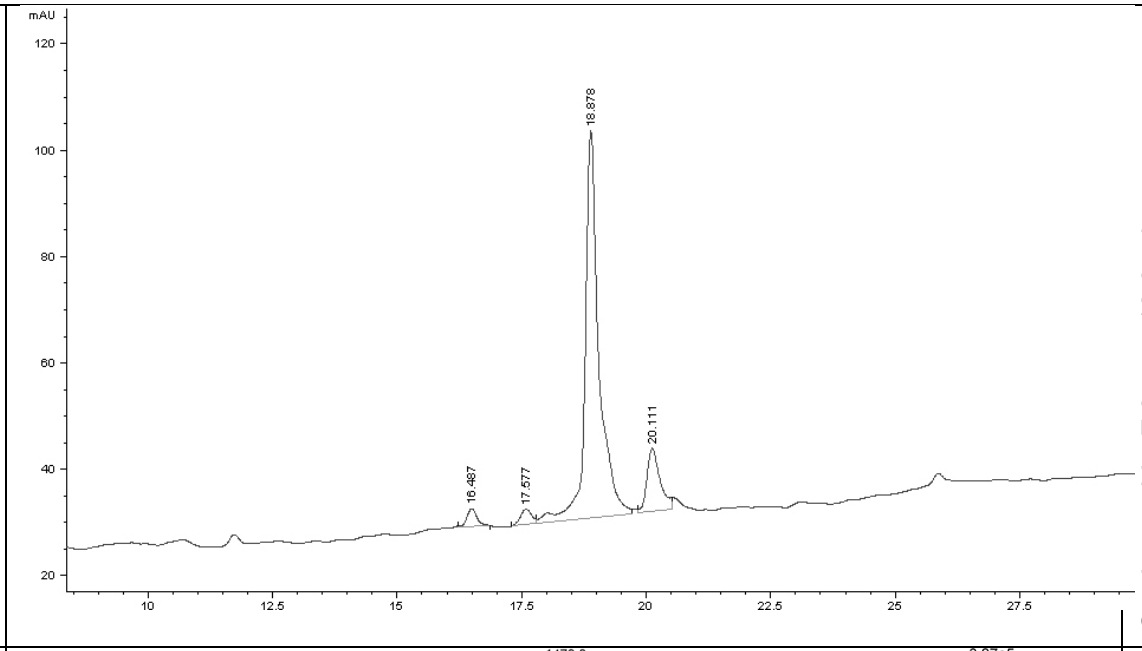

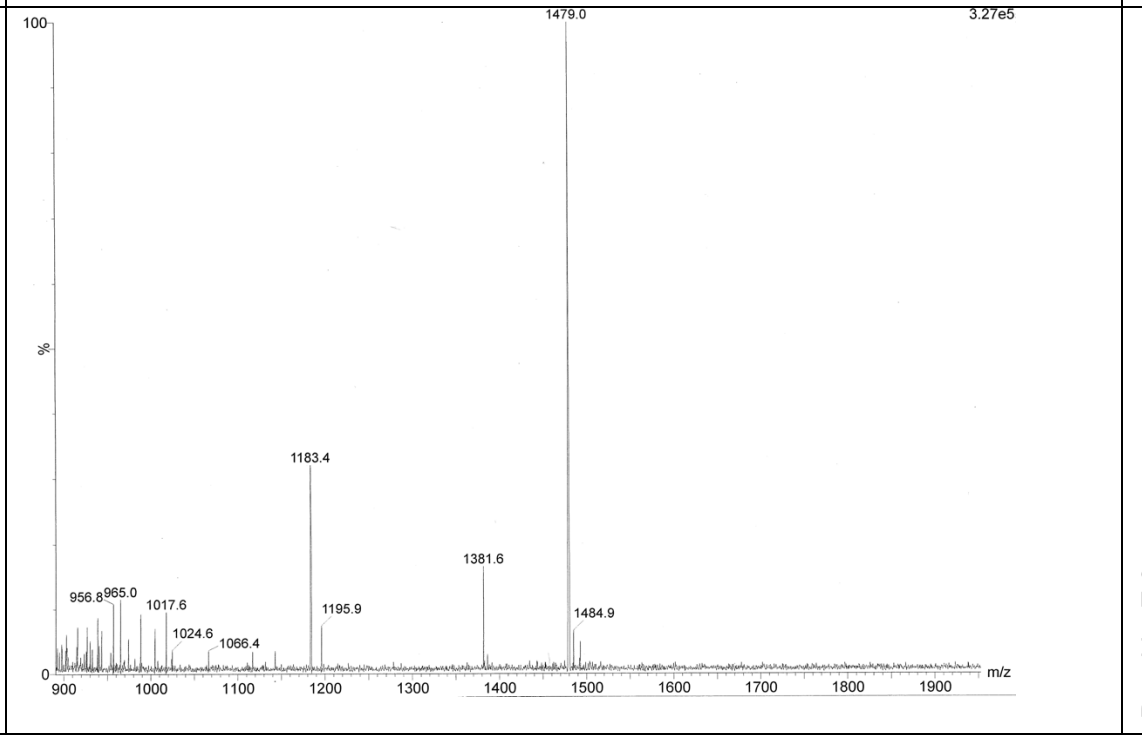

APPENDIX FIGURE 2.1I

Monocyclic A-B heterodimer of *c*[Δ^4A6,11]-dicarba human insulin chain *E*-6

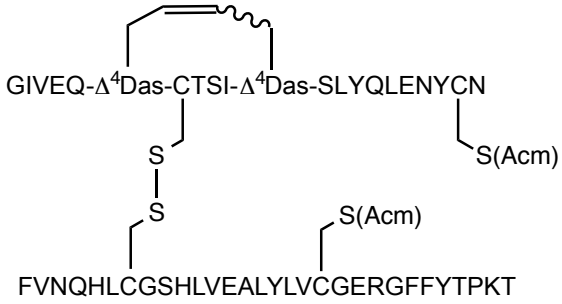

6

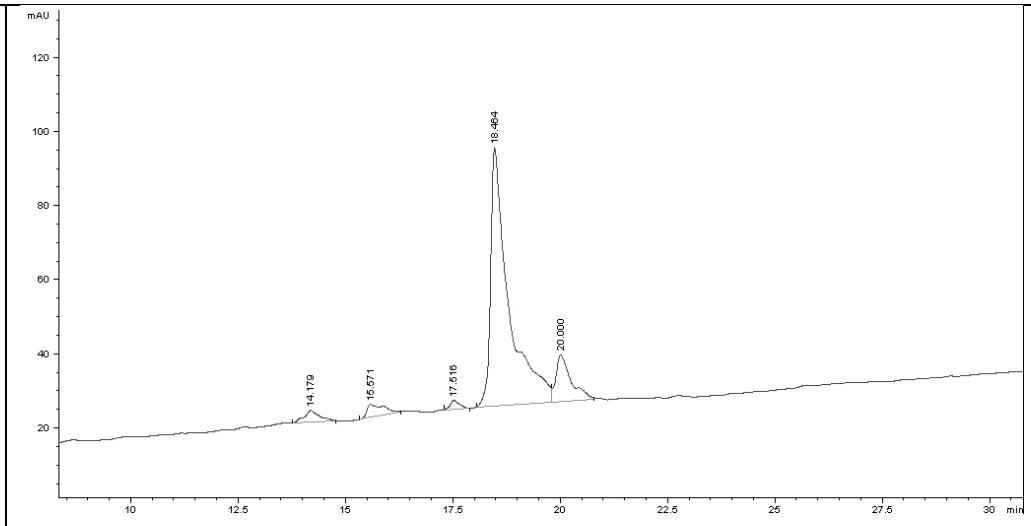

Crude peptide ***E*-6**; t_R = 18.5 min

6

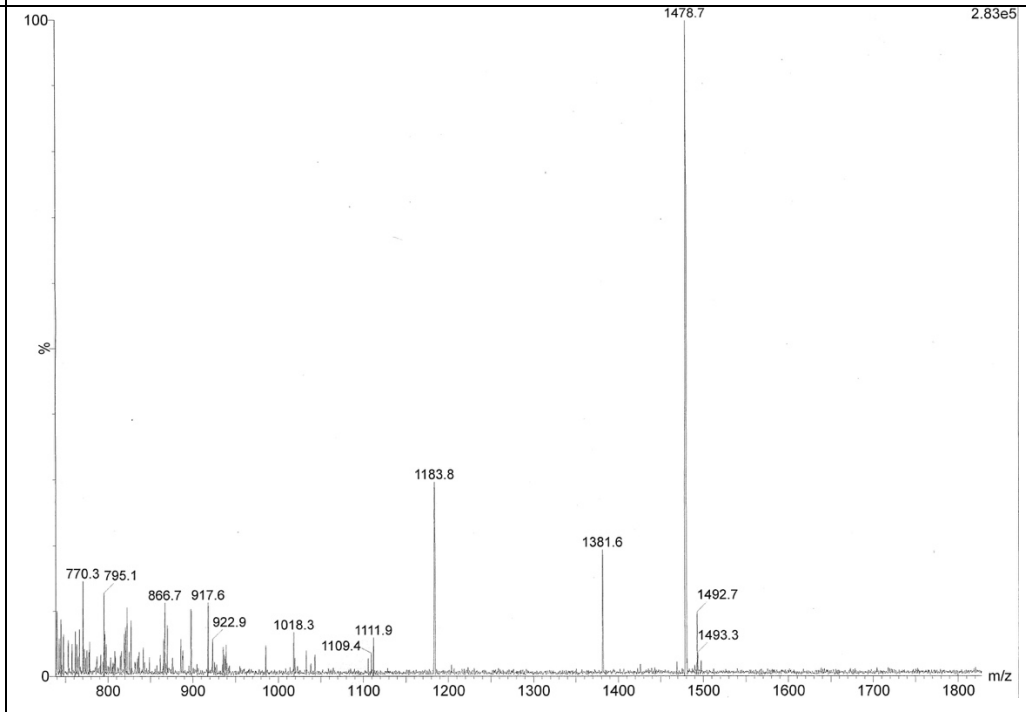

Purified peptide ***E*-6**

APPENDIX FIGURE 2.1J

c[Δ^4A6,11]-Dicarba human insulin Z-7

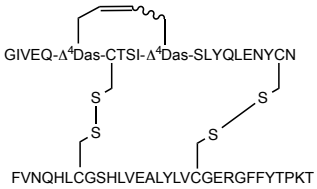

7

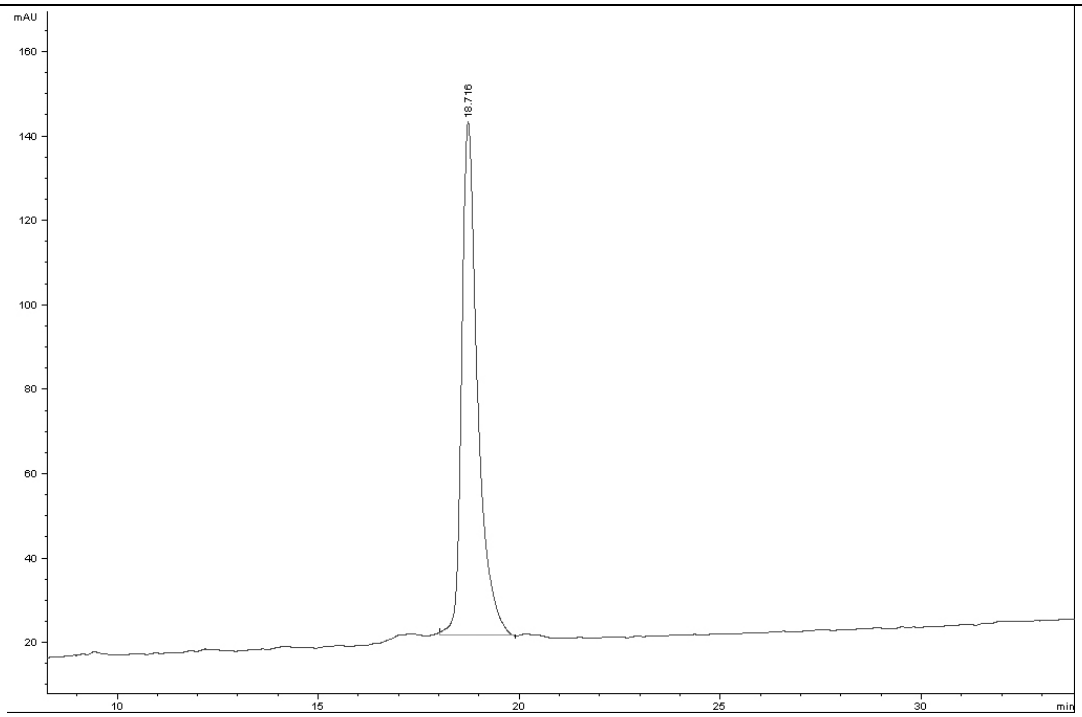

Purified peptide **Z-7**; t_R = 18.7 min

7

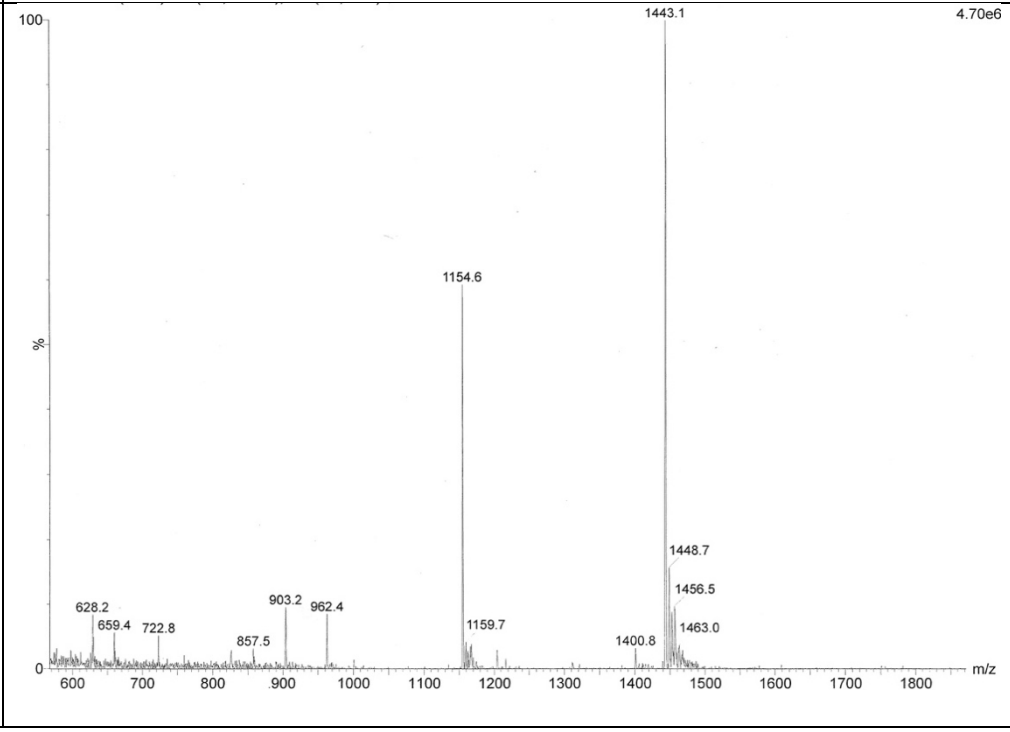

Purified **Z-7**

APPENDIX FIGURE 2.1K

c[Δ^4A6,11]-Dicarba human insulin *E*-7

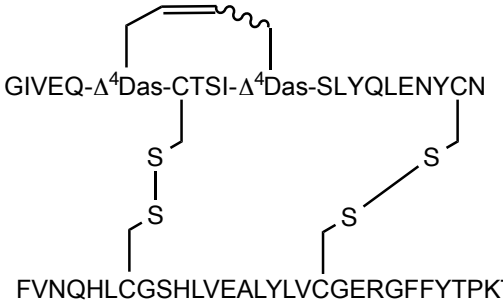

7

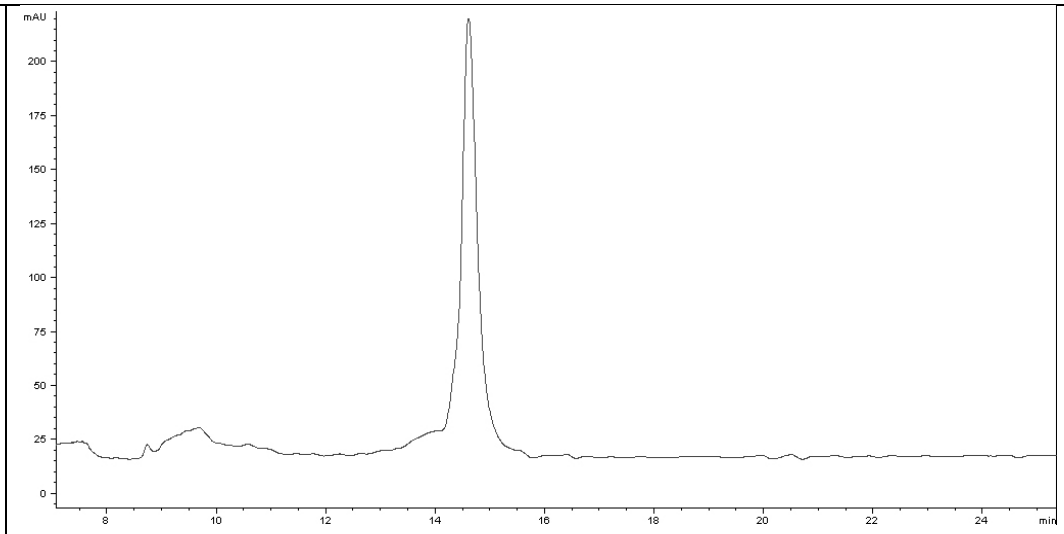

Purified peptide ***E-7***; t_R = 14.6 min

7

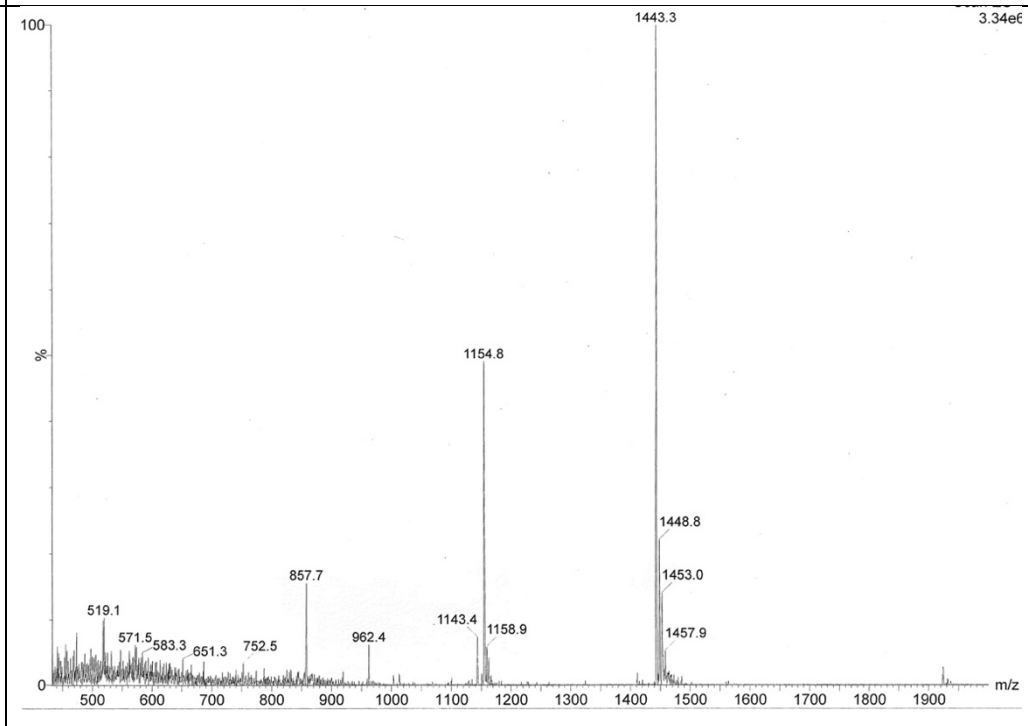

Purified peptide ***E-7***

APPENDIX FIGURE 2.1L
c[Δ⁴A6,11]-Dicarba-[A7]-Cys(ᵗBu)-[A20]-Cys(Acm) human insulin A-chain 3 *via Cis*-S1

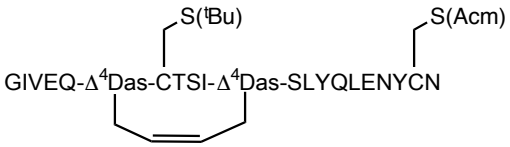

3.1

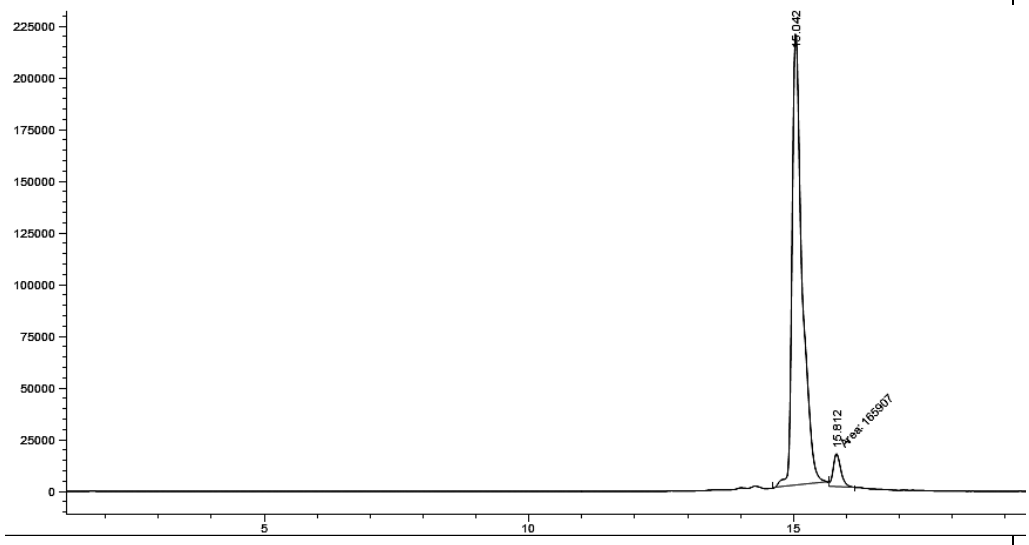

A-chain **3** synthesised using *Cis*-**S1**; t_R = 15.0 (**Z-3**) and 15.8 (***E*-3**), *25:1.*

3.1

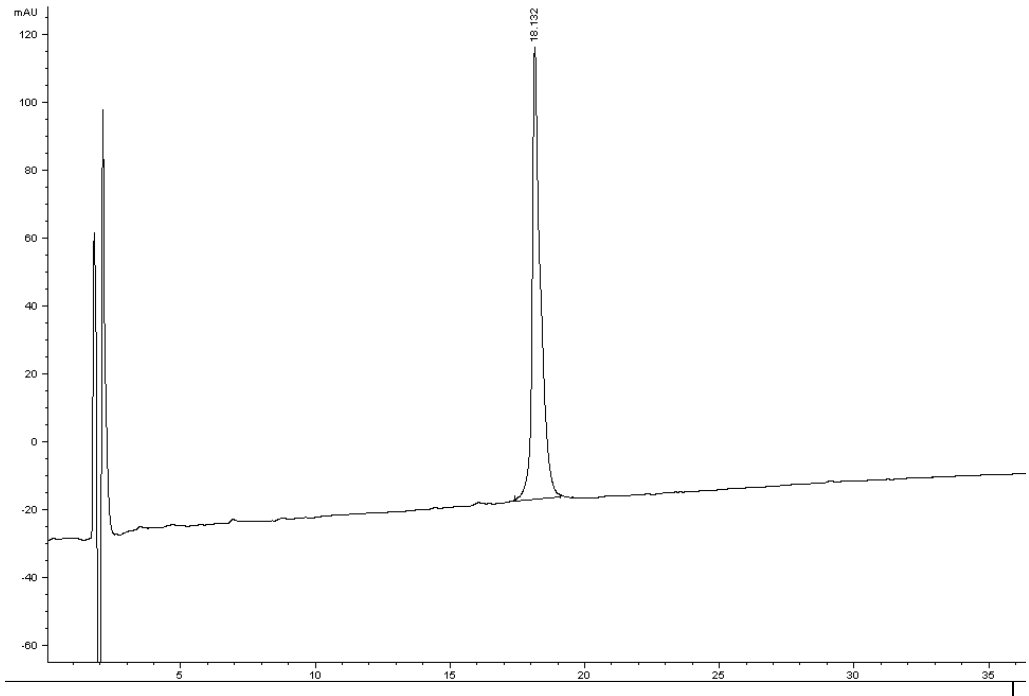

Co-injection of A-chain **3** (t_R = 15.0 (above)) with *cis*-isomer **Z-3** acquired *via* RCM method

APPENDIX FIGURE 2.2

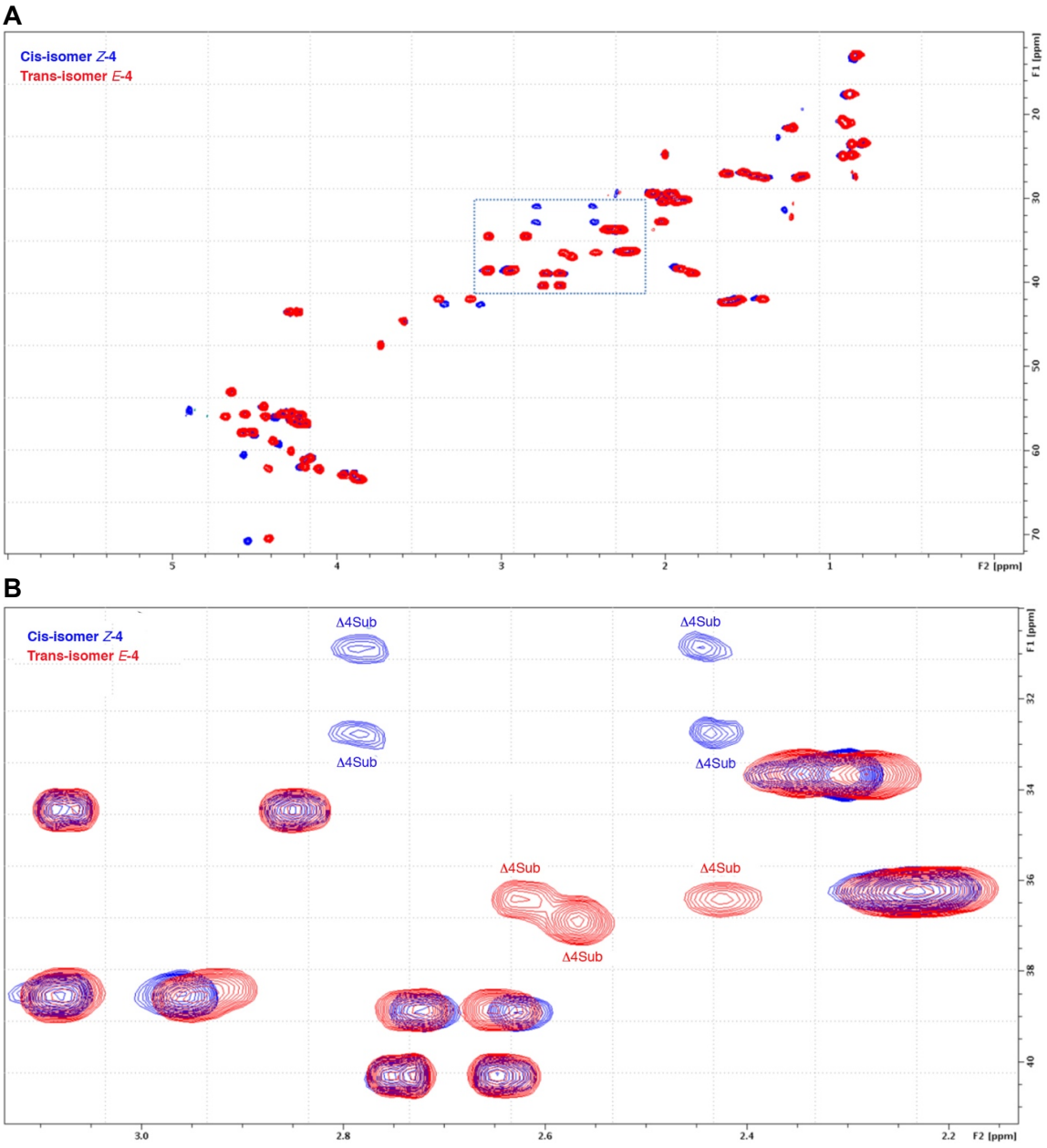

Appendix Figure 2.2A ^{13}C-HSQC spectra of *cis* dicarba (blue, *Z*-4) and *trans* dicarba (red, *E*-4) insulin A chain isomers. Differences in Δ^4Sub C$^{\beta}$ chemical shift are highlighted by the box. **B:** Crop of ^{13}C-HSQC spectra showing the difference between Δ^4Sub C$^{\beta}$ chemical shifts of *E*- and *Z*-isomers of the dicarba insulin A chain 4.

APPENDIX FIGURE 2.3

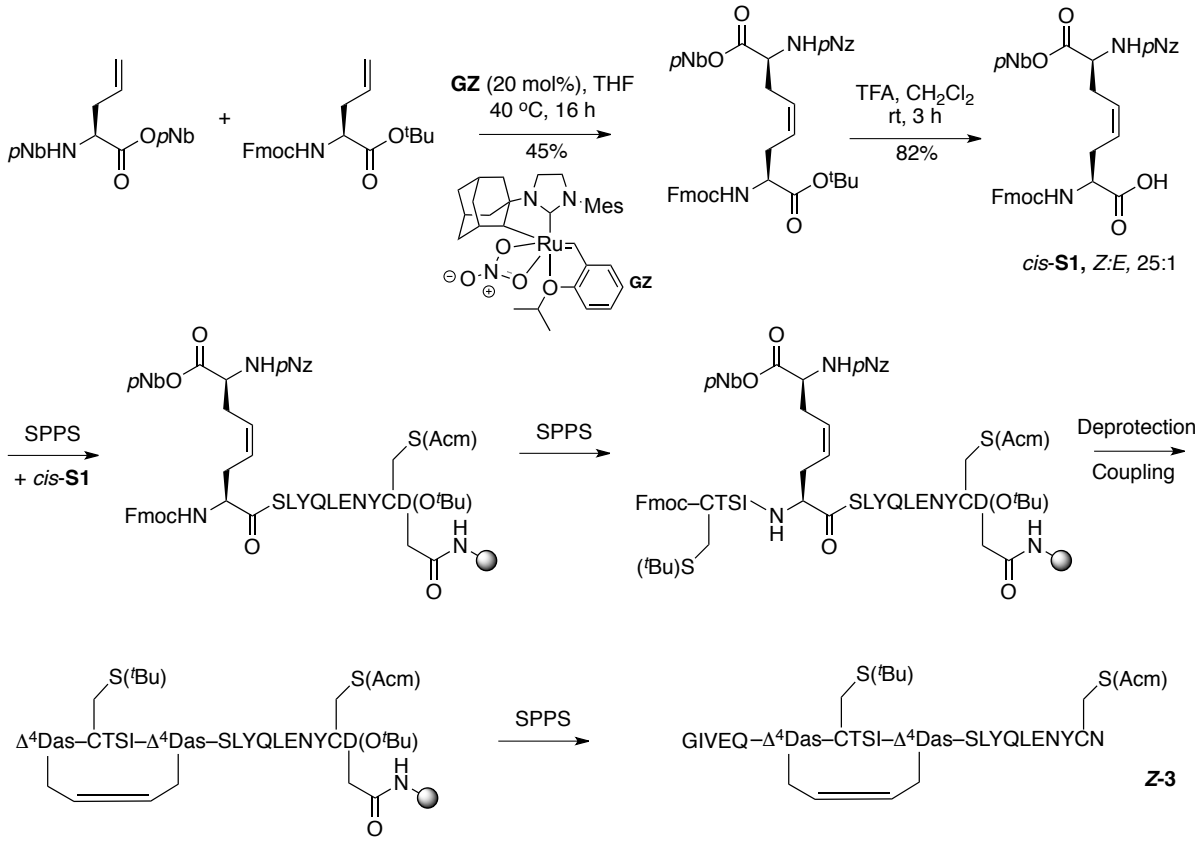

Appendix Figure 2.3 Stereochemical synthesis of insulin A-chain peptide *Z*-**3** using a preformed *Z*-configured, orthogonally protected Δ^4-diaminosuberic acid residue, *cis* **S1**.

APPENDIX FIGURE 2.4

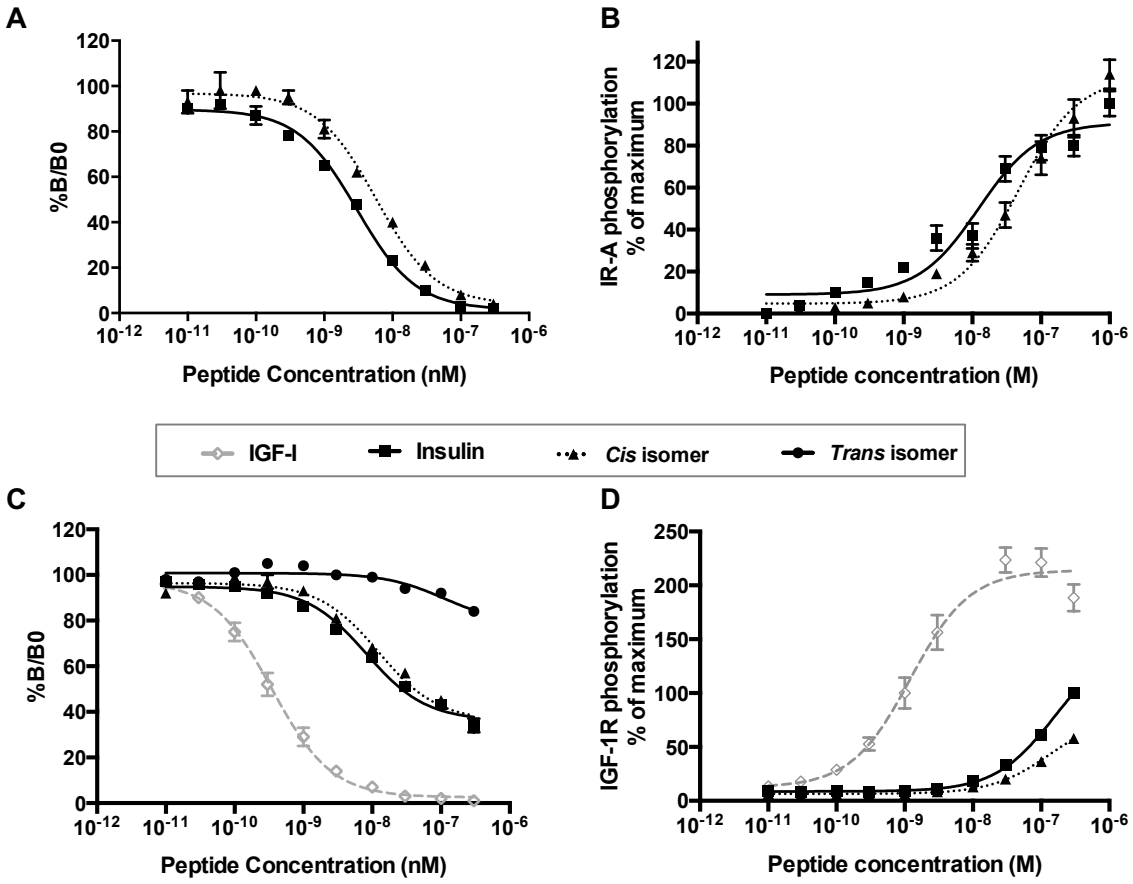

Appendix Figure 2.4 Insulin receptor isoform A and IGF-1R binding and activation activities of *cis*- and *trans* isomers. (A) Competition binding of insulin (squares) and *cis* isomer (triangles) with europium-labelled insulin. Results are expressed as a percentage of binding in the absence of competing ligand (%B/B0). (B) Activation of IR-A by increasing concentrations of dicarba insulins (10 min stimulation) is expressed as receptor phosphorylation as a percentage of the maximal phosphorylation induced by insulin. (C) Competition binding of IGF-I (diamonds), insulin (squares), *cis*- (triangles) and *trans* (circles) isomers with europium-labelled IGF-I. Results are expressed as a percentage of binding in the absence of competing ligand (%B/B0). (D) Activation of IGF-1R by increasing concentrations of dicarba insulins (10 min stimulation) is expressed as receptor phosphorylation as a percentage of the maximal phosphorylation induced by insulin. All data are the mean ± S.E.M. n = at least 3 independent experiments.

APPENDIX FIGURE 2.5

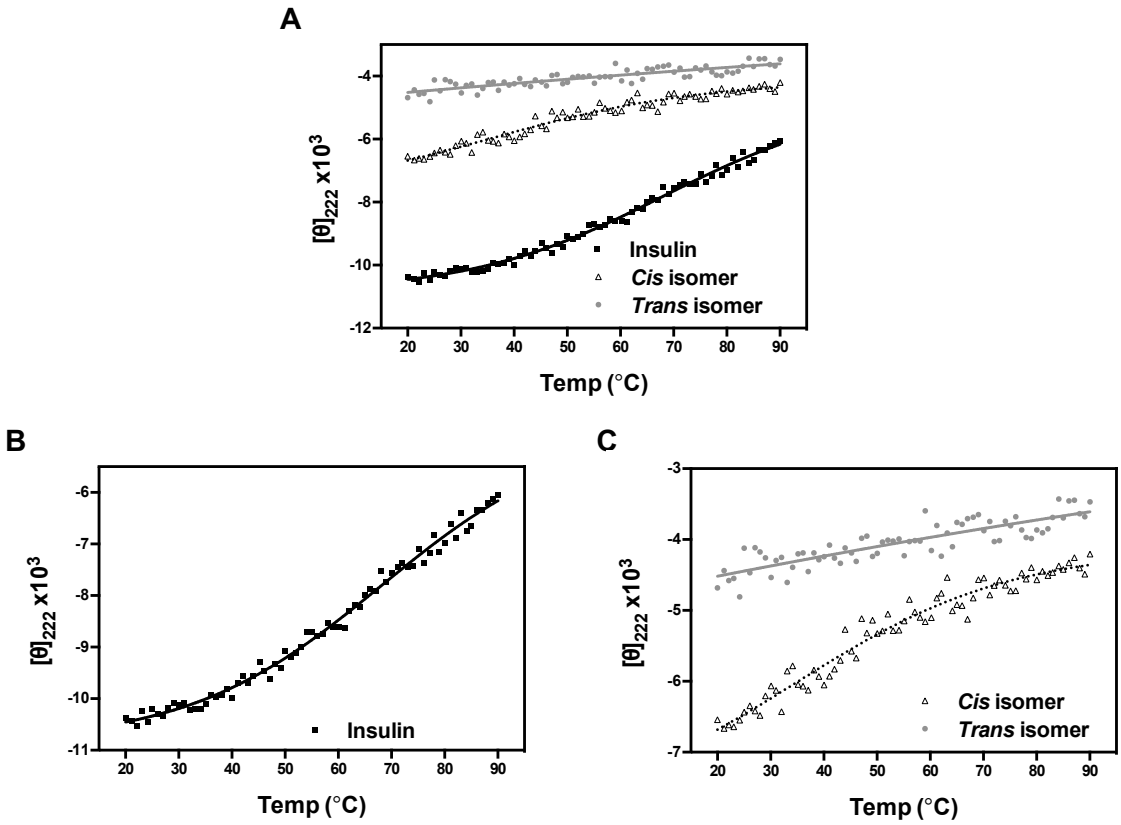

Appendix Figure 2.5 Thermal stability of dicarba insulin isomers in detail. (A) Circular dichroism far-UV spectra reveal lower helical propensities in both *cis*- and *trans* isomers. θ = ellipticity. Differences in thermal unfolding are monitored by ellipticity at 222 nm and show *trans* isomer is less stable than *cis* isomer. (B) and (C) are plotted on expanded scales to show detail.

APPENDIX FIGURE 2.6

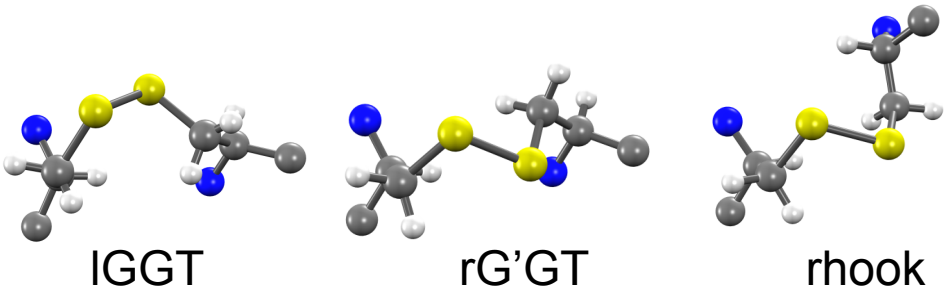

Appendix Figure 2.6 Schematic diagrams of the different disulfide bond conformations present in insulin structures listed in *Appendix Table 2.3*. lGGT = left-handed GGT, rG'GT = right-handed G'GT, rhook = right-handed hook.

APPENDIX FIGURE 2.7

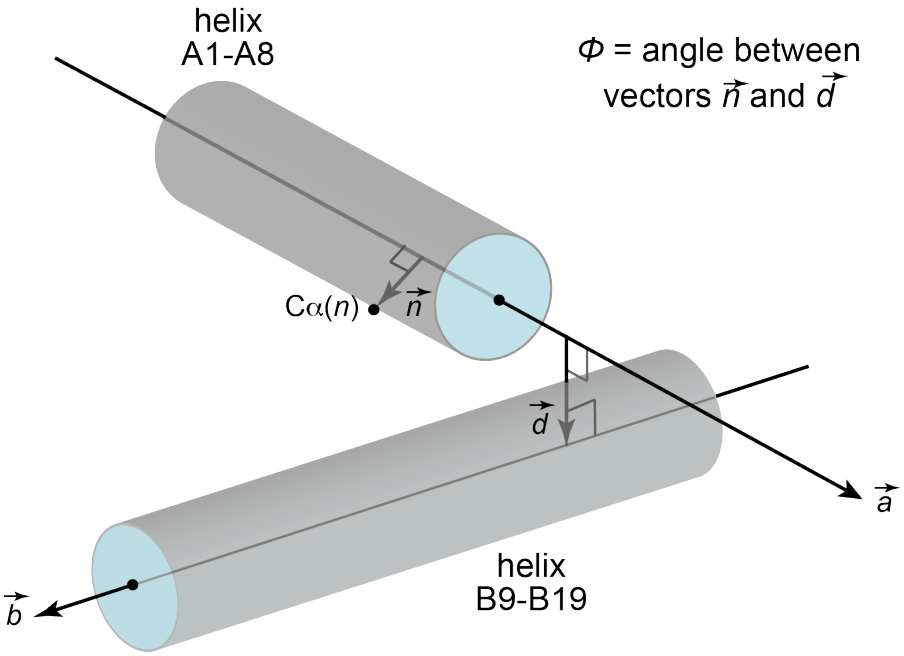

Appendix Figure 2.7 Definition of the azimuth angle ϕ of residue *n* within the segment A1–A10. The helix axial vectors $\vec{a}$ and $\vec{b}$ their vector of closest approach $\vec{d}$ were computed using HELIXANG within the CCP4 suite.(Winn et al., 2011)

APPENDIX FIGURE 2.8

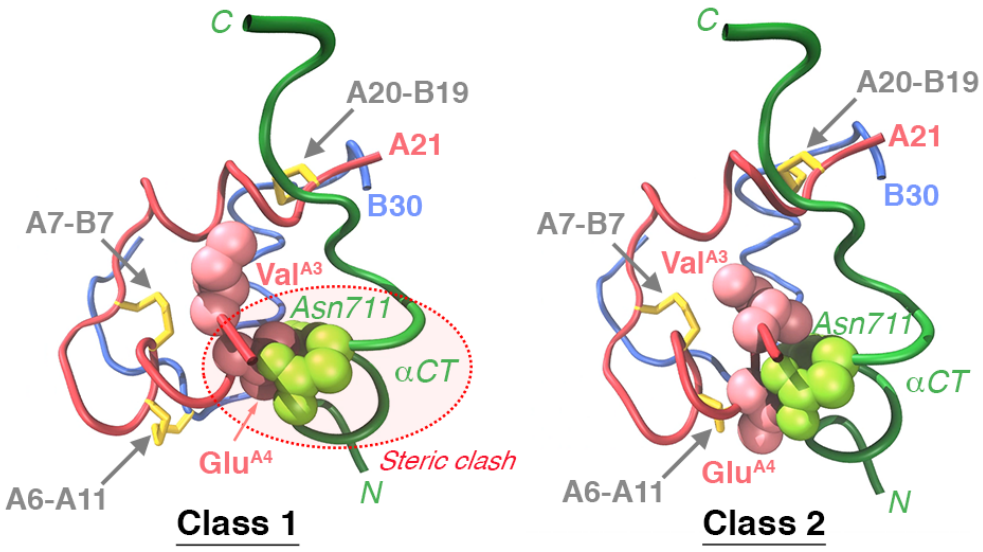

Appendix Figure 2.8 Shown above are snap shots of movie highlighting the difference in sidechain orientation of A1–A3 residues when transitioning between the tight and wide helical states of the first A-chain helix.

Movie can be found in this link: https://static-content.springer.com/esm/art%3A10.1038%2Fs41598-017-16876-3/MediaObjects/41598_2017_16876_MOESM2_ESM.mov

CHAPTER 3

"Probing the correlation between insulin activity and structural stability through introduction of the rigid A6–A11 bond."

The following chapter has been published in Journal of Biological Chemistry; Vol. 293(30)

on the 13th of June 2018

CHAPTER 3 PROBING THE CORRELATION BETWEEN INSULIN ACTIVITY AND STRUCTURAL STABILITY THROUGH THE INTRODUCTION OF THE RIGID A6–A11 BOND

3.1 INTRODUCTION

Since the discovery of insulin by Banting and Best, insulin therapy remains the primary treatment for type 1 (T1D) and late stage type 2 diabetes (T2D), being prescribed to effectively lower blood glucose levels (Banting and Best, 2007, Pandyarajan and Weiss, 2012, Mathieu et al., 2017). Long-acting (eg insulin glargine; Lantus®, Sanofi) and rapid-acting insulin analogues (eg lispro insulin or KP insulin[4]); Humalog®, Eli Lilly) currently in clinical use were developed to mimic the physiological basal-bolus insulin profile (recently reviewed in Mathieu *et al.* (Mathieu et al., 2017)). Although these analogues are undoubtedly life-savers for diabetic patients, their pharmacokinetic and pharmacodynamic performance remains suboptimal for some patients (Mathieu et al., 2017). Of high priority is the development of a new rapid-acting insulin analogue possessing faster onset of action and greater structural stability. To achieve this, a deeper understanding is required of the structural determinants of insulin necessary for receptor binding and function.

Insulin is a small globular protein synthesized in the pancreatic β-cells and secreted as a two-chain polypeptide comprising a 21-residue A chain and a 30-residue B chain. The secondary structure of insulin consists of three α-helices, two within the A chain (A1 to A8 and A12 to A18, respectively) and a single α-helix within the central segment of B chain (B9 to B19) (Fig. 3.1, *A* and *B*) (Adams et al., 1969a). It is stored in pancreatic β-cells as 2Zn-coordinated hexamers that, when released into the blood stream, rapidly dissociate into active monomers (Weiss, 2009b). The monomeric form then adopts the active conformation, and in doing so reveals essential residues within the hydrophobic core for binding (De Meyts, 2015) but also primes the molecule to the formation of higher order oligomers (Brange and Langkjoer, 1993, Hua and Weiss, 2004, Yang et al., 2010a). This is highlighted in the rapid-acting KP insulin, an analogue possessing an inversion of $Pro^{B28}Lys^{B29}$ in the B chain of native insulin to render the molecule essentially monomeric through disruption of the dimer interface (Fig. 3.1*A*) (Ciszak et al., 1995, Campbell et al., 1996). As a consequence, KP insulin is rapid acting, but concomitant exposure of core hydrophobic residues means that KP insulin readily forms fibrils (Ludwig et

al., 2011, Woods et al., 2012, Yang et al., 2010a). This highlights the fine balance between the competing requirements for stability and conformational plasticity needed for optimal activity.

High affinity binding to the insulin receptor (IR; a tyrosine kinase receptor (Lawrence and Ward, 2015b)) is achieved by interaction through two distinct binding surfaces (1 and 2) on the ligand (Menting et al., 2013, De Meyts, 2015, Jensen, 2000a, Whittaker et al., 2008). Insulin site 1 binding residues (also known as the "classical binding site") are also involved in insulin dimerization (Zoete et al., 2004, Zoete et al., 2005) while site 2 binding residues overlap with the hexamer-forming surfaces within a 2Zn-insulin hexamer (Fig. 3.1*A*) (Jensen, 2000a, De Meyts, 2015, Baker et al., 1988b). Recent crystallographic studies of an IR fragment comprised of the ectodomain and the αCT segment in complex with insulin through site 1 residues provided key insights into the mechanism of insulin:IR interaction (Menting et al., 2013, Menting et al., 2014b). Key conformational changes in insulin required for effective IR binding were identified. Movement of the *C*-terminal segment (B24–B30) of the B chain from the hormone core is required for engagement with the IR αCT and L1 domains (Hua et al., 1991). It is likely that the end of the B chain opens in a zipper-like fashion (Papaioannou et al., 2015) to allow accessibility to insulin site 1-binding residues that otherwise remain buried within the hydrophobic core (Menting et al., 2014b, Hua et al., 1991). Evident in our previous findings, insulin also undergoes further conformational change within the first A chain helix to enable binding. The helix rotates in order to avoid a steric clash between the first four residue sidechains and the αCT segment (van Lierop et al., 2017). In this conformation, residues A1 to A5 to form a single α-helical turn while residues A3 to A9 adopt a wider helix conformation, approximating an (*i*, *i*+5) π-helix (van Lierop et al., 2017). This conformation is also evident in the μIR: insulin crystal structure (PDB entries 4OGA) (Menting et al., 2014b, van Lierop et al., 2017) and can be artificially achieved by a mutation of residue B26 that also promotes opening of the B chain (Zakova et al., 2008, Zakova et al., 2004).

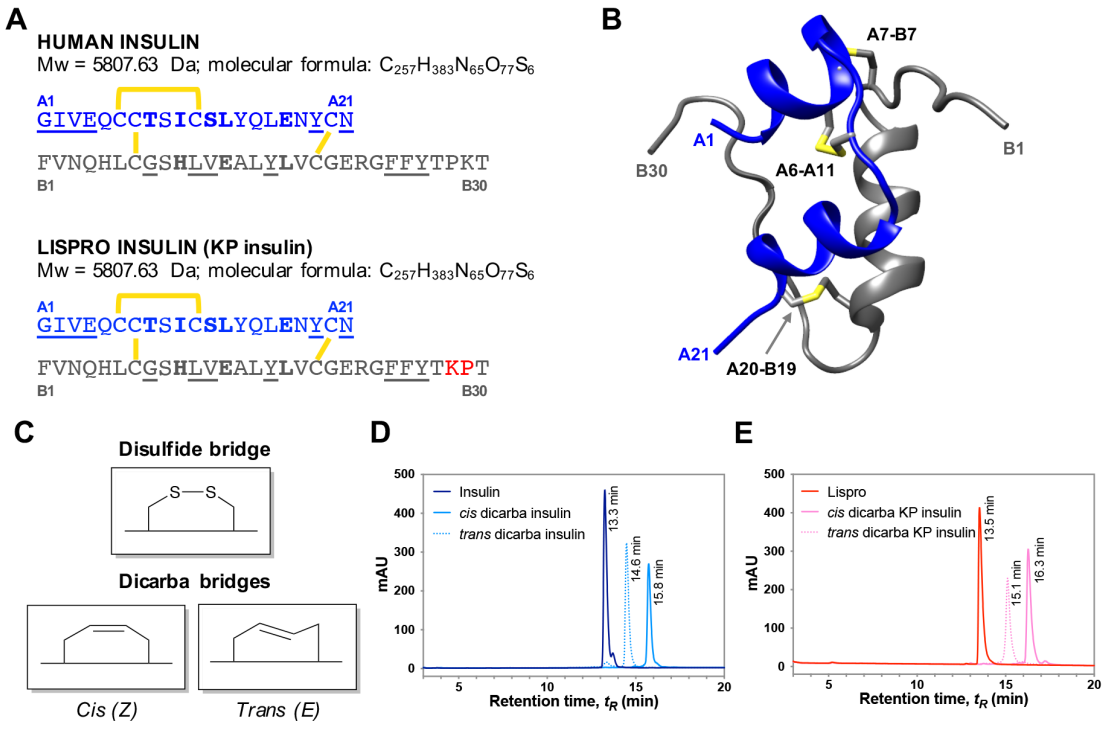

Figure 3.1 Insulin, KP insulin and dicarba insulin analogues. (A) Primary sequence comparison of human insulin (*top*) and KP insulin (*bottom*). Both consist of A (*blue*) and B (*grey*) chains stabilized by three disulfide bridges (yellow). *Underlined* are site 1-binding residues and *bold* are site 2-binding residues (Whittaker et al., 2008). Rapid-acting KP insulin has a reversal of B28 and B29 amino acids ($Lys^{B28}Pro^{B29}$) (*red*) compared to insulin. (B) Ribbon diagram of human insulin (2-Zn-coordinated T_6 conformation (Baker et al., 1988b) PDB entry 1MSO) showing the location of the three α-helices (A chain: *blue;* B chain: *grey*) and the three disulfide bonds (*yellow*). (C) Schematic diagram of native cystine and isomeric *cis*- and *trans*-dicarba bridges. RP-HPLC chromatograms of (D) native insulin, *cis*- and *trans* dicarba insulins; (E) KP insulin, *cis*- and *trans* dicarba KP insulins.

The correct folding and stabilization of the unique three-dimensional structure of mature insulin is supported by the three disulfide linkages: two inter-chain (Cys^{A7}–Cys^{B7} and Cys^{A20}–Cys^{B19}) and one intra-chain (Cys^{A6}–Cys^{A11}) (Fig. 3.1, *A* and *B*) (Chang et al., 2003, Weiss, 2009b). Correct disulfide combination is essential for function (Chang et al., 2003, Dai and Tang, 1996, Hua et al., 2002b, Sieber et al., 1978). The Cys^{A7}–Cys^{B7} bond is surface exposed and holds the *N*-termini of the two chains together. Both Cys^{A6}–Cys^{A11} and Cys^{A20}–Cys^{B19} linkages are buried within the hydrophobic core. Once folded, the Cys^{A20}–Cys^{B19} disulfide is constrained in a fixed configuration and buried deeply within the core, suggesting its most likely function is to maintain structural stability. The intra-chain Cys^{A6}–Cys^{A11} cystine, although buried, is relatively flexible and can adopt several different configurations (Sieber et al., 1978, Hua et al., 1995, Liu et al., 2004). Described in *Chapter 2*, the Cys^{A6}–Cys^{A11} linkage was identified as an important modulator of the structural transitions of the *N*-terminal A chain helix required for insulin activity. Introduction of two isomeric fixed A6–A11 dicarba bridges in insulin did not perturb the overall structure but resulted in strikingly different receptor potencies, where the *cis* isomer permits high affinity IR binding and the *trans* isomer does not (Fig. 2.2*A* and published in (van Lierop et al., 2017)). *Cis*- and *trans* isomer of native insulin are known as *cis*- and *trans* dicarba insulin, respectively, in this chapter.

Arising from the *in vivo* insulin tolerance testing of the *cis* dicarba insulin was the observation that this analogue promotes a more rapid lowering of blood glucose levels than native insulin (Figs. 2.2, *E* and *F,* and published in (van Lierop et al., 2017)). It is also less thermodynamically and chemically stable than native insulin (Fig. 2.3 and published in (van Lierop et al., 2017)). As these properties are reminiscent of the monomeric KP insulin (Brange and Langkjoer, 1993, Hua et al., 2011, Yang et al., 2010a), in this chapter, I investigate whether the A6–A11 linkage not only controls A chain flexibility but also influences the B chain conformation, leading to the monomeric state required for rapid receptor engagement.

In this chapter, through a combination of biophysical analyses of *cis* dicarba insulin and the monomeric *cis* dicarba KP insulin counterpart, I show that, despite its rapid action *in vivo* and its accelerated fibril formation relative to native insulin, the *cis* dicarba insulin is not inherently monomeric. Limited proteolysis studies alluded to an unexpected conformational change in the B-chain helix. Such a link between the A6–A11 disulfide and the conformational dynamics of the B chain has not been previously described. These findings suggest a key role for the A6–A11 linkage, not only in regulating A chain flexibility that primes insulin for receptor engagement, but also in influencing the B chain conformation and regulating insulin's stability.

3.2 MATERIALS & METHODS

3.2.1 Materials

Actrapid® insulin was purchased from Novo Nordisk Pharmaceuticals Pty Ltd. Humalog® lispro (KP insulin) was obtained from Eli Lilly Australia. Hybridoma cells expressing antibodies specific for the IR alpha subunit (83-7) and the insulin-like growth factor 1 receptor (IGF-1R) α-subunit (24-31) were a kind gift from Prof. K Siddle (Soos and Siddle, 1989, Soos et al., 1989, Ganderton et al., 1992). [^{3}H]-Thymidine and Eu-pY20 were purchased from Perkin Elmer Life Sciences. Sequencing grade chymotrypsin was purchased from Promega. The sodium salt of iodoacetic acid (IAA), HPLC grade acetonitrile (CH_3CN) and TFA and DTT were purchased from Sigma-Aldrich (St. Louis, MO, USA). Iodoacetamide (IAM) was a product of Bio-Rad (Hercules, CA, USA). All antibodies were purchased from Cell Signalling Technology (Danvers, MA) unless specified. The matrices for MALDI-TOF-MS (sinapinic acid (SA) and α-cyano-4-hydroxycinnamic acid (HCCA)) were products of Bruker Daltonics (Leipzig, Germany). All other reagents used were analytical grade.

3.2.2 Cell Lines and Cultures Conditions

For materials and method for maintaining R$^-$IR-A (R$^-$fibroblasts over-expressing hIR-A), R-IR-B (R$^-$fibroblasts over-expressing hIR-B), hIR-L6 (L6 rat myoblast over-expressing hIR-A) and P6 cells (BALB/c3T3 cells over-expressing the human IGF-1R); refer *Section 2.2.2.*

3.2.3 Synthesis of Dicarba Lispro Insulins

Chemical synthesis of all dicarba insulin analogues in this thesis were generated by our collaborator Dr Bianca van Lierop, Dr Alessia Belgi and Prof. Andrea J. Robinson in the School of Chemistry, Monash University. Clayton, Victoria, Australia. The details of the synthesis method for the dicarba KP insulins are provided in *Appendix 3A*. The synthesis method for dicarba insulins refer *Chapter 2*.

Methodology is briefly described here. The synthesis of c[Δ^4A6,11]-dicarba insulin (*cis*- and trans dicarba insulins) *(van Lierop et al., 2017)* and c[Δ^4A6,11]-dicarba KP insulins (*cis*- and trans dicarba KP insulins) were essentially the same. Synthesis of dicarba A chain was achieved through an interrupted solid-phase peptide synthesis (SPPS)-catalysis and ring-closing metathesis (RCM) procedures (van Lierop et al., 2017, van Lierop et al., 2011a). Construction of insulin and KP insulin B-chain was achieved through microwave-accelerated SPPS. The

monocyclic A-B conjugates were prepared by combination of the dicarba A chains with the insulin (or KP insulin) B chain under basic conditions resulting in spontaneous oxidation of the liberated free thiol groups generating cis- and trans dicarba insulins (or *cis*- and *trans* dicarba KP insulins).

3.2.4 Receptor Competition Binding Assays

IR-A, IR-B and IGF-1R competition binding with increasing concentrations of insulin, KP insulin and dicarba insulins was measured essentially as described in *Section 2.2.4*.

3.2.5 Kinase Receptor Activation Assays (KIRA)

IR-A, IR-B and IGF-1R phosphorylation in response to increasing concentrations of insulin, KP insulin and dicarba insulins was detected essentially as described in *Section 2.2.5.*

3.2.6 DNA synthesis Assay

DNA synthesis in response to increasing concentrations of *cis* dicarba KP insulin was carried out essentially as described in *Section 2.2.6.*

3.2.7 Glucose Uptake Assay

Glucose uptake in response to increasing concentrations of *cis* dicarba KP insulin was carried out essentially as described in *Section 2.2.7.*

3.2.8 Insulin Tolerance Test

Insulin tolerance tests for KP insulin (Humalog) and *cis* dicarba KP insulin were performed by our collaborator Assoc. Prof. Sofianos Andrikopoulos in the University of Melbourne, Department of Medicine, Parkville, Victoria, Australia.; as described in *Section 2.2.8.*

Additionally, a study was performed in order to compare the effect between semi-formulated and non-formulated KP insulin in insulin tolerance test. Semi-formulated KP insulin was prepared essentially as described in *Section 2.2.8* where formulated KP insulin was diluted to the correct dose in phosphate-buffered saline pH 7.4. To prepare non-formulated KP insulin, commercially available KP insulin was first purified *via* RP-HPLC chromatography. Lyophilised KP insulin was dissolved in 10 mM HCl and diluted to the correct dose in phosphate-buffered saline pH 7.4. As illustrated in *Appx. Fig. 3.10*, there is no difference between semi-formulated and non-

formulated KP insulin in an insulin tolerance test, demonstrating that the vehicles had no effect on the insulin tolerance test outcomes.

3.2.9 Circular Dichroism (CD)

Circular dichroism was carried out as described in *Section 2.2.9.*

3.2.10 Sedimentation Equilibrium Analytical Ultracentrifugation (SE-AUC)

SE-AUC analyses were conducted by our collaborator, Dr Chris MacRaild and Prof. Ray S. Norton in the School of Medical Chemistry, Monash Institute of Pharmaceutical Sciences, Monash University, Parkville, Victoria, Australia.

Analytical ultracentrifugation was conducted at 20 °C using a Beckman XLI analytical centrifuge in 12 mm path-length cells. Cis dicarba insulin was diluted from a 10 mg / ml stock in 10 mM HCl into 100 µL 10 mM sodium phosphate, 100 mM NaCl, pH 7.4, with or without 0.2 mM $ZnCl_2$ to a final concentration of 100 or 300 µg/mL. Radial concentration distributions were measured by absorbance at 230 nm. Sedimentation equilibrium was established at 25,000 and 40,000 rpm, as assessed by sequential absorbance scans 2 h apart. Data at both speeds were jointly fit to a single ideal sedimenting species or to various models of self-association in SEDPHAT (Houtman et al., 2007), using values of solution density and solute partial specific volume estimated from composition using SEDNTERP (Laue et al., 1992), neglecting any effect of the dicarba modification. Mass conservation was applied as a constraint on the fits by floating the position of the bottom of the cell. Reported errors describe the precision of the fit at 0.68 confidence level, estimated from Monte Carlo simulations as implemented in SEDPHAT.

3.2.11 Atomic Force Microscopy (AFM)

AFM analyses were conducted by Ms Carlie Delaine.

Analysis of fibrillation was monitored by AFM essentially as described (Manno et al., 2007). Briefly, lyophilized insulin, insulin lispro and dicarba isomers were re-suspended in 200 mM KCl-HCl in Milli-Q water, pH 1.6 at 200 µM (1.16 mg/mL) and incubated at 60 °C with gentle agitation. Samples (5 µL) were taken at different times, diluted 1: 10 in the same buffer and immediately frozen. 30 µL of the insulin solution was dropped onto a freshly cleaved mica substrate. Once dried, the sample was washed dropwise with Milli-Q water, and then dried with a gentle stream of dry nitrogen. Images of the protein aggregates were recorded with a

Multimode Nanoscope IV Atomic Force Microscope (Veeco Instruments, Santa Barbara, CA, USA), operating in Tapping Mode. Rigid cantilevers with resonance frequencies of 325 kHz and equipped with silicon tips (Mikromasch HQ: NSC15, Bulgaria) with nominal spring constant of 40 N/m and a nominal tip diameter of 16 nm were used. Typical scan size was 5 µm (512×512 points), and scan rate was 1-2 Hz. The scanner was calibrated in the x, y and z axes using silicon calibration grids (Bruker model numbers PG: 1 µm pitch, 110 nm depth and VGRP: 10 µm pitch, 180 nm depth). Images were analysed using the Nanoscope analysis program version 1.40.

3.2.12 In-solution Time Course Limited Proteolysis Assay

Limited proteolysis analyses were performed in 100 mM Tris-HCl pH 7.5 using sequencing grade chymotrypsin at final protease: peptide ratio of 1: 50 or 1: 250 (w/w); incubated at 37 °C. The final concentration of peptide was 0.5 mg/mL. The proteolytic reactions were analysed on a time-course basis by sampling 10 µL of proteolytic mixture (equivalent to 5 µg of insulin) into 100 µL 0.5% (v/v) TFA at t = 0, 1, 2 and 3 h. Digested samples were analysed and fractionated (fraction size: 0.25 mL or 0.5 mL) using RP-HPLC and lyophilised. The extents of proteolysis were analysed as follows:

Equation 3.1

$$\%\ of\ Undigested\ Peptide = \frac{Mass\ of\ Undigested\ Peptide\ at\ T = x}{Mass\ of\ Undigested\ Peptide\ at\ T = 0}\ x\ 100\ \%$$

3.2.13 Reversed-phase High Performance Liquid Chromatography (RP-HPLC)

Purification of insulin analogues was performed on a Vydac C_4 analytical column (214TP5210; 5 µm, 2.1 x 100 mm, 300 Å) connected to the Agilent 1260 Infinity Quaternary LC system. Buffer A: 0.1% aqueous TFA. Buffer B: 80% CH_3CN in 0.08% TFA. Peptides were eluted using a linear gradient of 20 – 25 % CH_3CN for 5 min, followed by a 25 – 38 % CH_3CN gradient over 13 min at flow rate of 0.5 mL/min. UV detection was at 280 nm and peak areas were used for quantitation of peptides.

3.2.14 Preparation of Proteolysed Insulin Samples for Mass Spectrometry

Lyophilised fractions were resuspended in 20 µL of 100 mM ammonium bicarbonate (NH_4HCO_3). Half of the volume was kept separately as non-reducing samples for mass

spectrometry analysis. The other half was reduced in 5 mM DTT for 45 min at 56 °C and alkylated with 14 mM IAM (for positive mode) or IAA (for negative mode) for 30 minutes in the dark at room temperature.

3.2.15 Matrix-Assisted Laser Desorption and Ionisation Time-of-Flight Mass Spectrometry (MALDI-TOF MS)

The molecular weights of intact insulin analogues and the proteolytically cleaved metabolites were identified using MALDI-TOF Autoflex™ III (Bruker Daltonics, Leipzig, Germany) equipped with a Nd: YAG laser (wavelength: 355nm). Either the entire cleavage mixture or isolated peaks separated by RP-HPLC were subjected to mass spectral analysis using combinations of positive or negative ion with linear or reflectron mode. Insulin digest samples intended for mass analysis using positive mode were desalted using Zip-Tip C_{18} (Millipore®, Billerica, MA, USA), eluted with 2 µL of 0.1 % TFA / CH_3CN (70: 30, v/v). Samples intended for negative mode analysis were desalted and eluted with no TFA. 1 µL of each sample was spotted onto the MTP 384 ground steel target plate (Bruker Daltonics), air dried, then 1 µL of SA matrix is spotted on top of each dried sample. Calibrations were performed using Bruker Daltonics' Peptide Calibration Standard II and Protein Calibration Standard I according to manufacturer's instructions.

3.2.16 Molecular Dynamics

Molecular dynamics analyses were conducted by our collaborator, Dr Naomi L. Haworth in the School of Chemistry, Monash University, Clayton, Victoria, Australia.

Previously, MD simulations of insulin and its *cis* dicarba analogue were performed, and the different behaviours of the *N*-terminal A chain helix analysed in detail (refer *Chapter 2 Methods*, also published in (van Lierop et al., 2017)). Here, these simulation data are further analysed to give insight into the effect of the A6–A11 linkage on insulin structural stability. Details of the simulation and analysis protocols are provided in *Chapter 2* (published in (van Lierop et al., 2017)). In brief, the AMBER14 program package (Case et al., 2014) in conjunction with *Amber ff14SB force field parameters*(Maier et al., 2015) (along with calculated parameters for the dicarba linkage) were used to perform 200 ns room-temperature MD simulations for insulin and its dicarba isomers based on four different starting structures derived from high-resolution X-ray crystallography experiments. Twelve independent 200 ns simulations were performed for insulin and 16 simulations for the *cis* dicarba insulin. Simulation frames recorded at 200 ps intervals

were used for the analysis in this paper (1000 frames per simulation). Data were processed and analysed using CPPTRAJ, (Roe and Cheatham, 2013) along with custom computer scripts. The torsional strain in the A7—B7 disulfide linkages was estimated based on the data reported in references (Haworth et al., 2010, Haworth et al., 2007). Insulin structures were superimposed on the crystal structure of a chymotrypsin-inhibitor complex (PDB: 4h4f) using Swiss-PDBViewer (Guex and Peitsch, 1997) and VMD (Humphrey et al., 1996).

3.2.17 Statistical Analyses

Statistical analysis of receptor binding, receptor activation and DNA synthesis assays were performed using a 2-way ANOVA with a Dunnett's multiple comparison. Data for glucose uptake assay and significance of the overall change of blood glucose levels in insulin tolerance test were analysed with paired *t*-test. Significance of the change of blood glucose levels at each time-point was also determined by 2-way ANOVA followed by Holm Sidak's multiple comparison test. Significance was accepted at $P < 0.05$.

3.3 RESULTS

3.3.1 Chemical Synthesis

Outline: Chemical synthesis of A6–A11 dicarba lispro (KP) insulin generates two isomeric cis- and trans dicarba KP insulin peptides.

This chapter aimed to understand the mechanism by which the *cis* dicarba insulin was apparently rapid acting *in vivo* by directly comparing it's *in vitro* and *in vivo* biological and biophysical activities with the monomeric c[Δ^4A6,11]-dicarba human lispro insulin (*cis*- and *trans* dicarba KP insulins). The *cis*- and *trans*-configured dicarba insulin A chains, in which a C=C dicarba bond replaces the A6–A11 intra-chain S–S bond (Fig. 3.1*C*), were synthesised as previously described using a RCM and SPPS-catalysis approach (van Lierop et al., 2017, van Lierop et al., 2011a). The modified dicarba insulin A chains were then combined with requisite insulin B chains to provide *cis* and *trans* isomers of c[Δ^4A6,11]-dicarba human insulin and c[Δ^4A6,11]-dicarba KP insulin. The dicarba analogues were purified by RP-HPLC (see Figs. 3.1, *D* and *E*, and Appx. Fig. 3.1) before being subjected to biological and biophysical analyses. The synthesis of dicarba lispro is summarized in *schematic 3.1*.

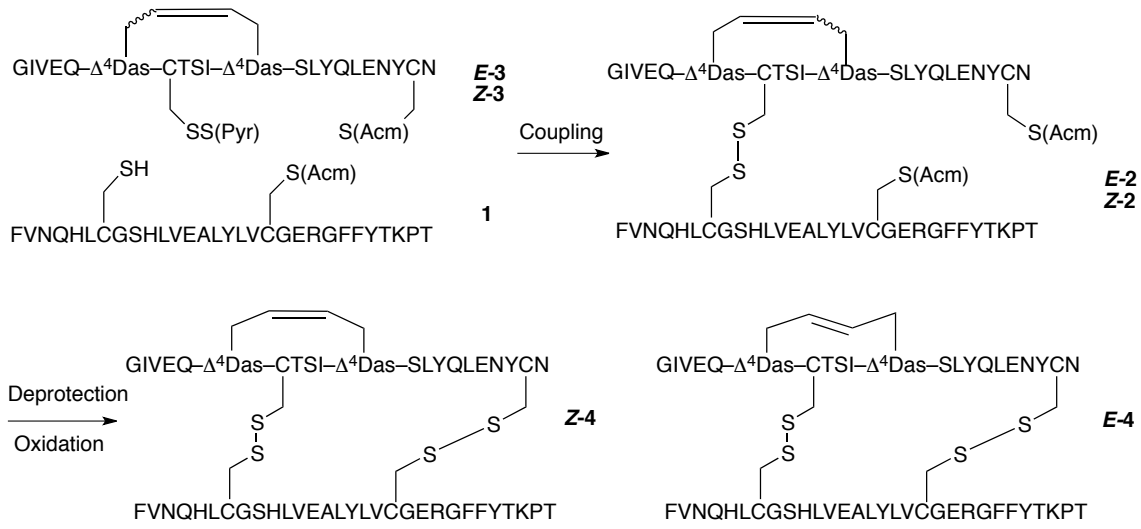

Schematic 3.1 Synthesis of *c*[Δ^{4}A6,11]-Dicarba lispro insulin 4 insulins was performed *via* ring-closing metathesis (RCM) and an interrupted solid phase peptide synthesis (SPPS)-catalysis approach. L-Allylglycine (Agl), tert-butyl (^{t}Bu), acetamidomethyl (Acm), pyridinyl (Pyr), cis isomer (Z), trans isomer (E).

3.3.2 Receptor Binding & Activation Analyses

Outline: Cis dicarba insulin and cis dicarba KP insulin are equally potent to native insulin in receptor binding and activation.

The binding affinities of the dicarba insulin analogues for the IR-B and IGF-1R were determined using competition binding assays (Figs. 3.2*A*, Appx. Fig. 3.2 and Appx. Table 3.1). Notably, the restrained A6–A11 *cis* and *trans* dicarba C=C bonds had the same effect when introduced into the monomeric KP insulin analogue as was previously seen with the *cis* and *trans* dicarba analogues of human insulin (van Lierop et al., 2017)). *Cis* dicarba insulin and *cis* dicarba KP insulin were equipotent to native insulin in binding and activation of both the IR-B (Fig. 3.2, *A* and *B*) and the IGF-1R (Appx. Fig. 3.2, *A* and *B*, and Appx. Table 3.1), suggesting that the restrained *cis* dicarba C=C bond allows both analogues to adopt a conformation that engages with both receptors in a manner similar to insulin. Conversely, *trans* dicarba insulin and *trans* dicarba KP insulin bind poorly to both the IR-B (Fig. 3.2*A*) and IGF-1R (Appx. Fig. 3.2*A* and Appx. Table 3.1), indicating that the *trans* dicarba configuration restricts both analogues from forming a high affinity interaction with these receptors. The *trans* dicarba insulins were subsequently excluded in this and further activity assays due to their poor receptor binding affinities.

3.3.3 *In vitro* Metabolic and Mitogenic Activity

Outline: The cis dicarba KP insulin promotes in vitro DNA synthesis and glucose uptake with equal potency to native insulin.

Corresponding with its IR-B binding and activation potency, the *cis* dicarba KP insulin was equipotent with native insulin in promoting DNA synthesis in L6 rat skeletal myoblast overexpressing IR-A. This is in contrast to the *cis* dicarba insulin, which was 5 to 10-fold less potent than insulin in promoting mitogenic activity (Fig. 3.2*C* and *(van Lierop et al., 2017)*). The *cis* dicarba KP insulin was equipotent with *cis* dicarba insulin and insulin in promoting glucose uptake in cultured NIH3T3-L1 adipocytes (Fig. 3.2*D*). There is a trend of lower activities for the *cis* dicarba insulin and *cis* dicarba KP insulin, however the effect was not significantly different.

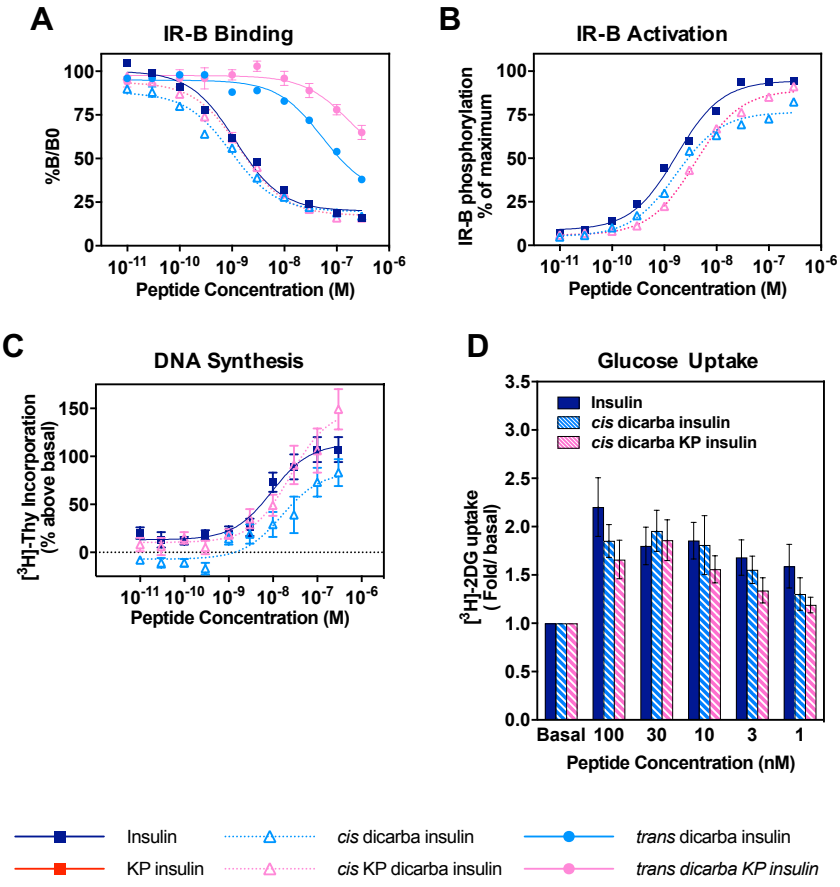

Figure 3.2 *In vitro* (A – D) activity of insulin, KP insulin and their respective dicarba insulin analogues. (A) Competition binding of insulin and dicarba insulins with europium-labelled insulin. Results are expressed as a percentage of binding in the absence of competing ligand (% B/B_0). (B) Activation of IR-B by increasing concentration of dicarba insulins (10 min stimulation) is expressed as receptor phosphorylation as a percentage of the maximal phosphorylation induced by insulin. Insulin *vs cis* dicarba insulin (ns); insulin *vs trans* dicarba insulin **** ($P \leq 0.0001$) (2-way ANOVA; Dunnett's multiple comparison) (C) DNA synthesis in response to increasing concentrations of dicarba insulins is shown as percentage incorporation of ^{3}H-thymidine (^{3}H-Thy) above basal. All data in (A –D) are the mean ± *S.E.M.* n = at least 3 independent experiments. (D) Glucose uptake stimulated by increasing concentrations of insulin, *cis* dicarba insulin or *cis* dicarba KP insulin is expressed as fold glucose uptake (pmol/min/mg) above basal. Insulin *vs cis* dicarba insulin *vs cis* dicarba KP insulin (ns) (paired *t*-test).

3.3.4 SE-AUC Analyses

Outline: The cis dicarba insulin demonstrates identical self-association behaviour to native insulin.

AUC was performed in order to determine whether the *cis* dicarba insulin is monomeric as suggested by its rapid action *in vivo* (Fig. 2.2, *E* and *F*, and (van Lierop et al., 2017)). In the presence of Zn^{2+}, sedimentation equilibrium data for the *cis* dicarba insulin was fitted to a single species of apparent mass 34,500 ± 400 Da (Fig. 3.3*A*), consistent with the expected mass of a 2-Zn^{2+} human insulin hexamer (34,726 Da). At higher concentrations the fit was not perfect (reduced $\chi^2 \sim 4$), suggesting the presence of other high molecular weight species, consistent with previous observations for native mammalian insulins (Milthorpe et al., 1977).

In contrast, the shape of the equilibrium concentration distributions in the absence of Zn^{2+} were clearly concentration dependent, implying reversible self-association (Fig. 3.3*B*). Accordingly, these data could not be fit as a single species, in sharp contrast to those that have recently described for the strictly monomeric venom insulin of *Conus geographus* (Appx. Fig. 3.11) (Menting et al., 2016). Native insulin shows similar concentration dependence in the shape of its equilibrium concentration distributions (Appx. Fig. 3.11), and also fails to fit to single-species models, consistent with its expected tendency for self-association. For an initial model-free assessment of the self-association of Zn^{2+}-free *cis* dicarba and native insulin, the data were plotted as the square of the radial position scaled by rotor speed $[\omega^2(r^2-r_0^2)]$ *vs* the logarithm of the equilibrium concentration (Fig. 3.3*C*). The slope of such a plot is proportional to the weight-average molecular weight of all species present at each point in the cell, and the observed non-linearity confirms the presence of multiple species in the sample. Over much of the accessible concentration range, the slopes of the *cis* dicarba and native insulin plots are similar, implying that the self-association behaviour of the two insulins are similar. At low concentration (< 10 μM), the slope was consistent with that expected for monomeric insulin, suggesting that monomer dominated at these concentrations. The slope increased with increasing concentration, indicating that oligomeric species were dominant over much of the experimental concentration range. Only at the highest concentrations is there evidence of some divergence between the two curves, suggesting the possibility of some difference in the tendency of *cis* dicarba insulin to form higher-order oligomers.

Attempts to fit the two datasets to a specific, consistent model of self-association were unsuccessful, due to numerical instabilities in relevant models (Jeffrey et al., 1976), and perhaps

also reflecting the putative subtle difference in higher-order oligomerisation. Nonetheless, under the conditions studied, the self-association behaviour of the *cis* dicarba insulin is qualitatively similar to that of native mammalian insulins. Like native insulin, *cis* dicarba insulin is only monomeric in the absence of Zn^{2+}, and only at low concentration.

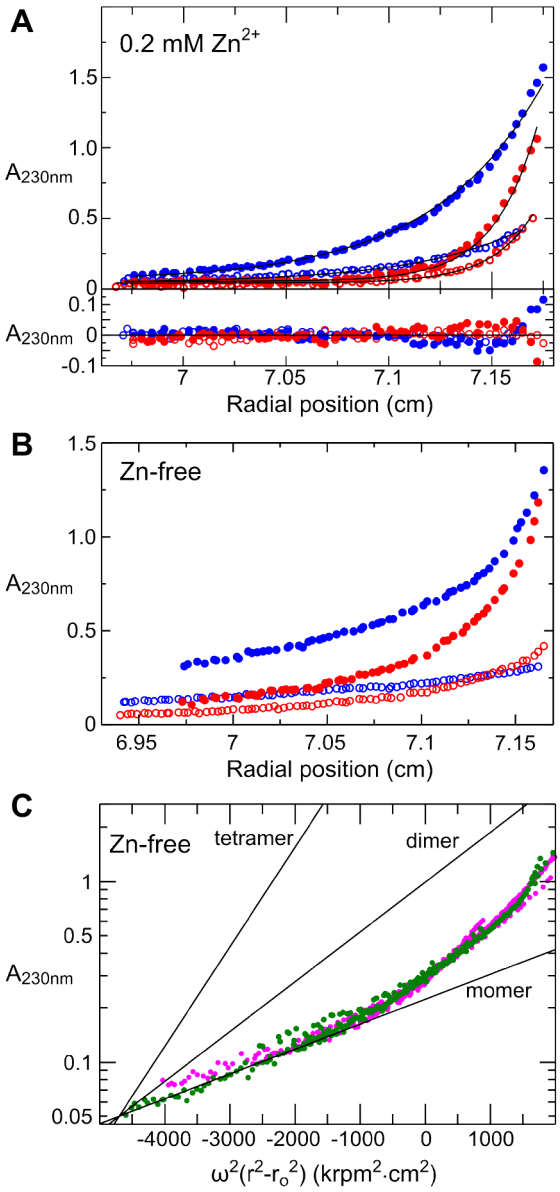

Figure 3.3 Sedimentation equilibrium data for *cis* dicarba insulin in the presence and absence of zinc ion (Zn^{2+}). Radial concentration distributions at sedimentation equilibrium for *cis* dicarba insulin in the (A) presence and (B) absence of 0.2 mM Zn^{2+} at loading concentrations of 100 (*open symbols*) and 300 µg/ml (*closed symbols*) at 25,000 (*blue*) and 40,000 rpm (*red*). In (A), data were globally fitted to a single species of 34,500 ± 400 Da (*solid lines*). Residuals to the fit (*bottom*) show some systematic deviation from an ideal fit. (C) Sedimentation equilibrium data for Zn-free *cis* dicarba (*green*) and native (*magenta*) insulin at each speed and loading concentration is plotted together as the square of the radial position scaled by rotor speed *vs* concentration on a logarithmic scale. The slopes expected for monomeric, dimeric and tetrameric insulin are shown for reference.

3.3.5 Insulin Tolerance Test

Outline: Cis dicarba KP insulin lowers blood glucose levels more effectively and more rapidly compared to the cis dicarba insulin, KP insulin and native human insulin.

Having established that the *cis* dicarba insulin is not monomeric I sought to compare the *in vivo* activities of this analogue with *cis* dicarba KP insulin, which we can assume is monomeric as per KP insulin. The *cis* dicarba KP insulin lowered blood glucose levels more effectively and more rapidly compared to native insulin and KP insulin when mice were treated with 0.75 IU/kg insulin or analogue under non-fasting conditions (Fig. 3.4, *A* and *B*). Notably, the *cis* dicarba KP insulin was even more effective and rapid acting than the *cis* dicarba insulin. The glucose-lowering effect was most evident and significant in insulin-resistant mice fed on high fat diet (Fig. 3.4*B*). The changes of blood glucose levels post-treatments are also presented as the inverse area under curve (AUC) (Figs. 3.4, *C* and *D*) and show a significant ($P \leq 0.01$) blood glucose lowering effect in the duration of 2 hours post-treatment with *cis* dicarba KP insulin in high-fat fed mice (Fig. 3.4*D*). The difference in activities between KP insulin and *cis* dicarba KP insulin, which are both expected to be monomeric, implies that the improved activity of the *cis* dicarba analogues is not the result of a change in self-association. This is consistent with the above observation that native and *cis* dicarba insulin show similar self-association behaviour.

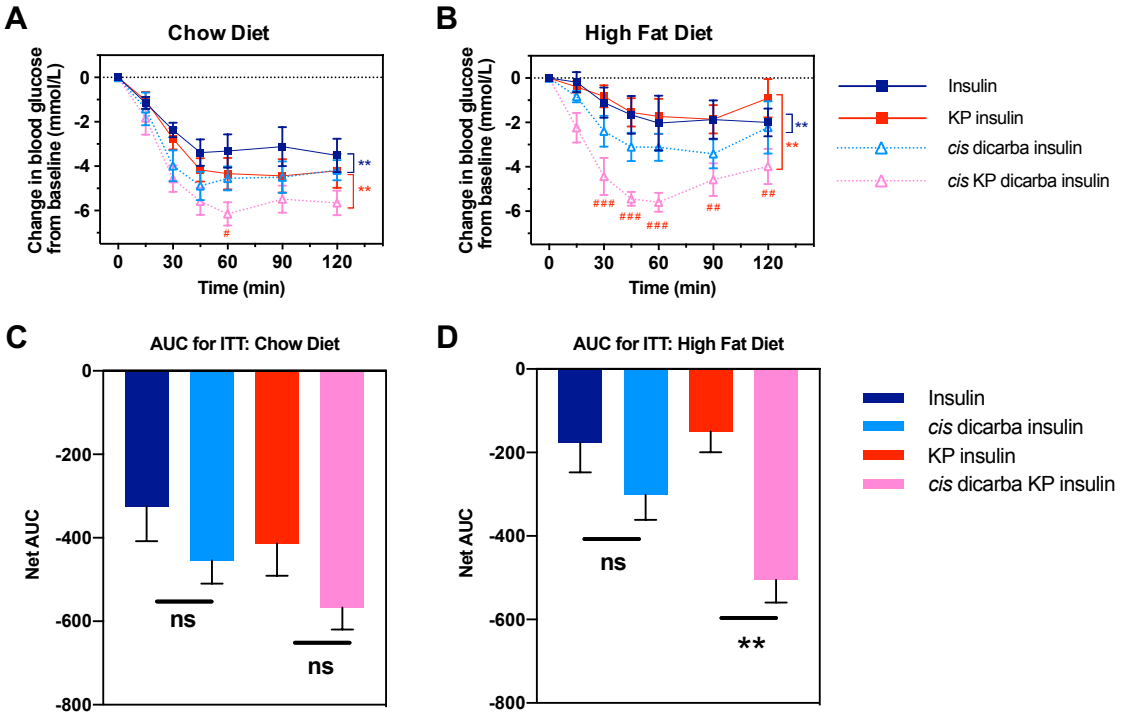

Figure 3.4 *In vivo* insulin tolerance test (ITT) of insulin, KP insulin and their respective dicarba insulin analogues. (A) Insulin tolerance test in mice fed on a normal diet (chow), or (B) on a high fat diet (HFD) were administered through intraperitoneal injection (*ip*) with 0.75 IU/kg insulin, KP insulin, *cis* dicarba insulin or *cis* dicarba KP insulin under non-fasting conditions and tail vein blood glucose was measured *via* glucose meter at indicated times. n = 5 – 6 per group. Blood glucose levels are expressed as change over basal levels (mmol/L). Chow diet: insulin *vs cis* dicarba insulin ** ($P \leq 0.01$); KP insulin *vs cis* dicarba KP insulin ** ($P \leq 0.01$) (paired *t*-test). High fat diet: insulin *vs cis* dicarba insulin ** ($P \leq 0.01$); KP insulin *vs cis* dicarba KP insulin ** ($P \leq 0.01$) (paired *t*-test). Significance of the change in blood glucose levels at each time-point was also determined by two-way ANOVA followed by Holm-Sidak's multiple comparison test. Chow diet: KP insulin *vs cis* dicarba KP insulin at $t = 60$ min $^{\#}$ ($p \leq 0.05$). High fat diet: KP insulin *vs cis* dicarba KP insulin at $t = 30$, 45 and 60 min $^{\#\#\#}$ ($p \leq 0.001$); $t = 90$ and 120 min $^{\#\#}$ ($p \leq 0.01$). (C – D) Area under curves (AUC) derived from insulin tolerance tests in (A) and (B). Chow diet: insulin *vs cis* dicarba insulin^{ns}; KP insulin *vs cis* dicarba KP insulin^{ns} (paired *T-test*). High fat diet: insulin *vs cis* dicarba insulin^{ns}; KP insulin *vs cis* dicarba KP insulin ** ($P \leq 0.01$) (paired *T-test*).

3.3.6 Atomic Force Microscopy (AFM) Analyses

Outline: Cis dicarba insulin and cis dicarba KP insulin more rapidly form fibrils than native human insulin.

While the rapid action of the *cis* dicarba insulin compared to insulin is not due to this analogue being monomeric, it must have different biophysical properties to insulin that lead to this difference in biological activity. To explore this further, AFM fibrillation assay was performed. The *cis* dicarba insulin formed fibrils more rapidly than native insulin, with fibrils first detected after 2 h compared to 6 h for native insulin at the same temperature and concentration (60 °C and 1.16 mg/mL, respectively; Fig. 3.5). Consistent with being monomeric, KP insulin also rapidly formed fibrils, with fibrils first detectable at 2 h. The *cis* dicarba KP insulin fibrillation is evident between t = 6–8 h. Interestingly, the fibrils formed by both *cis* dicarba insulin and *cis* dicarba KP insulin appeared shorter, thicker and of different morphology to those arising from native insulin and KP insulin (Fig. 3.5 see *cis* dicarba insulin at t = 15 h and *cis* dicarba KP insulin at t = 8 h). These observations are consistent with the fact that thioflavin T (ThT), a dye commonly used to detect insulin fibrils, did not bind cis dicarba insulin fibrils (data not shown). ThT normally binds to insulin fibrils at two sites (between fibers and/or between protofilaments) (Groenning et al., 2007).This data suggest that while *cis* dicarba insulin is not inherently monomeric it is conformationally different to native insulin.

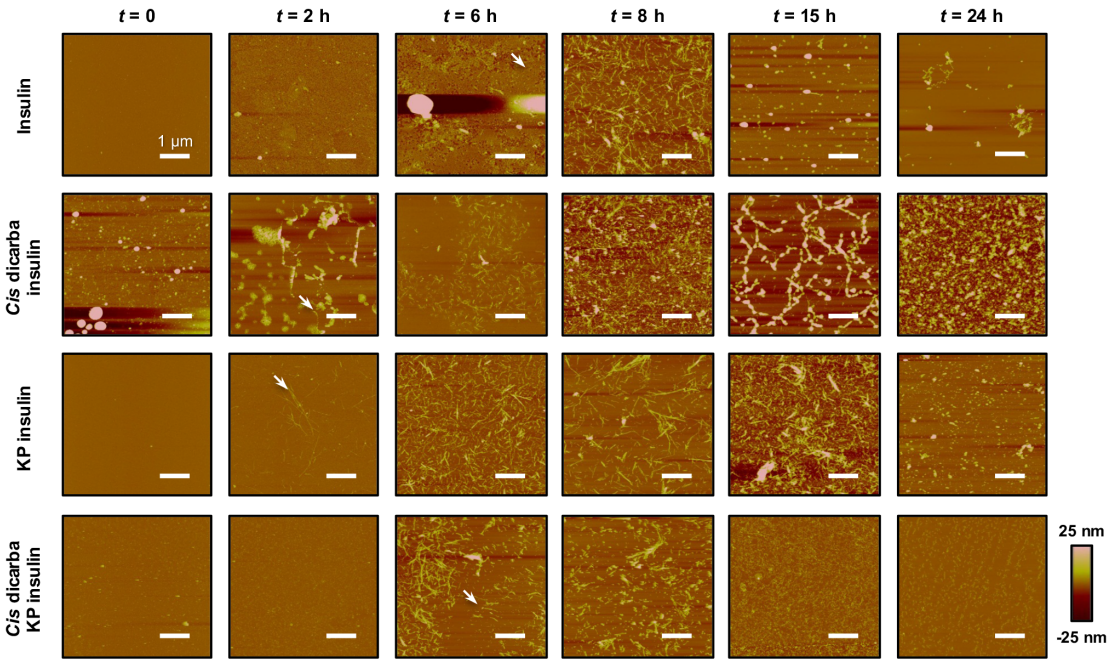

Figure 3.5 Time-course of fibril formation detected by AFM. Insulin fibrillation is first evident at t = 6 h. After t = 15 h, insulin has formed aggregates and fibrils are no longer easily detectable. Fibrillation of *cis* dicarba insulin is first evident after t = 2 h and is clearly detectable by t = 6 h. Fibrils formed by the *cis* dicarba insulin are of a different structure compared to insulin, particularly evident at t = 15 h. Fibrillation of the monomeric KP insulin is evident at earlier time-points across a wider incubation range (t = 2 – 15 h) compared to insulin. At t = 24 h, KP insulin fibrils are no longer easily detectable. Surprisingly, *cis* dicarba KP insulin fibrillation is only evident at t = 6 – 8 h with a rapid increase in formation of shorter and thicker fibrils at t = 6 h. In summary, the *cis* dicarba insulin adopts a different fibrillary pattern compared to insulin with an apparent increased complexity of fibrillary topology. These experiments are representative of n = 4 experiments for insulin, n = 3 for *cis* dicarba insulin, n = 5 for KP insulin and n = 3 for *cis* dicarba KP insulin. First detection of fibrils for each analogue is indicated by white arrows. The scale bar (*white*) corresponds to 1µm in all images.

3.3.7 Biophysical Characterisation

Outline: Cis dicarba insulin and cis dicarba KP insulin are thermodynamically less stable than native insulin.

Next, I compared the thermodynamic stability of the *cis* dicarba insulin with the *cis* dicarba KP insulin. Introduction of a dicarba A6–A11 bond into KP insulin also led to a decrease in thermal and chemical denaturation stabilities. The far-UV CD spectra (190 – 260 nm) of Zn^{2+}-free *cis*- and *trans* dicarba KP insulin exhibited lower helical content (34 % and 17 %, respectively) compared to KP insulin (44 %) (see Fig. 3.6*A* and Table 3.1). The $[\theta]_{222}$ values are directly proportional to the helical content of the proteins. As seen with the *cis* dicarba insulin *(van Lierop et al., 2017)*, the *cis* dicarba KP insulin (Fig. 3.6*B*) exhibited smaller $[\theta]_{222}$ negative magnitudes measured at 20 °C consistent with their lower initial helical content (Table 3.1). Denaturation induced by increasing temperature (20–70°C) (Fig. 3.6*B*) or GdnHCl concentrations (0–8M) (Fig. 3.6*C*) was monitored at wavelength 222 nm using CD. The relative thermodynamic stabilities of KP insulins were determined by comparing the relative change of ellipticity with increasing temperature at 1 °C intervals, *i.e.* by comparing the slope of temperature denaturation curves. Native and KP insulins exhibited similar thermal denaturation curves, whereas the *cis* dicarba KP insulin exhibited relatively small changes in ellipicity due to its significantly lower starting helical content (Fig. 3.6*B* and Table 3.1). The *cis* dicarba KP insulin is also considerably less stable upon GdnHCl denaturation, with $\Delta G°_u$ = 1.71 kcal mol^{-1}, as was seen with the dicarba insulin isomers of human insulin (Fig. 3.6*C*, Table 3.1 and *(van Lierop et al., 2017)*).

The effect of introduction of the *cis* dicarba bond on thermodynamic stability is striking and much greater than the introduction of the KP mutation (Fig. 3.6, *B* and *C*, and *(van Lierop et al., 2017)*). The observed reduction in stability is thus independent of being monomeric.

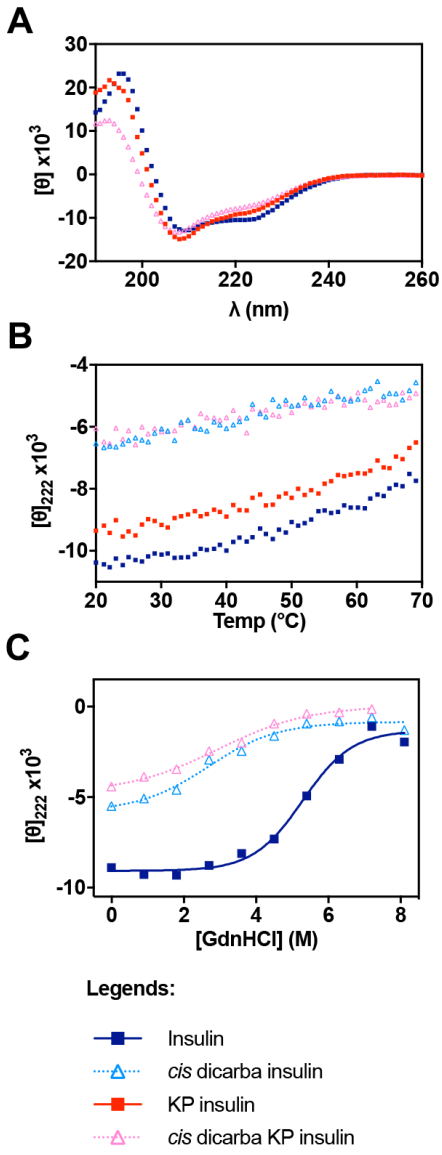

Figure 3.6 Thermal and chemical stability of *cis* dicarba insulin and *cis* dicarba KP insulin. (A) Circular dichroism far-UV spectrum of *cis* dicarba KP insulin suggests there is a difference in structure of the *cis* dicarba KP insulin compared to KP insulin and insulin, where lower helical propensities in the *cis* dicarba KP insulin is observed (see Table 3.1). θ = ellipticity. (B) Differences in thermal unfolding were monitored by ellipticity at λ = 222 nm and show both the *cis*- and *trans* dicarba insulins are considerably less stable than insulin. (C) Unfolding in the presence of guanidine hydrochloride demonstrates that both *cis* dicarba analogues are considerably destabilized compared to insulin. ΔG values derived from guanidine denaturation studies are listed in Table 3.1.

Table 3.1 Structural analyses of insulin, KP insulin and dicarba insulins using circular dichroism. Helical content calculated using the CONTINLL algorithm for deconvolution against the protein database reference set SP43. The program is available on the DICROWEB website (http://dichroweb.cryst.bbk.ac.uk/html/home.shtml). ΔG° values were derived from guanidine denaturation studies. †Data previously reported in *Chapter 2* and in (van Lierop et al., 2017).

Analogues	Secondary Structures Content (%)				Guanidine Denaturation
	Helix	Sheet	Turn	Unordered	$\Delta G°_U$ (kcal.mole^{-1})
Insulin†	48%	12%	14%	26%	4.74
***cis* dicarba insulin**†	37%	16%	20%	27%	1.98
***trans* dicarba insulin**†	23%	24%	22%	31%	1.61
KP Insulin	44%	14%	14%	28%	n.a.
***cis* dicarba KP insulin**	34%	19%	20%	27%	1.71
***trans* dicarba KP insulin**	17%	31%	22%	30%	n.a.

3.3.8 Limited-Proteolysis, Mass Spectrometry & Molecular Dynamics Analyses

Outline: The cis dicarba A6–A11 linkage promotes a structural change in the B chain helix, which leads to instability.

In order to explain why the *cis* dicarba peptides are less thermodynamically stable, I have performed a limited proteolysis study that allowed detection of structural differences between the *cis* dicarba peptides, native insulin and KP insulin. This involved RP-HPLC separation of fragments generated by chymotrypsin proteolysis and subsequent mass spectrometry. Firstly, I noticed that *cis*- and *trans* dicarba insulin isomers eluted later (15.8 and 14.6 min, respectively) than native insulin (13.3 min) when separated by RP-HPLC (Fig. 3.1*D*). Similarly, the *cis*- and *trans* KP isomers also eluted with delayed retention times (16.3 and 15.1 min, respectively) compared to KP insulin (13.5 min) (Fig. 3.1*E*). The relative delay in the retention times of dicarba insulins is an indication of an apparent increase in hydrophobicity compared to the native forms, with *cis* dicarba insulins being more surface hydrophobic. This was the first indication that the *cis* A6–A11 dicarba linkage induces a more open conformation of insulin than in the native hormone, and that it is likely that hydrophobic residues of the core are more exposed.

The enzymatic stability of dicarba insulin analogues was investigated through limited proteolysis by chymotrypsin under non-reducing conditions. The rate and kinetics of proteolysis were monitored through RP-HPLC as described in *sections 3.2.12 and 3.2.13*. The results show that *cis* dicarba insulin is significantly more rapidly cleaved by chymotrypsin compared to native insulin (Fig. 3.7*A*, also see Appx Fig. 3.3, *A – D*). At a protein: enzyme ratio of 86: 0.08 μM, the native insulin remained almost completely undigested after 3 h of proteolysis (> 95 % undigested peptide remaining), whereas almost no intact *cis* dicarba insulin remained. The monomeric KP insulin is more susceptible to proteolysis than insulin with ~ 65% undigested peptide remaining after 3 h (~ 30 % reduction compared to native insulin). However, the *cis* dicarba KP insulin is rapidly cleaved with only ~ 30% of undigested peptide remaining at 3 h (~ 30% reduction compared to KP insulin) (see Appx. Fig 3.4, *A – D*). As different batches of chymotrypsin were used in the *cis* dicarba insulin and *cis* dicarba KP insulin experiments (Fig. 3.7*A vs* Appx. Fig. 3.4*A*) I cannot determine if the difference in cleavage rates between the two *cis* dicarba analogues is significant. Nonetheless, clearly both are much more rapidly cleaved than native insulin and KP insulin, respectively.

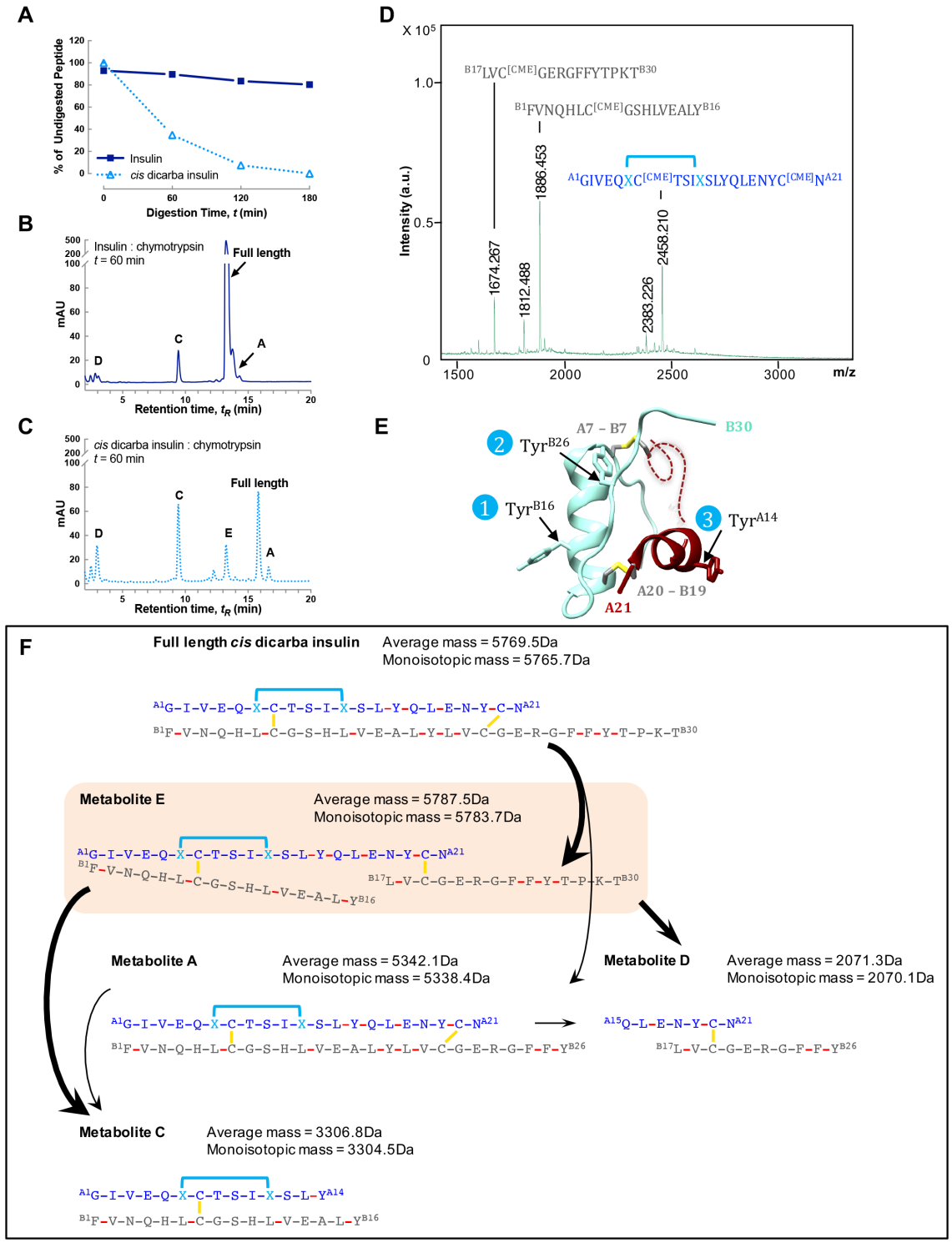
A
% of Undigested Peptide
Insulin
cis dicarba insulin
Digestion Time, t (min)
B
Insulin : chymotrypsin
t = 60 min
Full length
mAU
Retention time, tR (min)
C
cis dicarba insulin : chymotrypsin
t = 60 min
Full length
D
X 10^5
B17LVC[CME]GERGFFYTPKTB30
B1FVNQHLC[CME]GSHLVEALYB16
A1GIVEQXC[CME]TSIXSLYQLENYC[CME]NA21
1886.453
1674.267
1812.488
2383.226
2458.210
Intensity (a.u.)
m/z
E
A7 – B7
B30
Tyr B26
Tyr B16
Tyr A14
A20 – B19
A21
F
Full length cis dicarba insulin
Average mass = 5769.5Da
Monoisotopic mass = 5765.7Da
Metabolite E
Average mass = 5787.5Da
Monoisotopic mass = 5783.7Da
Metabolite A
Average mass = 5342.1Da
Monoisotopic mass = 5338.4Da
Metabolite D
Average mass = 2071.3Da
Monoisotopic mass = 2070.1Da
Metabolite C
Average mass = 3306.8Da
Monoisotopic mass = 3304.5Da

Figure 3.7 Limited proteolysis of insulin and *cis* dicarba insulin using chymotrypsin. (A) Rate of proteolysis plotted as percentage of undigested peptide over time. *Non-reducing* (B) insulin and (C) *cis* dicarba insulin digested for t = 60 min were analysed and fractionated using RP-HPLC. Metabolite **A** – **E** were identified *via* MALDI analyses in combinations of different conditions: whole sample *vs* RP-HPLC-fractionated samples; non-reducing *vs* reducing; positive *vs* negative detection mode (see Appx. Figs. 3.5 and 3.6). Indicated in (B), (C) and (F) are: full length, undigested peptide; metabolite **A**, non-reduced metabolite resulting from single cleavage at Tyr^{B26}; metabolite **C**, *C*-terminal- and metabolite **D**, *N*-terminal non-reduced metabolites resulting from cleavage at Tyr^{B26} followed by cleavages at Tyr^{A14} and Tyr^{B16}; metabolite **E** is only present in *cis* dicarba insulin cleavage reactions and resulted from single cleavage at Tyr^{B16}. (D) Metabolite **E** of *cis* dicarba insulin was identified in fractioned sample proteolysed with chymotrypsin for t = 60 min. The sample was treated with DTT (reduction) and IAA (alkylation) prior to MALDI analysis under negative mode detection. [CME], Carboxymethylcystine residues with monoisotopic mass of 58.005 Da. (E) *Cis* dicarba insulin crystal structure (reported in (van Lierop et al., 2017); model coordinates not in the PDB database) with circled numbers indicating the order in which *cis* dicarba insulin peptide bonds are cleaved by chymotrypsin. (F) A simplified chymotryptic digestion kinetics of *cis* dicarba insulin showing sequences of peptides arising from chymotrypsin cleavage. A6–A11 dicarba bond (*blue solid line*). Insulin is cleaved first to metabolite **A** and then into metabolites **C** and **D**, with *no* metabolite **E** being detected. The rate of synthesis of each metabolite is presented in *Appendix Figures 3.3 and 3.4*. Subspecies of each metabolite were also identified *via* MALDI analyses (see Appx. Figs. 3.5 – 3.7).

The RP-HPLC chromatograms of a chymotrypsin-cleaved insulin (Fig. 3.7*B*; also see Appx. Fig. 3.3*E*) and the *cis* dicarba insulin (Fig. 3.7*C*; also see Appx. Fig. 3.3*F*) were comparable to previously reported data, which identified 4 non-reduced metabolites (termed **A**, **B**, **C**, **D**) post-cleavage (Schilling and Mitra, 1991). Through positive ion mode of MALDI mass analysis of the entire digest, the native insulin metabolites **A**, **C** and **D** were detected following the chymotrypsin digest (protein: enzyme ratio of 86: 0.08 μM; t = 60 min) but metabolite **B** was not detected (see HPLC chromatograms in Figs. 3.7*B* and Appx. Fig. 3.3*E*, MALDI analysis in Appx. Fig. 3.5 and schematic diagram in Appx Fig. 3.7). By MALDI analysis of individual RP-HPLC fractions, I could assign the different masses to individual peaks (Appx. Figs. 3.5 and 3.6). Metabolite **A** eluted ≈ 1 min after the undigested peptide (Fig. 3.7, *B* and *C*), as was seen for all digested insulins (native and dicarba analogues) (labelled as *'2'* (Metabolite **A***; grey*) in Appx. Figs. 3.3 and 3.4, *E – G*). Peptides equivalent to metabolite **C** and metabolite **D** eluted at t_R ≈ 3.5 min and ≈ 9.5 min respectively for all insulins (see Fig. 3.7, *B* and *C*; labelled as *'3'* (Metabolite **C**; *orange*) and '*4'* (Metabolite **D**; *green*) in Appx. Figs. 3.3 and 3.4, *E – G*). Refer *Figure 3.7F* for sequence of each metabolite.

Close comparison of the RP-HPLC chromatograms revealed the presence of an apparently unique metabolite in chymotrypsin digests of *cis* dicarba insulins (Metabolite **E** in Fig. 3.7*C*; labelled as *'5'* (Metabolite **E**; *purple*), in Appx. Figs. 3.3*F* and 3.4*F*) that was not detected in native insulin (Fig. 3.7*B*) or KP insulin (Appx. Fig. 3.4*E*). Metabolite **E** was detected in proteolytic samples of *cis* dicarba insulin as early as t = 1 h (kinetics of cleavage shown in Appx. Fig. 3.3*C* and *F*). Analysis from MALDI data in *negative ion* mode identified the *cis* dicarba insulin metabolite **E** from a fractionated and *reduced* sample (Fig. 3.7*D*). As shown in the simplified schematic diagram, *Figure 3.7F (orange box)*, the new metabolite is a full-length two-chain peptide (with intact A6–A11 dicarba bond and A7–B7 and A19–B20 disulfide bonds) with a single cleavage at the *C*-terminal end of Tyr^{B16} of B chain (indicated in *cis* dicarba insulin crystal structure in Fig. 3.7*E*, *blue circled 1*). This new metabolite **E** was not identified in native insulin or KP insulin cleaved with chymotrypsin, suggesting that chymotrypsin is able to access Tyr^{B16} in *cis* dicarba insulin more readily than in insulin or KP insulin.

In order to understand why only *cis* dicarba insulin is cleaved at this new site, insulin structures were superimposed on the active site of chymotrypsin, ensuring that the tyrosine residue that is recognised by the enzyme was localised in the appropriate binding pocket (Fig. 3.8). Significant steric interactions between the insulin structure and chymotrypsin (Fig. 3.8*B*) revealed that it would be necessary for the B chain helix of insulin to bend significantly to allow Tyr^{B16} to

engage with the chymotrypsin enzyme. Such bending behaviour is evident in the previously reported MD simulations of insulin and its *cis* dicarba analogue (published in (van Lierop et al., 2017)). It is significant that this bending motion occurs more frequently and persists longer in *cis* dicarba insulin (see below). Hydrogen bonds between Val^{B12} and Tyr^{B16}, Glu^{B13} and Leu^{B17}, and Tyr^{B16} and Gly^{B20} must all be broken, allowing the Cα-Cα distances between Glu^{B13} and Tyr^{B16} and between Tyr^{B16} and Gly^{B20} to increase from their unperturbed values of ~ 5.5 Å to ≥ 7 Å (Fig. 3.8*A*). This allows Tyr^{B16} to occupy the chymotrypsin binding pocket, with the two neighbouring loops of the helix wrapping around the binding pocket walls (compare Fig. 3.8*B vs* 8*C*). These changes in the B chain helix structure are concomitant with the twisting of Cys^{B7}, generally resulting in a decrease of the Cα-Cα distance across the A7–B7 disulfide linkage and an increase in its torsional strain. The effects of the bulging in the B chain helix are thereby transmitted to the *N*-terminal helix of the A chain. This results in the *N*-terminal end of this latter helix being tilted away from the B chain helix, although it is important to note that this conformation of the A chain is also seen in the absence of B helix bulging, and also in circumstances when Cys^{B7} is not twisted.

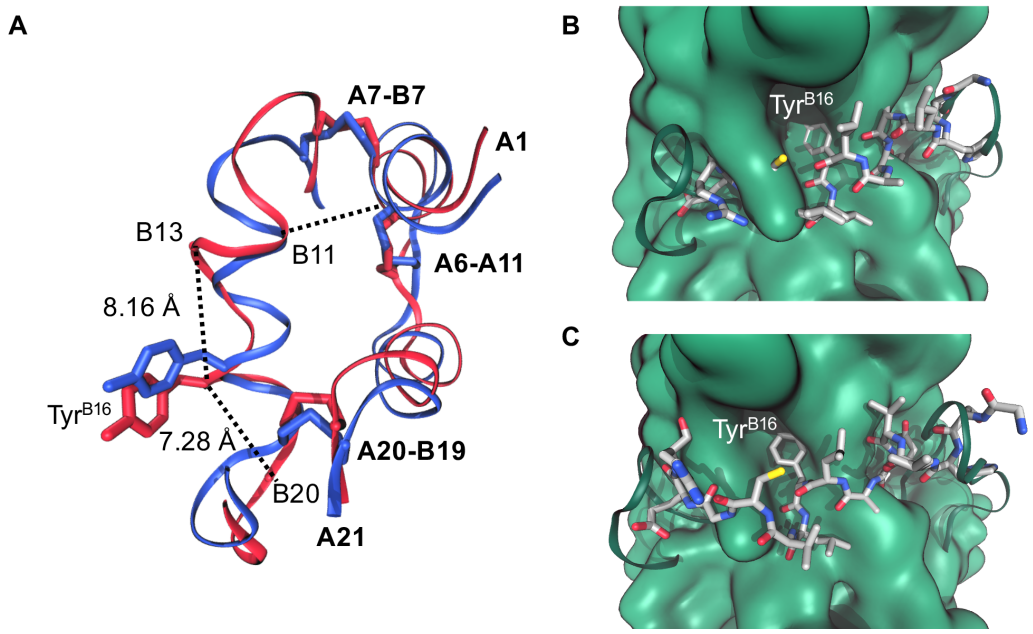

Figure 3.8 Bending of the B chain helix required to enable chymotrypsin proteolysis. (A) Overlay of the bent structure (*red;* MD simulation frame for *cis* dicarba insulin) with a reference insulin crystal structure (*blue*; PDB: 1MSO chains C and D). Residues A1 to A21 and B9 to B23 are superimposed. Hydrogen bonds in the B chain helix connecting residues Val^{B12} and Tyr^{B16}, Glu^{B13} and Leu^{B17} and Tyr^{B16}, and Gly^{B20} are broken, allowing the Cα-Cα distances between Glu^{B13} and Tyr^{B16} and between Tyr^{B16} and Gly^{B20} to increase from ~ 5.5 Å to > 7 Å. The bending rotates and compresses the A7—B7 disulfide bond and increases the distance between the *N*-terminal A chain and B chain helices (as measured by the Cα-Cα distance between residues A6 and B11). (B) Superimposition of the B chain helix of the un-bent insulin crystal structure (stick model; PDB: 1MSO chains C and D) on the active site of chymotrypsin (dark green; PDB: 4h4f – chymotrypsin in complex with inhibitor eglin C). For proteolysis to occur, Tyr^{B16} must be recognized by the active site of the enzyme. Superimposition of the backbone atoms of Tyr^{B16} as well as N and CA of Leu^{B17} on those of the corresponding residues in the inhibitor reveals that the un-bent structure cannot engage correctly with the peptidase: residues B12, B13 and all residues beyond B18 overlap significantly with the chymotrypsin structure, and the sidechain of Tyr^{B16} cannot sit properly in the active site cavity. (B) Superimposition of the B chain helix of the bent *cis* dicarba insulin simulation frame on the active site of chymotrypsin. Bulging of the B chain helix allows both the B12-B16 and B16-B20 loops to fit over the surface of the chymotrypsin molecule, with Tyr^{B16} sitting in the middle of the binding pocket. (Note: in both B and C the sidechains of B16, B17 and chymotrypsin residues 143 and 192 have been rotated to give the best possible engagement of the two molecules.) Loops of chymotrypsin which must move out of the way to allow insulin engagement are shown as *dark green ribbons*.

The propensity of the B chain helices of both insulin and the *cis* dicarba insulin to undergo bulging can be assessed through the MD simulation data. In *Figure 3.9*, this bulging is monitored *via* the Glu^{B13} - Tyr^{B16} Cα-Cα distance (*green*). The corresponding Cys^{A7}–Cys^{B7} Cα-Cα distances (*purple*) and the strain in the A7—B7 disulfide linkages (*blue*) are also shown. It is clear that, while bending of the B chain helix can occur in both insulin and the *cis* dicarba insulin, it occurs far more frequently in the *cis* dicarba analogue (Fig. 3.9, *A* and *B*, outlined in *black boxes*), with the bulging events being more prolonged and showing increased spreading of the loops of the helix (Fig. 3.9*A*). As noted previously, the A chain *N*-terminal helix is far more labile in the *cis* dicarba insulin than in insulin (van Lierop et al., 2017). It appears that in the more stable insulin structure, the A6–A11 disulfide linkage rapidly dampens the bending of the B chain helix and restores its helical structure. In contrast, this conformational lability of αAN in the *cis* dicarba insulin allows the bulge in the B chain helix to form more readily and to persist long enough to allow engagement with and digestion by chymotrypsin. It is important to note that there does not appear to be any correlation between bulging of the B chain and the unwinding motion of the A chain necessary for complexation of the insulin receptor (Appx. Fig. 3.9).

A second important consequence of enhanced B chain bulging for the *cis* dicarba insulin is that the hydrophobic core of the hormone is opened up, resulting in increased exposure to solvent (Fig. 3.9, *red*). This is consistent with the longer observed elution time of the *cis* dicarba insulin in the RP-HPLC experiments (Fig. 3.1*D*).

In summary, the limited proteolytic-MS integrated analyses revealed that the kinetics of dicarba insulins proteolysis are different from those of native insulin, leading to the formation of new metabolites. This supports the notion that installation of the intra-A-chain dicarba bridge enhances structural perturbation near Tyr^{B16} to permit access of chymotrypsin to this site.

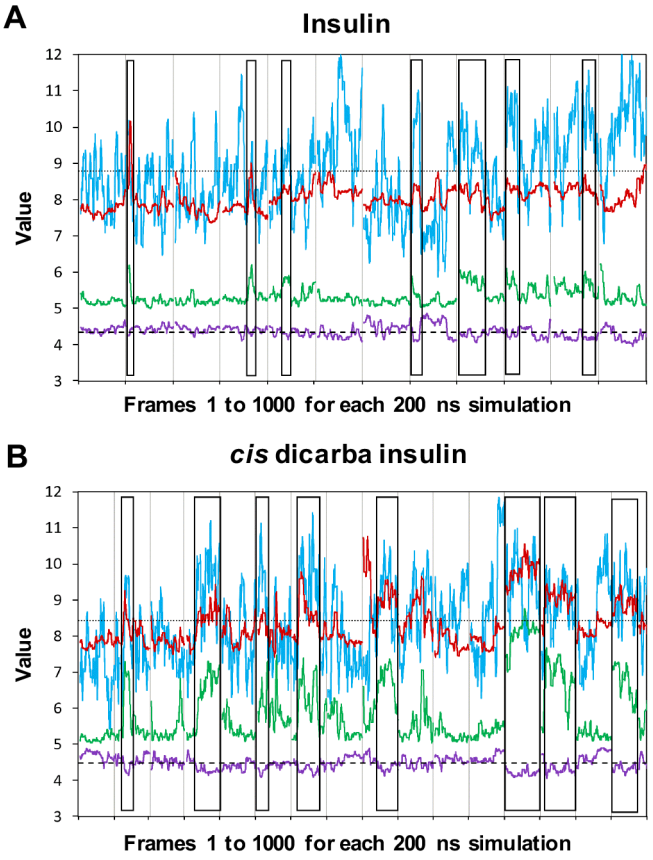

Figure 3.9 Variations in structural parameters associated with B chain helix bending from MD simulations. *Green*: *r*(Cα-Cα) between Glu^{B13} and Tyr^{B16}; this is a direct measure of helix bending. *Red*: *r*(Cα-Cα) between residue A6 and B11; a measure of the distance between the *N*-terminal A chain and B chain helices. *Purple*: *r*(Cα-Cα) between Cys^{A7} and Cys^{B7}; the length of the A7—B7 interchain linker. *Blue*: the relative torsional energy of the A7—B7 disulfide linkage. Data are presented as 50 period moving averages to highlight trends. Full data are presented in *Appendix Figure 3.8*. Overall averages for the purple and blue traces are shown with dashed and dotted lines, respectively. Bond distances are given in Å and relative energies in kJ mol^{-1}. Bending events in the B chain helix are outlined in black boxes. Note that each bin on the horizontal axis represents an independent 200 ns simulations; traces are therefore not continuous between bins.

3.4 DISCUSSION

For the last decade, insulin analogue design has focused on improving insulin efficacy and stability. Ideally, we require new rapid-acting insulin analogues that perfectly mimic the normal rapid onset of bolus insulin action. Desirably, insulin analogues would also be physically and chemically stable during pump delivery or at sites of injection. The 'bottleneck' to creating the perfect insulin arises from our incomplete understanding of the relationship between insulin's structure and function, particularly with respect to the fine balance between activity and stability.

Previously, in *Chapter 2*, using *cis*- and *trans* dicarba stereoisomers, I revealed an insight into the previously unexplored function of the insulin A6–A11 disulfide bond in modulating insulin activity. Unique to these insulin analogues, only *cis* dicarba insulin is biologically active while *trans* dicarba insulin is inactive. I proposed that the underlying cause of this difference lies in the structural dynamics of the A6–A11 linkage, and that this dictates insulin's ability to transition into its active conformation. *Chapter 2* demonstrated that the configuration of the A6–A11 linkage could modulate insulin's ability to engage with the receptor through its influence on the conformational flexibility of the *N*-terminal A chain helix (also published in (van Lierop et al., 2017)).

In this chapter, I seek to explain why *in vivo* the *cis* dicarba insulin promotes more rapid lowering of blood glucose than native insulin. Taken together with the previous observation of reduced thermal and chemical denaturation stabilities I hypothesised the rapid action might be attributed to the *cis* dicarba insulin being monomeric. To address this, I performed biophysical analyses of the *cis* dicarba insulin in comparison to the *cis* isomer of dicarba KP insulin, which we assume is monomeric as per KP insulin.

I first compared receptor binding and biological activity of the dicarba KP insulins with the *cis*- and *trans* dicarba insulins and native insulin. Consistent with the unique biological characteristics of *cis*- and *trans* dicarba isomers of native insulin, the *cis* dicarba KP insulin was also equipotent to native insulin (receptor binding, receptor activation, DNA synthesis in myoblasts and glucose uptake by adipocytes) while the *trans* dicarba KP insulin was inactive. This confirms the functional role of the native A6–A11 cystine bridge. Even in the context of a disrupted dimer interface induced by the B chain *C*-terminal KP mutation, the A6–A11 bond still influences the ability of insulin to engage with the receptor.

Next, we determined that the *cis* dicarba insulin is not inherently monomeric. The AUC results clearly showed that the distribution of *cis* dicarba insulin into monomeric and dimeric forms

under zinc free conditions was similar to that of native insulin. This was surprising and prompted us to further explore the biophysical differences between the *cis* dicarba insulin and native insulin that might account for the more rapid action of the *cis* dicarba analogue.

Further evidence of structural differences between the dicarba insulins and native insulin was provided by the fibrillation assays. The qualitative differences in fibrillation rate and fibril conformation between the *cis* dicarba insulin and native insulin are additional indicators of conformational differences in their structures. It is well established that the movement of the B chain *C*-terminus away from the B chain helix and hydrophobic core promotes fibrillation, as is seen with KP insulin (Fig. 3.5 and (Hua et al., 2011, Hua and Weiss, 2004, Phillips et al., 2012, Brange et al., 1997a)). The AUC results show that the *cis* dicarba insulin is not inherently monomeric, suggesting that the dimer interface is not disrupted, and hence this is not the source of the increased fibrillation rate of the *cis* dicarba insulin. Another key feature of fibril formation is the transition of the A chain *N*-terminal helix to a β-sheet, a process which requires displacement of the A chain away from the B chain helix and from the hormone core (Hua et al., 2011, Yang et al., 2010a). Therefore, it is postulated that *cis* dicarba insulin's increased rate of fibrillation compared to native insulin was likely to be connected to its increased flexibility and altered helicity (more π-like) at the *N*-terminus of the A chain.

However, upon further investigation using limited chymotrypsin proteolysis I was able to detect an unexpected difference in the structure of the B chain between the *cis* dicarba insulin and native insulin. The initial cleavage in the *cis* dicarba insulin occurs at the *C*-terminal end of Tyr^{B16} of B chain. This site is not the first site of cleavage in native insulin (the product was not detected), suggesting that the enzyme is unable to readily access this site in fully intact native insulin; cleavage at Tyr^{B16} only occurs after the molecule has been cleaved at other sites. In the *cis* dicarba insulin, initial cleavage at Tyr^{B16} indicates that chymotrypsin can readily access this site, implying that the *C*-terminal end of the B chain has a tendency to be in a non-native, partially open, or bulged, conformation, thereby allowing enzyme access. Interestingly, this bulged conformation does not affect the ability of the *cis* dicarba insulin to bind the insulin receptor. Previous mutation studies at Tyr^{B16} (*e.g.* to His or Ala) highlighted the importance of this residue in receptor binding as well as being involved in the dimer interface. Interestingly, the Tyr^{B16}Ala insulin mutant behaves as a monomer on size exclusion chromatography (Chen et al., 2004).

Previously, MD simulations have captured insulin in both "open" and "wide open (receptor bound)" states (Papaioannou et al., 2015). In that study, the open state referred to a zipper-like opening from the end of the B chain. This state was also observed in our MD investigations of native insulin and its *cis* dicarba analogue. However, here it was additionally observed that simulations of the *cis* dicarba insulin show a significantly enhanced propensity for outward bulging of the B chain helix. This opens up the helix loop between Val^{B12} and Leu^{B17}, exposing Tyr^{B16} for chymotrypsin cleavage (see Fig. 3.8). Hence, the *cis* dicarba linkage causes two fundamental changes to the dynamics of the insulin structure. On the one hand, it increases the mobility of the A chain *N*-terminal helix, enhancing its ability to engage favourably with the insulin receptor. On the other, it decreases the stability of the overall structure. This is seen in both the destabilisation of the B chain helix, increasing its susceptibility to chymotrypsin digestion, and in an increase in the solvent exposure of the hydrophobic core of insulin, leaving the hormone vulnerable to degradation *via* the formation of fibrils.

Recently Wade *et al* reported that the dicarba substitution of the intra-A-chain disulfide bond of the insulin-like peptide H2 relaxin resulted in significantly reduced stability to enzyme degradation in plasma, despite maintaining the ability to bind relaxin's cognate receptor RXFP1. The mechanisms underlying the instability were not explored. Similar to dicarba insulins, dicarba H2 relaxins also displayed structural differences to the native peptide (Hossain et al., 2015). It is hence postulated that the role of intra-A-chain disulfide bond in regulating peptide stability is conserved across the insulin-relaxin superfamily. However, further investigation is required to confirm this.

The rapid action of both *cis* dicarba insulin and *cis* dicarba KP insulin in lowering blood glucose (in comparison with native insulin) is most likely explained by the increased mobility of the A chain *N*-terminal helix, as observed in the MD simulations. This enhances the ability of *cis* dicarba insulin to adopt a conformation consistent with IR engagement. By restraining the A6–A11 linkage through introduction of a *cis* dicarba bond, the bioactive conformation of the molecule is favoured, and hence the *in vivo* metabolism of glucose is promoted. It is as yet unclear whether the accompanying destabilisation of the B chain helix also contributes to the enhanced glucose consumption.

3.5 CONCLUSION

In conclusion, through introduction of a non-reducible A6–A11 dicarba bridge of fixed configuration into insulin and KP insulin, this study reveals the functional and structural roles of

this linkage. It not only regulates structural flexibility at the *N*-terminus of the A chain helix, which is necessary for receptor binding, but also influences the frequency at which the B-chain helix "bulges", thereby increasing insulin mimetic's vulnerability to heat, chemical and enzymatic degradation.

These findings suggest there is potential for the development of ultra-rapid insulin analogues through only minimal manipulation of native insulins or existing insulin analogues. Importantly, this study provides a deeper insight into the function of the A6–A11 bond in regulating the balance between optimal insulin potency and structural stability. We anticipate that this detailed understanding of the structural dynamics of insulin will aid in future design of rapid-acting insulin analogues with improved stability. Defining the determinants of receptor binding (including mechanisms driving necessary A- and B- chain flexibility), stability and fibrillation will allow us to design analogues that permit high affinity binding but avoid instability and fibrillation.

CHAPTER 3

APPENDICES

CHAPTER 3 APPENDICES

APPENDIX 3A Synthesis for Dicarba KP Insulins

c[Δ^4A6,11]-Dicarba KP insulin (dicarba lispro insulin, E/Z-4) transformations

[B19]-Cys(Acm) KP insulin B-chain 1

1

An automated, microwave-accelerated SPPS procedure as described by Robinson *et al.* (van Lierop et al., 2011a) was used for the synthesis of peptide **1** on Fmoc-Thr(^{t}Bu)-PEG-PS resin (1.11 g, 0.20 mmol). After sequence completion, the resin was transferred into a fritted syringe, washed with DMF (7 mL; 3 × 1 min), DCM (7 mL; 3 × 1 min) and MeOH (7 mL; 3 × 1 min), then left to dry *in vacuo* for 1 h. Fmoc-deprotection and TFA-mediated cleavage of the peptide **1** from the resin (2.17 g) gave a pale yellow solid (630 mg) which was purified by RP-HPLC (Agilent: Vydac C18 preparative column, 25 → 45% buffer B over 30 min, t_R = 19.8 min). Selected fractions were combined and lyophilised to give the desired insulin B chain **1** as a colourless solid (82 mg, 12%) in 94% purity. Mass spectrum (ESI$^+$, MeCN : H_2O): *m/z* 701.4 [M + 5H]$^{5+}$, $^1\!/_5$($C_{161}H_{244}N_{41}O_{43}S_2$) requires 700.8; 876.0 [M + 4H]$^{4+}$, $C_{161}H_{243}N_{41}O_{43}S_2$ requires 875.7; 1167.7 [M + 3H]$^{3+}$, $^1\!/_3$($C_{161}H_{242}N_{41}O_{43}S_2$) requires 1167.2. RP-HPLC (Agilent: Vydac C18 analytical column, 20 → 50% buffer B over 30 min): t_R = 15.7 min.

Monocyclic A-B heterodimer of c[Δ⁴A6,11]-dicarba KP insulin 3

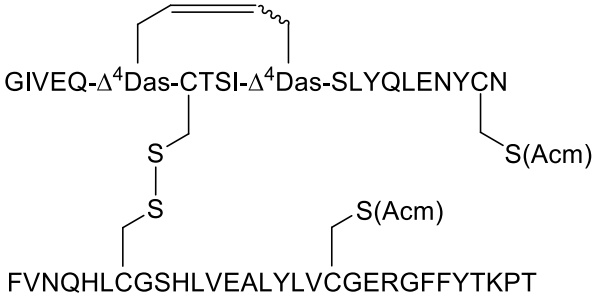

Cis-**(3)** and *trans*-**(3)**

<u>*Cis*-isomer:</u>

A solution of *cis*-*c*[Δ⁴A6,11]-Dicarba-[A7]-Cys(Pyr)-[A20]-Cys(Acm) insulin A-chain **2** (26 mg, 10.3 μmol), prepared on Fmoc-Asn(Trt)-PEG-PS resin as described in Robinson *et al*. (van Lierop et al., 2017)[†], in 50 mM NH_4HCO_3 (13 mL) was added dropwise to a stirred solution of the modified insulin B-chain **1** (36 mg, 10.3 μmol) in H_2O : MeCN (36 mL; 9 : 1). Reaction progress was monitored by RP-HPLC and mass spectrometry and after 3 h, the oxidation was terminated by addition of AcOH. The reaction mixture was then lyophilised to give the target peptide *Z*-**3** as a pale yellow solid (62 mg). Mass spectrum (ESI^+, MeCN : H_2O : HCOOH): *m/z* 1183.6 $[M + 5H]^{5+}$, ⅕($C_{265}H_{402}N_{67}O_{79}S_4$) requires 1183.0; 1478.7 $[M + 4H]^{4+}$, ¼($C_{265}H_{401}N_{67}O_{79}S_4$) requires 1478.5. RP-HPLC (Agilent: Vydac C18 analytical column, 0 → 25% buffer B over 5 min then 25 → 45% buffer B over 30 min): t_R = 20.3 min.

<u>*Trans*-isomer:</u>

A solution of *trans*-*c*[Δ⁴A6,11]-Dicarba-[A7]-Cys(Pyr)-[A20]-Cys(Acm) insulin A-chain **2** (1.5 mg, 0.59 μmol), prepared on Fmoc-Asn(Trt)-PEG-PS resin (van Lierop et al., 2017)[†] in 50 mM NH_4HCO_3 (750 μL) was added dropwise to a stirred solution of the modified insulin B-chain **1** (2.08 mg, 0.59 μmol) in H_2O : MeCN (2.1 mL; 9 : 1). Reaction progress was monitored by RP-HPLC and mass spectrometry and after 3 h, the oxidation was terminated by addition of AcOH. The reaction mixture was then lyophilised to give the target peptide *E*-**3** as a pale yellow solid (5 mg). Mass spectrum (ESI^+, MeCN : H_2O : HCOOH): *m/z* 1183.5 $[M + 5H]^{5+}$, ⅕($C_{265}H_{402}N_{67}O_{79}S_4$) requires 1183.0; 1479.1 $[M + 4H]^{4+}$, ¼($C_{265}H_{401}N_{67}O_{79}S_4$) requires 1478.5; 1971.3 $[M + 3H]^{3+}$, ⅓($C_{265}H_{400}N_{67}O_{79}S_4$) requires 1970.9. RP-HPLC (Vydac C18 analytical column, 0 → 25% buffer B over 5 min then 25 → 50% buffer B over 30 min): t_R = 20.7 min.

[†] *Cis*- and *trans*-*c*[Δ⁴A6,11]-Dicarba-[A7]-Cys(Pyr)-[A20]-Cys(Acm) insulin A-chain were also synthesised on Fmoc-Asp-O^{t}Bu loaded Rink-amide resin and combined with [B19]-Cys(Acm) KP insulin B-chain to make the dicarba lispro insulins used in this study.

c[Δ⁴A6,11]-Dicarba KP insulin (dicarba lispro insulin) 4

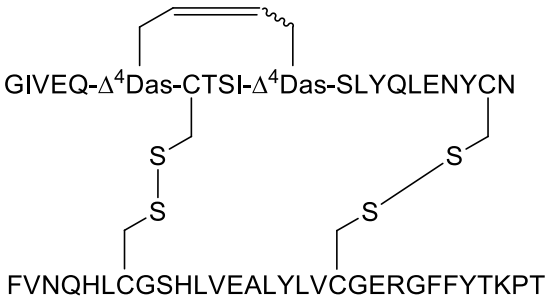

Cis-**(4)** and *trans*-**(4)**

<u>*Cis*-isomer:</u>

A 20 mM solution of iodine in glacial acetic acid (13.8 mL) was added to a stirred solution of the monocyclic peptide *Z*-**3** (31 mg, 5.24 μmol) in glacial acetic acid (34.8 mL) and 60 mM HCl (2.7 mL). Reaction progress was monitored by RP-HPLC and after 2.75 h, ice-cold Et_2O (5 ×35 mL) was added to induce peptide precipitation. The resultant yellow solid was collected by centrifugation (1 × 10 min) and 20 mM ascorbic acid (1 mL) was then added to quench any excess iodine before analysis *via* RP-HPLC and mass spectrometry.

The remaining A-B conjugate *Z*-**3** (31 mg, 5.24 μmol) in glacial acetic acid (34.8 mL) and 60 mM HCl (2.7 mL) was subjected to identical reaction conditions in the presence of a 20 mM solution of iodine in glacial acetic acid (138 mL), and the combined batches were then purified by RP-HPLC (Agilent: Vydac C18 analytical column, 0 → 25% buffer B over 5 min then 25 → 40% buffer B over 60 min: t_R = 34.6 and 35.5 min). Selected fractions were combined and lyophilised to give the desired *c*[Δ^4A6,11]-dicarba human insulin lispro analogue *Z*-**4** as a colourless solid (2.87 mg, 5%) in >99% purity. *Z*-**4**: Mass spectrum (ESI^+, MeCN : H_2O : HCOOH): *m/z* 1154.6 $[M + 5H]^{5+}$, ⅕($C_{259}H_{390}N_{65}O_{77}S_4$) requires 1154.1; 1442.9 $[M + 4H]^{4+}$, ¼($C_{259}H_{389}N_{65}O_{77}S_4$) requires 1442.4; 1924.7 $[M + 3H]^{3+}$, ⅓($C_{259}H_{388}N_{65}O_{77}S_4$) requires 1922.9. RP-HPLC (Agilent: Vydac C18 analytical column, 0 → 30% buffer B over 5 min then 30 → 40% buffer B over 30 min): t_R = 17.9 min.

<u>*Trans*-isomer:</u>

A 20 mM solution of iodine in glacial acetic acid (2.2 mL) was added to a stirred solution of the mono-cyclic peptide *E*-**3** (5.0 mg, 0.85 μmol) in glacial acetic acid (5.7 mL) and 60 mM HCl (420 μL). Reaction progress was monitored by RP-HPLC and after 2.75 h, ice-cold Et_2O (35

mL) was added to induce peptide precipitation. The resultant solid was collected by centrifugation (1 × 10 min) and 20 mM ascorbic acid (1 mL) was then added to quench any excess iodine before analysis *via* RP-HPLC and mass spectrometry. Following purification by RP-HPLC (Agilent: Vydac C18 analytical column, 0 → 25% buffer B over 5 min then 25 → 45% buffer B over 60 min, t_R = 32.9 and 33.5 min), selected fractions were combined and lyophilised to give the desired *c*[Δ^4A6,11]-dicarba human insulin lispro analogue *E*-**4** as a colourless solid (0.15 mg, 3%) in 95% purity. *E*-**4**: Mass spectrum (ESI^+, MeCN : H_2O : HCOOH): *m/z* 1154.7 $[M + 5H]^{5+}$, ⅕($C_{259}H_{390}N_{65}O_{77}S_4$) requires 1154.1; 1443.1 $[M + 4H]^{4+}$, ¼($C_{259}H_{389}N_{65}O_{77}S_4$) requires 1442.4. RP-HPLC (Agilent: Vydac C18 analytical column, 0 → 30% buffer B over 5 min then 30 → 40% buffer B over 30 min): t_R = 14.8 min.

APPENDIX TABLES 3

APPENDIX TABLE 3.1

Binding affinities to IR-B and IGF-1R. Inhibition of europium-labeled insulin and IGF-I for binding to the IR-B and IGF-1R, respectively, by insulin, dicarba insulin isomers and IGF-I.

	IR-B		IGF-1R	
	IC_{50} (nM)	Affinity (% Insulin ± SEM)	IC_{50} (nM)	Affinity (% Insulin ± SEM)
Insulin	1.07 ± 0.09	100	> 300	100
cis dicarba insulin	1.07 ± 0.30	100 ± 26[ns]	> 300	~100
trans dicarba insulin	40.4 ± 7.2[a]	1.8 ± 0.3****	-	-
KP insulin	-	84 ± 6[Ψ]	-	156 ± 16[Ψ]
cis dicarba KP insulin	1.13 ± 0.06	95 ± 5 [ns]	> 300	n.a.
trans dicarba KP insulin	>300	n.a		-
IGF-I	-	-	0.60 ± 0.07	4704 ±468 ****

n = 3 or more, [a]n=2, - not performed, [ns]non-statistically significant, [Ψ]derived from Kurtzhals *et al*. (Kurtzhals et al., 2000), $P > 0.05$, ** $P \leq 0.01$, *** $P \leq 0.001$, **** $P \leq 0.0001$. Errors shown are S.E.M.

APPENDIX FIGURES 3

APPENDIX FIGURE 3.1

***Cis-c*[Δ^4A6,11]-Dicarba KP insulin (*cis* dicarba lispro insulin) Z-4**

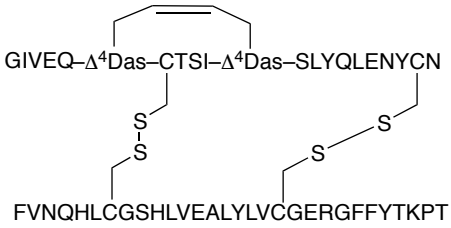

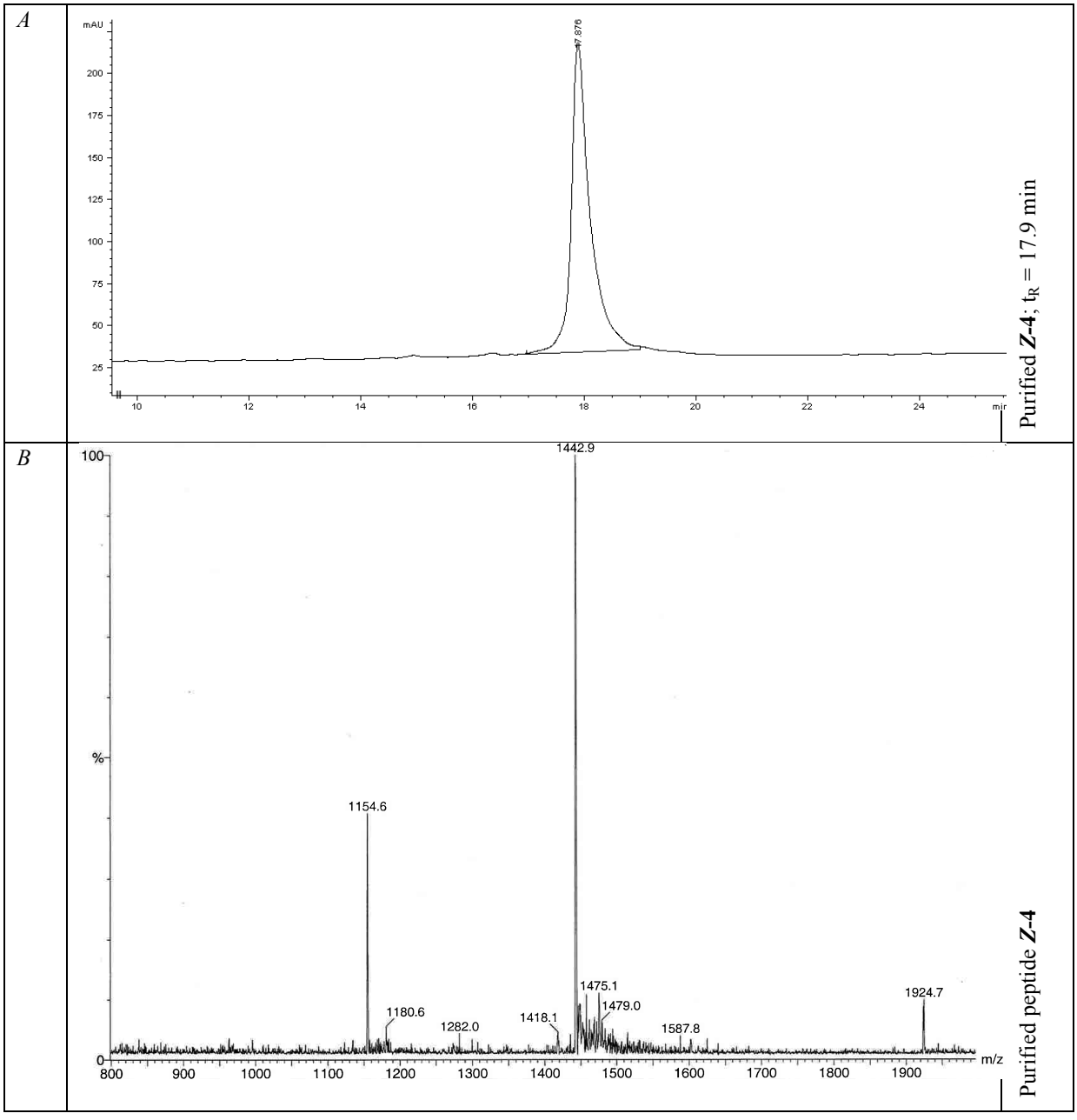

***Trans-c*[Δ⁴A6,11]-Dicarba KP insulin (*trans* dicarba lispro insulin) *E*-4**

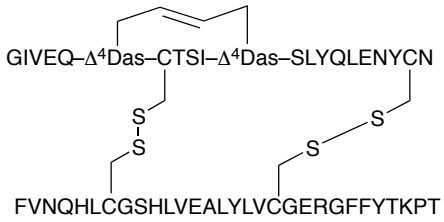

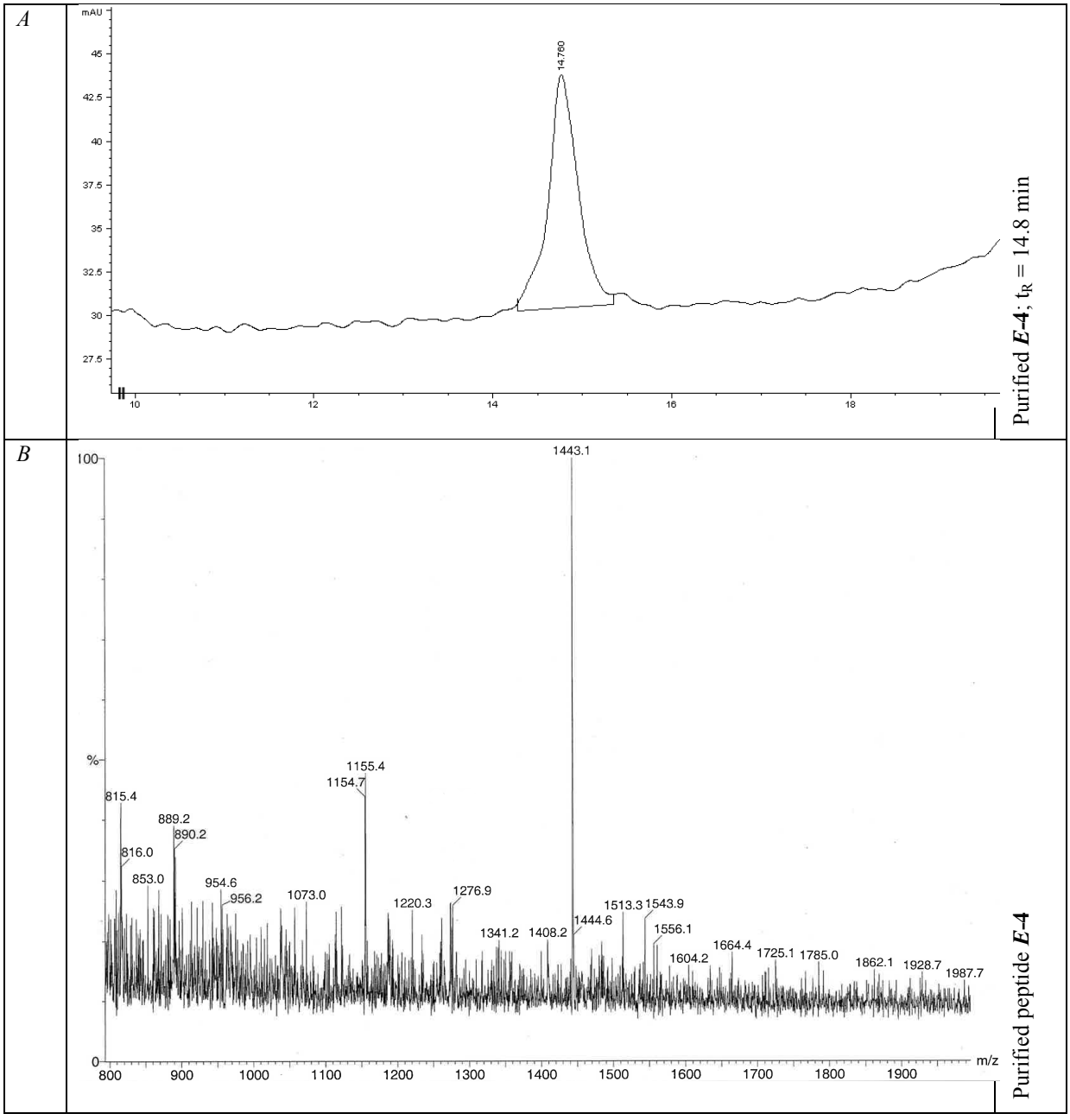

Appendix Figure 3.1 HPLC chromatograms and **B:** mass spectra of purified dicarba lispro insulins (*Z*-**4** and *E*-**4**).

APPENDIX FIGURE 3.2

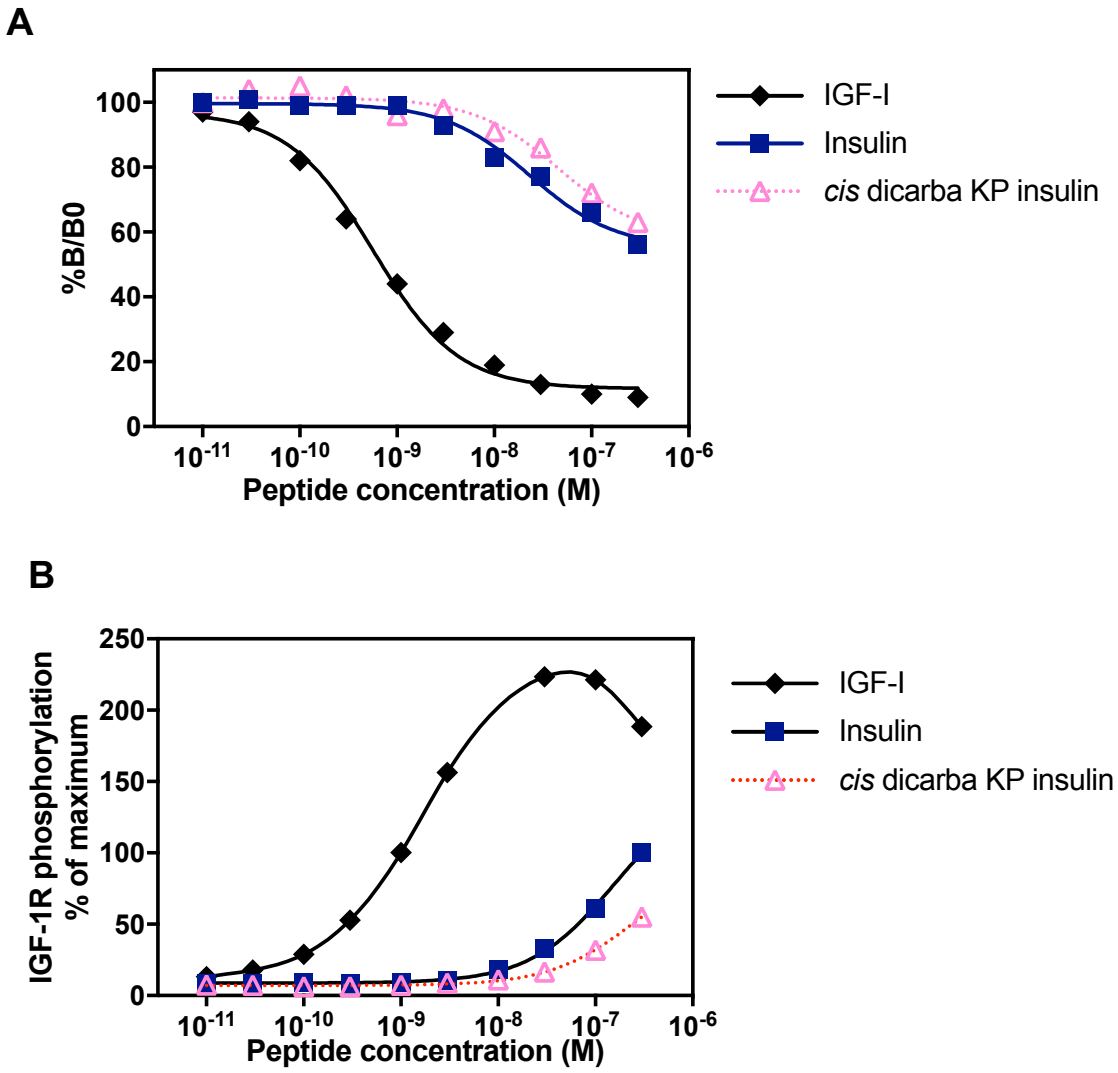

Appendix Figure 3.2 (A) Competition binding of IGF-I, insulin and *cis* dicarba KP insulin with europium-labelled IGF-I. Results are expressed as a percentage of binding in the absence of competing ligand (%B/B0). (B) Activation of IGF-1R by increasing concentrations of insulin and *cis* dicarba KP insulin (10 min stimulation) is expressed as receptor phosphorylation as a percentage of the maximal phosphorylation induced by IGF-I. Insulin *vs cis* dicarba KP insulin (non significant); insulin *vs* IGF-I **** ($P \leq 0.0001$) (2-way ANOVA; Dunnett's multiple comparison).

APPENDIX FIGURE 3.3

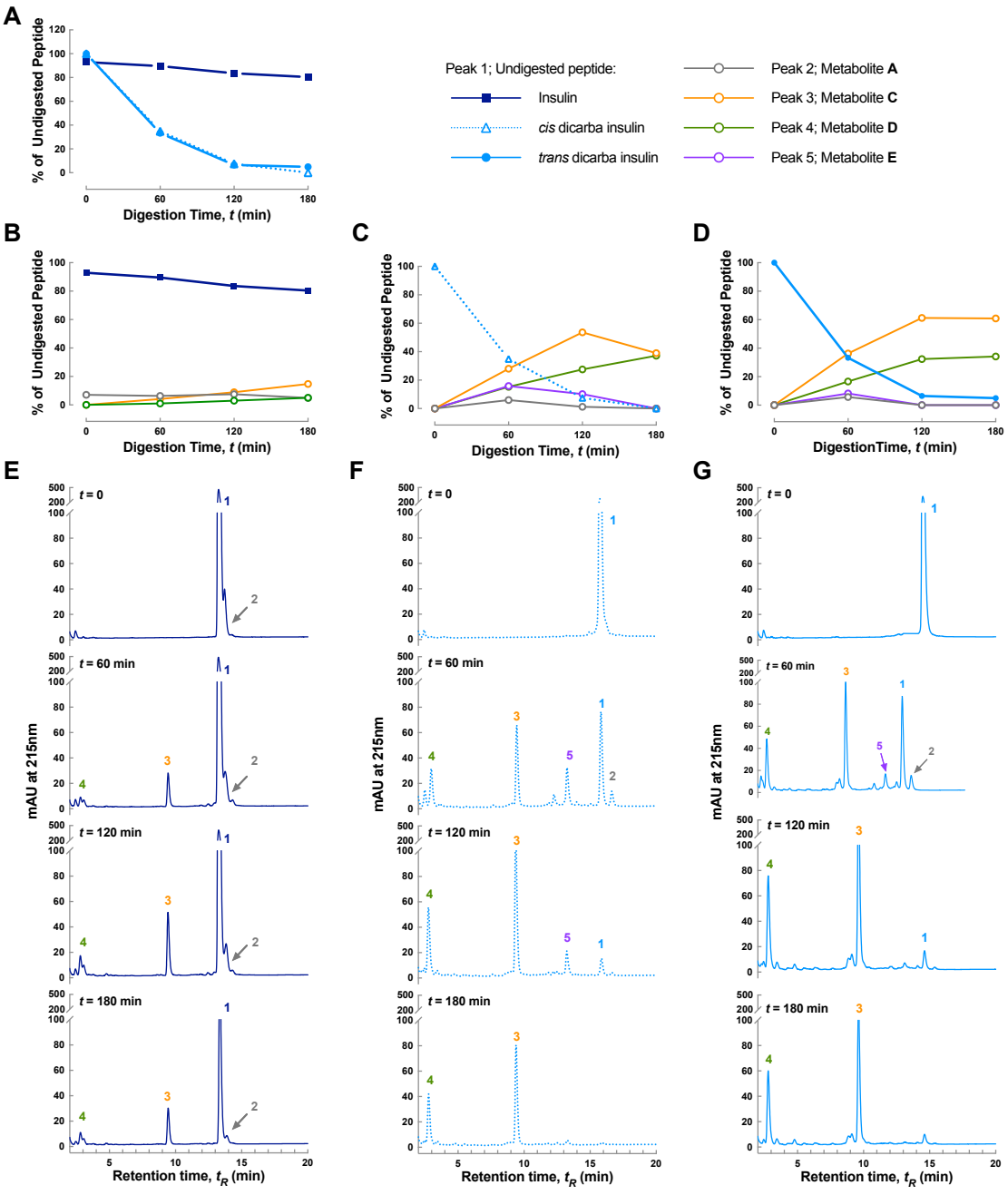

Appendix Figure 3.3 Chymotrypsin proteolysis of insulin and *cis*- and *trans* dicarba insulins. (A) Rate of proteolysis plotted and rate of metabolite synthesis (B –D) as percentage of undigested peptide over time. RP-HPLC purification of (E) insulin, (F) *cis* dicarba insulin and (G) *trans* dicarba insulin metabolites digested under *non-reducing* conditions for t = 0, 60, 120, 180 minutes at 37 °C. Peptides presented are: Undigested peptide (1; *blue*), Metabolite **A** (2; *grey*): non-reduced metabolite resulting from single cleavage at Tyr^{B26} , Metabolite **C** (3; *orange*): *C*-terminal-, and Metabolite **D** (4; *green*): *N*-terminal non-reduced metabolites resulting from cleavage at Tyr^{B26} followed by cleavages at Tyr^{A14} and Tyr^{B16}. Metabolite **E** (5; *purple*) is only present in the *cis* dicarba insulin (and in small amount in the *trans* dicarba insulin) cleavage reactions; resulted from single cleavage at Tyr^{B16}

APPENDIX FIGURE 3.4

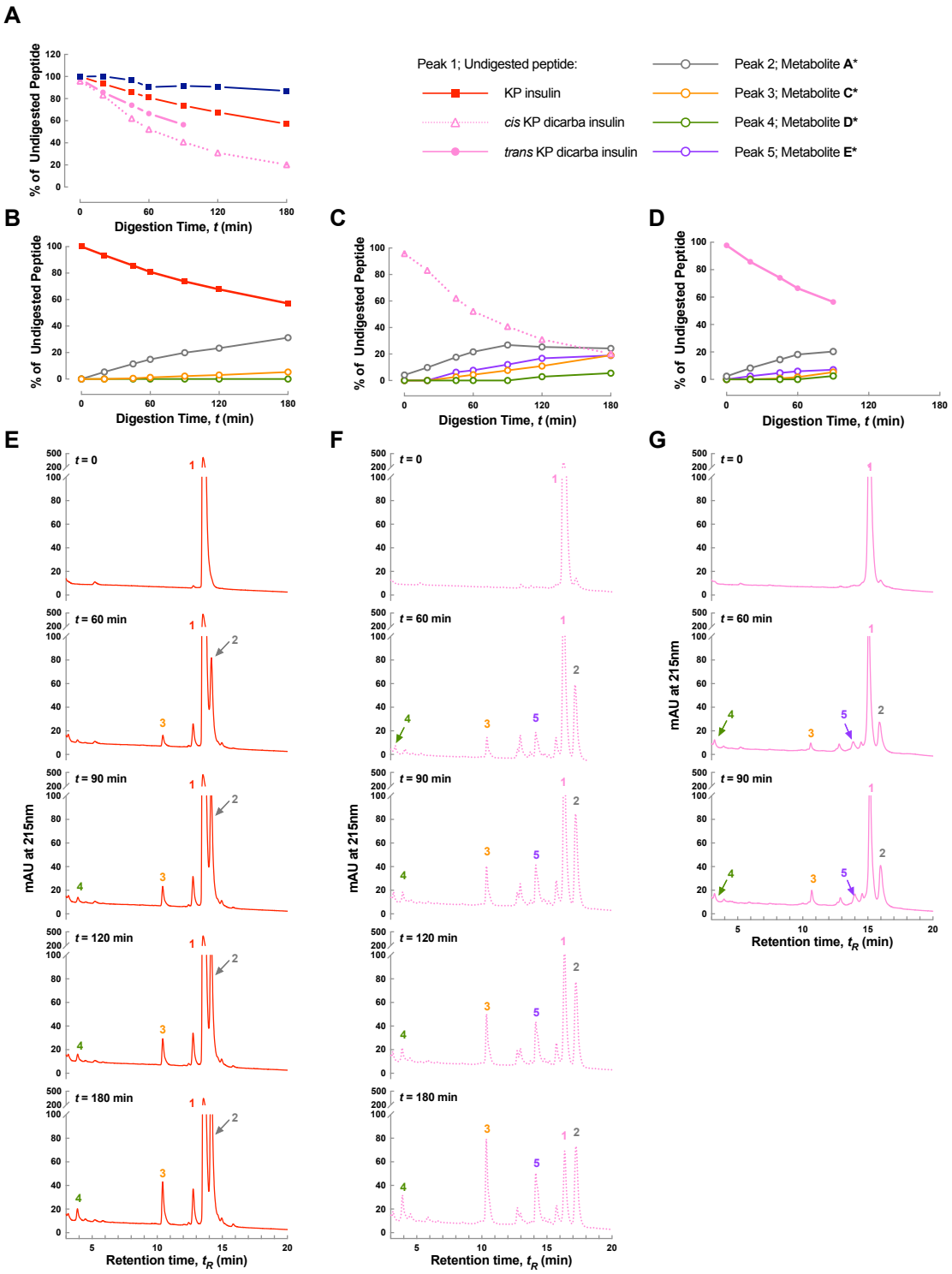

Appendix Figure 3.4 Chymotrypsin proteolysis of KP insulin, cis- and trans dicarba KP insulins. (A) Rate of proteolysis plotted and rate of metabolites synthesis (B –D) as percentage of undigested peptide over time. RP-HPLC purification of (E) KP insulin, (F) *cis* dicarba KP insulin and (G) *trans* dicarba KP insulin metabolites digested in *non-reducing* condition for t = 0, 15, 45, 60, 90, 120, 180 minutes at 37°C. Due to limited material, *trans* dicarba KP insulin was only proteolysed for t = 0, 15, 45, 60, 90 minutes. *Metabolites are predicted from analyses of insulin and *cis* dicarba insulin (see Appx. Figs. 3.3, 3.5 and 3.6): Undigested peptide (1; *blue*), Metabolite **A*** (2; *grey*): non-reduced metabolite resulting from single cleavage at Tyr^{B26}, Metabolite **C*** (3; *orange*): *C*-terminal- and Metabolite **D*** (4; *green*): *N*-terminal non-reduced metabolites resulting from cleavage at Tyr^{B26} followed by cleavages at Tyr^{A14} and Tyr^{B16}. Metabolite **E*** (5; *purple*) is only present in *cis* dicarba KP insulin (and in small amount in *trans* dicarba KP insulin) cleavage reactions; resulted from single cleavage at Tyr^{B16}.

APPENDIX FIGURE 3.5

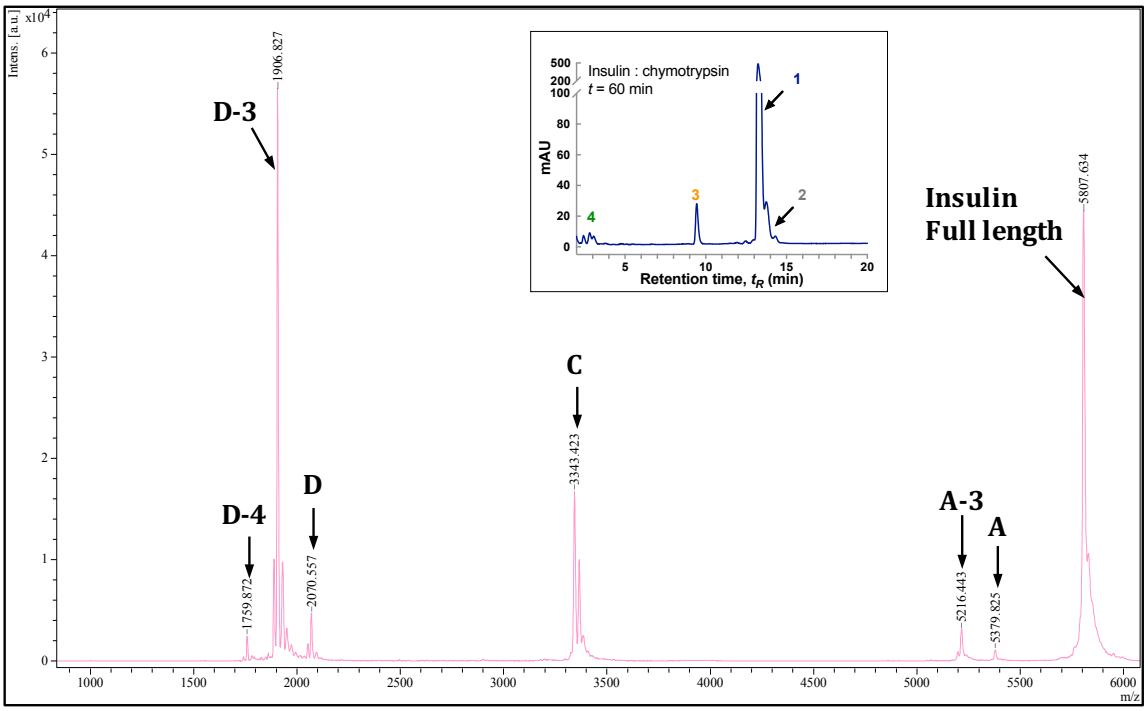

Metabolites	HPLC	Calculated mass, [M+H]⁺		Measured mass, [M+H]⁺			
				Whole Digestβ	Whole Digestβ	Fractionsα	Fractionsα
	Peak #	*Monoisotopic*	*Average*	*Monoisotopic*	*Average*	*Monoisotopic*	*Average*
Full length	1	5804.68	5808.67	5808.52	5807.63	5805.18	5808.24
A	2	5377.44	5381.17	5382.39	5379.83	-	-
A-2	2	5214.38	5217.99	5219.11	5216.44	-	-
B	-	5162.39	5165.92	-	-	-	-
C	3	3343.55	3345.87	3343.85	3343.42	3343.41	3344.43
D	4	2070.91	2072.32	2070.85	2070.56	2070.93	-
D-3	4	1907.85	1909.15	1907.81	1906.83	1907.90	-
D-4	4	1760.79	1761.97	-	1759.87	-	-

α Chymotryptic peptides purified *via* rpHPLC were collected as 0.5mL-fractions. Samples were freeze-dried and resuspended in 0.1% TFA for MALDI analysis.
β Whole sample of chymotryptic peptides were desalted using C18 ZipTip for MALDI analysis.
Peptide calibration range : ~ 1,000 – 3 ,500 Da
Protein calibration range : ~ 4,000 – 20,000 Da

Appendix Figure 3.5 Chymotrypsin limited proteolysis and MALDI analysis of native insulin. MALDI analysis of insulin digested by chymotrypsin in *non-reducing* condition for 60 minutes. Full length insulin and metabolites were detected in linear positive mode. Digested sample was also fractionated *via* RP-HPLC (chromatogram of proteolysed sample at t = 60 min; *inner box*) for MALDI analysis. Calculated mass and measured mass of metabolites identified are presented in the table (*bottom panel*).

APPENDIX FIGURE 3.6

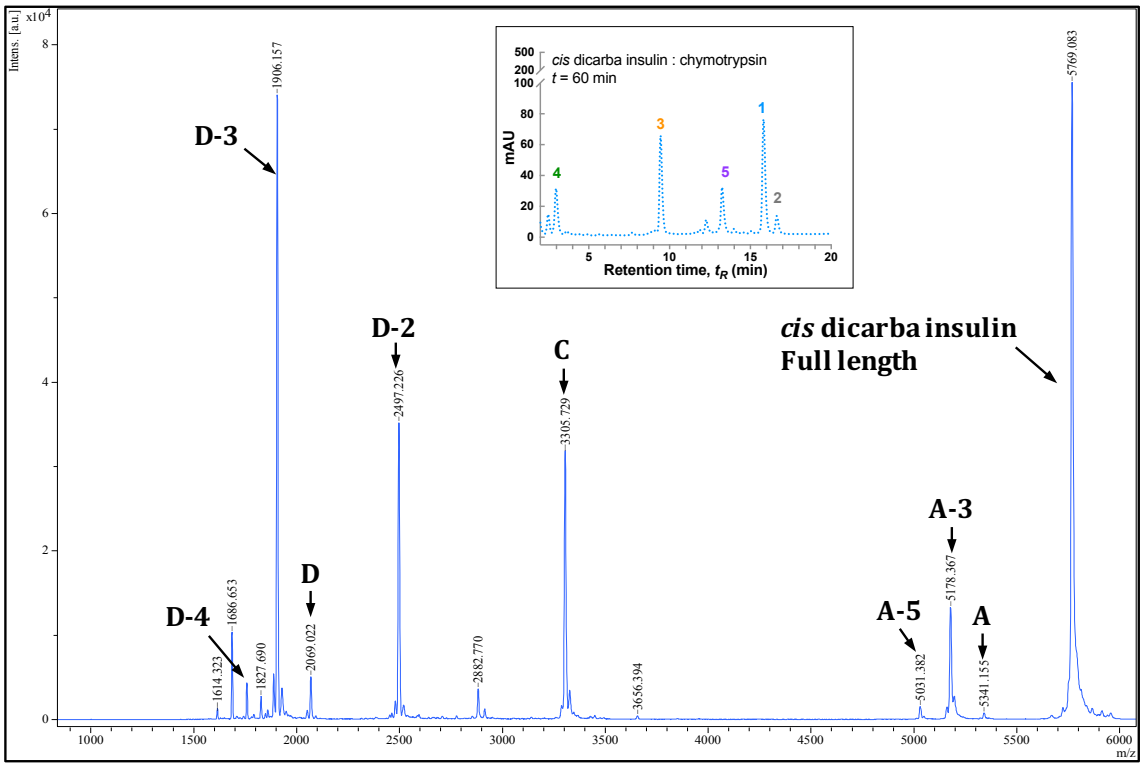

Metabolites	HPLC	Calculated mass, $[M+H]^+$		Measured mass $[M+H]^+$			
				Whole Digest$^{\beta}$	Whole Digest$^{\beta}$	Fractions$^{\alpha}$	Fractions $^{\alpha}$
	Peak #	*Monoisotopic*	*Average*	*Monoisotopic*	*Average*	*Monoisotopic*	*Average*
Full length	1	5766.68	5770.67	5766.50	5769.08	-	5769.70
A	2	5339.44	5343.17	-	5341.55	-	-
A-2	2	5176.38	5179.99	5176.37	5178.37	-	-
A-3		5029.31	5032.82	-	5031.38	-	-
B	-	5124.39	5127.92	-	-	-	-
C	3	3305.55	3307.87	3304.65	3305.73	3305.97	-
D	4	2070.10	2071.30	2070.76	2069.02	-	-
D-2	4	2498.15	2499.82	2497.77	2497.23	2498.16	-
D-3	4	1907.85	1909.15	1907.78	1906.15	1907.90	-
D-4	4	1760.79	1761.97	1760.76	1757.75	1760.80	-
D-5	4	1258.56	1259.46	-	-	1260.60	-

$^{\alpha}$ Chymotryptic peptides purifed *via* rpHPLC were collected as 0.5 mL-fractions. Samples were freeze-dried and resuspended in 0.1% TFA for MALDI analysis.
$^{\beta}$ Whole sample of chymotryptic peptides were desalted using C18 ZipTip for MALDI analysis.
Peptide calibration range : ~ 1,000 – 3,500 Da
Protein calibration range : ~ 4,000 – 20,000 Da

Appendix Figure 3.6 Chymotrypsin limited proteolysis and MALDI analysis of *cis* dicarba insulin. MALDI analysis of *cis* dicarba insulin digested by chymotrypsin in *non-reducing* condition for 60 minutes. Full length *cis* dicarba insulin and metabolites were detected in linear positive mode. Digested sample was also fractionated *via* RP-HPLC (chromatogram of proteolysed sample at t = 60min; *inner box*) for MALDI analysis. Calculated mass and measured mass of metabolites identified are presented in the table (*bottom panel*).

APPENDIX FIGURE 3.7

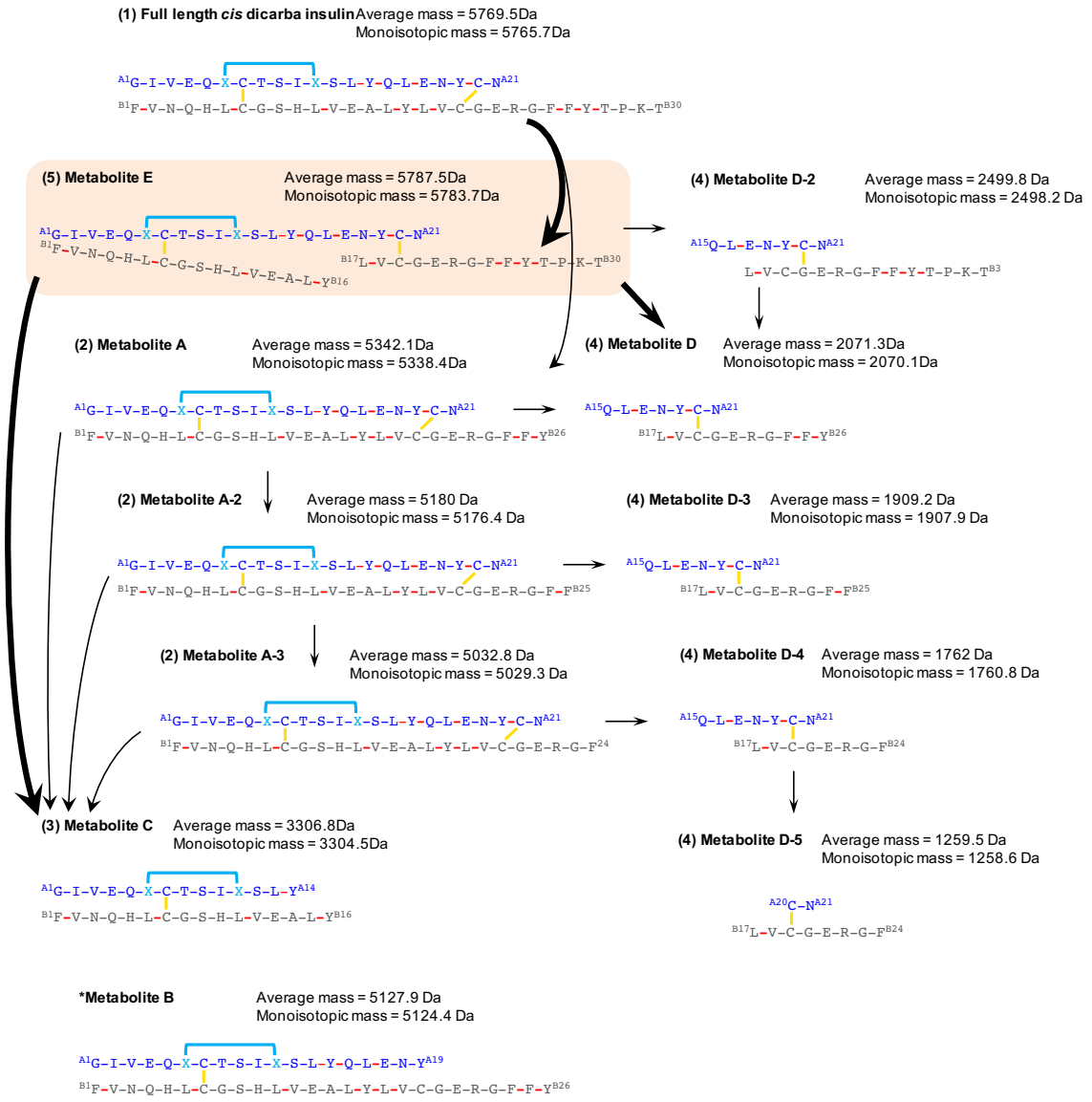

Appendix Figure 3.7 Peptides arising from chymotrypsin cleavage of the *cis* dicarba insulin. Chymotryptic digestion kinetics of *cis* dicarba insulin showing all identified sequences of peptides arising from chymotrypsin cleavage. Metabolites were identified *via* MALDI analyses in combination of different conditions: whole sample *vs* RP-HPLC-fractionated samples; non-reducing *vs* reducing; positive *vs* negative MALDI detection mode. Peak number indicated in brackets. (1) Full length: Undigested peptide; (2) metabolite **A** and subspecies; (3) metabolite **C**; (4) metabolite **D** and subspecies; and (5) metabolite **E**. Sequence of B-chain was confirmed by ESI-MS (data not presented). *Metabolite **B** that was detected by Schilling *et al* (Schilling and Mitra, 1991) was not detected in this experiment.

APPENDIX FIGURE 3.8

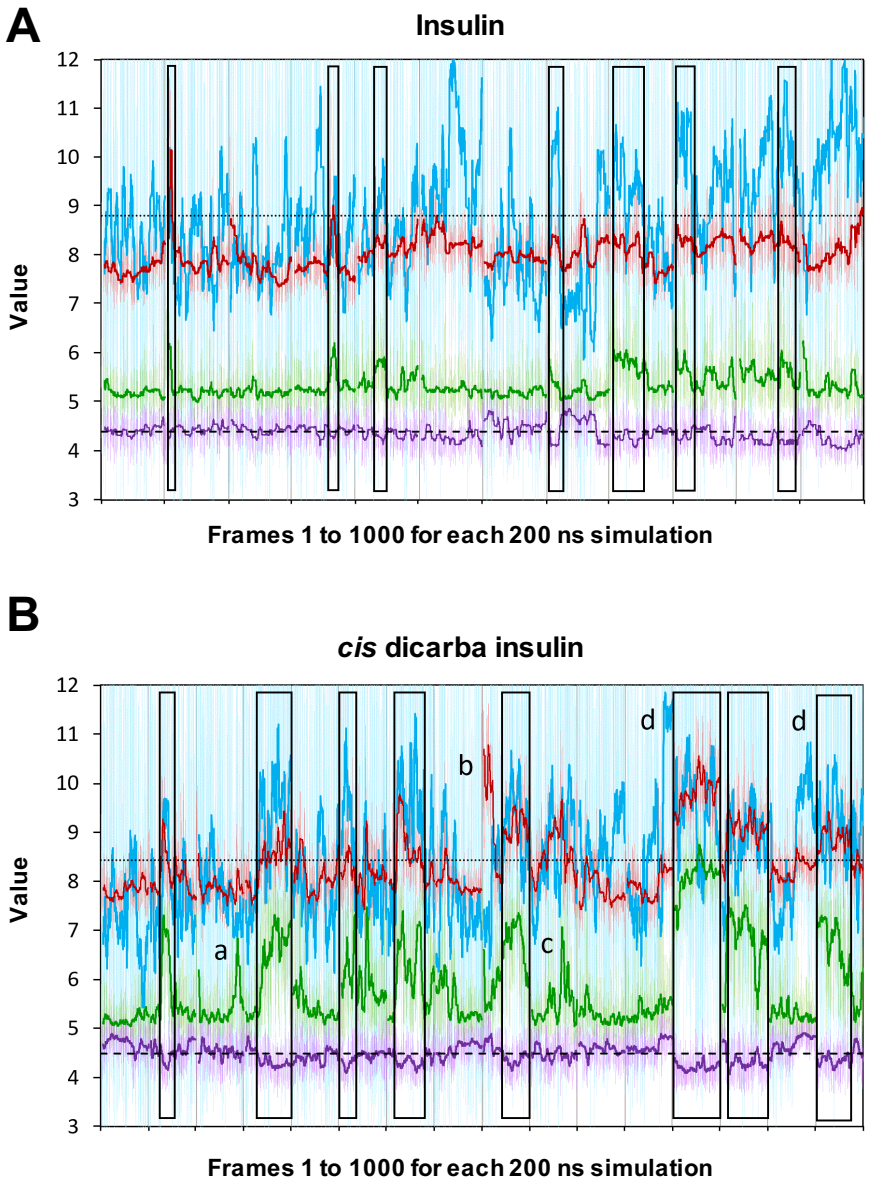

Appendix Figure 3.8 Full data for figure 3.9 - variations in structural parameters associated with B chain helix bending from MD simulations. Green: *r*(Cα-Cα) between Glu^{B13} and Tyr^{B16}; this is a direct measure of helix bending. Red: *r*(Cα-Cα) between residues A6 and B11; this is a measure of the distance between the *N*-terminal A chain and B chain helices. Purple: *r*(Cα-Cα) between Cys^{A7} and Cys^{B7}; the length of the A7—B7 interchain linker. Blue: the relative torsional energy of the A7—B7 disulfide linkage. In all cases, pale colours represent the actual values, while dark colours show a 50 period moving average of the data. The overall averages for the purple and blue traces are shown with dashed and dotted lines, respectively. Bond distances are given in Å and relative torsional energies in kJ mol^{-1}. Bending events in the B chain helix are outlined in black boxes. Note that each bin on the horizontal axis represents an independent 200 ns simulations; traces are therefore not continuous between bins.

APPENDIX FIGURE 3.9

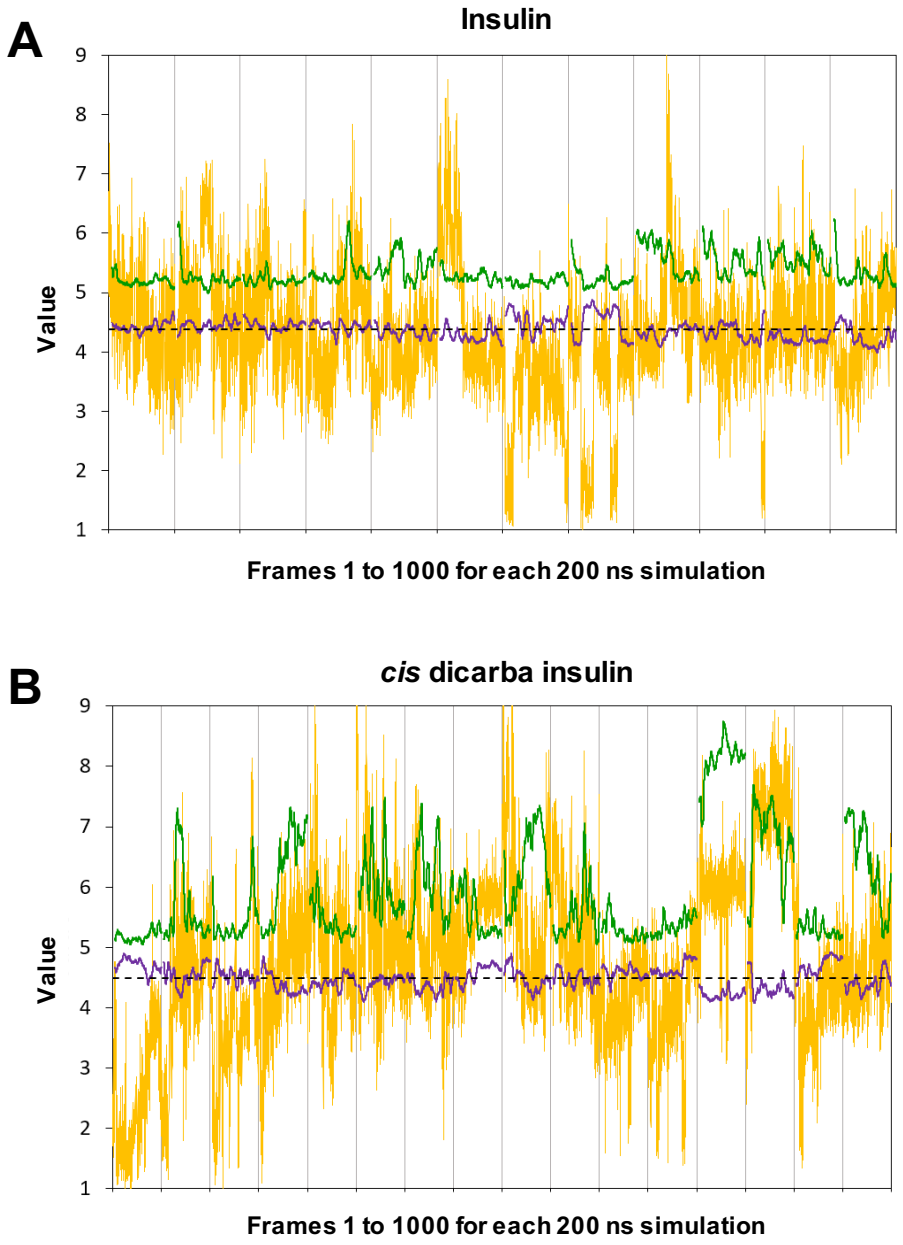

Appendix Figure 3.9 B chain bulging is not associated with twisting of the *N*-terminus of the A chain to the "receptor binding" conformation (Class 2 conformation). All atom RMSDs for residues A1 to A4 from a representative Class 2 structure are shown in yellow; values below 2.5 Å are consistent with a Class 2 conformation. Class 2 conformations tend to be associated with $r(C\alpha^{A7}\text{-}C\alpha^{B7})$ values (purple) that are significantly above the average (black dashed line). In contrast, B chain bulging (leading to large values of $r(C\alpha^{B13}\text{-}C\alpha^{B16})$, shown in green) tends to correlate with below average $r(C\alpha^{A7}\text{-}C\alpha^{B7})$ values.

APPENDIX FIGURE 3.10

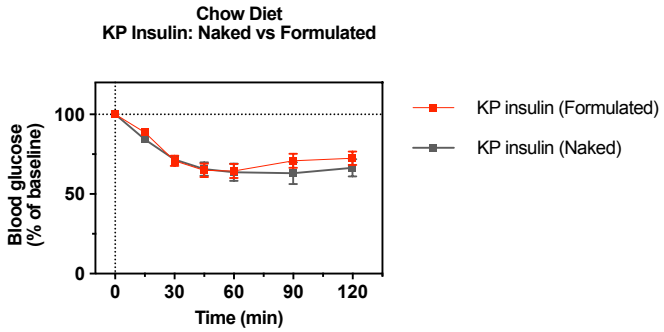

Appendix Figure 3.10 Insulin tolerance tset in mice fed on a normal diet (chow) were administered through intraperitoneal injection (*ip*) with 0.75 IU/kg of *semi-formulated* or *non-formulated* KP insulin under non-fasting conditions and tail vein blood glucose was measured *via* glucose meter at indicated times. n = 10 per group. Blood glucose levels are expressed as % blood glucose over baseline

APPENDIX FIGURE 3.11

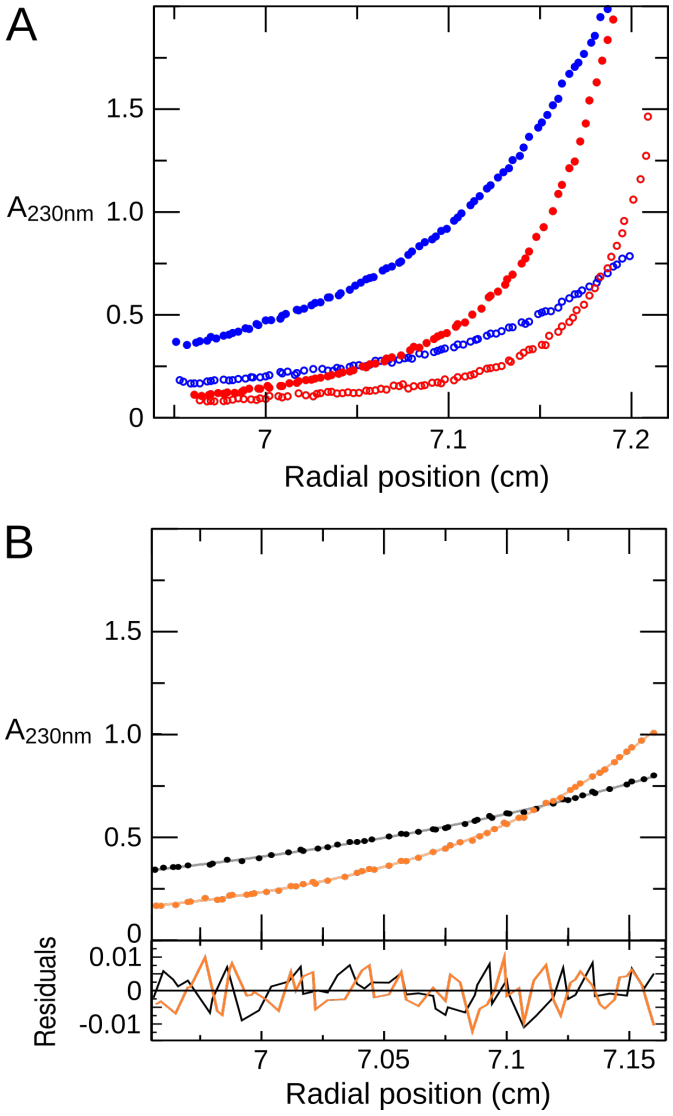

Appendix Figure 3.11 Sedimentation equilibrium data for *native* insulin (A) and monomeric cone snail insulin Con-Ins G1 (B) in the absence of zinc ion (Zn^{2+}). Radial concentration distributions at sedimentation equilibrium for native insulin at loading concentrations of 100 (*open symbols*) and 300 µg/ml (*closed symbols*) at 25,000 (*blue*) and 40,000 rpm (*red*). Radial concentration distributions at sedimentation equilibrium for cone snail insulin at loading concentrations of 100 µg/ml at 30,000 rpm (*black*) and 45,000 rpm (*orange*). It is clearly evident that Con-Ins G1 curves are flatter even though these experiments were conducted at higher speeds than for insulin. Analysis of the Con-Ins G1 data describes a single sedimenting species with an apparent mass of 5,380 ± 55 Da. On the basis of a calculated theoretical mass of 5,143 Da, it was concluded that Con-Ins G1 is predominantly monomeric in solution, with at most 5% being dimeric (data previously published by Menting et al. (Menting et al., 2016) and reproduced here with permission from the journal).

CHAPTER 4

"Metabolically potent dicarba insulin analogues exhibit reduced mitogenic potential."

CHAPTER 4 METABOLICALLY POTENT DICARBA INSULIN ANALOGUES EXHIBIT REDUCED MITOGENIC POTENTIAL

4.1 INTRODUCTION

Since the termination of preclinical safety testing of the "highly mitogenic" insulin X10 (Drejer, 1992) great emphasis has been placed on reducing any potential carcinogenic risk of newly developed insulin mimetics (Janssen and Varewijck, 2014). While there is no definitive reports to suggest insulin analogues currently in clinical use promote higher cancer risk, controversial discussions surrounding the complex relationships between insulin therapy, diabetes and cancer are nonetheless a concerning topic (Johnson and Gale, 2010, Karlstad et al., 2013, Tennagels and Werner, 2013, Janssen and Varewijck, 2014, Vigneri et al., 2009, Sciacca et al., 2018). Ideally, a perfect insulin analogue would be a biased agonist of insulin receptor with selective therapeutic traits – metabolically effective and mitogenically safe.

To this end, a detailed understanding of the mechanisms that mediate the differential signalling for insulin's 'metabolic' *versus* 'mitogenic' responses is fundamental and can be achieved through characterisation of biased ligands. For instance, although the therapeutic promise of insulin X10 was short-lived, it represents an important mitogenically-biased insulin agonist that revealed several key insights that may explain insulin's mitogenecity. In addition to its apparent increased binding affinity for the growth-promoting insulin-like growth factor receptor 1 (IGF-1R), a second mechanism that may attribute to insulin X10 enhanced mitogenic potency is its reduced rate of dissociation from insulin receptor (IR). The prolonged residence time on the IR has been shown to correlate with a sustained phosphorylation of IR and an increased rate of receptor internalisation (reviewed in (Hansen et al., 2011)).

On the other hand, metabolically-biased insulin mimetics have also been reported. For example, the metabolically-biased S597 peptide, has been extensively studied by Jensen *et al*. (Jensen et al., 2007) and recently in our laboratory (Rajapaksha and Forbes, 2015). Importantly, they demonstrated that perturbed IR-A internalisation correlates strongly with reduced mitogenic potential mediated by Shc and Erk activation. Full metabolic action *via* Akt activated at the cell surface is retained (Jensen et al., 2007, Rajapaksha and Forbes, 2015). Another example is IR-A48, an IR agonistic aptamer that highly activates metabolic signalling *via* Akt and effectively lowers blood glucose in mice but does not promote MAPK signalling and cell proliferation (Yunn et al., 2017, Yunn et al., 2015). Collectively, this evidence suggests that ligand-induced

IR mitogenic signalling bias is correlated to a reduced rate of ligand dissociation from the IR and an increased rate of receptor internalisation that results in sustainable activation of Shc and MAPK signalling (Hansen et al., 1996, De Meyts and Shymko, 2000, Jensen and De Meyts, 2009, Rajapaksha and Forbes, 2015).

Until now the studies investigating the link between receptor internalisation and mitogenic activity used insulin analogues with single amino acid changes or peptide mimetics. Although insulin mimetics such as S597 and IR-A48 peptides are great models to study mechanism of signalling bias they do not truly represent insulin, especially as they activate the IR *via* binding to allosteric sites away from the conventional insulin binding pockets (Yunn et al., 2015, Pillutla et al., 2002). In contrast, in this study the dicarba insulin analogues provided a unique opportunity to compare the differential signalling properties between peptides that contain identical amino acid sequences but differ only in their chemical composition at the A6–A11 bond.

As described for the other biased 'insulin' agonists, the mechanisms that contribute to the differential metabolic-mitogenic outcomes can be scrutinised at several "checkpoints" throughout the activation cascade. Using similar approaches, I was interested in further investigating the relationship between phosphorylation kinetics of key adaptor proteins, receptor internalisation and the receptor phosphorylation pattern. Here, using *cis* dicarba insulin and *cis* dicarba glargine insulin I definitively demonstrated that reduced Erk1/2 phosphorylation strongly correlates to impaired rate of IR-A internalisation. In the case of *cis* dicarba glargine remarkably this resulted in a marked reduction in mitogenecity to a potency equivalent to native insulin.

Finally, these observations suggested that the first regulatory signal that stimulates receptor internalisation must lie within the unique phosphorylation pattern on the intracellular domains of insulin receptor. Nevertheless, no one has ever been able to conclusively define the complete phosphorylation "barcode" for IR metabolic /mitogenic signalling. Hansen *et al*. suggested that the preferential phosphorylation of the Y972 and Y1158 promotes mitogenic responses, whereas preferential phosphorylation of the *C*-terminal end of IR (Y1334) leads to metabolic signalling (Hansen et al., 2011). Yunn *et al.* revealed metabolic-biased signalling is associated with preferential phosphorylation of the Y1150 residue (Yunn et al., 2015). Rajapaksha & Forbes also revealed a slight differential phosphorylation of IR-A Y1322 residue (located in *C*-terminal domain) in response to the stimulation of a metabolically biased S597 peptide. Interestingly, IR activation by S597 also exhibits a slower IR-A tyrosine phosphorylation kinetics on all tested

residues; Y960, Y1146, Y1150, Y1151, Y1316 and Y1322 (Rajapaksha and Forbes, 2015). This may also explain the lower IRS-1 activation reported earlier by Jensen *et al.* (Jensen et al., 2007). Clearly, there is a huge knowledge gap in the understanding of the mechanism of receptor phosphorylation. My final aim of this project was, therefore, to identify the different phosphorylation "barcode" on the IR-A that contributes to the reduced mitogenicity of *cis* dicarba insulins. Correlation of this information to structural analysis of the *cis* dicarba insulins may reveal the secret to regulating insulin differential signalling with precision, a vital knowledge for designing safer insulin analogues.

4.2 MATERIALS & METHODS

4.2.1 Materials

Actrapid® insulin was purchased from Lyppard Australia Pty Ltd. Lantus® glargine insulin was purchased from Sanofi Pty Ltd. Western Lightning Plus-ECL, Enhanced Chemiluminescence Substate was purchased from Perkin Elmer, Amersham™ Protran™ 0.2 μm nitrocellulose membrane was obtained from GE Healthcare Life Sciences. Precision Plus Protein™ Dual Color Standards and Affi-Gel 10 were purchased from Bio-Rad. Hybridoma cells expressing antibodies specific for the IR α-subunit (83-7; conformational epitope at exon 3 and 83-14; epitope at exon 7/8 amino acids 469-592 (Soos et al., 1986, Soos and Siddle, 1989), IGF-1R α-subunit (24-31; epitope at amino acids 283-440) (Soos et al., 1992) and IR β-subunit (CT-1; epitope at *C*-terminal domain (KKNGRILTLPRSNPS)) (Ganderton et al., 1992) were a gift from Prof. K Siddle. The monoclonal anti-IR antibody 83-14 was labelled with europium (Eu-83-14) according to instructions provided by Perkin Elmer Life Sciences. [^{3}H]-Thymidine was purchased from Perkin Elmer Life Sciences. hIR-A and hIR-B over-expressing R^{-}fibroblast cells (derived from IGF-1R knockout mouse embryonic fibroblasts, a gift from Prof. R. Baserga (Philadelphia, USA) (Sell et al., 1994) were produced according to Denley *et al.*(Denley et al., 2004). hIR-A over expressing L6 myoblasts were provided by Dr B.F. Hansen (Novo Nordisk A/S, Denmark). P6 cells (BALB/c3T3 cells overexpressing the human IGF-1R) were from Prof. R. Baserga (Pietrzkowski et al., 1992). CNBr-activated sepharose 4B was a product of GE Healthcare. CT-1 competing peptide (KKKKKNGRILTLPRSNPS) was a gift from Prof. Michael Lawrence.

Table 4.1 Primary antibodies used for Western Blot analysis.

Commercial Names	Vendor/Cat. No.	Source/Isotype	Target Protein		Dilutions
			Specificity	Mw (kDa)	
PathScan® Multiplex Western Cocktail I*	Cell Signalling Technology #5301	Rabbit	p-Akt (Ser473) #9271	60	1: 200
		Rabbit IgG	p-ERK 1/2 (Thr202/Tyr204) #4370	44, 42	
		Rabbit IgG	p-p90RSK (Ser380) #9335	90	
		Rabbit IgG	p-S6 Ribosomal (Ser235/236) #4858	32	
		Rabbit IgG	Rab 11 #5589	25	
Phospho-Akt (Thr308)Antibody	Cell Signalling Technology #9275	Rabbit	p-Akt (Thr308)	60	1: 1000
Phospho-GSK3β (Ser9) (D3A4) Rabbit mAb	Cell Signalling Technology #9322	Rabbit IgG	p-GSK3β (Ser9)	46	1: 1000
Phospho-AS160 (Thr642) (D27E6) Rabbit mAb	Cell Signalling Technology #8881	Rabbit IgG	p-AS160	160	1: 1000
Mouse anti-β-Tubulin	Invitrogen #32-2600	Mouse IgG_1- κ	β-Tubulin	50	1: 1000

* This product is discontinued. Individual antibodies in the cocktail system is still available; catalogue numbers provided.

Table 4.2 Secondary antibodies used for Western Blot analysis.

Commercial Names	Vendor/Cat. No.	Host	Target	Conjugate	Dilutions
Peroxidase AffiniPure Donkey Anti-Rabbit IgG (H+L)	Jackson ImmunoResearch Laboratories #711-035-152	Donkey	Rabbit IgG	Horseradish Peroxidase	1:5000
Goat anti-mouse IgG (H+L) Secondary Antibody, HRP	Thermo Fisher #31430	Goat	Mouse IgG	Horseradish Peroxidase	1: 5000
IRDye® 800CW Donkey Anti-Rabbit IgG (H+L)	LI-COR Biosciences #926-32213	Donkey	Rabbit IgG	IRDye 800CW Excitation λ: 778 nM Emission λ: 795nM	1: 50, 000
IRDye® 680RD Donkey Anti-Mouse IgG (H+L)	LICOR Biosciences #926-68072	Donkey	Mouse IgG	IRDye 680RD Excitation λ: 676 nm Emission λ: 694 nm	1: 50, 000

4.2.2 Cell Lines and Culture Conditions

For materials and method for maintaining R$^-$IR-A (R$^-$fibroblasts over-expressing hIR-A), R-IR-B (R$^-$fibroblasts over-expressing hIR-B), hIR-L6 (L6 rat myoblast over-expressing hIR-A) and P6 cells (BALB/c3T3 cells over-expressing the human IGF-1R); refer to *Section 3.2.2*.

4.2.3 Synthesis of Dicarba Glargine Insulins

Chemical synthesis of dicarba glargine insulins was performed by our collaborators Dr Bianca van Lierop, Dr Alessia Belgi and Prof. Andrea J. Robinson in the School of Chemistry, Monash University. Clayton, Victoria, Australia. The details of the synthesis method for the dicarba glargine insulins are provided in the *Appendix 4A*. The synthesis method for dicarba insulins has been previously described in *Chapter 2* and in *(van Lierop et al., 2017)*.

The methods of synthesis of c[Δ^4A6,11]-dicarba insulin (*cis*- and *trans* dicarba insulins) *(van Lierop et al., 2017)* and c[Δ^4A6,11]-dicarba insulin glargine (*cis*- and *trans* dicarba glargines) were essentially the same. Synthesis of dicarba A chain was achieved through an interrupted solid-phase peptide synthesis (SPPS)-catalysis and ring-closing metathesis (RCM) procedures *(van Lierop et al., 2017, van Lierop et al., 2011a)*. Construction of glargine insulin A- and B-chain was achieved through microwave-accelerated SPPS. The monocyclic A-B conjugates were prepared by combination of the dicarba glargine A chain with the glargine insulin B chain under basic conditions resulting in spontaneous oxidation of the liberated free thiol groups generating *cis*- and *trans* dicarba insulins (or *cis*- and *trans* dicarba glargine insulins).

4.2.4 Receptor Competition Binding Assays

IR-A, IR-B and IGF-1R competition binding with increasing concentrations of insulin, glargine insulin and dicarba insulins was measured essentially as described in *Section 2.2.4*.

4.2.5 Kinase Receptor Activation Assays (KIRA)

IR-A, IR-B and IGF-1R phosphorylation in response to increasing concentrations of insulin, glargine insulin and dicarba insulins was detected essentially as described in *Section 2.2.5*.

4.2.6 DNA synthesis Assay

DNA synthesis in response to increasing concentrations of glargine insulin and *cis* dicarba glargine insulin was measured essentially as described in *Section 2.2.6*.

4.2.7 Glucose Uptake Assay

Glucose uptake in response to increasing concentrations of *cis* dicarba glargine insulin was measured essentially as described in *Section 2.2.7.*

4.2.8 Insulin Tolerance Test

Insulin tolerance tests were performed by our collaborator Prof. Sofianos Andrikopoulos in the University of Melbourne, Department of Medicine, Parkville, Victoria, Australia.; as described in *Section 2.2.8.*

4.2.9 Circular Dichroism (CD)

Circular dichroism was carried out as described in *Section 2.2.9.*

4.2.10 Western Blot Analysis

7.5 % glycine mini-gels were prepared in-house. Gels were run at 100 V for approximately 1.5 – 2 hours in 1 x GTS running buffer (192 mM glycine, 25mM Tris, 0.1 % (w/v) SDS, pH8.3; prepared in house). Separated proteins were transferred to Amersham™ Protran™ 0.2 µm nitrocellulose membrane performed in Bio-Rad Wet-Tank Blotting System at 100V for 1.5 hours. Transfer buffer used were prepared fresh in-house (25 mM Tris, 250 mM glycine, 20 % (v/v) methanol, pH8.3).

4.2.10.1 Dose Response Analysis

R⁻IR-B (80,000 cells/well) or hIR-A L6 cells (240,000 cells/well) were seeded in 6-well plates and allowed to grow to confluence (~ 48 hours). Prior to stimulation, cells were serum starved in serum-free media (SFM) containing 1 % (w/v) bovine serum albumin (BSA) for 4 hours. Dose-response analyses were performed by stimulating cells with 0.1, 1, 10 and 100nM of insulin or insulin analogues for 10 min at 37°C. After stimulation, cells were washed with warm PBS, aspirated, followed by 60-min incubation in 200 µL of pre-chilled RIPA lysis buffer (50 mM Tris, 150 mM NaCl, 1 % (v/v) NP-40, 0.25 % sodium deoxycholate, 1 mM EDTA, pH8.0) supplemented with Roche cOmplete™ Protease Inhibitor Cocktail and PhosSTOP™ phosphatase inhibitor tablets. Lysates were scraped off from the well and transferred into pre-chilled 1.5-mL microcentrifuge tubes. Tubes were spun at 13,000 rpm for 3 min at 0°C to remove cell debris. Lysates were transferred into fresh pre-chilled 1.5-mL microcentrifuge tubes and stored at -80°C. Lysates protein concentrations were quantified using Bio-Rad DC™ Protein Assay and 20 µg of each sample was separated in 10 % glycine gel under reducing conditions

for western blot analysis. Samples were boiled for 5 minutes at 95 °C in approximately 5 µL of 5 x protein loading dye (300 mM Tris-HCl pH 6.8, 10 % SDS, 0.25 % bromophenol blue, 50 % glycerol and 25 % (v/v) β-mercaptoethanol) and spun at 13,000 rpm for 2 minutes prior to loading. Transferred blots were blocked for 1 h at room temperature in TBST (20 mM Tris, 150 mM NaCl and 0.01 % (v/v) Tween 20) containing 3 % BSA and probed with primary antibodies (listed in Table 4.1) in blocking solution overnight at 4°C. All blots were also probed with anti-β-tubulin as a loading control. Blots were washed six times for 5 minutes each in TBS/0.01 % (v/v) Tween-20 then probed with HRP-conjugated secondary antibodies (listed in Table 4.2) for 1 hour at room temperature. The washing was then repeated. Blots were developed in ECL reagent according to manufacturer's instruction and imaged in Fujiflim LAS-4000 Luminescent Image Analyzer. All blots were performed at least three times.

4.2.10.2 ***Time-Course Analysis***

hIR-A L6 cells (160,000 cells/well) were seeded in 6-well plates and allowed to grow to confluence (~ 48 hours). Prior to stimulation, cells were serum starved in SFM containing 1 % BSA for 4 hours. Time-course analyses were performed at 10 nM ligand concentration stimulating for 0, 0.33 (20s), 0.5 (30s), 1, 3, 5, 8, 10, 20 and 30 min. After stimulation, cells were washed with warm PBS, aspirated, followed by 30-min incubation in 200 µL of pre-chilled 20 % (v/v) trichloroacetic acid (TCA). Lysates were scraped off from the well and transferred into cold 1.5-mL microcentrifuge tubes. Wells were washed once with 400 µL of 5 % (v/v) TCA and combined into the initial 200 µL of lysates. Tubes were spun at 13,000 rpm for 3 min at 0°C. Supernatant removed, and pellets were resuspended in 50 µL of reducing loading buffer (100mM Tris-HCl pH6.8, 4 % SDS, 0.2 % bromophenol blue, 20 % glycerol and 100mM of DTT). Samples were neutralized with 30 µL of 1M Tris pH 8.0. Samples were boiled for 2 minutes at 95 °C and spun at 13,000 rpm for 2 minutes prior to loading or stored at -80 °C. 20 µL of each sample was separated in 10 % glycine gel in reducing condition for western blot analysis. Transferred blots were blocked for 1 h at room temperature in 3 % BSA/TBST and probed with primary antibodies (listed in Table 4.1) in blocking solution overnight at 4°C. All blots were also probed with anti-β-tubulin as loading control. Blots were washed six times for 5 minutes each in TBST then probed with fluorophore-conjugated (listed in Table 4.2) for 1 hour at room temperature. Repeat washing. Blots were imaged with Odyssey® CLx Imaging System. All blots were performed at least three times.

4.2.10.3 *Analysis*

All data were analysed with LI-COR Image Studio™ software. Each band intensity was normalised to tubulin of its respective lane.

Densitometric analyses were performed to demonstrate dose-response (*Equation 5.1*) and time-course (*Equation 5.2*) effects of dicarba insulin analogues on phosphorylation levels of intracellular proteins involve in metabolic and (or) mitogenic signallings.

Equation 5.1: Dose-response Analysis

$$\%\ of\ phosphorylation\ (over\ phosphorylation\ level\ stimulated\ by\ 100\ nM\ insulin) = \frac{Normalised\ signal\ stimulated\ by\ x\ nM\ insulin/analogue}{Normalised\ signal\ stimulated\ by\ 100\ nM\ insulin}\ x\ 100\ \%$$

Data were analysed individually, averaged and plotted as mean ± S.E.M. in bar graphs.

Equation 5.2: Time-course Analysis

$$\%\ of\ phosphorylation\ (over\ 30\ \text{min}\ insulin\ \ stimulation) = \frac{Normalised\ signal\ stimulated\ by\ 10\ nM\ insulin/analogue\ at\ t = x\ min}{Normalised\ signal\ stimulated\ by\ 10\ nM\ insulin\ at\ t = 30\ min}\ x\ 100\ \%$$

Data were analysed individually, averaged and plotted as mean ± S.E.M. in XY line graphs.

4.2.11 Receptor Internalisation

Receptor internalisation assays were performed based on methods described previously with some modifications *(Daunt et al., 1997, Rajapaksha, 2013, Jensen et al., 2007)*. Briefly, R$^-$IR-A cells (10,000 cells/well) were seeded in Falcon 96-well plates in duplicate sets: one to measure surface receptor after stimulation (*surface receptor plate*); the other to measure total receptors (*total receptor plate*). Cells were allowed to grow for ~48 hours to confluence. Prior to stimulation, cells were serum starved in SFM/1 % BSA for 4 hours. Time-course analyses were performed with 10 nM ligand concentration stimulating for *t* = 0, 5, 10, 20, 30, 60 and 120 min. After stimulation, medium was aspirated, and cells in the *surface receptor plate* were fixed with 4 % paraformaldehyde/PBS for 15 min and washed three times with TBS. Plates were blocked overnight with TBS containing 1 % BSA. The cells in the separate *total receptor plate* were lysed in 110 µL ice-cold RIPA lysis buffer and incubated for 1 h, at 4 °C. Receptors were captured in white Greiner Lumitrac 600 96-well plates pre-coated with anti-IR antibody 83-7 (250 ng/well). Following overnight incubation at 4 °C, both plates were washed three times with

TBST. Approximately 500,000 fluorescent counts of Eu-83-14 antibody were added to each well diluted with europium binding buffer (100 mM HEPES, 100 mM NaCl, 0.05 % BSA, 2 µM DTPA, pH 8.0) in final volume of 100 µL/well and incubated in dark for 1 h. Wells were washed three times with TBST. Then DELFIA enhancement solution was added into both plates (100 µL/well). After 10 min, the solutions in the *surface receptor plate* were transferred to a white Greiner Lumitrac 600 96-well plate. Finally, time-resolved fluorescence was measured using 340 nm excitation and 612 nm emission filters with a BMG Lab Technologies Polarstar fluorometer (Mornington, Australia). Assays were performed in triplicate in at least three independent experiments. The extent of receptor internalisation upon ligand stimulation at each time-point was analysed using *Equation 5.3* followed by normalization with % surface receptor under non-stimulated conditions (SFM) at $t = 0$.

Equation 5.3:

$$\%\ of Surface/Total\ Receptor = \frac{Surface\ Receptor\ at\ T = x}{Average\ Total\ Receptor}\ x\ 100\ \%$$

Data were analysed individually, averaged and plotted as mean ± S.E.M. in XY line graphs.

4.2.12 Preparation of the 83-7 Column

Prior to coupling, 83-7 antibodies were dialysed (CelluSep® T2 regenerated cellulose tubular membrane, 6,000 -8,000 MWCO) in 2.5 L of coupling buffer (20 mM HEPES, pH 7.5) for 24 hours; changing fresh dialysate buffer at least 3 times in between. Affi-Gel 10 was washed with 3 column volume (CV) of cold MQ water, followed by 2 CV of coupling buffer through a sintered glass filter facilitated by applying vacuum. Within 20 minutes after washing, each mL of Affi-Gel 10 was mixed with 4 mg of 83-7 antibody at a ratio of 1: 3 (v/v) in a siliconized tube and allowed to couple overnight at 4 °C with gentle rotation. Final concentration of antibody was approximately 1 mg/mL. Small sample (20 µL) of the *pre-coupling supernatant* was collected immediately after mixing for SDS-PAGE analysis. On the following day, the antibody-coupled Affi-Gel 10 was allowed to settle at room temperature. *Post-coupling supernatant* was collected and 20 µL were kept separately for SDS-PAGE analysis. Resin was washed with 5 CV coupling buffer and excess active groups were blocked with 0.5 M glycine pH 8.0, for 2 h at room temperature with gentle rocking. Blocked resins were packed into glass columns under gravitation. Resins were washed with 5CV of PBST (2.68 mM KCl, 1.46 mM KH_2PO_4, 136.9 mM NaCl, 8.1 mM $NaHPO_4$, pH 7.4 and 0.01 % (v/v) Tween-20) at 1 mL/min *via* Peristaltic

Pump P-1 (Pharmacia Fine Chemicals). Packed column was stored in PBST containing 0.02% sodium azide at 4 °C.

4.2.13 CT-1 Antibody Purification using a Protein G Column

CT-1 antibodies expressing hybridomas were maintained in Gibco® CD Hybridoma Medium in T-175 flasks at 37 °C, 5 % CO_2. Hybridomas were starved at 0 or 1 % of FCS for 3 – 7 days. Supernatant were collected, centrifuged at 4,000 rpm at 4 °C for 5 min prior to purification. For each 2-mL protein G column, the maximum capacity of supernatant loaded were 100 mL; equivalent to supernatant collected from 4 – 5 x T-175 flasks. Protein G column was equilibrated with 5 CV of ice-cold PBST then supernantant was pumped into the column at a rate of 1 mL/min. Column washed with 5 CV of ice-cold PBST. CT-1 antibodies were eluted with elution buffer (0.1 M glycine, pH 2.6) at a rate of 0.5 mL/min. Fifteen 1-mL fractions were collected, each fraction was immediately neutralised with 90 µL of Tris pH 9.0. Protein concentrations of eluted samples were determined using NanoDrop™ 2000 Spectrometer detected at 280 nm wavelength. Fractions containing CT-1 antibodies were pooled and stored at -20 °C until use.

4.2.14 Preparation of the CT-1 Column

Purified antibodies were dialysed (CelluSep® T2 regenerated cellulose tubular membrane, 6,000 -8,000 MWCO) in 2.5 L of coupling buffer (0.1 M $NaHCO_3$; pH 8.3 containing 0.5 M NaCl) for 24 hours; changing fresh dialysate buffer at least 3 times in between. To prepare sepharose for coupling, x g of lyophilised sepharose (each gram of lyophilised powder = 3.5 mL final volume of medium) were weighed out and washed in 200 mL of 1mM HCl through a sintered glass filter facilitated by applying vacuum. Within 20 minutes after washing, CNBr-activated sepharose was mixed with CT-1 antibody. For each gram of lyophilised sepharose powder, 5 mL of CT-1 solution was used. Final concentration of antibody was 1 mg/mL. Coupling was performed overnight in a siliconized tube at 4 °C with gentle rotation. Small sample (20 µL) of the *pre-coupling supernatant* was collected immediately after mixing for SDS-PAGE analysis. On the following day, antibody-coupled sepharose was allowed to settle at room temperature. *Post-coupling supernatant* was collected and 20 µL were kept separately for SDS-PAGE analysis. Sepharose medium was washed with 5CV coupling buffer and excess active groups were blocked with 0.1 M of Tris-HCl buffer; pH 8.0, for 2 h at room temperature with gentle rocking. Medium was washed with 3 cycles of alternating pH; 5 CV each buffer. Wash buffer 1: 0.1 M sodium acetate pH 4.0 containing 0.5 M NaCl. Wash buffer 2: 0.1 M Tris-HCl pH 8.0 containing

0.5 M NaCl. Resins were packed into glass column under gravitation and column was stored in PBST containing 0.02% sodium azide at 4 °C.

4.2.15 Preparation of the Pre-clearing Column

Pre-clearing columns were prepared exactly the same as described for their affinity column counterparts (see *section 4.2.12* for Affi-Gel 10 and *section 4.2.14* for CNBr-activated sepharose) except resin was incubated overnight in coupling buffer in place of antibody solution.

4.2.16 Optimisation for the Purification of Stimulated Insulin Receptor

R$^-$IR-A cells were grown to approximately 90 % confluency in 10 x Corning® cell culture flasks, surface area 175 cm^2 at 37 °C, 5 % CO_2. Cells were serum starved overnight (~ 18 hrs) at 37 °C in filtered-sterilised SFM/1 % BSA. Cells were stimulated in SFM/1% BSA supplemented with 10 mM insulin (10 mL/flask) for 20 minutes at 37 °C. To stop stimulation, supernatant was aspirated and cells were washed gently in PBS, buffer aspirated and cells were then lysed in ice-cold RIPA lysis buffer (see section 5.2.9.1 for recipe) supplemented with Roche cOmplete™ Protease Inhibitor Cocktail and PhosSTOP™ phosphatase inhibitor tablets; at 4 °C for 1 hr with gently rocking. Lysates were centrifuged at 2,200 x g for 20 min at 4 °C to remove aggregates or cell debris. Meanwhile, pre-clearing and affinity columns were washed in 5CV of TBST followed by 3 CV of RIPA lysis buffer at 4 °C at a rate of 2 mL/min. Supernatant (*pre-loading lysate*) was first pumped through an equilibrated 2 mL pre-clearing column at a rate of 1 mL/min. *Pre-cleared lysate* was collected and pumped through the affinity column at a rate of 1 mL/min. *Post-loading lysate* was collected and stored at -20 °C. The affinity column was washed with 5 CV of cold lysis buffer followed by 5CV of cold TBS; *flow-through* collected. IR-A bound to the column was eluted with various elution buffer conditions listed below:

4.2.16.1 Elution buffers

Elution Buffer A: 0.1 M glycine, 0.15 M NaCl and 0.01 % (v/v) Triton-x 100, pH 1.7 (Adapted from (Rajapaksha, 2013))

Elution Buffer B: 25 mM Tris pH 8.0, 200 mM NaCl, 1M $MgCl_2$ and 0.01 % (v/v) Triton-x 100 (Adapted from (Kavran et al., 2014))

Elution Buffer C: 50 mM sodium acetate pH 5.0, 1 M NaCl and 0.01 % (v/v) Triton-x 100 (Adapted from (Fujita-Yamaguchi et al., 1983))

Elution Buffer D: CT-1 competing peptide in 50 mM HEPES pH 7.4, 10 % glycerol and 0.005 % (v/v) Triton-x 100 (Adapted from (Ganderton et al., 1992))

4.2.16.2 *Elution Methods*

4.2.16.2.1 *Insulin receptor elution via 83-7 affinity chromatography):*

Two Oakridge tubes containing 20 mL of 100 % acetone were pre-chilled prior to elution. Resin was drained to a minimal reservoir volume and 1 mL of *Elution Buffer A* was added to the resin and allowed 5 min incubation. Eluate was collected directly into the pre-chilled 100% acetone solution; mixed gently. Immediately, 2 mL of elution buffer was added into the resin, incubated, eluted into the same Oakridge tube and repeat. The final eluate: acetone concentration is 20: 80 % (v/v). Samples were stored overnight at -20 °C. Acetone precipitated samples were pelleted *via* ultracentrifugation at 40,000 x g for 45 min at 4 °C. Acetone solution removed gently, pellet was resuspended in 40 µL of 2 x NuPAGE load buffer containing freshly added 1 M DTT. Sample was boiled at 85 °C for 5 min and separated on either 7.5 % glycine gel (prepared in-house) or Bio-Rad 4 – 20 % Mini-PROTEAN® Bis-Tris Precast Protein Gel.

4.2.16.2.2 *Insulin receptor elution via CT-1 affinity chromatography*

Samples were eluted at a rate of 0.5 mL/min. Each collected 1-mL fraction was immediately neutralised with 90 µL of Tris pH 9.0. Protein concentrations of eluted samples were determined using NanoDrop™ 2000 Spectrometer detected at 280 nm wavelength. Fractions containing protein were pooled and concentrated to at least 40 µL and resuspended with 10 µL 4x NuPAGE load buffer containing freshly added 2 M DTT. Sample was boiled at 85 °C for 5 min and separated on either 7.5 % glycine gel (prepared in-house) or Bio-Rad 4 – 20 % Mini-PROTEAN® Bis-Tris Precast Protein Gel.

4.2.17 Statistical Analyses

Statistical analysis of receptor binding, receptor activation and DNA synthesis assays were performed using a 2-way ANOVA with a Dunnett's multiple comparison. Data for glucose uptake assay and significance of the overall change of blood glucose levels in insulin tolerance tests were analysed by paired *t*-test. Significance of the change of blood glucose levels at each time-point was also determined by 2-way ANOVA followed by Holm Sidak's multiple comparison test. Significance was accepted at $P < 0.05$.

4.3 RESULTS

4.3.1 Chemical Synthesis

Outline: Chemical synthesis of A6–A11 dicarba glargine insulin generates two isomeric cis- and trans dicarba glargine insulin peptides.

The *cis*- and *trans*-configured dicarba glargine insulin A chains, in which a C=C dicarba bond replaces the A6–A11 intra-chain S-S bond (Fig. 4.1*C*), were synthesised as previously described using a RCM and SPPS-catalysis approach (van Lierop et al., 2017, van Lierop et al., 2011a). The modified dicarba glargine insulin A chains were then combined with requisite insulin B chains to provide *cis* and *trans* isomers of c[Δ^4A6,11]-dicarba glargine insulin. The dicarba analogues were purified by RP-HPLC (see Figs. 4, *D* and *E*) before being subjected to biological and downstream signalling analyses. The synthesis of dicarba glargine is summarized in *schematic 4.1*.

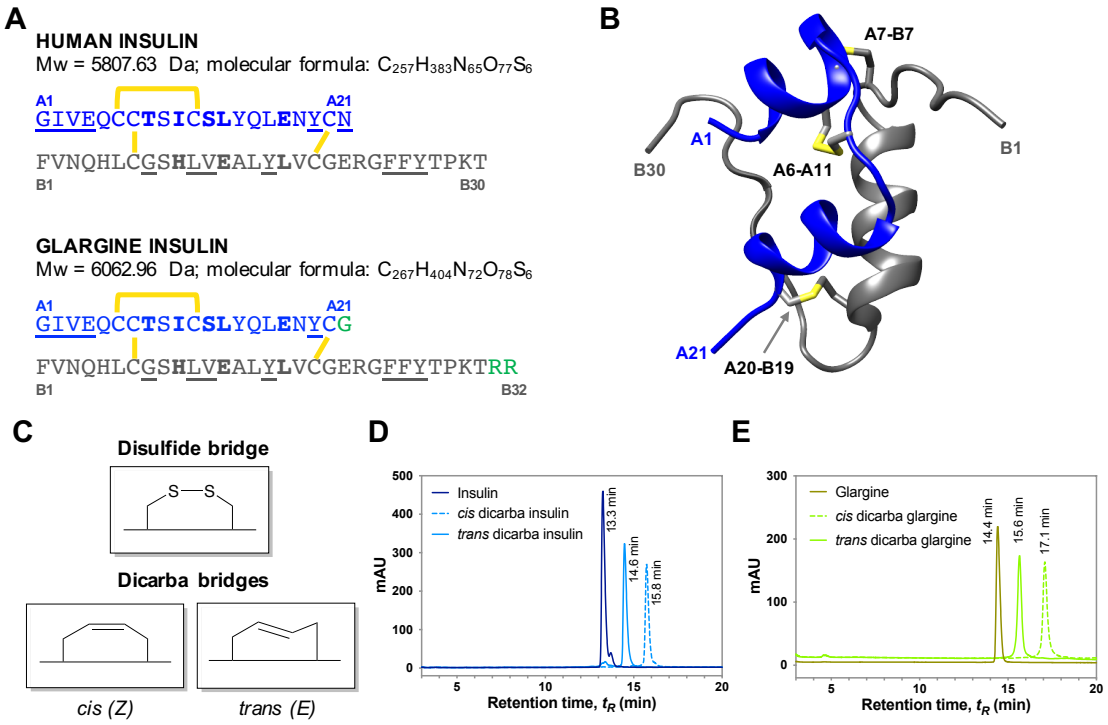

Figure 4.1 Insulin, insulin glargine and dicarba insulin analogues. (A) Primary sequence comparison of human insulin (top) and insulin glargine (*bottom*). Both consist of A (*blue*) and B (*grey*) chains stabilized by three disulfide bridges (yellow). *Underlined* are site 1-binding residues and *bold* are site 2-binding residues (Whittaker et al., 2008). Long-acting insulin glargine has a substitution of Asn^{A21} ➛ Gly^{A21} residue and an addition of $Arg^{B31}Arg^{B32}$ residues on the *C*-terminal end of B chain (highlighted in *green*). (B) Ribbon diagram of human insulin (2-Zn-coordinated T_6 conformation (Baker et al., 1988b) PDB entry 1MSO) showing the location of the three a-helices (*A chain: blue; B chain: grey*) and the three disulfide bonds (*yellow*). (C) Schematic diagram of native cystine and isomeric *cis*- and *trans*-dicarba bridges. RP-HPLC chromatograms of (D) insulin, *cis* dicarba insulin (*cis* insulin) and *trans* dicarba insulin (*trans* insulin); (E) insulin glargine, *cis* dicarba glargine and *trans* dicarba glargine.

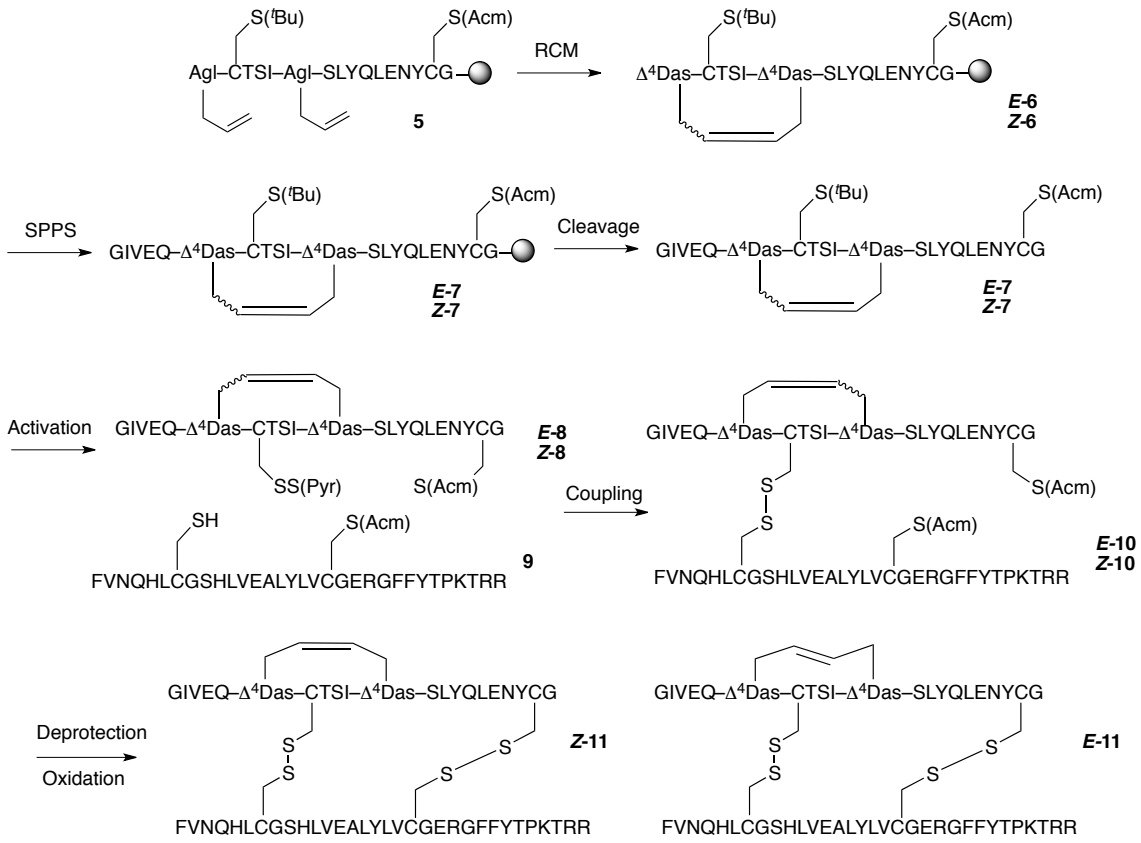

Schematic 4.1 Synthesis of *c*[Δ^4A6,11]-Dicarba glargine insulin (*E*-11) Synthesis of dicarba glargine insulins was performed *via* ring-closing metathesis (RCM) and an interrupted solid phase peptide synthesis (SPPS)-catalysis approach. L-Allylglycine (Agl), tert-butyl (^{t}Bu), acetamidomethyl (Acm), pyridinyl (Pyr), cis isomer (Z), trans isomer (E). The synthesis of dicarba glargine analogues was from Robinson, A.J. *et al.* and schematic is included with their permission.

4.3.2 Receptor Binding & Activation Analyses

Outline: Cis dicarba glargine showed reduced receptor binding and activation potency compared to glargine.

The binding affinities of the dicarba insulin analogues for the IR-B and IGF-1R were determined using competition binding assays (Fig. 4.2, *A* and *B*, and Table 4.3). Similar to the effect of dicarba bonds on native insulin (Chapter 2) and KP insulin (Chapter 3), only the *cis* isomer of dicarba glargine is potent while the *trans* isomer binds poorly to IR-B. The *trans* dicarba glargine was subsequently excluded in further activity assays due to its poor receptor binding affinity. Consistent with the literature, glargine binds and activates IR-B with a potency similar or slightly lower compared to insulin (60–80% of native insulin reported in (Kurtzhals et al., 2000, Sommerfeld et al., 2010); 88% reported in this study) and showed increased affinity for the IGF-1R compared with insulin (460–650 % of native insulin reported in (Sommerfeld et al., 2010, Kurtzhals et al., 2000); 480 % increased in this study) (Kurtzhals et al., 2000, Sommerfeld et al., 2010). Interestingly, the *cis* dicarba glargine showed approximately 2-fold reduced binding affinities for both IR-B and IGF-1R compared to glargine (Fig. 4.2, *A* and *B*, and Table 4.3). The *cis* dicarba glargine also activates IR-B with a reduced potency compared to glargine (Fig. 4.2*C*) and activates IGF-1R poorly with equal potency to insulin (Fig. 4.2*D*).

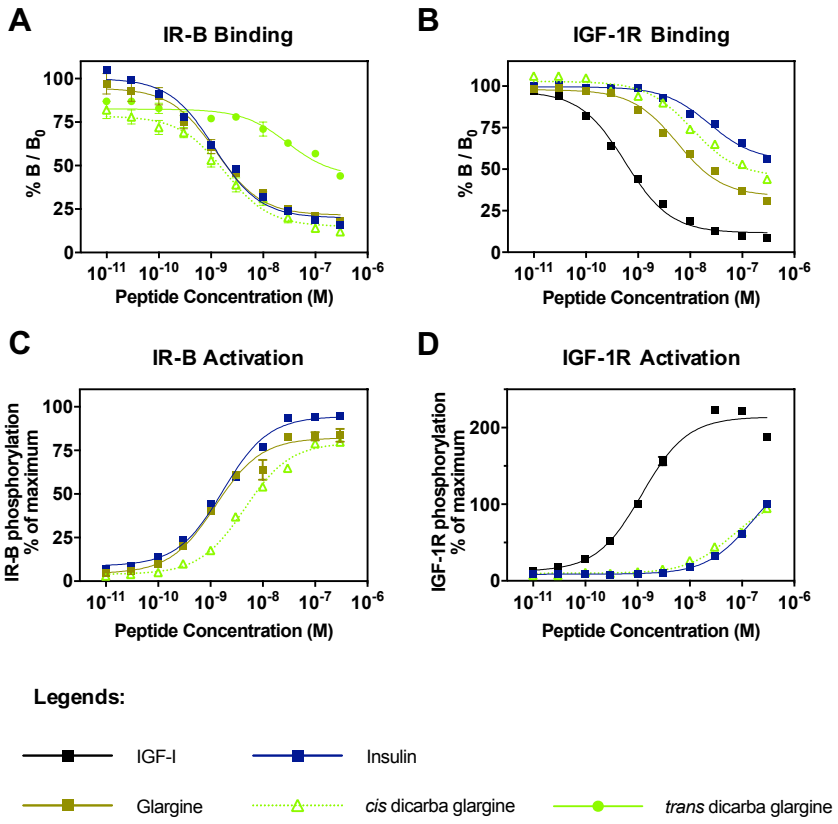

Figure 4.2 Receptor binding and activation of insulin, glargine and dicarba glargine analogues. (A) Competition binding of insulin, glargine and dicarba glargine analogues with europium-labelled insulin for the IR-B and (B) with europium-labelled IGF-I for the IGF-1R. Results are expressed as a percentage of binding in the absence of competing ligand (%B/B_0). (C) Activation of IR-B and (D) IGF-1R by increasing concentrations of each insulin analogue (10 min stimulation) is expressed as a percentage of the maximal receptor phosphorylation induced by insulin. IR-B binding: Insulin *vs* glargine (non significant); glargine *vs cis* dicarba glargine **** ($P \leq 0.0001$); glargine *vs trans* dicarba glargine **** ($P \leq 0.0001$). IGF-1R binding: IGF-I *vs* Insulin **** ($P \leq 0.0001$); Insulin *vs* glargine **** ($P \leq 0.0001$); glargine *vs cis* dicarba glargine **** ($P \leq 0.0001$) (2-way ANOVA; Dunnett's multiple comparison). All data are the mean ± S.E.M. n = at least 3 independent experiments. Error bars are shown when greater than the size of the symbols.

Table 4.3 Binding affinities of IR-B and IGF-1R.

Competition for europium-labelled insulin and IGF-I binding to the IR-B and IGF-1R, respectively, by insulin, insulin lispro (KP), insulin glargine, dicarba insulin analogues and IGF-I. These data were derived from IR-B receptor binding curves *in Figures 2.2A, 3.2A* and *4.2A*, and IGF-1R receptor binding curves in *Appendix Figures 2.4A, 3.2A* and *Figure 4.2B*.

	IR-B		**IGF-1R**	
	IC_{50} (nM)	Affinity (% Insulin ± SEM)	IC_{50} (nM)	Affinity (% Insulin ± SEM)
Insulin	1.07 ± 0.09	100	> 300	100
cis dicarba insulin	1.07 ± 0.30	100 ± 26[ns]	> 300	~100
trans dicarba insulin	40.4 ± 7.2[a]	1.8 ± 0.3****	-	-
KP insulin	-	84 ± 6[ψ]	-	156 ± 16[ψ]
cis dicarba KP insulin	1.13 ± 0.06	95 ± 5 [ns]	> 300	n.a.
trans dicarba KP insulin	>300	n.a		-
Glargine	1.22 ± 0.13	88 ± 9 [ns]	6.71 ± 3.9	> 484 ± 281 ****
cis dicarba glargine	1.95 ± 0.38	55 ± 10****	11.5 ± 3.16	> 261 ± 76 ****
trans dicarba glargine	30.8 ± 15	3.48 ± 3.6****	-	-
IGF-I	-	-	0.60 ± 0.07	4704 ±468 ****

n = 3 or more, [a]n=2, - not performed, n.a. not analysed, [ns]non-statistically significant, [ψ]derived from Kurtzhals *et al.*, $P > 0.05$, ** $P \leq 0.01$, *** $P \leq 0.001$, **** $P \leq 0.0001$. Errors shown are S.E.M

4.3.3 *In vitro* Metabolic and Mitogenic Activity

Outline: Cis dicarba glargine insulin is significantly less potent than glargine in promoting DNA synthesis activity while effectively promoting glucose uptake in vitro.

Corresponding to its slightly lower IR-B binding and activation potencies, the *cis* dicarba glargine showed a trend of lower glucose uptake activity compared to *cis* dicarba insulin and native insulin, however the effect was not significantly different (Fig. 4.3*A*), suggesting the introduction of the dicarba linkage has little effect on the ability to activate metabolic signalling pathways upon IR-B binding.

There is, however, a discrepancy between the receptor binding affinities of *cis* dicarba glargine and its ability to activate DNA synthesis. Glargine, that binds to IGF-1R with approximately 5-fold increased affinity compared to insulin, promotes a proportionate ~5-fold increase in mitogenic potency as measured by the DNA synthesis assay (Fig. 4.3*B*). In contrast, despite *cis* dicarba glargine binding to IGF-1R and the IR-B with only less than 2-fold lower affinity compared to glargine, this analogue promotes DNA synthesis at a significant 5-fold lower potency compared to glargine. In fact, the *cis* dicarba glargine is equipotent to native insulin in promoting DNA synthesis. We hypothesize that lower ability of *cis* dicarba glargine to activate DNA synthesis arises not only due to its slightly reduced receptor binding affinities but also by engaging the receptors differently to glargine.

It is important to acknowledge that the DNA synthesis assays were performed in L6 myoblasts overexpressing IR-A and the affinity of *cis* dicarba glargine has not been measured as yet. However, we know that *cis* dicarba to the IR-A binds with a 2-fold lower affinity than insulin, (personal communication; data not shown). Also, as mentioned above, *cis* dicarba glargine has a 2-fold lower affinity for the IR-B and IGF-1R compared to insulin. Thus, we can reasonably expect that *cis* dicarba glargine will have a similar 2-fold lower affinity for the IR-A compared to insulin, although it would be good in the future to definitively measure this.

Importantly, *cis* dicarba glargine retains a metabolic potency similar to insulin and allows the analogue to effectively promote glucose uptake *via* stimulation of IR-B despite the reduction in receptor binding affinities and the disproportionately reduced mitogenic action.

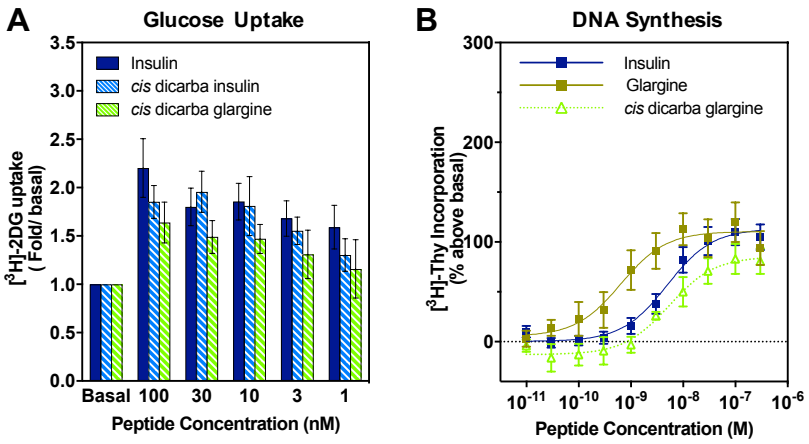

Figure 4.3 *In vitro* metabolic and mitogenic studies of insulin, glargine and *cis* dicarba analogue. (A) Glucose uptake stimulated by increasing concentrations of insulin, *cis* dicarba insulin or *cis* dicarba glargine is expressed as fold glucose uptake (pmol/min/mg) above basal. Insulin *vs cis* dicarba insulin *vs cis* dicarba glargine (ns) (paired *T-test*). (B) DNA synthesis in response to increasing concentrations of stimulating insulin analogue is shown as percentage incorporation of [^{3}H]-thymidine (^{3}H-Thy) above basal. All data are the mean ± S.E.M. n = at least 3 independent experiments. Error bars are shown when greater than the size of the symbols.

4.3.4 Insulin Tolerance Test

Outline: Cis dicarba glargine showed varying blood glucose lowering capacities in mice fed with chow and high-fat diets.

Similar to the effect of A6–A11 *cis* dicarba bond in native insulin (*Chapter 2*) and lispro insulin (*Chapter 3*), the introduction of the A6–A11 dicarba bond into glargine (*cis* dicarba glargine) leads to an analogue that lowers blood glucose levels in insulin resistant mice fed a high-fat diet more rapidly than glargine (Fig. 4.4*B*). The change of blood glucose levels post-treatments are also presented as the inverse area under curve (AUC) and show a significant ($P \leq 0.01$) blood glucose lowering effect in the duration of 2 hours post-treatment with *cis* dicarba glargine in high-fat fed mice (Fig. 4.4*D*). Interestingly, the blood glucose lowering effects of both glargine and *cis* dicarba glargine are only as effective as saline treatment in mice fed with a chow diet (data not shown). As glargine was designed to precipitate upon subcutaneous injection to allow its slow and long duration of action, *in vivo* testings *via* intraperitoneal (ip) injection cannot provide an accurate measurement of glargine action. Subcutaneous insulin tolerance testing is not a standard method (Ayala et al., 2010).

Until now, I have demonstrated that the introduction of A6–A11 *cis* dicarba bond to the native insulin (Fig. 2.3), lispro insulin (Fig. 3.2) and glargine insulin, all resulted in signalling bias towards a metabolic response. The *cis* dicarba insulin analogues more rapidly lowered blood glucose levels in mice and showed reduced mitogenic potency *in vitro* compared to their respective parent peptides. Such effects were most prominent in the *cis* dicarba analogue of glargine insulin. Additionally, the *cis* dicarba insulin analogue also binds to IR with an affinity very similar to their parent peptides but is at least 5–10 fold less mitogenically potent, suggesting that post-IR binding a mechanism exists to promote this signalling bias. Thus, I present here the perfect tools to further scrutinise the mechanism of signalling bias using analogues of the closest resemblance to the native insulins.

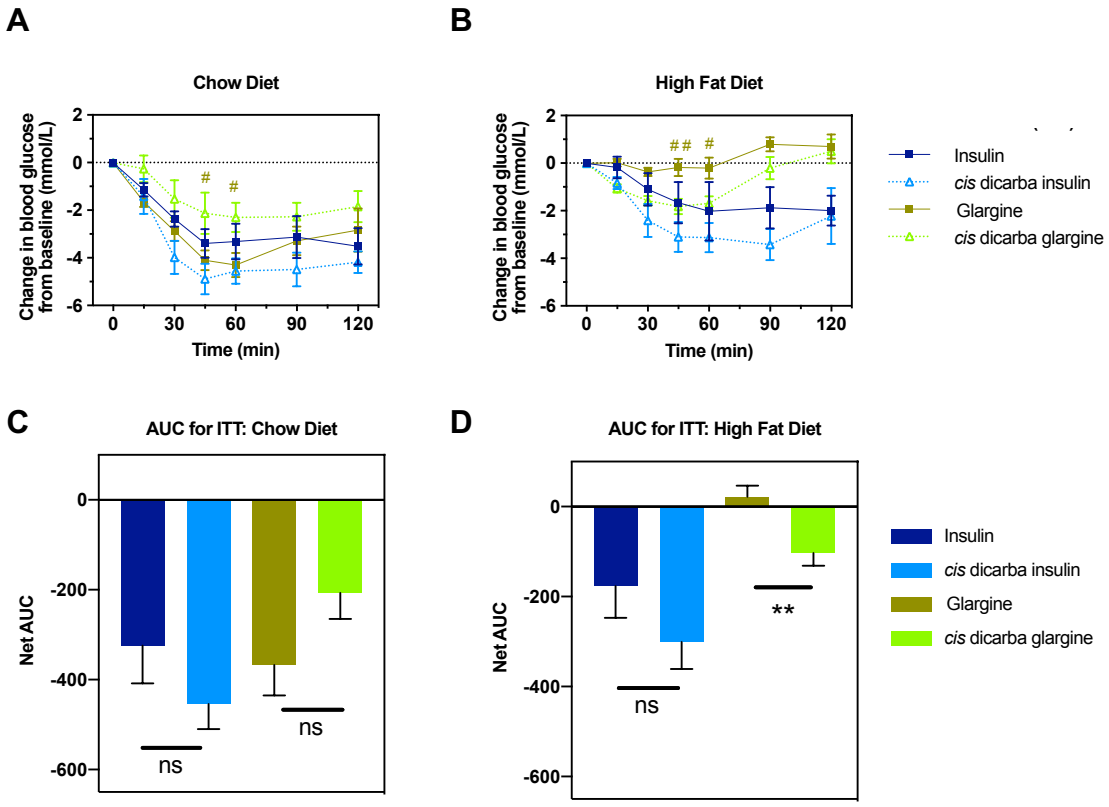

Figure 4.4 *In vivo* insulin tolerance test (ITT) with insulin, glargine and *cis* dicarba analogues. (A) Insulin tolerance tests were conducted in mice fed on a normal diet (chow), or (B) on a high fat diet. Insulins and insulin analogues were administered through intraperitoneal injection (ip) with 0.75 IU/kg insulin, glargine, *cis* dicarba insulin or *cis* dicarba glargine under non-fasting conditions. and Tail vein blood glucose was measured *via* glucose meter at indicated times. n = 5-6 per group. Error bars are shown when greater than the size of the symbols. Blood glucose levels are expressed as change over basal levels (mmol / L). Statistical significance of each time-point was determined *via* 2-way ANOVA followed by Holm-Sidak's multiple comparison test. Chow diet: glargine insulin *vs cis* dicarba glargine insulin at t = 45$^{\#}$ and 60 min $^{\#}$ ($p \leq 0.05$). High fat diet: glargine insulin *vs cis* dicarba glargine insulin at t = 45 min$^{\#\#}$ ($P \leq 0.01$); t = 60 min $^{\#}$ ($p \leq 0.05$). (C – D) Area under curves (AUC) derived from insulin tolerance tests in (A) and (B). Chow diet: insulin *vs cis* dicarba insulin^{ns}; glargine *vs cis* dicarba glargine^{ns} (paired *T-test*). High fat diet: insulin *vs cis* dicarba insulin^{ns}; glargine *vs cis* dicarba glargine ** ($P \leq 0.01$) (paired *T-test*).

4.3.5 Dose-response effects on P13K and MAPK signalling

Outline: Cis dicarba insulin analogues showed dose-dependent reduced potencies for activating MAPK signalling. The effect is more prominent in IR-A overexpressing cells.

Insulin signalling is generally involves two major pathways – the metabolic PI3K and the mitogenic MAPK pathway (Taniguchi et al., 2006). A metabolic response *via* PI3K is associated with phosphorylation of Akt and its downstream activation of AS160 to promote glucose uptake and GSK-3β to promote glycogen synthesis. A mitogenic response *via* MAPK is regulated by phosphorylation of Erk1/2 and p90RSK. Thus, by measuring the phosphorylation levels of these adaptor proteins in response to ligand stimulation, it is possible to discern which pathways are involved in signalling bias described above promoted by *cis* dicarba insulin analogues.

Dose-response effects of insulin, lispro (KP), glargine and their respective *cis* dicarba analogues were investigated using both IR-B overexpressing fibroblasts (Figs. 4.5–4.10) and IR-A overexpressing L6 myoblasts (Figs 4.11–4.16). Phosphorylation levels of selected key effector proteins involved in PI3K and MAPK pathways were measured and compared as percentage of phosphorylation when stimulated by native insulin at 100 nM concentration for 10 min (see simplified schematic diagram of PI3K/MAPK signalling in Fig. 1.16).

For the PI3K pathway, phosphorylation of Akt at Ser473 and Thr308 were detected separately. Activation of Akt is tightly associated with signalling *via* mTOR complex 1 and 2 (mTORC1 and mTORC2) (Yang et al., 2015, Vadlakonda et al., 2013, Laplante and Sabatini, 2012). Briefly, upon stimulation, PDK1 phosphorylates Akt at Thr308, partially activating Akt kinase activity. pAkt Thr308 in turn activates mTORC2 that acts as a positive feedback loop for the full activation of Akt by phosphorylating Ser473 (Yang et al., 2015). Activated Akt acts as a master kinase acting on an extensive range of downstream proteins involved in both mitogenic and metabolic responses. For instance, activated Akt can activate mTORC1 directly or indirectly *via* TSC2, and subsequently promotes responses key to cell growth and survival (Laplante and Sabatini, 2012, Potter et al., 2002). In this study, I also measured phosphorylation of S6 ribosomal at Ser235/236, a key downstream effector of Akt/mTORC1 activation for initiation of protein synthesis in cells (Yang et al., 2015).

Importantly, in response to insulin stimulation, Akt also plays a vital role in regulating glucose metabolism. Activated Akt promotes glycogen synthesis *via* phosphorylation (at Ser9) and inhibition of GSK-3β (Cross et al., 1995). Similarly, Akt can also phosphorylate AS160 at

multiple sites (Ser318, Ser570, Ser588, Thr642, and Thr751) increasing GLUT4 translocation to plasma membrane for glucose uptake in muscle and adipose tissue (Middelbeek et al., 2013, Kramer et al., 2006). Of the 5 phosphorylation sites, the phosphorylation at Thr642 (studied in this chapter) is one of the most crucial as it is required for interaction with 14-3-3 regulatory proteins necessary for GLUT4 translocation (Kramer et al., 2006, Ramm et al., 2006).

For the mitogenic MAPK pathway, activation and phosphorylation of Erk 1 (Thr202/Tyr204), Erk 2 (Thr185/Tyr187) and its downstream p90RSK (Ser380) were measured. Activation of the Erk/p90RSK family is a common indicator of mitogenic response stimulated by growth factors and hormones including insulin (Chang et al., 1995, Anjum and Blenis, 2008, Bedinger and Adams, 2015). In recent studies increased MAPK signalling was associated with increased cell proliferation when stimulated by a number of insulin analogues (Vigneri et al., 2010, Sciacca et al., 2010).

Overall in dose-response activation experiments, the *cis* dicarba analogues showed a trend of lower activation of both PI3K and MAPK pathways compared to their respective parent peptides, with a greater effect evident on the MAPK pathway (Figs. 4.5–4.16). Such differential potencies were seen in both tested cell types but were more evident in the IR-A overexpressing L6 myoblasts (Figs 4.11–4.16) than in IR-B overexpressing fibroblasts (Figs4.5–4.10). Of the three *cis* dicarba analogues, the *cis* dicarba insulin (IR-B: Figs. 4.5 and 4.6; IR-A: Figs. 4.11 and 4.12) and *cis* dicarba glargine (IR-B: Figs. 4.9 and 4.10; IR-A: Figs. 4.15 and 4.16) showed the most drastic reductions in activation of MAPK pathway, with significantly reduced phosphorylation levels of Erk 1, Erk 2 and p90RSK in the concentration range of 0.5 – 10 nM at t = 10 min (significance ranging from p* ≤ 0.05 to p**** ≤ 0.0001). Compared to the MAPK pathway, the difference in activation of PI3K between native parent peptides and their respective *cis* dicarba analogues was less distinctive. Significant difference (p* ≤ 0.05) in phosphorylation level of Akt at Ser473 was only evident at concentrations < 0.1 nM in both cell types. Interestingly, the dose-dependent effect was slightly more evident in phosphorylation of Akt at Thr308 (particularly for *cis* dicarba glargine).

Downstream of Akt, GSK-3β achieved maximal phosphorylation at Ser9 even at concentrations as low as 0.1 nM for all analogues. Hence, no potency differences between analogues were detected for GSK-3β. This is also the case for AS160 activation in IR-B cells. Phosphorylation of AS160 in L6 myoblasts was not detected.

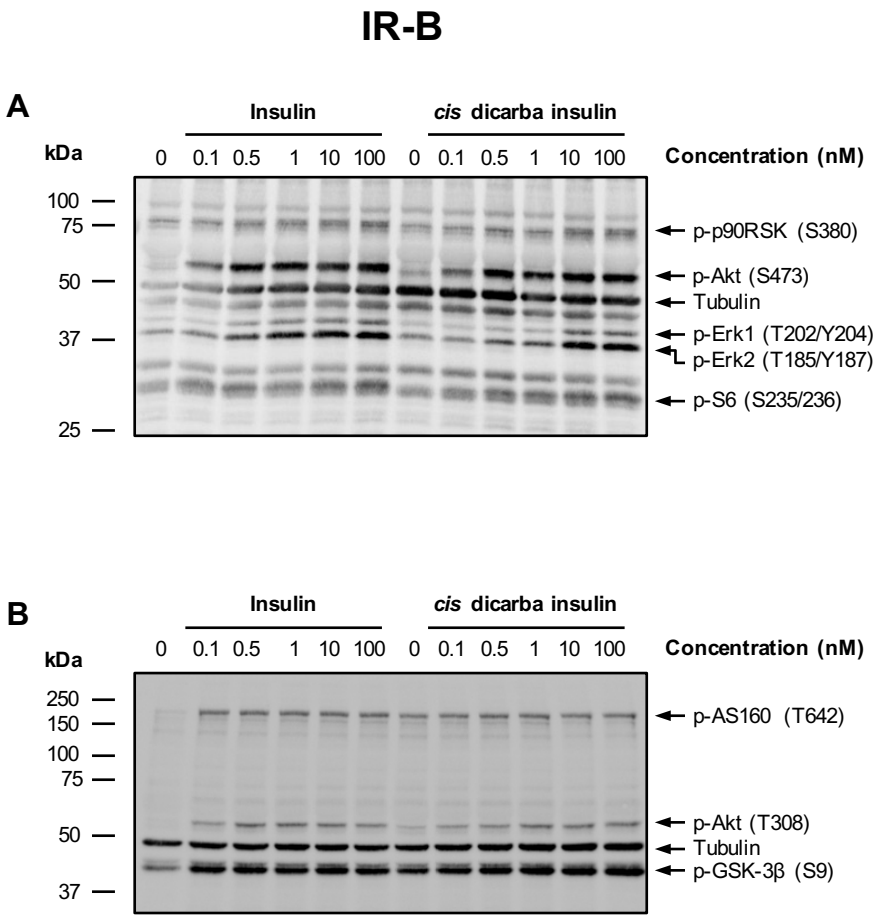

Figure 4.5 Representative western blot of IR-B stimulated by increasing concentration of insulin and *cis* dicarba insulin. Serum starved R⁻IR-B fibroblasts were stimulated with increasing concentrations (0, 0.1, 0.5 1, 10 and 100 nM) of insulin or *cis* dicarba insulin for 10 min. Whole cells lysates were prepared and 20 mg of each sample were separated in duplicate 10% glycine gels followed by immunoblotting. Blot (A) probed with Pathscan® Multiplex Western Cocktail allowed detection of phospho-p90RSK (S380), phospho-Akt (S473), phospho-ERK1 (T202/Y204), phospho-ERK2 (T185/Y187) and phospho-S6 ribosomal (S235/236) simultaneously. Blot (B) was probed for phospho-AS160 (T642), phospho-Akt (T308) and phospho-GSK3b (S9). Each blot was also probed with anti-b-Tubulin as loading control. All repeat blots were included in *Appendix Figure 4.1*.

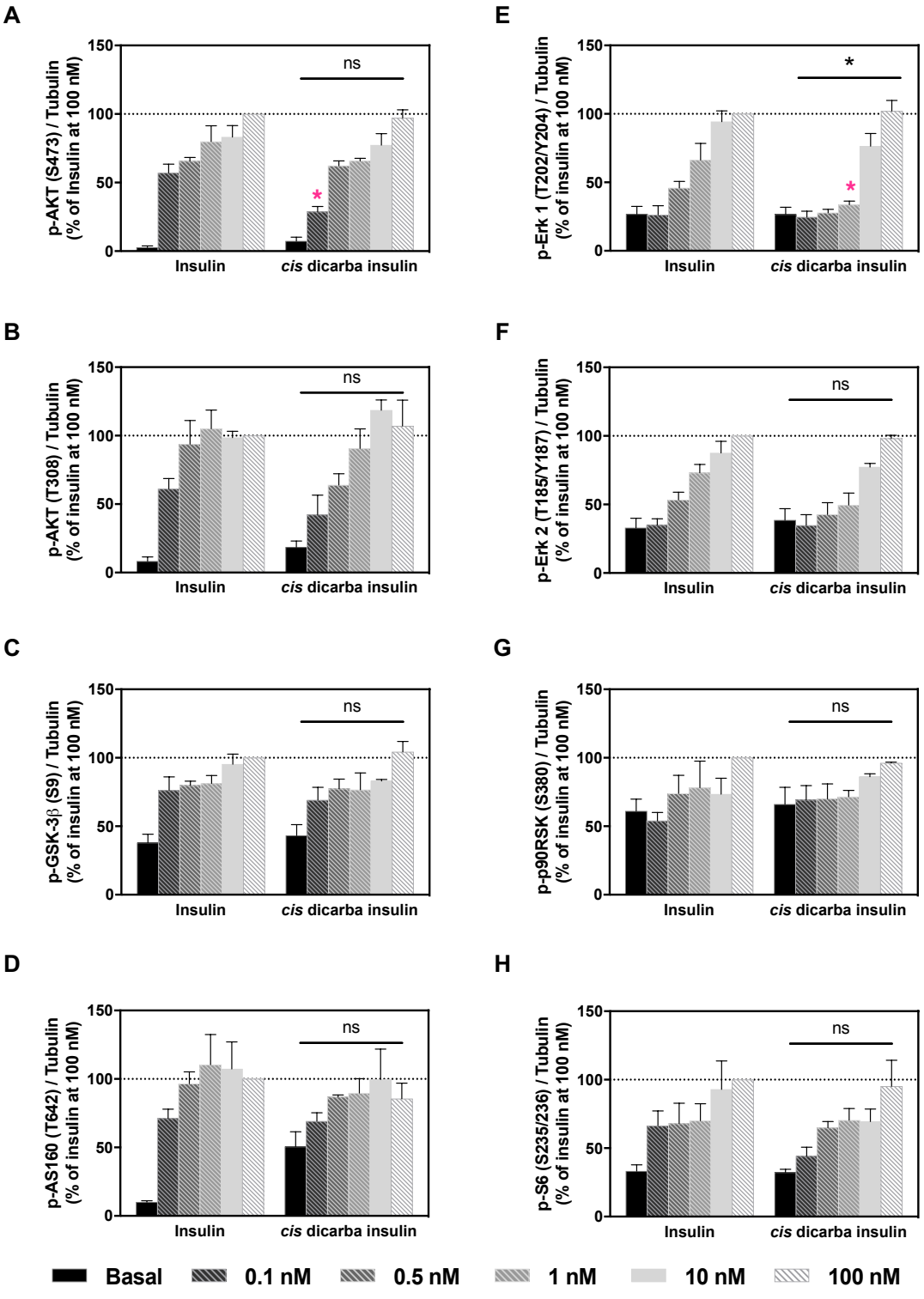
A
p-AKT (S473) / Tubulin (% of insulin at 100 nM)
ns
*
Insulin
cis dicarba insulin
E
p-Erk 1 (T202/Y204) / Tubulin (% of insulin at 100 nM)
*
*
Insulin
cis dicarba insulin
B
p-AKT (T308) / Tubulin (% of insulin at 100 nM)
ns
Insulin
cis dicarba insulin
F
p-Erk 2 (T185/Y187) / Tubulin (% of insulin at 100 nM)
ns
Insulin
cis dicarba insulin
C
p-GSK-3β (S9) / Tubulin (% of insulin at 100 nM)
ns
Insulin
cis dicarba insulin
G
p-p90RSK (S380) / Tubulin (% of insulin at 100 nM)
ns
Insulin
cis dicarba insulin
D
p-AS160 (T642) / Tubulin (% of insulin at 100 nM)
ns
Insulin
cis dicarba insulin
H
p-S6 (S235/236) / Tubulin (% of insulin at 100 nM)
ns
Insulin
cis dicarba insulin
150
100
50
0
Basal
0.1 nM
0.5 nM
1 nM
10 nM
100 nM

Figure 4.6 Quantitation of IR-B dose-response signalling stimulated by insulin and *cis* dicarba insulin. Quantitation of western blots presented in *Figure 4.5* and *Appendix Figure 4.1*. Serum starved R^- IR-B fibroblasts were stimulated with increasing concentrations (0, 0.1, 0.5 1, 10 and 100 nM) of insulin or *cis* dicarba insulin for 10 min. Phosphorylation levels of (A) Akt (phosho-S473), (B) Akt (phosho-T308), (C) GSK-3β (phospho-S9), (D) AS160 (phospho-T642), (E) Erk 1 (phospho-T202/Y204), (F) Erk2 (phsopho-T185/Y187), (G) p90RSK (phospho-S380) and (H) S6 ribosomal (phospho-S235/236) are expressed as percentage of level detected when cells were stimulated with 100 nM of insulin for 10 min. All data are the mean ± S.E.M presented as bar graphs. n = at least 3 independent experiments. In each case, data are normalized to the loading control β-tubulin. Statistical significance of the overall difference in phosphorylation levels stimulated by *cis* dicarba insulin compared to native insulin was determined *via* 2-way ANOVA (bars above graph); difference comparing each stimulating concentration (pink asterisks) were further analyzed using Holm-Sidak test. ns: non significant; * $P \leq 0.05$.

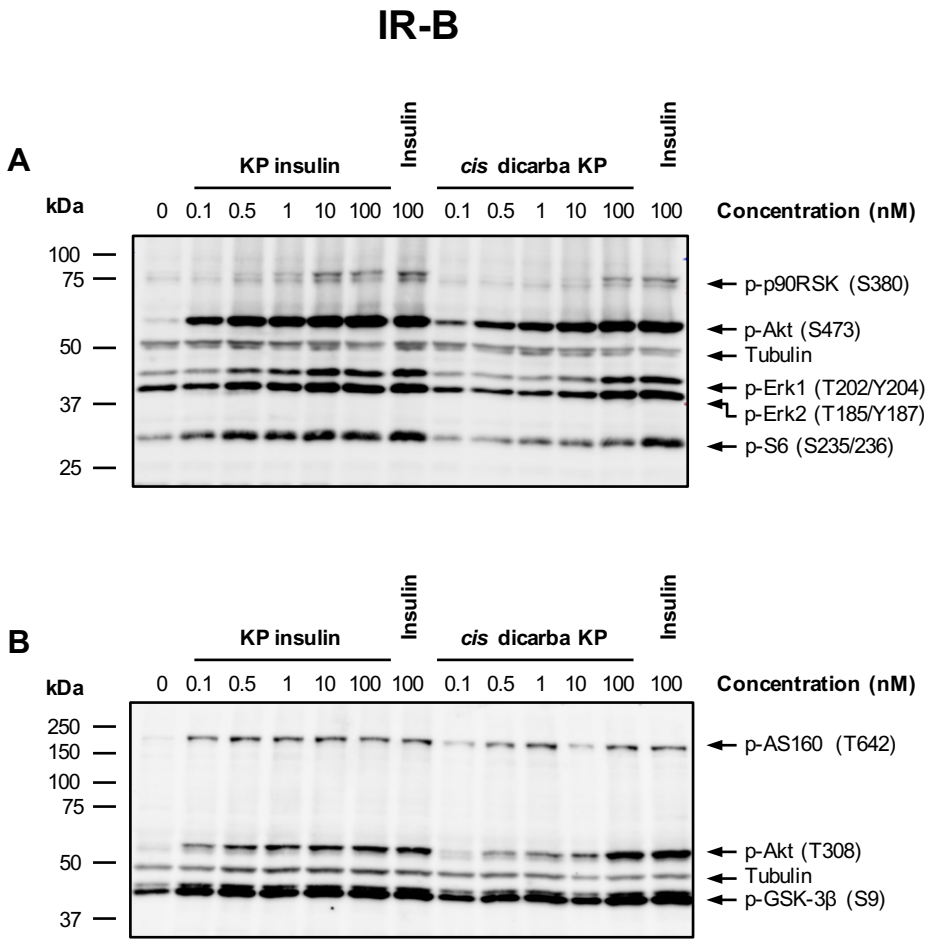

Figure 4.7 Representative western blot of IR-B stimulated by increasing concentration of lispro (KP) insulin and *cis* dicarba KP insulin. Serum starved R⁻IR-B fibroblasts were stimulated with increasing concentrations (0, 0.1, 0.5 1, 10 and 100 nM) of KP insulin or *cis* dicarba KP insulin for 10 min. Stimulation by 100 nM of insulin was also included as a control and for normalization to obtained relative phosphorylation levels of of each protein when stimulated by different insulin analogues. Whole cells lysates were prepared and 20 mg of each sample were separated in duplicate 10% glycine gels followed by immunoblotting. Blot (A) probed with Pathscan® Multiplex Western Cocktail allowed detection of phospho-p90RSK (S380), phospho-Akt (S473), phospho-ERK1 (T202/Y204), phospho-ERK2 (T185/Y187) and phospho-S6 ribosomal (S235/236) simultaneously. Blot (B) was probed for phospho-AS160 (T642), phospho-Akt (T308) and phospho-GSK3b (S9). Each blot was also probed with anti-b-Tubulin as loading control. All repeat blots were included in *Appendix Figure 4.2*.

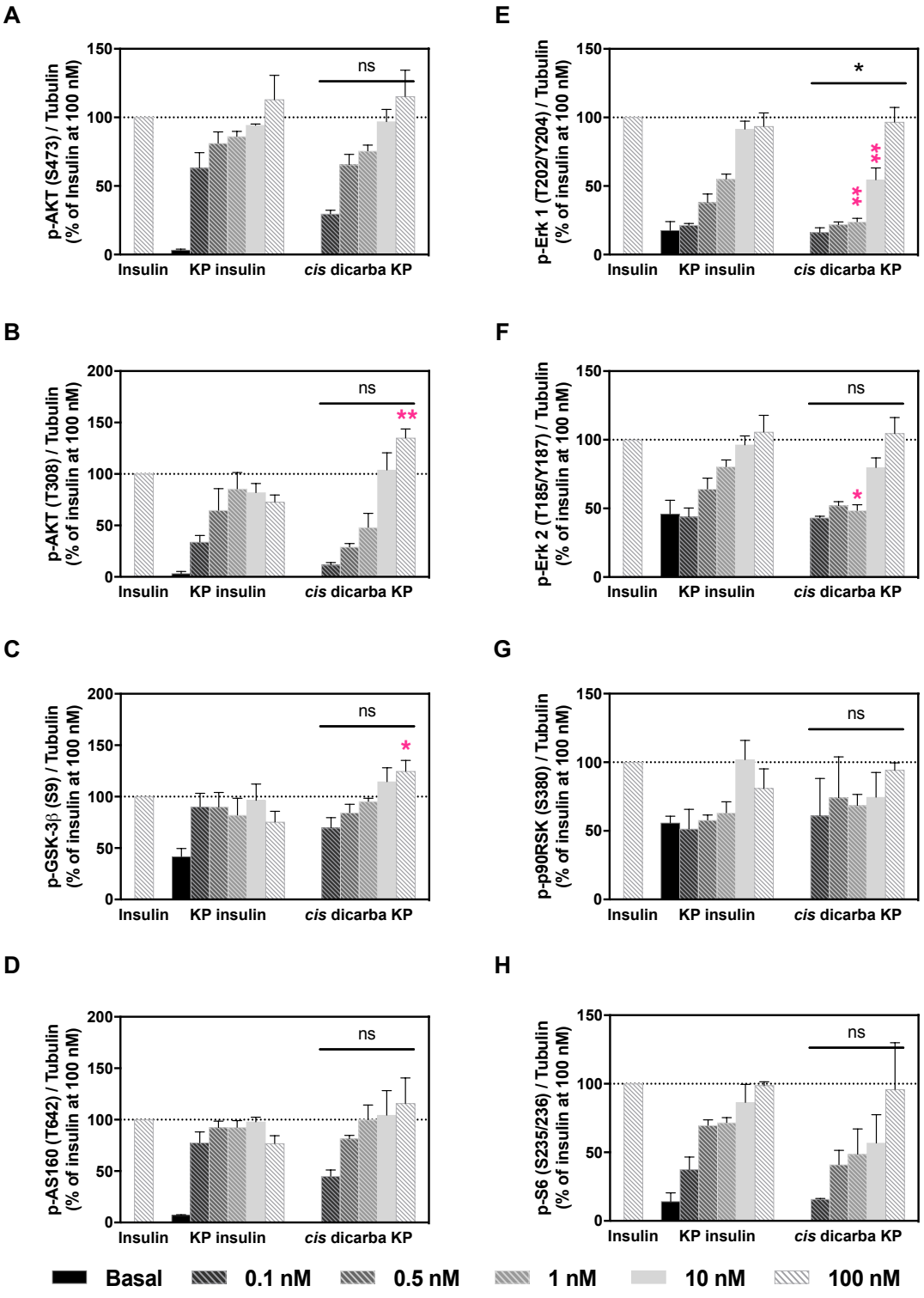
A
p-AKT (S473) / Tubulin (% of Insulin at 100 nM)
ns
Insulin
KP insulin
cis dicarba KP
B
p-AKT (T308) / Tubulin (% of insulin at 100 nM)
ns
**
C
p-GSK-3β (S9) / Tubulin (% of insulin at 100 nM)
ns
*
D
p-AS160 (T642) / Tubulin (% of insulin at 100 nM)
ns
E
p-Erk 1 (T202/Y204) / Tubulin (% of insulin at 100 nM)
*
**
**
F
p-Erk 2 (T185/Y187) / Tubulin (% of insulin at 100 nM)
ns
*
G
p-p90RSK (S380) / Tubulin (% of insulin at 100 nM)
ns
H
p-S6 (S235/236) / Tubulin (% of insulin at 100 nM)
ns
Basal
0.1 nM
0.5 nM
1 nM
10 nM
100 nM

Figure 4.8 Quantitation of IR-B dose-response signalling analyses stimulated by lispro (KP) insulin and *cis* dicarba KP insulin. Quantitation of western blots presented in *Figure 4.7* and *Appendix Figure 4.2*. Serum starved R$^-$IR-B fibroblasts were stimulated increasing concentrations (0, 0.1, 0.5 1, 10 and 100 nM) KP insulin or *cis* dicarba KP insulin for 10 min. Stimulation with 100 nM of insulin were also included as a control and for normalization to obtained relative phosphorylation levels of of each protein when stimulated by different insulin analogues. Phosphorylation levels of (A) Akt (phosho-S473), (B) Akt (phosho-T308), (C) GSK-3β (phospho-S9), (D) AS160 (phospho-T642), (E) Erk 1 (phospho-T202/Y204), (F) Erk2 (phsopho-T185/Y187), (G) p90RSK (phospho-S380) and (H) S6 ribosomal (phospho-S235/236) are expressed as percentage of level detected when cells were stimulated with 100 nM of insulin for 10 min. All data are the mean ± S.E.M presented as bar graphs. n = at least 3 independent experiments. In each case, data are normalized to the loading control β-tubulin. Representative blots are shown in *Figure 4.7*. Statistical significance of the overall difference in phosphorylation levels stimulated by *cis* dicarba KP insulin compared to KP insulin was determined *via* 2-way ANOVA (bars above graph); difference comparing each stimulating concentration (pink asterisks) were further analyzed using Holm-Sidak test. ns: non significant; * $P \leq 0.05$; ** $P \leq 0.01$.

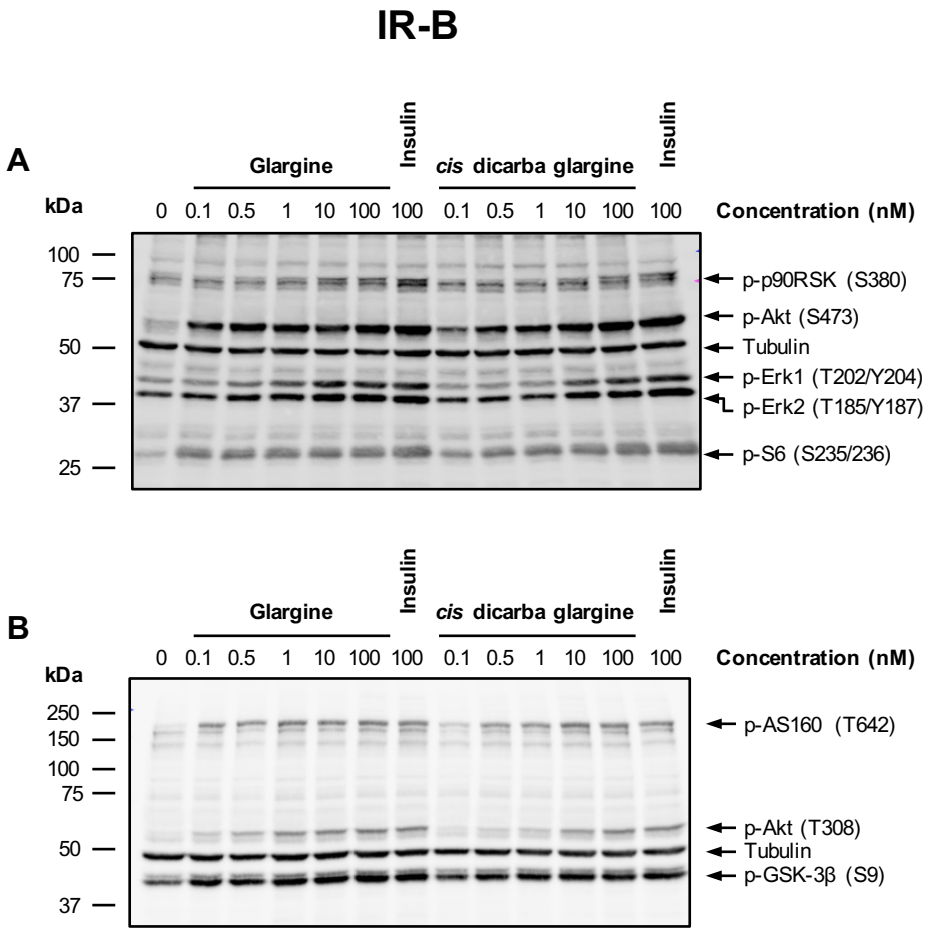

Figure 4.9 Representative western blot of IR-B stimulated by increasing concentration of glargine insulin and *cis* dicarba glargine insulin. Serum starved R⁻IR-B fibroblasts were stimulated with increasing concentrations (0, 0.1, 0.5 1, 10 and 100 nM) of glargine insulin or *cis* dicarba glargine insulin for 10 min. Stimulation with 100 nM of insulin were also included as a control and for normalization to obtained relative phosphorylation levels of of each protein when stimulated by different insulin analogues. Whole cells lysates were prepared and 20 mg of each sample were separated in duplicate 10% glycine gels followed by immunoblotting. Blot (A) probed with Pathscan® Multiplex Western Cocktail allowed detection of phospho-p90RSK (S380), phospho-Akt (S473), phospho-ERK1 (T202/Y204), phospho-ERK2 (T185/Y187) and phospho-S6 ribosomal (S235/236) simultaneously. Blot (B) was probed for phospho-AS160 (T642), phospho-Akt (T308) and phospho-GSK3b (S9). Each blot was also probed with anti-b-Tubulin as loading control. All repeat blots were included in *Appendix Figure 4.3.*

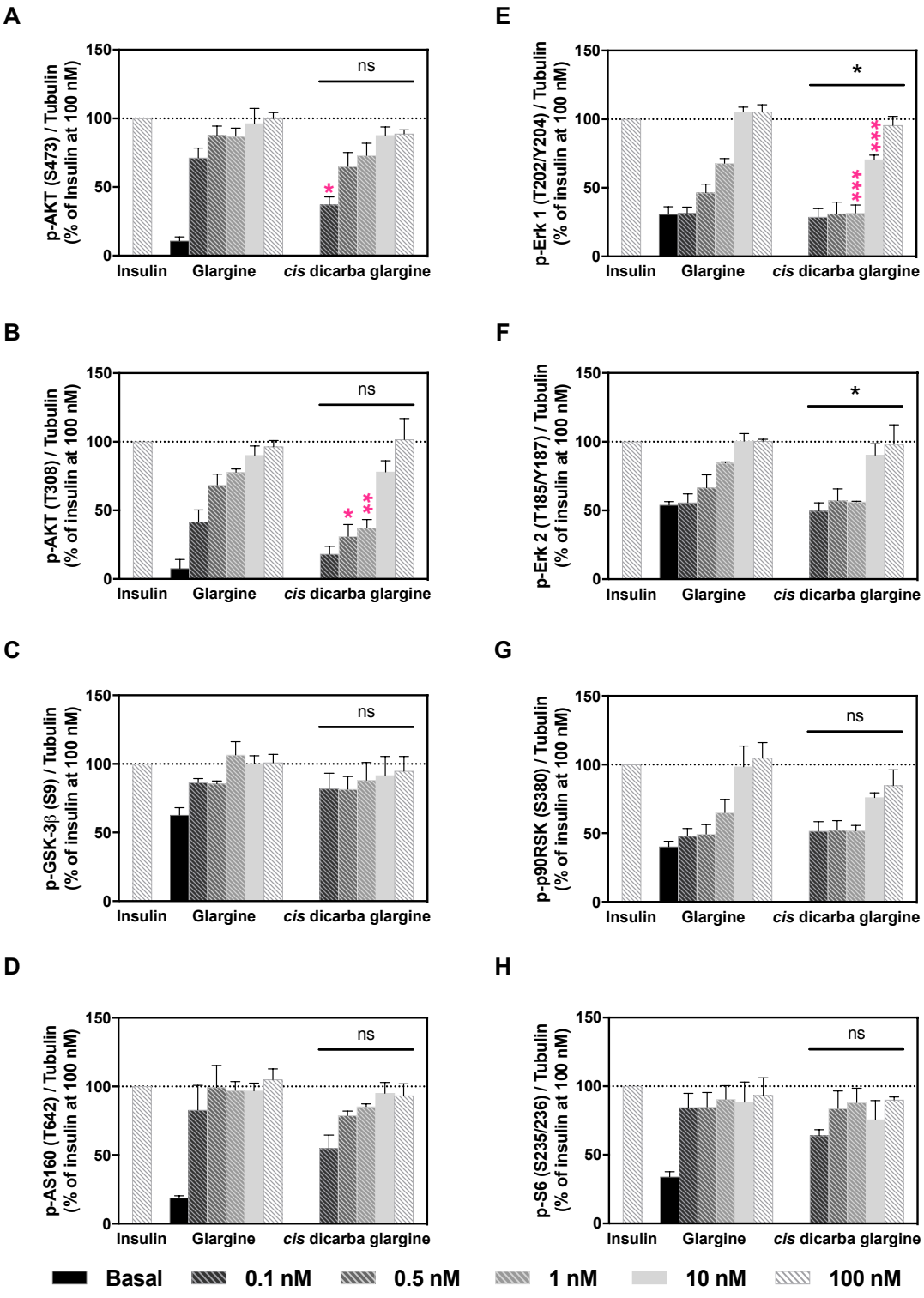
A
p-AKT (S473) / Tubulin (% of Insulin at 100 nM)
ns
*
B
p-AKT (T308) / Tubulin (% of insulin at 100 nM)
ns
*
**
C
p-GSK-3β (S9) / Tubulin (% of insulin at 100 nM)
ns
D
p-AS160 (T642) / Tubulin (% of insulin at 100 nM)
ns
E
p-Erk 1 (T202/Y204) / Tubulin (% of insulin at 100 nM)
*
***
***
F
p-Erk 2 (T185/Y187) / Tubulin (% of insulin at 100 nM)
*
G
p-p90RSK (S380) / Tubulin (% of insulin at 100 nM)
ns
H
p-S6 (S235/236) / Tubulin (% of insulin at 100 nM)
ns
150
100
50
0
Insulin
Glargine
cis dicarba glargine
Basal
0.1 nM
0.5 nM
1 nM
10 nM
100 nM

Figure 4.10 Quantitation of IR-B dose-response signalling analyses stimulated by glargine insulin and *cis* dicarba glargine insulin. Quantitation of western blots presented in *Figure 4.9* and *Appendix Figure 4.3*. Serum starved R$^-$IR-B fibroblasts were stimulated with increasing concentrations (0, 0.1, 0.5 1, 10 and 100 nM) of glargine insulin or *cis* dicarba glargine insulin for 10 min. Phosphorylation levels of (A) Akt (phosho-S473), (B) Akt (phosho-T308), (C) GSK-3β (phospho-S9), (D) AS160 (phospho-T642), (E) Erk 1 (phospho-T202/Y204), (F) Erk2 (phsopho-T185/Y187), (G) p90RSK (phospho-S380) and (H) S6 ribosomal (phospho-S235/236) are expressed as percentage of level detected when cells were stimulated with 100 nM of insulin for 10 min. All data are the mean ± S.E.M presented as bar graphs. n = at least 3 independent experiments. In each case, data are normalized to the loading control β-tubulin. Representative blots are shown in *Figure 4.9*. Statistical significance of the overall difference in phosphorylation levels stimulated by *cis* dicarba glargine compared to glargine insulin was determined *via* 2-way ANOVA (bars above graph); difference comparing each stimulating concentration (pink asterisks) were further analyzed using Holm-Sidak test. ns: non significant; * $P \leq 0.05$; ** $P \leq 0.01$; *** $P \leq 0.001$.

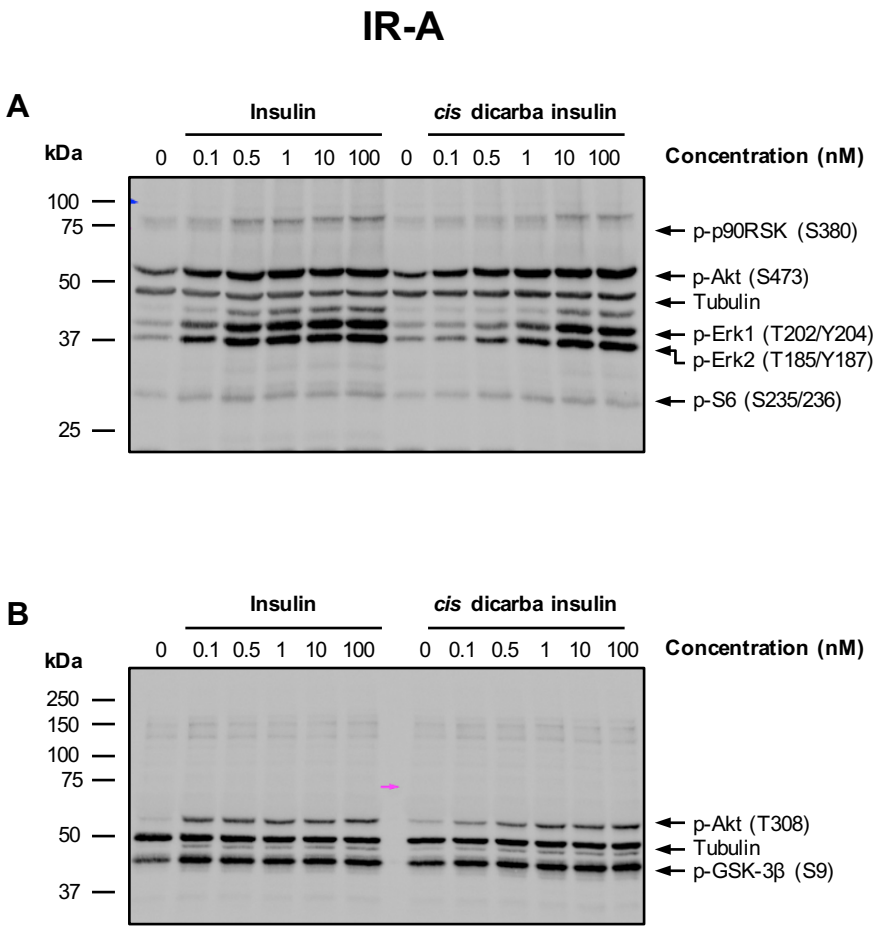

Figure 4.11 Representative western blot of IR-A stimulated by increasing concentration of insulin and *cis* dicarba insulin. Serum starved IR-A overexpressing L6 myoblasts (hIR-A L6) were stimulated with increasing concentrations (0, 0.1, 0.5 1, 10 and 100 nM) of insulin or *cis* dicarba insulin for 10 min. Whole cells lysates were prepared and 20 mg of each sample were separated in duplicate 10% glycine gels followed by immunoblotting. Blot (A) probed with Pathscan® Multiplex Western Cocktail allowed detection of phospho-p90RSK (S380), phospho-Akt (S473), phospho-ERK1 (T202/Y204), phospho-ERK2 (T185/Y187) and phospho-S6 ribosomal (S235/236) simultaneously. Blot (B) was probed for phospho-AS160 (T642), phospho-Akt (T308) and phospho-GSK3b (S9). Each blot was also probed with anti-b-Tubulin as loading control. All repeat blots were included in *Appendix Figure 4.4*. Pink arrow aligns to 75 kDa marker.

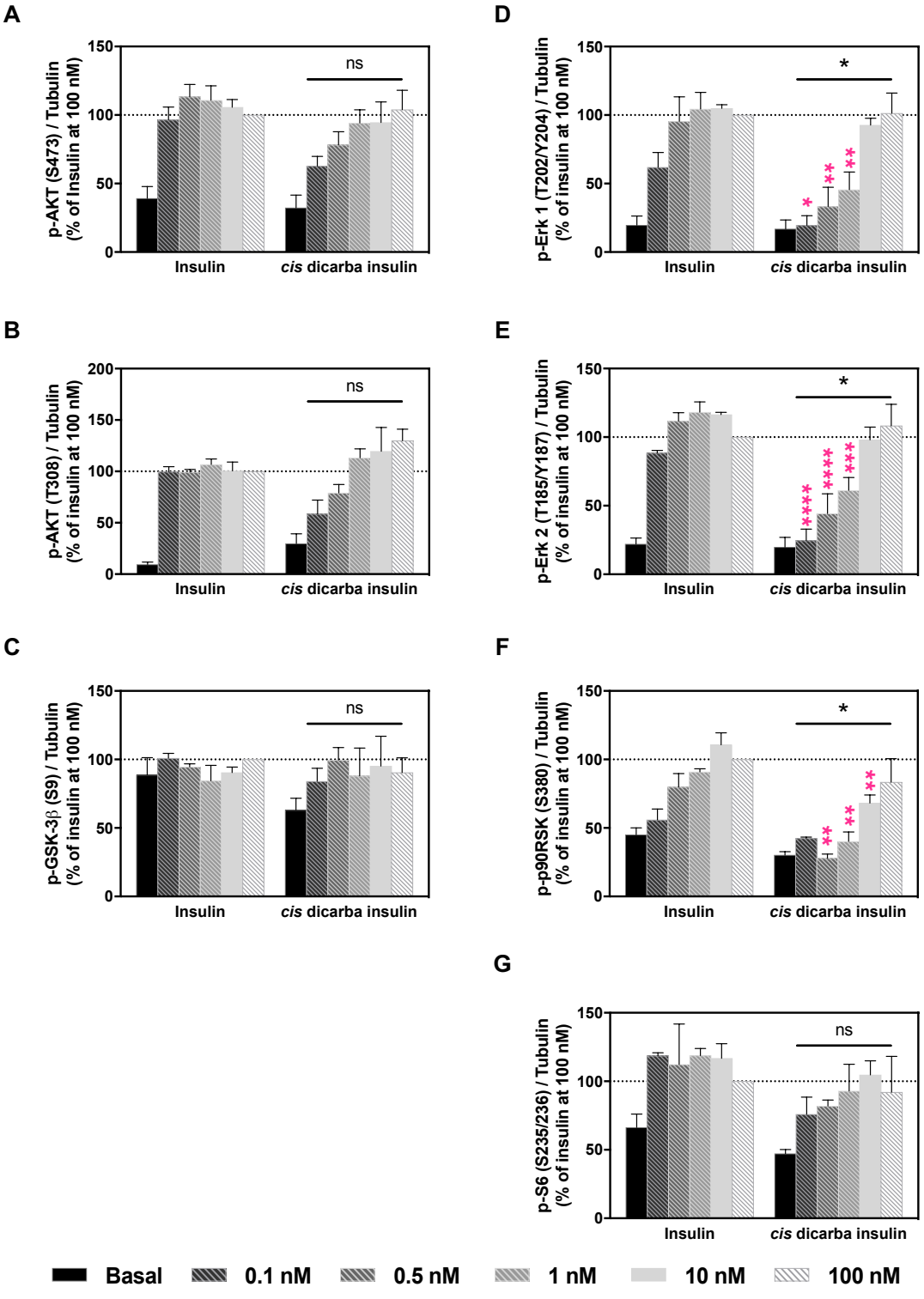
A
p-AKT (S473) / Tubulin (% of Insulin at 100 nM)
ns
Insulin
cis dicarba insulin
D
p-Erk 1 (T202/Y204) / Tubulin (% of insulin at 100 nM)
*
B
p-AKT (T308) / Tubulin (% of insulin at 100 nM)
E
p-Erk 2 (T185/Y187) / Tubulin (% of insulin at 100 nM)
C
p-GSK-3β (S9) / Tubulin (% of insulin at 100 nM)
F
p-p90RSK (S380) / Tubulin (% of insulin at 100 nM)
G
p-S6 (S235/236) / Tubulin (% of insulin at 100 nM)
Basal
0.1 nM
0.5 nM
1 nM
10 nM
100 nM

Figure 4.12 Quantitation of IR-A dose-response signalling analyses stimulated by insulin and *cis* dicarba insulin. Quantitation of western blots presented in *Figure* 4.11 and *Appendix Figure 4.4.* Serum starved IR-A overexpressing L6 myoblasts were stimulated with increasing concentrations (0, 0.1, 0.5 1, 10 and 100 nM) of insulin or *cis* dicarba insulin for 10 min. Phosphorylation levels of (A) Akt (phosho-S473), (B)Akt (phosho-T308), (C) GSK-3β (phospho-S9), (D) AS160 (phospho-T642), (E) Erk 1 (phospho-T202/Y204), (F) Erk2 (phsopho-T185/Y187), (G) p90RSK (phospho-S380) and (H) S6 ribosomal (phospho-S235/236) are expressed as percentage of level detected when cells were stimulated with 100 nM of insulin for 10 min. All data are the mean ± S.E.M presented as bar graphs. n = at least 3 independent experiments. In each case, data are normalized to the loading control β-tubulin. Representative blots are shown in *Figure 4.11.* Statistical significance of the overall difference in phosphorylation levels stimulated by *cis* dicarba insulin compared to native insulin were determined *via* 2-way ANOVA (bars above graph); difference comparing each stimulating concentration (pink asterisks) were further analyzed using Holm-Sidak test. ns: non significant; * ($P \leq 0.05$), ** ($P \leq 0.01$); *** ($P \leq 0.001$); **** ($P \leq 0.0001$).

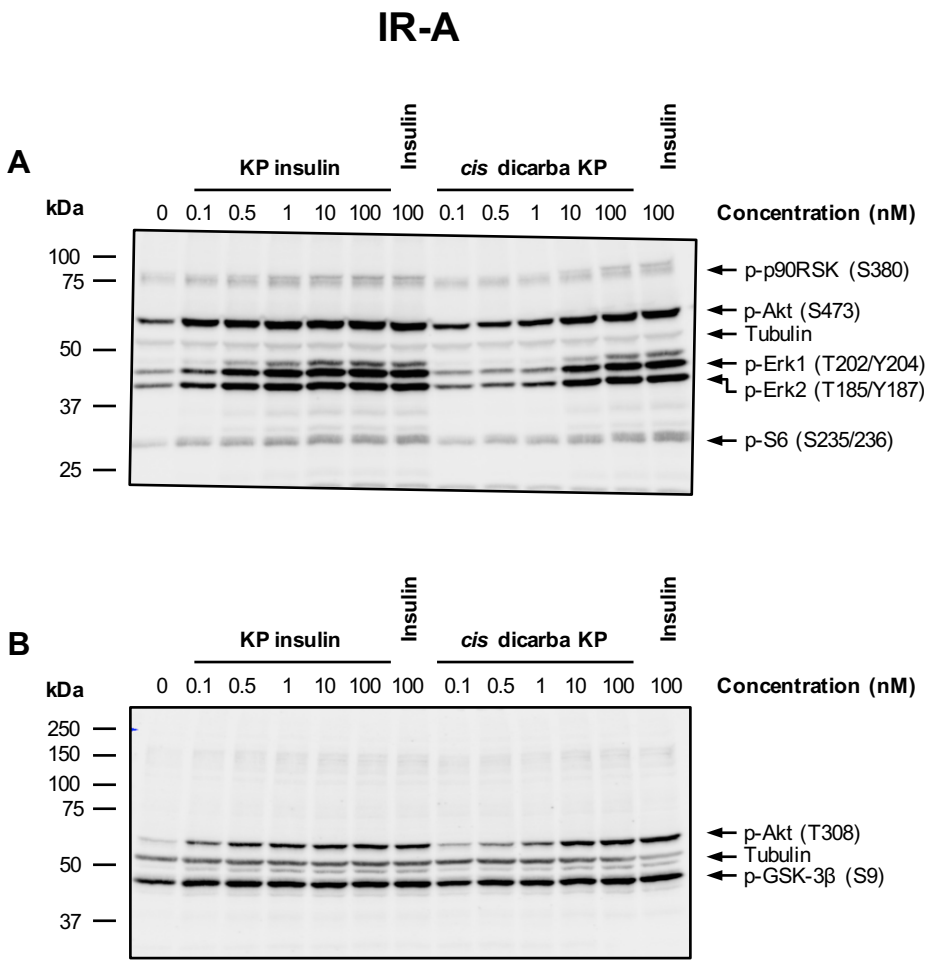

Figure 4.13 Representative western blot of IR-A stimulated by increasing concentration of lispro (KP) insulin and *cis* dicarba KP insulin. Serum starved IR-A overexpressing L6 myoblasts (hIR-A L6) were stimulated with increasing concentrations (0, 0.1, 0.5 1, 10 and 100 nM) of KP insulin or *cis* dicarba KP insulin for 10 min. Stimulation with 100 nM of insulin were also included as a control and for normalization to obtained relative phosphorylation levels of of each protein when stimulated by different insulin analogues. Whole cells lysates were prepared and 20 mg of each sample were separated in duplicate 10% glycine gels followed by immunoblotting. Blot (A) probed with Pathscan® Multiplex Western Cocktail allowed detection of phospho-p90RSK (S380), phospho-Akt (S473), phospho-ERK1 (T202/Y204), phospho-ERK2 (T185/Y187) and phospho-S6 ribosomal (S235/236) simultaneously. Blot (B) was probed for phospho-AS160 (T642), phospho-Akt (T308) and phospho-GSK3b (S9). Each blot was also probed with anti-b-Tubulin as loading control. All repeat blots were included in *Appendix Figure 4.5*.

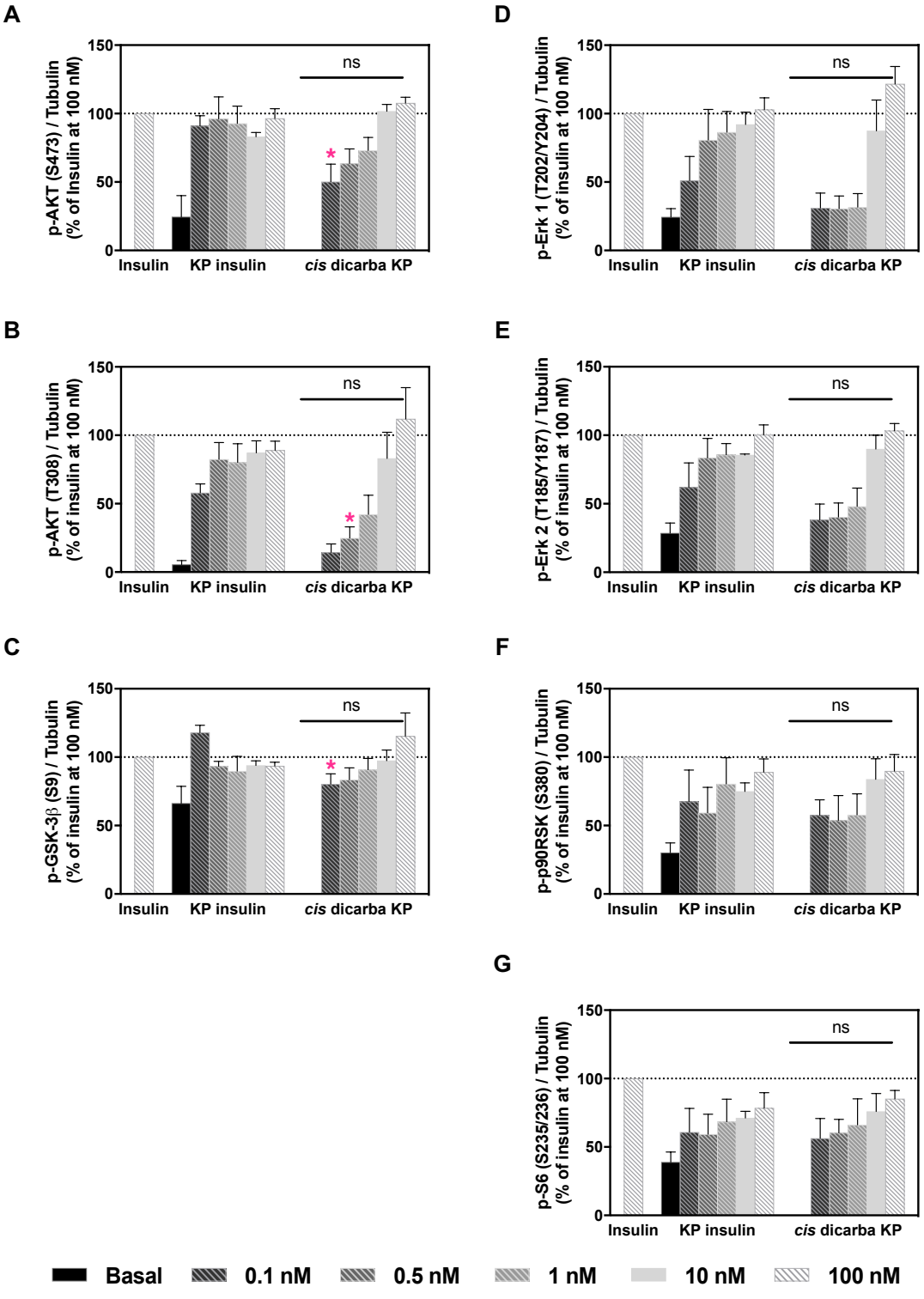
A
p-AKT (S473) / Tubulin (% of Insulin at 100 nM)
B
p-AKT (T308) / Tubulin (% of insulin at 100 nM)
C
p-GSK-3β (S9) / Tubulin (% of insulin at 100 nM)
D
p-Erk 1 (T202/Y204) / Tubulin (% of insulin at 100 nM)
E
p-Erk 2 (T185/Y187) / Tubulin (% of insulin at 100 nM)
F
p-p90RSK (S380) / Tubulin (% of insulin at 100 nM)
G
p-S6 (S235/236) / Tubulin (% of insulin at 100 nM)
150
100
50
0
ns
*
Insulin
KP insulin
cis dicarba KP
Basal
0.1 nM
0.5 nM
1 nM
10 nM
100 nM

Figure 4.14 Quantitation of IR-A dose-response signalling analyses stimulated by lispro (KP) insulin and *cis* dicarba KP insulin. Quantitation of western blots presented in *Figure 4.13* and *Appendix Figure 4.5*. Serum starved IR-A overexpressing L6 myoblasts were stimulated with increasing concentrations (0, 0.1, 0.5 1, 10 and 100 nM) of KP insulin or *cis* dicarba KP insulin for 10 min. Phosphorylation levels of (A) Akt (phosho-S473), (B)Akt (phosho-T308), (C) GSK-3β (phospho-S9), (D) AS160 (phospho-T642), (E) Erk 1 (phospho-T202/Y204), (F) Erk2 (phsopho-T185/Y187), (G) p90RSK (phospho-S380) and (H) S6 ribosomal (phospho-S235/236) are expressed as percentage of level detected when cells were stimulated with 100 nM of insulin for 10 min. All data are the mean ± S.E.M presented as bar graphs. n = at least 3 independent experiments. In each case, data are normalized to the loading control β-tubulin. Representative blots are shown in *Figure 4.7*. Statistical significance of the overall difference in phosphorylation levels stimulated by *cis* dicarba KP insulin compared to KP insulin were determined *via* 2-way ANOVA (bars above graph); difference comparing each stimulating concentration (pink asterisks) were further analyzed using Holm-Sidak test. ns: non significant; * ($P \leq 0.05$).

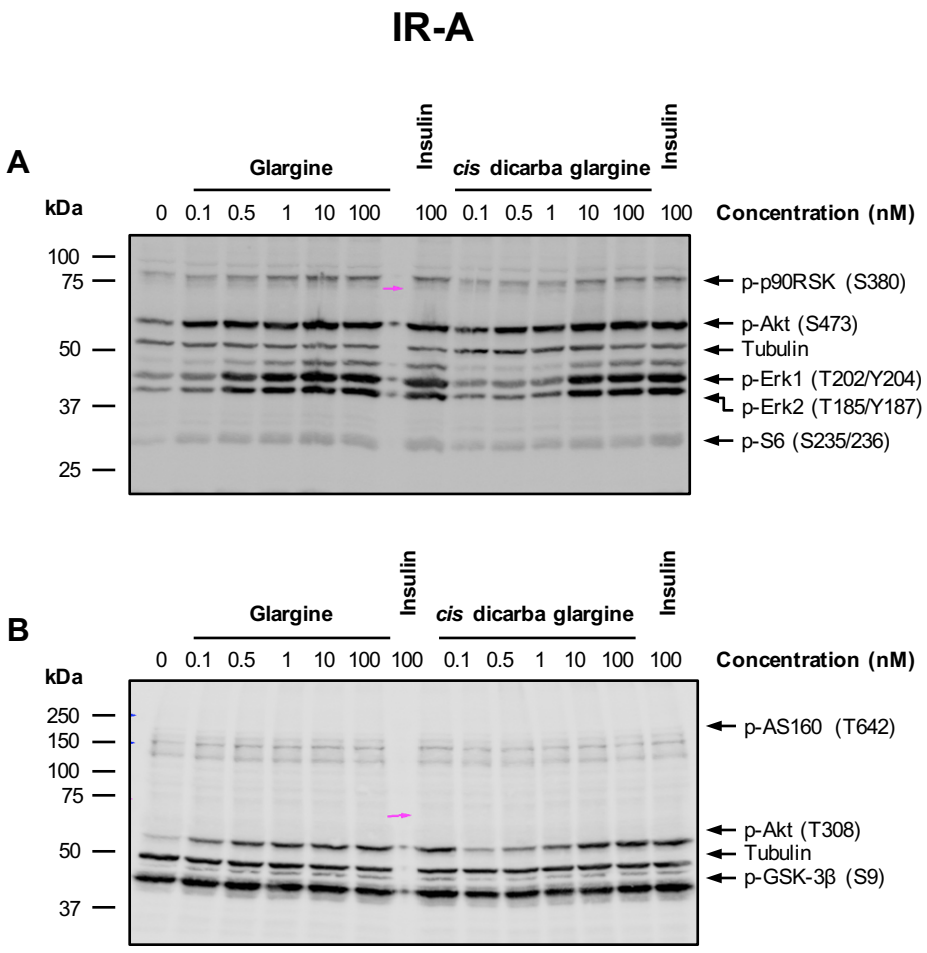

Figure 4.15 Representative western blot of IR-A stimulated by increasing concentration of glargine insulin and *cis* dicarba glargine insulin. Serum starved IR-A overexpressing L6 myoblasts (hIR-A L6) were stimulated with increasing concentrations (0, 0.1, 0.5 1, 10 and 100 nM) of glargine insulin or *cis* dicarba glargine insulin for 10 min. Stimulation with 100 nM of insulin were also included as a control and for normalization to obtained relative phosphorylation levels of of each protein when stimulated by different insulin analogues. Whole cells lysates were prepared and 20 mg of each sample were separated in duplicate 10% glycine gels followed by immunoblotting. Blot (A) probed with Pathscan® Multiplex Western Cocktail allowed detection of phospho-p90RSK (S380), phospho-Akt (S473), phospho-ERK1 (T202/Y204), phospho-ERK2 (T185/Y187) and phospho-S6 ribosomal (S235/236) simultaneously. Blot (B) was probed for phospho-AS160 (T642), phospho-Akt (T308) and phospho-GSK3b (S9). Each blot was also probed with anti-b-Tubulin as loading control. All repeat blots were included in *Appendix Figure 4.6*. Pink arrows align to 75 kDa marker.

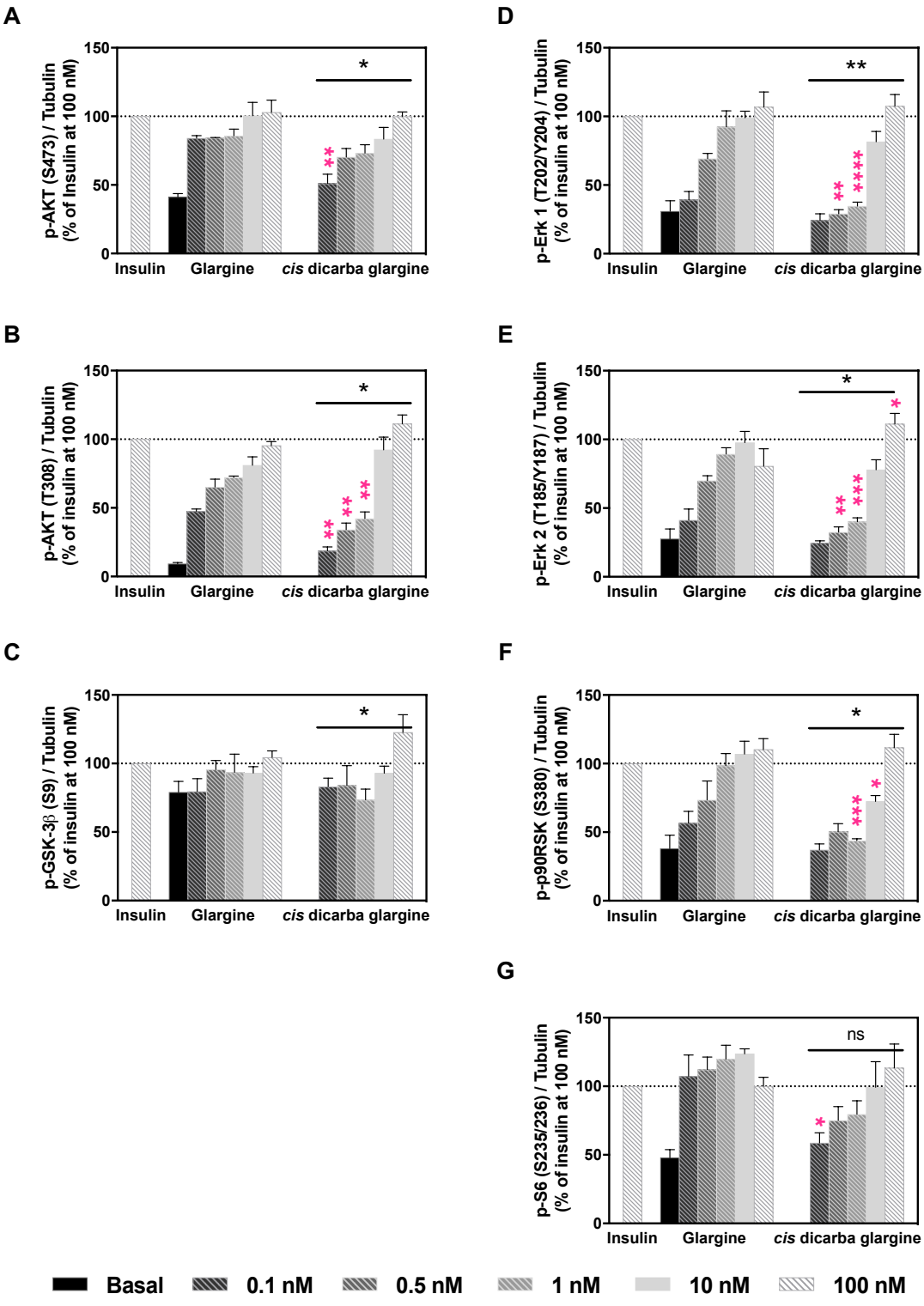
A
p-AKT (S473) / Tubulin (% of Insulin at 100 nM)
B
p-AKT (T308) / Tubulin (% of insulin at 100 nM)
C
p-GSK-3β (S9) / Tubulin (% of insulin at 100 nM)
D
p-Erk 1 (T202/Y204) / Tubulin (% of insulin at 100 nM)
E
p-Erk 2 (T185/Y187) / Tubulin (% of insulin at 100 nM)
F
p-p90RSK (S380) / Tubulin (% of insulin at 100 nM)
G
p-S6 (S235/236) / Tubulin (% of insulin at 100 nM)
150
100
50
0
Insulin
Glargine
cis dicarba glargine
*
**
***
****
ns
Basal
0.1 nM
0.5 nM
1 nM
10 nM
100 nM

Figure 4.16 Quantitation of IR-A dose-response signalling analyses stimulated by glargine insulin and *cis* dicarba glargine insulin. Quantitation of western blots presented in *Figure 4.15* and *Appendix Figure 4.6*. Serum starved IR-A overexpressing L6 myoblasts were stimulated with increasing concentrations (0, 0.1, 0.5 1, 10 and 100 nM) of glargine insulin or *cis* dicarba glargine insulin for 10 min. Phosphorylation levels of (A) Akt (phosho-S473), (B)Akt (phosho-T308), (C) GSK-3β (phospho-S9), (D) AS160 (phospho-T642), (E) Erk 1 (phospho-T202/Y204), (F) Erk2 (phsopho-T185/Y187), (G) p90RSK (phospho-S380) and (H) S6 ribosomal (phospho-S235/236) are expressed as percentage of level detected when cells were stimulated with 100 nM of insulin for 10 min. All data are the mean ± S.E.M presented as bar graphs. n = at least 3 independent experiments. In each case, data are normalized to the loading control β-tubulin. Representative blots are shown in *Figure 4.15.* Statistical significance of the overall difference in phosphorylation levels stimulated by *cis* dicarba glargine compared to glargine insulin were determined *via* 2-way ANOVA (bars above graph); difference comparing each stimulating concentration (pink asterisks) were further analyzed using Holm-Sidak test. ns: non significant; * $P \leq 0.05$; ** $P \leq 0.01$; *** $P \leq 0.001$; **** $P \leq 0.0001$

4.3.6 Time-course effects on PI3K and MAPK signalling

Outline: Cis dicarba insulin and cis dicarba glargine insulin showed significantly delayed activation of MAPK signalling in IR-A overexpressing cells.

Following the investigation of dose-dependent response of *cis* dicarba analogues, I was also interested in comparing the kinetics of PI3K and MAPK signalling stimulated by *cis* dicarba insulin (native insulin, Fig. 4.17; *cis* dicarba insulin, Fig. 4.18) and *cis* dicarba glargine insulin (glargine, Fig. 4.19; *cis* dicarba glargine, Fig. 4.20). For this study, the kinetics were investigated in IR-A overexpressing L6 myoblasts stimulated with a constant 10 nM concentration of ligand at time course of t = 0, 0.33 (20s), 0.5 (30s), 1, 3, 5, 8, 10, 20 and 30 min. At a glance, the kinetics between PI3K (Fig. 4.21) and MAPK (Fig. 4.22) signalling were quite different; Akt and GSK-3β showed a rapid response reaching optimal phosphorylation within 20s post-stimulation and remained at maximal phosphorylation throughout the duration of experiment up to t = 30 min. On the other hand, phosphorylation of Erk1/2 and p90RSK progressed gradually, reaching maximal phosphorylation at t = 10 min post-stimulation and then reducing at t = 10 – 30 min.

The time-course analyses supported the findings from dose-response analyses presented above, although the differences between *cis* dicarba analogues and their parent peptides with respect to their intracellular signalling behaviour were more apparent in the time-course analyses (Figs. 4.17–4.22). The kinetics of activation of the Akt pathway (p-Akt (Ser473), p-Akt (Thr308), p-GSK3β (Ser9) and p-S6 (Ser235/236)) were essentially the same for insulin, *cis* dicarba insulin and *cis* dicarba glargine (Fig 4.21), with the exception of p-Akt (Ser473), which did not reach the same level of maximal phosphorylation when stimulated by *cis* dicarba insulin compared to insulin (Fig. 4.21). Phosphorylation kinetics of Akt (Ser473 and Thr308) and GSK-3β are similar, achieving maximal activation rapidly within 20s and maintaining high level of activation throughout the time-course. This is consistent with the ability of *cis* dicarba analogues to maintain a high level of metabolic activity *in vitro* (glucose uptake assays; Fig. 4.3*A*) and *in vivo* (insulin tolerance tests; Fig. 4.4). Interestingly, downstream of Akt/mTORC1, the kinetics for activation of S6 ribosomal protein is quite distinctive, showing low and gradual phosphorylation levels throughout the time-course.

In contrast, a lower level of activation of MAPK signalling by *cis* dicarba insulin and *cis* dicarba glargine was characterised by the more gradual and lower responses in the activation of Erk1/2 and p90RSK (Fig. 4.22). The effect is most prominent when comparing *cis* dicarba glargine to

glargine (Fig. 4.22). Although the *cis* dicarba insulin eventually promotes a phosphorylation level similar to the native insulin at t = 30 min, the initial response was also significantly delayed. Moreover, when activated by *cis* dicarba insulin and *cis* dicarba glargine, Erk 1, Erk 2 and p90RSK phosphorylation never achieved the maximal level attained *via* the stimulation of their corresponding parent peptides (insulin and glargine, respectively) (Fig. 4.22). These findings correlate well with the lower mitogenic potency of *cis* dicarba analogues measured *in vitro via* the DNA synthesis assay (Fig. 5.3B) reported above, and provide an explanation as to why metabolic potency is retained but mitogenic potency is reduced.

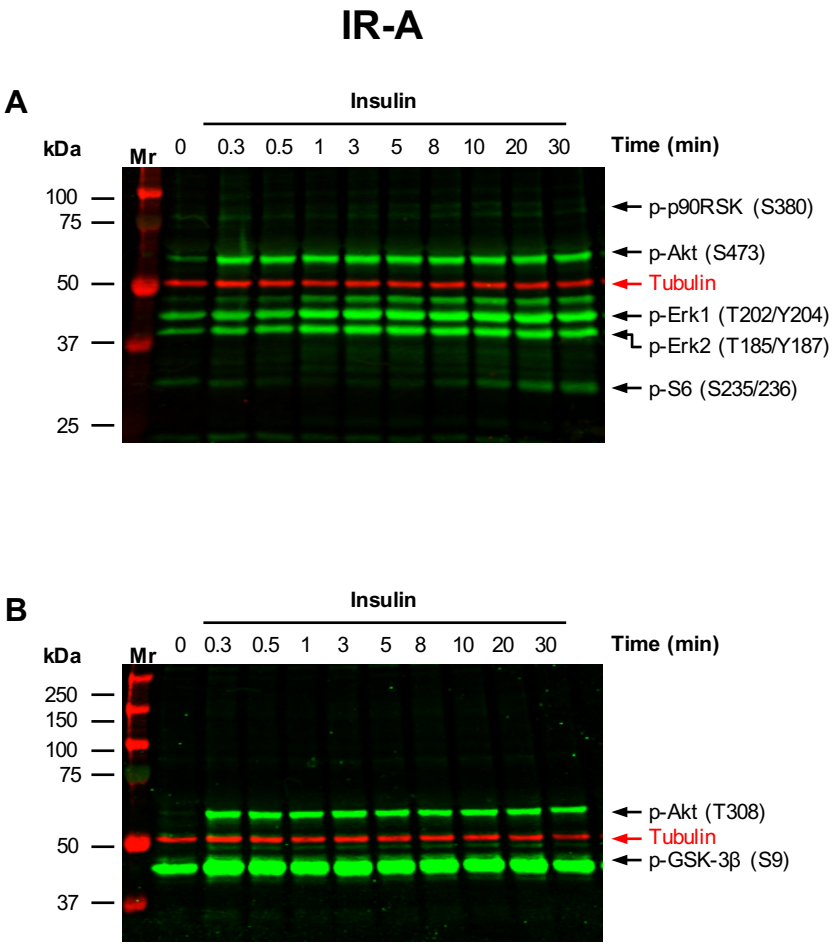

Figure 4.17 Representative western blot of IR-A stimulated by 10 nM of insulin in a time-course analysis. Serum starved IR-A overexpressing L6 myoblasts (hIR-A L6) were stimulated with 10 nM of insulin in a time-course of t = 0, 0.33 (20 s), 0.5 (30 s), 1, 3, 5, 8, 10, 20 and 30 min. Whole cells lysates were prepared and 20 mg of each sample were separated in duplicate 10% glycine gels followed by immunoblotting. Blot (A) probed with Pathscan® Multiplex Western Cocktail allowed detection of phospho-p90RSK (S380), phospho-Akt (S473), phospho-ERK1 (T202/Y204), phospho-ERK2 (T185/Y187) and phospho-S6 ribosomal (S235/236) simultaneously. Blot (B) was probed for phospho-AS160 (T642) (*not detected*), phospho-Akt (T308) and phospho-GSK3b (S9). Each blot was also probed with anti-b-Tubulin as loading control. All repeat blots were included in *Appendix Figure 4.7*.

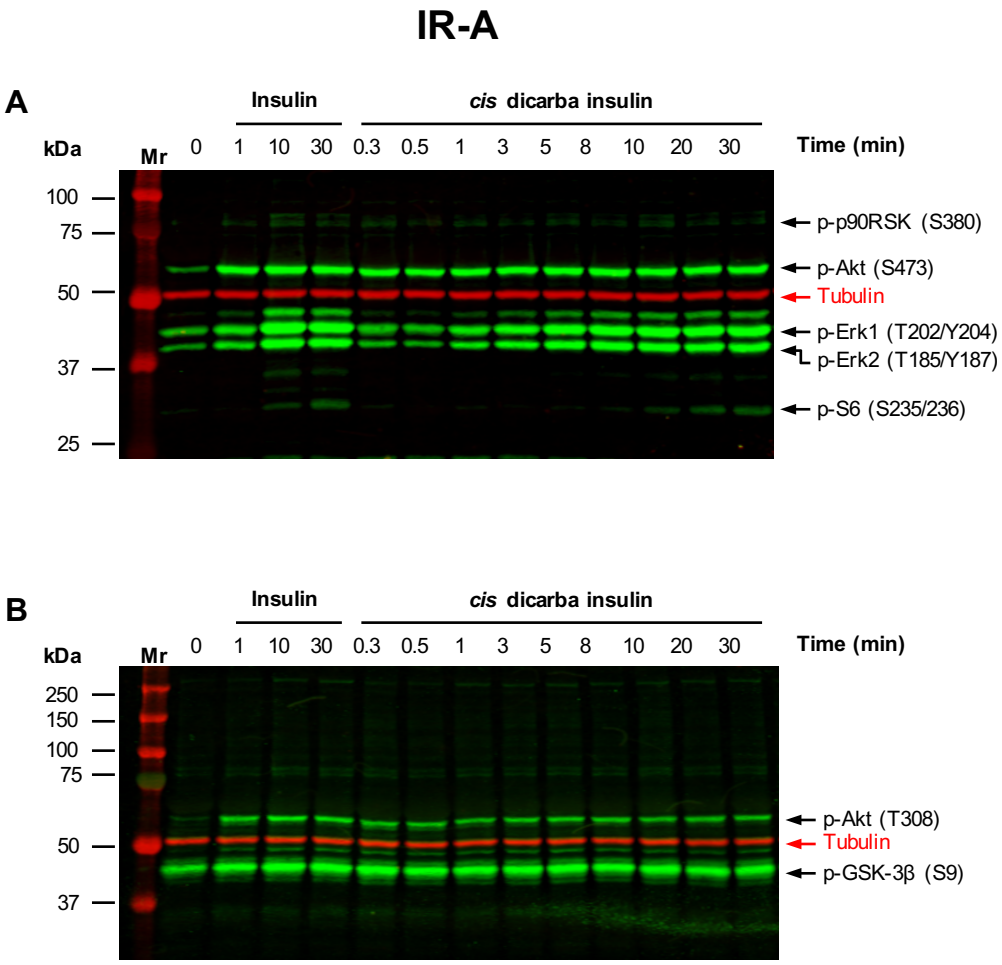

Figure 4.18 Representative western blot of IR-A stimulated by 10 nM of *cis* dicarba insulin in a time-course analysis. Serum starved IR-A overexpressing L6 myoblasts (hIR-A L6) were stimulated with 10 nM of *cis* dicarba insulin in a time-course of t = 0, 0.33 (20 s), 0.5 (30 s), 1, 3, 5, 8, 10, 20 and 30 min. Stimulation with 10 nM of insulin at t = 1, 10 and 30 minutes were also included as controls. Whole cells lysates were prepared and 20 mg of each sample were separated in duplicate 10% glycine gels followed by immunoblotting. Blot (A) probed with Pathscan® Multiplex Western Cocktail allowed detection of phospho-p90RSK (S380), phospho-Akt (S473), phospho-ERK1 (T202/Y204), phospho-ERK2 (T185/Y187) and phospho-S6 ribosomal (S235/236) simultaneously. Blot (B) was probed for phospho-AS160 (T642) (*not detected*), phospho-Akt (T308) and phospho-GSK3b (S9). Each blot was also probed with anti-b-Tubulin as loading control. All repeat blots were included in *Appendix Figure 4.8*.

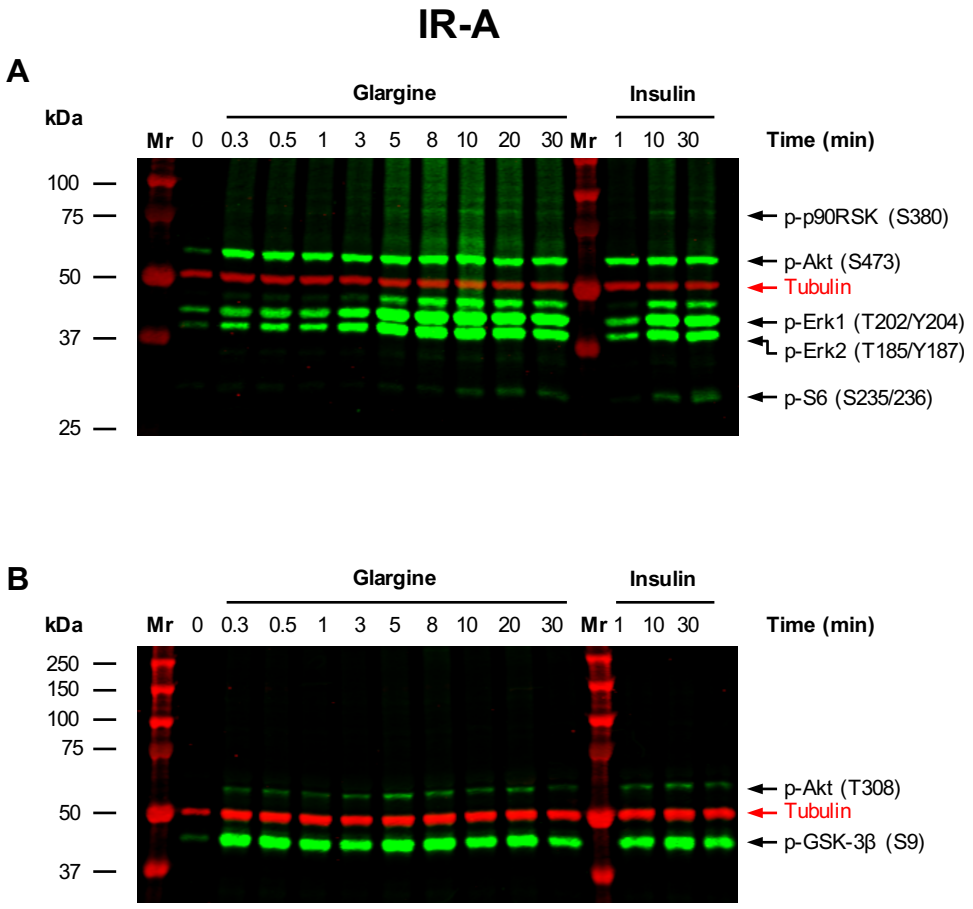

Figure 4.19 Representative western blot of IR-A stimulated by 10 nM of glargine insulin in a time-course analysis. Serum starved IR-A overexpressing L6 myoblasts (hIR-A L6) were stimulated with 10 nM of glargine insulin in a time-course of t = 0, 0.33 (20 s), 0.5 (30 s), 1, 3, 5, 8, 10, 20 and 30 min. Stimulation with 10 nM of insulin at t = 1, 10 and 30 minutes were also included as controls. Whole cells lysates were prepared and 20 mg of each sample were separated in duplicate 10% glycine gels followed by immunoblotting. Blot (A) probed with Pathscan® Multiplex Western Cocktail allowed detection of phospho-p90RSK (S380), phospho-Akt (S473), phospho-ERK1 (T202/Y204), phospho-ERK2 (T185/Y187) and phospho-S6 ribosomal (S235/236) simultaneously. Blot (B) was probed for phospho-AS160 (T642) (*not detected*), phospho-Akt (T308) and phospho-GSK3b (S9). Each blot was also probed with anti-b-Tubulin as loading control. All repeat blots were included in *Appendix Figure 4.9*.

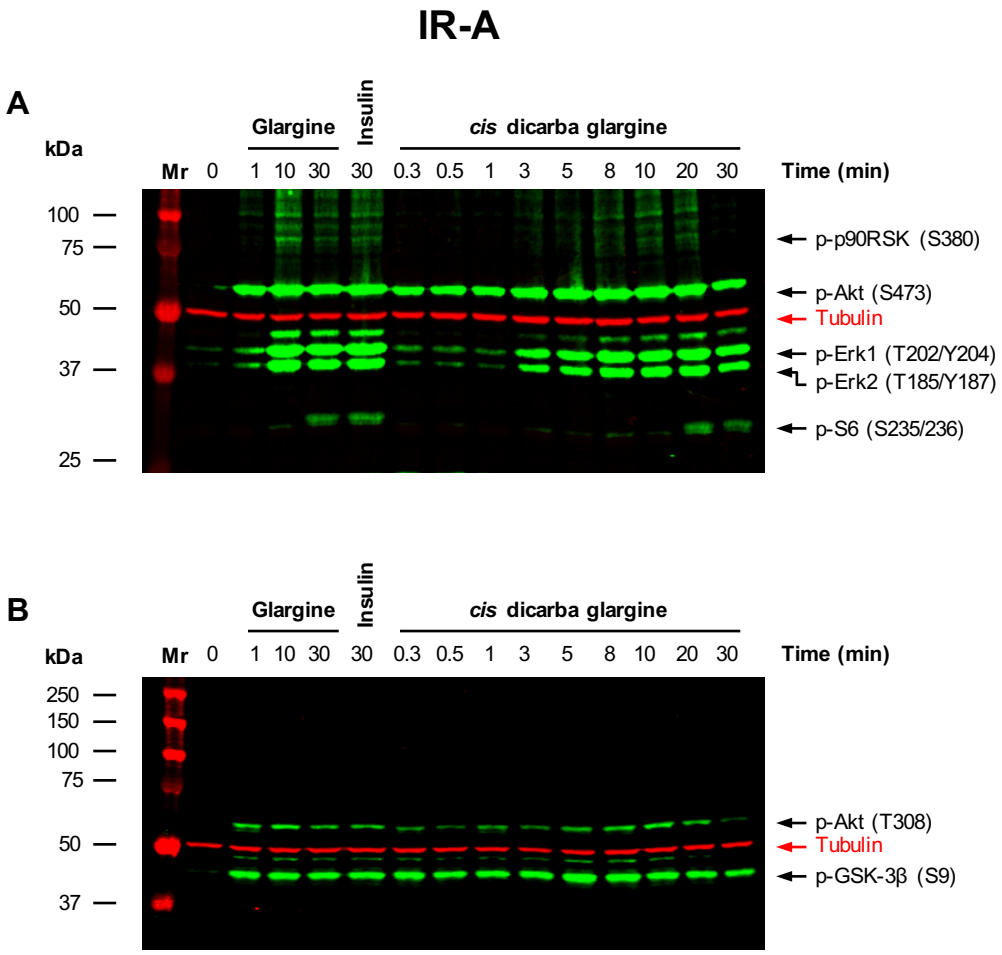

Figure 4.20 Representative western blot of IR-A stimulated by 10 nM of *cis* dicarba glargine insulin in a time-course analysis. Serum starved IR-A overexpressing L6 myoblasts (hIR-A L6) were stimulated with 10 nM of *cis* dicarba glargine insulin in a time-course of t = 0, 0.33 (20 s), 0.5 (30 s), 1, 3, 5, 8, 10, 20 and 30 min. Stimulation with 10 nM of glargine at t = 1, 10 and 30 minutes and insulin at t = 30 min were also included as controls. Whole cells lysates were prepared and 20 mg of each sample were separated in duplicate 10% glycine gels followed by immunoblotting. Blot (A) probed with Pathscan® Multiplex Western Cocktail allowed detection of phospho-p90RSK (S380), phospho-Akt (S473), phospho-ERK1 (T202/Y204), phospho-ERK2 (T185/Y187) and phospho-S6 ribosomal (S235/236) simultaneously. Blot (B) was probed for phospho-AS160 (T642) (*not detected*), phospho-Akt (T308) and phospho-GSK3b (S9). Each blot was also probed with anti-b-Tubulin as loading control. All repeat blots were included in *Appendix Figure 4.10*.

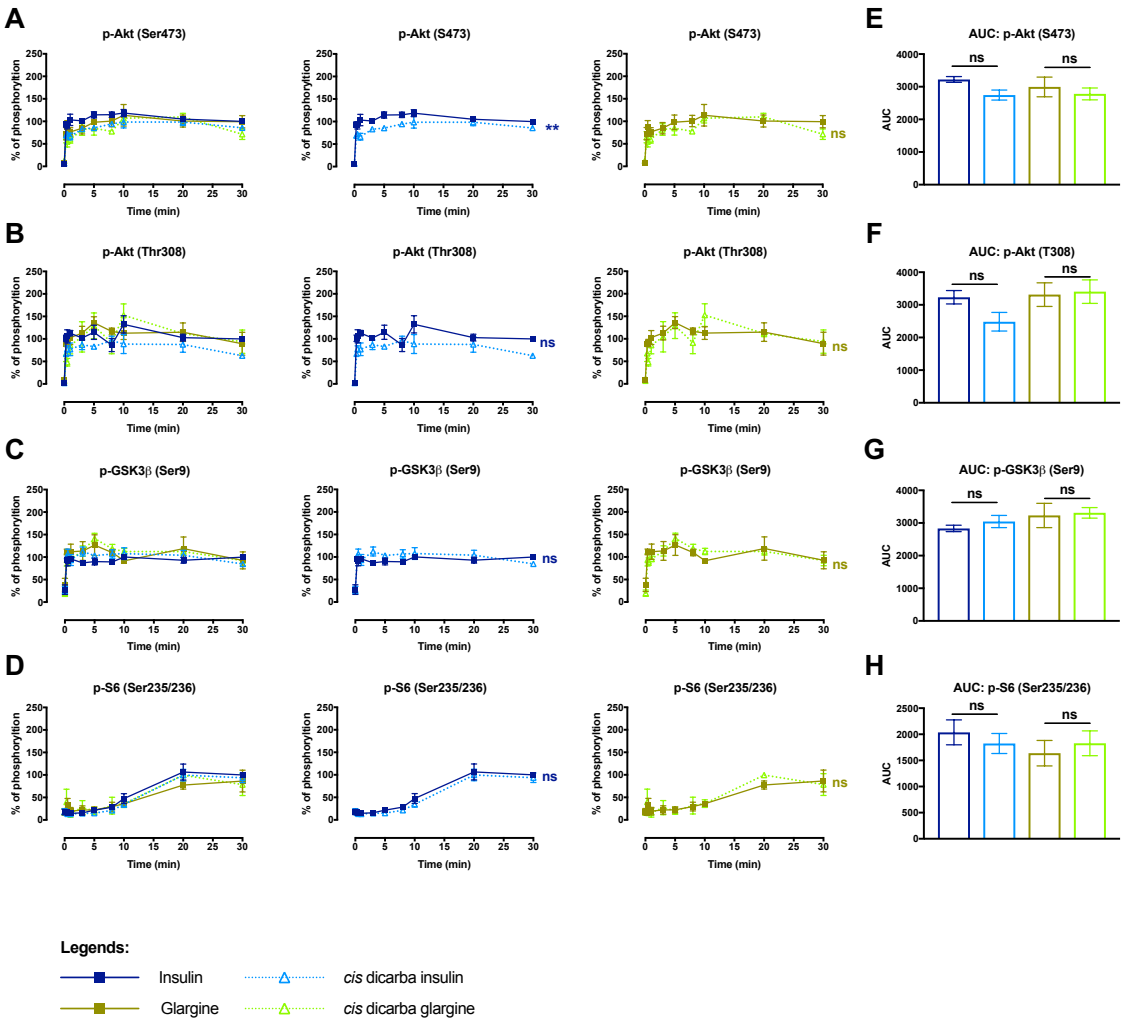

Figure 4.21 Quantitation of IR-A time-course of P13K signalling when stimulated by insulin, glargine insulin, *cis* dicarba insulin and *cis* dicarba glargine. Serum starved IR-A overexpressing L6 myoblasts were stimulated in a 0 – 30 min time-course at 10 nM of insulin (solid line, dark blue), *cis* dicarba insulin (dotted line, light blue), glargine insulin (solid line, olive green) or *cis* dicarba glargine insulin (dotted line, lime green). Phosphorylation levels of (A) Akt (phosho-S473), (B) Akt (phosho-T308), (C) GSK-3β (phospho-S9) and (D) S6 ribosomal (phospho-S235/236) are expressed as percentage of level detected when cells were stimulated with 10 nM of insulin for 30 min. All data are the mean ± S.E.M presented as XY graphs. n = at least 3 independent experiments. Error bars are shown when greater than the size of the symbols. In each case, data are normalized to the loading control β-tubulin. Representative blots are shown in *Figures 4.17 –4.20.* Statistical significance of the difference in phosphorylation levels when stimulated by *cis* dicarba insulin compared to insulin or *cis* dicarba glargine compared to glargine insulin were determined *via* 2-way ANOVA. (E – H) Area under curves derived from % of phosphorylation over 30 minutes. Statistical significance of the difference in total phosphorylation over 30 minutes measured as area under curves when stimulated by *cis* dicarba insulin compared to insulin or *cis* dicarba glargine compared to glargine insulin were determined *via* ordinary one-way ANOVA. ns ($P > 0.05$), ** ($P \leq 0.01$).

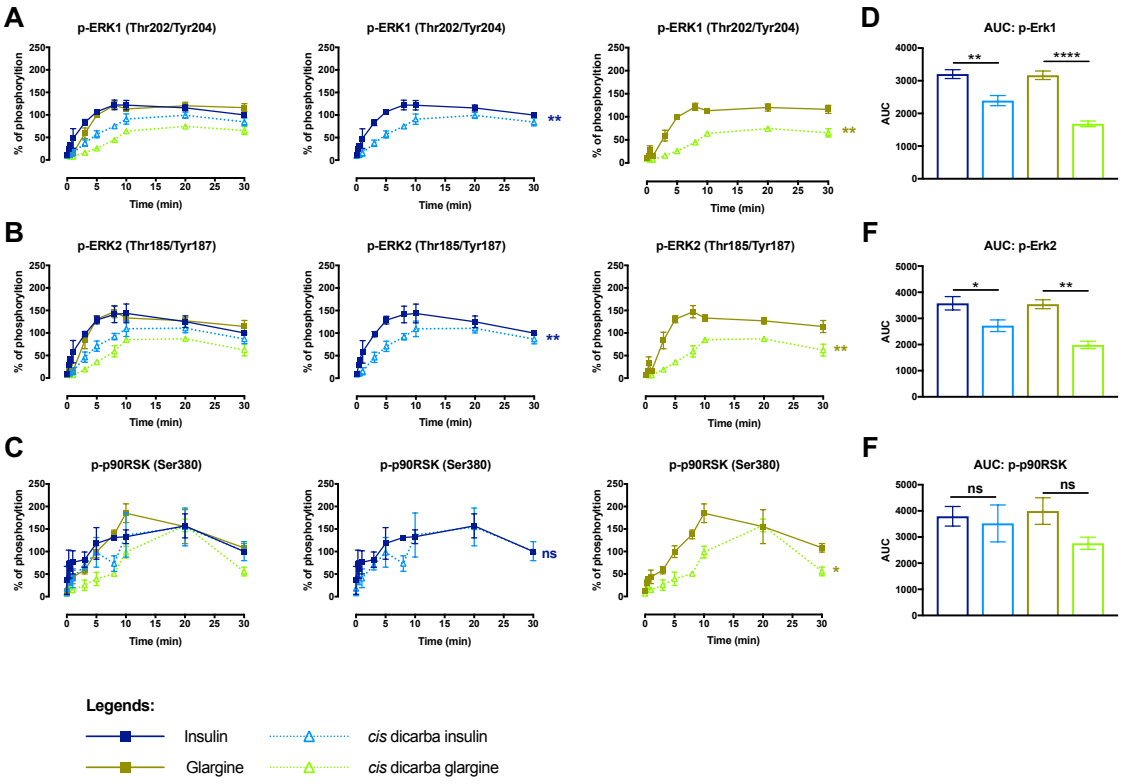

Figure 4.22 Quantitation of IR-A time-course of MAPK signalling when stimulated by insulin, glargine insulin, *cis* dicarba insulin and *cis* dicarba glargine. Serum starved IR-A overexpressing L6 myoblasts were stimulated in a 0 – 30 min time-course at 10 nM of insulin (solid line, dark blue), *cis* dicarba insulin (dotted line, light blue), glargine insulin (solid line, olive green) or *cis* dicarba glargine insulin (dotted line, lime green). Phosphorylation levels of (A) Erk 1 (phospho-T202/Y204), (B) Erk2 (phsopho-T185/Y187) and (C) p90RSK (phospho-S380) are expressed as percentage of level detected when cells were stimulated with 10 nM of insulin for 30 min. All data are the mean ± S.E.M presented as XY graphs. n = at least 3 independent experiments. Error bars are shown when greater than the size of the symbols. In each case, data are normalized to the loading control β-tubulin. Representative blots are shown in *Figures 4.17 –4.20.* Statistical significance of the difference in phosphorylation levels when stimulated by *cis* dicarba insulin compared to insulin or *cis* dicarba glargine compared to glargine insulin were determined *via* 2-way ANOVA. (D – F) Area under curves derived from % of phosphorylation over 30 minutes. Statistical significance of the difference in total phosphorylation over 30 minutes measured as area under curves when stimulated by *cis* dicarba insulin compared to insulin or *cis* dicarba glargine compared to glargine insulin were determined *via* ordinary one-way ANOVA. ns ($P > 0.05$), * ($P \leq 0.05$), ** ($P \leq 0.01$), **** ($P \leq 0.0001$).

4.3.7 IR-A receptor internalisation

Outline: Cis dicarba insulins showed strongly impaired ability to promote IR-A internalisation.

Having established the correlation between biological outputs and their upstream intracellular signalling kinetics, we hypothesized that the reduced mitogenic signalling of *cis* dicarba insulins must be regulated by a receptor-dependent event that occurs after the initial receptor engagement. Previously, other groups (Hamer et al., 2002, Ceresa et al., 1998, Jensen et al., 2007) and our laboratory (Rajapaksha and Forbes, 2015) provided evidence supporting the hypothesis that activation of mitogenic signalling *via* MAPK pathway is dependent on IR-A internalisation, although the underlying mechanism that triggers the receptor internalisation is not fully understood. Similarly, I was interested to validate this hypothesis with the *cis* dicarba insulin analogues.

It is important to emphasize here that the *cis* dicarba insulin analogues are unique and ideal for the purpose of this investigation for three reasons. Firstly, the *cis* dicarba analogues are identical in sequence to their parent peptide and only differ in the A6–A11 linkage. Secondly, they exhibit similar binding affinities (less than 2-fold different) to their respective parent peptides. Thirdly and most importantly, they are significantly less mitogenically active while maintaining an unchanged level of metabolic potency.

Based on the collective findings in glucose uptake, DNA synthesis and signalling analyses, of the three *cis* dicarba analogues the *cis* dicarba analogues of insulin and glargine showed most significant metabolic-mitogenic signalling bias. Hence, only these two *cis* dicarba analogues were investigated in the receptor internalisation assay; *cis* dicarba KP was excluded for this study. The method used in this study for measuring receptor internalisation was optimised based on several published literatures and performed in IR-A overexpressing fibroblasts (R^-IR-A cell) (Daunt et al., 1997, Jensen et al., 2007, Rajapaksha, 2013, Rajapaksha and Forbes, 2015).

As predicted, the less mitogenic *cis* dicarba insulin and *cis* dicarba glargine showed strongly impaired ability to promote IR-A internalisation, with virtually all receptor remaining on the surface 2 hours post-stimulation (Fig. 4.23). Insulin and glargine rapidly induced receptor internalisation immediately post-stimulation. Within t = 2 h, only 60% of IR-A remained on the cell surface. Interestingly, the native insulin and the "mitogenic" glargine did not show any difference in ability to promote receptor internalisation and effectively promoted IR-A receptor internalisation at a similar rate.

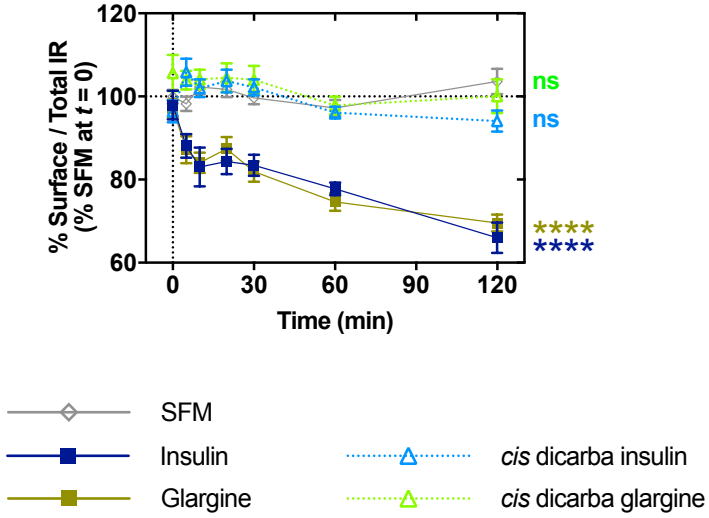

Figure 4.23 IR-A internalisation stimulated by insulin, glargine and their respective *cis* dicarba analogues. Serum starved IR-A overexpressing L6 myoblasts were treated with serum-free media (SFM; non-stimulated condition, grey) or 10 nM of insulin (dark blue), glargine (olive green), *cis* dicarba insulin (light blue) and *cis* dicarba glargine insulin (light green) in a time-course of t = 0, 5, 10, 20, 30, 60 and 120 min. Data are presented as % of surface receptor/total receptor (see Equation 4.3) followed by normalisation with % of surface receptor in SFM at t = 0; ie. SFM at t = 0 is equivalent to 100%. All data are the mean ± S.E.M. n = at least 3 independent experiments. Error bars are shown when greater than the size of the symbols. Statistical significance of the difference in rates of internalisation were determined *via* one-way repeated measures ANOVA followed by Dunnets multiple test. SFM *vs* insulin**** ($P \leq 0.0001$); SFM *vs* glargine**** ($P \leq 0.0001$); SFM *vs cis* dicarba insulin^{ns}; SFM *vs cis* dicarba glargine^{ns}; insulin *vs cis* dicarba insulin**** ($P \leq 0.0001$); glargine *vs cis* dicarba glargine**** ($P \leq 0.0001$).

4.3.8 Optimisation of IR-A Purification for Mass Spectrometry

Outline: The cis dicarba insulin represent an ideal tool for the investigation of receptor phosphorylation patterns underlying metabolic vs mitogenic differential signalling.

At this stage, the presented evidence suggested that the "check-point" of initiating metabolic *versus* mitogenic signalling is determined by the ability of each ligand to induce insulin receptor internalisation. With consideration that the *cis* dicarba insulin and native insulin are equipotent in receptor binding and total receptor phosphorylation, we proposed that the message to the different signalling outputs is "coded" within the phosphorylation pattern on the receptor tyrosine kinase domain. The most direct approach to map out the unique "codes" that contribute to insulin's "mitogenicity" is to compare the phosphorylation level of several known sites on the tyrosine kinase domain when stimulated by native insulin or *cis* dicarba insulin. We hypothesised this could be achieved *via* targeted mass spectrometry (MRM/SRM) of known phosphorylation sites, 14 of which had previously been identified in our laboratory through a mass spectrometry discovery project. A large quantity of stimulated insulin receptor (30 μg) is required for this approach. The proposed workflow for the purification of stimulated IR-A for MRM analysis is summarized in *schematic 4.2*.

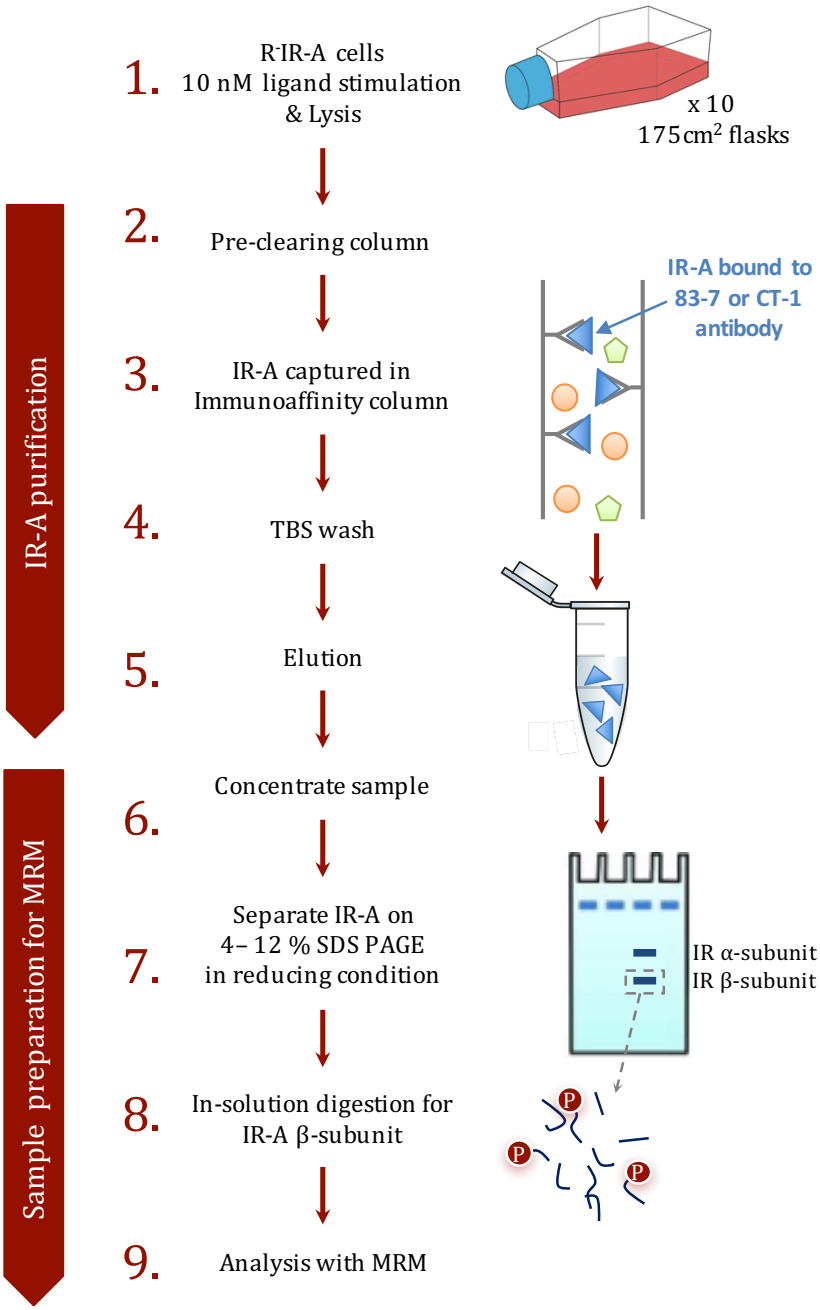

Schematic 4.2 Proposed workflow for purification of stimulated IR-Afor phosphopeptide mass spectrometry analysis. (1) R-IR-A cells stimulated 10 nM of insulin or *cis* dicarba insulin for 20 min followed by cell lysis in cold. (2) Pre-cleared lysates in blocked column and collect flow-through. (3) Capture stimulated IR-A using a column coupled with anti-IR antibodies, 83-7 or CT-1 antibody, and collect flow-through. (4) Wash column in ice-cold TBS. (5) Elute IR-A; see elution conditions in section 4.2.16.1. (6) Concentrate sample; see section 4.2.16.2. (7) Purified IR-A separated in a 4 – 12% SDS PAGE. The band corresponding to the IR-A beta subunit is excised from the gel and subjected to (8) in-solution trypsin digestion. (9) Analysis via targeted mass spectrometry; multiple reaction monitoring (MRM).

4.3.8.1 *Optimisation of IR-A purification via 83-7 affinity column*

Previously, Dr Rajapaksha from our laboratory had taken a similar approach for the investigation using affinity column containing anti-IR antibody, 83-7. Although Dr Rajapaksha had successfully purified IR-A in his study, the method was not optimal. The protein recovery was not consistent across batches and each batch also required a large volume of cell culture (Rajapaksha, 2013).

As an initial attempt, I aimed to further improve the protocol developed by Dr Rajapaksha for IR-A purification using 83-7 affinity column. The 83-7 antibody binds to IR-A ectodomain in the cysteine rich (CR) region with very high affinity and does not compete with ligand binding, and is thus ideal for purification of ligand-bound receptors (Adams et al., 2000). Purified 83-7 antibodies were coupled to Affi-Gel 10 resin as described in *section 4.2.12*. Affi-Gel 10 contains an N-hydroxysucinide (NHS) ester group with a 10-atom spacer arm. Displacement of the NHS groups allows ligand with free alkyl or aryl amino groups, such as 83-7 antibodies, to couple spontaneously to the resin. The coupling reaction is most optimal in NH_2-free buffer at pH close to the isoelectric point (IP) of the binding ligand. In this case, as the pI of 83-7 is ~ pH 7 a coupling buffer 20 mM HEPES at pH 7.5 was used. The coupling efficiency was monitored by comparing 83-7 depletion in the coupling solution pre- and post-coupling. As indicated in *Figure 4.24*, there was more than 50% depletion of 83-7 antibodies post-coupling suggesting an effective (but not optimal) coupling of 83-7 antibodies. Both the pre-clearing column and the 83-7 affinity column were blocked with 0.5 M glycine; pH 8.0.

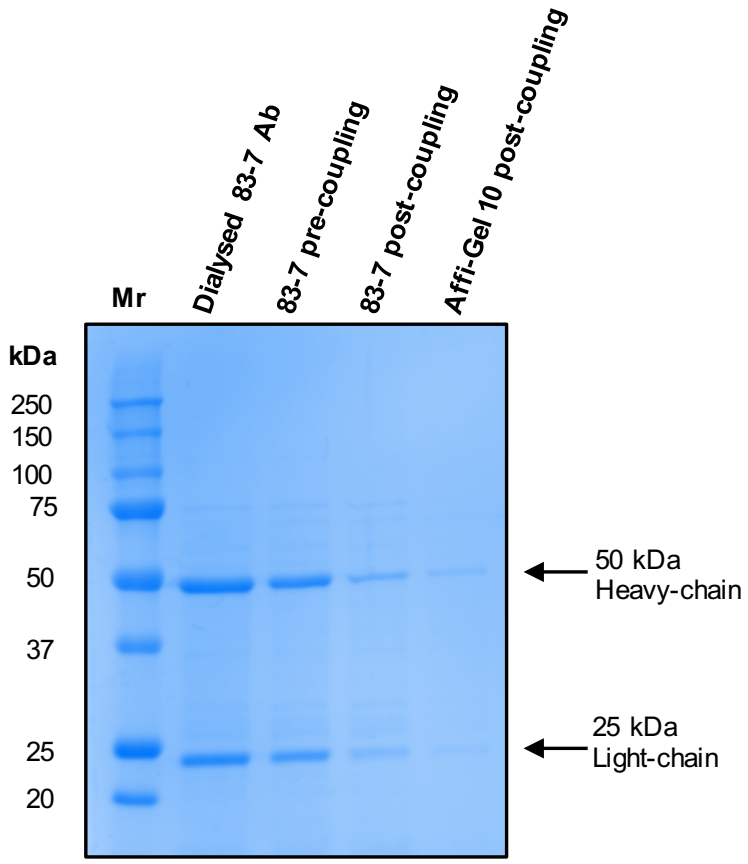

Figure 4.24 Coupling 83-7 on Affi-Gel 10. 83-7 antibodies (56 mg at 14.2 mg/mL) were dialysed overnight in coupling buffer (20mM HEPES buffer at pH 7.5). Dialysed 83-7 was coupled to Affi-Gel 10 at 4 mg antibody: 1 mL Affi-Gel ratio. After an overnight coupling at 4C, post-coupling buffer was collected. Resin was washed with 5 CV coupling buffer. In order to estimate coupling efficiency, 20 µg of dialysed 83-7, pre- (15µL) and post-coupling (15 µL) of 83-7 containing coupling supernatant; and post-coupling resin (5 µL) were separated in a 7.5 % SDS-PAGE in reducing condition; stained with Coomassie Blue R250. Less than 50 % of 83-7 antibodies remain in the post-coupling sample suggesting an effective (but not optimal) coupling efficiency.

IR-A purification was performed as described in *section 4.2.16* and receptor was eluted in *Elution Buffer A* (see recipe in section 4.2.16.1) *via* method described in *section 4.2.16.2.1* which involve acetone precipitation of the eluted samples. A small sample (10 µL) was kept aside for western blot analysis. The remaining eluates were treated with 100% pre-chilled acetone and stored overnight at – 20°C in order to preserve the protein phosphorylation state of the samples. Western blot analysis indicated the presence of insulin receptors in the eluted samples (Fig. 4.25). However, no proteins were detected in the acetone precipitated eluate when separated on SDS-PAGE under reducing conditions and stained with Colloidal Coomassie Brilliant Blue (Fig. 4.26). This suggested the overall recovery of IR-A was below the level of detection (*i.e.* < 30 ng).

As initial attempt suggested most of the receptor may still be tightly bound on the column (see '*83-7 resin post-elution*' in Fig. 4.25) different elution conditions were explored. Magnesium was introduced into the elution buffers to provide ionic interference to assist with dissociation of receptors from the column. Thus, following elution with *Elution Buffer A*, a second elution with same elution buffer containing 1 M or 2 M of $MgCl_2$ was conducted. However, the introduction of $MgCl_2$ did not improve elution, as shown in *Figure 4.27*.

Considering the minimal success in the prior efforts performed by Dr Rajapksha (Rajapaksha, 2013) and Dr Peter McCarthy (unpublished), we concluded that we may have saturated the options for improvement using 83-7 affinity column for IR-A purification.

Several factors that may have affected the IR-A purification *via* 83-7 column are:

(i) 83-7 coupling efficiency
(ii) Very high affinity binding of 83-7 antibody to IR-A may reduce elution efficiency
(iii) IR-A: 83-7 ratio during binding

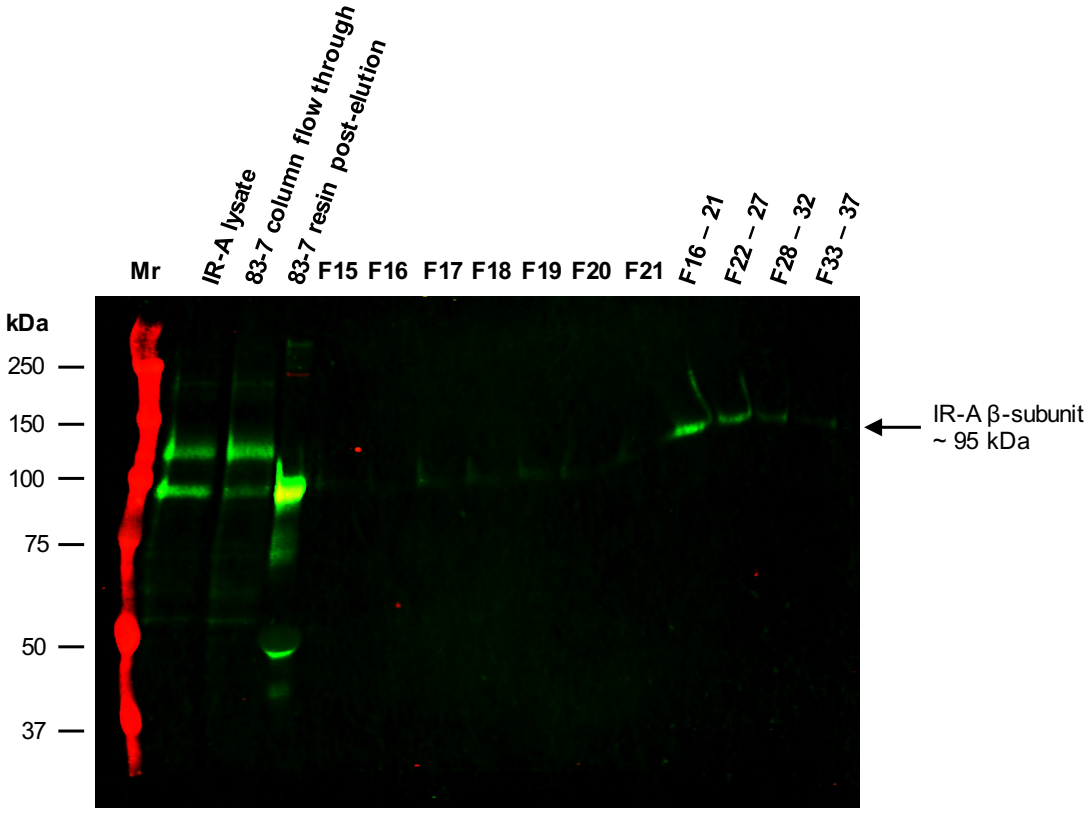

Figure 4.25 IR-A purification *via* 83-7 affinity column using *Elution A (acidic conditions).* Stimulated IR-A lysate were pre-cleared then captured on 83-7 affinity column (total lysate volume of 135 mL). The IR-A bound 83-7 column were eluted with Elution Buffer A (0.1 M glycine, 0.15 M NaCl and 0.01 % (v/v) Triton-x 100, pH 1.7). Eluted samples were collected as 1 mL fractions. fraction 15 – 21 were separated on gel individually. However, amount of phosphorylated IR-A detected in individual fraction was too low. Elution fractions were pooled into 4 batches. 20 µL of each sample were separated in a reducing 7.5 % SDS PAGE. A 50 µL of eluted 83-7 column was boiled in 2 x protein dye; supernatant was also separate in gel to determine amount of IR-A remained on column after elution. The transferred blot was probed with phospho-3Y antibody for the detection of phosphorylated IR-A.

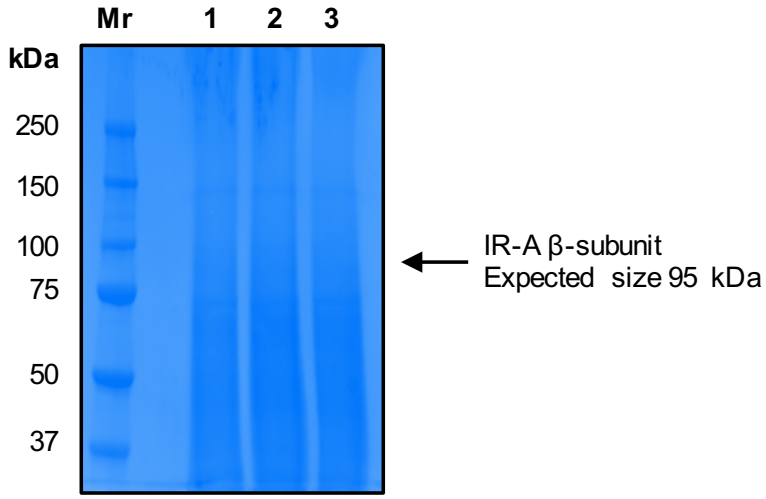

Figure 4.26 Acetone precipitated IR-A purified *via* 83-7 affinity chromatography. Pooled elution sample 1, 2 and 3 (refer Fig. 4.25) were acetone precipitated. Each pellet was resuspended in 40 µL of 2 x protein dye; pooled into a total volume of 120 µL and boiled for 5 minutes. Pooled sample was separated in a reducing 4 – 20 % SDS PAGE; loading 40 µL each lane. Gel was stained with Colloidal Coomassie Briliant Blue.

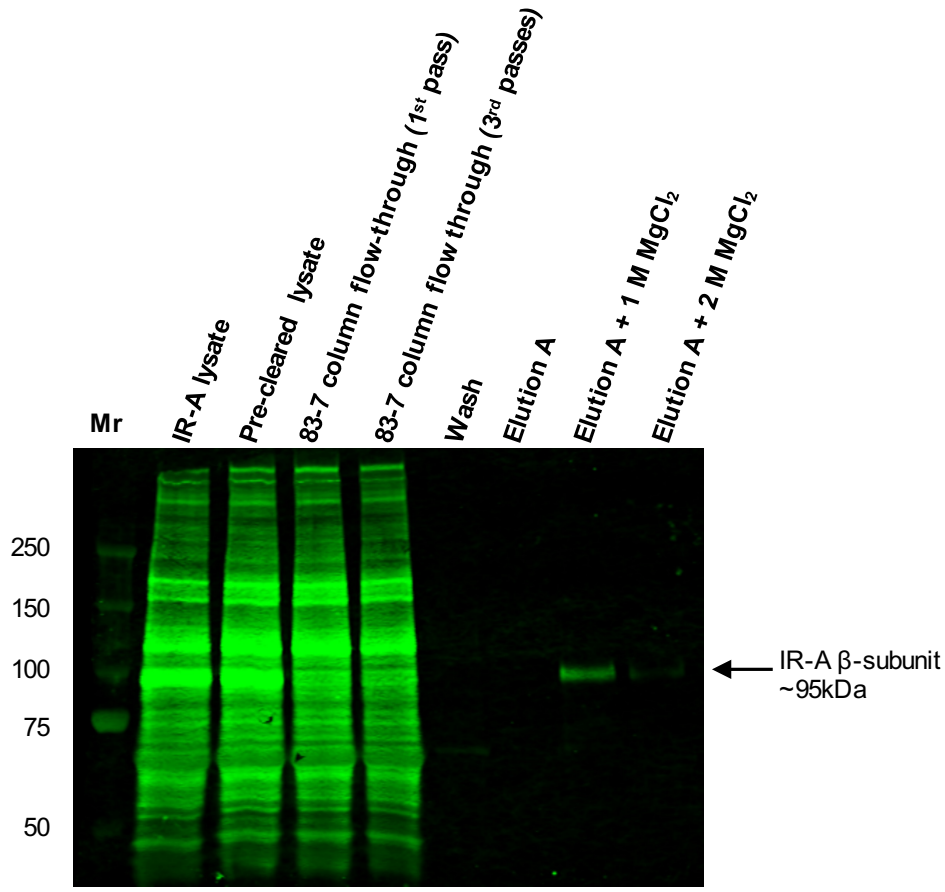

Figure 4.27 IR-A purification *via* 83-7 affinity column using *Elution A* with added 1 or 2 M Mg Cl_2. Stimulated IR-A lysate (total lysate volume 135 mL) were pre-cleared and loaded on 83-7 column for three passes. The affinity column was washed with 5 CV of cold lysis buffer followed by 5 CV of TBS. The IR-A bound 83-7 column was first eluted with the acidic *Elution Buffer A* (0.1 M glycine, 0.15 M NaCl and 0.01 % (v/v) Triton-x 100, pH 1.7), followed by *Elution A* added with 1M $MgCl_2$ and 2 M Mg Cl_2 at 0.5ml/min. Eluted samples were collected as 3 mL-fractions. 20 µL of each sample was separated in a 7.5 % reducing SDS PAGE. The transferred blot was probed with phospho-3Y antibody for the detection of phosphorylated IR-A. IR-A were captured efficiently on 83-7 column. However, all elution conditions tested did not elute IR-A efficiently.

4.3.8.2 *Optimisation of IR-A purification via CT-1 affinity column*

In order to improve the elution efficiency, I considered using a different ligand for the affinity column that either binds to the receptors with lower affinity or has a competing peptide at the receptor binding epitope on the antibody. Personal discussion with Dr John Menting (WEHI) suggested the purification of IR may be more effective using a CT-1 affinity column and eluting with buffer containing CT-1 competing peptide. He has successfully used this method for the purification of the holo insulin receptor.

The use of CT-1 antibody in an immunoaffinity purification of IR with a short competing peptide was first introduced by Ganderton *et al*. The CT-1 antibody has an epitope of YKKNGRILTLPRSNPS located at the *C*-terminal domain of insulin receptor β-subunit. A hexadecapeptide of the same epitope sequence was shown to effectively compete for IR-bound to the CT-1 column and hence allow effective IR purification (Ganderton et al., 1992). In this study, a modified version of peptide was used and is a kind gift from John Menting and Prof. Mike Lawrence. The peptide was modified to include three additional lysine residues at the *N*-terminus (KKKKKNGRILTLPRSNPS) that improves peptide solubility and receptor elution. CT-1 antibodies were harvested from hybridomas and purified *via* Protein G column as described in *section 4.2.13*. Presented in *Figure 4.28* is the representation of CT-1 antibodies collected in 1-mL fractions from one batch of purification. Fraction 5 – 11 were separated in SDS-PAGE to confirm protein purity. Protein concentrations of the collected fractions were determined using Nanodrop (Fig. 4.28*B*); fractions containing the highest protein concentration were highlighted in *red*). Several batches of purifications were made and pooled together in order to collect a sufficient amount of CT-1 for setting up a CT-1 affinity column. Specificity of the purified CT-1 antibody was confirmed by using the antibody to probe for insulin receptor in lysates harvested from insulin receptor knockout cell lines that overexpress IR-A (R^-IR-A) or IGF-1R (P6 cells). The purified CT-1 detected a band ~95 KDa for β-subunit of IR-A in R^-IR-A lysate, but not in P6 lysate (see Fig. 4.29).

A

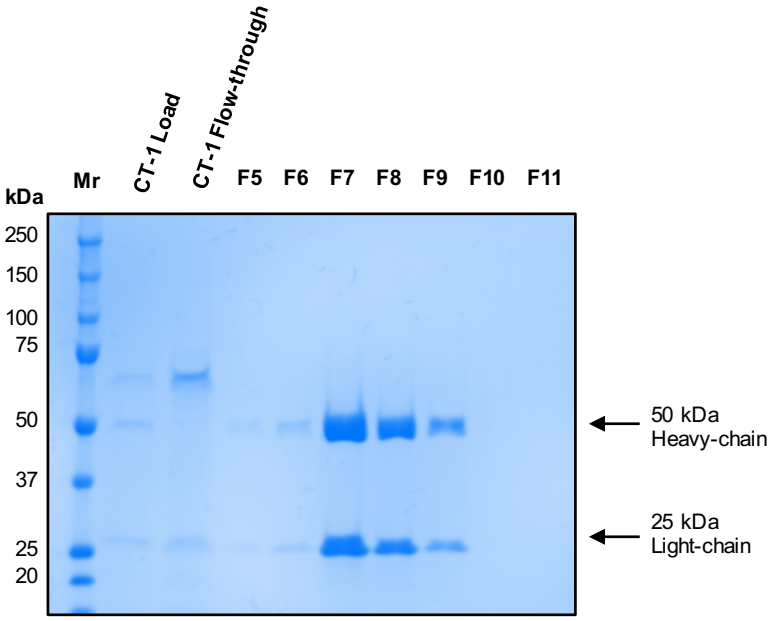

B

Sample	Protein Concentration (mg/mL)	Protein Amount (mg)
Blank	0.002	
Fraction 1	0.049	0.049
Fraction 2	0.04	0.04
Fraction 3	0.031	0.031
Fraction 4	0.024	0.024
Fraction 5	0.039	0.039
Fraction 6	0.136	0.136
Fraction 7	3.954	3.954
Fraction 8	1.489	1.489
Fraction 9	0.467	0.467
Fraction 10	0.032	0.032

Figure 4.28 CT-1 purification *via* Protein G column. (A) CT-1 antibody expressing hybridomas starved with no fetal calf serum for 3 – 7 days. Supernatant were collected, centrifuged at 4, 000 rpm at 4 ° C for 5 minutes prior to protein G purification. CT-1 hybridoma supernatant was loaded onto the column at a rate of 1 mL/min and flow-through was collected. CT-1 antibodies were eluted with elution buffer (0.1 M glycine, pH 2.6) at a rate of 0.5 mL/min. 1 mL fractions were collected. 20 µL of CT-1 supernantant, flow-through and fraction 5 – 11 were separated in a reducing 7.5 % SDS PAGE. Gel was stained with Coomassie Blue R250. (B) Protein concentrations of eluted fractions were determined using NanoDrop™ 2000 Spectrometer at 280 nm wavelength. Protein amount in each fraction was calculated. Fractions highlighted in red contained the highest protein concentration and are pooled together for setting up CT-1 affinity column described in *Section 4.2.14*.

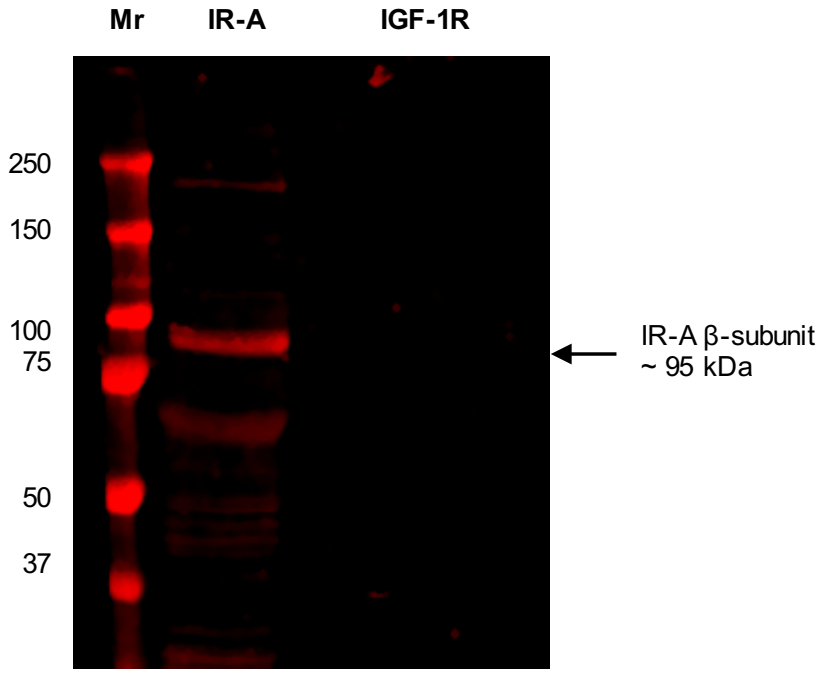

Figure 4.29 Purified CT-1 antibody binds to β-subunit of insulin receptor in R⁻IR-A lysate but not IGF-1R. 20 µL of R⁻IR-A (overexpressing IR-A) and P6 (overexpressing IGF-1R) lysates were separated in a reducing 7.5% SDS PAGE. Transferred blot was probed with purified CT-1 antibody (refer Fig. 4.28) at 9 µg/mL in TBS/0.1% Tween-20 with 1 % BSA. The purified CT-1 detected a band ~95 KDa for b-subunit of IR-A in R⁻IR-A lysate, but not in P6 lysate. Additional bands detected > 250 kDa and ~60kDa are likely to be pro-receptor and receptor breakdown, respectively.

The CT-1 antibodies were coupled to a cyanogen bromide-activated sepharose 4B from GE Healthcare as described in *Section 4.2.14*. Similar to Affi-Gel 10, the CnBr-activated sepharose is optimal for immobilising antibodies that contain -NH_2 groups. The resin however does not contain an intermediate spacer arm, a feature not required for coupling large proteins such as in this case. For optimal compatibility, a pre-clearing column of the CnBr-activated sepharose was also set-up as described in *Section 4.2.15*. Although a different coupling ligand was used (CT-1 instead of 83-7 antibodies), it appeared that the coupling efficiency of CnBr-activated sepharose was greater than the Affi-Gel 10. As shown in *Figure 4.30*, the majority of CT-1 antibody was depleted from the solution during coupling (as seen by comparing the antibody concentrations before and after coupling).

IR-A purification using CT-1 affinity chromatography was essential the same as described for 83-7 affinity chromatography described in *Section 4.2.16.* and a different elution method was adopted (described in Section 4.2.16.2.2). Acetone precipitation step was avoided from this stage onwards as I found the precipitated pellets were hard to re-dissolve in SDS solution and may have contributed to the loss of protein. Through personal communication with Dr John Menting (WEHI), a competing peptide concentration of 0.1 – 0.5 mg/mL was chosen, a range he had used for eluting holo-insulin receptor from the CT-1 column. The CT-1 competing peptide was first resuspended in a small volume of DMSO then further diluted in TBS at pH 7 for elution. To our surprise, although all IR-A was successfully captured in the CT-1 affinity column (compare '*pre-cleared IR-A lysate*' and '*CT-1 column flow-through*' at ~95kDa in Fig. 4.31), elution using the suggested peptide concentration at 0.5 mg / mL did not result in elution of the receptor (no band detected at ~95 kDa in '*elution fraction 5 – 12*'; as presented in Fig. 4.31). The column was also further treated with the low pH *Elution Buffer A* but again no receptor was eluted (*far right lane* in Fig. 4.31).

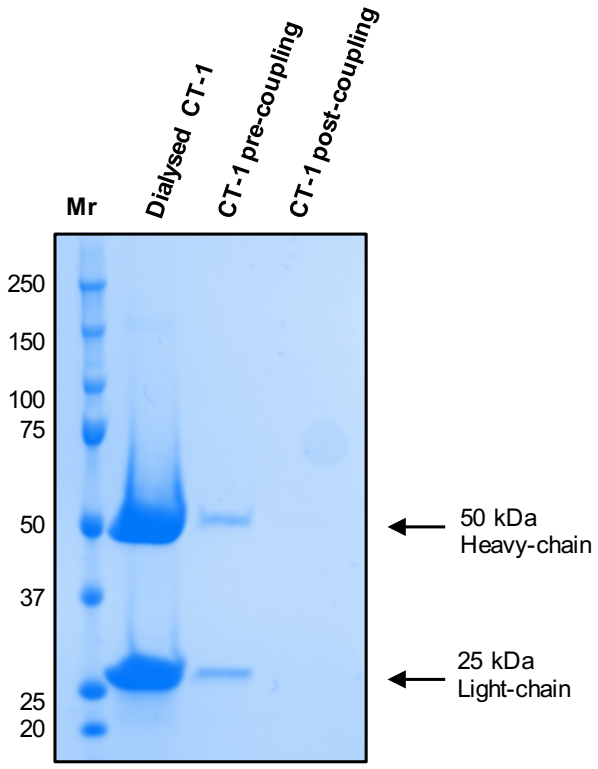

Figure 4.30 CT-1 coupling to cynogen bromide (CnBr)-activated sepharose. CT-1 antibodies (30 mg at 7 mg/mL) were dialysed overnight in coupling buffer (0.1 M $NaHCO_3$, 0.5 M NaCl; pH 8.3). Dialysed CT-1 was coupled to cyanogen bromide (CnBr)-activated sepharose 4B at 4.28 mg CT-1 antibody: 1 mL CnBr-activated sepharose ratio. 20 µg of dialysed CT-1 antibody, 15 µL of pre-coupling and 15 µL post-coupling of CT-1 containing buffer were separated in a reducing 7.5% SDS PAGE. The gel was stained with Coomassie Blue R250. No antibody was detected in post-coupling sample suggest a CT-1 antibody has been successfully coupled to CnBr-activated sepharose.

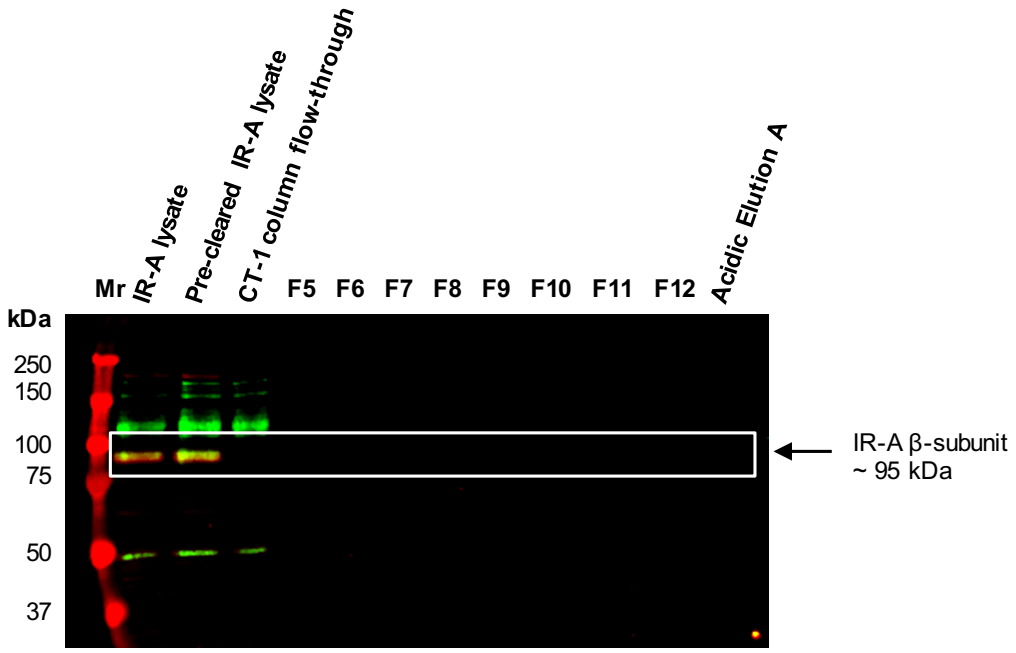

Figure 4.31 IR-A purification *via* CT-1 affinity chromatography using competing peptide. Stimulated IR-A lysate (total lysate volume 135 mL) were pre-cleared then captured on the CT-1 column. *Flow through* (150 mL) was collected and the CT-1 column was washed with 5 CV of cold lysis buffer followed by 5CV of TBS. The IR-A bound CT-1 column was eluted with 0.5 mg/mL of competing peptide in tris-base saline (TBS) buffer at pH 7.4; followed by an acidic elution with Elution buffer A. Eluted samples were collected as 1 mL-fractions. 20 µL of each sample was separated in a reducing 7.5 % glycine gel. Transferred blot was probe with both phospho-3Y antibody (green bands; detected at λ = 800 nm) and CT-1 antibody (red bands; detected at λ = 680 nm) for detection of phosphorylated and non-phosphorylated IR-A, respectively. Blot presented is an overlay of the same blot detected at two wavelengths.

As use of the CT-1 column had been developed for the purification of the holo insulin receptor we wondered if it was possible that the elution of the receptor was hindered when bound to insulin. Therefore, the next aim was (i) to investigate whether stimulation of the IR-A receptor interferes with the elution of the receptor from the antibody and (ii) to compare elution using several different buffer conditions. The experiments were set up in a 1: 150 scaled down condition performed in 1.5-mL lo-bind centrifuged tubes. IR-A cells were grown in two T-175 flasks as described before, one non-stimulated ('– *insulin Load'*; Fig. 4.32) and the other stimulated with 10 nM insulin for 20 min ('+ *insulin Load'*; Fig. 4.32). Lysates (700 µL) harvested were incubated with CT-1 resin (50 µL) in separate tubes (one for each condition – see details panel above Fig. 4.32) and rotated overnight at 4 °C. The different elution buffer conditions (*Elution buffer B – D*; see recipe in section 4.2.16.1) were adapted from several published literatures, referenced accordingly in the *Method Section 4.2.16.1*.

The next day, the supernatants from each tube were collected in separate tubes (only one representative sample from each non-stimulated and stimulated condition was analysed on western blot – see '*FT'*; Fig. 4.32). Beads were washed followed by incubation for 2 hours at 10 °C with agitation in 100 µL of *Elution Buffer B, C or D*. *Elution Buffer D* were pre-resuspended with 0.5 or 2.5 mg/mL of competing peptides. The eluates were transferred to fresh tubes and beads were washed 5 times with TBS. For western blot analysis, 20 µL of each eluate was reduced in SDS buffer containing final concentration of 5 % β-mercaptoethanol (βME). Beads were also incubated in 50 µL of 2 x SDS buffer / 10% βME. Samples were boiled in 95 °C for 5 minutes, centrifuged and separated on SDS-PAGE gel followed by western blot transfer. Blots were probed for non-phosphorylated (CT-1 antibody) and phosphorylated (phospho-3Y) insulin receptor.

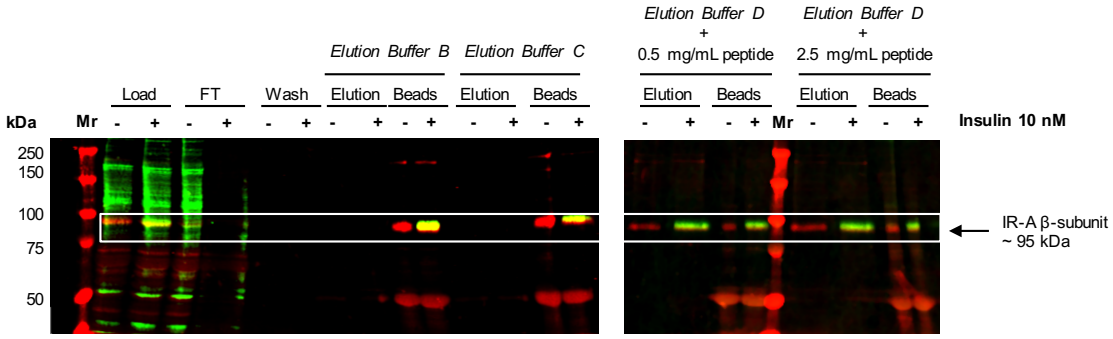

Figure 4.32 Optimization of elution condition for IR-A purification *via* CT-1 affinity chromatography. A small-scale IR-A purification *via* CT-1 affinity column were set-up to investigate the efficiency of several elution buffers. For each condition, 50 µL of CT-1 mini-column were captured with 700 µL of non-stimulated or insulin-stimulated (100 nM for 20 minutes) IR-A lysates. Flow through (FT) were collected and column washed with TBS buffer. CT-1 mini columns were eluted in 100 µL of specified elution condition (refer section *4.2.16.1.* for details) overnight at 4°C with shaking. The CT-1 mini columns were washed with 5CV of TBS buffer and subsequently boiled 5 minutes in 2 x protein dye with freshly added 0.5 M DTT. 20 µL of each sample was separated in reducing 7.5 % glycine gels. Transferred blot was probe with both phospho-3Y antibody (green bands; detected at λ = 800 nm) and CT-1 antibody (red bands; detected at λ = 680 nm) for detection of phosphorylated and non-phosphorylated IR-A, respectively. Blot presented is an overlay of the blots detected at two wavelengths.

Presented in *Figure* 4.32, the *Elution Buffer B* adapted from Kavran *et al.* for IGF-1R purification and *Elution Buffer C* from *Fujita-Yamaguchi et al.* did not effectively elute the IR-A bound to CT-1 column. Both non-stimulated and stimulated IR-A remained tightly bound to the resin (see *Elution Buffer B* and *Elution Buffer C* in Fig. 4.32, *left blot*). Interestingly, in this trial experiment, the IR-A were *partially* eluted when competed with peptide at 0.5 mg/mL and 2.5 mg/mL (see Fig. 4.32; *right blot*). Note that in this trial experiment, the peptides were buffered with HEPES (*Elution Buffer D*) rather than a tris-buffered saline (TBS) as described in *Figure 4.31*. The effective pH range of Tris buffer is pH 7.5–9.0 at 25°C; while HEPES has an optimal pH range of pH 6.8-8.2. At 25°C, Tris buffer prepared at pH7.4 is at its limit of buffering capacity. Furthermore, Tris buffer, but not HEPES buffer, is also sensitive to temperature change. At 4°C, Tris buffer prepared at a neutral pH 7.4 would shift to pH 8.0. Purification of IR was conducted at 4°C, the slightly more alkaline pH of Tris buffer may reduce the solubility of the highly basic (PI = 12.57) CT-1 competing peptide; thus, a reduced efficiency in the elution of IR. Future experiments should, therefore, avoid using Tris-base buffer in the purifications step. Most importantly, this experiment also showed that in all eluting conditions, the ligand-binding state of the IR-A did not affect the elution efficacy. Nevertheless, significant amount of IR still remained bound on the CT-1 column. Additional optimisation may be required to improve IR purification using this method. Current method of IR-A purification *via* CT-1 affinity column optimised in this study is summarized in *Schematic diagram 4.3.*

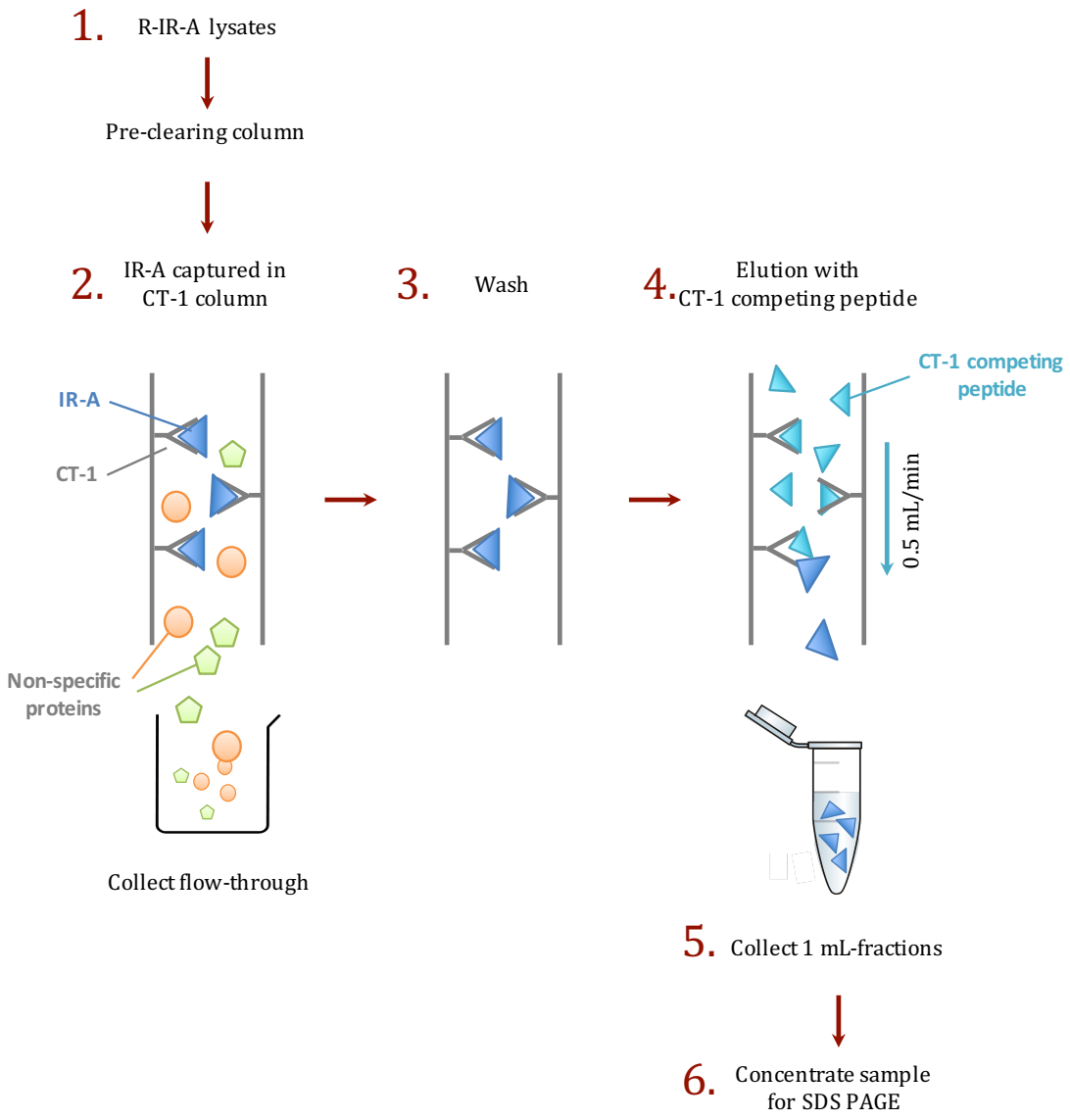

Schematic 4.3 Current workflow for purification of stimulated IR-A *via* CT-1 column.(1) Load stimulated R-IR-A lysate into pre-clearing column. (2) Capture stimulated IR-A using CT-1 antibody, and collect flow-through. (3) Wash column in 5 column volume (CV) of ice-cold lysis buffer followed by 5CV of TBS. (4) Elute IR-A with 0.5 mg/mL of CT-1 competing peptide in 50 mM HEPES pH 7.4, 10 % glycerol and 0.005 % (v/v) Triton-x 100 (Elution Buffer D). (5) Collect 1-mL fractions and pool fractions with highest protein concentration. (6) Concentrate samples and separate in a 4 –12% reducing SDS PAGE.

4.4 DISCUSSION

Design of signalling biased agonists has been an emerging trend and ambition for peptide-based drug discovery including for the design of insulin peptide analogues. Current research aims to enhance the therapeutic index of insulin analogues not only by improving the rate and precision of action but also by conferring to the analogues the ability to selectively promote signalling for metabolic responses without inducing the undesirable mitogenic response. Critical to such advancement is the understanding of how insulin regulates its multifaceted action through both insulin receptor. This, however, is not without challenge.

Often findings from the investigation of insulin-dependent signalling are difficult to interpret as it has been almost impossible to establish models that allow us to discern the regulation of each specific signalling pathway within the complex insulin signalling network that involves crosstalk between the signals. Some of the known factors that affect insulin signalling are the concentrations of circulating insulin, receptor isoform, receptor binding affinities, ligand residence times on receptor (or dissociation rate), rate of receptor internalisation and expression of downstream signalling molecules by different cell types (Haeusler et al., 2018).

Previously, studies using insulin peptidomimetics, S597 (Rajapaksha and Forbes, 2015, Jensen et al., 2007) and IR-A48 (Yunn et al., 2015), demonstrated a correlation between the rate of insulin receptor internalisation and the differential activation of its downstream PI3K and MAPK signalling. Although the studies were great examples that demonstrate the potential of designing a metabolically-biased IR agonist, lacking from these investigations is the understanding of how the mechanism of binding and activation by these insulin mimetic peptides relates to the mechanisms used by insulin.

Using dicarba insulins as tools, for the first time, the underlying mechanism that allow differential activation of the PI3K and MAPK signalling upon IR activation can be validated. The *cis* dicarba insulin is comprised of sequences identical to insulin with the only modification being the substitution of Cys^{A6}–Cys^{A11} disulfide bond with a non-reducible dicarba (C=C) bond. Earlier, insulin tolerance testings using *cis* dicarba insulin (*Chapter 2*) and *cis* dicarba KP insulin (*Chapter 3*) suggested that the introduction of a rigid bond in *cis* configuration could improve insulin pharmacokinetics. Both *cis* dicarba analogues were shown to lower blood glucose levels more rapidly than their parent peptides in normal and insulin tolerance mice. Interestingly, these analogues also demonstrated reduced mitogenic potencies (DNA synthesis assays) in *in vitro* testing performed on IR-A overexpressing cells.

In this chapter, I showed that the altered metabolic-mitogenic properties of *cis* dicarba insulins is even more evident in the *cis* dicarba glargine. For the first time, I have shown the ability to reduced mitogenic potency of glargine insulin to a significant 5-fold lower potency *in vitro* as evident in the *cis* dicarba glargine. Essentially, the mitogenecity of *cis* dicarba glargine is now similar to native insulin (*in vitro*) and still effectively lowers blood glucose levels in mice, at least within 2 hours after treatment *via* intraperitoneal injection.

The increased mitogenecity of glargine is mostly correlated to its increased binding affinity for IGF-1R (Sommerfeld et al., 2010, Kurtzhals et al., 2000, Varewijck et al., 2010) . Consistent to the previous findings, glargine binds to IR-B with similar (or slightly lower) affinity to native insulin and binds to IGF-1R with approximately 5-fold higher affinity. The *cis* dicarba glargine binds to both IR-B and IGF-1R with less than 2-fold lower affinity relative to glargine. Compared to insulin, *cis* dicarba glargine binds to IGF-IR with approximately 2–3-fold higher affinity than the native insulin and is equipotent to insulin in IGF-1R activation. Although it is possible that the reduced mitogenecity of the *cis* dicarba glargine may be partly attributed by its altered binding and activation capacity for IGF-1R, I have demonstrated that *cis* dicarba glargine (and other dicarba insulin analogues) can indeed regulate signalling bias predominantly through IR-A that accounts for its reduced mitogenic potency measured in DNA synthesis assay. Here, I also provided further evidence that may describe the mechanism underlying the signalling-biased properties of the *cis* dicarba analogues through investigations on the signalling kinetics and its correlated receptor dynamics upstream of these observed biological outputs in IR-A overexpressing cells.

Firstly, the dose-dependent signalling analyses has provided us a broad overview of the signalling pattern of PI3K and MAPK pathways when stimulated by the *cis* dicarba analogues. The effect of differential signalling was more evident in IR-A compared to IR-B-overexpressing cells; supporting our initial suspicion that the signalling biased of *cis* dicarba analogues is most likely IR-A dependent. As described in results section, the reduced Erk 1 and 2 activations were most drastic in the concentration range of 0.5–10 nM (Figs. 4.5 –4.16); this is also consistent with the observation in the dose-response DNA synthesis analyses; albeit the latter were measured after an 18 h-stimulation (Fig 4.3*B*). Interestingly, the relative Erk 1/2 phosphorylation activated by *cis* dicarba glargine within the tested concentration range were only < 2-fold lower than glargine; as oppose to the 5-fold lower mitogenic potency measured in DNA synthesis assay. The time-course signalling analyses would suggest that the delayed Erk 1/2 activations

upon *cis* dicarba insulins stimulation plays an additional and important role that attribute to their lower mitogenic response. Activation kinetics of Akt-PI3K was unaffected.

Importantly, both *cis* dicarba insulin (Figs. 4.17, 4.18, 4.21 and 4.22) and *cis* dicarba glargine (Figs. 4.19–4.22) were unable to stimulate phosphorylation of Erk 1/2 to the maximal level seen in insulin or glargine stimulation (see kinetic curves in Fig. 4.22). Phosphorylation levels of Erk 1/2 reached a maximum after 10 min stimulation where maximum level of phospho-Erk 1/2 when stimulated by *cis* dicarba analogues were only approximately half of the level achieved by insulin or glargine stimulation. The *cis* dicarba glargine promotes the lowest and slowest Erk 1/2 activations amongst all tested peptides. These data suggest that the difference in the "long-term" mitogenic potency (up to 18 hours as in DNA synthesis) between the analogues was established soon after stimulation (*i.e.* by 10 min).

Supporting the findings in the western blot analyses, reduced mitogenic MAPK signalling correlates strongly with the reduced capability of promoting IR-A receptor internalisation when stimulated by the *cis* dicarba insulin analogues. Both *cis* dicarba insulin and *cis* dicarba glargine, showed no sign of promoting IR-A internalisation after stimulation for up to two hours. On the other hand, native insulin and glargine are equally effective in promoting receptor internalisation, inducing ~5 % of IR-A internalisation within 5 minutes post-stimulation and only 60% of total receptor remained on the surface after 2 hours (see Fig. 4.23). This is somewhat consistent with the data published from several groups. Rajapaksha *et al.* reported 80 % of IR-A receptor remained on cell surface after 30 minutes stimulation with 10 nM insulin (Rajapaksha and Forbes, 2015). Morcavello *et al*. showed 70% of IR-A remained on the cell surface after 60 minutes stimulation with 1, 5 or 30 nM of insulin (Morcavallo et al., 2012). Using an indirect approach, Jensen *et al.* measured receptor internalisation through detection of surface bound and internalised ^{125}I-insulin and reported only 20 % of ^{125}I-insulin remained surface bound after 2 h-stimulation (Jensen et al., 2007). However, it is important to acknowledge that each group performed receptor internalisation assay using different experimental approach and stimulating conditions, thus data cannot be compared directly. Interestingly, although the *cis* dicarba insulin analogues are completely incapable of inducing IR-A internalisation they can activate ERK1/2, although with poorer efficiency than insulin or glargine. It is possible that the pathway can also be activated through a surface bound IR-A albeit less effectively.

Summarized in *Table 4.4*, in this study, I have definitively demonstrated a strong correlation between insulin's mitogenicity, MAPK signalling and IR-A internalisation. Using the

metabolically-biased *cis* dicarba insulin analogues, I further validated that IR-A receptor internalisation is an important mechanism that promotes the maximal phosphorylations of Erk 1/2 in MAPK signalling responsible for a sustainable downstream mitogenic response. *Cis* dicarba insulin analogues with impaired ability to promote receptor internalisation result in significantly delayed and reduced MAPK activation that attribute to its lower downstream mitogenic response measured in DNA synthesis assay. On the other hand, the activation of the metabolic responses *via* the PI3K pathway are not affected by the perturbed receptor internalisation. The rapid activation of PI3K signalling is most likely activated through cell surface receptors. These findings are also consistent with the previously described mechanism for ligand-dependent signalling biased through IR-A (Jensen et al., 2007, Rajapaksha and Forbes, 2015, Morcavallo et al., 2012, Yunn et al., 2015).

Table 4.4 Summary of metabolic-mitogenic signalling profile and biological outputs promoted by insulin, glargine, *cis* dicarba insulin and *cis* dicarba glargine. Each * represents approximately 25% change relative to insulin.

The *cis* dicarba insulin is equipotent to native insulin in receptor binding and activation, whereas *cis* dicarba glargine has receptor potencies ≤ 2-fold lower than glargine. *In vitro* studies suggest that both *cis* dicarba insulin analogues are mitogenically less potent (~ 5-fold less) compared to their respective parent peptides while retaining their metabolic potency as indicated in glucose uptake assay and in insulin tolerance testings (ITT) on high fat (HF) diet mice. The reduced mitogenicity of *cis* dicarba insulins is clearly correlated to their almost complete loss of ability to promote IR-A internalisation. The *cis* dicarba insulins also exhibit an apparent biased PI3K-MAPK signalling profile. The intracellular signalling potency presented in this table represent a summary of data derived from the time-course western blot analyses. Within 10 min stimulation, the *cis* dicarba insulins exhibit a delayed MAPK signalling and achieve maximal Erk1/2 phosphorylation of only ~ 50% of the levels promoted by insulin and glargine. Activation of PI3K was not affected. In summary, the *cis* dicarba analogues are metabolically biased and exhibit significantly reduced mitogenic responses. The reduced mitogenic potency is correlated to the perturbed IR-A internalisation that is also reflected in the delayed and lowered activation of MAPK signalling.

Experiments	**Receptor binding**		**Receptor activation (Total pY)**		**Metabolic potency**	**Mitogenic Potency**	**ITT**	**IR-A internali-zation**	**Intracellular Signalling Potency**						
									IR-B fibroblasts / IR-A L6 myoblasts						
									P13K Signalling				**MAPK Signalling**		
	Solubilised IR-B	*Solubilised IGF-1R*	*Solubilised IR-B*	*Solulibised IGF-1R*	*3T3-L1 adipocytes*	*IR-A L6 myoblasts*	*HF diet mice*	*IR-A L6 myoblasts*	p-Akt (S473)	p-Akt (T308)	p-GSK3β (S9)	p-S6 (pS235/236)	p-Erk1 (pT202/pY204)	p-Erk2 (pT185/pY187)	p-p90RSK (S380)
Insulin	****	****	****	****	****	****	****	****	****	****	****	****	****	****	****
***cis* dicarba insulin**	****	****	****	****	****	*	**** **	*	****	****	****	****	***	***	****
glargine	****	**** x5	****	****	n.a.	**** x5	*	****	****	****	****	****	****	****	****
***cis* dircarba glargine**	***	**** x2.5	**	****	****	****	***	*	****	****	****	****	**	**	***

Finally, the logical next goal of this chapter was to identify the first signal that activates the machinery of IR-A internalisation responsible for mitogenic signalling. We proposed that in order for insulin to specifically instruct the activation of different machineries that initiate the metabolic or mitogenic outcome, the receptor needs to be able to convey the message systematically using different 'barcode' combinations.

Previously, several groups (Jensen et al., 2007, Hansen et al., 2012, Yunn et al., 2015) and our group (Rajapaksha and Forbes, 2015) have reported a change in phosphorylation pattern and preferential phosphorylation on several specific residues on the IR that are suggestively associated to the receptor's metabolic-mitogenic signalling bias. For instance, the highly mitogenic insulin X10 promotes preferential phosphorylation at Y960 located on the juxtamembrane (JM) domain an essential docking site for Shc that subsequently initiate MAPK signalling (Hansen et al., 2012). In contrast, the metabolically-biased IR-A48 peptide was reported to preferentially promotes phosphorylation on Y1150 residue on the IR kinase domain. The group proposed that phosphorylated Y1150 residue acts as a selective binding site for IRS-1/2 for inducing metabolic activity *via* Akt activation (Yunn et al., 2017).

Most recently, Dr Rajapaksha from our laboratory reported the reduced mitogenecity of S597 peptide is associated to a reduced phosphorylation rate and a change in phosphorylation kinetics of several IR-A tyrosine residues including Y960, Y1146/Y1150/Y1151, Y1316 and Y1322 residues (Rajapaksha and Forbes, 2015) The altered IR-A phosphorylation pattern stimulated by the 'less mitogenic' S597 peptide may also explains the reduced phosphorylation for IRS-1 and IRS-2 reported earlier by Jensen *et al.* (Jensen et al., 2007). These evidence reemphasise the need to further explore the different phosphorylation patterns of insulin receptor.

We aim to also expand the study by examining all available phosphorylation sites on IR-A: Y953, Y960, Y972, S994, Y999, S1023, S1025, Y1110, Y1198, S1275, S1293, S1294, S1308, S1309, S1315, Y1316, Y1322, T1323, T1336, S1340. By investigating the phosphorylation kinetics/pattern of IR-A stimulated by *cis* dicarba insulin, we envisage to map the distinctive IR-A phosphorylation "barcode" responsible promoting mitogenic signalling. Although the study was interrupted due to time constraint, this chapter provides a strong basis to future investigation on IR-A signalling bias using the *cis* dicarba insulin.

4.5 CONCLUSION

In conclusion, this chapter studied two ideal models for the investigation of IR-A signalling bias – *cis* dicarba insulin and *cis* dicarba glargine. The dicarba insulin analogues provide us with a fundamental opportunity to validate the correlation between IR-A internalisation and MAPK signalling without the discrepancy of using analogues widely different to insulin. I confirmed that the activation of MAPK signalling *via* IR-A is accelerated by the rate of IR-A internalisation. Replacing insulin/glargine's A6–A11 disulfide bond with a dicarba bond does not affect metabolic potency but significantly reduced mitogenic potential. The effects of signalling bias were also clearly reflected in the change of MAPK signalling kinetics. The findings presented also created a strong foundation for future studies that would assist in the mapping of IR-A phosphorylation kinetics/patterns that regulates the selective mechanism for the metabolic or mitogenic signalling.

Astoundingly, the *cis* dicarba glargine that has mitogenic potential equivalent to native insulin may be a great solution for improving the glargine analogue without compromising its metabolic potential. Further pharmacokinetics/pharmacodynamics studies of this analogue are required to expand its therapeutic potential.

CHAPTER 4

APPENDICES

CHAPTER 4 APPENDICES

APPENDIX 4A Synthesis of Dicarba Glargine Insulins

c[Δ4A6,11]-Dicarba human insulin glargine transformations

desA1-5-[A6,11]-Agl-[A7]-Cys(tBu)-[A20]-Cys(Acm) human insulin glargine A-chain 5

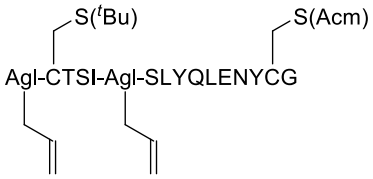

5

The automated, microwave-accelerated procedure as described by Robinson *et al.*[1] was used for the synthesis of peptide **5** on Fmoc-Gly-PEG-PS resin (1.10 g, 200 μmol). After sequence completion, the resin-bound peptide was transferred into a fritted syringe and treated with an acetic anhydride solution (7 mL; DMF : acetic anhydride : NMM; 94 : 5 : 1) for 2 h. The resin was then washed with DMF (7 mL; 3 × 1 min), DCM (7 mL; 3 × 1 min) and MeOH (7 mL; 3 × 1 min), then left to dry *in vacuo* for 1 h. Prior to treatment with MeOH, a small aliquot of the resin-bound peptide was removed and subjected to Fmoc-deprotection in the presence of 20% v/v piperidine in DMF (1 mL; 1 × 1 min, 2 × 10 min), then washed with DMF (1 mL; 5 × 1 min), DCM (1 mL; 3 × 1 min) and MeOH (1 mL; 3 × 1 min). The aliquot of Fmoc-deprotected resin-tethered peptide was subjected to TFA-mediated cleavage for RP-HPLC and mass spectral analysis. This supported formation of the desired peptide **5** in 70% purity. Mass spectrum (ESI^+, MeCN : H_2O : HCOOH): *m/z* 958.3 $[M + 2H]^{2+}$, ½($C_{85}H_{133}N_{19}O_{27}S_2$) requires 958.0. RP-HPLC (Agilent: Vydac C18 analytical column, 15 → 45% buffer B over 30 min): t_R = 18.9 min.

desA1-5-c[Δ4A6,11]-Dicarba-[A7]-Cys(tBu)-[A20]-Cys(Acm) human insulin glargine A-chain 6

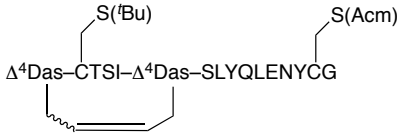

Cis-**6** and *trans*-**6**

Resin-bound peptide **5** was subjected to the microwave-accelerated RCM procedure as described by Robinson *et al.*[1] under the following conditions: Resin-bound **5** (1.35 g, 0.20 mmol), DCM (13 mL), 0.4 M LiCl in DMF (0.5 mL), 2nd generation Grubbs' catalyst (34 mg, 40 μmol), 100 W μwave, 100 ºC, 4 h, 100% conversion into **6**. Post metathesis, a small aliquot of resin-bound peptide was subjected to Fmoc-deprotection in the presence of 20% v/v piperidine in DMF (1 mL; 1 × 1 min, 2 × 10 min), then washed with DMF (1 mL; 5 × 1 min), DCM (1 mL; 3 × 1 min) and MeOH (1 mL; 3 × 1 min). The aliquot of Fmoc-deprotected resin-tethered peptide was subjected to TFA-mediated cleavage for RP-HPLC and mass spectral analysis. This supported formation of the desired peptide as two isomers, *Z*-**6** and *E*-**6**, in a 7 : 3 ratio. *Cis*-**6**: Mass spectrum (ESI^+, MeCN : H_2O : HCOOH): *m/z* 944.0 $[M + 2H]^{2+}$, ½($C_{83}H_{129}N_{19}O_{27}S_2$) requires 943.9. RP-HPLC (Agilent: Vydac C18 analytical column, 15 → 45% buffer B over 30 min): t_R = 17.8 min. *Trans*-**6**: Mass spectrum (ESI^+, MeCN : H_2O : HCOOH): *m/z* 944.2 $[M + 2H]^{2+}$, ½($C_{83}H_{129}N_{19}O_{27}S_2$) requires 943.9. RP-HPLC (Agilent: Vydac C18 analytical column, 15 → 45% buffer B over 30 min): t_R = 17.9 min.

c[Δ4A6,11]-Dicarba-[A7]-Cys(tBu)-[A20]-Cys(Acm) human insulin glargine A-chain 7

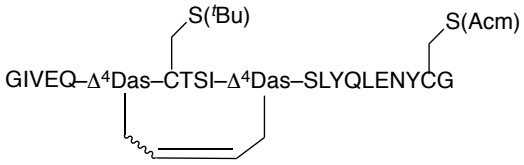

Cis-**7** and *trans*-**7**

The automated, microwave-accelerated procedure as described by Robinson *et al.*[1] was used to attach the remaining five residues on resin-bound peptide **6** (1.16 g, 0.20 mmol). After sequence completion, the resin-bound peptide was transferred into a fritted syringe and subjected to Fmoc-deprotection in the presence of 20% v/v piperidine in DMF (7 mL; 1 × 1 min, 2 × 10 min). The resin was washed with DMF (7 mL; 5 × 1 min), DCM (7 mL; 3 × 1 min) and MeOH (7 mL; 3 × 1 min), then left to dry *in vacuo* for 1 h. The resin-bound peptide (0.98 g) was subjected to TFA-mediated cleavage and RP-HPLC and mass spectral analysis of the resultant pale brown solid (300 mg) supported formation of the desired peptide as two isomers, *Z*-**7** and *E*-**7**, in a 7 : 3 ratio. *Cis*-**7**: Mass spectrum (ESI^+, MeCN : H_2O : HCOOH): *m/z* 1207.2 $[M + 2H]^{2+}$, ½($C_{106}H_{167}N_{25}O_{35}S_2$) requires 1207.1. RP-HPLC (Agilent: Vydac C18 analytical column, 15 → 45% buffer B over 30 min): t_R = 18.6 min. *Trans*-**7**: Mass spectrum (ESI^+, MeCN : H_2O : HCOOH): *m/z* 1207.2 $[M + 2H]^{2+}$, ½($C_{106}H_{167}N_{25}O_{35}S_2$) requires 1207.1. RP-HPLC (Agilent: Vydac C18 analytical column, 15 → 45% buffer B over 30 min): t_R = 19.5 min.

c[Δ4A6,11]-Dicarba-[A7]-Cys(Pyr)-[A20]-Cys(Acm) human insulin glargine A-chain 8

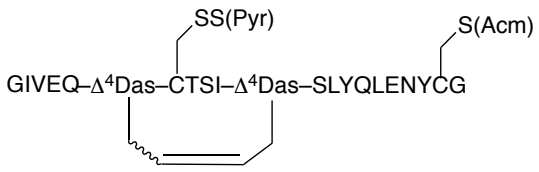

Cis-**8** and *trans*-**8**

The concerted *tert*-butyl-deprotection and pyridinyl-reprotection of Cys_7 was carried out according to a procedure described by Bullesback *et al.*.[2] A solution of ice-cold TFA : TfOH (8 mL; 4 : 1) was added to a stirred solution of the cyclic peptide **7** (300 mg, 114 μmol) and 2,2'-DPDS (0.251 g, 1.14 mmol) in TFA : anisol (8 mL; 9 : 1) at 0°C. After 1.5 h, the reaction mixture was reduced under a constant stream of air and ice-cold Et_2O (40 mL) was added to induce peptide precipitation. The resultant solid was collected by centrifugation (3 × 10 min), lyophilised and analysed by RP-HPLC and mass spectrometry. This supported formation of the *S*-activated peptide **8** as two isomers, *Z*-**8** and *E*-**8**, in a 7 : 3 ratio. Following purification by RP-HPLC (Agilent: Vydac C18 preparative column, 15 → 45% buffer B over 30 min, t_R = 22.9 and 21.9 min), selected fractions were combined and lyophilised to give two isomers, *Z*-**8** and *E*-**8**, of the desired peptide as colourless solids in 64% and 51% purity respectively. Repurification of *cis*-**8** isomer (Agilent: Vydac C18 analytical column, 15 → 45% buffer B over 30 min: t_R = 17.5 min) then gave insulin analogue *Z*-**8** as a colourless solid (2.96 mg, 1%) in 90% purity. *Cis*-**8**: Mass spectrum (ESI^+, MeCN : H_2O : HCOOH): *m/z* 822.7 $[M + H]^+$, $C_{107}H_{163}N_{26}O_{35}S_3$ requires 822.7; 1233.8 $[M + 2H]^{2+}$, ½($C_{107}H_{162}N_{26}O_{35}S_3$) requires 1233.5. RP-HPLC (Agilent: Vydac C18 analytical column 15 → 45% buffer B over 30 min): t_R = 17.8 min. Repurification of *trans*-**8** isomer (Agilent: Vydac C18 analytical column, 15 → 45% buffer B over 30 min: t_R = 19.5 min) then gave insulin analogue *E*-**8** as a colourless solid (1.95 mg, 0.8%) in 94% purity. *Trans*-**8**: Mass spectrum (ESI^+, MeCN : H_2O : HCOOH): *m/z* 822.7 $[M + H]^+$, $C_{107}H_{163}N_{26}O_{35}S_3$ requires 822.7; 1233.5 $[M + 2H]^{2+}$, ½($C_{107}H_{162}N_{26}O_{35}S_3$) requires 1233.5. RP-HPLC (Agilent: Vydac C18 analytical column, 15 → 45% buffer B over 30 min): t_R = 18.7 min.

[B19]-Cys(Acm) human insulin glargine B-chain 9

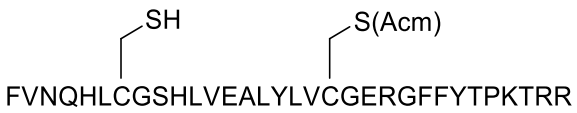

9

The automated, microwave-accelerated procedure as described by Robinson *et al.*[1] was used for the synthesis of peptide **9** on Fmoc-Thr(^{t}Bu)-PEG-PS resin (0.95 g, 0.20 mmol). After sequence completion, the resin was transferred into a fritted syringe, washed with DMF (7 mL; 3 × 1 min), DCM (7 mL; 3 × 1 min) and MeOH (7 mL; 3 × 1 min), then left to dry *in vacuo* for 1 h. A small aliquot of resin-bound peptide was subjected to the cleavage procedure as described by Robinson *et al.*[1] for RP-HPLC and mass spectral analysis. This supported formation of the desired peptide **9** in 48% purity. Following global Fmoc-deprotection and TFA-mediated cleavage of the remaining peptide from the resin (1.59 g), the resultant colourless solid (520 mg) was purified by RP-HPLC (Agilent: Vydac C18 preparative column, 0 → 25% buffer B over 5 min then 25 → 45% buffer B over 30 min, t_R = 18.9 min). Selected fractions were combined and lyophilised to give the desired peptide **9** as a colourless solid (48 mg, 6%) in 96% purity. Mass spectrum (ESI$^+$, MeCN : H_2O : HCOOH): *m/z* 636.5 $[M + 6H]^{6+}$, $^1/_6(C_{173}H_{269}N_{49}O_{45}S_2)$ requires 636.2; 763.6 $[M + 5H]^{5+}$, $^1/_5(C_{173}H_{268}N_{49}O_{45}S_2)$ requires 763.2; 954.2 $[M + 4H]^{4+}$, $^1/_4(C_{173}H_{267}N_{49}O_{45}S_2)$ requires 953.7; 1271.9 $[M + 3H]^{3+}$, $^1/_3(C_{173}H_{266}N_{49}O_{45}S_2)$ requires 1271.3. RP-HPLC (Agilent: Vydac C18 analytical column, 0 → 25% buffer B over 5 min then 25 → 45% buffer B over 30 min): t_R = 17.6 min.

The monocyclic A-B heterodimer of c[Δ4A6,11]-dicarba human insulin glargine 10

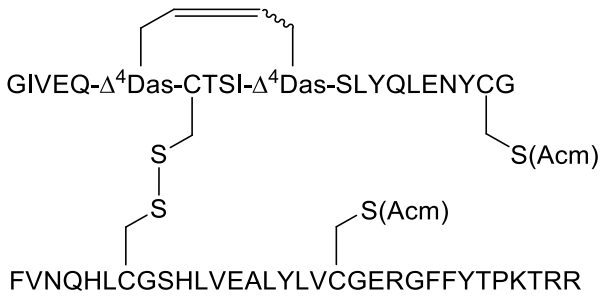

Cis-**10** and *trans*-**10**

<u>*Cis*-isomer:</u>

The modified insulin A-chain *Z*-**8** (1.96 mg, 0.79 μmol) in 50 mM NH_4HCO_3 (1.0 mL) was added dropwise to a stirred solution of the modified insulin B-chain **9** (3.03 mg, 0.79 μmol) in H_2O : MeCN (3.0 mL; 9 : 1). Reaction progress was monitored by RP-HPLC and mass spectrometry, and after 2 h the oxidation was terminated by addition of AcOH. Mass spectrum (ESI^+, MeCN : H_2O : HCOOH): *m/z* 1029.1 $[M + 6H]^{6+}$, ⅙($C_{275}H_{424}N_{74}O_{80}S_4$) requires 1028.5; 1234.3 $[M + 5H]^{5+}$, ⅕($C_{275}H_{423}N_{74}O_{80}S_4$) requires 1234.0; 1543.0 $[M + 4H]^{4+}$, ¼($C_{275}H_{422}N_{74}O_{80}S_4$) requires 1542.3. RP-HPLC (Agilent: Vydac C18 analytical column, 0 → 25% buffer B over 5 min then 25 → 45% buffer B over 30 min): t_R = 20.2 min.

<u>*Trans*-isomer:</u>

The modified insulin A-chain *E*-**8** (1.95 mg, 0.79 μmol) in 50 mM NH_4HCO_3 (1.0 mL) was added dropwise to a stirred solution of the modified insulin B-chain **9** (3.01 mg, 0.79 μmol) in H_2O : MeCN (3.0 mL; 9 : 1). Reaction progress was monitored by RP-HPLC and mass spectrometry, and after 2 h the oxidation was terminated by addition of AcOH. Mass spectrum (ESI^+, MeCN : H_2O : HCOOH): *m/z* 1028.8 $[M + 6H]^{6+}$, ⅙($C_{275}H_{424}N_{74}O_{80}S_4$) requires 1028.5; 1234.5 $[M + 5H]^{5+}$, ⅕($C_{275}H_{423}N_{74}O_{80}S_4$) requires 1234.0; 1543.1 $[M + 4H]^{4+}$, ¼($C_{275}H_{422}N_{74}O_{80}S_4$) requires 1542.3. RP-HPLC (Agilent: Vydac C18 analytical column, 0 → 25% buffer B over 5 min then 25 → 45% buffer B over 30 min): t_R = 20.7 min.

c[Δ4A6,11]-Dicarba human insulin glargine 11

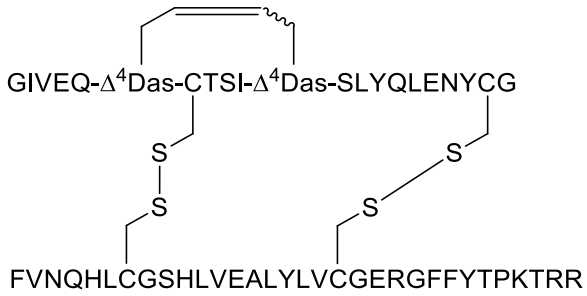

Cis-**11** and *trans*-**11**

<u>*Cis*-isomer:</u>

The iodine-catalysed disulfide oxidation was carried out according to a procedure described by Lin *et al.*.[3] A 20 mM solution of iodine in glacial acetic acid (2.2 mL) was added to a stirred solution of the mono-cyclic peptide *Z*-**10** (5.0 mg, 0.81 μmol) in glacial acetic acid (5.6 mL) and 60 mM HCl (420 μL). Reaction progress was monitored by RP-HPLC and after 2.75 h, ice-cold Et_2O (35 mL) was added to induce peptide precipitation. The resultant yellow solid was collected by centrifugation (1 × 10 min) and 20 mM ascorbic acid (1 mL) was then added to quench any excess iodine before analysis *via* RP-HPLC and mass spectrometry. Following purification by RP-HPLC (Agilent: Vydac C18 analytical column, 0 → 30% buffer B over 5 min then 30 → 40% buffer B over 60 min, t_R = 21.5 min), selected fractions were combined and lyophilised to give the desired *c*[Δ^4A6,11]-dicarba human insulin glargine analogue *Z*-**11** as a colourless solid (635 μg, 13%) in >99% purity. Mass spectrum (ESI^+, MeCN : H_2O : HCOOH): *m/z* 1004.9 $[M + 6H]^{6+}$, $\frac{1}{6}(C_{269}H_{412}N_{72}O_{78}S_4)$ requires 1004.5; 1205.4 $[M + 5H]^{5+}$, $\frac{1}{5}(C_{269}H_{411}N_{72}O_{78}S_4)$ requires 1205.2; 1506.4 $[M + 4H]^{4+}$, $\frac{1}{4}(C_{269}H_{410}N_{72}O_{78}S_4)$ requires 1506.2. RP-HPLC (Agilent: Vydac C18 analytical column, 0 → 30% buffer B over 5 min then 30 → 40% buffer B over 30 min): t_R = 18.7 min.

<u>*Trans*-isomer:</u>

The iodine-catalysed disulfide oxidation was carried out according to a procedure described by Lin *et al.*.[3] A 20 mM solution of iodine in glacial acetic acid (2.2 mL) was added to a stirred solution of the mono-cyclic peptide *E*-10 (5.0 mg, 0.81 μmol) in glacial acetic acid (5.6 mL) and 60 mM HCl (420 μL). Reaction progress was monitored by RP-HPLC and after 2.75 h, ice-cold Et_2O (35 mL) was added to induce peptide precipitation. The resultant solid was collected by

centrifugation (1 × 10 min) and 20 mM ascorbic acid (1 mL) was then added to quench any excess iodine before analysis *via* RP-HPLC and mass spectrometry. Following purification by RP-HPLC (Agilent: Vydac C18 analytical column, 0 → 25% buffer B over 5 min then 25 → 40% buffer B over 60 min, t_R = 32.6 min), selected fractions were combined and lyophilised to give the desired *c*[Δ^4A6,11]-dicarba human insulin glargine analogue *E*-11 as a colourless solid (620 μg, 13%) in >99% purity. Mass spectrum (ESI^+, MeCN : H_2O : HCOOH): *m/z* 1004.8 $[M + 6H]^{6+}$, $^1/_6(C_{269}H_{412}N_{72}O_{78}S_4)$ requires 1004.5; 1205.8 $[M + 5H]^{5+}$, $^1/_5(C_{269}H_{411}N_{72}O_{78}S_4)$ requires 1205.2; 1506.9 $[M + 4H]^{4+}$, $^1/_4(C_{269}H_{410}N_{72}O_{78}S_4)$ requires 1506.2. RP-HPLC (Agilent: Vydac C18 analytical column, 0 → 30% buffer B over 5 min then 30 → 40% buffer B over 30 min): t_R = 14.6 min.

APPENDIX FIGURES 4
APPENDIX FIGURE 4.1

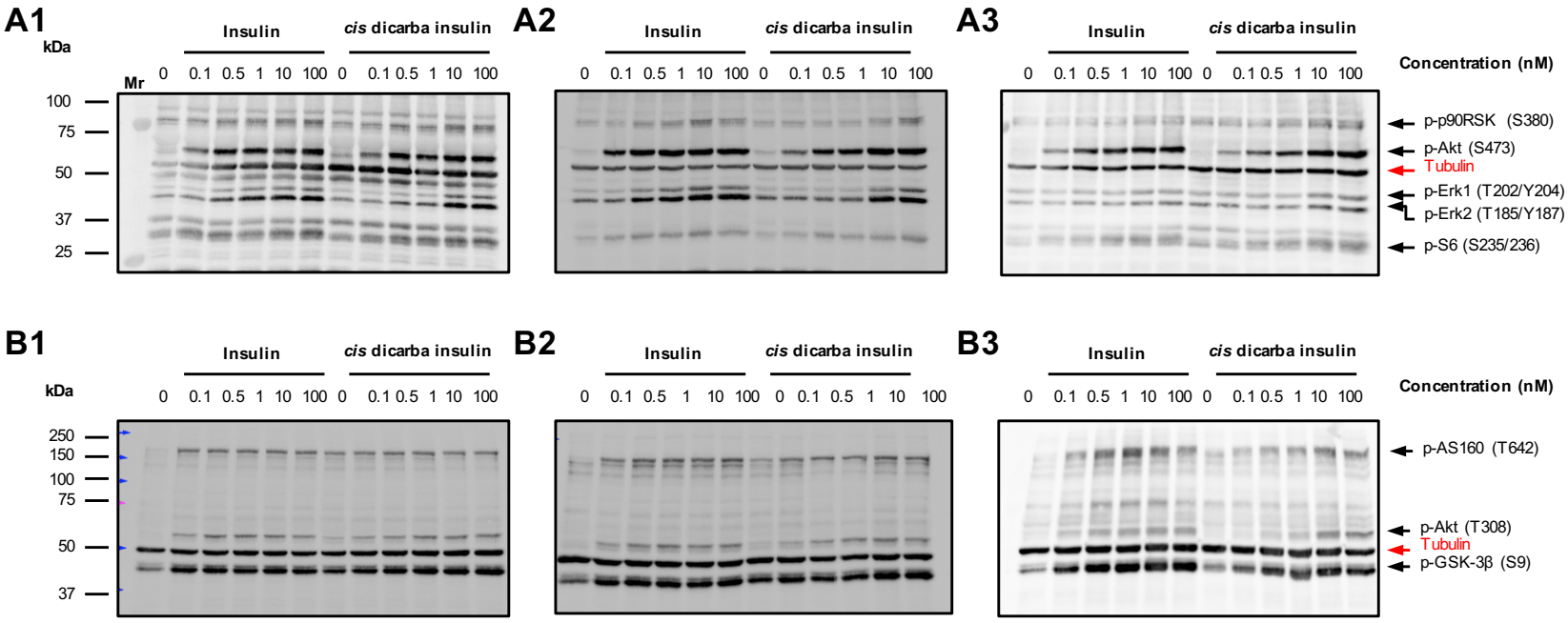

Appendix Figure 4.1 Western blots of IR-B stimulated by increasing concentration of insulin and *cis* dicarba insulin. Serum starved R⁻IR-B fibroblasts were stimulated with increasing concentrations (0, 0.1, 0.5 1, 10 and 100 nM) of insulin or *cis* dicarba insulin for 10 min. Whole cells lysates were prepared and 20 µg of each sample was separated in duplicate 10% glycine gels followed by immunoblotting. Blots (A1 –A3) probed with Pathscan® Multiplex Western Cocktail allowed detection of phospho-p90RSK (S380), phospho-Akt (S473), phospho-ERK1 (T202/Y204), phospho-ERK2 (T185/Y187) and phospho-S6 ribosomal (S235/236) simultaneously. Blots (B1 – B3) were probed for phospho-AS160 (T642), phospho-Akt (T308) and phospho-GSK3β (S9). Each blot was also probed with anti-β-Tubulin as loading control. *Figure A1* and *B1* are also presented in *Figure 4.5* as representative blots.

APPENDIX FIGURE 4.2

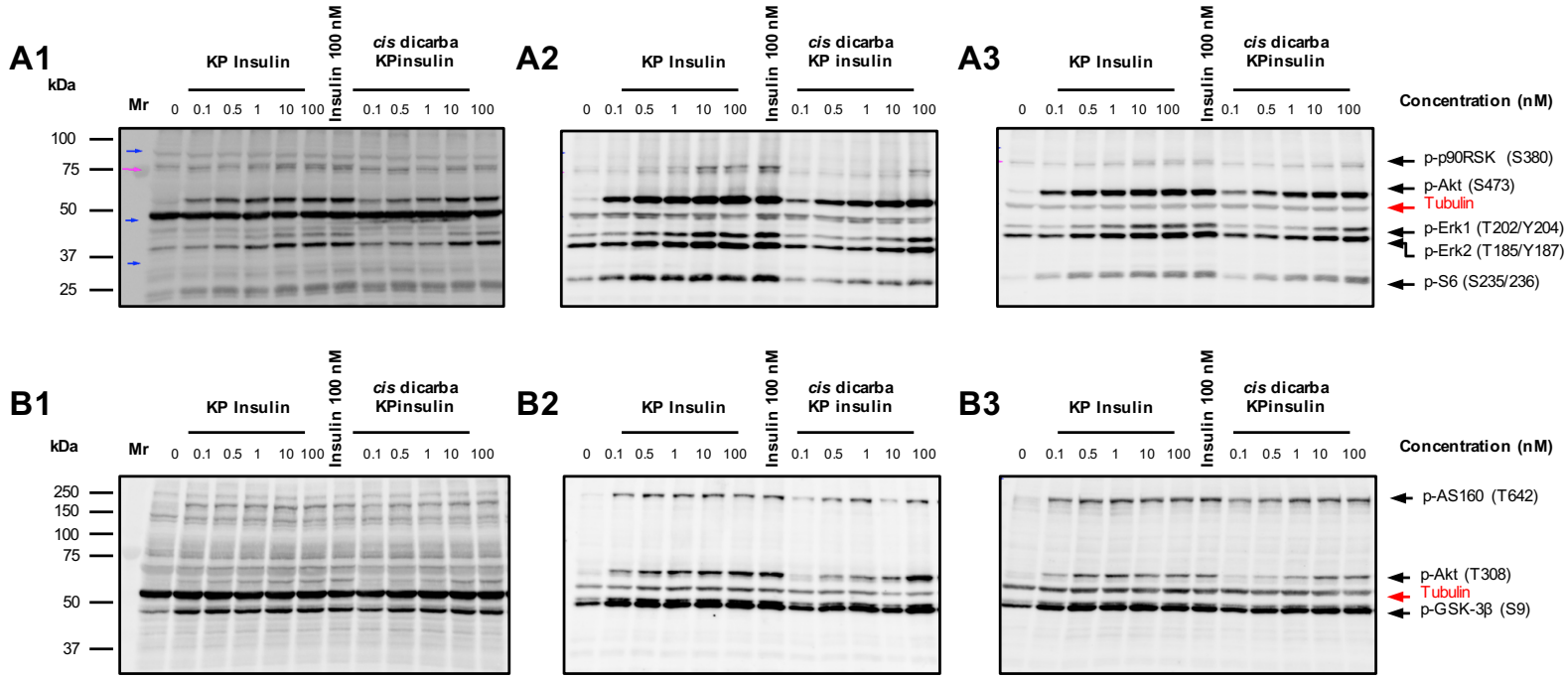

Appendix Figure 4.2 Western blots of IR-B stimulated by increasing concentration of lispro (KP) insulin and *cis* dicarba KP insulin. Serum starved R⁻IR-B fibroblasts were stimulated with increasing concentrations (0, 0.1, 0.5 1, 10 and 100 nM) of KP insulin or *cis* dicarba KP insulin for 10 min. Stimulation by 100 nM of insulin was also included as a control and for normalization to obtained relative phosphorylation levels of of each protein when stimulated by different insulin analogues. Whole cells lysates were prepared and 20 µg of each sample was separated in duplicate 10% glycine gels followed by immunoblotting. Blots (A1 – A3) probed with Pathscan® Multiplex Western Cocktail allowed detection of phospho-p90RSK (S380), phospho-Akt (S473), phospho-ERK1 (T202/Y204), phospho-ERK2 (T185/Y187) and phospho-S6 ribosomal (S235/236) simultaneously. Blots (B1 – B3) were probed for phospho-AS160 (T642), phospho-Akt (T308) and phospho-GSK3β (S9). Each blot was also probed with anti-β-Tubulin as loading control. *Figure A2* and *B2* are also presented in *Figure 4.7* as representative blots. Pink and blue arrows align to markers.

APPENDIX FIGURE 4.3

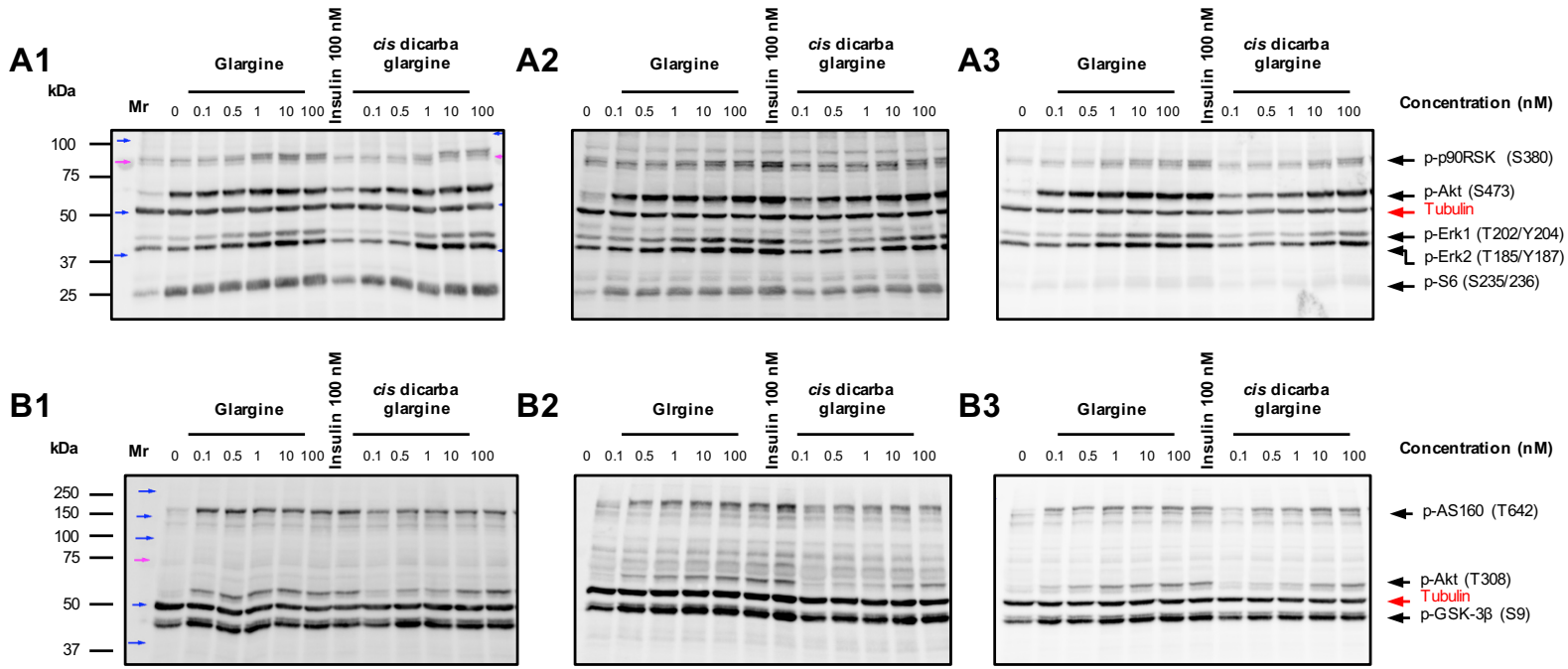

Appendix Figure 4.3 Western blots of IR-B stimulated by increasing concentration of glargine insulin and *cis* dicarba glargine insulin. Serum starved R⁻IR-B fibroblasts were stimulated with increasing concentrations (0, 0.1, 0.5 1, 10 and 100 nM) of glargine insulin or *cis* dicarba glargine insulin for 10 min. Stimulation with 100 nM of insulin were also included as a control and for normalization to obtained relative phosphorylation levels of of each protein when stimulated by different insulin analogues. Whole cells lysates were prepared and 20 µg of each sample was separated in duplicate 10% glycine gels followed by immunoblotting. Blots (A1 – A3) probed with Pathscan® Multiplex Western Cocktail allowed detection of phospho-p90RSK (S380), phospho-Akt (S473), phospho-ERK1 (T202/Y204), phospho-ERK2 (T185/Y187) and phospho-S6 ribosomal (S235/236) simultaneously. Blots (B1 – B3) were probed for phospho-AS160 (T642), phospho-Akt (T308) and phospho-GSK3β (S9). Each blot was also probed with anti-β-Tubulin as loading control. *Figure A2* and *B3* are also presented in *Figure 4.9* as representative blots. Pink and blue arrows align to markers.

APPENDIX FIGURE 4.4

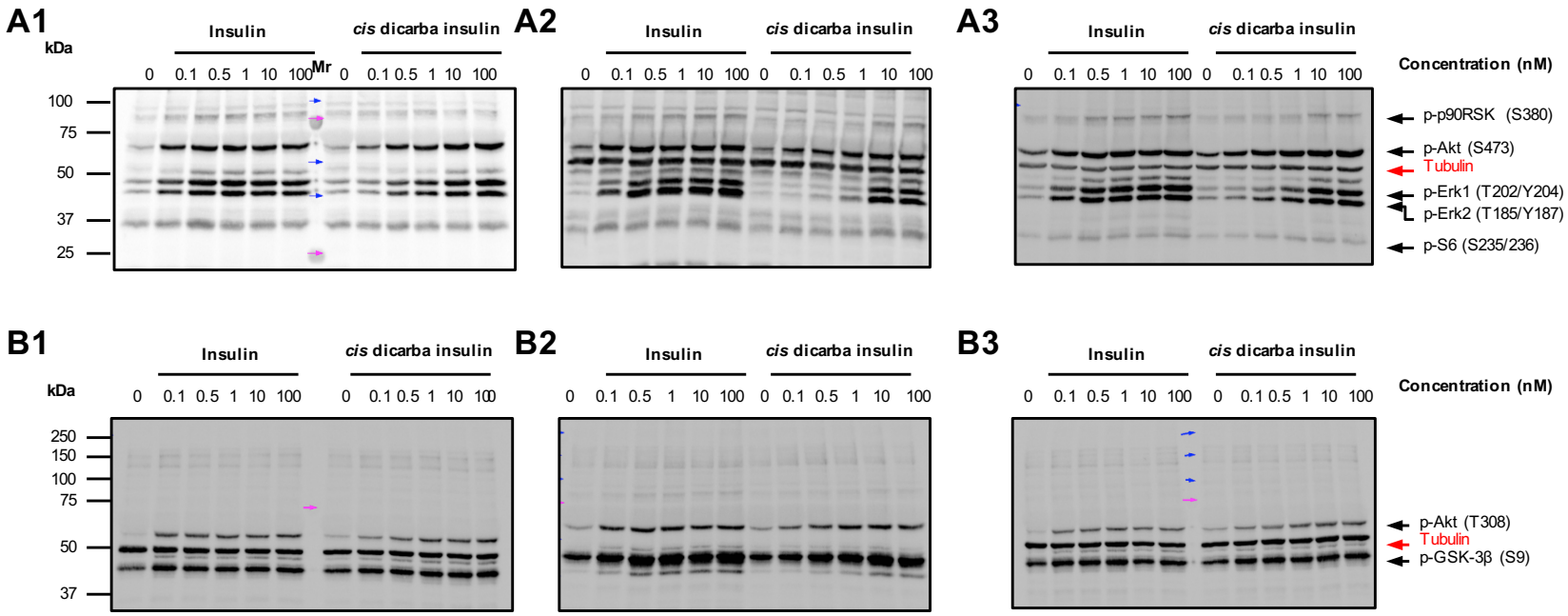

Appendix Figure 4.4 Western blots of IR-A stimulated by increasing concentration of insulin and *cis* dicarba insulin. Serum starved IR-A overexpressing L6 myoblasts (hIR-A L6) were stimulated with increasing concentrations (0, 0.1, 0.5 1, 10 and 100 nM) of insulin or *cis* dicarba insulin for 10 min. Whole cells lysates were prepared and 20 µg of each sample was separated in duplicate 10% glycine gels followed by immunoblotting. Blots (A1 – A3) probed with Pathscan® Multiplex Western Cocktail allowed detection of phospho-p90RSK (S380), phospho-Akt (S473), phospho-ERK1 (T202/Y204), phospho-ERK2 (T185/Y187) and phospho-S6 ribosomal (S235/236) simultaneously. Blots (B1 – B3) were probed for phospho-AS160 (T642), phospho-Akt (T308) and phospho-GSK3β (S9). Each blot was also probed with anti-β-Tubulin as loading control. *Figure A3* and *B1* are also presented in *Figure 4.11* as representative blots. Pink and blue arrows align to markers.

APPENDIX FIGURE 4.5

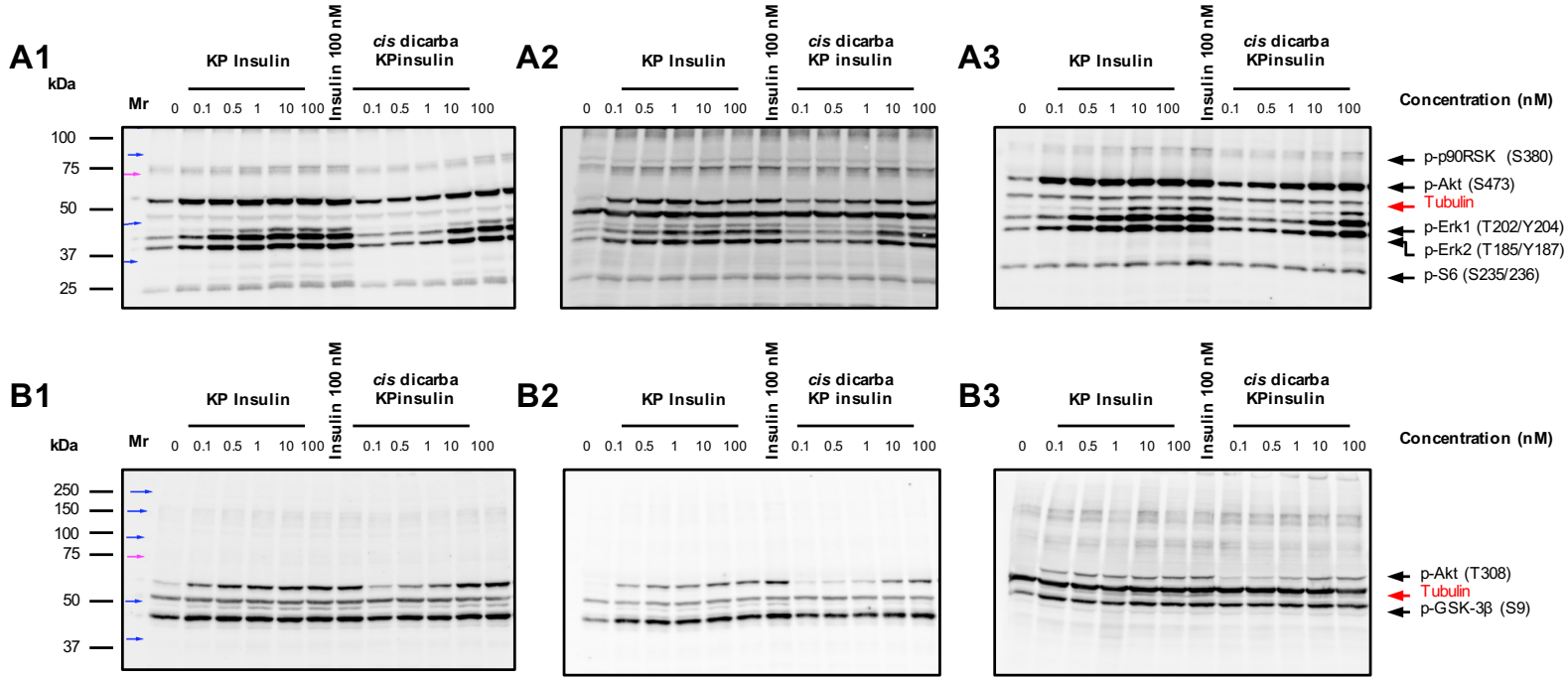

Appendix Figure 4.5 Western blots of IR-A stimulated by increasing concentration of lispro (KP) insulin and *cis* dicarba KP insulin. Serum starved IR-A overexpressing L6 myoblasts (hIR-A L6) were stimulated with increasing concentrations (0, 0.1, 0.5 1, 10 and 100 nM) of KP insulin or *cis* dicarba KP insulin for 10 min. Stimulation with 100 nM of insulin were also included as a control and for normalization to obtained relative phosphorylation levels of of each protein when stimulated by different insulin analogues. Whole cells lysates were prepared and 20 µg of each sample was separated in duplicate 10% glycine gels followed by immunoblotting. Blots (A1 – A3) probed with Pathscan® Multiplex Western Cocktail allowed detection of phospho-p90RSK (S380), phospho-Akt (S473), phospho-ERK1 (T202/Y204), phospho-ERK2 (T185/Y187) and phospho-S6 ribosomal (S235/236) simultaneously. Blots (B1 – B3) were probed for phospho-AS160 (T642), phospho-Akt (T308) and phospho-GSK3β (S9). Each blot was also probed with anti-β-Tubulin as loading control. *Figure A1* and *B1* are also presented in *Figure 4.13* as representative blots. Pink and blue arrows align to markers.

APPENDIX FIGURE 4.6

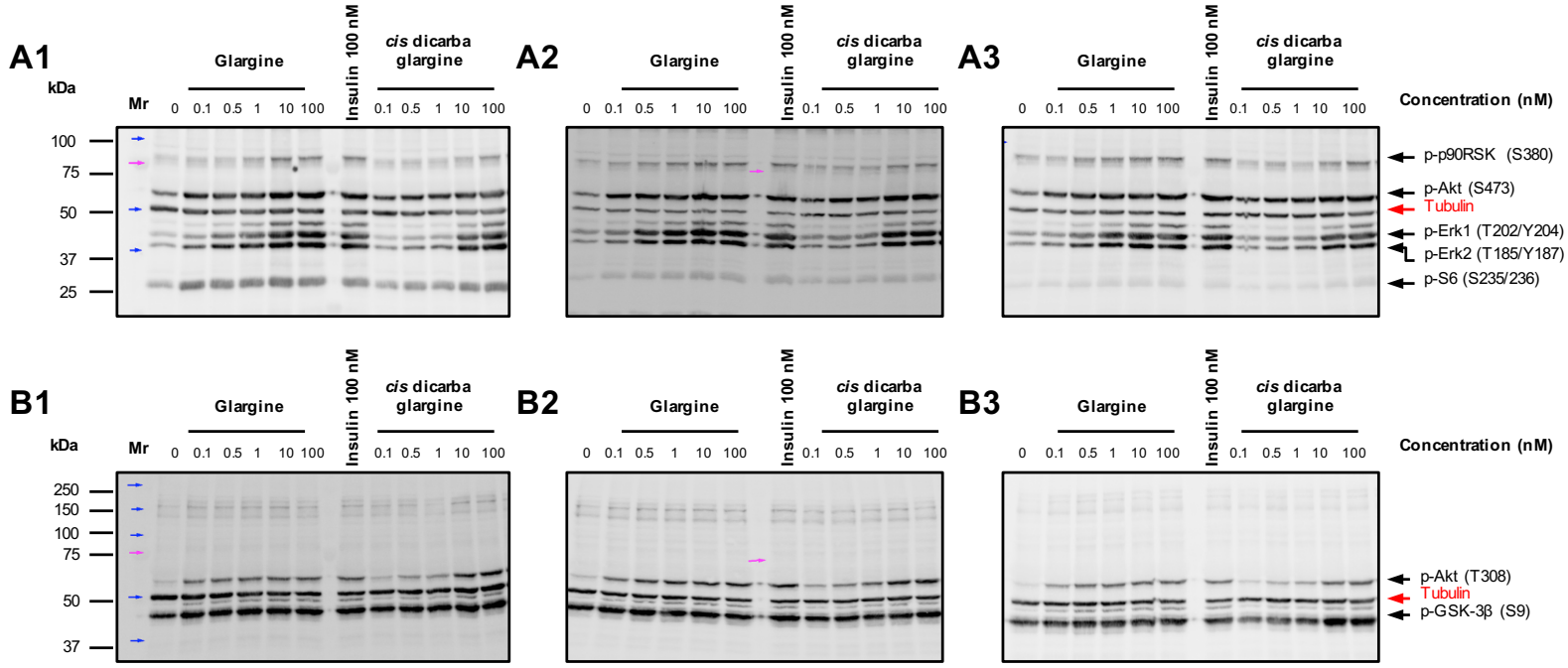

Appendix Figure 4.6 Western blots of IR-A stimulated by increasing concentration of glargine insulin and *cis* dicarba glargine insulin. Serum starved IR-A overexpressing L6 myoblasts (hIR-A L6) were stimulated with increasing concentrations (0, 0.1, 0.5 1, 10 and 100 nM) of glargine insulin or *cis* dicarba glargine insulin for 10 min. Stimulation with 100 nM of insulin were also included as a control and for normalization to obtained relative phosphorylation levels of of each protein when stimulated by different insulin analogues. Whole cells lysates were prepared and 20 µg of each sample was separated in duplicate 10% glycine gels followed by immunoblotting. Blot (A) probed with Pathscan® Multiplex Western Cocktail allowed detection of phospho-p90RSK (S380), phospho-Akt (S473), phospho-ERK1 (T202/Y204), phospho-ERK2 (T185/Y187) and phospho-S6 ribosomal (S235/236) simultaneously. Blot (B) was probed for phospho-AS160 (T642), phospho-Akt (T308) and phospho-GSK3β (S9). Each blot was also probed with anti-β-Tubulin as loading control. *Figure A2* and *B2* are also presented in *Figure 4.15* as representative blots. Pink and blue arrows align to markers.

APPENDIX FIGURE 4.7

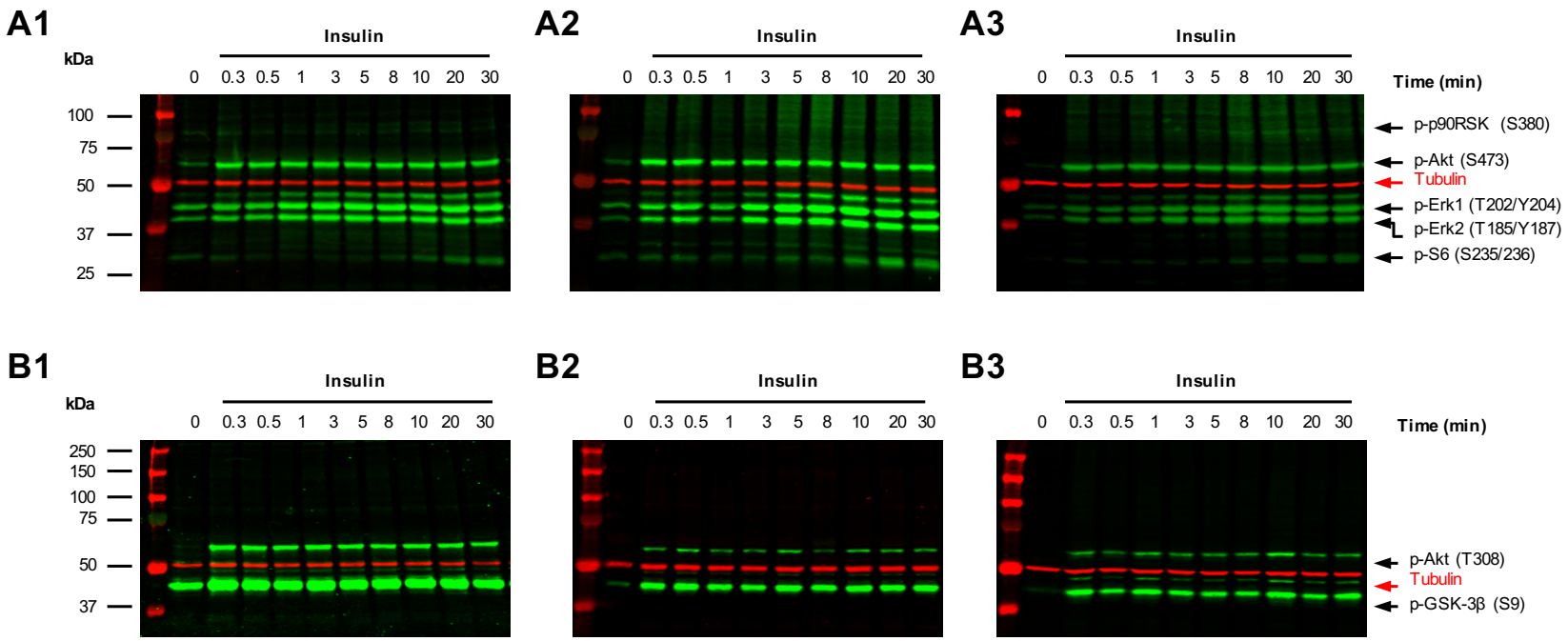

Appendix Figure 4.7 Western blots of IR-A stimulated by 10 nM of insulin in a time-course analysis. Serum starved IR-A overexpressing L6 myoblasts (hIR-A L6) were stimulated with 10 nM of insulin in a time-course of t = 0, 0.33 (20 s), 0.5 (30 s), 1, 3, 5, 8, 10, 20 and 30 min. Whole cells lysates were prepared and 20 µg of each sample were separated in duplicate 10% glycine gels followed by immunoblotting. Blots (A1 – A3) probed with Pathscan® Multiplex Western Cocktail allowed detection of phospho-p90RSK (S380), phospho-Akt (S473), phospho-ERK1 (T202/Y204), phospho-ERK2 (T185/Y187) and phospho-S6 ribosomal (S235/236) simultaneously. Blots (B1 – B3) were probed for phospho-AS160 (T642) (*not detected*), phospho-Akt (T308) and phospho-GSK3β (S9). Each blot was also probed with anti-β-Tubulin as loading control. *Figure A1* and *B1* are also presented in *Figure 4.17* as representative blots.

APPENDIX FIGURE 4.8

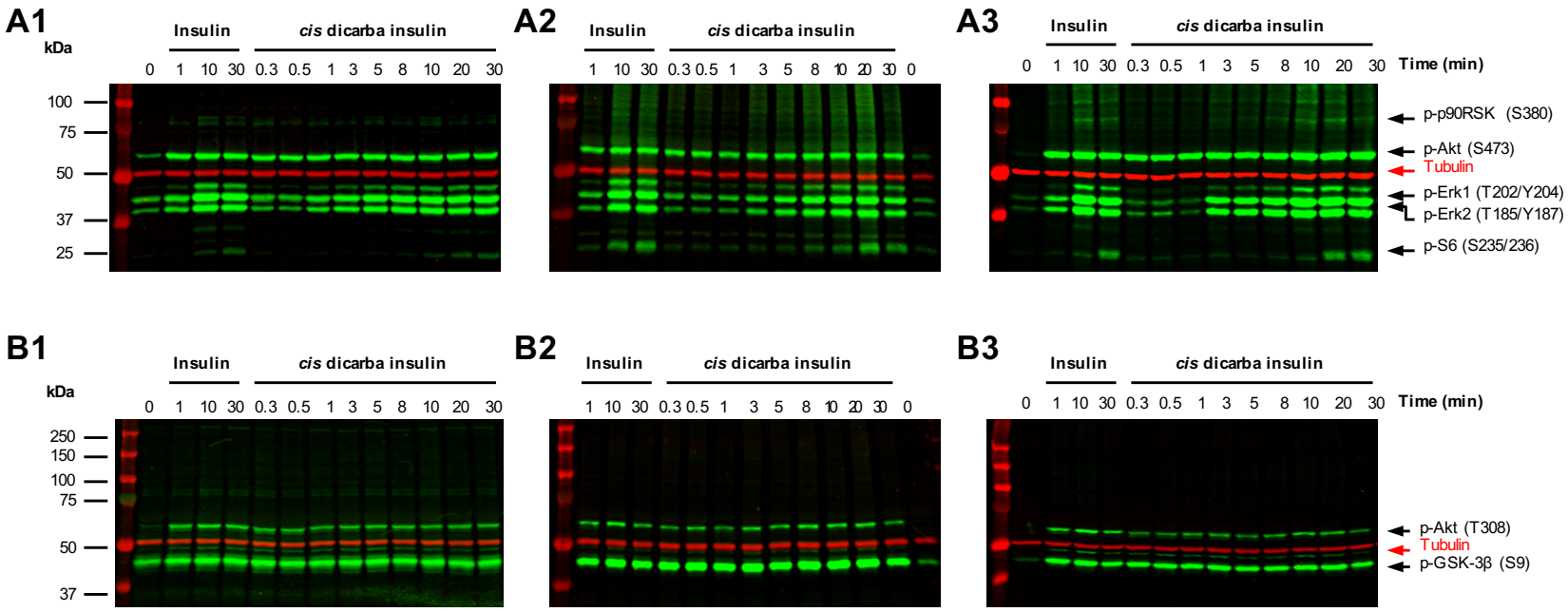

Appendix Figure 4.8 Western blot of IR-A stimulated by 10 nM of *cis* dicarba insulin in a time-course analysis. Serum starved IR-A overexpressing L6 myoblasts (hIR-A L6) were stimulated with 10 nM of *cis* dicarba insulin in a time-course of t = 0, 0.33 (20 s), 0.5 (30 s), 1, 3, 5, 8, 10, 20 and 30 min. Stimulation with 10 nM of insulin at t = 1, 10 and 30 minutes were also included as controls. Whole cells lysates were prepared and 20 µg of each sample was separated in duplicate 10% glycine gels followed by immunoblotting. Blots (A1 – A3) probed with Pathscan® Multiplex Western Cocktail allowed detection of phospho-p90RSK (S380), phospho-Akt (S473), phospho-ERK1 (T202/Y204), phospho-ERK2 (T185/Y187) and phospho-S6 ribosomal (S235/236) simultaneously. Blots (B1 – B3) were probed for phospho-AS160 (T642) (*not detected*), phospho-Akt (T308) and phospho-GSK3β (S9). Each blot was also probed with anti-β-Tubulin as loading control. *Figure A1* and *B1* are also presented in *Figure 4.18* as representative blots.

APPENDIX FIGURE 4.9

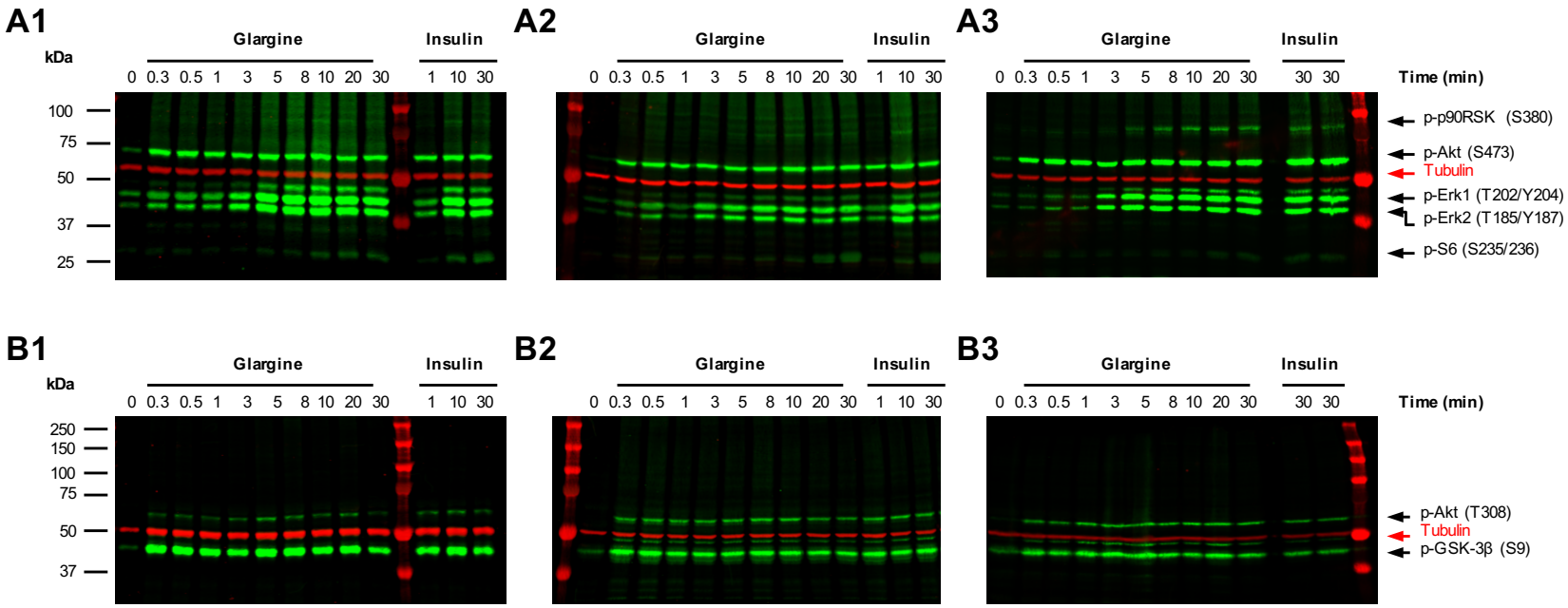

Appendix Figure 4.9 Western blots of IR-A stimulated by 10 nM of glargine insulin in a time-course analysis. Serum starved IR-A overexpressing L6 myoblasts (hIR-A L6) were stimulated with 10 nM of glargine insulin in a time-course of t = 0, 0.33 (20 s), 0.5 (30 s), 1, 3, 5, 8, 10, 20 and 30 min. Stimulation with 10 nM of insulin at t = 1, 10 and 30 minutes were also included as controls. Whole cells lysates were prepared and 20 µg of each sample was separated in duplicate 10% glycine gels followed by immunoblotting. Blots (A1 – A3) probed with Pathscan® Multiplex Western Cocktail allowed detection of phospho-p90RSK (S380), phospho-Akt (S473), phospho-ERK1 (T202/Y204), phospho-ERK2 (T185/Y187) and phospho-S6 ribosomal (S235/236) simultaneously. Blots (B1 – B3) were probed for phospho-AS160 (T642) (*not detected*), phospho-Akt (T308) and phospho-GSK3β (S9). Each blot was also probed with anti-β-Tubulin as loading control. *Figure A1* and *B1* are also presented in *Figure 4.19* as representative blots.

APPENDIX FIGURE 4.10

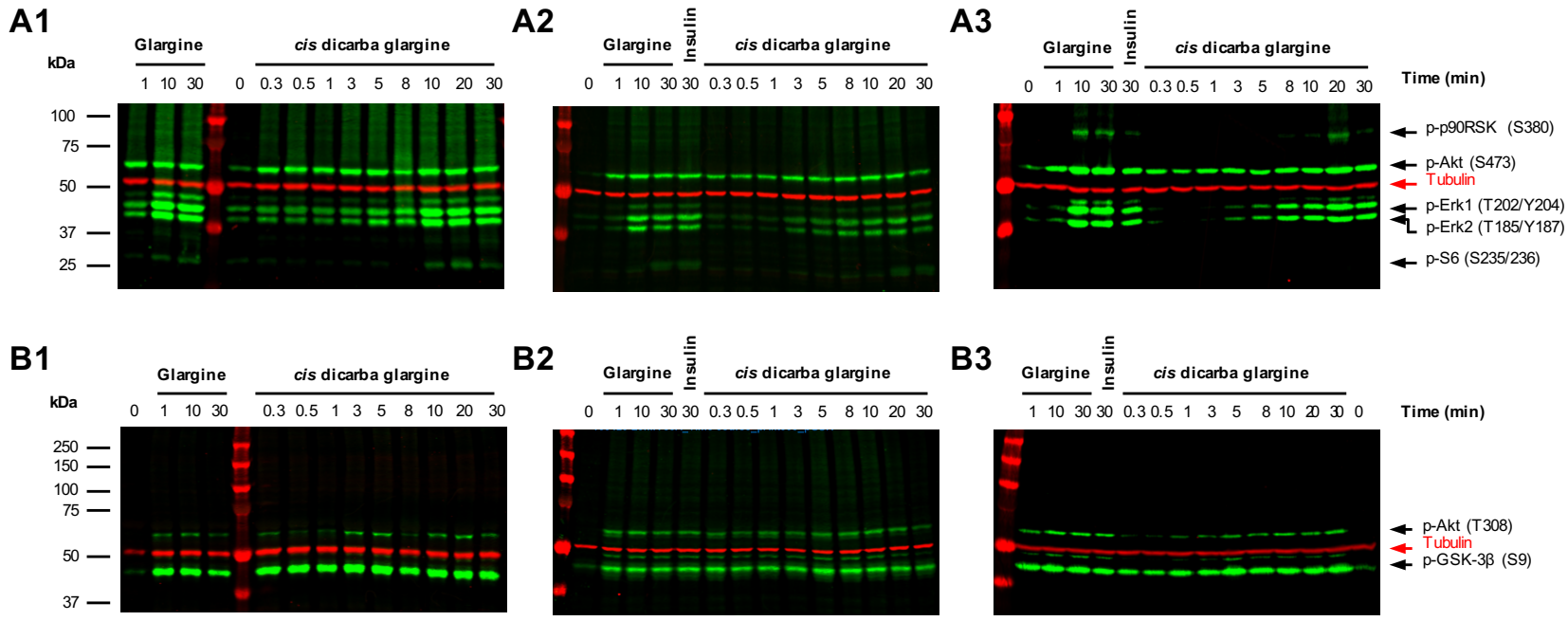

Appendix Figure 4.10 Western blots of IR-A stimulated by 10 nM of *cis* dicarba glargine insulin in a time-course analysis. Serum starved IR-A overexpressing L6 myoblasts (hIR-A L6) were stimulated with 10 nM of *cis* dicarba glargine insulin in a time-course of t = 0, 0.33 (20 s), 0.5 (30 s), 1, 3, 5, 8, 10, 20 and 30 min. Stimulation with 10 nM of glargine at t = 1, 10 and 30 minutes and insulin at t = 30 min were also included as controls. Whole cells lysates were prepared and 20 µg of each sample was separated in duplicate 10% glycine gels followed by immunoblotting. Blots (A1 – A3) probed with Pathscan® Multiplex Western Cocktail allowed detection of phospho-p90RSK (S380), phospho-Akt (S473), phospho-ERK1 (T202/Y204), phospho-ERK2 (T185/Y187) and phospho-S6 ribosomal (S235/236) simultaneously. Blots (B1 – B3) were probed for phospho-AS160 (T642) (*not detected*), phospho-Akt (T308) and phospho-GSK3β (S9). Each blot was also probed with anti-β-Tubulin as loading control. *Figure A2* and *B3* are also presented in *Figure 4.20* as representative blots.

CHAPTER 5

Final Discussion & Conclusions

CHAPTER 5 FINAL DISCUSSION & CONCLUSIONS

Our understanding of insulin has come a long way since it was first identified by Banting and Best in 1921. The discovery of insulin has saved millions of lives and is still the most effective treatment for diabetes today. After nearly a century, insulin is one of the most intensively investigated hormone peptide and yet we still do not fully understand the small protein in many aspects. Particularly lacking is the knowledge to decipher the mechanism(s) underlying the conformational dynamics of insulin to achieve optimal function and stability.

Physiologically, insulin stability is maintained through self-association into Zn^{2+}-coordinated hexamers comprised of 3 sets of insulin dimers (Steiner, 1988). However, it is the monomeric form that engages the insulin receptor, a receptor tyrosine kinase (Lawrence and Ward, 2015b). Thus, current rapid-acting insulin analogues were engineered with reduced self-association propensity; effectively increasing the concentration of active monomers for insulin action. A major drawback of such design is that the exposure of the hydrophobic surfaces in its monomeric form also primes the protein to the events of misfolding and fibrillation (Brange and Langkjoer, 1993, Hua and Weiss, 2004, Yang et al., 2010a). Inevitably, the many limitations of current insulin analogues suggest an urgency for a new avenue to improve insulin stability, without compensating its therapeutic efficacy.

Furthermore, the suboptimal pharmacodynamics of current insulin analogues has also raised a renewed interest to probe the receptor-ready active conformation of insulin. At the start of this investigation insulin structure had been broadly categorised as T-state or R-state; the latter characterised by the extended helix at the *N*-terminus of B8-B20 helix (Weiss, 2009b). Whether either of these states represents the fully active conformation of insulin molecule is debatable. From a molecular perspective, the ability to probe the conformational state of insulin that allows gain of both high receptor binding ability and high structural stability may be the most fitting solution to producing a stable yet active therapeutic analogue.

In line with aforementioned ambition, we recognized that the role of the insulin disulfide bonds has not been fully understood. Typically assumed as a structural motif for insulin, the stereochemistry and the structural contribution of disulfide bonds in the regulation of insulin function and activity have never been thoroughly investigated. Although disulfide bonds are the foundation to peptide stability, reduction of disulfide bonds through redox reactions is also a main contributing factor to peptide denaturation (Bechtel and Weerapana, 2017). The recent

trend of introducing non-reducible disulfide isosteres within the small polypeptides (Hossain and Wade, 2017) thus presents a promising possibility to enhance peptide stability. In some cases, disulfide isosteres also demonstrate improved bioactivity (Chhabra et al., 2014, Hossain et al., 2011, Hossain et al., 2015, Hossain et al., 2009, Karas et al., 2013, Noda et al., 1987, Stymiest et al., 2003, van Lierop et al., 2013, Zhang et al., 2010). On these grounds, we speculated that the substitution of insulin A6–A11 disulfide bond with a non-interconvertible and non-reducible dicarba linkage could also benefit in similar ways.

5.1 FINDINGS AND RESEARCH CONTRUBUTIONS

While the initial concept of designing the A6–A11 dicarba insulin analogues aimed to provide greater stability to the molecule, these investigations led to some surprising insights to the molecular mechanisms that modulate insulin receptor engagement, insulin stability and signalling selectivity. Integral to our findings are the unique structural and biological elements of the *cis*- and *trans* dicarba insulin analogues. Previously, dicarba substitution of disulfide bonds in other polypeptides (Noda et al., 1987, Stymiest et al., 2003, van Lierop et al., 2013, Hossain et al., 2015, Hossain et al., 2009, Zhang et al., 2010), generally generated *cis*- and *trans* isomers with similar biological properties. This, however, was not the case for insulin dicarba analogues. As evident in receptor binding and activation assays, only the *cis* dicarba insulins are fully active while the *trans* dicarba insulins are inactive.

More remarkably, the novel *cis* dicarba insulin analogues in this study are also shown to be more rapid-acting compared to their respective parent peptides. However, contrary to our expectations, substitution of a non-reducible dicarba linkage at the A6–A11 position did not improve the thermostability of insulin. Rather, the *cis* dicarba insulins exhibited a surprisingly desirable therapeutic trait – all *cis* dicarba insulins exhibited significantly reduced mitogenic potential in *in vitro* testings compared to their respective parent peptides. The unique attributes of these dicarba insulin analogues were characterised in detail in this thesis and provided us an inspiring insight to the structure-function relationships of insulin molecule that has never been described before.

First and foremost, the subtle differences in the *cis* and *trans* configurations that results in a strikingly different biological activity in the insulin molecule sparked my curiosity to further elucidate the underlying cause of such a dramatic effect. Whilst the full activity of at least three *cis* dicarba insulins suggests that redox reaction of A6–A11 disulfide bond is not required for insulin action, it was unclear why the insulin molecule did not tolerate a substitution of dicarba

linkage in the *trans* configuration. We hypothesized that the topology of A6–A11 linkage could be an important element that dictates insulin's ability to bind its receptor. As described in Chapter 2, the *cis* and *trans* dicarba insulins presented the ideal tools to test our hypothesis through direct structural comparison as they essentially represent the active and inactive insulin conformation of insulin.

Prior to my investigation, it has been long-predicted that the movement of *C*-terminal segment of B-chain may be required to allow receptor engagement (Hua et al., 1991). Supporting this earlier hypothesis, structural and functional analyses of insulin analogues with a truncated *C*-terminal segment of B-chain, such as in the des [24-30]-insulin (Bao et al., 1997) and NMeAla-B26-DTI (Jiracek et al., 2010), also revealed the importance of retaining the β-turn structures in the B20-B24 region for receptor binding. Recently high-resolution crystallographic structures of the insulin: μIR complex confirmed the proposed model, revealing two key insights into the mechanism of interactions: (1) the movement of *C*-terminal segment (B24-B30) of B-chain away from the hydrophobic core that is driven by the rotation of β-turn in B20-B23 region and the reorientation of B24 residue allowing accessibility to the insulin site 1-binding residues, including the Ile^{A2} and Val^{A3} residues on the *N*-terminal helix of A-chain; and (2) the receptor-bound insulin adopts a conformation that is similar to a classical T-state structure; where *N*-terminal segment of insulin B-chain is folded back against the insulin core (Menting et al., 2013, Menting et al., 2014b).

At the start of my investigation little had been described of the conformational dynamics within the A-chain helix involved in receptor engagement. It had been shown that the reposition of *C*-terminal end of B-chain also influences the movement of A-chain *N*-terminal helix (Bao et al., 1997, Jiracek et al., 2010). Weiss *et al.* also reported that the removal of A6–A11 linkage severely perturbed insulin activity as a result of the disordered *N*-terminal A-chain, suggesting the A6–A11 linkage plays an important role in retaining a pre-formed A-chain helix necessary for receptor binding (Weiss et al., 2000). In agreement to these observations, my investigation revealed that in addition to assisting the maintenance of a helical conformation, the A6–A11 disulfide bond plays a more important role, whereby it functions as a "toggle" that modulates the conformational flexibility of the first A-chain helix that in turns dictates its ability to engage the IR αCT domain. Having a helical structure at the *N*-terminal segment of A-chain that lacks such flexibility prevents receptor engagement, as demonstrated in the case of *trans* dicarba insulin that retains native-like *N*-terminal A-chain helix but has poor binding affinity for IR.

In the pursuance of probing the structural differences that led to the potency discrimination between the two dicarba insulin isomers, this study also presented a renewed definition of the classical T-state insulin structures. Based on the conformation of A-chain *N*-terminal helix, T-state insulin structures are now partitioned into two classes: the inactive Class 1 and the active Class 2 conformation, whereby Class 2 insulins adopt a wider A-chain *N*-terminal helix. We noted that the receptor-bound insulin conformation also adopts a Class 2 conformation. The Class 2 conformation of the A-chain *N*-terminal helix is also observed in the des [24-30]-insulin and NMeAla-B26-DTI insulin analogues (Bao et al., 1997, Jiracek et al., 2010). In the case of des [23-30]-insulin, however, the analogue is inactive due to the loss of β-turn in the *C*-terminal end of the B-chain. A crystal structure of inactive *trans* dicarba insulin presented in this study revealed it only adopts the Class 1 conformation and never adopts the Class 2 conformation. Collectively, it appeared that the ability to transition between the tight (inactive Class 1) to the wider (active Class 2) A-chain *N*-terminal helix conformation is independent of the movement of the *C*-terminal segment of B-chain; both mechanisms are nevertheless equally important and necessary to allow receptor binding.

Concomitant to the characterisation of the two new T-state subclasses, this study also described the two key elements of A6–A11 linkage that dictates insulin's ability to engage receptor: (1) the flexibility of A6–A11 disulfide bond as in native insulin allows dynamic transitions between the inactive and active conformation of insulin (2) the configuration of A6–A11 bond influences the A6–A11 Cα-Cα distance which in turns influence the position of the A1-A8 helix. Evidently, the shorter distance of A6–A11 bond seen in the active Class 2 conformation is necessary to allow helix rotation of the A-chain *N*-terminal helix, which in turns positions the side-chain of A2 to A4 classical binding sites in an orientation compatible to receptor binding. In contrast, the longer A6–A11 bond, such as seen in the *trans* isomer, prevents the necessary rotation and leads to a steric clash between the A-chain *N*-terminal helix and the IR αCT domain, thereby explaining the inactivity of *trans* isomer.

Interestingly, the rapid-acting *cis* dicarba insulin is not inherently more monomeric than native insulin. *Cis* dicarba KP-insulin also lowered blood glucose levels more rapidly and more effectively than its parent peptide, monomeric KP-insulin, currently used clinically. This further emphasizes that the increased flexibility of A-chain *N*-terminal helix can improve the pharmacokinetics of insulin molecule; independent of its self-dissociation propensity to active monomers. However, a major drawback of the increased flexibility of A-chain *N*-terminal helix is the increased vulnerability to fibrillation; a mechanism that was suggested driven by the

transition of A-chain *N*-terminal helix to a β-sheet. Furthermore, it appeared that the rigidity of the A6–A11 linkage also causes a structural change that led to its increased vulnerability to heat, chemical and enzymatic degradation.

Through an intensive investigation integrating mass spectrometry analyses of the controlled proteolytic cleavage of *cis* dicarba insulin and molecular dynamic simulations, this study revealed an important structural change on the B-chain helix in *cis* dicarba insulin that contributes to its instability. Taken together, I was able to demonstrate that the introduction of a rigid A6–A11 dicarba bond promoted two fundamental changes to the conformational dynamics of insulin structure. While the increased flexibility of A-chain *N*-terminal helix favours improved bioactivity, the rigid bond also causes increase frequency of B-chain helix bulging outwards that results in a decrease stability of overall insulin structure.

Similar to the unique attributes of *cis* dicarba insulin, the intra-A-chain dicarba substitution of insulin-like peptide H2 relaxin was also recently reported to have significantly reduced stability to enzyme degradation in plasma despite retaining strong receptor potency (Hossain et al., 2015). We speculate that the role of intra-A-chain bond on the regulation of peptide stability is possibly conserved across the insulin superfamily. The influence of dicarba intra-A-chain bond on the B-chain conformation may also promote a B-chain bulge in dicarba analogues of insulin-related peptides allowing greater access for enzymatic breakdown.

More recently, Hossain and colleagues also discovered that replacing the intra-A-chain bond with a cystathionine linkage yields A[S-CH_2] insulin analogue that also binds to IR-B with equal affinity to native insulin. Interestingly, in contrast to the *cis* dicarba insulin, the A[S-CH_2] insulin exhibits remarkably enhanced thermostability and retains a tertiary structure identical to native insulin as indicated by its CD spectrum (Karas et al., 2016). The cystathionine is an intermediate in the synthesis of cysteine. In the case of A[S-CH_2] insulin, the Cys11 was synthesized with a γ-carbon moiety; while the CysA6 retained its γ-sulphur moiety. Evidently the 'native-like' flexibility at the A6 region of A[S-CH_2] insulin allows the analogue to retain a 'native-like' conformational flexibility of the A-chain *N*-terminal helix (residues A1 to A8), leading to the CD spectrum that is similar to native insulin. This is in contrast to the *cis* dicarba insulin that exhibits an enhanced helix flexibility due to the configuration constraint of the C=C bond. It seems that the structural difference between the *cis* dicarba insulin and A[S-CH_2] insulin correlates to the different structural stability of the analogues. While both dicarba and cystathionine linkages are non-reducible and may be protected from chemical denaturation via

disulfide exchange, the rigidity of dicarba bond increases the overall insulin vulnerability to denaturation through structural change as a consequence of enhanced flexibility. We speculate that if the directionality of the A6–A11 cystathionine linkage is reversed, the insulin molecule would exhibit biological and structural attributes similar to *cis* dicarba insulin.

On a positive note, although the design of *cis* dicarba insulins did not meet our initial expectation of designing an ultra-rapid insulin with improved stability, this study directed us to a new perspective of understanding the role of A6–A11 linkage in regulating the fine balance between optimal insulin activity and structural stability. We believe that the findings in this thesis have revealed several unexplored determinants of receptor binding, stability and fibrillation that will aid the future design of insulin analogues that permit high-affinity binding with greater stability.

Aside from the valuable insights to the structural implication of A6–A11 bond, perhaps the most surprising and appreciated feature of the *cis* dicarba insulins is the evidently metabolic-biased signalling property. Defining the mechanism that regulates the differential signalling for insulin's 'metabolic' versus 'mitogenic' responses has been an important aspect of characterising insulin action. A recently proposed model suggests that prolonged residence of insulin on IR results in sustained phosphorylation of IR and increased rate of receptor internalisation that correlates to preferential activation of the mitogenic Erk-MAPK signalling (Hansen et al., 1996, De Meyts and Shymko, 2000, Jensen and De Meyts, 2009, Rajapaksha and Forbes, 2015). So far, this model has been tested using IR binding ligands that have different composition to native insulin; either insulin analogues with amino acid changes, IGF-II or peptide mimetics that bind to the IR at allosteric sites away from the conventional insulin binding pockets (Morcavallo et al., 2012, Rajapaksha and Forbes, 2015, Jensen et al., 2007, De Meyts and Shymko, 2000, Hansen et al., 1996). In this study, the *cis* dicarba insulins have identical amino acid sequences to their respective parent peptides but differ only in their chemical composition at the A6–A11 bond. Thus, we believe that the dicarba analogues represent the best model to study the mechanism of insulin signalling selectivity through IR.

Herein, as described in *Chapter 4*, I definitively demonstrated that the reduced potency and delayed activation of the mitogenic Erk1/2 signalling strongly correlates to the impaired rate of IR-A internalisation. Both *cis* dicarba analogues of regular human insulin and insulin glargine are unable to promote detectable IR-A internalisation. These findings also correlate with the significantly reduced mitogenic activity of the analogues as measured in the DNA synthesis assays. Remarkably, I was able to demonstrate a possibility to markedly reduce mitogenecity of

glargine to the level equivalent to native insulin. On the other hand, as the metabolic potency of the *cis* dicarba insulins is clearly not affected by the impaired receptor internalisation, we also proposed that the rapid activation of PI3K for metabolic signalling is mainly activated *via* cell surface receptor. These findings are also consistent with the previously described mechanism for ligand-dependent signalling biased through IR-A (Jensen et al., 2007, Rajapaksha and Forbes, 2015, Morcavallo et al., 2012, Yunn et al., 2015). Furthermore, it also appeared that the effect of signalling bias promoted by the *cis* dicarba insulins are well-established soon after the initial receptor activation; within 10 minutes. Interestingly, this effect is also long-term, as prolonged stimulation with *cis* dicarba insulin for up to 18 hours (DNA synthesis assays) did not seems to compensate for its reduced potency for Erk signalling.

Taken together, I believe that this thesis has provided us valuable information on the role of intra-A-chain A6–A11 linkage in receptor binding, insulin stability and signalling selectivity. I have demonstrated that the A6–A11 bond configuration and flexibility are both important elements for modulating the conformational dynamics of insulin A-chain *N*-terminal helix; key determinant to receptor engagement. I have also demonstrated that the of A6–A11 linkage is a key modulator for a balanced regulation between insulin activity and stability. Introducing a rigid A6–A11 linkage increased flexibility of A-chain *N*-terminal helix and B-chain helix that result in a more open and dynamic conformation that led to increased vulnerability to insulin instability. Finally, The A6–A11 bond also plays a role in regulating structural change that defines its signalling properties, possibly through the change receptor engagement dynamics.

5.2 FUTURE DIRECTIONS

The final goal of this project aimed to decipher the phosphorylation patterns within the intracellular domains of the insulin receptor β-subunit that signals the initiation of mitogenic response. Due to time constraints, the project was temporarily halted at the stage of insulin receptor purification. However, as described in Chapter 4, in a small scale experiment I have now optimised the purification of insulin receptor using CT-1 column that can be eluted with competing peptides. It should now be relatively straight forward to scale up this purification method to harvest a sufficient amount of IR for the investigation of IR phosphopeptides *via* targeted mass spectrometry (MRM/SRM). The ability to decode the preferential phosphorylation pattern of insulin receptor mitogenic response would be an immensely important breakthrough to the understanding of insulin action that would revolutionize the future design of insulin analogues.

Furthermore, an additional mechanism that was correlated to the upregulation of mitogenic signalling is the reduced rate of ligand dissociation from the insulin receptor. Several groups also suggest that the increased residence time of ligand on insulin receptor is correlated to its increased rate of receptor internalization (Hansen et al., 2011, Morcavallo et al., 2012, De Meyts, 1994). In the case of *cis* dicarba insulin analogues, the dicarba analogues have binding affinities for IR very similar to their respective parent peptides (less than 2-fold difference) but showed a complete loss of receptor internalization capability. We proposed the mitogenicity of insulin is influenced by the conformational flexibility of the *N*-terminal helix of A-chain important for regulating residence time on receptor. The binding affinities of *cis* dicarba analogues does not accurately reflect its association/dissociation rate on the receptor. We hypothesis that although the hormone is capable of initiating receptor engagement, the residence time may be brief. Thus, an extended experiment measuring the dissociation rate of the metabolically-biased *cis* dicarba insulin analogues may be important to complete our understanding of the receptor binding dynamics.

Finally, up to this point of the investigation, we concluded that the rapid-action of *cis* dicarba insulin analogues is mainly attributed to its increased flexibility of the A-chain *N*-terminal helix. It is yet unclear whether the structural change on the B-chain helix may also possess an added contribution to the enhanced glucose lowering effects. As several hexamer binding surfaces (Glu^{B13} and Leu^{B17}) reside on the B-chain central helix, we speculate that the bulging of B-chain helix may influence its propensity to associate as *cis* dicarba hexamers and dissociate into monomers. Through analytical ultracentrifugation analyses (described in *Chapter 3*), the self-association tendency of *cis* dicarba insulin was explored. The *cis* dicarba insulin demonstrated a self-association behaviour similar to native insulin at the highest accessible concentrations (0.5 mg/mL). However, due to the limited resources of the *cis* dicarba insulin peptides, we were unable to explore the hexamer dissociation mechanism of *cis* dicarba insulin. In future, this could be achieved through static light scattering analyses as described for KP insulin in (Bakaysa et al., 1996) . It would also be interesting to examine if the increased structural flexibility of *cis* dicarba insulin could influence its ability to form different hexamer species; *ie.* T_6, T_3R3, $T_3R_3^f$ or R_6 complexes, in the presence of zinc and/or phenol. We believe that further exploration in the physiochemical properties of the *cis* dicarba insulin may be key to understanding its rapid *in vivo* glucose lowering action.

5.3 CONCLUSIONS

Through structural, biophysical and biological analyses of the intra-A-chain dicarba insulin analogues, this investigation has provided us with the first descriptions of the allosteric role of insulin A6–A11 bond in insulin activity, stability and signalling outcome. We proposed that the *cis* dicarba insulin analogue may be a close representative of a receptor-ready active conformation of native insulin. Astoundingly, the introduction of *cis* dicarba linkage in at least three insulin types demonstrates an improved blood glucose lowering efficacy in mice and significantly reduced their mitogenic potentials. Thus, from a therapeutic point of view, the *cis* dicarba analogues represent metabolically-biased agonists with promising clinical potentials. On the other hand, from a basic research perspective, the dicarba insulin analogues also represent ideal models for future investigation of insulin signalling-biased mechanisms. Although further efforts are required to improve the stability of the dicarba insulin analogues, I hope the findings in this thesis will bring us a step forward towards the creation of the perfect insulin.

REFERENCES

ABE, H., YAMADA, N., KAMATA, K., KUWAKI, T., SHIMADA, M., OSUGA, J., SHIONOIRI, F., YAHAGI, N., KADOWAKI, T., TAMEMOTO, H., ISHIBASHI, S., YAZAKI, Y. & MAKUUCHI, M. 1998. Hypertension, hypertriglyceridemia, and impaired endothelium-dependent vascular relaxation in mice lacking insulin receptor substrate-1. *J Clin Invest,* 101**,** 1784-8.

ADAMS, M. J., BLUNDELL, T. L., DODSON, E. J., DODSON, G. G., VIJAYAN, M., BAKER, E. N., HARDING, M. M., HODGKIN, D. C., RIMMER, B. & SHEAT, S. 1969a. Structure of Rhombohedral 2 Zinc Insulin Crystals. *Nature,* 224**,** 491-495.

ADAMS, M. J., BLUNDELL, T. L., DODSON, E. J., DODSON, G. G., VIJAYAN, M., BAKER, E. N., HARDING, M. M., HODGKIN, D. C., RIMMER, B. & SHEAT, S. 1969b. Structure of Rhombohedral 2 Zinc Insulin Crystals. *Nature,* 224**,** 491-495.

ADAMS, T. E., EPA, V. C., GARRETT, T. P. & WARD, C. W. 2000. Structure and function of the type 1 insulin-like growth factor receptor. *Cell Mol Life Sci,* 57**,** 1050-93.

AGGARWAL, R. S. 2014. What's fueling the biotech engine-2012 to 2013. *Nat Biotechnol,* 32**,** 32-9.

AHMAD, S. I. 2013. *Introduction to Diabetes Mellitus*, Springer New York.

AIHW. *Australian Instutute of Health and Welfare* [Online]. Available: http://www.aihw.gov.au/ [Accessed 20 Sept 2014].

AKAJI, K., FUJINO, K., TATSUMI, T. & KISO, Y. 1993. Total synthesis of human insulin by regioselective disulfide formation using the silyl chloride-sulfoxide method. *Journal of the American Chemical Society,* 115**,** 11384-11392.

ALESSI, D. R., JAMES, S. R., DOWNES, C. P., HOLMES, A. B., GAFFNEY, P. R., REESE, C. B. & COHEN, P. 1997. Characterization of a 3-phosphoinositide-dependent protein kinase which phosphorylates and activates protein kinase Balpha. *Curr Biol,* 7**,** 261-9.

ALVINO, C. L., MCNEIL, K. A., ONG, S. C., DELAINE, C., BOOKER, G. W., WALLACE, J. C., WHITTAKER, J. & FORBES, B. E. 2009. A Novel Approach to Identify Two Distinct Receptor Binding Surfaces of Insulin-like Growth Factor II. *J Biol Chem,* 284**,** 7656-64.

ANDERSEN, G., ALLUIS, B., MEIFFREN, G., RANSON, A., SEROUSSI, C., GAUDIER, M., SOULA, O., FISCHER, A., NOSEK, L. & HEISE, T. Ultra-rapid BioChaperone insulin lispro (BC LIS): linear dose-response and faster absorption than insulin Lispro (LIS). 2015 2015. Diabetes, A248-A248.

ANDRALI, S. S., SAMPLEY, M. L., VANDERFORD, N. L. & OZCAN, S. 2008. Glucose regulation of insulin gene expression in pancreatic beta-cells. *Biochem J,* 415**,** 1-10.

ANJUM, R. & BLENIS, J. 2008. The RSK family of kinases: emerging roles in cellular signalling. *Nat Rev Mol Cell Biol,* 9**,** 747-58.

ARKUN, Y. 2016. Dynamic Modeling and Analysis of the Cross-Talk between Insulin/AKT and MAPK/ERK Signaling Pathways. *PLoS One,* 11**,** e0149684.

ARMISHAW, C. J., DALY, N. L., NEVIN, S. T., ADAMS, D. J., CRAIK, D. J. & ALEWOOD, P. F. 2006. Alpha-selenoconotoxins, a new class of potent alpha7 neuronal nicotinic receptor antagonists. *J Biol Chem,* 281**,** 14136-43.

ARNOLD, S., JOWETT, J. & BALLANCE, J. Synergistic Action of PE0139, a Super-Long-Acting Basal Insulin, and PB1023 a Weekly GLP-1 Receptor Agonist. American Diabetes Association 75th Scientifc Sessions, 2015 2015. American Diabetes Association, A44-A44.

ASLUND, F., BERNDT, K. D. & HOLMGREN, A. 1997. Redox potentials of glutaredoxins and other thiol-disulfide oxidoreductases of the thioredoxin superfamily determined by direct protein-protein redox equilibria. *J Biol Chem,* 272**,** 30780-6.

ATKINSON, M. A., EISENBARTH, G. S. & MICHELS, A. W. 2014. Type 1 diabetes. *Lancet,* 383**,** 69-82.

AUCLAIR, J. R., JOHNSON, J. L., LIU, Q., SALISBURY, J. P., ROTUNNO, M. S., PETSKO, G. A., RINGE, D., BROWN, R. H., JR., BOSCO, D. A. & AGAR, J. N. 2013. Post-translational modification by cysteine protects Cu/Zn-superoxide dismutase from oxidative damage. *Biochemistry,* 52**,** 6137-44.

AUWERX, J., ISACSSON, O., SODERLUND, J., BALZARINI, J., JOHANSSON, M. & LUNDBERG, M. 2009. Human glutaredoxin-1 catalyzes the reduction of HIV-1 gp120 and CD4 disulfides and its inhibition reduces HIV-1 replication. *Int J Biochem Cell Biol,* 41**,** 1269-75.

AVRUCH, J. 1998. Insulin signal transduction through protein kinase cascades. *Mol Cell Biochem,* 182**,** 31-48.

AYALA, J. E., SAMUEL, V. T., MORTON, G. J., OBICI, S., CRONIGER, C. M., SHULMAN, G. I., WASSERMAN, D. H., MCGUINNESS, O. P. & CONSORTIUM, N. I. H. M. M. P. C. 2010. Standard operating procedures for describing and performing metabolic tests of glucose homeostasis in mice. *Dis Model Mech,* 3**,** 525-34.

BACKER, J. M., SCHROEDER, G. G., CAHILL, D. A., ULLRICH, A., SIDDLE, K. & WHITE, M. F. 1991. Cytoplasmic juxtamembrane region of the insulin receptor: a critical role in ATP binding, endogenous substrate phosphorylation, and insulin-stimulated bioeffects in CHO cells. *Biochemistry,* 30**,** 6366-72.

BACKER, J. M., SHOELSON, S. E., WEISS, M. A., HUA, Q. X., CHEATHAM, R. B., HARING, E., CAHILL, D. C. & WHITE, M. F. 1992. The insulin receptor juxtamembrane region contains two independent tyrosine/beta-turn internalization signals. *J Cell Biol,* 118**,** 831-9.

BAKAYSA, D. L., RADZIUK, J., HAVEL, H. A., BRADER, M. L., LI, S., DODD, S. W., BEALS, J. M., PEKAR, A. H. & BREMS, D. N. 1996. Physicochemical basis for the rapid time-action of LysB28ProB29-insulin: dissociation of a protein-ligand complex. *Protein Sci,* 5**,** 2521-31.

BAKER, E. N., BLUNDELL, T. L., CUTFIELD, J. F., CUTFIELD, S. M., DODSON, E. J., DODSON, G. G., HODGKIN, D. M., HUBBARD, R. E., ISAACS, N. W., REYNOLDS, C. D. & ET AL. 1988a. The structure of 2Zn pig insulin crystals at 1.5 A resolution. *Philos Trans R Soc Lond B Biol Sci,* 319**,** 369-456.

BAKER, E. N., BLUNDELL, T. L., F. R. S., CUTFIELD, J. F., CUTFIELD, S. M., DODSON, E. J., DODSON, G. G., HODGKIN, D. M., F. R. S., HUBBARD, R. E., ISAACS, N. W., REYNOLDS, C. D., SAKABE, K., SAKABE, N. & VIJAYAN, N. M. 1988b. The structure of 2Zn pig insulin crystals at 1.5 A resolution. *Philos Trans R Soc Lond B Biol Sci,* 319**,** 369-456.

BAKER IDI HEART & DIABETES INSTITUTE. 2012. *Diabetes: The silent pandemic and its impact on Australia* [Online]. Available: https://www.diabeteswa.com.au/UserDir/Documents/14814 Diabetes management booklet 5 Mar_FINAL.pdf [Accessed].

BANTING, F. G. & BEST, C. H. 2007. The internal secretion of the pancreas. 1922. *Indian J Med Res,* 125**,** 251-66.

BAO, S. J., XIE, D. L., ZHANG, J. P., CHANG, W. R. & LIANG, D. C. 1997. Crystal structure of desheptapeptide(B24-B30)insulin at 1.6 A resolution: implications for receptor binding. *Proc Natl Acad Sci U S A,* 94**,** 2975-80.

BAYLY, C. I., CIEPLAK, P., CORNELL, W. & KOLLMAN, P. A. 1993. A well-behaved electrostatic potential based method using charge restraints for deriving atomic charges: the RESP model. *The Journal of Physical Chemistry,* 97**,** 10269-10280.

BECHTEL, T. J. & WEERAPANA, E. 2017. From structure to redox: The diverse functional roles of disulfides and implications in disease. *Proteomics,* 17.

BECKER, R. H. 2015. New insulin glargine 300 Units·mL−1 provides a more even activity profile and prolonged glycemic control at steady state compared with insulin glargine 100 Units·mL−1. *Diabetes Care,* 38**,** 637-643.

BECKER, R. H., FRICK, A. D., BURGER, F., POTGIETER, J. H. & SCHOLTZ, H. 2005. Insulin glulisine, a new rapid-acting insulin analogue, displays a rapid time-action profile in obese non-diabetic subjects. *Exp Clin Endocrinol Diabetes,* 113**,** 435-43.

BEDINGER, D. H. & ADAMS, S. H. 2015. Metabolic, anabolic, and mitogenic insulin responses: A tissue-specific perspective for insulin receptor activators. *Mol Cell Endocrinol,* 415**,** 143-56.

BELFIORE, A., FRASCA, F., PANDINI, G., SCIACCA, L. & VIGNERI, R. 2009. Insulin receptor isoforms and insulin receptor/insulin-like growth factor receptor hybrids in physiology and disease. *Endocr Rev,* 30**,** 586-623.

BELFIORE, A., MALAGUARNERA, R., VELLA, V., LAWRENCE, M. C., SCIACCA, L., FRASCA, F., MORRIONE, A. & VIGNERI, R. 2017. Insulin Receptor Isoforms in Physiology and Disease: An Updated View. *Endocr Rev,* 38**,** 379-431.

BELGI, A., AKHTER HOSSAIN, M., W. TREGEAR, G. & WADE, J. 2011. The Chemical Synthesis of Insulin: From the Past to the Present. *In:* MORISHITA, R. (ed.) *Immunology Endocrine & Metabolic Agents - Medicinal Chemistry (Formerly Current Medicinal Chemistry - Immunology Endocrine & Metabolic Agents).* Bentham Science Publishers.

BENTLEY, G., DODSON, E., DODSON, G., HODGKIN, D. & MERCOLA, D. 1976. Structure of insulin in 4-zinc insulin. *Nature,* 261**,** 166-8.

BENTLEY, G., DODSON, G. & LEWITOVA, A. 1978. Rhombohedral insulin crystal transformation. *J Mol Biol,* 126**,** 871-5.

BI RU, C., DAUTER, Z., DODSON, E., DODSON, G., GIORDANO, F. & REYNOLDS, C. 1984. Insulin's structure as a modified and monomeric molecule. *Biopolymers,* 23**,** 391-395.

BIENER, Y., FEINSTEIN, R., MAYAK, M., KABURAGI, Y., KADOWAKI, T. & ZICK, Y. 1996. Annexin II is a novel player in insulin signal transduction. Possible association between annexin II phosphorylation and insulin receptor internalization. *J Biol Chem,* 271**,** 29489-96.

BILLINGS, L. K., DOSHI, A., GOUET, D., OVIEDO, A., RODBARD, H. W., TENTOLOURIS, N., GRON, R., HALLADIN, N. & JODAR, E. 2018. Efficacy and Safety of IDegLira Versus Basal-Bolus Insulin Therapy in Patients With Type 2 Diabetes Uncontrolled on Metformin and Basal Insulin: The DUAL VII Randomized Clinical Trial. *Diabetes Care,* 41**,** 1009-1016.

BLISS, M. 1982. Banting's, Best's, and Collip's accounts of the discovery of insulin. *Bull Hist Med,* 56**,** 554-68.

BLUNDELL, T. L., CUTFIELD, J. F., DODSON, G. G., DODSON, E., HODGKIN, D. C. & MERCOLA, D. 1971a. The structure and biology of insulin. *Biochem J,* 125**,** 50P-51P.

BLUNDELL, T. L., DODSON, G. G., DODSON, E., HODGKIN, D. C. & VIJAYAN, M. 1971b. X-ray analysis and the structure of insulin. *Recent Prog Horm Res,* 27**,** 1-40.

BONNESEN, C., NELANDER, G. M., HANSEN, B. F., JENSEN, P., KRABBE, J. S., JENSEN, M. B., HEGELUND, A. C., SVENDSEN, J. E. & OLEKSIEWICZ, M. B. 2010. Synchronization in G0/G1 enhances the mitogenic response of cells overexpressing the human insulin receptor A isoform to insulin. *Cell Biol Toxicol,* 26**,** 293-307.

BOUCHARD, M., ZURDO, J., NETTLETON, E. J., DOBSON, C. M. & ROBINSON, C. V. 2000. Formation of insulin amyloid fibrils followed by FTIR simultaneously with CD and electron microscopy. *Protein Sci,* 9**,** 1960-7.

BRAIMAN, L., ALT, A., KUROKI, T., OHBA, M., BAK, A., TENNENBAUM, T. & SAMPSON, S. R. 2001. Insulin induces specific interaction between insulin receptor

and protein kinase C delta in primary cultured skeletal muscle. *Mol Endocrinol,* 15**,** 565-74.

BRANGE, J. 1992. Chemical stability of insulin. 4. Mechanisms and kinetics of chemical transformations in pharmaceutical formulation. *Acta Pharm Nord,* 4**,** 209-22.

BRANGE, J., ANDERSEN, L., LAURSEN, E. D., MEYN, G. & RASMUSSEN, E. 1997a. Toward understanding insulin fibrillation. *J Pharm Sci,* 86**,** 517-25.

BRANGE, J., DODSON, G. G., EDWARDS, D. J., HOLDEN, P. H. & WHITTINGHAM, J. L. 1997b. A model of insulin fibrils derived from the x-ray crystal structure of a monomeric insulin (despentapeptide insulin). *Proteins,* 27**,** 507-16.

BRANGE, J., HALLUND, O. & SORENSEN, E. 1992a. Chemical stability of insulin. 5. Isolation, characterization and identification of insulin transformation products. *Acta Pharm Nord,* 4**,** 223-32.

BRANGE, J., HANSEN, J. F., LANGKJAER, L., MARKUSSEN, J., RIBEL, U. & SORENSEN, A. R. 1992b. Insulin analogues with improved absorption characteristics. *Horm Metab Res Suppl,* 26**,** 125-30.

BRANGE, J., HAVELUND, S. & HOUGAARD, P. 1992c. Chemical stability of insulin. 2. Formation of higher molecular weight transformation products during storage of pharmaceutical preparations. *Pharm Res,* 9**,** 727-34.

BRANGE, J. & LANGKJAER, L. 1992. Chemical stability of insulin. 3. Influence of excipients, formulation, and pH. *Acta Pharm Nord,* 4**,** 149-58.

BRANGE, J., LANGKJAER, L., HAVELUND, S. & VOLUND, A. 1992d. Chemical stability of insulin. 1. Hydrolytic degradation during storage of pharmaceutical preparations. *Pharm Res,* 9**,** 715-26.

BRANGE, J. & LANGKJOER, L. 1993. Insulin structure and stability. *Pharm Biotechnol,* 5**,** 315-50.

BROWN, J., JONES, E. Y. & FORBES, B. E. 2009. Interactions of IGF-II with the IGF2R/cation-independent mannose-6-phosphate receptor mechanism and biological outcomes. *Vitam Horm,* 80**,** 699-719.

BULLESBACH, E. E. & SCHWABE, C. 2001. Synthesis and conformational analysis of the insulin-like 4 gene product. *J Pept Res,* 57**,** 77-83.

BURNLEY, B. T., AFONINE, P. V., ADAMS, P. D. & GROS, P. 2012. Modelling dynamics in protein crystal structures by ensemble refinement. *Elife,* 1**,** e00311.

BURNLEY, J., JACKSON, W. R. & ROBINSON, A. J. 2015. One-Pot Selective Homodimerization/Hydrogenation Strategy for Sequential Dicarba Bridge Formation. *J Org Chem,* 80**,** 9057-63.

BUTERA, D., COOK, K. M., CHIU, J., WONG, J. W. & HOGG, P. J. 2014. Control of blood proteins by functional disulfide bonds. *Blood,* 123**,** 2000-7.

CABRERA-FREITAG, P., ESCALADA, J., GOIKOETXEA, M. J., LAGUNA, S., SANZ, M. L. & GASTAMINZA, G. 2011. A severe case of lipoatrophy due to human insulin and insulin analogs in a patient with diabetes: is an immunological mechanism involved? *J Investig Allergol Clin Immunol,* 21**,** 417-9.

CAMPBELL, R. K., CAMPBELL, L. K. & WHITE, J. R. 1996. Insulin lispro: its role in the treatment of diabetes mellitus. *Ann Pharmacother,* 30**,** 1263-71.

CAMPBELL, R. K. & WHITE, J. R., JR. 2002. Insulin therapy in type 2 diabetes. *J Am Pharm Assoc (Wash),* 42**,** 602-11.

CAREL, K., KUMMER, J. L., SCHUBERT, C., LEITNER, W., HEIDENREICH, K. A. & DRAZNIN, B. 1996. Insulin stimulates mitogen-activated protein kinase by a Ras-independent pathway in 3T3-L1 adipocytes. *J Biol Chem,* 271**,** 30625-30.

CARPENTIER, J. L., PACCAUD, J. P., BACKER, J., GILBERT, A., ORCI, L., KAHN, C. R. & BAECKER, J. 1993. Two steps of insulin receptor internalization depend on different domains of the beta-subunit. *J Cell Biol,* 122**,** 1243-52.

CASE, D. A., BABIN, V., BERRYMAN, J. T., BETZ, R. M., CAI, Q., CERUTTI, D. S., CHEATHAM III, T. E., DARDEN, T. A., DUKE, R. E., GOHLKE, H., GOETZ, A. W., GUSAROV, S., HOMEYER, N., JANOWSKI, P., KAUS, J., KOLOSSVÁRY, I., KOVALENKO, A., LEE, T. S., LEGRAND, S., LUCHKO, T., LUO, R., MADEJ, B., MERZ, K. M., PAESANI, F., ROE, D. R., ROITBERG, A., SAGUI, C., SALOMON-FERRER, R., SEABRA, G., SIMMERLING, C. L., SMITH, W., SWAILS, J., WALKER, R. C., WANG, J., WOLF, R. M., WU, X. & KOLLMAN, P. A. 2014. AMBER 14. University of California, San Francisco.

CERESA, B. P., KAO, A. W., SANTELER, S. R. & PESSIN, J. E. 1998. Inhibition of clathrin-mediated endocytosis selectively attenuates specific insulin receptor signal transduction pathways. *Mol Cell Biol,* 18**,** 3862-70.

CHANG, P. Y., LE MARCHAND-BRUSTEL, Y., CHEATHAM, L. A. & MOLLER, D. E. 1995. Insulin stimulation of mitogen-activated protein kinase, p90rsk, and p70 S6 kinase in skeletal muscle of normal and insulin-resistant mice. Implications for the regulation of glycogen synthase. *J Biol Chem,* 270**,** 29928-35.

CHANG, S. G., CHOI, K. D., JANG, S. H. & SHIN, H. C. 2003. Role of disulfide bonds in the structure and activity of human insulin. *Mol Cells,* 16**,** 323-30.

CHANG, S. G., KIM, D. Y., CHOI, K. D., SHIN, J. M. & SHIN, H. C. 1998. Human insulin production from a novel mini-proinsulin which has high receptor-binding activity. *Biochem J,* 329 (Pt 3)**,** 631-5.

CHARDIN, P., CAMONIS, J. H., GALE, N. W., VAN AELST, L., SCHLESSINGER, J., WIGLER, M. H. & BAR-SAGI, D. 1993. Human Sos1: a guanine nucleotide exchange factor for Ras that binds to GRB2. *Science,* 260**,** 1338-43.

CHEN, H. & FENG, Y. M. 1998. Hydrophilic Thr can replace the hydrophobic and absolutely conservative A3Val in insulin. *Biochim Biophys Acta,* 1429**,** 69-73.

CHEN, R. H., SARNECKI, C. & BLENIS, J. 1992. Nuclear localization and regulation of erk- and rsk-encoded protein kinases. *Mol Cell Biol,* 12**,** 915-27.

CHEN, Y., YOU, Y., JIN, R., GUO, Z. Y. & FENG, Y. M. 2004. Sequences of B-chain/domain 1-10/1-9 of insulin and insulin-like growth factor 1 determine their different folding behavior. *Biochemistry,* 43**,** 9225-33.

CHHABRA, S., BELGI, A., BARTELS, P., VAN LIEROP, B. J., ROBINSON, S. D., KOMPELLA, S. N., HUNG, A., CALLAGHAN, B. P., ADAMS, D. J., ROBINSON, A. J. & NORTON, R. S. 2014. Dicarba analogues of alpha-conotoxin RgIA. Structure, stability, and activity at potential pain targets. *J Med Chem,* 57**,** 9933-44.

CHRISTOFFERSEN, C. T., BORNFELDT, K. E., ROTELLA, C. M., GONZALES, N., VISSING, H., SHYMKO, R. M., TEN HOEVE, J., GROFFEN, J., HEISTERKAMP, N. & DE MEYTS, P. 1994. Negative cooperativity in the insulin-like growth factor-I receptor and a chimeric IGF-I/insulin receptor. *Endocrinology,* 135**,** 472-5.

CISZAK, E., BEALS, J. M., FRANK, B. H., BAKER, J. C., CARTER, N. D. & SMITH, G. D. 1995. Role of C-terminal B-chain residues in insulin assembly: the structure of hexameric LysB28ProB29-human insulin. *Structure,* 3**,** 615-22.

CISZAK, E. & SMITH, G. D. 1994. Crystallographic evidence for dual coordination around zinc in the T3R3 human insulin hexamer. *Biochemistry,* 33**,** 1512-7.

COSMATOS, A. & KATSOYANNIS, P. G. 1975. Elongation of the interchain disulfide bridges of insulin. A synthetic analog. *J Biol Chem,* 250**,** 5315-21.

COUVERTIER, S. M., ZHOU, Y. & WEERAPANA, E. 2014. Chemical-proteomic strategies to investigate cysteine posttranslational modifications. *Biochim Biophys Acta,* 1844**,** 2315-30.

CROLL, T. I., SMITH, B. J., MARGETTS, M. B., WHITTAKER, J., WEISS, M. A., WARD, C. W. & LAWRENCE, M. C. 2016a. Higher-Resolution Structure of the Human Insulin Receptor Ectodomain: Multi-Modal Inclusion of the Insert Domain. *Structure,* 24**,** 469-76.

CROLL, T. I., SMITH, B. J., MARGETTS, M. B., WHITTAKER, J., WEISS, M. A., WARD, C. W. & LAWRENCE, M. C. 2016b. Higher-Resolution Structure of the Human Insulin Receptor Ectodomain: Multi-Modal Inclusion of the Insert Domain. *Structure*.

CROSS, D. A., ALESSI, D. R., COHEN, P., ANDJELKOVICH, M. & HEMMINGS, B. A. 1995. Inhibition of glycogen synthase kinase-3 by insulin mediated by protein kinase B. *Nature,* 378**,** 785-9.

D.A. CASE, V. B., J.T. BERRYMAN, R.M. BETZ, Q. CAI, D.S. CERUTTI, T.E. CHEATHAM, III, T.A. DARDEN, R.E., DUKE, H. G., A.W. GOETZ, S. GUSAROV, N. HOMEYER, P. JANOWSKI, J. KAUS, I. KOLOSSVÁRY, A. KOVALENKO,, T.S. LEE, S. L., T. LUCHKO, R. LUO, B. MADEJ, K.M. MERZ, F. PAESANI, D.R. ROE, A. ROITBERG, C. SAGUI,, R. SALOMON-FERRER, G. S., C.L. SIMMERLING, W. SMITH, J. SWAILS, R.C. WALKER, J. WANG, R.M. WOLF, X. & KOLLMAN, W. A. P. A. 2014. AMBER 14. University of California, San Francisco.

DAI, Y. & TANG, J. G. 1996. Characteristic, activity and conformational studies of [A6-Ser, A11-Ser]-insulin. *Biochim Biophys Acta,* 1296**,** 63-8.

DANN, S. G., SELVARAJ, A. & THOMAS, G. 2007. mTOR Complex1-S6K1 signaling: at the crossroads of obesity, diabetes and cancer. *Trends Mol Med,* 13**,** 252-9.

DAUNT, D. A., HURT, C., HEIN, L., KALLIO, J., FENG, F. & KOBILKA, B. K. 1997. Subtype-specific intracellular trafficking of alpha2-adrenergic receptors. *Mol Pharmacol,* 51**,** 711-20.

DE LUCA, A., MAIELLO, M. R., D'ALESSIO, A., PERGAMENO, M. & NORMANNO, N. 2012. The RAS/RAF/MEK/ERK and the PI3K/AKT signalling pathways: role in cancer pathogenesis and implications for therapeutic approaches. *Expert Opin Ther Targets,* 16 Suppl 2**,** S17-27.

DE MEYTS, P. 1994. The structural basis of insulin and insulin-like growth factor-I receptor binding and negative co-operativity, and its relevance to mitogenic versus metabolic signalling. *Diabetologia,* 37 Suppl 2**,** S135-48.

DE MEYTS, P. 2004. Insulin and its receptor: structure, function and evolution. *Bioessays,* 26**,** 1351-62.

DE MEYTS, P. 2015. Insulin/receptor binding: the last piece of the puzzle? What recent progress on the structure of the insulin/receptor complex tells us (or not) about negative cooperativity and activation. *Bioessays,* 37**,** 389-97.

DE MEYTS, P., PALSGAARD, J., SAJID, W., THEEDE, A. M. & ALADDIN, H. 2004. Structural biology of insulin and IGF-1 receptors. *Novartis Found Symp,* 262**,** 160-71; discussion 171-6, 265-8.

DE MEYTS, P., ROTH, J., NEVILLE, D. M., JR., GAVIN, J. R., 3RD & LESNIAK, M. A. 1973. Insulin interactions with its receptors: experimental evidence for negative cooperativity. *Biochem Biophys Res Commun,* 55**,** 154-61.

DE MEYTS, P. & SHYMKO, R. M. 2000. Timing-dependent modulation of insulin mitogenic versus metabolic signalling. *Novartis Found Symp,* 227**,** 46-57; discussion 57-60.

DE MEYTS, P., VAN OBBERGHEN, E. & ROTH, J. 1978. Mapping of the residues responsible for the negative cooperativity of the receptor-binding region of insulin. *Nature,* 273**,** 504-9.

DE MEYTS, P. & WHITTAKER, J. 2002. Structural biology of insulin and IGF1 receptors: implications for drug design. *Nat Rev Drug Discov,* 1**,** 769-83.

DENLEY, A., BONYTHON, E. R., BOOKER, G. W., COSGROVE, L. J., FORBES, B. E., WARD, C. W. & WALLACE, J. C. 2004. Structural determinants for high-affinity binding of insulin-like growth factor II to insulin receptor (IR)-A, the exon 11 minus isoform of the IR. *Mol Endocrinol,* 18**,** 2502-12.

DENLEY, A., COSGROVE, L. J., BOOKER, G. W., WALLACE, J. C. & FORBES, B. E. 2005. Molecular interactions of the IGF system. *Cytokine Growth Factor Rev,* 16**,** 421-39.

DEPREZ, J., VERTOMMEN, D., ALESSI, D. R., HUE, L. & RIDER, M. H. 1997. Phosphorylation and activation of heart 6-phosphofructo-2-kinase by protein kinase B and other protein kinases of the insulin signaling cascades. *J Biol Chem,* 272**,** 17269-75.

DEPUYDT, M., MESSENS, J. & COLLET, J. F. 2011. How proteins form disulfide bonds. *Antioxid Redox Signal,* 15**,** 49-66.

DEREWENDA, U., DEREWENDA, Z., DODSON, E. J., DODSON, G. G., REYNOLDS, C. D., SMITH, G. D., SPARKS, C. & SWENSON, D. 1989. Phenol stabilizes more helix in a new symmetrical zinc insulin hexamer. *Nature,* 338**,** 594-6.

DI GUGLIELMO, G. M., BAASS, P. C., OU, W. J., POSNER, B. I. & BERGERON, J. J. 1994. Compartmentalization of SHC, GRB2 and mSOS, and hyperphosphorylation of Raf-1 by EGF but not insulin in liver parenchyma. *EMBO J,* 13**,** 4269-77.

DIABETES AUSTALIA. Available: http://www.diabetesaustralia.com.au/ [Accessed 15 Sept 2014].

DIAO, J. 2003. Crystallographic titration of cubic insulin crystals: pH affects GluB13 switching and sulfate binding. *Acta Crystallogr D Biol Crystallogr,* 59**,** 670-6.

DOBSON, C. M. & KARPLUS, M. 1999. The fundamentals of protein folding: bringing together theory and experiment. *Curr Opin Struct Biol,* 9**,** 92-101.

DREJER, K. 1992. The bioactivity of insulin analogues from in vitro receptor binding to in vivo glucose uptake. *Diabetes Metab Rev,* 8**,** 259-85.

DREYER, M., PRAGER, R., ROBINSON, A., BUSCH, K., ELLIS, G., SOUHAMI, E. & VAN LEENDERT, R. 2005. Efficacy and safety of insulin glulisine in patients with type 1 diabetes. *Horm Metab Res,* 37**,** 702-7.

DU, Y. C., ZHANG, Y. S., LU, Z. X. & TSOU, C. L. 1961. Resynthesis of insulin from its glycyl and phenylalanyl chains. *Sci Sin,* 10**,** 84-104.

DU, Y. T., JIANG, R. Q. & TSOU, C. L. 1965. Conditions for successful resynthesis of insulin from its glycyl and phenylalanyl chains. *Sci. Sin. ,* 14**,** 229–236.

DUPRADEAU, F.-Y., PIGACHE, A., ZAFFRAN, T., SAVINEAU, C., LELONG, R., GRIVEL, N., LELONG, D., ROSANSKI, W. & CIEPLAK, P. 2010. The R.E.D. tools: advances in RESP and ESP charge derivation and force field library building. *Physical Chemistry Chemical Physics,* 12**,** 7821-7839.

ELI LILLY & CO. *Product Information: Humalin R & Humalin NPH* [Online]. Available: https://www.lilly.com.au/en/products/index.aspx [Accessed 20 Sept 2014].

EMSLEY, P. & COWTAN, K. 2004. Coot: model-building tools for molecular graphics. *Acta Crystallogr D Biol Crystallogr,* 60**,** 2126-32.

F. WANG, J.-P. B., P. CIEPLAK & F.-Y. DUPRADEAU 2013. R.E.D. Python: Object oriented programming for Amber force fields. Université de Picardie - Jules Verne, Sanford Burnham Prebys Medical Discovery Institute.

FAGERHOLM, S., ORTEGREN, U., KARLSSON, M., RUISHALME, I. & STRALFORS, P. 2009. Rapid insulin-dependent endocytosis of the insulin receptor by caveolae in primary adipocytes. *PLoS One,* 4**,** e5985.

FAROOQ, A., PLOTNIKOVA, O., ZENG, L. & ZHOU, M. M. 1999. Phosphotyrosine binding domains of Shc and insulin receptor substrate 1 recognize the NPXpY motif in a thermodynamically distinct manner. *J Biol Chem,* 274**,** 6114-21.

FEDERICI, M., PORZIO, O., LAURO, D., BORBONI, P., GIOVANNONE, B., ZUCARO, L., HRIBAL, M. L. & SESTI, G. 1998. Increased abundance of insulin/insulin-like growth factor-I hybrid receptors in skeletal muscle of obese subjects is correlated with in vivo insulin sensitivity. *J Clin Endocrinol Metab,* 83**,** 2911-5.

FEIGE, M. J. & HENDERSHOT, L. M. 2011. Disulfide bonds in ER protein folding and homeostasis. *Curr Opin Cell Biol,* 23**,** 167-75.

FORBES, B. E., MCCARTHY, P. & NORTON, R. S. 2012. Insulin-like growth factor binding proteins: a structural perspective. *Front Endocrinol (Lausanne),* 3**,** 38.

FOTI, M., MOUKIL, M. A., DUDOGNON, P. & CARPENTIER, J. L. 2004. Insulin and IGF-1 receptor trafficking and signalling. *Novartis Found Symp,* 262**,** 125-41; discussion 141-7, 265-8.

FRAME, S. & COHEN, P. 2001. GSK3 takes centre stage more than 20 years after its discovery. *Biochem J,* 359**,** 1-16.

FRANKAER, C. G., KNUDSEN, M. V., NOREN, K., NAZARENKO, E., STAHL, K. & HARRIS, P. 2012. The structures of T6, T3R3 and R6 bovine insulin: combining X-ray diffraction and absorption spectroscopy. *Acta Crystallogr D Biol Crystallogr,* 68**,** 1259-71.

FRANKE, T. F. 2008. PI3K/Akt: getting it right matters. *Oncogene,* 27**,** 6473-88.

FRASCA, F., PANDINI, G., SCALIA, P., SCIACCA, L., MINEO, R., COSTANTINO, A., GOLDFINE, I. D., BELFIORE, A. & VIGNERI, R. 1999. Insulin receptor isoform A, a newly recognized, high-affinity insulin-like growth factor II receptor in fetal and cancer cells. *Mol Cell Biol,* 19**,** 3278-88.

FREEMAN, J. S. 2009. Insulin analog therapy: improving the match with physiologic insulin secretion. *J Am Osteopath Assoc,* 109**,** 26-36.

FRISCH, M. J. Gaussian, Inc., Wallingford CT, 2009. Gaussian 09, revision d.01.

FUJITA-YAMAGUCHI, Y., CHOI, S., SAKAMOTO, Y. & ITAKURA, K. 1983. Purification of insulin receptor with full binding activity. *J Biol Chem,* 258**,** 5045-9.

GANDERTON, R. H., STANLEY, K. K., FIELD, C. E., COGHLAN, M. P., SOOS, M. A. & SIDDLE, K. 1992. A monoclonal anti-peptide antibody reacting with the insulin receptor beta-subunit. Characterization of the antibody and its epitope and use in immunoaffinity purification of intact receptors. *Biochem J,* 288 (Pt 1)**,** 195-205.

GAUGUIN, L., DELAINE, C., ALVINO, C. L., MCNEIL, K. A., WALLACE, J. C., FORBES, B. E. & DE MEYTS, P. 2008a. Alanine scanning of a putative receptor binding surface of insulin-like growth factor-I. *J Biol Chem,* 283**,** 20821-9.

GAUGUIN, L., KLAPROTH, B., SAJID, W., ANDERSEN, A. S., MCNEIL, K. A., FORBES, B. E. & DE MEYTS, P. 2008b. Structural basis for the lower affinity of the insulin-like growth factors for the insulin receptor. *J Biol Chem,* 283**,** 2604-13.

GEHART, H., KUMPF, S., ITTNER, A. & RICCI, R. 2010. MAPK signalling in cellular metabolism: stress or wellness? *EMBO Rep,* 11**,** 834-40.

GIANI, C., CAMPANI, D., RASMUSSEN, A., FIERABRACCI, P., MICCOLI, P., BEVILACQUA, G., PINCHERA, A. & CULLEN, K. J. 2002. Insulin-like growth factor II (IGF-II) immunohistochemistry in breast cancer: relationship with the most important morphological and biochemical prognostic parameters. *Int J Biol Markers,* 17**,** 90-5.

GILBERT, H. F. 1990. Molecular and cellular aspects of thiol-disulfide exchange. *Adv Enzymol Relat Areas Mol Biol,* 63**,** 69-172.

GIUDICE, J., BARCOS, L. S., GUAIMAS, F. F., PENAS-STEINHARDT, A., GIORDANO, L., JARES-ERIJMAN, E. A. & COLUCCIO LESKOW, F. 2013. Insulin and insulin like growth factor II endocytosis and signaling via insulin receptor B. *Cell Commun Signal,* 11**,** 18.

GIUDICE, J., LESKOW, F. C., ARNDT-JOVIN, D. J., JOVIN, T. M. & JARES-ERIJMAN, E. A. 2011. Differential endocytosis and signaling dynamics of insulin receptor variants IR-A and IR-B. *J Cell Sci,* 124**,** 801-11.

GLEESON, E. C., JACKSON, W. R. & ROBINSON, A. J. 2017. Ring closing metathesis of unprotected peptides. *Chem Commun (Camb),* 53**,** 9769-9772.

GLEESON, E. C., WANG, Z. J., ROBINSON, S. D., CHHABRA, S., MACRAILD, C. A., JACKSON, W. R., NORTON, R. S. & ROBINSON, A. J. 2016. Stereoselective synthesis and structural elucidation of dicarba peptides. *Chem Commun (Camb),* 52**,** 4446-9.

GLENDORF, T., STIDSEN, C. E., NORRMAN, M., NISHIMURA, E., SORENSEN, A. R. & KJELDSEN, T. 2011. Engineering of insulin receptor isoform-selective insulin analogues. *PLoS One,* 6**,** e20288.

GLIDDEN, M. D., ALDABBAGH, K., PHILLIPS, N. B., CARR, K., CHEN, Y. S., WHITTAKER, J., PHILLIPS, M., WICKRAMASINGHE, N. P., REGE, N., SWAIN, M., PENG, Y., YANG, Y., LAWRENCE, M. C., YEE, V. C., ISMAIL-BEIGI, F. & WEISS, M. A. 2018a. An ultra-stable single-chain insulin analog resists thermal inactivation and exhibits biological signaling duration equivalent to the native protein. *J Biol Chem,* 293**,** 47-68.

GLIDDEN, M. D., YANG, Y., SMITH, N. A., PHILLIPS, N. B., CARR, K., WICKRAMASINGHE, N. P., ISMAIL-BEIGI, F., LAWRENCE, M. C., SMITH, B. J. & WEISS, M. A. 2018b. Solution structure of an ultra-stable single-chain insulin analog connects protein dynamics to a novel mechanism of receptor binding. *J Biol Chem,* 293**,** 69-88.

GLOBAL CLINICAL REGISTRY & NOVO NORDISK A/S 2016. A Trial Investigating the Safety, Tolerability, Pharmacokinetics (the Exposure of the Trial Drug in the Body) and Pharmacodynamics (the Effect of the Investigated Drug on the Body) of Insulin 287 in Subjects With Type 2 Diabetes.

GONNET, G. H., COHEN, M. A. & BENNER, S. A. 1992. Exhaustive matching of the entire protein sequence database. *Science,* 256**,** 1443-5.

GOUGH, S. C., JAIN, R. & WOO, V. C. 2016. Insulin degludec/liraglutide (IDegLira) for the treatment of type 2 diabetes. *Expert Rev Endocrinol Metab,* 11**,** 7-19.

GOVERS, R., COSTER, A. C. & JAMES, D. E. 2004. Insulin increases cell surface GLUT4 levels by dose dependently discharging GLUT4 into a cell surface recycling pathway. *Mol Cell Biol,* 24**,** 6456-66.

GROENNING, M., FROKJAER, S. & VESTERGAARD, B. 2009. Formation mechanism of insulin fibrils and structural aspects of the insulin fibrillation process. *Curr Protein Pept Sci,* 10**,** 509-28.

GROENNING, M., NORRMAN, M., FLINK, J. M., VAN DE WEERT, M., BUKRINSKY, J. T., SCHLUCKEBIER, G. & FROKJAER, S. 2007. Binding mode of Thioflavin T in insulin amyloid fibrils. *J Struct Biol,* 159**,** 483-97.

GUEX, N. & PEITSCH, M. C. 1997. SWISS-MODEL and the Swiss-PdbViewer: An environment for comparative protein modeling. *Electrophoresis,* 18**,** 2714-2723.

GUO, Z. Y., SHEN, L. & FENG, Y. M. 2002. The different folding behavior of insulin and insulin-like growth factor 1 is mainly controlled by their B-chain/domain. *Biochemistry,* 41**,** 1556-67.

HAEUSLER, R. A., MCGRAW, T. E. & ACCILI, D. 2018. Biochemical and cellular properties of insulin receptor signalling. *Nat Rev Mol Cell Biol,* 19**,** 31-44.

HAMER, I., FOTI, M., EMKEY, R., CORDIER-BUSSAT, M., PHILIPPE, J., DE MEYTS, P., MAEDER, C., KAHN, C. R. & CARPENTIER, J. L. 2002. An arginine to cysteine(252) mutation in insulin receptors from a patient with severe insulin resistance inhibits receptor internalisation but preserves signalling events. *Diabetologia,* 45**,** 657-67.

HANSEN, B. F., DANIELSEN, G. M., DREJER, K., SORENSEN, A. R., WIBERG, F. C., KLEIN, H. H. & LUNDEMOSE, A. G. 1996. Sustained signalling from the insulin receptor after stimulation with insulin analogues exhibiting increased mitogenic potency. *Biochem J,* 315 (Pt 1)**,** 271-9.

HANSEN, B. F., GLENDORF, T., HEGELUND, A. C., LUNDBY, A., LUTZEN, A., SLAABY, R. & STIDSEN, C. E. 2012. Molecular characterisation of long-acting insulin analogues in comparison with human insulin, IGF-1 and insulin X10. *PLoS One,* 7**,** e34274.

HANSEN, B. F., KURTZHALS, P., JENSEN, A. B., DEJGAARD, A. & RUSSELL-JONES, D. 2011. Insulin X10 revisited: a super-mitogenic insulin analogue. *Diabetologia,* 54**,** 2226-31.

HATAHET, F. & RUDDOCK, L. W. 2009. Protein disulfide isomerase: a critical evaluation of its function in disulfide bond formation. *Antioxid Redox Signal,* 11**,** 2807-50.

HAWORTH, N. L., GREADY, J. E., GEORGE, R. A. & WOUTERS, M. A. 2007. Evaluating the stability of disulfide bridges in proteins: A torsional potential energy surface for diethyl disulfide. *Molecular Simulation,* 33**,** 475-485.

HAWORTH, N. L., LIU, J. Y., FAN, S. W., GREADY, J. E. & WOUTERS, M. A. 2010. Estimating relative disulfide energies: an accurate *ab initio* potential energy surface. *Aust. J. Chem.,* 63**,** 379-387.

HEINEMANN, L., LINKESCHOVA, R., RAVE, K., HOMPESCH, B., SEDLAK, M. & HEISE, T. 2000. Time-action profile of the long-acting insulin analog insulin glargine (HOE901) in comparison with those of NPH insulin and placebo. *Diabetes Care,* 23**,** 644-9.

HILGENFELD, R., SEIPKE, G., BERCHTOLD, H. & OWENS, D. R. 2014. The evolution of insulin glargine and its continuing contribution to diabetes care. *Drugs,* 74**,** 911-27.

HIRSCH, I. B. 2005. Insulin analogues. *N Engl J Med,* 352**,** 174-83.

HOGG, P. J. 2013. Targeting allosteric disulphide bonds in cancer. *Nat Rev Cancer,* 13**,** 425-31.

HOLSTEIN, A., STEGE, H. & KOVACS, P. 2010. Lipoatrophy associated with the use of insulin analogues: a new case associated with the use of insulin glargine and review of the literature. *Expert Opin Drug Saf,* 9**,** 225-31.

HOME, P. D. 2012. The pharmacokinetics and pharmacodynamics of rapid-acting insulin analogues and their clinical consequences. *Diabetes Obes. Metab.,* 14**,** 780-788.

HORNBECK, P. V., KORNHAUSER, J. M., TKACHEV, S., ZHANG, B., SKRZYPEK, E., MURRAY, B., LATHAM, V. & SULLIVAN, M. 2012. PhosphoSitePlus: a comprehensive resource for investigating the structure and function of experimentally determined post-translational modifications in man and mouse. *Nucleic Acids Res,* 40**,** D261-70.

HOSSAIN, M. A., GUILHAUDIS, L., SONNEVEND, A., ATTOUB, S., VAN LIEROP, B. J., ROBINSON, A. J., WADE, J. D. & CONLON, J. M. 2011. Synthesis, conformational analysis and biological properties of a dicarba derivative of the antimicrobial peptide, brevinin-1BYa. *Eur Biophys J,* 40**,** 555-64.

HOSSAIN, M. A., HAUGAARD-KEDSTROM, L. M., ROSENGREN, K. J., BATHGATE, R. A. & WADE, J. D. 2015. Chemically synthesized dicarba H2 relaxin analogues retain strong RXFP1 receptor activity but show an unexpected loss of in vitro serum stability. *Org Biomol Chem,* 13**,** 10895-903.

HOSSAIN, M. A., ROSENGREN, K. J., ZHANG, S., BATHGATE, R. A., TREGEAR, G. W., VAN LIEROP, B. J., ROBINSON, A. J. & WADE, J. D. 2009. Solid phase synthesis and structural analysis of novel A-chain dicarba analogs of human relaxin-3 (INSL7) that exhibit full biological activity. *Org Biomol Chem,* 7**,** 1547-53.

HOSSAIN, M. A. & WADE, J. D. 2017. Novel Methods for the Chemical Synthesis of Insulin Superfamily Peptides and of Analogues Containing Disulfide Isosteres. *Acc Chem Res,* 50**,** 2116-2127.

HOUTMAN, J. C. D., BROWN, P. H., BOWDEN, B., YAMAGUCHI, H., APPELLA, E., SAMELSON, L. E. & SCHUCK, P. 2007. Studying multisite binary and ternary protein interactions by global analysis of isothermal titration calorimetry data in SEDPHAT: application to adaptor protein complexes in cell signaling. *Protein Science,* 16**,** 30-42.

HOWEY, D. C., BOWSHER, R. R., BRUNELLE, R. L. & WOODWORTH, J. R. 1994. [Lys(B28), Pro(B29)]-human insulin. A rapidly absorbed analogue of human insulin. *Diabetes,* 43**,** 396-402.

HRIBAL, M. L., FEDERICI, M., PORZIO, O., LAURO, D., BORBONI, P., ACCILI, D., LAURO, R. & SESTI, G. 2000. The Gly-->Arg972 amino acid polymorphism in insulin receptor substrate-1 affects glucose metabolism in skeletal muscle cells. *J Clin Endocrinol Metab,* 85**,** 2004-13.

HUA, Q.-X., GOZANI, S. N., CHANCE, R. E., HOFFMANN, J. A., FRANK, B. H. & WEISS, M. A. 1995. Structure of a protein in a kinetic trap. *Nat Struct Mol Biol,* 2**,** 129-138.

HUA, Q. X., CHU, Y. C., JIA, W., PHILLIPS, N. F., WANG, R. Y., KATSOYANNIS, P. G. & WEISS, M. A. 2002a. Mechanism of insulin chain combination. Asymmetric roles of A-chain alpha-helices in disulfide pairing. *J Biol Chem,* 277**,** 43443-53.

HUA, Q. X., HU, S. Q., FRANK, B. H., JIA, W., CHU, Y. C., WANG, S. H., BURKE, G. T., KATSOYANNIS, P. G. & WEISS, M. A. 1996. Mapping the functional surface of insulin by design: structure and function of a novel A-chain analogue. *J Mol Biol,* 264**,** 390-403.

HUA, Q. X., JIA, W., FRANK, B. H., PHILLIPS, N. F. & WEISS, M. A. 2002b. A protein caught in a kinetic trap: structures and stabilities of insulin disulfide isomers. *Biochemistry,* 41**,** 14700-15.

HUA, Q. X., JIA, W. & WEISS, M. A. 2011. Conformational dynamics of insulin. *Front Endocrinol (Lausanne),* 2**,** 48.

HUA, Q. X., NAKAGAWA, S., HU, S. Q., JIA, W., WANG, S. & WEISS, M. A. 2006. Toward the active conformation of insulin: stereospecific modulation of a structural switch in the B chain. *J Biol Chem,* 281**,** 24900-9.

HUA, Q. X., NAKAGAWA, S. H., JIA, W., HUANG, K., PHILLIPS, N. B., HU, S. Q. & WEISS, M. A. 2008. Design of an active ultrastable single-chain insulin analog: synthesis, structure, and therapeutic implications. *J Biol Chem,* 283**,** 14703-16.

HUA, Q. X., SHOELSON, S. E., KOCHOYAN, M. & WEISS, M. A. 1991. Receptor binding redefined by a structural switch in a mutant human insulin. *Nature,* 354**,** 238-41.

HUA, Q. X. & WEISS, M. A. 1990. Toward the solution structure of human insulin: sequential 2D 1H NMR assignment of a des-pentapeptide analogue and comparison with crystal structure. *Biochemistry,* 29**,** 10545-55.

HUA, Q. X. & WEISS, M. A. 1991. Comparative 2D NMR studies of human insulin and des-pentapeptide insulin: sequential resonance assignment and implications for protein dynamics and receptor recognition. *Biochemistry,* 30**,** 5505-15.

HUA, Q. X. & WEISS, M. A. 2004. Mechanism of insulin fibrillation: the structure of insulin under amyloidogenic conditions resembles a protein-folding intermediate. *J Biol Chem,* 279**,** 21449-60.

HUANG, K., CHAN, S. J., HUA, Q. X., CHU, Y. C., WANG, R. Y., KLAPROTH, B., JIA, W., WHITTAKER, J., DE MEYTS, P., NAKAGAWA, S. H., STEINER, D. F., KATSOYANNIS, P. G. & WEISS, M. A. 2007. The A-chain of insulin contacts the insert domain of the insulin receptor. Photo-cross-linking and mutagenesis of a diabetes-related crevice. *J Biol Chem,* 282**,** 35337-49.

HUANG, K., XU, B., HU, S. Q., CHU, Y. C., HUA, Q. X., QU, Y., LI, B., WANG, S., WANG, R. Y., NAKAGAWA, S. H., THEEDE, A. M., WHITTAKER, J., DE MEYTS, P., KATSOYANNIS, P. G. & WEISS, M. A. 2004. How insulin binds: the B-chain alpha-helix contacts the L1 beta-helix of the insulin receptor. *J Mol Biol,* 341**,** 529-50.

HUBBARD, S. R. & MILLER, W. T. 2007. Receptor tyrosine kinases: mechanisms of activation and signaling. *Curr Opin Cell Biol,* 19**,** 117-23.

HUBER-WUNDERLICH, M. & GLOCKSHUBER, R. 1998. A single dipeptide sequence modulates the redox properties of a whole enzyme family. *Fold Des,* 3**,** 161-71.

HUH, Y., YUN, N., KIL, S., SON, J. & CHAPEL, S. 2015. Use of PKPD model to design and analyze results of a euglycemic clamp study for a very long-acting insulin analogue HM12470. *American Diabetes Association's 75th Scientific Sessions*.

HUMBEL, R. E. 1990. Insulin-like growth factors I and II. *Eur J Biochem,* 190**,** 445-62.

HUMPHREY, S. J., AZIMIFAR, S. B. & MANN, M. 2015. High-throughput phosphoproteomics reveals in vivo insulin signaling dynamics. *Nat Biotechnol,* 33**,** 990-5.

HUMPHREY, W., DALKE, A. & SCHULTEN, K. 1996. VMD - Visual Molecular Dynamics. *J. Molec. Graphics,* 14**,** 33-38.

HWANG, S. Y., CHOI, I. Y., KIM, J. Y., JUNG, S. Y., KIM, D. J., LEE, Y. M., KIM, Y. H., TRAUTMANN, M., HOMPESCH, M. & SON, J. W. 2014. A Novel Very Long-Acting Insulin Analog (HM12470) with Potential for Once-Weekly Dosing, Has a Favorable PK, PD and Mitogenic Profile. *Insulin,* 100**,** 100.

INOUE, G., CHEATHAM, B., EMKEY, R. & KAHN, C. R. 1998. Dynamics of insulin signaling in 3T3-L1 adipocytes. Differential compartmentalization and trafficking of insulin receptor substrate (IRS)-1 and IRS-2. *J Biol Chem,* 273**,** 11548-55.

INOUYE, K., WATANABE, K., TOCHINO, Y., KOBAYASHI, M. & SHIGETA, Y. 1981. Semisynthesis and properties of some insulin analogs. *Biopolymers,* 20**,** 1845-1858.

INTERNATIONAL DIABETES FEDERATION. Available: http://www.idf.org/ [Accessed 15 Sept 2014].

JACOBY, E., KRUGER, P., KARATAS, Y. & WOLLMER, A. 1993. Distinction of structural reorganisation and ligand binding in the T<==>R transition of insulin on the basis of allosteric models. *Biol Chem Hoppe Seyler,* 374**,** 877-85.

JANSSEN, J. A. & VAREWIJCK, A. J. 2014. Insulin analogs and cancer: a note of caution. *Front Endocrinol (Lausanne),* 5**,** 79.

JEFFREY, P. D., MILTHORPE, B. K. & NICHOL, L. W. 1976. Polymerization pattern of insulin at pH 7.0. *Biochemistry,* 15**,** 4660-5.

JENSEN, K. S., HANSEN, R. E. & WINTHER, J. R. 2009. Kinetic and thermodynamic aspects of cellular thiol-disulfide redox regulation. *Antioxid Redox Signal,* 11**,** 1047-58.

JENSEN, M. 2000a. *Analysis of structure-activity relationships at the insulin molecule by alanine-scaning mutagenesis.* Master Thesis, University of Copenhagen.

JENSEN, M. 2000b. Analysis of Structure-activity Relationships at the Insulin Molecule by Alanine-scanning Mutagenesis. *Masters Thesis,* University of Copenhagen.

JENSEN, M. & DE MEYTS, P. 2009. Molecular mechanisms of differential intracellular signaling from the insulin receptor. *Vitam Horm,* 80**,** 51-75.

JENSEN, M., HANSEN, B., DE MEYTS, P., SCHAFFER, L. & URSO, B. 2007. Activation of the insulin receptor by insulin and a synthetic peptide leads to divergent metabolic and mitogenic signaling and responses. *J Biol Chem,* 282**,** 35179-86.

JIRACEK, J. & ZAKOVA, L. 2017. Structural Perspectives of Insulin Receptor Isoform-Selective Insulin Analogs. *Front Endocrinol (Lausanne),* 8**,** 167.

JIRACEK, J., ZAKOVA, L., ANTOLIKOVA, E., WATSON, C. J., TURKENBURG, J. P., DODSON, G. G. & BRZOZOWSKI, A. M. 2010. Implications for the active form of human insulin based on the structural convergence of highly active hormone analogues. *Proc Natl Acad Sci U S A,* 107**,** 1966-70.

JOHNSON, J. A. & GALE, E. A. 2010. Diabetes, insulin use, and cancer risk: are observational studies part of the solution-or part of the problem? *Diabetes,* 59**,** 1129-31.

JONASSEN, I., HAVELUND, S., HOEG-JENSEN, T., STEENSGAARD, D. B., WAHLUND, P. O. & RIBEL, U. 2012. Design of the novel protraction mechanism of insulin degludec, an ultra-long-acting basal insulin. *Pharm Res,* 29**,** 2104-14.

KAARSHOLM, N. C. & LUDVIGSEN, S. 1995. The high resolution solution structure of the insulin monomer determined by NMR. *Receptor,* 5**,** 1-8.

KAARSHOLM, N. C., NORRIS, K., JORGENSEN, R. J., MIKKELSEN, J., LUDVIGSEN, S., OLSEN, O. H., SORENSEN, A. R. & HAVELUND, S. 1993. Engineering stability of the insulin monomer fold with application to structure-activity relationships. *Biochemistry,* 32**,** 10773-8.

KABSCH, W. 2010. Integration, scaling, space-group assignment and post-refinement. *Acta Crystallogr D Biol Crystallogr,* 66**,** 133-44.

KABSCH, W. & SANDER, C. 1983. Dictionary of protein secondary structure - pattern-recognition of hydrogen-bonded and geometrical features. *Biopolymers,* 22**,** 2577-2637.

KAPUSTIN, J. F. 2012. Uncomplicating insulin therapy: strategies for initiation in patients with type 2 diabetes. *Adv NPs PAs,* 3**,** 20-6; quiz 27.

KARAS, J., SHABANPOOR, F., HOSSAIN, M. A., GARDINER, J., SEPAROVIC, F., WADE, J. D. & SCANLON, D. B. 2013. Total chemical synthesis of a heterodimeric interchain bis-lactam-linked Peptide: application to an analogue of human insulin-like Peptide 3. *Int J Pept,* 2013**,** 504260.

KARAS, J. A., PATIL, N. A., TAILHADES, J., SANI, M. A., SCANLON, D. B., FORBES, B. E., GARDINER, J., SEPAROVIC, F., WADE, J. D. & HOSSAIN, M. A. 2016. Total Chemical Synthesis of an Intra-A-Chain Cystathionine Human Insulin Analogue with Enhanced Thermal Stability. *Angew Chem Int Ed Engl,* 55**,** 14743-14747.

KARAS, J. A., SCANLON, D. B., FORBES, B. E., VETTER, I., LEWIS, R. J., GARDINER, J., SEPAROVIC, F., WADE, J. D. & HOSSAIN, M. A. 2014. 2-nitroveratryl as a photocleavable thiol-protecting group for directed disulfide bond formation in the chemical synthesis of insulin. *Chemistry,* 20**,** 9549-52.

KARLSTAD, O., STARUP-LINDE, J., VESTERGAARD, P., HJELLVIK, V., BAZELIER, M. T., SCHMIDT, M. K., ANDERSEN, M., AUVINEN, A., HAUKKA, J., FURU, K., DE VRIES, F. & DE BRUIN, M. L. 2013. Use of insulin and insulin analogs and risk of cancer - systematic review and meta-analysis of observational studies. *Curr Drug Saf,* 8**,** 333-48.

KATSO, R., OKKENHAUG, K., AHMADI, K., WHITE, S., TIMMS, J. & WATERFIELD, M. D. 2001. Cellular function of phosphoinositide 3-kinases: implications for development, homeostasis, and cancer. *Annu Rev Cell Dev Biol,* 17**,** 615-75.

KATSOYANNIS, P. G., TOMETSKO, A. & ZALUT, C. 1966. Insulin peptides. XII. Human insulin generation by combination of synthetic A and B chains. *J Am Chem Soc,* 88**,** 166-7.

KAVRAN, J. M., MCCABE, J. M., BYRNE, P. O., CONNACHER, M. K., WANG, Z., RAMEK, A., SARABIPOUR, S., SHAN, Y., SHAW, D. E., HRISTOVA, K., COLE, P. A. & LEAHY, D. J. 2014. How IGF-1 activates its receptor. *Elife,* 3.

KISELYOV, V. V., VERSTEYHE, S., GAUGUIN, L. & DE MEYTS, P. 2009. Harmonic oscillator model of the insulin and IGF1 receptors' allosteric binding and activation. *Mol Syst Biol,* 5**,** 243.

KOSINOVA, L., VEVERKA, V., NOVOTNA, P., COLLINSOVA, M., URBANOVA, M., MOODY, N. R., TURKENBURG, J. P., JIRACEK, J., BRZOZOWSKI, A. M. & ZAKOVA, L. 2014. Insight into the structural and biological relevance of the T/R transition of the N-terminus of the B-chain in human insulin. *Biochemistry,* 53**,** 3392-402.

KRAMER, H. F., WITCZAK, C. A., TAYLOR, E. B., FUJII, N., HIRSHMAN, M. F. & GOODYEAR, L. J. 2006. AS160 regulates insulin- and contraction-stimulated glucose uptake in mouse skeletal muscle. *J Biol Chem,* 281**,** 31478-85.

KRASNER, A., BRAZG, R. L., BLEVINS, T. C., CANNEY, L., SIMMS, P., PICHOTTA, P., STRANGE, P. & DE SOUZA, E. Safety and efficacy of ultra-rapid-acting human insulin formulation BIOD-123 in patients with type 1 diabetes. American Diabetes Association's 74th Scientific Sessions, 2014. American Diabetes Association, A34-A34.

KRISTENSEN, C., KJELDSEN, T., WIBERG, F. C., SCHAFFER, L., HACH, M., HAVELUND, S., BASS, J., STEINER, D. F. & ANDERSEN, A. S. 1997. Alanine scanning mutagenesis of insulin. *J Biol Chem,* 272**,** 12978-83.

KUNG, Y. T., DU, Y. C., HUANG, W. T., CHEN, C. C. & KE, L. T. 1965. Total synthesis of crystalline bovine insulin. *Sci Sin,* 14**,** 1710-6.

KURTZHALS, P., SCHAFFER, L., SORENSEN, A., KRISTENSEN, C., JONASSEN, I., SCHMID, C. & TRUB, T. 2000. Correlations of receptor binding and metabolic and mitogenic potencies of insulin analogs designed for clinical use. *Diabetes,* 49**,** 999-1005.

LAPLANTE, M. & SABATINI, D. M. 2012. mTOR signaling in growth control and disease. *Cell,* 149**,** 274-93.

LAUE, T., SHAH, D., RIDGEWAY, T. & PELLETIER, S. 1992. Computer-aided interpretation of analytical sedimentation data for proteins. *In:* HARDING, S., ROWE, A. & HORTON, J. (eds.) *Analytical Ultracentrifugation in Biochemistry and Polymer Science.* Cambridge, UK: Royal Society of Chemistry.

LAWRENCE, M. C. & WARD, C. W. 2015a. *Structural Features of the Receptor Tyrosine Kinase Ectodomains,* New York, Humana Press.

LAWRENCE, M. C. & WARD, C. W. 2015b. Structural Features of the Receptor Tyrosine Kinase Ectodomains. *In:* WHEELER, D. L. & YARDEN, Y. (eds.) *Receptor Tyrosine Kinases: Structure, Functions and Role in Human Disease.* New York, NY: Springer New York.

LEOF, E. B. 2000. Growth factor receptor signalling: location, location, location. *Trends Cell Biol,* 10**,** 343-8.

LI, N., BATZER, A., DALY, R., YAJNIK, V., SKOLNIK, E., CHARDIN, P., BAR-SAGI, D., MARGOLIS, B. & SCHLESSINGER, J. 1993. Guanine-nucleotide-releasing factor hSos1 binds to Grb2 and links receptor tyrosine kinases to Ras signalling. *Nature,* 363**,** 85-8.

LI, Y., GONG, H., SUN, Y., YAN, J., CHENG, B., ZHANG, X., HUANG, J., YU, M., GUO, Y., ZHENG, L. & HUANG, K. 2012. Dissecting the role of disulfide bonds on the amyloid formation of insulin. *Biochem Biophys Res Commun,* 423**,** 373-8.

LILLIG, C. H. & HOLMGREN, A. 2007. Thioredoxin and related molecules--from biology to health and disease. *Antioxid Redox Signal,* 9**,** 25-47.

LIN, T. Y. & KIM, P. S. 1989. Urea dependence of thiol-disulfide equilibria in thioredoxin: confirmation of the linkage relationship and a sensitive assay for structure. *Biochemistry,* 28**,** 5282-7.

LINDENBAUM, C., MENZIN, A. & LUDMIR, J. 1993. Diabetic ketoacidosis in pregnancy resulting from insulin pump failure. A case report. *J Reprod Med,* 38**,** 306-8.

LIU, F., ZAYKOV, A. N., LEVY, J. J., DIMARCHI, R. D. & MAYER, J. P. 2016. Chemical synthesis of peptides within the insulin superfamily. *J Pept Sci,* 22**,** 260-70.

LIU, Y., WANG, Z. H. & TANG, J. G. 2004. Flexibility exists in the region of [A6-A11, A7-B7] disulfide bonds during insulin precursor folding. *J Biochem,* 135**,** 1-6.

LUDWIG, D. B., WEBB, J. N., FERNÁNDEZ, C., CARPENTER, J. F. & RANDOLPH, T. W. 2011. Quaternary conformational stability: The effect of reversible self-association on the fibrillation of two insulin analogs. *Biotechnology and Bioengineering,* 108**,** 2359-2370.

MAEGAWA, H., MCCLAIN, D. A., FREIDENBERG, G., OLEFSKY, J. M., NAPIER, M., LIPARI, T., DULL, T. J., LEE, J. & ULLRICH, A. 1988. Properties of a human insulin receptor with a COOH-terminal truncation. II. Truncated receptors have normal kinase activity but are defective in signaling metabolic effects. *J Biol Chem,* 263**,** 8912-7.

MAHMOOD, D. F., ABDERRAZAK, A., EL HADRI, K., SIMMET, T. & ROUIS, M. 2013. The thioredoxin system as a therapeutic target in human health and disease. *Antioxid Redox Signal,* 19**,** 1266-303.

MAIER, J. A., MARTINEZ, C., KASAVAJHALA, K., WICKSTROM, L., HAUSER, K. E. & SIMMERLING, C. 2015. ff14SB: Improving the Accuracy of Protein Side Chain and Backbone Parameters from ff99SB. *Journal of Chemical Theory and Computation,* 11**,** 3696-3713.

MALAGUARNERA, R., MORCAVALLO, A. & BELFIORE, A. 2012. The insulin and igf-I pathway in endocrine glands carcinogenesis. *J Oncol,* 2012**,** 635614.

MANNO, M., CRAPARO, E. F., PODESTA, A., BULONE, D., CARROTTA, R., MARTORANA, V., TIANA, G. & SAN BIAGIO, P. L. 2007. Kinetics of different processes in human insulin amyloid formation. *J Mol Biol,* 366**,** 258-74.

MANOUSOS, O., SOUGLAKOS, J., BOSETTI, C., TZONOU, A., CHATZIDAKIS, V., TRICHOPOULOS, D., ADAMI, H. O. & MANTZOROS, C. 1999. IGF-I and IGF-II in relation to colorectal cancer. *Int J Cancer,* 83**,** 15-7.

MARASCHIN JDE, F., MURUSSI, N., WITTER, V. & SILVEIRO, S. P. 2010. Diabetes mellitus classification. *Arq Bras Cardiol,* 95**,** e40-6.

MARGLIN, A. & MERRIFIELD, R. B. 1966. The synthesis of bovine insulin by the solid phase method. *J Am Chem Soc,* 88**,** 5051-2.

MARINO-BUSLJE, C., MARTIN-MARTINEZ, M., MIZUGUCHI, K., SIDDLE, K. & BLUNDELL, T. L. 1999. The insulin receptor: from protein sequence to structure. *Biochem Soc Trans,* 27**,** 715-26.

MARKI, F., DE GASPARO, M., EISLER, K., KAMBER, B., RINIKER, B., RITTEL, W. & SIEBER, P. 1979. Synthesis and biological activity of seventeen analogues of human insulin. *Hoppe Seylers Z Physiol Chem,* 360**,** 1619-32.

MARKUSSEN, J., JORGENSEN, K. H., SORENSEN, A. R. & THIM, L. 1985. Single chain des-(B30) insulin. Intramolecular crosslinking of insulin by trypsin catalyzed transpeptidation. *Int J Pept Protein Res,* 26**,** 70-7.

MARQUEZ, F., BRAZG, R., CHRISTIANSEN, M., FREE, A., MATSON, M., JONES, S., GEORGOPOULOS, L., MALATESTA, J., ARNOLD, S. & KRAMER, W. PE0139, the first recombinant fully human monomeric super-long-acting basal insulin to display a sustained nearly peakless insulin profile following a single subcutaneous dose in subjects with T2DM supporting weekly dosing. American Diabetes Association 75th Scientifc Sessions, 2015 2015. American Diabetes Association, A26-A26.

MATHIEU, C., GILLARD, P. & BENHALIMA, K. 2017. Insulin analogues in type 1 diabetes mellitus: getting better all the time. *Nat Rev Endocrinol,* 13**,** 385-399.

MAYER, J. P., ZHANG, F. & DIMARCHI, R. D. 2007. Insulin structure and function. *Biopolymers,* 88**,** 687-713.

MAYFIELD, J. A. & WHITE, R. D. 2004. Insulin therapy for type 2 diabetes: rescue, augmentation, and replacement of beta-cell function. *Am Fam Physician,* 70**,** 489-500.

MCCLAIN, D. A. & OLEFSKY, J. M. 1988. Evidence for two independent pathways of insulin-receptor internalization in hepatocytes and hepatoma cells. *Diabetes,* 37**,** 806-15.

MCCOY, A. J., GROSSE-KUNSTLEVE, R. W., ADAMS, P. D., WINN, M. D., STORONI, L. C. & READ, R. J. 2007. Phaser crystallographic software. *J Appl Crystallogr,* 40**,** 658-674.

MCKERN, N. M., LAWRENCE, M. C., STRELTSOV, V. A., LOU, M. Z., ADAMS, T. E., LOVRECZ, G. O., ELLEMAN, T. C., RICHARDS, K. M., BENTLEY, J. D., PILLING, P. A., HOYNE, P. A., CARTLEDGE, K. A., PHAM, T. M., LEWIS, J. L., SANKOVICH, S. E., STOICHEVSKA, V., DA SILVA, E., ROBINSON, C. P., FRENKEL, M. J., SPARROW, L. G., FERNLEY, R. T., EPA, V. C. & WARD, C. W. 2006. Structure of the insulin receptor ectodomain reveals a folded-over conformation. *Nature,* 443**,** 218-21.

MCPHILLIPS, T. M., MCPHILLIPS, S. E., CHIU, H. J., COHEN, A. E., DEACON, A. M., ELLIS, P. J., GARMAN, E., GONZALEZ, A., SAUTER, N. K., PHIZACKERLEY, R. P., SOLTIS, S. M. & KUHN, P. 2002. Blu-Ice and the Distributed Control System: software for data acquisition and instrument control at macromolecular crystallography beamlines. *J Synchrotron Radiat,* 9**,** 401-6.

MEIENHOFER, J., SCHNABEL, E., BREMER, H., BRINKHOFF, O., ZABEL, R., SROKA, W., KLOSTERMAYER, H., BRANDENBURG, D., OKUDA, T. & ZAHN, H. 1963. [Synthesis of Insulin Chains and Their Combination to Insulin-Active Preparations]. *Z Naturforsch B,* 18**,** 1120-1.

MENDOZA, M. C., ER, E. E. & BLENIS, J. 2011. The Ras-ERK and PI3K-mTOR pathways: cross-talk and compensation. *Trends Biochem Sci,* 36**,** 320-8.

MENTING, J. G., GAJEWIAK, J., MACRAILD, C. A., CHOU, D. H., DISOTUAR, M. M., SMITH, N. A., MILLER, C., ERCHEGYI, J., RIVIER, J. E., OLIVERA, B. M., FORBES, B. E., SMITH, B. J., NORTON, R. S., SAFAVI-HEMAMI, H. & LAWRENCE, M. C. 2016. A minimized human insulin-receptor-binding motif revealed in a Conus geographus venom insulin. *Nat Struct Mol Biol,* 23**,** 916-920.

MENTING, J. G., WHITTAKER, J., MARGETTS, M. B., WHITTAKER, L. J., KONG, G. K., SMITH, B. J., WATSON, C. J., ZAKOVA, L., KLETVIKOVA, E., JIRACEK, J., CHAN, S. J., STEINER, D. F., DODSON, G. G., BRZOZOWSKI, A. M., WEISS, M. A., WARD, C. W. & LAWRENCE, M. C. 2013. How insulin engages its primary binding site on the insulin receptor. *Nature,* 493**,** 241-5.

MENTING, J. G., YANG, Y., CHAN, S. J., PHILLIPS, N. B., SMITH, B. J., WHITTAKER, J., WICKRAMASINGHE, N. P., WHITTAKER, L. J., PANDYARAJAN, V., WAN, Z. L., YADAV, S. P., CARROLL, J. M., STROKES, N., ROBERTS, C. T., JR., ISMAIL-BEIGI, F., MILEWSKI, W., STEINER, D. F., CHAUHAN, V. S., WARD, C. W., WEISS, M. A. & LAWRENCE, M. C. 2014a. Protective hinge in insulin opens to enable its receptor engagement. *Proc Natl Acad Sci U S A,* 111**,** E3395-404.

MENTING, J. G., YANG, Y., CHAN, S. J., PHILLIPS, N. B., SMITH, B. J., WHITTAKER, J., WICKRAMASINGHE, N. P., WHITTAKER, L. J., PANDYARAJAN, V., WAN, Z. L., YADAV, S. P., CARROLL, J. M., STROKES, N., ROBERTS, C. T., JR., ISMAIL-BEIGI, F., MILEWSKI, W., STEINER, D. F., CHAUHAN, V. S., WARD, C. W., WEISS, M. A. & LAWRENCE, M. C. 2014b. Protective hinge in insulin opens to enable its receptor engagement. *Proc Natl Acad Sci U S A*.

MERRIFIELD, R. B. 1963. Solid phase peptide synthesis. I. The synthesis of a

tetrapeptide. *J. Am. Chem. Soc.,* 85**,** 2149–2154.

MIDDELBEEK, R. J., CHAMBERS, M. A., TANTIWONG, P., TREEBAK, J. T., AN, D., HIRSHMAN, M. F., MUSI, N. & GOODYEAR, L. J. 2013. Insulin stimulation regulates AS160 and TBC1D1 phosphorylation sites in human skeletal muscle. *Nutr Diabetes,* 3**,** e74.

MILLER, J. A., NARHI, L. O., HUA, Q. X., ROSENFELD, R., ARAKAWA, T., ROHDE, M., PRESTRELSKI, S., LAUREN, S., STONEY, K. S., TSAI, L. & ET AL. 1993. Oxidative refolding of insulin-like growth factor 1 yields two products of similar thermodynamic stability: a bifurcating protein-folding pathway. *Biochemistry,* 32**,** 5203-13.

MILTHORPE, B. K., NICHOL, L. W. & JEFFREY, P. D. 1977. The polymerization pattern of zinc(II)-insulin at pH 7.0. *Biochim Biophys Acta,* 495**,** 195-202.

MIRMIRA, R. G., NAKAGAWA, S. H. & TAGER, H. S. 1991. Importance of the character and configuration of residues B24, B25, and B26 in insulin-receptor interactions. *J Biol Chem,* 266**,** 1428-36.

MIRMIRA, R. G. & TAGER, H. S. 1989. Role of the phenylalanine B24 side chain in directing insulin interaction with its receptor. Importance of main chain conformation. *J Biol Chem,* 264**,** 6349-54.

MORCAVALLO, A., GENUA, M., PALUMMO, A., KLETVIKOVA, E., JIRACEK, J., BRZOZOWSKI, A. M., IOZZO, R. V., BELFIORE, A. & MORRIONE, A. 2012. Insulin and insulin-like growth factor II differentially regulate endocytic sorting and stability of insulin receptor isoform A. *J Biol Chem,* 287**,** 11422-36.

MORCAVALLO, A., STEFANELLO, M., IOZZO, R. V., BELFIORE, A. & MORRIONE, A. 2014. Ligand-mediated endocytosis and trafficking of the insulin-like growth factor receptor I and insulin receptor modulate receptor function. *Front Endocrinol (Lausanne),* 5**,** 220.

MURAKAMI, M. S. & ROSEN, O. M. 1991. The role of insulin receptor autophosphorylation in signal transduction. *J Biol Chem,* 266**,** 22653-60.

MYERS, M. G., BACKER, J. M., SIDDLE, K. & WHITE, M. F. 1991. The insulin receptor functions normally in Chinese hamster ovary cells after truncation of the C terminus. *J Biol Chem,* 266**,** 10616-23.

MYNARCIK, D. C., WILLIAMS, P. F., SCHAFFER, L., YU, G. Q. & WHITTAKER, J. 1997. Analog binding properties of insulin receptor mutants. Identification of amino acids interacting with the COOH terminus of the B-chain of the insulin molecule. *J Biol Chem,* 272**,** 2077-81.

MYNARCIK, D. C., YU, G. Q. & WHITTAKER, J. 1996. Alanine-scanning mutagenesis of a C-terminal ligand binding domain of the insulin receptor alpha subunit. *J Biol Chem,* 271**,** 2439-42.

NAGATA, K., HATANAKA, H., KOHDA, D., KATAOKA, H., NAGASAWA, H., ISOGAI, A., ISHIZAKI, H., SUZUKI, A. & INAGAKI, F. 1995. Three-dimensional solution structure of bombyxin-II an insulin-like peptide of the silkmoth Bombyx mori: structural comparison with insulin and relaxin. *J Mol Biol,* 253**,** 749-58.

NAKAGAWA, S. H. & TAGER, H. S. 1992. Importance of aliphatic side-chain structure at positions 2 and 3 of the insulin A chain in insulin-receptor interactions. *Biochemistry,* 31**,** 3204-3214.

NAKAGAWA, S. H., TAGER, H. S. & STEINER, D. F. 2000. Mutational Analysis of Invariant Valine B12 in Insulin: Implications for Receptor Binding. *Biochemistry,* 39**,** 15826-15835.

NAKAGAWA, S. H., ZHAO, M., HUA, Q. X., HU, S. Q., WAN, Z. L., JIA, W. & WEISS, M. A. 2005. Chiral mutagenesis of insulin. Foldability and function are inversely regulated by a stereospecific switch in the B chain. *Biochemistry,* 44**,** 4984-99.

NIELSEN, L., FROKJAER, S., BRANGE, J., UVERSKY, V. N. & FINK, A. L. 2001a. Probing the mechanism of insulin fibril formation with insulin mutants. *Biochemistry,* 40**,** 8397-409.

NIELSEN, L., KHURANA, R., COATS, A., FROKJAER, S., BRANGE, J., VYAS, S., UVERSKY, V. N. & FINK, A. L. 2001b. Effect of environmental factors on the kinetics of insulin fibril formation: elucidation of the molecular mechanism. *Biochemistry,* 40**,** 6036-46.

NODA, T., MORITA, K., UZAWA, T., KINOSHITA, H. & HORI, M. 1987. Synthesis of an analog of human calcitonin gene related peptide, [Asu]-h-CGRP. *Experientia,* 43**,** 890-2.

OLSEN, H. B., LUDVIGSEN, S. & KAARSHOLM, N. C. 1996. Solution structure of an engineered insulin monomer at neutral pH. *Biochemistry,* 35**,** 8836-45.

OLSEN, H. B., LUDVIGSEN, S. & KAARSHOLM, N. C. 1998. The relationship between insulin bioactivity and structure in the NH2-terminal A-chain helix. *J Mol Biol,* 284**,** 477-88.

OTTO-BUCZKOWSKA, E. & JAINTA, N. 2018. Pharmacological Treatment in Diabetes Mellitus Type 1 - Insulin and What Else? *Int J Endocrinol Metab,* 16**,** e13008.

OWENS, D. R. 2013. Clinical evidence for the earlier initiation of insulin therapy in type 2 diabetes. *Diabetes Technol Ther,* 15**,** 776-85.

PANDINI, G., FRASCA, F., MINEO, R., SCIACCA, L., VIGNERI, R. & BELFIORE, A. 2002. Insulin/insulin-like growth factor I hybrid receptors have different biological characteristics depending on the insulin receptor isoform involved. *J Biol Chem,* 277**,** 39684-95.

PANDYARAJAN, V. & WEISS, M. A. 2012. Design of non-standard insulin analogs for the treatment of diabetes mellitus. *Curr Diab Rep,* 12**,** 697-704.

PAPAIOANNOU, A., KUYUCAK, S. & KUNCIC, Z. 2015. Molecular Dynamics Simulations of Insulin: Elucidating the Conformational Changes that Enable Its Binding. *PLoS One,* 10**,** e0144058.

PAPAIOANNOU, A., KUYUCAK, S. & KUNCIC, Z. 2017. Computational study of the activity, dynamics, energetics and conformations of insulin analogues using molecular dynamics simulations: Application to hyperinsulinemia and the critical residue B26. *Biochem Biophys Rep,* 11**,** 182-190.

PASTORE, A. & PIEMONTE, F. 2012. S-Glutathionylation signaling in cell biology: progress and prospects. *Eur J Pharm Sci,* 46**,** 279-92.

PHILLIPS, N. B., WHITTAKER, J., ISMAIL-BEIGI, F. & WEISS, M. A. 2012. Insulin fibrillation and protein design: topological resistance of single-chain analogs to thermal degradation with application to a pump reservoir. *J. Diabetes Sci. Technol.,* 6**,** 277-288.

PIERRE-EUGENE, C., PAGESY, P., NGUYEN, T. T., NEUILLE, M., TSCHANK, G., TENNAGELS, N., HAMPE, C. & ISSAD, T. 2012. Effect of insulin analogues on insulin/IGF1 hybrid receptors: increased activation by glargine but not by its metabolites M1 and M2. *PLoS One,* 7**,** e41992.

PIETRZKOWSKI, Z., LAMMERS, R., CARPENTER, G., SODERQUIST, A. M., LIMARDO, M., PHILLIPS, P. D., ULLRICH, A. & BASERGA, R. 1992. Constitutive expression of insulin-like growth factor 1 and insulin-like growth factor 1 receptor abrogates all requirements for exogenous growth factors. *Cell Growth Differ,* 3**,** 199-205.

PILLUTLA, R. C., HSIAO, K. C., BEASLEY, J. R., BRANDT, J., OSTERGAARD, S., HANSEN, P. H., SPETZLER, J. C., DANIELSEN, G. M., ANDERSEN, A. S., BRISSETTE, R. E., LENNICK, M., FLETCHER, P. W., BLUME, A. J., SCHAFFER, L. & GOLDSTEIN, N. I. 2002. Peptides identify the critical hotspots involved in the biological activation of the insulin receptor. *J Biol Chem,* 277**,** 22590-4.

PINEDA-MOLINA, E., KLATT, P., VAZQUEZ, J., MARINA, A., GARCIA DE LACOBA, M., PEREZ-SALA, D. & LAMAS, S. 2001. Glutathionylation of the p50 subunit of NF-kappaB: a mechanism for redox-induced inhibition of DNA binding. *Biochemistry,* 40**,** 14134-42.

PLATEAU, P., SAVEANU, C., LESTINI, R., DAUPLAIS, M., DECOURTY, L., JACQUIER, A., BLANQUET, S. & LAZARD, M. 2017. Exposure to selenomethionine causes selenocysteine misincorporation and protein aggregation in Saccharomyces cerevisiae. *Sci Rep,* 7**,** 44761.

POL, A., CALVO, M. & ENRICH, C. 1998. Isolated endosomes from quiescent rat liver contain the signal transduction machinery. Differential distribution of activated Raf-1 and Mek in the endocytic compartment. *FEBS Lett,* 441**,** 34-8.

POTTER, C. J., PEDRAZA, L. G. & XU, T. 2002. Akt regulates growth by directly phosphorylating Tsc2. *Nat Cell Biol,* 4**,** 658-65.

PRONK, G. J., MCGLADE, J., PELICCI, G., PAWSON, T. & BOS, J. L. 1993. Insulin-induced phosphorylation of the 46- and 52-kDa Shc proteins. *J Biol Chem,* 268**,** 5748-53.

PRYCE, R. 2009. Diabetic ketoacidosis caused by exposure of insulin pump to heat and sunlight. *BMJ,* 338**,** a2218.

QIAO, Z. S., GUO, Z. Y. & FENG, Y. M. 2001. Putative disulfide-forming pathway of porcine insulin precursor during its refolding in vitro. *Biochemistry,* 40**,** 2662-8.

RAJAPAKSHA, H. 2013. *Molecular mechanism of insulin receptor isoform-A signalling.* PhD, The University of Adelaide.

RAJAPAKSHA, H. & FORBES, B. E. 2015. Ligand-Binding Affinity at the Insulin Receptor Isoform-A and Subsequent IR-A Tyrosine Phosphorylation Kinetics are Important Determinants of Mitogenic Biological Outcomes. *Front Endocrinol (Lausanne),* 6**,** 107.

RAMM, G., LARANCE, M., GUILHAUS, M. & JAMES, D. E. 2006. A role for 14-3-3 in insulin-stimulated GLUT4 translocation through its interaction with the RabGAP AS160. *J Biol Chem,* 281**,** 29174-80.

REINEHR, T. 2013. Type 2 diabetes mellitus in children and adolescents. *World J Diabetes,* 4**,** 270-81.

RENDELL, M., AKTURK, H. K. & TELLA, S. H. 2013. Glargine safety, diabetes and cancer. *Expert Opin Drug Saf,* 12**,** 247-63.

RETNAKARAN, R. & ZINMAN, B. 2012. Short-term intensified insulin treatment in type 2 diabetes: long-term effects on beta-cell function. *Diabetes Obes Metab,* 14 Suppl 3**,** 161-6.

RHEE, S. Y., KIM, H. J., KO, S. H., HUR, K. Y., KIM, N. H., MOON, M. K., PARK, S. O., LEE, B. W., CHOI, K. M., KIM, J. H. & COMMITTEE OF CLINICAL PRACTICE GUIDELINE OF KOREAN DIABETES, A. 2017. Monotherapy in Patients with Type 2 Diabetes Mellitus. *Diabetes Metab J,* 41**,** 349-356.

ROBERTS, B. K., WANG, X., ROSENDAHL, M. & MANTRIPRIGADA, S. The extended duration single dose pharmacokinetics (PK) and pharmacodynamics (PD) of AB101, a potential once weekly basal subcutaneous (SC) insulin, in diabetic miniature swine. American Diabetes Association 76th Scientific Sessions 2016. American Diabetes Association.

ROBINSON, A. J. & VAN LIEROP, B. J. 2011. Insulin analogues. *Patent US20120225811.*

ROBINSON, A. J., VAN LIEROP, B. J., GARLAND, R. D., TEOH, E., ELARIDI, J., ILLESINGHE, J. P. & JACKSON, W. R. 2009. Regioselective formation of interlocked dicarba bridges in naturally occurring cyclic peptide toxins using olefin metathesis. *Chem Commun (Camb)***,** 4293-5.

RODBARD, H. W., BUSE, J. B., WOO, V., VILSBOLL, T., LANGBAKKE, I. H., KVIST, K. & GOUGH, S. C. 2016. Benefits of combination of insulin degludec and liraglutide are independent of baseline glycated haemoglobin level and duration of type 2 diabetes. *Diabetes Obes Metab,* 18**,** 40-8.

ROE, D. R. & CHEATHAM, T. E., 3RD 2013. PTRAJ and CPPTRAJ: Software for Processing and Analysis of Molecular Dynamics Trajectory Data. *J Chem Theory Comput,* 9**,** 3084-95.

ROSENBLOOM, D., SCIME, J., ELVISS, O. D., MAYHEW, B., THOMPSON, W. J., THORNLEY, P. & WILDEMAN, M. 1994. Measurement of insulin wastage in five Ontario hospitals. *Can J Hosp Pharm,* 47**,** 5-7.

ROY, M., BRADER, M. L., LEE, R. W., KAARSHOLM, N. C., HANSEN, J. F. & DUNN, M. F. 1989. Spectroscopic signatures of the T to R conformational transition in the insulin hexamer. *J Biol Chem,* 264**,** 19081-5.

ROY, M., LEE, R. W., BRANGE, J. & DUNN, M. F. 1990. 1H NMR spectrum of the native human insulin monomer. Evidence for conformational differences between the monomer and aggregated forms. *J Biol Chem,* 265**,** 5448-52.

RYLE, A. P. & SANGER, F. 1955. Disulphide interchange reactions. *Biochem J,* 60**,** 535-40.

SACCO, A., MORCAVALLO, A., PANDINI, G., VIGNERI, R. & BELFIORE, A. 2009. Differential signaling activation by insulin and insulin-like growth factors I and II upon binding to insulin receptor isoform A. *Endocrinology,* 150**,** 3594-602.

SALTIEL, A. R. & KAHN, C. R. 2001. Insulin signalling and the regulation of glucose and lipid metabolism. *Nature,* 414**,** 799-806.

SATO, Y. & INABA, K. 2012. Disulfide bond formation network in the three biological kingdoms, bacteria, fungi and mammals. *FEBS J,* 279**,** 2262-71.

SATTAR, A. A., BERHANU, C., GEBRESELASSIE, S. & BERHANU, P. 2007. Human insulin receptor juxtamembrane domain independent insulin signaling. *Cell Biol Int,* 31**,** 815-24.

SAWKA-VERHELLE, D., TARTARE-DECKERT, S., WHITE, M. F. & VAN OBBERGHEN, E. 1996. Insulin receptor substrate-2 binds to the insulin receptor through its phosphotyrosine-binding domain and through a newly identified domain comprising amino acids 591-786. *J Biol Chem,* 271**,** 5980-3.

SCHILLING, R. J. & MITRA, A. K. 1991. Degradation of insulin by trypsin and alpha-chymotrypsin. *Pharm Res,* 8**,** 721-7.

SCHMIDT, B., HO, L. & HOGG, P. J. 2006. Allosteric disulfide bonds. *Biochemistry,* 45**,** 7429-33.

SCHMIDT, B. & HOGG, P. J. 2007. Search for allosteric disulfide bonds in NMR structures. *BMC Struct Biol,* 7**,** 49.

SCHWABE, C. & MCDONALD, J. K. 1977. Relaxin: a disulfide homolog of insulin. *Science,* 197**,** 914-5.

SCIACCA, L., CASSARINO, M. F., GENUA, M., PANDINI, G., LE MOLI, R., SQUATRITO, S. & VIGNERI, R. 2010. Insulin analogues differently activate insulin receptor isoforms and post-receptor signalling. *Diabetologia,* 53**,** 1743-53.

SCIACCA, L., VELLA, V., FRITTITTA, L., TUMMINIA, A., MANZELLA, L., SQUATRITO, S., BELFIORE, A. & VIGNERI, R. 2018. Long-acting insulin analogs and cancer. *Nutr Metab Cardiovasc Dis,* 28**,** 436-443.

SEINO, S. & BELL, G. I. 1989. Alternative splicing of human insulin receptor messenger RNA. *Biochem Biophys Res Commun,* 159**,** 312-6.

SEINO, S., SEINO, M., NISHI, S. & BELL, G. I. 1989. Structure of the human insulin receptor gene and characterization of its promoter. *Proc Natl Acad Sci U S A,* 86**,** 114-8.

SELL, C., DUMENIL, G., DEVEAUD, C., MIURA, M., COPPOLA, D., DEANGELIS, T., RUBIN, R., EFSTRATIADIS, A. & BASERGA, R. 1994. Effect of a null mutation of the insulin-like growth factor I receptor gene on growth and transformation of mouse embryo fibroblasts. *Mol Cell Biol,* 14**,** 3604-12.

SESTI, G. 2000. Insulin receptor substrate polymorphisms and type 2 diabetes mellitus. *Pharmacogenomics,* 1**,** 343-57.

SEVIER, C. S. & KAISER, C. A. 2002. Formation and transfer of disulphide bonds in living cells. *Nat Rev Mol Cell Biol,* 3**,** 836-47.

SHABANPOOR, F., HOSSAIN, M. A., LIN, F. & WADE, J. D. 2013. Sequential formation of regioselective disulfide bonds in synthetic peptides with multiple disulfide bonds. *Methods Mol Biol,* 1047**,** 81-7.

SHAUL, Y. D. & SEGER, R. 2007. The MEK/ERK cascade: from signaling specificity to diverse functions. *Biochim Biophys Acta,* 1773**,** 1213-26.

SHNEINE, J., VOSWINKEL, M., FEDERWISCH, M. & WOLLMER, A. 2000. Enhancing the T-->R transition of insulin by helix-promoting sequence modifications at the N-terminal B-chain. *Biol Chem,* 381**,** 127-33.

SHOELSON, S., HANEDA, M., BLIX, P., NANJO, A., SANKE, T., INOUYE, K., STEINER, D., RUBENSTEIN, A. & TAGER, H. 1983. Three mutant insulins in man. *Nature,* 302**,** 540-3.

SHOELSON, S. E., BONI-SCHNETZLER, M., PILCH, P. F. & KAHN, C. R. 1991. Autophosphorylation within insulin receptor beta-subunits can occur as an intramolecular process. *Biochemistry,* 30**,** 7740-6.

SIEBENLIST, U., FRANZOSO, G. & BROWN, K. 1994. Structure, regulation and function of NF-kappa B. *Annu Rev Cell Biol,* 10**,** 405-55.

SIEBER, P., EISLER, K., KAMBER, B., RINIKER, B., RITTEL, W., MARKI, F. & DE GASPARO, M. 1978. Synthesis and biological activity of two disulphide bond isomers of human insulin: [A7-A11,A6-B7-cystine]- and [A6-A7,A11-B7-cystine]insulin (human). *Hoppe Seylers Z Physiol Chem,* 359**,** 113-23.

SLAWIK, M., SCHORIES, M., BUSSE GRAWITZ, A., REINCKE, M. & PETERSEN, K. G. 2006. Treatment with insulin glargine does not suppress serum IGF-1. *Diabet Med,* 23**,** 814-7.

SMALLWOOD, C., LAMARCHE, D. & CHEVRIER, A. 2017. Examining Factors That Impact Inpatient Management of Diabetes and the Role of Insulin Pen Devices. *Canadian Journal of Diabetes,* 41**,** 102-107.

SMITH, G. D. & CISZAK, E. 1994. The structure of a complex of hexameric insulin and 4'-hydroxyacetanilide. *Proc Natl Acad Sci U S A,* 91**,** 8851-5.

SMITH, G. D., CISZAK, E., MAGRUM, L. A., PANGBORN, W. A. & BLESSING, R. H. 2000. R6 hexameric insulin complexed with m-cresol or resorcinol. *Acta Crystallogr D Biol Crystallogr,* 56**,** 1541-8.

SMITH, G. D., PANGBORN, W. A. & BLESSING, R. H. 2003. The structure of T6 human insulin at 1.0 A resolution. *Acta Crystallogr D Biol Crystallogr,* 59**,** 474-82.

SMITH, R. M. & JARETT, L. 1990. Differences in adenosine triphosphate dependency of receptor-mediated endocytosis of alpha 2-macroglobulin and insulin correlate with separate routes of ligand-receptor complex internalization. *Endocrinology,* 126**,** 1551-60.

SMITH, R. M., SEELY, B. L., SHAH, N., OLEFSKY, J. M. & JARETT, L. 1991. Tyrosine kinase-defective insulin receptors undergo insulin-induced microaggregation but do not concentrate in coated pits. *J Biol Chem,* 266**,** 17522-30.

SOMMERFELD, M. R., MULLER, G., TSCHANK, G., SEIPKE, G., HABERMANN, P., KURRLE, R. & TENNAGELS, N. 2010. In vitro metabolic and mitogenic signaling of insulin glargine and its metabolites. *PLoS One,* 5**,** e9540.

SOOS, M. A., FIELD, C. E., LAMMERS, R., ULLRICH, A., ZHANG, B., ROTH, R. A., ANDERSEN, A. S., KJELDSEN, T. & SIDDLE, K. 1992. A panel of monoclonal antibodies for the type I insulin-like growth factor receptor. Epitope mapping, effects on ligand binding, and biological activity. *J Biol Chem,* 267**,** 12955-63.

SOOS, M. A., O'BRIEN, R. M., BRINDLE, N. P., STIGTER, J. M., OKAMOTO, A. K., WHITTAKER, J. & SIDDLE, K. 1989. Monoclonal antibodies to the insulin receptor mimic metabolic effects of insulin but do not stimulate receptor autophosphorylation in transfected NIH 3T3 fibroblasts. *Proc Natl Acad Sci U S A,* 86**,** 5217-21.

SOOS, M. A. & SIDDLE, K. 1989. Immunological relationships between receptors for insulin and insulin-like growth factor I. Evidence for structural heterogeneity of insulin-like growth factor I receptors involving hybrids with insulin receptors. *Biochem J,* 263**,** 553-63.

SOOS, M. A., SIDDLE, K., BARON, M. D., HEWARD, J. M., LUZIO, J. P., BELLATIN, J. & LENNOX, E. S. 1986. Monoclonal antibodies reacting with multiple epitopes on the human insulin receptor. *Biochem J,* 235**,** 199-208.

SØRENSEN, A. R., STIDSEN, C. E., RIBEL, U., NISHIMURA, E., STURIS, J., JONASSEN, I., BOUMAN, S. D., KURTZHALS, P. & BRAND, C. L. 2010. Insulin detemir is a fully efficacious, low affinity agonist at the insulin receptor. *Diabetes, Obesity and Metabolism,* 12**,** 665-673.

STAMMBERGER, I., SEIPKE, G. & BARTELS, T. 2006. Insulin glulisine--a comprehensive preclinical evaluation. *Int J Toxicol,* 25**,** 25-33.

STEINER, D. D., G. 1988. The role of assembly in insulin's biosynthesis. *Elsevier ScienceDirect,* 8**,** 189-194.

STYMIEST, J. L., MITCHELL, B. F., WONG, S. & VEDERAS, J. C. 2003. Synthesis of biologically active dicarba analogues of the peptide hormone oxytocin using ring-closing metathesis. *Org Lett,* 5**,** 47-9.

SUBIABRE, M., SILVA, L., TOLEDO, F., PAUBLO, M., LOPEZ, M. A., BORIC, M. P. & SOBREVIA, L. 2018. Insulin therapy and its consequences for the mother, foetus, and newborn in gestational diabetes mellitus. *Biochim Biophys Acta*.

SURINYA, K. H., FORBES, B. E., OCCHIODORO, F., BOOKER, G. W., FRANCIS, G. L., SIDDLE, K., WALLACE, J. C. & COSGROVE, L. J. 2008. An investigation of the ligand binding properties and negative cooperativity of soluble insulin-like growth factor receptors. *J Biol Chem,* 283**,** 5355-63.

TAKATA, Y., WEBSTER, N. J. & OLEFSKY, J. M. 1991. Mutation of the two carboxyl-terminal tyrosines results in an insulin receptor with normal metabolic signaling but enhanced mitogenic signaling properties. *J Biol Chem,* 266**,** 9135-9.

TANG, J. G., WANG, Z. H., TREGEAR, G. W. & WADE, J. D. 2003. Human gene 2 relaxin chain combination and folding. *Biochemistry,* 42**,** 2731-9.

TANIGUCHI, C. M., EMANUELLI, B. & KAHN, C. R. 2006. Critical nodes in signalling pathways: insights into insulin action. *Nat Rev Mol Cell Biol,* 7**,** 85-96.

TENNAGELS, N. & WERNER, U. 2013. The metabolic and mitogenic properties of basal insulin analogues. *Arch Physiol Biochem,* 119**,** 1-14.

THOMAS, B. & WOLLMER, A. 1989. Cobalt probing of structural alternatives for insulin in solution. *Biol Chem Hoppe Seyler,* 370**,** 1235-44.

THOMPSON, R., CHRISTIE, D. & HINDMARSH, P. C. 2006. The role for insulin analogues in diabetes care. *Current Paediatrics,* 16**,** 117-122.

ULLRICH, A., BELL, J. R., CHEN, E. Y., HERRERA, R., PETRUZZELLI, L. M., DULL, T. J., GRAY, A., COUSSENS, L., LIAO, Y. C., TSUBOKAWA, M. & ET AL. 1985. Human insulin receptor and its relationship to the tyrosine kinase family of oncogenes. *Nature,* 313**,** 756-61.

VADLAKONDA, L., DASH, A., PASUPULETI, M., ANIL KUMAR, K. & REDDANNA, P. 2013. The Paradox of Akt-mTOR Interactions. *Front Oncol,* 3**,** 165.

VAJO, Z., FAWCETT, J. & DUCKWORTH, W. C. 2001. Recombinant DNA technology in the treatment of diabetes: insulin analogs. *Endocr Rev,* 22**,** 706-17.

VAN DAM, E. M., GOVERS, R. & JAMES, D. E. 2005. Akt activation is required at a late stage of insulin-induced GLUT4 translocation to the plasma membrane. *Mol Endocrinol,* 19**,** 1067-77.

VAN LIEROP, B., BORNSCHEIN, C., ROY JACKSON, W. & ROBINSON, A. 2011a. Ring-closing Metathesis in Peptides – the Sting is in the Tail! *Aust. J. Chem.,* 64**,** 806.

VAN LIEROP, B., ONG, S. C., BELGI, A., DELAINE, C., ANDRIKOPOULOS, S., HAWORTH, N. L., MENTING, J. G., LAWRENCE, M. C., ROBINSON, A. J. & FORBES, B. E. 2017. Insulin in motion: The A6-A11 disulfide bond allosterically modulates structural transitions required for insulin activity. *Sci. Rep.,* 7**,** 17239.

VAN LIEROP, B. J., BORNSCHEIN, C., JACKSON, W. R. & ROBINSON, A. J. 2011b. Ring-closing metathesis in peptides – the sting is in the tail! *Aust. J. Chem.,* 64**,** 806-811.

VAN LIEROP, B. J., ROBINSON, S. D., KOMPELLA, S. N., BELGI, A., MCARTHUR, J. R., HUNG, A., MACRAILD, C. A., ADAMS, D. J., NORTON, R. S. & ROBINSON, A. J. 2013. Dicarba alpha-conotoxin Vc1.1 analogues with differential selectivity for nicotinic acetylcholine and GABAB receptors. *ACS Chem Biol,* 8**,** 1815-21.

VAN LIEROP, B. J., WHELAN, A. N., ANDRIKOPOULOS, S., MULDER, R. J., JACKSON, W. R. & ROBINSON, A. J. 2010. Methods for Enhancing Ring Closing Metathesis Yield in Peptides: Synthesis of a Dicarba Human Growth Hormone Fragment. *International Journal of Peptide Research and Therapeutics,* 16**,** 133-144.

VANQUELEF, E., SIMON, S., MARQUANT, G., GARCIA, E., KLIMERAK, G., DELEPINE, J. C., CIEPLAK, P. & DUPRADEAU, F.-Y. 2011. R.E.D. Server: a web service for deriving RESP and ESP charges and building force field libraries for new molecules and molecular fragments. *Nucleic Acids Research,* 39**,** W511-W517.

VAREWIJCK, A. J., GOUDZWAARD, J. A., BRUGTS, M. P., LAMBERTS, S. W., HOFLAND, L. J. & JANSSEN, J. A. 2010. Insulin glargine is more potent in activating the human IGF-I receptor than human insulin and insulin detemir. *Growth Horm IGF Res,* 20**,** 427-31.

VERSTEYHE, S., KLAPROTH, B., BORUP, R., PALSGAARD, J., JENSEN, M., GRAY, S. G. & DE MEYTS, P. 2013. IGF-I, IGF-II, and Insulin Stimulate Different Gene Expression Responses through Binding to the IGF-I Receptor. *Front Endocrinol (Lausanne),* 4**,** 98.

VIENBERG, S. G., BOUMAN, S. D., SORENSEN, H., STIDSEN, C. E., KJELDSEN, T., GLENDORF, T., SORENSEN, A. R., OLSEN, G. S., ANDERSEN, B. &

NISHIMURA, E. 2011. Receptor-isoform-selective insulin analogues give tissue-preferential effects. *Biochem J,* 440**,** 301-8.

VIGNERI, P., FRASCA, F., SCIACCA, L., PANDINI, G. & VIGNERI, R. 2009. Diabetes and cancer. *Endocr Relat Cancer,* 16**,** 1103-23.

VIGNERI, R., SQUATRITO, S. & SCIACCA, L. 2010. Insulin and its analogs: actions via insulin and IGF receptors. *Acta Diabetol,* 47**,** 271-8.

VINTHER, T. N., KJELDSEN, T. B., JENSEN, K. J. & HUBALEK, F. 2015a. The road to the first, fully active and more stable human insulin variant with an additional disulfide bond. *J Pept Sci,* 21**,** 797-806.

VINTHER, T. N., NORRMAN, M., RIBEL, U., HUUS, K., SCHLEIN, M., STEENSGAARD, D. B., PEDERSEN, T. A., PETTERSSON, I., LUDVIGSEN, S., KJELDSEN, T., JENSEN, K. J. & HUBALEK, F. 2013. Insulin analog with additional disulfide bond has increased stability and preserved activity. *Protein Sci,* 22**,** 296-305.

VINTHER, T. N., PETTERSSON, I., HUUS, K., SCHLEIN, M., STEENSGAARD, D. B., SORENSEN, A., JENSEN, K. J., KJELDSEN, T. & HUBALEK, F. 2015b. Additional disulfide bonds in insulin: Prediction, recombinant expression, receptor binding affinity, and stability. *Protein Sci,* 24**,** 779-88.

WALI, J. A., THOMAS, H. E. & SUTHERLAND, A. P. 2014. Linking obesity with type 2 diabetes: the role of T-bet. *Diabetes Metab Syndr Obes,* 7**,** 331-40.

WARD, C. W. & LAWRENCE, M. C. 2009. Ligand-induced activation of the insulin receptor: a multi-step process involving structural changes in both the ligand and the receptor. *Bioessays,* 31**,** 422-34.

WEISS, M. 2013a. Design of ultra-stable insulin analogues for the developing world. *Journal of Health Specialties,* 1**,** 59.

WEISS, M. 2014. *Halogen-stabilized insulin*. US Patent 8921313.

WEISS, M. 2015. *Insulin analogues with chlorinated amino acids*. US Patent 9079975.

WEISS, M. A. 2009a. Proinsulin and the genetics of diabetes mellitus. *J Biol Chem,* 284**,** 19159-63.

WEISS, M. A. 2009b. The structure and function of insulin: decoding the TR transition. *Vitam Horm,* 80**,** 33-49.

WEISS, M. A. 2013b. Diabetes mellitus due to the toxic misfolding of proinsulin variants. *FEBS Lett,* 587**,** 1942-50.

WEISS, M. A., HUA, Q. X., JIA, W., CHU, Y. C., WANG, R. Y. & KATSOYANNIS, P. G. 2000. Hierarchical protein "un-design": insulin's intrachain disulfide bridge tethers a recognition alpha-helix. *Biochemistry,* 39**,** 15429-40.

WEISS, R. C., VAN AMERONGEN, D., BAZALO, G., AAGREN, M. & BOUCHARD, J. R. 2011. Economic benefits of improved insulin stability in insulin pumps. *Manag Care,* 20**,** 42-7.

WHITTAKER, L., HAO, C., FU, W. & WHITTAKER, J. 2008. High-Affinity Insulin Binding: Insulin Interacts with Two Receptor Ligand Binding Sites. *Biochemistry,* 47**,** 12900-9.

WHITTINGHAM, J. L., YOUSHANG, Z., ZAKOVA, L., DODSON, E. J., TURKENBURG, J. P., BRANGE, J. & DODSON, G. G. 2006. I222 crystal form of despentapeptide (B26-B30) insulin provides new insights into the properties of monomeric insulin. *Acta Crystallogr D Biol Crystallogr,* 62**,** 505-11.

WILDEN, P. A., KAHN, C. R., SIDDLE, K. & WHITE, M. F. 1992. Insulin receptor kinase domain autophosphorylation regulates receptor enzymatic function. *J Biol Chem,* 267**,** 16660-8.

WILLIAMS, P. F., MYNARCIK, D. C., YU, G. Q. & WHITTAKER, J. 1995. Mapping of an NH2-terminal ligand binding site of the insulin receptor by alanine scanning mutagenesis. *J Biol Chem,* 270**,** 3012-6.

WINN, M. D., BALLARD, C. C., COWTAN, K. D., DODSON, E. J., EMSLEY, P., EVANS, P. R., KEEGAN, R. M., KRISSINEL, E. B., LESLIE, A. G., MCCOY, A.,

MCNICHOLAS, S. J., MURSHUDOV, G. N., PANNU, N. S., POTTERTON, E. A., POWELL, H. R., READ, R. J., VAGIN, A. & WILSON, K. S. 2011. Overview of the CCP4 suite and current developments. *Acta Crystallogr D Biol Crystallogr,* 67**,** 235-42.

WONG, N., FAM, B. C., CEMPAKO, G. R., STEINBERG, G. R., WALDER, K., KAY, T. W., PROIETTO, J. & ANDRIKOPOULOS, S. 2011. Deficiency in interferon-gamma results in reduced body weight and better glucose tolerance in mice. *Endocrinology,* 152**,** 3690-9.

WOODS, R. J., ALARCÓN, J., MCVEY, E. & PETTIS, R. J. 2012. Intrinsic Fibrillation of Fast-Acting Insulin Analogs. *Journal of Diabetes Science and Technology,* 6**,** 265-276.

WOUTERS, M. A., FAN, S. W. & HAWORTH, N. L. 2010. Disulfides as redox switches: from molecular mechanisms to functional significance. *Antioxid Redox Signal,* 12**,** 53-91.

WOUTERS, M. A., LAU, K. K. & HOGG, P. J. 2004. Cross-strand disulphides in cell entry proteins: poised to act. *Bioessays,* 26**,** 73-9.

WU, J., TSENG, Y. D., XU, C. F., NEUBERT, T. A., WHITE, M. F. & HUBBARD, S. R. 2008. Structural and biochemical characterization of the KRLB region in insulin receptor substrate-2. *Nat Struct Mol Biol,* 15**,** 251-8.

WUNDERLICH, M. & GLOCKSHUBER, R. 1993. Redox properties of protein disulfide isomerase (DsbA) from Escherichia coli. *Protein Sci,* 2**,** 717-26.

XU, B., HU, S. Q., CHU, Y. C., WANG, S., WANG, R. Y., NAKAGAWA, S. H., KATSOYANNIS, P. G. & WEISS, M. A. 2004. Diabetes-associated mutations in insulin identify invariant receptor contacts. *Diabetes,* 53**,** 1599-602.

XU, P., JACOBS, A. R. & TAYLOR, S. I. 1999. Interaction of insulin receptor substrate 3 with insulin receptor, insulin receptor-related receptor, insulin-like growth factor-1 receptor, and downstream signaling proteins. *J Biol Chem,* 274**,** 15262-70.

YAMADA, S. 2009. Insulin glulisine in the management of diabetes. *Diabetes Metab Syndr Obes,* 2**,** 111-5.

YANG, G., MURASHIGE, D. S., HUMPHREY, S. J. & JAMES, D. E. 2015. A Positive Feedback Loop between Akt and mTORC2 via SIN1 Phosphorylation. *Cell Rep,* 12**,** 937-43.

YANG, Y., PETKOVA, A., HUANG, K., XU, B., HUA, Q. X., YE, I. J., CHU, Y. C., HU, S. Q., PHILLIPS, N. B., WHITTAKER, J., ISMAIL-BEIGI, F., MACKIN, R. B., KATSOYANNIS, P. G., TYCKO, R. & WEISS, M. A. 2010a. An Achilles' heel in an amyloidogenic protein and its repair: insulin fibrillation and therapeutic design. *J Biol Chem,* 285**,** 10806-21.

YANG, Y., PETKOVA, A., HUANG, K., XU, B., HUA, Q. X., YE, I. J., CHU, Y. C., HU, S. Q., PHILLIPS, N. B., WHITTAKER, J., ISMAIL-BEIGI, F., MACKIN, R. B., KATSOYANNIS, P. G., TYCKO, R. & WEISS, M. A. 2010b. An Achilles' heel in an amyloidogenic protein and its repair. Insulin fibrillation and therapeutic design. *J Biol Chem*.

YU, N. T., JO, B. H., CHANG, R. C. & HUBER, J. D. 1974. Single-crystal Raman spectra of native insulin. Structures of insulin fibrils, glucagon fibrils, and intact calf lens. *Arch Biochem Biophys,* 160**,** 614-22.

YUNN, N. O., KIM, J., KIM, Y., LEIBIGER, I., BERGGREN, P. O. & RYU, S. H. 2017. Mechanistic understanding of insulin receptor modulation: Implications for the development of anti-diabetic drugs. *Pharmacol Ther*.

YUNN, N. O., KOH, A., HAN, S., LIM, J. H., PARK, S., LEE, J., KIM, E., JANG, S. K., BERGGREN, P. O. & RYU, S. H. 2015. Agonistic aptamer to the insulin receptor leads to biased signaling and functional selectivity through allosteric modulation. *Nucleic Acids Res,* 43**,** 7688-701.

ZAKOVA, L., BARTH, T., JIRACEK, J., BARTHOVA, J. & ZORAD, S. 2004. Shortened insulin analogues: marked changes in biological activity resulting from replacement of

TyrB26 and N-methylation of peptide bonds in the C-terminus of the B-chain. *Biochemistry,* 43**,** 2323-31.

ZAKOVA, L., KAZDOVA, L., HANCLOVA, I., PROTIVINSKA, E., SANDA, M., BUDESINSKY, M. & JIRACEK, J. 2008. Insulin analogues with modifications at position B26. Divergence of binding affinity and biological activity. *Biochemistry,* 47**,** 5858-68.

ZAKOVA, L., KLETVIKOVA, E., LEPSIK, M., COLLINSOVA, M., WATSON, C. J., TURKENBURG, J. P., JIRACEK, J. & BRZOZOWSKI, A. M. 2014. Human insulin analogues modified at the B26 site reveal a hormone conformation that is undetected in the receptor complex. *Acta Crystallogr D Biol Crystallogr,* 70**,** 2765-74.

ZAKOVA, L., KLETVIKOVA, E., VEVERKA, V., LEPSIK, M., WATSON, C. J., TURKENBURG, J. P., JIRACEK, J. & BRZOZOWSKI, A. M. 2013. Structural integrity of the B24 site in human insulin is important for hormone functionality. *J Biol Chem,* 288**,** 10230-40.

ZAYKOV, A. N., MAYER, J. P. & DIMARCHI, R. D. 2016. Pursuit of a perfect insulin. *Nat Rev Drug Discov,* 15**,** 425-39.

ZAYKOV, A. N., MAYER, J. P., GELFANOV, V. M. & DIMARCHI, R. D. 2014. Chemical synthesis of insulin analogs through a novel precursor. *ACS Chem Biol,* 9**,** 683-91.

ZHANG, S., HUGHES, R. A., BATHGATE, R. A., SHABANPOOR, F., HOSSAIN, M. A., LIN, F., VAN LIEROP, B., ROBINSON, A. J. & WADE, J. D. 2010. Role of the intra-A-chain disulfide bond of insulin-like peptide 3 in binding and activation of its receptor, RXFP2. *Peptides,* 31**,** 1730-6.

ZHANG, Z., TANG, Y., YAO, S., ZHU, S. & FENG, Y. 2003. Protein engineering of insulin: Two novel fast-acting insulins [B16Ala]insulin and [B26Ala]insulin. *Sci China C Life Sci,* 46**,** 474-80.

ZHENG, X. & CARTEE, G. D. 2016. Insulin-induced Effects on the Subcellular Localization of AKT1, AKT2 and AS160 in Rat Skeletal Muscle. *Sci Rep,* 6**,** 39230.

ZHOU, B., BALDUS, I. B., LI, W., EDWARDS, S. A. & GRATER, F. 2014. Identification of allosteric disulfides from prestress analysis. *Biophys J,* 107**,** 672-681.

ZIEGLER, A. N., CHIDAMBARAM, S., FORBES, B. E., WOOD, T. L. & LEVISON, S. W. 2014. Insulin-like growth factor-II (IGF-II) and IGF-II analogs with enhanced insulin receptor-a binding affinity promote neural stem cell expansion. *J Biol Chem,* 289**,** 4626-33.

ZOETE, V., MEUWLY, M. & KARPLUS, M. 2004. A comparison of the dynamic behavior of monomeric and dimeric insulin shows structural rearrangements in the active monomer. *J Mol Biol,* 342**,** 913-29.

ZOETE, V., MEUWLY, M. & KARPLUS, M. 2005. Study of the insulin dimerization: binding free energy calculations and per-residue free energy decomposition. *Proteins,* 61**,** 79-93.